JOURNAL OF THE ELECTROCHEMICAL SOCIETY

LECTROCHEMICAL
CIENCE AND TECHNOLOGY

OLID-STATE
CIENCE AND TECHNOLOGY

EVIEWS AND NEWS

VOL. 122, NO. 1 JANUARY 1975

JESOAN 122 (1) 1-158, 1C-18C

FUTURE MEETINGS
Of The Electrochemical Society

TORONTO, CANADA—MAY 11, 12, 13, 14, 15 & 16, 1975
Headquarters at the Royal York Hotel

Planned symposia for the Toronto Meeting include the following Divisions and subjects:

Battery and Electronics—Materials Problems in Battery and Fuel Cell Technology; **Dielectrics and Insulation**—Aging and Time Dependent Breakdown in Dielectrics and Insulators, General Session; **Dielectrics and Insulation and Corrosion**—Anodic Oxide Films; **Dielectrics and Insulation and Electronics**—Protective Coatings and Encapsulation, Thin-Film and Interfacial Reaction Studies by Rutherford Scattering; **Electronics**—Large-Scale Integration (LSI) Process Technology, Semiconductor General Sessions, Phosphor Efficiency, Luminescence General Sessions, Materials and Processes for Solar Energy Conversion; **Electronics and Electrothermics and Metallurgy**—Growth and Processing of Large Crystals; **Electrothermics and Metallurgy**—General Session; **Electrothermics and Metallurgy and Corrosion**—International Symposium on Metal-Slag-Gas Reactions and Processes; **Electrothermics and Metallurgy and Industrial Electrolytic**—Chemistry and Physics of Aqueous Gas Solutions; **Industrial Electrolytic**—Electrochemical Separators, General Session; **Organic and Biological Electrochemistry**—General Session; **Organic and Biological Electrochemistry, Corrosion, and Physical Electrochemistry**—Bioelectrochemistry—Interfacial Phenomena in Biological Systems; **Physical Electrochemistry**—General Session; **New Technology Subcommittee, Electronics, and Electrothermics and Metallurgy**—Analysis of Trace Constituents; **Education Committee**—Teaching of Electrochemistry.

DALLAS, TEXAS—OCTOBER 5, 6, 7, 8, 9 & 10, 1975
Headquarters at the Sheraton Dallas Hotel

Planned symposia for the Dallas Meeting include the following Divisions and subjects:

Battery—Leclanché Cells, Nonaqueous Cells, General Session; **Corrosion**—Repassivation Kinetics, General Session; **Corrosion and Electrodeposition**—Electrodeposition of Organic Coatings; **Corrosion, Electronics, Electrothermics and Metallurgy, and Dielectrics and Insulation**—Techniques for Surface and Thin-Film Analysis and Depth Profiling; **Dielectrics and Insulation**—Dielectric Materials for Hybrid and Thin-Film Circuits, Thermal and Photostimulated Current in Insulators, General Session; **Dielectrics and Insulation and Electronics**—Recent Developments in MOS Technology; **Electrodeposition**—General Session; **Electronics**—Electrochemical Techniques for Electronic Device Fabrication, Semiconductor General Session, Materials and Processes General Session; **Electrothermics and Metallurgy**—High Temperature Processes Induced in Materials by the Absorption of Radiation, General Session; **Electrothermics and Metallurgy and Electronics**—Liquid Phase and Molecular Beam Epitaxy: Electronic and Magnetic Materials; **New Technology Subcommittee and Electrothermics and Metallurgy**—Energy Storage.

WASHINGTON, D.C.—MAY 2, 3, 4, 5, 6 & 7, 1976
Headquarters at the Sheraton Park Hotel

Planned symposia for the Washington Meeting include the following Divisions and subjects:

Battery and Electronics—Materials for Batteries and Fuel Cells; **Corrosion**—Magnetohydrodynamics, General Session; **Dielectrics and Insulation**—Dielectrics for Image and Hologram Storage and Display Devices, Refractory Materials for Display Devices, General Session; **Dielectrics and Insulation and Electronics**—Etching of Dielectrics and Insulators; **Dielectrics and Insulation, Electronics, and Electrothermics and Metallurgy**—Control and Utilization of Defects in Solids; **Electronics**—Semiconductor General Session, Surface Properties of Phosphors and Photoconductors, Luminescence General Session, Materials and Processes General Session; **Electronics and Electrothermics and Metallurgy**—International Symposium on Solar Energy, Seventh International Conference on Electron and Ion Beam Science and Technology; **Electrothermics and Metallurgy and Industrial Electrolytic**—Electrochemical Extraction Processes; **Industrial Electrolytic**—Engineering Analysis and Scale-Up of Electrochemical Systems; **Industrial Electrolytic and Organic and Biological Electrochemistry**—Industrial Electro-Organic Processes; **Physical Electrochemistry**—Spectroscopic Methods in Electrochemical Studies, General Session; **New Technology Subcommittee and Corrosion**—Corrosion in Molten Salts.

LAS VEGAS, NEVADA—OCTOBER 17, 18, 19, 20, 21 & 22, 1976
Headquarters at the Caesar's Palace Hotel

Planned symposia for the Las Vegas Meeting include the following Divisions and subjects:

Battery—Low Maintenance and Maintenance-Free Lead-Acid Batteries, Porous Electrodes, Theory and Practice, General Session; **Corrosion**—Corrosion in Scrubber Systems, Corrosion Problems in Geothermal Energy Systems, General Session; **Corrosion and Electrothermics and Metallurgy**—Properties of High Temperature Alloys; **Dielectrics and Insulation and Electronics**—Dielectrics and Semiconductors on Insulating Electronic Materials and Devices for Storage and Display; **Dielectrics and Insulation, Electronics, and Electrothermics and Metallurgy**—The Chemistry and Crystallography of Chemical Vapor Deposition of Electronic Materials; **Electrodeposition**—General Session; **Electrodeposition and Industrial Electrolytic**—High Current Density Electrode Processes; **Electronics**—LED's Mechanisms and Injection Lasers: Process Technology and Degradation, Semiconductor General Session, Materials and Structures for Integrated Optical Networks, Materials and Processes General Session; **Electrothermics and Metallurgy**—High Temperature Processes of Geological Interest; **New Technology Subcommittee**—Power Conditioning and Power Transport.

We told you it was versatile

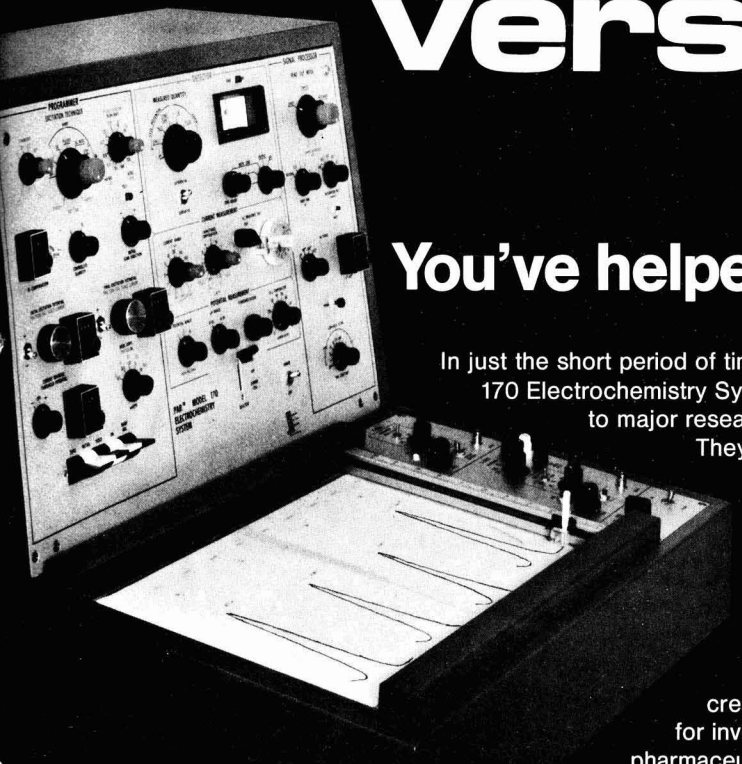

You've helped us prove it!

In just the short period of time since we introduced our Model 170 Electrochemistry System we've sold hundreds of units to major research facilities throughout the world. They're being used for studies ranging from trace analysis to electrode kinetics to corrosion. And they're helping to bring about widespread use of electroanalytical techniques.

The dozens of experiments this instrument can perform have increased the value of electrochemistry for investigations of organics, inorganics, pharmaceuticals and heavy metals. Complete information about the Model 170 and our full line of electrochemical instruments and accessories is available on request. We'll be happy to include a copy of the paper "Renaissance in Polarography" reprinted from Analytical Chemistry and a copy of our bibliography of applications literature. Use the reader service card number given below or contact Princeton Applied Research Corporation, P.O. Box 2565, Princeton, N.J. 08540. Telephone (609) 452-2111. European Headquarters: Princeton Applied Research GmbH, D8034 Unterpfaffenhofen, Waldstrasse 2, West Germany.

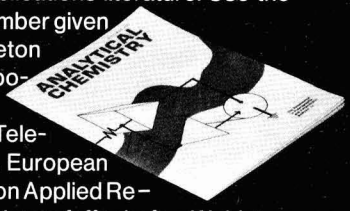

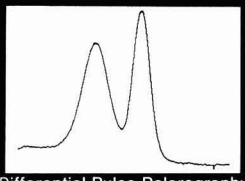
Differential Pulse Polarography

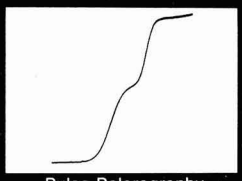
Pulse Polarography

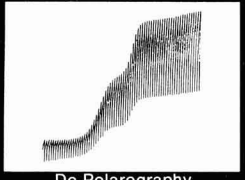
Dc Polarography

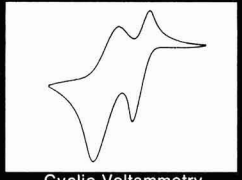
Cyclic Voltammetry

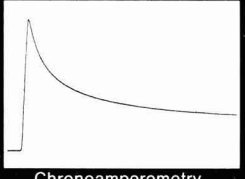
Chronoamperometry

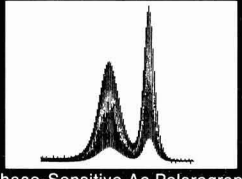
Phase-Sensitive Ac Polarography

PRINCETON APPLIED RESEARCH

SAVE 50%
ON SYMPOSIUM VOLUMES

Value for $$$. In order to reduce inventory, The Electrochemical Society, Inc. is offering a 50% discount, while supplies last, on the following five highly successful symposium volumes.

- **HIGH TEMPERATURE METALLIC CORROSION OF SULFUR AND ITS COMPOUNDS**

  edited by Z. A. Foroulis (1970)

  276 pages

  Regularly $9.00—**NOW ONLY $4.50**

  Sulfur and its compounds have been a contributing factor to corrosion in the field of high-temperature oxidation studies during the past several years. This volume approaches the problem by use of electrochemical analysis to interpret and predict corrosion behavior of metals and alloys in oxygen and sulfur-containing environments; by study of the kinetics and mechanism of sulfidation reactions; and by evaluation and/or development of suitable alloys for industrial applications.

- **ELECTRON AND ION BEAM SCIENCE AND TECHNOLOGY**
  4th International Conference

  edited by R. Bakish (1971)

  680 pages

  Regularly $15.00—**NOW ONLY $7.50**

  The aim is to survey the field at a given moment and to present the status of the technology as reflected by the newest theoretical advances on the one hand and by industrially adopted innovations on the other. Included are papers on the physics of electron and ion beams; electron beams in welding, materials processing, and radiation processing; and electron and ion beams in microelectronics.

- **FUNDAMENTALS OF ELECTROCHEMICAL MACHINING**

  edited by C. L. Faust (1971)

  365 pages

  Regularly $9.00—**NOW ONLY $4.50**

  This volume bridges the gap between empirical equations relating the variables with theoretical analysis. Papers present laboratory data on ECM which help clarify factors that are important for attaining accuracy, minimizing and controlling overcut, avoiding pitting and intergranular attack, and achieving smooth finishes. Results of studying the anodic dissolution of metals under conditions simulating those used for ECM are analyzed.

- **ELECTRON AND ION BEAM SCIENCE AND TECHNOLOGY**
  5th International Conference

  edited by R. Bakish (1972)
  420 pages
  Regularly $11.00—**NOW ONLY $5.50**

  Low energy electron and ion beams related to the field of microelectronics including physical aspects of the beams with material interactions and devices. A review of ion implantation technologies as used by industry. High power electron beams in welding. All are discussed in the Proceedings of this successful 5th International Conference.

- **ELECTROCHEMICAL CONTRIBUTIONS TO ENVIRONMENTAL PROTECTION**

  edited by T. R. Beck, O. B. Cecil, C. G. Enke, J. McCallum, and S. T. Wlodek (1972)
  173 pages
  Regularly $8.00—**NOW ONLY $4.00**

  Air, water, and land are natural chemical systems on which we depend for survival. Electrochemistry acts as interface between these and our man-made, electrical signaling systems to help monitor the environment. A direct product of current popular interest in our environment, this symposium volume shows how electrochemical and solid-state processes in pollution control and monitoring can help.

AVOID DISAPPOINTMENT—SEND YOUR ORDER TODAY TO:

The Electrochemical Society, Inc., P.O. Box 2071 Princeton, N.J. 08540

PAYMENT MUST ACCOMPANY ORDER

a first edition free!

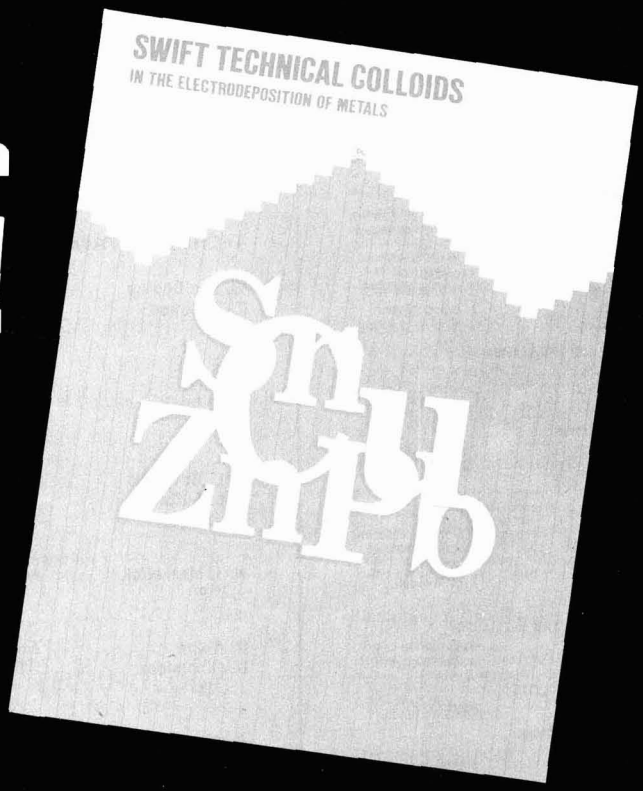

Write today for this new brochure on the role of colloidal proteins in the electrodeposition of metals.

To our knowledge, this is the first publication of information dealing with the theories of the function of colloidal proteins in electrolytes, as well as the practical results. Technically oriented and well illustrated, it concisely describes past and present uses of colloidal proteins in electrodeposition with emphasis on the role of molecular weight. It also describes the Swift Technical Colloids available and the economics of their use. Fill out the coupon for your free copy today.

Please send me, without obligation, my personal copy of the brochure, "Swift Technical Colloids in the Electrodeposition of Metals."

Company _____
(Please print)

Street _____

City _____ State _____ Zip _____

Your name and title _____

JESA5

SWIFT **TECHNICAL COLLOIDS**

Swift Chemical Company
An Estech Company
111 W. Jackson Blvd.
Chicago, Illinois 60604

JOURNAL OF THE

JANUARY 1975

ELECTROCHEMICAL SCIENCE AND TECHNOLOGY

TECHNICAL PAPERS

ELECTROCHEMICAL SOCIETY

Vol. 122 • No. 1

Manuscripts submitted to the Journal should be sent, in triplicate, to the Editorial Office at P.O. Box 2071, Princeton, N.J. 08540. They should conform to the revised "Instructions to Authors" available from Society Headquarters. Manuscripts so submitted, as well as papers presented before a Society technical meeting, become the property of the Society and may not be published elsewhere in whole or in part without written permission of the Society. Address such requests to the Editor.

The Electrochemical Society does not maintain a supply of reprints of papers appearing in its Journal. A photoprint copy of any particular paper may be obtained from University Microfilms, Inc., 300 N. Zeeb St., Ann Arbor, Mich. 48106.

Inquiries regarding positive microfilm copies of volumes should be addressed to University Microfilms, Inc., 300 N. Zeeb St., Ann Arbor, Mich. 48106.

Walter J. Johnson, Inc., 355 Chestnut St., Norwood, N.J. 07648, have reprint rights to out-of-print volumes of the Journal, and also have available for sale back volumes and single issues, with the exception of the current calendar year. Anyone interested in securing back copies should correspond directly with them.

Published monthly by The Electrochemical Society, Inc., at 215 Canal St., Manchester, N.H.; **Executive Offices, Editorial Office and Circulation Dept.,** and **Advertising Office** at P.O. Box 2071, Princeton, N.J. 08540, combining the JOURNAL and TRANSACTIONS OF THE ELECTROCHEMICAL SOCIETY. Statements and Opinions given in articles and papers in the JOURNAL OF THE ELECTROCHEMICAL SOCIETY are those of the contributors, and The Electrochemical Society assumes no responsibility for them.

Claims for missing numbers will not be allowed if received more than 60 days from date of mailing plus time normally required for postal delivery of JOURNAL and claim. No claims allowed because of failure to notify the Circulation Dept., The Electrochemical Society, P.O. Box 2071, Princeton, N.J. 08540, of a change of address, or because copy is "missing from files." Subscription to members as part of membership service; subscription to nonmembers $50.00 plus $5.00 for postage outside U.S. and Canada. Single copies $3.25 to members, $5.00 to nonmembers.

Second Class Postage Paid at Princeton, New Jersey, and at additional mailing offices. Printed in U.S.A.

SOLID-STATE SCIENCE (Cont.)

TECHNICAL NOTES

REVIEWS AND NEWS

NEWS

JOURNAL OF THE ELECTROCHEMICAL SOCIETY

ELECTROCHEMICAL SCIENCE
AND TECHNOLOGY

JANUARY
1975

Supersaturated Zincate Solutions

W. Van Doorne and T. P. Dirkse*

Department of Chemistry, Calvin College, Grand Rapids, Michigan 49506

ABSTRACT

A study of supersaturated zincate solutions is made using light scattering and nuclear magnetic resonance techniques. The results indicate strongly that the excess zinc is present as a solute species rather than in a colloidal form. The solute species appears to be the same as that in solutions of ZnO in aqueous KOH, viz., $Zn(OH)_4^{2-}$. There is no strong evidence to indicate the presence of other solute species.

When metallic zinc is treated anodically in aqueous KOH the surface often becomes dark in color and, if the treatment is continued long enough, a white solid precipitates from the solution. Both the white solid and the dark film on the metal are zinc oxide. Thus, the end product of the anodic treatment appears to be ZnO. However, ZnO is soluble in aqueous KOH. For some time it was believed that the solution from which the white solid precipitated was a saturated solution of ZnO in KOH. But further investigation (1) disproved this assumption. Instead, it was shown that the dissolved Zn(II) content of the electrolyte decreased and after about a year approached that of a saturated solution of ZnO. Meanwhile, a white solid continued to precipitate from the solution.

This phenomenon has been known for some 20 years and it is of significance for batteries containing a metallic zinc electrode and an aqueous KOH electrolyte. However, very little work has been done with these so-called "supersaturated" zincate solutions (szs).

A variety of evidence suggests that in a saturated solution of ZnO in aqueous KOH the dissolved Zn(II) species is primarily $Zn(OH)_4^{2-}$ (2-4). Very little work has been done to determine the nature of the dissolved Zn(II) species in the szs. Dirkse (1) measured the emf of a zinc electrode in various szs and interpreted the results as indicating that $Zn(OH)_4^{2-}$ is also the predominant species in szs. However, this suggestion has been called into question. It has been suggested, *e.g.*, that the excess Zn(II) in the szs is in a colloidal form and there is evidence to support this, *e.g.*, the slow precipitation of the excess Zn(II) as ZnO. Hampson *et al.* (5) on the basis of emf measurements concluded that the excess Zn(II) in szs is electrochemically inactive. A Raman spectra investigation (6) showed that the Zn(II) species in saturated solutions of ZnO in aqueous KOH is a tetrahedral zinc-hydroxy arrangement. With anodic treatment of zinc in a 40% KOH solution saturated with ZnO the dissolved Zn(II) content increased about 70%, but the area under a band typical of $Zn(OH)_4^{2-}$ increased only about 12% and no new bands were observed. The conclusion is that about 1/6 of the excess Zn(II) is converted to $Zn(OH)_4^{2-}$. The nature of the remaining 5/6 was not determined.

In the early work with szs, it was observed (1) that the specific conductance of the solution decreased with increasing excess Zn(II). This may have been due to increased viscosity of the solutions and/or to replacement of OH^- ions by the zinc-hydroxy species.

In summary, on the basis of the work done to date it is not possible to describe precisely the nature of the excess Zn(II) in the szs. The work reported here was carried out in an attempt to gather more information about these szs solutions. Two techniques were used: (*i*) light scattering, and (*ii*) nuclear magnetic resonance (NMR). The light scattering technique may give information as to whether or not the Zn(II) in the szs is in a colloidal form. The NMR technique provides information about the environment of the protons in the solutions. This environment is averaged over all possible proton locations (*i.e.*, in water, hydroxide ions, and Zn species). Because of rapid exchange of protons among these locations the NMR technique cannot distinguish between the various proton-containing species.

The initial investigation of the ZnO-aqueous KOH system by NMR techniques was reported by Newman and Blomgren (4). Their investigation covered a series of KOH concentrations ranging from 3.89 to 13.62 molal and ZnO concentrations nearly up to the saturation point for each of the KOH solutions. The analysis of Newman and Blomgren shows that the formulation $Zn(OH)_4^{2-}$, as the primary Zn(II) species, is consistent with the chemical shift values. The present work employs a similar technique but extends the range of ZnO concentrations into those of the szs.

Experimental

The light scattering results were obtained by the use of a Coleman Universal spectrophotometer with a nephelometric attachment. The NMR spectra were obtained using a Jeolco MH60 spectrometer, operating at 60 MHz. Water was used as the external reference. After allowing time for obtaining temperature equilibrium in the sample, each spectrum was scanned five consecutive times.

Three stock solutions of KOH were prepared using reagent grade KOH. Saturated solutions of ZnO were made by dissolving the maximum of reagent grade

* Electrochemical Society Active Member.

Key words: supersaturated zincate solutions, light scattering, nuclear magnetic resonance.

ZnO in each of the KOH solutions, followed by filtration through a Pyrex frit. Unsaturated solutions of varying ZnO concentrations were prepared by mixing appropriate amounts of pure KOH solution and the KOH solutions saturated with ZnO. A supersaturated Zn(II) solution was made by anodic oxidation of metallic zinc in a saturated ZnO solution. Solutions with varying degrees of supersaturation were made by mixing the saturated and supersaturated solutions in varying ratios. All zinc analyses were made by titration with EDTA.

Results and Discussion

Light scattering.—A saturated solution of ZnO in 2.8*M* KOH [0.13*M* in Zn(II)] was used as a reference and to set the galvanometer to 0. Next a szs solution [2.8*M* KOH + 0.35*M* Zn(II)] was placed in the same cuvette and the galvanometer then read 3%. This is within the experimental uncertainty associated with making these measurements. In a second run a saturated solution of ZnO [10.2*M* KOH + 1.12*M* Zn(II)] was placed in the cuvette and the galvanometer set to read 0. When a szs [10.2*M* KOH + 1.5*M* Zn(II)] was placed in the same cuvette the galvanometer read 0%. Thus, in both these cases the szs showed no or negligible increased light scattering compared to the saturated ZnO solutions. These results indicate the absence of colloidal material. It has been argued that the light scattering results are dependent on the refractive indices of the substances involved and that in these cases the refractive indices are such that even though there is colloidal material present no light scattering is observed. It has been observed under magnification that a pronounced refractive index change occurred around the zinc electrodes during discharge, *i.e.*, during anodic treatment (6, p. 34). This argument has been used often when solutions of ZnO in aqueous KOH are said to be optically clear. However, the fact that NMR results also support the absence of colloidal material (see below), seems to make it reasonable to state that the szs solutions contain no appreciable amounts of colloidal material.

Nuclear Magnetic Resonance.—All spectra showed a single peak for the external reference and a sharp, single, downfield peak for the KOH-ZnO solution. A typical scan is shown on Fig. 1.

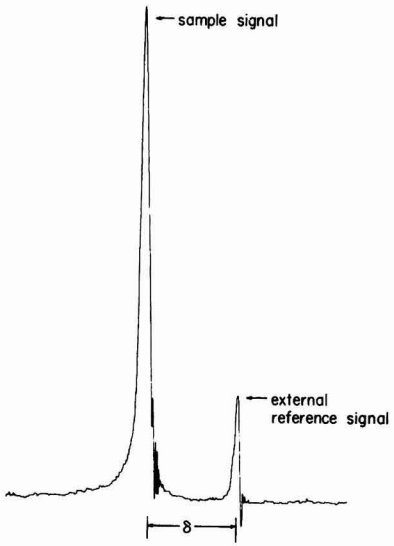

Fig. 1. Typical nuclear magnetic resonance scan

The five chemical shifts relative to water were measured for each sample and averaged to give the uncorrected chemical shift, δ. The standard deviation was 0.4 Hz for a typical set of five values.

Since an external reference was used, bulk susceptibility corrections were made using the equation given by Pople, Schneider, and Bernstein (7)

$$\delta = [(H - H_r)/H_r] + (2\pi/3)(\chi_{v,r} - \chi_v) \qquad [1]$$

χ_{v1} and χ_v refer to the volume magnetic susceptibilities of reference and sample. χ values were obtained from the table given by Selwood (8) and it was assumed that the additivity law

$$\chi_v = \phi_1\chi_1 + \phi_2\chi_2 + \ldots + \phi_n\chi_n \qquad [2]$$

was obeyed. (ϕ represents the volume fraction of each component.)

The change in the chemical shift, δ, from that of the pure KOH solution, caused by the addition of ZnO, is defined as Δδ.

As is shown in Fig. 2, Δδ increases with increasing Zn concentrations, and the slope of the lines increases with increasing KOH concentrations. The linearity of these plots, as has been observed by Newman and Blomgren (4), is consistent with the existence of a single Zn-containing species. Evidence from other authors suggests that this species is the tetra-coordinated ion $Zn(OH)_4^{2-}$ (2, 3).

Figure 3 gives a plot of Δδ *vs.* the increasing mole ratio of KOH to ZnO. In a similar graph, Newman and Blomgren found possible discontinuities in the two curves of lowest KOH concentrations (2.89 and 4.83*M*). These discontinuities were tentatively attributed to second coordination sphere effects. Although our curve for the lowest KOH concentration (2.9*M*) also shows an increase at a mole ratio of about 11, we feel that this must be viewed with caution since the increase is less than twice the standard deviation of the δ-values, and may be due to normal statistical scatter.

In Fig. 2, 3, and 4 the dotted vertical line indicates the limit of normal solubility of ZnO in each of the KOH solutions. Neither Fig. 2 nor Fig. 3 shows a statistically significant discontinuity or change of slope on passing from the unsaturated into the supersaturated region. The absence of such a discontinuity is consistent with the view that in both the unsaturated and supersaturated regions only one type of Zn complex exists, namely $Zn(OH)_4^{2-}$.

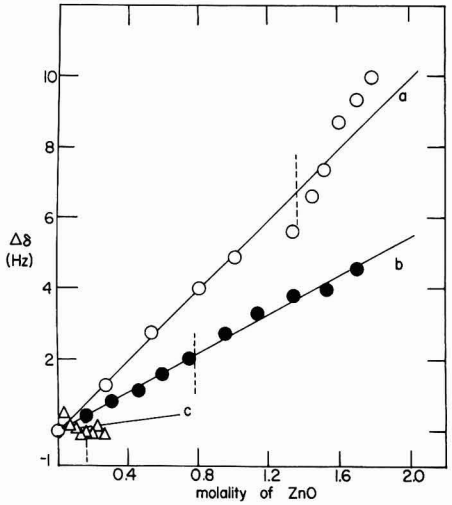

Fig. 2. Change in chemical shift with added ZnO at different base strengths: a, 12.2M KOH; b, 7.3M KOH; c, 2.9M KOH.

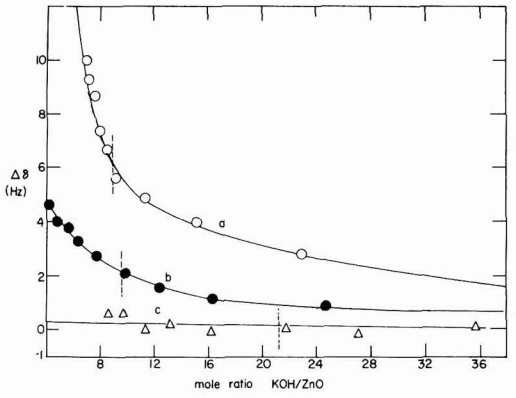

Fig. 3. Change of chemical shift with increasing mole ratio of KOH to ZnO at different base strengths: a, 12.2M KOH; b, 7.3M KOH; c, 2.9M KOH.

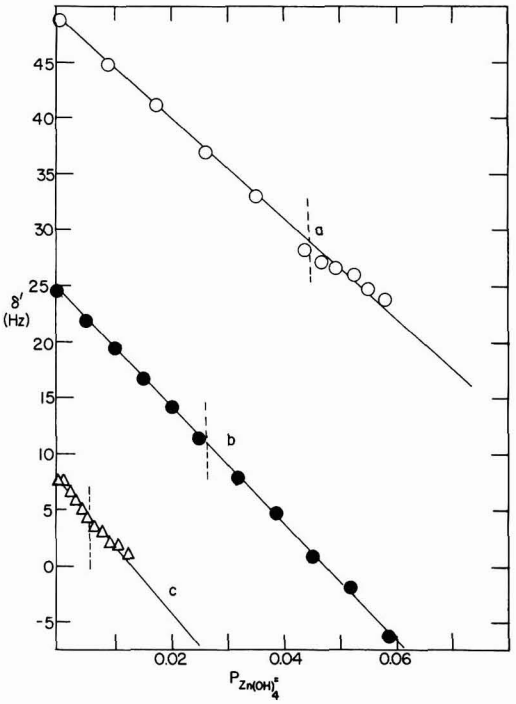

Fig. 4. Plot of δ' with increasing proton fraction of $Zn(OH)_4^{2-}$ at different base strengths: a, 12.2M KOH; b, 7.3M KOH; c, 2.9M KOH.

The total chemical shift with respect to the reference signal may be expressed by the equation

$$\delta = P_{OH^-}\,\delta^\circ_{OH^-} + P_{Zn(OH)_4^{2-}}\,\delta^\circ_{Zn(OH)_4^{2-}} \quad [3]$$

in which the following definitions apply

δ = chemical shift corrected for bulk susceptibility

P_{OH^-} = proton fraction of OH^- in solution

$$= (M_{KOH} - 2M_{ZnO})/(M_{KOH} + 2 \times 55.51) \quad [4]$$

$P_{Zn(OH)_4^{2-}}$ = proton fraction of $Zn(OH)_4^{2-}$ in solution

$$P_{Zn(OH)_4^{2-}} = 4M_{ZnO}/M_{KOH} + 2 \times 55.51) \quad [5]$$

$\delta^\circ_{OH^-}$ = ratio of change of chemical shift with change in mole fraction of OH^- at infinite dilution

$\delta^\circ_{Zn(OH)_4^{2-}}$ = ratio of change of chemical shift with change in proton fraction of $Zn(OH)_4^{2-}$

The above definitions are identical to those used by Newman and Blomgren (4).

The value for $\delta^\circ_{OH^-}$ found by Newman and Blomgren is 20.0 ppm or 1200 Hz.

This value was found by measuring the chemical shift, δ, *vs.* the proton fraction of OH^- ion and measuring the slope of the curve at zero concentration.

Both our values and those of Newman and Blomgren (4) show positive deviations from linearity which the latter authors have attributed to ion-pairing between the K^+ and OH^- ions. The magnitude of this deviation should depend on the concentration of KOH and, since water solutions are strongly hydrogen-bonded, the deviation should also be temperature dependent (7, p. 400).

The differences in the deviation from linearity (Fig. 5) for identical KOH concentrations may be attributed to different spectrometer probe temperatures.

Newman and Blomgren do not report a temperature value. Ambient probe temperature in our instrument is 40° ± 2°C. In any case, the value of the slope of the curve extrapolated to zero concentration corroborates the value of 20.0 ppm for $\delta^\circ_{OH^-}$.

From the value of $\delta^\circ_{OH^-}$ and the known KOH concentration the value of δ' may be calculated for each solution.

$$\delta' = P_{Zn(OH)_4^{2-}}\,\delta^\circ_{Zn(OH)_4^{2-}} = \delta - P_{OH^-}\,\delta^\circ_{OH^-} \quad [6]$$

A plot of δ' *vs.* $P_{Zn(OH)_4^{2-}}$ will then give as its slope, the value of $\delta^\circ_{Zn(OH)_4^{2-}}$ (Fig. 4).

The following values were found:

Molality of KOH	$\delta^\circ_{Zn(OH)_4^{2-}}$, ppm
2.9	−9.60
7.3	−8.60
12.2	−7.32

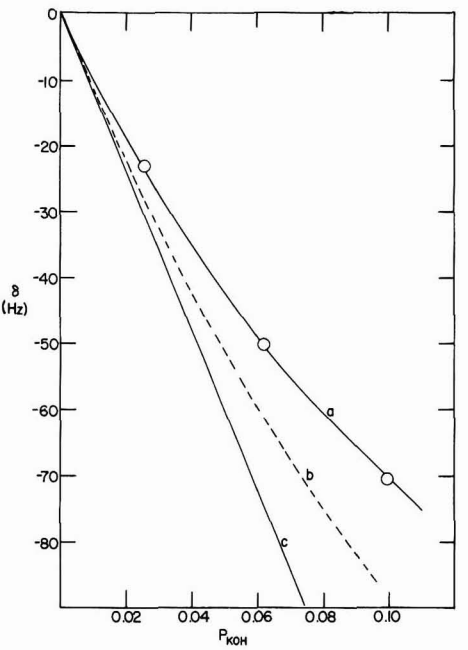

Fig. 5. Plot of proton resonance shift, δ, with increasing proton fraction of base: a, our values; b, approximate experimental values of Newman and Blomgren (4); c, slope of curves at $P_{KOH} = 0$. Used as values of δ°_{KOH}.

In view of the small magnitude of the effect being measured and the uncertainty in the temperature, these values compare well with those found by Newman and Blomgren (4) which ranged from −6.44 to −6.04 ppm. Although our values are slightly higher, the change in $\delta_{Zn(OH)_4^{2-}}$ with changing KOH concentrations is similar, though somewhat more pronounced.

In calculating the data in Fig. 4, it was assumed that $\delta^o_{OH^-}$ has a constant value of 20.0 ppm. The error introduced by the deviations from this value (see Fig. 5) causes the nonzero intercepts of the curves in Fig. 4, but should not affect the slopes appreciably.

The plots of δ' *vs.* $P_{Zn(OH)_4^{2-}}$ do not show a significant deviation from linearity on passing from the unsaturated to the supersaturated region. In view of this, no difference in the zinc-containing species existing in those two regions is indicated. Should a second, different, zinc species exist in the supersaturated region, a change in slope might be expected.

If, for example, the excess zinc (above the normal limit of solubility) existed as simple Zn^{++} ions, the slope of the curves in Fig. 4 should approach zero in the supersaturated region. The species which cannot be eliminated by those arguments are other complexes of zinc containing 4 protons, namely, $Zn(H_2O)_2^{++}$ and $Zn(OH)_2(H_2O)$. The existence of these, however, is placed in doubt by the work of Fordyce and Baum (3).

Finally, the linearity of the plots in Fig. 4, and the lack of signal broadening in the spectra eliminate the possibility that the excess zinc exists as a colloid or suspended solid.

Acknowledgment

The work reported here was carried out with grants from the Aero Propulsion Laboratory of the United States Air Force, the United States Office of Naval Research, and the General Electric Company.

Manuscript submitted Feb. 26, 1974; revised manuscript received July 22, 1974.

Any discussion of this paper will appear in a Discussion Section to be published in the December 1975 JOURNAL. All discussions for the December 1975 Discussion Section should be submitted by Aug. 1, 1975.

Publications costs of this article were partially assisted by Calvin College.

REFERENCES

1. T. P. Dirkse, *This Journal.* **102,** 497 (1955).
2. T. P. Dirkse, *ibid.*, **101,** 328 (1954).
3. J. S. Fordyce and R. L. Baum, *J. Chem. Phys.*, **43,** 843 (1965).
4. G. H. Newman and G. E. Blomgren, *ibid.*, **43,** 2794 (1965).
5. N. A. Hampson, G. A. Herdman, and R. Taylor, *Electroanal. Chem.*, **25,** 9 (1970).
6. J. F. Jackovitz and A. Langer, "Zinc-Silver Oxide Batteries," J. J. Lander and A. Fleischer, Editors, Chap. 4, p. 29, John Wiley & Sons, Inc., New York (1971).
7. J. P. Pople, W. G. Schneider, and H. J. Bernstein, "High-Resolution Nuclear Magnetic Resonance," p. 81, McGraw-Hill Book Co., New York (1959).
8. P. W. Selwood, "Magnetochemistry," p. 78, Interscience Publishers, Inc., New York (1956).

The Sealed Nickel-Hydrogen Secondary Cell

Jose Giner*,[1]

Tyco Laboratories, Waltham, Massachusetts 02154

and James D. Dunlop*

COMSAT Laboratories, Clarksburg, Maryland 20734

ABSTRACT

A recently developed sealed nickel-hydrogen cell offers considerable promise to develop lightweight, long-life, rechargeable batteries. The most apparent advantages of this cell are its higher energy and power density as compared with other rechargeable systems including nickel-cadmium, lead-acid, and silver-zinc cells and the regenerative H_2-O_2 fuel cell. The energy density for lightweight 50 A-hr cells shown is 28 W-hr/lb. The cell enjoys a unique overdischarge protection mechanism which allows for long cycle life at high depth of discharge. Experimental data are presented to define the characteristics of the cell. Over 5000 high rate cycles have been completed on small 1.5 A-hr cells with good voltage performance. A 50 A-hr cell has completed to date over 800 cycles discharge to 70% of measured capacity in 1.2 hr.

A recently developed sealed nickel-hydrogen cell (1) offers considerable promise for the development of light, long-life, rechargeable batteries. This system competes favorably in many applications with such rechargeable systems as the lead-acid and nickel-cadmium (Ni-Cd) cells and with systems in the developmental stage, such as the regenerative H_2-O_2 fuel cells and Cd-O_2 cells. The most apparent advantages of the cell are its attractive energy and power densities for both charge and discharge. In addition, it shows high reliability, long cycle life, storage life which is insensitive to the state of charge, considerable overcharge protection, and a unique overdischarge protection mechanism which makes it eminently suited for connecting cells in series. It also promises attractive low-temperature performance. The specific application of this system to synchronous satellite operation has already been discussed (2). In the following the characteristics of the cell are defined, based on experimental measurements, and the lightweight 66 W-hr (50 A-hr) cell design.

Description of the System

In its construction the nickel-hydrogen cell resembles the Ni-Cd cell, except that the cadmium electrode is replaced by a catalyst electrode capable of oxidiz-

* Electrochemical Society Active Member.
[1] Present address: Giner, Inc., 144 Moody Street, Waltham, Massachusetts 02154.
Key words: batteries, rechargeable batteries, nickel-hydrogen batteries, aerospace batteries.

ing hydrogen gas on discharge and evolving it on charge at low polarizations. Figure 1 is a schematic representation which shows the basic electrode arrangement for the cell. In this arrangement, the positive plates, the separators, and the electrolyte are identical to those used in the Ni-Cd cell, while the hydrogen electrode structure consists of Teflon-bonded platinum supported within a thin, fine mesh, Ni screen. A gas diffusion mesh Teflon screen is placed on the back side of each hydrogen electrode to facilitate hydrogen diffusion to the platinum electrode. The total electrode-electrolyte separator stack is surrounded by an atmosphere of hydrogen under pressure.

Under normal discharge conditions, the reaction on the positive electrode is

$$NiOOH + H_2O + e^- \rightarrow Ni(OH)_2 + OH^- \quad [1]$$

and, at the negative electrode

$$\tfrac{1}{2} H_2 + OH^- \rightarrow H_2O + e^- \quad [2]$$

which results in the over-all cell reaction

$$NiOOH + \tfrac{1}{2} H_2 \rightarrow Ni(OH)_2 \quad [3]$$

During charge, the reverse reactions occur. From reaction [3], it can be concluded that there is no water production or consumption during operation other than that caused by differences in the amount of water of crystallization in the different nickel hydroxides. As shown by Eq. [1] and [2], there are local water concentration changes at each electrode.

On overcharge, when most of the bivalent nickel oxide has been oxidized, oxygen is evolved according to the reaction

$$2OH^- \rightarrow H_2O + \tfrac{1}{2} O_2 + 2e^- \quad [4]$$

This oxygen reacts immediately at the abundant catalytic surface with an equivalent amount of the hydrogen (which is being produced at equivalent stoichiometric rates) according to

$$H_2 + \tfrac{1}{2} O_2 \rightarrow H_2O$$

or is reduced at the negative electrode according to the reverse of reaction [4]. The Ni-H_2 cell is intrinsically positive electrode limited on charge because of the practically unlimited supply of water for the charging reaction at the negative electrode.

Cell reversal protection can be achieved by introducing a hydrogen precharge (*i.e.*, an amount of hydrogen gas) in the cell while it is in the discharged state. Under these conditions, the cell becomes positive electrode limited on discharge. When all the trivalent nickel hydroxide has been reduced in the discharge part of the cycle and further current is passed, hydrogen is evolved on the nickel electrode surface (since it is extremely difficult to reduce nickel hydroxide to pure nickel under these conditions). The evolved hydrogen is compensated for by an equivalent amount of hydrogen which is oxidized at the hydrogen electrode.

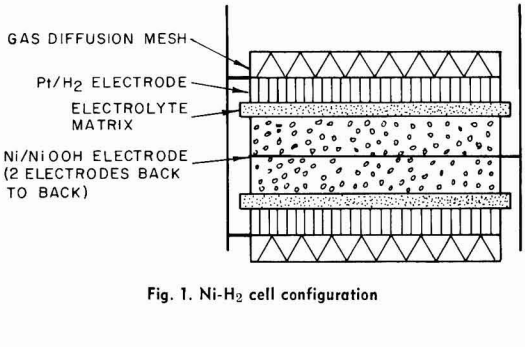

Fig. 1. Ni-H_2 cell configuration

Experimental Results

All experimental data presented were obtained using demountable heavy-walled pressure vessels. Two types of experimental cells were fabricated, a single 1.5 A-hr Ni-H_2 electrode cell, and multielectrode 5, 15, 25, and 50 A-hr cells. All of these cells used sintered nickel hydroxide positive electrodes, polypropylene separators, and Teflon-bonded platinum black negative electrodes, with a 30% KOH solution as electrolyte.

Single nickel hydroxide electrode cells (Fig. 1) were used to characterize electrochemical performance for cycle life, overcharge protection, temperature performance, and electrolyte management. Multielectrode cells (Fig. 2) were used to determine the effects of connecting a number of electrodes in parallel. In all cases the hydrogen gas was contained within the pressure vessel.

Parametric Data

The multielectrode cells were used to characterize the Ni-H_2 cell behavior in terms of temperature, pressure, and voltage with cycling. The cover of the heavy-walled container had an inlet tube to allow for hydrogen precharge filling and for pressure monitoring via a pressure transducer. The electrical feedthroughs were Ziegler-type plastic compression seals (3). A thermocouple was located in the cavity of the hydrogen electrode at the center of the electrode stack to determine the temperature under operating conditions. The thermocouple was encapsulated in polysulfone to avoid corrosion.

Conventional aerospace sintered nickel electrodes used in these cells were chemically impregnated and had a thickness of 0.76 mm and a measured flooded capacity of 0.12 A-hr/g. Two of these electrodes were used back to back to construct one positive electrode.

The hydrogen electrodes used in most cells were constructed from platinum black, bonded with Teflon, and pressed onto a thin nickel screen. Some of the electrodes had a porous Teflon backing on the gas side. A few cells used hydrogen electrodes consisting of a lightly platinized, graphite felt material (Energy Research Corporation proprietary electrode).

Pressure and voltage characteristics on cycling.—The pressure and voltage *vs.* time over a charge and discharge cycle are presented in Fig. 3. On charge at the C/1 rate,[2] the pressure increases linearly as hydrogen is evolved. The voltage rise at end of charge is

[2] The C/t rate is the rate in amperes for charging or discharging a cell, defined as the cell capacity in ampere-hours divided by the time, t, in hours (in this case, 1 hr).

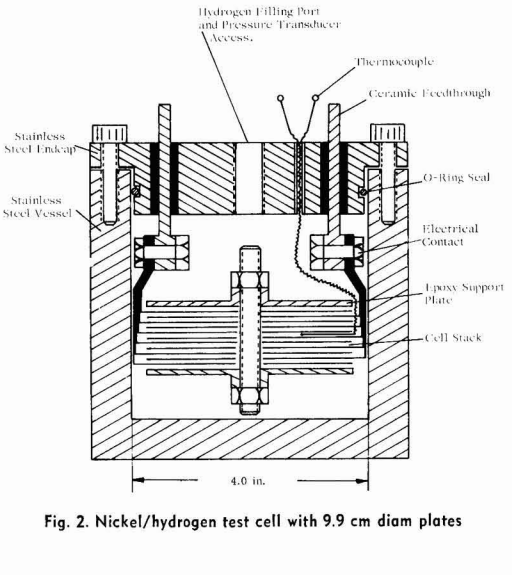

Fig. 2. Nickel/hydrogen test cell with 9.9 cm diam plates

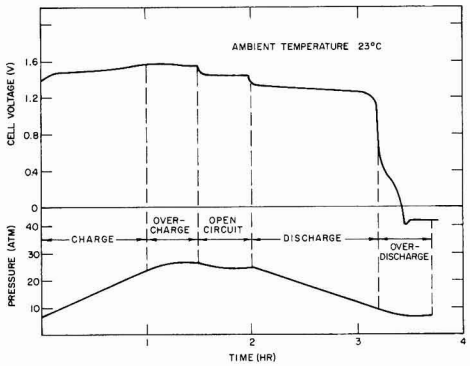

Fig. 3. Ni-H_2 cell pressure and cell voltage characteristics

caused by the onset of oxygen evolution at the nickel electrode. A slight voltage decrease observed during overcharge after O_2 evolution occurs is attributed to a temperature rise caused by O_2 and H_2 recombination. The pressure levels off and becomes constant. The partial pressure of oxygen measured during overcharge is less than 1% of the total cell pressure.

On discharge at the C/1 rate, the pressure decreases linearly as hydrogen is consumed. The voltage on discharge is characteristic of the nickel hydroxide electrode. A second plateau observed below 1V may be attributed either to reduction of chemisorbed oxygen on the positive electrode or to reduction of higher valent nickel. The cell voltage on discharge is not appreciably affected by the partial pressure of hydrogen at these temperatures and discharge rates.

During reversal on overdischarge of the positive electrode, the cell voltage reverses polarity and becomes slightly negative while the pressure levels off. This capability for continuous overdischarging of the cell with no adverse effects or pressure buildup is a unique feature of this cell.

Temperature characteristics.—Temperature data presented in Fig. 4 are for the thermocouple located in the center of the cell stack. On charge at a C/10 rate, the cell is slightly endothermic, and the cell temperature is practically constant. All of the power delivered to the cell on overcharge is dissipated as heat. Oxygen is evolved at the positive electrode, while hydrogen is evolved at the negative electrode in equivalent Faradaic rates. This oxygen and hydrogen react to form water (see Eq. [4] and [5]), causing the temperature to rise.

On discharge at the C/2 rate, part of the electrochemical energy is dissipated as heat, primarily because of polarization at the positive electrode which results in a temperature rise. A very high transient temperature rise occurs at the end of discharge because of the high polarization at the positive electrode.

During reversal at the C/2 rate, the temperature decreases and stabilizes to a value lower than that observed on discharge. Hydrogen is generated at the positive electrode and consumed at the negative electrode with low polarization.

In general the thermal and temperature characteristics of the Ni-H_2 cell are very similar to those of the Ni-Cd cell with the exception of behavior on reversal.

Temperature effects on capacity.—The voltage *vs.* time discharge characteristics with temperature as a parameter are shown in Fig. 5. The cell has been overcharged by 60% at the C/10 rate and then discharged completely to 0V. From 0° to −10°C there is a significant loss in capacity and also above 40°C a significant loss is observed. As with an Ni-Cd system, the desirable temperature range of operation is from 0° to approximately 25°C. However, the Ni-H_2 cell does not have the low temperature limitation of the Ni-Cd cell attributed to the poor charge acceptance of the cadmium electrode.

Self-discharge.—The self-discharge characteristics for the Ni-H_2 cells standing on open circuit are shown in Fig. 6. Starting with a fully charged cell, the self-discharge can be directly related to a loss of hydrogen pressure. As shown in Fig. 6, the self-discharge, similar to that of a Ni-Cd cell, occurs in a diminishing exponential fashion; after one day of standing on open circuit, the cell retains approximately 80% of its full capacity. This self-discharge is attributable either to

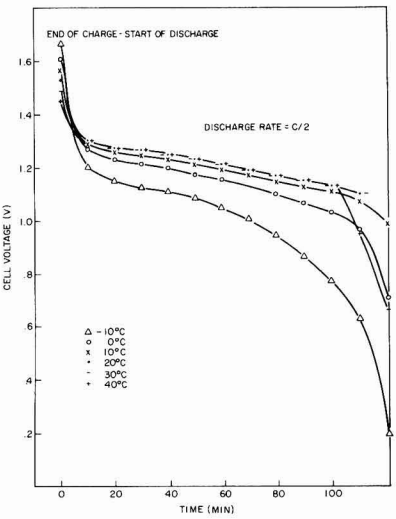

Fig. 5. Temperature effects on capacity

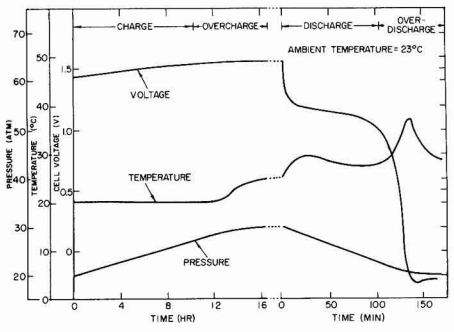

Fig. 4. Ni-H_2 cell temperature characteristics

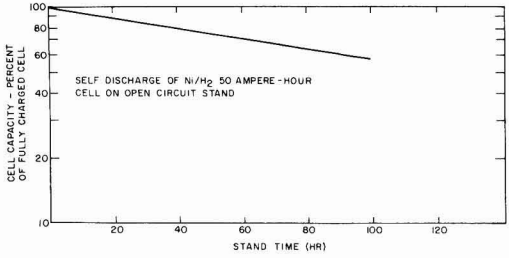

Fig. 6. Self-discharge characteristics

the direct reduction of Ni^{+3} to Ni^{+2} or to the reduction of chemisorbed oxygen on the nickel electrode.

Effects of charge and discharge rates.—Both the nickel hydroxide and the hydrogen electrodes are capable of high-rate charge and discharge. Figure 7 shows the cell voltage *vs.* the charge rate (up to the 5C rate) as a function of the state of charge of the positive electrode at room temperature. Figure 8 shows the cell voltage *vs.* the discharge rate (up to the 5C rate) as a function of the state of discharge.

Figure 9 shows the effect of the charge rate on charge acceptance. The charge acceptance was determined by charging the cell at different rates to return 5 A-hr of capacity to the cell and then discharging it at the C/1.2 rate to 1V. Maximum charge efficiency is achieved at the C/1 charge rate.

The effects of the rate of discharge on measured cell capacity after the cell is charged at the C rate to 33% overcharge are shown in Fig. 10. The capacity obtained on discharge at the 5C rate is only 10% less than that obtained at the C rate. Thus, in addition to providing a high energy density (approximately 66 W-hr/kg), the Ni-H_2 system has an excellent power density capability (over 300 W/kg).

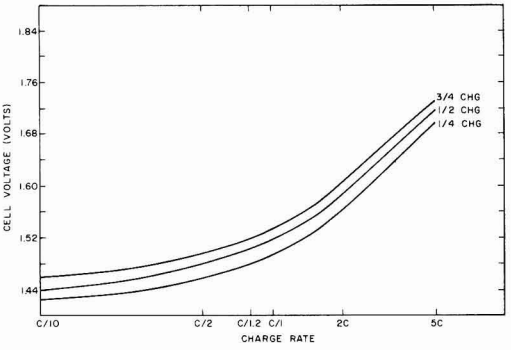

Fig. 7. Polarization on charge

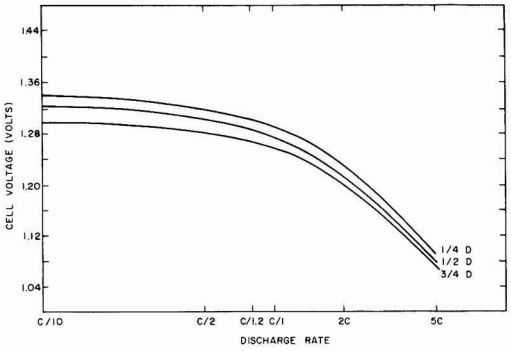

Fig. 8. Polarization on discharge

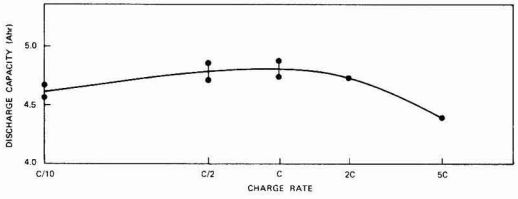

Fig. 9. Charge efficiency

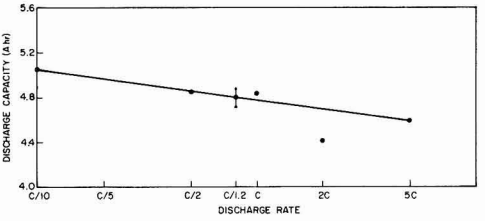

Fig. 10. Discharge rate effects on capacity

Cyclic Life Data

The nickel hydroxide electrode and the Teflon-bonded H_2 electrode are the two most stable electrodes developed for sealed secondary cells to date. Since the sealed Ni-H_2 cell is a recent development, the major failure mechanisms must still be determined. Data are presented for cyclic test results to date.

High-rate cycle test.—The purpose of this test is to evaluate different combinations of commercially available electrodes and separator materials in terms of cyclic life performance. Data are presented for five cells with electrode and separator materials identified in Table I. These cells are subjected to a 1 hr cycle test consisting of discharge for 26 min at a C/1.5 rate which corresponds to 28.6% depth of discharge (DOD) and charge for 34 min at a C/1.5 rate corresponding to 30% overcharge.

High-rate cycle test results.—Cell S/N 123 has completed over 5000 cycles to date. (Figure 11 shows the end-of-charge and end-of-discharge voltages for this cell.) The other cells have failed at 3000, 1674, 1068, and 468 cycles. The cells are considered to have failed when the discharge voltage drops below 1V.

Cell S/N 122 failed after 3000 cycles. The measured impedance of this cell increased from 70 mohm at the start of the test to over 200 mohm at failure. The increase in impedance results from a loss of electrolyte from the separator. Examination of the separator after failure revealed that the polypropylene had dried out and would not absorb electrolyte. Examination of the positive electrodes showed that they were still structurally sound, but that the thickness had changed from 0.76 to 1.16-1.30 mm.

This cell was rebuilt by using the same positive electrodes, but with a Hercules polypropylene separator and ERC Teflon-backed hydrogen electrodes. It has now completed 2000 additional cycles.

Cell S/N 115 failed after 1674 cycles. The hydrogen electrode in this cell did not have Teflon backing. The measured impedance increased from 70 mohm at the start of the test to 620 mohm at failure. Examination of the separator after failure again revealed that the polypropylene had dried out and would not absorb electrolyte. Examination of these positive electrodes showed

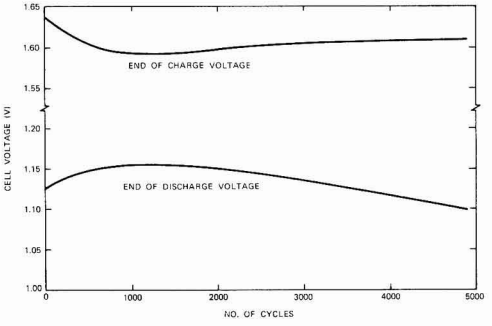

Fig. 11. Cyclic life performance of cell S/N 123

Table I. Electrode materials for use with polypropylene separators

Cell S/N	Nickel positive electrode	Separator	Negative
122	SAFT sintered nickel (slurry process) Nickel-plated perforated iron support Double electrodes back to back Each electrode 0.76 mm thick	Hercules polypropylene	ERC platinum and PTFE on nickel screen, Teflon backing
123	SAFT sintered nickel (slurry process) Nickel-plated perforated iron support Double electrodes back to back Each electrode 0.76 mm thick	Hercules polypropylene	ERC platinum and PTFE on nickel screen, Teflon backing
115	Eagle Picher sintered nickel (dry process) Nickel screen support Double electrodes back to back Each electrode 0.76 mm thick	Hercules polypropylene	ERC platinum and PTFE on nickel screen without Teflon backing
126	Eagle Picher sintered nickel (dry process) Nickel screen support Double electrodes back to back Each electrode 0.76 mm thick	Hercules polypropylene	ERC platinum on graphite without Teflon backing
127	Eagle Picher sintered nickel (dry process) Nickel screen support Double electrodes back to back Each electrode 0.76 mm thick	Hercules polypropylene	ERC platinum on graphite without Teflon backing
128	GE sintered nickel (slurry process) Nickel-plated perforated iron support Double electrodes back to back Each electrode 0.76 mm thick	Pellon polypropylene	ERC platinum and PTFE on nickel screen, Teflon backing
129	SAFT sintered nickel (slurry process) Nickel-plated perforated iron support Double electrodes back to back Each electrode 0.76 mm thick	Pellon polypropylene	ERC platinum and PTFE on nickel screen, Teflon backing

Table II. Electrode materials for use with nylon and potassium titanate separators

Cell S/N	Nickel positive electrode	Separator	Negative
130	SAFT double electrodes back to back Each electrode 0.76 mm thick	Nylon	ERC platinum and PTFE on nickel screen, Teflon backing
131	SAFT double electrodes back to back Each electrode 0.76 mm thick	Potassium titanate	ERC platinum and PTFE on nickel screen, Teflon backing
132	SAFT double electrodes back to back Each electrode 0.76 mm thick	Potassium titanate	ERC platinum and PTFE on nickel screen, Teflon backing
136	SAFT double electrodes back to back Each electrode 0.76 mm thick	Nylon	ERC platinum and PTFE on nickel screen, Teflon backing

that they also were still structurally sound, but that the thickness had changed from 0.76 to 1.16-1.30 mm.

Cells S/N 126 and 127 failed after 468 and 1068 cycles, respectively. These cells had the ERC graphite hydrogen electrodes without Teflon backing. Both failed because of loss of electrolyte, resulting in high impedance. These cells were rebuilt, S/N 126 with an ERC hydrogen electrode without Teflon backing and S/N 127 with an ERC hydrogen electrode with Teflon backing, using the same positive electrodes. These rebuilt cells have now completed over 3000 additional cycles and are still running (see Fig. 12).

Two new cells, cells S/N 128 and S/N 129, were built to evaluate the Pellon polypropylene separator material. The electrode and separator materials are identified in Table I.

Cell S/N 128 failed after 1488 cycles, again because of high impedance. The Pellon polypropylene was dried out and would not readily absorb electrolyte. This cell was rebuilt by changing the separator to Pellon nylon 2505. A significant improvement in voltage performance has been observed with the nylon separator (see Fig. 13).

Conclusions of the high-rate cycle test.—The thin graphite hydrogen electrodes and also the electrodes on nickel screen without Teflon backing have limited cycle lifetimes because of electrolyte entrainment, resulting in a loss of electrolyte from the separator. In addition, the polypropylene separators, both Hercules and Pellon, with wetting agents are becoming hydrophobic with cycling. Because of the problems with the polypropylene separator additives, cyclic tests have been initiated to investigate nylon and potassium titanate separator materials (see Table II). The cells are subjected to a 3 hr cycle test consisting of discharge for 72 min at a C/1.5 rate to 85% DOD and charge for 1.8 hr at a C/1.96 rate to 15% overcharge. They are being cycled at a very deep DOD (85% of the measured capacity). To date they have completed 500 cycles demonstrating good voltage performance (see Fig. 14).

Cycle test data for the 50A-hr cell.—This cell electrode stack is similar in construction to the lightweight

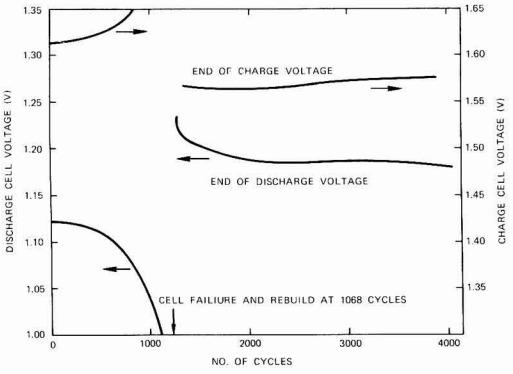

Fig. 12. Cyclic life performance of cell S/N 127

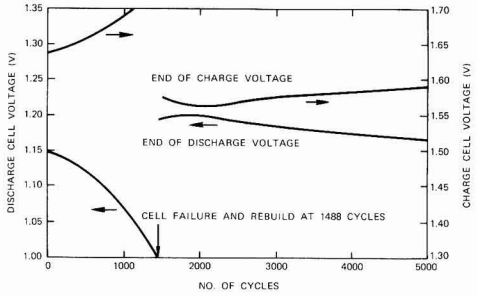

Fig. 13. Voltage performance of cell S/N 128 rebuilt with Pellon nylon 2505 separator.

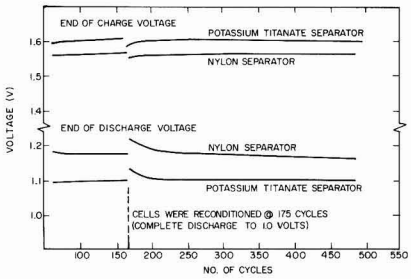

Fig. 14. Cyclic life performance of KT and nylon separator

prototype cells being fabricated. It has a 22 multi-electrode plate stack with the positive and negative electrodes connected in parallel. The hydrogen electrodes are Teflon-backed platinum and PTFE on nickel screen. SAFT aerospace positive electrodes, each 0.76 mm thick, are used back to back with the Hercules polypropylene separator.

Over 1000 cycles have been completed, demonstrating the ampere-hour turnover necessary to meet a 7 yr synchronous satellite mission (Fig. 15). A second 50 A-hr cell has now completed over 200 cycles on test. A positive SAFT nickel electrode has been manufactured specifically for this Ni-H_2 cell. Each nickel electrode is 0.96 mm thick; again they are used back to back to make one positive electrode, and all edges are coined. The cell has nylon separators.

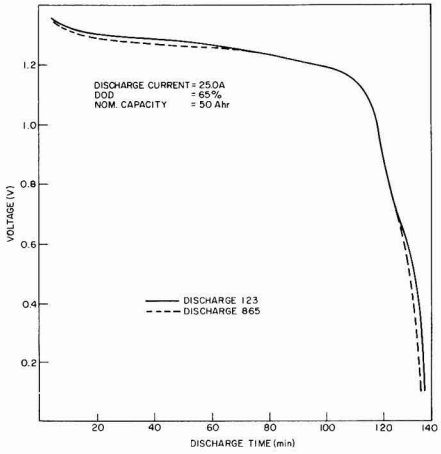

Fig. 15. Cyclic performance of the 50 A-hr cell

Lightweight Cell Design

For synchronous satellite applications, the cell design has been optimized for maximum energy density, subject to the practical restrictions discussed below.

A computer study has as the main variables cell capacity, capacity per unit area of the positive plates, cell diameter, and operating range of the cell pressure. The cell configuration for this study is a cylindrical single cell with the hydrogen contained within the pressure vessel. To characterize the electrode stack, state-of-the-art commercially available hydrogen electrodes, separators, gas diffusion screens, etc., are assumed. Inconel 625 is assumed to be the material used for the pressure vessel.

A practical cell design has been selected on the basis of the following criteria. The cell is sized to provide 66 W-hr (52 A-hr) of energy. The corresponding energy density for a cell of this capacity is 62-64 W-hr/kg (Fig. 16). Increasing the cell capacity does not significantly improve the energy density; however, if the cell capacity is reduced, there is a drop in energy density.

The cell capacity per unit area of the positive plates does have a significant effect on energy density (see Fig. 17). The practical limitations are the plate thickness that can be achieved in commercial production of the nickel plaque and the utilization of active material for thicker plates. For these reasons positive plates are used back to back in the fabrication of the multi-electrode cells.

Once the cell capacity is selected, the number of electrodes is dependent on the cell diameter selected. For the 66 W-hr cell the effect of the cell diameter and the current density on the energy density and the number of electrodes in the stack is shown in Fig. 18.

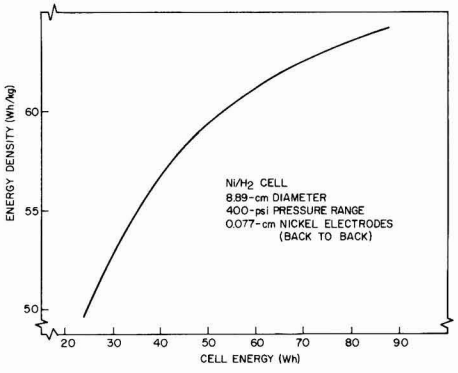

Fig. 16. Ni-H_2 cell, energy density vs. energy

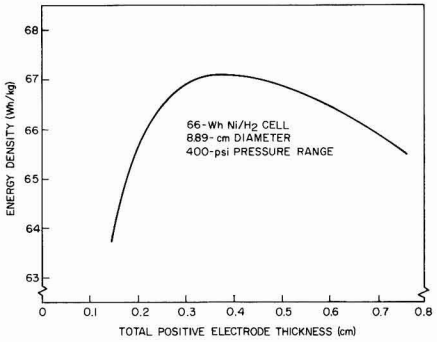

Fig. 17. Ni-H_2 cell, energy density vs. positive electrode thickness

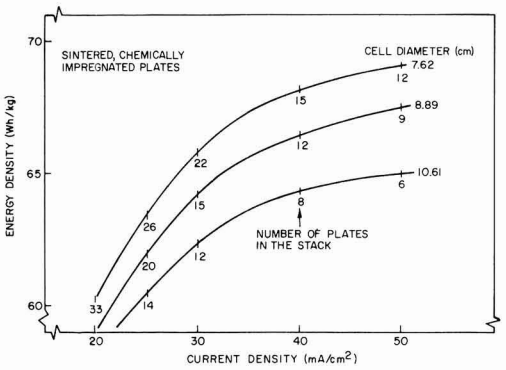

Fig. 18. Ni-H_2 cell, energy density vs. current density

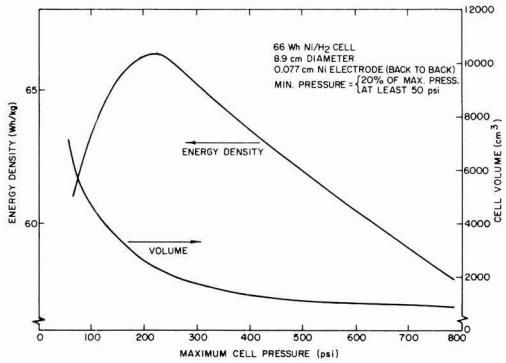

Fig. 19. Ni-H_2 cell, energy density vs. cell pressure

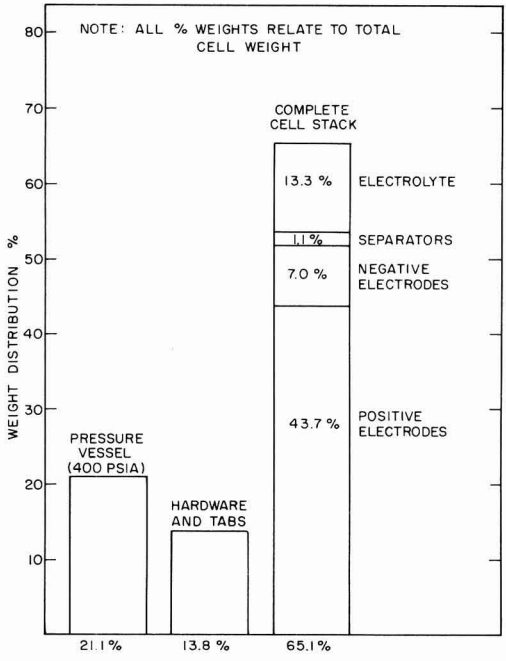

Fig. 20. Ni-H_2 cell, weight distribution

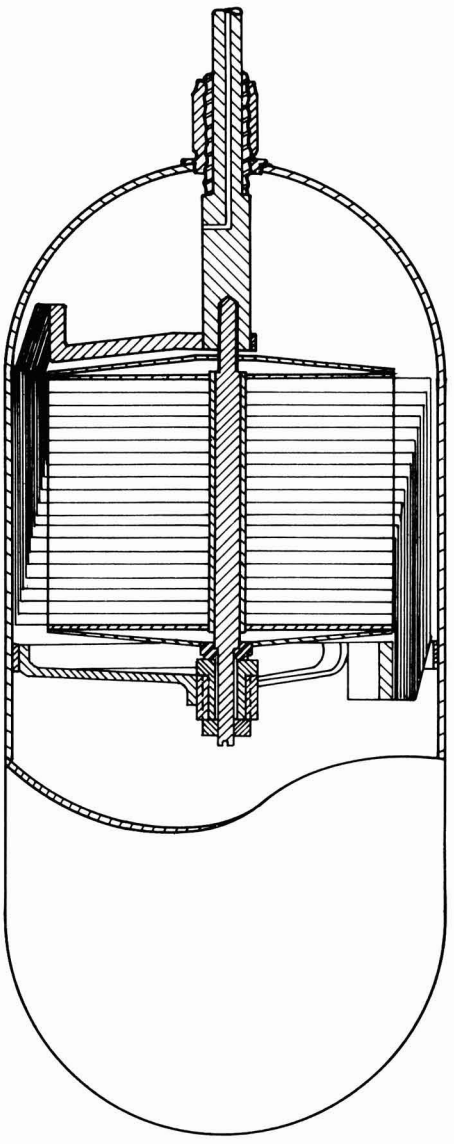

Fig. 21. Lightweight Ni-H_2 cell design

A diameter of 8.89 cm has been selected. At a current density of 25 mA/cm², the number of electrodes in the stack is 20. Decreasing the diameter makes it possible to achieve somewhat higher energy densities at the expense of an increased number of electrodes in the cell stack. The present design is a compromise between energy density and reliability.

The energy density and cell volume as functions of the maximum cell pressure are shown in Fig. 19 for an initial hydrogen pressure of 100 psi. A maximum pressure of 27 atm has been selected. Again, this is a trade off between maximum energy density and cell volume.

Figure 20 shows the weight breakdown for the 66 W-hr cell design. It should be noted that the weight of the nickel hydroxide electrodes is 44% of the total weight.

Lightweight Ni-H_2 cells are now being fabricated to the design shown in Fig. 21. Characteristics of the

sintered nickel electrodes are as follows:

thickness:	0.76 mm each, 0.152 mm back to back
density:	3.25 g/cm^3
capacity:	0.12 A-hr/g (measured, flooded)
utilization:	96% (measured in electrode stack)
current density:	25 mA/cm^2 (for 1.2-hr discharge)

This cell is designed to provide 66 W-hr at an energy density of 62-64 W-hr/kg.

The cylindrical pressure vessel is 8.89 cm in diameter by 19.9 cm high. The insulated feedthrough is a Ziegler plastic seal.

Conclusions

Experimental data presented from laboratory investigations demonstrate the capability of the Ni-H_2 system to meet the 7-10 year cyclic life requirements for a synchronous satellite application. In addition, the Ni-H_2 system has demonstrated performance characteristics superior to those of the Ni-Cd system in terms of higher overcharge capability, overdischarge capability, better low-temperature operation, and higher power density.

Lightweight cells have been designed and are now being fabricated. These cells are expected to demonstrate three to four times the usable energy density of Ni-Cd cells. For an INTELSAT V (2 kW) satellite, this represents a potential weight reduction of 200-300 lb for the battery system.

Acknowledgments

The work discussed in this paper was supported by the International Telecommunications Satellite Organization (Intelsat). Lightweight cell (Fig. 21) was designed by Mr. L. Swette.

Manuscript submitted Dec. 20, 1973; revised manuscript received June 28, 1974.

Any discussion of this paper will appear in a Discussion Section to be published in the December 1975 JOURNAL. All discussions for the December 1975 Discussion Section should be submitted by Aug. 1, 1975.

Publication costs of this article were partially assisted by COMSAT Laboratories.

REFERENCES

1. James D. Dunlop, Jose Giner, Gerrit van Ommering, and Joseph F. Stockel, Patent pending.
2. J. F. Stockel, G. Van Ommering, L. Swette, and L. Gaines, in "Proceedings of the 7th Intersociety Energy Conversion Engineering Conference," San Diego, California, September 1972, p. 87.
3. E. J. McHenry and P. Hubbauer, *This Journal*, **119**, 564 (1972).

The Effect of Solvent on the Electrochemistry of Iron

A. L. Bacarella

Chemistry Division, Oak Ridge National Laboratory, Oak Ridge, Tennessee 37830

and A. L. Sutton

Chemical Technology Division, Oak Ridge National Laboratory, Oak Ridge, Tennessee 37830

ABSTRACT

A study was made of the electrochemical behavior of the active iron electrode in acidic ethanol-water media. The pA (pH in pure water solvent) and potential dependence of the iron dissolution and hydrogen evolution reactions were determined. The results of this investigation served to resolve the role of water in the iron dissolution mechanism. Basic to the proposed mechanism was the validity of an "absolute acidity scale" for EtOH-HOH solutions.

A study has been made of the electrochemical behavior of the active iron electrode in acidic ethanol-water media. The purpose of the investigation was to test the applicability of an "absolute acidity scale" postulated for ethanol-water (1), and in the application of the "acidity scale," to determine the kinetic order with respect to water and protons in the corrosion mechanism.

It has been shown by Kelly (2) and Bockris (3) that the steady-state anodic dissolution of zone-refined iron in aqueous acid sulfate solutions is characterized by a Tafel slope of 2/3(2.303 $RT/\mathbf{F}$), *i.e.*, 40 mV/decade of current, and first order dependency on the hydroxyl ion activity. The results were interpreted in terms of the following mechanism

$$Fe + H_2O \rightleftarrows Fe(H_2O)_{ad} \quad [1]$$

$$Fe(H_2O)_{ad} \rightleftarrows Fe(OH^-)_{ad} + H^+ \quad [2]$$

$$Fe(OH^-)_{ad} \rightleftarrows Fe(OH)_{ad} + e \quad [3]$$

$$Fe(OH)_{ad} \rightarrow (FeOH)^+ + e \text{ (rate determining)} \quad [4]$$

$$(FeOH)^+ + H^+ \rightleftarrows Fe^{+2} + H_2O \quad [5]$$

These equations take formal account of the simultaneous coverage of the surface by adsorbed water molecules, hydroxyl ions, and the surface intermediate $Fe(OH)_{ad}$, and lead to the kinetic expression

$$i_+ = 2Fk_4^w(k_3^w k_2^w/a_{(H^+)}k_{-3}^w k_{-2}^w)\,\theta_1 \exp(3\mathbf{F}E/2RT) \quad [6]$$

where $\theta_1 = (k_1^w a_w/(k_1^w a_w + k_{-1}^w)$ is the fraction of the total possible adsorption sites occupied by $Fe(H_2O)_{ad}$, a_w is the activity of water, and the k_i^w are the rate constants with infinitely dilute water solvent as the reference state. Since the infinitely dilute water solvent is the reference state for all solvent compositions including pure alcohol, the superscript "w" will be omitted in subsequent rate expressions.

In a subsequent paper, Kelly (4) reported on the results obtained for the iron dissolution and hydrogen evolution reactions on zone-refined iron in hydrogen-saturated sodium benzoate solutions (referred to as the inhibited system). The mechanism proposed for the iron dissolution reaction in the inhibited system involved the formation of an electrochemically active surface intermediate from the adsorbed anion, $(FeB_z^-)_{ad}$, and $(FeOH)_{ad}$. Then by analogy with the inhibited system, an alternate mechanism for the noninhibited system was proposed. If to the reactions

Key words: absolute acidity, electrochemical kinetics, corrosion, iron, ethanol-water.

represented by Eq. [1]-[3] are added the reactions represented by Eq. [7] and [8]

$$(FeOH)_{ad} + Fe(HOH)_{ad} = [(FeOH) \cdot Fe(HOH)]_{ad} \equiv (I)_{ad} \quad [7]$$

$$(I)_{ad} \rightarrow (FeOH)^+ + Fe(HOH)_{ad} + e \text{ (rds)} \quad [8]$$

where [8] is now the rate determining step, Eq. [6] becomes

$$i_+ = 2FK_8k_7k_3k_2/[k_{-7}k_{-3}k_{-2}(a_{H^+})]\ \theta_1^2 \exp(3\mathbf{F}E/2RT) \quad [9]$$

The steady-state current is now second order with respect to θ_1, but remains unchanged with respect to pH and potential. In pure water $\theta_1 \sim 1$ and the effect of water on the anodic dissolution cannot be determined. The addition of ethanol to the aqueous acidic sulfate solution may provide a test for the alternate mechanisms as represented by Eq. [6] and [9]. However, changing the solvent system from HOH to EtOH-HOH introduces alternate reaction paths via other intermediates, *e.g.*, $(FeOEt)_{ad}$ and $Fe(EtOH)_{ad}$, and also introduces a junction potential into the measured cell potential when the measurements are made with respect to the aqueous calomel reference electrode. In order to compare the rates at constant potential and with respect to the same reference state (infinitely dilute water solvent), the measurements must be made with respect to an aqueous reference electrode. Here, the saturated aqueous calomel electrode was chosen as the reference electrode. Since the aqueous calomel electrode is in a constant environment (saturated aqueous KCl), its potential is constant and independent of changes in the solution composition on the other side of the liquid junction. The term potential is used here as a contraction for potential difference, *i.e.*, a Galvani potential difference, ${}^{M}\Delta^{S_1}\phi \equiv \phi_M - \phi_{S_1}$, between some point in the metal phase and some point S_1 in the solution phase. Although the absolute value of this potential cannot be determined, changes in this potential are obtained when the measurements are made with respect to some unchanging reference electrode. Here, however, the measured cell potential difference, E^s_{cell}, includes a liquid junction potential difference as well as the Galvani potential differences at the metal/solution interfaces, *i.e.*

$$(\phi_M - \phi_{Hg_2Cl_2/Hg} \equiv E^s_{cell} = (\phi_M - \phi_{S_1}) + (\phi_{S_1} - \phi_{S_2}) + (\phi_{S_2} - \phi_{Hg_2Cl_2/Hg})$$

where $(\phi_M - \phi_{S_1}) \equiv E^s_M$ is the Galvani potential difference for the metal electrode, (Fe or Pt), $(\phi_{S_1} - \phi_{S_2}) \equiv -E^s_L$ the liquid junction potential difference between EtOH-HOH solvent and saturated aqueous KCl, and $(\phi_2 - \phi_{Hg_2Cl_2/Hg}) \equiv -E_{SCE}$ is the Galvani potential difference for the reference electrode. Therefore, $E^s_{Fe,Pt} = E^s_{cell} + E^s_L + E_{SCE}$, and changes in the Galvani potential for iron or platinum are obtained when the cell potential E^s_{cell} is measured and the junction potentials E^s_L are known.

Junction Potentials

In solvents other than water it is useful to distinguish between two acidity measuring functions, pA and pH (5), defined as follows

$$pA = -\log a_+ = -\log c_{H^+}\, y^s_{H^+}\, f_{H^+} \quad [10]$$

$$pH = -\log a_{H^+} = -\log c_{H^+}\, y^s_{H^+} \quad [11]$$

where $y^s_{H^+}$ is the conventional molar lyonium ion activity coefficient in solvent S, and f_{H^+} is the "degenerate activity coefficient" for the transfer of proton from infinite dilution in solvent S to infinite dilution in H_2O (the reference state). The parameter f_{H^+} is also referred to as the "primary medium effect" term (6, 7). The pA function measures the actual proton activity, a_+, of the given solution, whereas pH measures the molar lyonium ion activity referred to the extremely dilute solution in the given solvent. Therefore, to correlate the rates of iron dissolution with respect to proton activity using the infinitely dilute water solvent, *w*, as the reference state, the pA of the solution must be measured. The pA can be obtained from a measurement of the emf of the Pt/H_2 electrode in the EtOH-HOH solvent with respect to the saturated aqueous calomel electrode, SCE

$$Pt\text{-}H_2 \text{ (1 atm)/Soln. (X)} \quad \text{in EtOH-HOH/}E^s_L\text{/KCl (sat. aq.) } Hg_2Cl_2\text{-Hg} \quad [1']$$

where

$$pA = -\log a_+ = -\log c_{H^+}\, y^s_{H^+}\, f_{H^+} = -E^s_{Pt}/0.06 \quad [12]$$

where $E^s_{Pt} = E^s_{cell(Pt)} + E_{SCE} + E^s_L$. Again, however, for measurements in each solvent system S, the liquid junction potential E^s_L must be known, and this is known if values for f_{H^+} in each solvent can be determined. Grunwald (1, 8) and co-workers Gutbezahl and Berkowetz have determined the thermodynamic dissociation constants, (pK^s), of weak uncharged acids HA (acetic acid type) and cation acids HA^+ (ammonium type) in ethanol-water solvents. An extrathermodynamic relationship, the activity postulate (9), was used to obtain values for the "degenerate" activity coefficient of the hydrogen ions, f_{H^+}. From a knowledge of f_{H^+} it was then possible to calculate the junction potentials in cells like (1'). Rearranging Eq. [12], the liquid junction potential

$$E^s_L = 0.06 \log (c_{H^+}\, y^s_{H^+}\, f_{H^+}) - (E_{cell(Pt)} + E_{SCE}) \quad [13]$$

where for dilute solutions, $y^s_{H^+}$ can be estimated from the Debye-Huckel limiting law, all other quantities on the right-hand side of Eq. [13] are known or measurable, and E^s_L may be calculated (1). Values of E^s_L as a function of EtOH-HOH composition are shown in Fig. 1. The measurements reported here are for a solution containing 0.5*M* H_2SO_4, which is not dilute, but is constant for all solvents S. The assumption is made that the liquid junction potential is approximately independent of acid concentration to 0.5*M* acid. This assumption could lead to errors of about 0.1 pA units (5).

Aleksandrov and Izmailov (10, 11) obtained values for the "degenerate" activity coefficient of the hydrogen ion, f_{H^+}, which were not too greatly different from those of Grunwald and Gutbezahl. However, more recently, Popovych and Dill (12, 13) have obtained values which were greatly different. Liquid junction potentials calculated from these values were not only different in magnitude but also in sign. It will be shown later that these values are not consistent with the present study.

With this background and the values for E^s_L in Fig. 1, the analysis of the anodic dissolution of iron can be attempted. The experimental system can be represented as

$$(Pt \text{ or } Fe) - H_2 \text{ (1 atm)/0.50}M\ H_2SO_4 \quad \text{in EtOH-HOH//}E'^s_L\text{//0.50}M\ H_2SO_4 \quad \text{in HOH//}E^w_L\text{//KCl (sat. aq.) HgCl-Hg} \quad [2']$$

where $E'^s_L + E^w_L = E^s_L$ and

$$E^s_{Fe} = E^s_{cell(Fe)} + E_{SCE} + E^s_L$$
$$E^s_{Pt} = E^s_{cell(Pt)} + E_{SCE} + E^s_L \quad [14]$$

where $E_{cell(Fe\text{ or }Pt)}$ is the experimental measured potential *vs.* the saturated aqueous calomel electrode. The calomel electrode becomes inoperable in solutions of

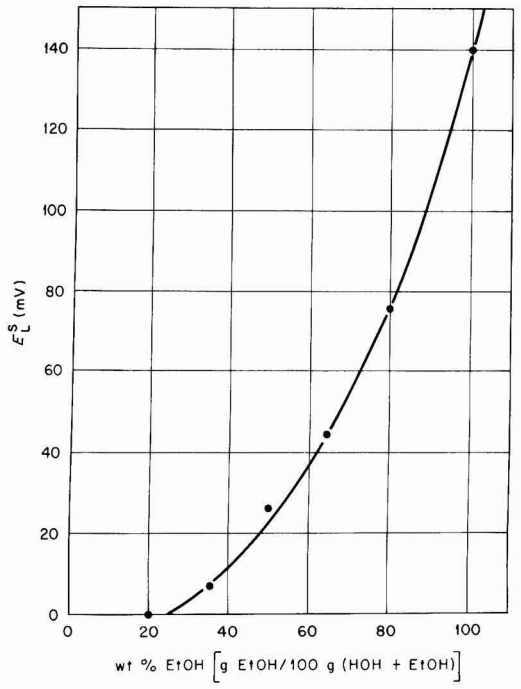

Fig. 1. Liquid junction potentials, E^s_L, between soln X in EtOH-HOH solvent and saturated aqueous KCl as a function of weight per cent EtOH in EtOH-HOH solvent.

high ethanol content due to plugging of the asbestos wick with KCl precipitation. According to [2'] a solution 0.5*M* H_2SO_4 in water was interposed between the calomel electrode and the ethanol-water solution. The liquid junction potential E^s_L now becomes the sum of the two junctions E'^s_L and E^w_L. Several measurements in cells like [1'] and [2'] showed that $E^s_L \sim E'^s_L + E^w_L$ within about 5 mV. An additional iron electrode was included in the cell for the polarization measurements. The liquid junction potential E^w_L was constant and probably less than 5 mV (14).

Experimental

The high purity zone-refined iron[1] electrodes used in this investigation were cut from ¼ in. rod stock and were ¼ in. to ⅜ in. long. The electrodes were mounted in conventional Teflon electrode holders (15). The entire cell assembly was made from Pyrex glass and Teflon. The apparatus was designed so that the addition and removal of solution could be accomplished without opening the apparatus to the atmosphere. The test electrode compartment was a flat bottom cylinder made from a 55/50 TS ground glass joint. The ground surface was carefully removed by fire polishing. A glass jacket was provided for circulating water, so that the solution temperature could be maintained at 30.00° ± 0.03°C. The cap to the test electrode compartment was machined from Teflon and had seven convenience ports. The ports were ¼ in. Teflon Swagelock fittings which were epoxied into holes drilled through the Teflon cap. One port provided for the delivery of H_2 saturated 0.5*M* H_2SO_4 in water. A glass tube passed from the bottom of the test electrode compartment (cell) through the walls of the water jacket, to a Teflon Nupro plastic valve,[2] diaphragm stem model. This tube and valve arrangement provided for solution sample removal for the electrometric Karl Fischer water analysis,[3] and also for solution drainage, so that in conjunction with the solvent delivery facilities, varying EtOH-HOH compositions could be obtained. Ultrapure H_2 gas was provided by a Matheson generator. The H_2 gas passed successively through a presaturator containing 0.5*M* H_2SO_4 in absolute EtOH, a reservoir containing the 0.5*M* H_2SO_4 in absolute EtOH which is to be delivered to the electrochemical cell, the electrochemical cell, a reservoir containing the 0.5*M* H_2SO_4 in water, finally exiting to the atmosphere through a bubbler-trap which prevented back diffusion of atmospheric oxygen into the aqueous acid reservoir. Other ports in the test cell cap provided for the Fe test electrode, an Fe polarizing electrode for *p*A determinations, H_2 gas exit, and a Haber-Luggin capillary probe. Another glass tube for H_2 gas inlet passed through the wall of the water jacket near the top of the test cell and extended down to the bottom of the cell. An external saturated aqueous calomel electrode was used as a reference electrode in conjunction with the Haber-Luggin capillary probe. Flexible Teflon "spaghetti" tubing (⅛ in. or ¼ in.) was used for convenient connections. A Teflon-coated bar magnet was used for stirring in the test cell.

The absolute ethanol and reagent grade sulfuric acid were used without further purification. The water was triply distilled. The iron electrodes were etched in 50/50 H_2SO_4-water, rinsed in distilled water and ethanol, dried, then vacuum annealed at 800°C for 12 hr at 10^{-7} Torr, and slow cooled. The annealed electrodes were again etched in 50/50 H_2SO_4-water, rinsed in distilled water and ethanol, and transferred to the cell. In a typical experiment the iron electrodes were first exposed to the aqueous acid environment from one to several days, during which the solution was frequently replaced with fresh solution. As with Kelly (2), a well-behaved system exhibited no polarization hysteresis phenomenon, and this fact was used as the basic criterion by which the suitability of the system for investigation was determined. The solution was then drained and the 0.5*M* H_2SO_4 in absolute ethanol was delivered to the cell. Again, the above criterion was used for suitability for investigation. Usually, when no polarization hysteresis was observed in the aqueous environment, none was observed in the absolute ethanol environment. The absolute ethanol solvent composition was increased in water content by partial drainage of the cell and addition of the aqueous acid. When the "hysteresis" criterion was met in the aqueous and absolute ethanol environment, the solvent composition could be varied at will with increasing or decreasing water content, and no polarization hysteresis was observed at any intermediate solvent composition. Sometimes, polarization data on a given electrode were accumulated over a period of one week's time.

The polarizing currents were furnished by using the Research Model Anotrol Potentiostat in the galvanostatic mode. The currents were measured by recording the voltage drop across precision resistors in the polarizing circuit. The potentials were measured with a 610B Keithley Electrometer and recorded with a 10 mV Brown recorder.

Results

The anodic polarization data in the acidic ethanol-water environments are shown in Fig. 2. Here the total net dissolution current is plotted as a function of $E^s_{cell(Fe)}$ (*i.e.*, the potential of the iron electrode *vs.* the saturated aqueous calomel electrode). The Tafel slope $(dE/d \log i) = 2/3(2.3\ RT/\mathbf{F})$, and is independent of solvent composition. This implies that in each solvent S, a mechanism similar to that in pure water prevails. The alphabetical listing reveals the sequence in which

[1] Prepared and analyzed by Materials Research Corporation.
[2] Manufactured by Swagelock.

[3] The authors wish to express their appreciation to Dr. Richard Raridon of the ORNL Chemistry Division for the electrometric Karl Fischer water analysis.

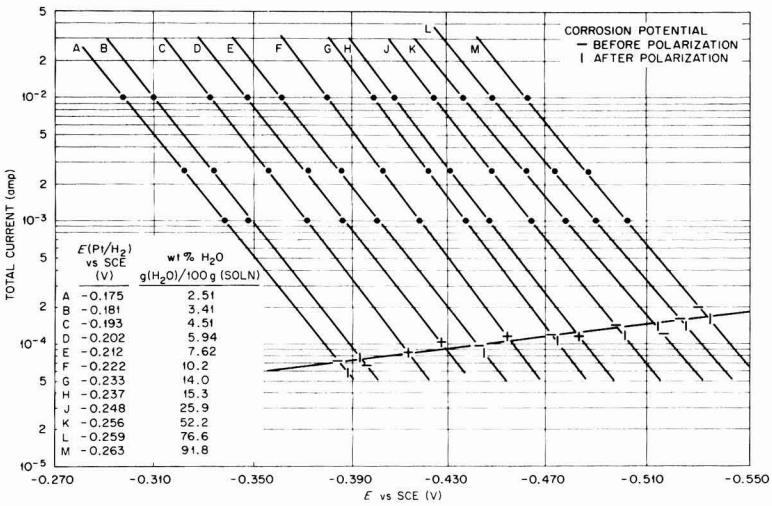

Fig. 2. Anodic polarization of iron in H_2-saturated 0.50M H_2SO_4 in various EtOH-HOH solvents, T = 30°C, electrode area 0.97 cm².

the polarizations were made, starting generally with the least aqueous environment. The polarization in pure water was indistinguishable from the polarization in 91.8% water shown in Fig. 2. The pure water result was repeated numerous times, and was in excellent agreement with the results reported by Eichkorn, Lorenz, Albert, and Fischer (16) for zone-refined iron. Also included in Fig. 2 are the weight per cent H_2O (as $g[H_2O]/100g$ [soln]), the potentials of the Pt-H_2 electrode *vs.* SCE and the corrosion potentials before polarization (horizontal slash) and after polarization (vertical slash). In Fig. 1 the liquid junction potentials between the acidic ethanol-water solution and the saturated aqueous KCl solution are plotted as a function of weight per cent H_2O in EtOH-H_2O solvent, where the weight per cent H_2O was calculated on the basis of $g(H_2O)/100g$ (EtOH + HOH). The weight per cent reported in Fig. 2 is calculated on the basis of g(HOH)/100g (EtOH + HOH + H_2SO_4). Consequently to obtain values for the liquid junction potentials from Fig. 1, the Karl-Fischer determinations of the water content in Fig. 2 are corrected to weight per cent (HOH)/100g (EtOH + HOH). For this calculation it was assumed that the density of the solution was the same as the density of the pure EtOH-HOH solvent at the Karl Fischer estimated water content. With these values for E^s_L, the results in Fig. 2 are replotted. Here, in Fig. 3, the polarizations are reported as current density (amperes/square centimeter) *vs.* the absolute potential of the iron electrode, E^s_{Fe}, *i.e.*, the potential of the iron electrode in solvent S *vs.* the standard hydrogen electrode in water, (SHE)^w. Also included in Fig. 3 are the potentials of the Pt/H_2 electrode *vs.* the (SHE)^w. At this point, it is probably worthwhile to emphasize that the measurement of the *p*A of the solutions, which is identically *p*H in pure water solvent, is defined according to Eq. [10]-[12]. The validity of such measurements is a test of the extra-thermodynamic postulates used for the estimation of the "degenerate" activity coefficients f_{H^+}, as a function of solvent composition. Such an application of the *p*A scale to inorganic reaction kinetics (in our case the corrosion of iron) has not heretofore been demonstrated. Unfortunately, the introduction of the measured *p*A values into the rate expression (to be derived for the EtOH-HOH solvent) does not provide

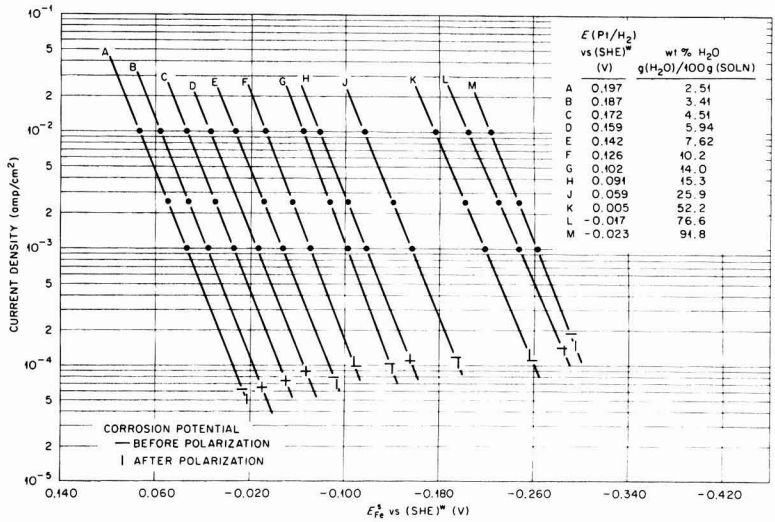

Fig. 3. Anodic polarization of iron in H_2-saturated 0.50M H_2SO_4 in various EtOH-HOH solvents, T = 30°C, electrode area 0.97 cm².

a direct test. In changing the solvent from pure water to EtOH-HOH, the activity of the water as well as the *p*A is changed, and some assumption must probably be made relating to the water activity, and presumably also to the activity of ethanol. It should be emphasized that the absolute potentials reported in Fig. 3 are based on the junction potentials provided by Grunwald and Gutbezahl. An interpretation of the results using the junction potentials provided by Popovych and Dill (12, 13) will be considered later.

The derivation of the rate expression for EtOH-HOH solvent follows very closely the mechanism proposed by Kelly (4) for the inhibited system. It is postulated that in pure EtOH the dissolution of iron proceeds by a mechanism similar to that in pure water, and in mixed solvents a simultaneous dissolution occurs by both water and alcohol, *i.e.*, $i_+ = i_w + i_a$, where i_+ is the total net anodic dissolution current, and i_w and i_a are the currents due to water and alcohol, respectively. Equations [16]-[27] give a formal description of the mechanism proposed

$$\mathrm{Fe} + \mathrm{HOH} \overset{1}{=} \mathrm{Fe(HOH)_{ad}} \qquad [16]$$

$$\mathrm{Fe(HOH)_{ad}} \overset{2}{=} \mathrm{(FeOH^-)_{ad}} + \mathrm{H^+} \qquad [17]$$

$$\mathrm{(FeOH^-)_{ad}} \overset{3}{=} \mathrm{(FeOH)_{ad}} + e \qquad [18]$$

$$\mathrm{(FeOH)_{ad}} + \mathrm{Fe(HOH)_{ad}} \overset{4}{=} [\mathrm{(FeOH)\cdot(Fe(HOH)]_{ad}} \equiv \mathrm{(I)_w} \qquad [19]$$

$$\mathrm{(I)_w} \overset{5}{\rightarrow} \mathrm{(FeOH^+)} + \mathrm{Fe(HOH)_{ad}} + e \quad \text{rds} \qquad [20]$$

$$\mathrm{(FeOH^+)} + \mathrm{H^+} \overset{6}{=} \mathrm{Fe^{++}} + \mathrm{HOH} \qquad [21]$$

and simultaneously

$$\mathrm{Fe} + \mathrm{EtOH} \overset{7}{=} \mathrm{Fe(EtOH)_{ad}} \qquad [22]$$

$$\mathrm{Fe(EtOH)_{ad}} \overset{8}{=} \mathrm{(FeOEt^-)_{ad}} + \mathrm{H^+} \qquad [23]$$

$$\mathrm{(FeOET^-)_{ad}} \overset{9}{=} \mathrm{(FeOEt)_{ad}} + e \qquad [24]$$

$$\mathrm{(FeOET)_{ad}} + \mathrm{Fe(EtOH)_{ad}} \overset{10}{=} [\mathrm{(FeOEt)\cdot Fe(EtOH)]_{ad}} \equiv \mathrm{(I)_a} \qquad [25]$$

$$\mathrm{(I)_a} \overset{11}{\rightarrow} \mathrm{(FeOEt^+)} + e \qquad \text{rds} \qquad [26]$$

$$\mathrm{(FeOEt^+)} + \mathrm{H^+} \overset{12}{=} \mathrm{Fe^{++}} + \mathrm{EtOH} \qquad [27]$$

These equations take account of the simultaneous coverage by the several intermediates, where $[\mathrm{Fe(HOH)_{ad}}] = \beta\theta_1$, $[\mathrm{(FeOH^-)_{ad}}] = \beta\theta_2$, $[\mathrm{(FeOH)_{ad}}] = \beta\theta_3$, $[\mathrm{(I)_w}] = \beta\theta_1$, $[\mathrm{Fe(EtOH)_{ad}}] = \beta\theta_4$, $[\mathrm{(FeOEt^-)_{ad}}] = \beta\theta_5$, $[\mathrm{(FeOEt)_{ad}}] = \beta\theta_6$, $[\mathrm{(I)_a}] = \beta\theta_a$, and $a_+ = c_{H^+} y^s_{H^+} f_{H^+}$, where θ_i is the fraction of the total possible adsorption sites occupied by $[i]$, and the surface concentrations ($\beta\theta_i$), are expressed in moles/square centimeter, with β a proportionality constant, y^s_i the conventional molar activity coefficient in solvent S, and f_i the "degenerate" activity coefficient. The reference state for f_i is the infinitely dilute aqueous solvent for all solvent compositions including pure ethanol. A kinetic description of this mechanism in the steady state is given by Eq. [28]-[37]

$$\frac{i_w}{\mathbf{F}} = \bar{k}_3[\beta\theta_2] - \bar{k}_{-3}[\beta\theta_3] + \bar{k}_5[\beta\theta_{I_w}] \qquad [28]$$

$$\beta\left(\frac{\partial\theta_{I_w}}{dt}\right)_{ss} = 0 = \bar{k}_4[\beta\theta_3][\beta\theta_1] - \bar{k}_{-4}[\beta\theta_{I_w}] - \bar{k}_5[\beta\theta_{I_w}] \qquad [29]$$

$$\beta\left(\frac{\partial\theta_3}{\partial t}\right)_{ss} = 0 = \bar{k}_3[\beta\theta_2] - \bar{k}_{-3}[\beta\theta_3] - \bar{k}_4[\beta\theta_3][\beta\theta_1] + \bar{k}_4[\beta\theta_{I_w}] \qquad [30]$$

$$\beta\left(\frac{\partial\theta_2}{\partial t}\right)_{ss} = 0 = \bar{k}_2[\beta\theta_1] - \bar{k}_{-2}[\beta\theta_2][a_+] - \bar{k}_3[\beta\theta_2] + \bar{k}_{-3}[\beta\theta_3] \qquad [31]$$

$$\beta\left(\frac{\partial\theta_1}{\partial t}\right)_{ss} = 0 = \bar{k}_1[a_w][(1-\theta_T)] - \bar{k}_{-1}[\beta\theta_1] + \bar{k}_2[\beta\theta_1] - \bar{k}_{-2}[\beta\theta_2][a_+] - \bar{k}_4[\beta\theta_3][\beta\theta_1] + \bar{k}_{-4}[\beta\theta_{I_w}] \qquad [32]$$

and similarly for dissolution by ethanol

$$\frac{i_a}{\mathbf{F}} = \bar{k}_9[\beta\theta_5] - \bar{k}_{11}[\beta\theta_{I_a}] \qquad [33]$$

$$\beta\left(\frac{\partial\theta_{I_a}}{\partial t}\right)_{ss} = 0 = \bar{k}_{10}[\beta\theta_6][\beta\theta_4] - \bar{k}_{-10}[\beta\theta_{I_a}] - \bar{k}_{11}[\beta\theta_{I_a}] \qquad [34]$$

$$\beta\left(\frac{\partial\theta_6}{\partial t}\right)_{ss} = 0 = \bar{k}_9[\beta\theta_5] - \bar{k}_{-9}[\beta\theta_6] - \bar{k}_{10}[\beta\theta_6][\beta\theta_4] + \bar{k}_{-10}[\beta\theta_{I_a}] \qquad [35]$$

$$\beta\left(\frac{\partial\theta_5}{\partial t}\right)_{ss} = 0 = \bar{k}_8[\beta\theta_4] - \bar{k}_{-8}[\beta\theta_5][a_+] - \bar{k}_9[\beta\theta_5] + \bar{k}_{-9}[\beta\theta_6] \qquad [36]$$

$$\beta\left(\frac{\partial\theta_4}{\partial t}\right)_{ss} = 0 = \bar{k}_7[a_a][(1-\theta_T)] - \bar{k}_{-7}[\beta\theta_4] - \bar{k}_8[\beta\theta_4][\beta\theta_6] + \bar{k}_{-8}[\beta\theta_5][a_+] - \bar{k}_{10}[\beta\theta_4][\beta\theta_6] + \bar{k}_{-10}[\beta\theta_{I_a}] \qquad [37]$$

Here, a_w, a_a are the activities of water and alcohol, respectively, in the mixed solvent and a_+ is the "absolute activity" of the proton (*vide* Eq. [12]). The $\bar{k}$'s are again the electrochemical rate constants referred to the extremely dilute aqueous solvent as the reference state. Equations [28]-[37] reduce to the steady-state solution

$$\frac{i_+}{\mathbf{F}} = \frac{i_w}{\mathbf{F}} + \frac{i_a}{\mathbf{F}} = \frac{k_5}{[a_+]}\left(\frac{k_4}{k_{-4}}\frac{k_3}{k_{-3}}\frac{k_2}{k_{-2}}(\theta_1)^2 \exp\frac{3\mathbf{F}E^s_{Fe}}{2\kappa T}\right] + \frac{k_{11}}{[a_+]}\left[\frac{k_{10}}{k_{-10}}\frac{k_9}{k_{-9}}\frac{k_8}{k_{-8}}(\theta_4)^2 \exp\frac{3\mathbf{F}E^s_{Fe}}{2RT}\right] \qquad [38]$$

where $\theta_1 = \dfrac{1}{1 + \dfrac{k_{-1}k_7 a_a}{k_1 k_{-7} a_w}}$ and $\theta_4 = \dfrac{1}{1 + \dfrac{k_1 k_{-7} a_w}{k_{-1} k_7 a_a}}$.

Equation [38] assumes that the surface coverage is mostly adsorbed water and alcohol; $\theta_1 + \theta_4 \sim \theta_T$ and $\theta_T \sim 1$. In the detailed derivation of Eq. [38], $(\theta_1 + \theta_4) \sim 1$ implies $k_{-1}\,k_{-7} << k_{-1}\,k_7\,a_a + k_1\,k_7\,a_w$, and $k_{-1}\,k_{-7} \sim 0$. It is now further assumed that over the range of solvent composition studied $i_w >> i_a$, leading to Eq. [39]

$$i_+ = \frac{k}{[a_+]}\left[\frac{1}{1 + \lambda'\dfrac{a_a}{a_w}}\right]^2 \exp\frac{3\mathbf{F}E^s_{Fe}}{2RT} \qquad [39]$$

where $k = \mathbf{F}\left(k_5\dfrac{k_4}{k_{-4}}\dfrac{k_3}{k_{-3}}\dfrac{k_2}{k_{-2}}\right)$ and $\lambda' = \dfrac{k_{-1}k_7}{k_1 k_{-7}}$.

It is assumed that the activity ratio $a_a/a_w = N_a/N_w$ where N_a and N_w are the mole fractions of alcohol and water, respectively. Further, it can be shown that $N_a/N_w = 18/46$ [weight per cent (EtOH)/ weight per cent (HOH)] which leads to Eq. [40]

$$i_+^s = \frac{k}{[a_+]}\left[\frac{1}{1+\lambda\dfrac{\text{w/o (EtOH)}}{\text{w/o (HOH)}}}\right]^2 \exp\frac{3FE^s_{Fe}}{2RT} \quad [40]$$

The value for k in Eq. [40] was obtained from the results in pure water where $\dfrac{\text{w/o EtOH}}{\text{w/o HOH}} = 0$, and knowing k, the value for λ was a grand average value calculated from all data for solvent compositions ranging from *ca.* 10-50 w/o (HOH). In logarithmic form Eq. [40] becomes

$$\log(i_+^s) = 3.1833 - E^s_{Pt}/0.06 + E^s_{Fe}/0.04 + 2\log\left[\frac{1}{1+1.4R}\right] \quad [41]$$

where R = w/o (EtOH)/w/o (HOH), $-\log(a_+) = -E^s_{Pt}/0.06$, $\log k = 3.1833$ and $\lambda = 1.4$. It should be recalled that the "absolute" acidity, $pA = -\log(a_+) = -E^s_{Pt}/0.06$. A plot of the experimental anodic current densities, (i_+^s), at constant potential $E^s_{Fe} = -0.222\bar{v}$ *vs.* $(SHE)^w$, as a function of solvent composition, for the results reported in Fig. 3, is presented in Fig. 4. The calculated values in Fig. 4 were obtained from Eq. [41]. Also included in Fig. 4 are the results from another iron electrode of larger surface area. A better fit of the data would be obtained if λ was recalculated for each electrode. The value for λ is not expected to be the same for different electrodes since it is a ratio of rate constants. The experimental current densities reported in Fig. 4 were obtained analytically as follows. In pure water at $E^s_{Fe} = -0.222\bar{v}$, the current density is 10^{-2} A/cm^2, for which $\log(i_+^s) = -2.0$. Therefore, it follows from Fig. 3 that

$$\log(i_+^s)_{E^s_{Fe}} = -2.0\,\frac{(E^s_{Fe})_{i+} - (-0.222)}{0.040} \quad [42]$$

where $(i_+^s)_{E^s_{Fe}}$ is the anodic current density at solvent composition S and constant potential $E^s_{Fe} = -0.222\bar{v}$ *vs.* $(SHE)^w$, $(E^s_{Fe})_{i+}$ is the potential of the iron electrode *vs.* $(SHE)^w$ at $(i_+^s) = 10^{-2}$ A/cm^2 and solvent composition S, and 0.040 is the anodic Tafel slope, $\partial(E^s_{Fe})/\partial(\log i_+)_{s,a+}$, at constant solvent composition S and proton activity, a_+.

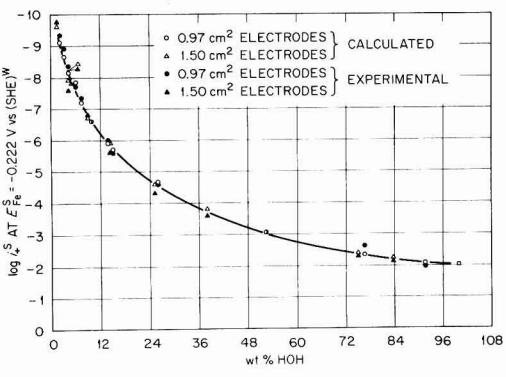

Fig. 4. Anodic current density for iron in H_2-saturated 0.50M H_2SO_4-EtOH-HOH as a function of weight per cent (HOH) at fixed potential, $E^s_{Fe} = -0.222\bar{v}$ *vs.* $(SHE)^w$ at 30°C.

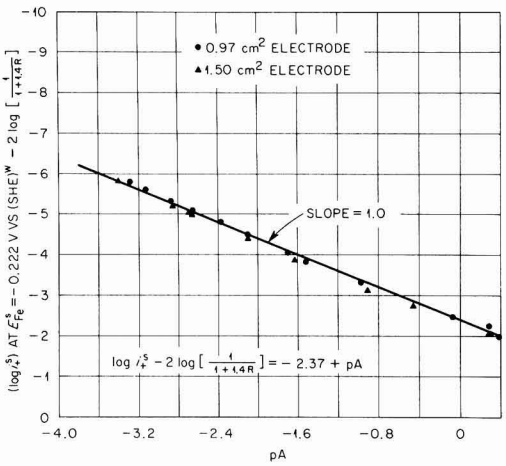

Fig. 5. The anodic current density for iron in H_2-saturated 0.50M H_2SO_4-EtOH-HOH as a function of pA at fixed potential, $E^s_{Fe} = -0.222\bar{v}$ *vs.* $(SHE)^w$ at 30°C.

The calculated values for the anodic current density at constant $E^s_{Fe} = -0.222v$ are again presented in Fig. 5. The results are corrected for the solvent dependence, $2\log\left(\dfrac{1}{1+\lambda R}\right)$, and plotted as a function of $pA = -E^s_{Pt}/0.06$. According to Eq. [41]

$$\left(\partial\left[\log(i_+^s)_{E^s_{Fe}} - 2\log\left(\frac{1}{1+\lambda R}\right)\right] \Big/ \partial pA\right) = 1$$

if the reaction is first order in the reciprocal of the proton activity. The theoretical solid line drawn with unit slope provides an excellent fit to the data. Similarly, according to Eq. [41], after accounting for the coverage factor, and at constant anodic current density, the electrode potential should be a linear function of pA. The proportionality constant should be equal to −0.040 V/pA if the dissolution reaction is first order in the reciprocal of the proton activity. The electrode potential at constant anodic current density of 10^{-2} A/cm^2 is plotted as a function of pA in Fig. 6. The straight line drawn with a slope of −0.042 V/pA fits the data, further confirming the first order dependence and the coverage factor term.

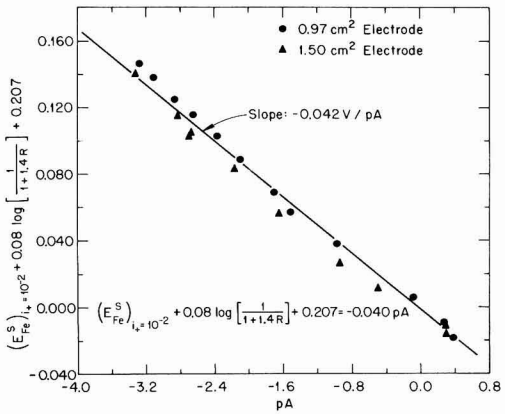

Fig. 6. The variation of the iron electrode potential in H_2-saturated 0.50M H_2SO_4-EtOH-HOH as a function of pA, at a constant anodic current density of 1×10^{-2} A/cm^2, at 30°C.

The cathodic evolution of H_2 as a function of solvent has been investigated here to only a limited extent. The polarizations which have been made covered the range of solvent composition from pure water to about 98 w/o (EtOH), and have shown Tafel slopes, $(\partial E^s_{Fe}/\partial \log i_-)_{s,a+}$, of 109-119 mV [approximately 2.3 $(2\ RT/\mathbf{F})$]. Since the results containing EtOH are similar to that which is observed in pure water solvent, it was postulated that the cathodic current was first order with respect to protons and that discharge occurred at both the adsorbed water sites, $Fe(H_2O)_{ads} \equiv \theta_1$, and at the adsorbed alcohol sites, $Fe(EtOH)_{ads} \equiv \theta_4$. A kinetic description of this mechanism is given by Eq. [43]

$$-\frac{(i_-{}^s)}{\mathbf{F}} = k_w a_+ \theta_1 \exp\frac{-\mathbf{F}E^s_{Fe}}{2RT} + k_a a_+ \theta_4 \exp\frac{-\mathbf{F}E^s_{Fe}}{2RT} \qquad [43]$$

where recalling the anodic dissolution mechanism

$$\theta_1 = \frac{1}{1+\lambda R} \text{ and } \theta_4 = \frac{\lambda R}{1+\lambda R}$$

in the steady state. Again it is assumed that the rate via the aqueous mechanism is much greater than via the alcohol mechanism, and

$$-i_-{}^s = k_w a_+ \left(\frac{1}{1+\lambda R}\right) \exp\frac{-\mathbf{F}E^s_{Fe}}{2RT} \qquad [44]$$

From Eq. [39] and [44] the corrosion potential and corrosion current as a function of pA and θ_1 may be obtained. It is recalled that at the corrosion potential, $E^s_{Fe(corr)}$, $i_-{}^s = i_+{}^s = i^s_{(corr)}$, and therefore

$$\log i^s_{(corr)} - 5/4 \log\left(\frac{1}{1+1.4R}\right) + 3.562 = -1/2\ pA \qquad [45]$$

$$E^s_{Fe(corr)} + 0.03 \log\left(\frac{1}{1+1.4R}\right) + 0.270 = -0.06\ pA \qquad [46]$$

The constants in Eq. [45] and [46] were obtained from the results in pure water where $R = 0$, $E^s_{Fe(corr)} = -0.292\bar{v}$ *vs.* $(SHE)^w$, $i^s_{(corr)} = 1.8 \times 10^{-4}$ A/cm², and $E_s{}^{Pt} = -0.022\bar{v}$ *vs.* $(SHE)^w$. Figure 7 shows the corrosion current, $\log i^s_{(corr)}$, (corrected for coverage), as a function of pA, and the theoretical line with slope $-1/2$ provides a satisfactory fit to the data. Similarly, the corrosion potential, $E^s_{Fe(corr)}$, (corrected for coverage) as a function of pA is shown in Fig. 8 and again the theoretical line with slope -0.060 provides an excellent fit to the data, *i.e.*, $\partial(E^s_{Fe(corr)} + 0.03 \log \theta_1)/\partial pA = -2.303\ RT/\mathbf{F}$.

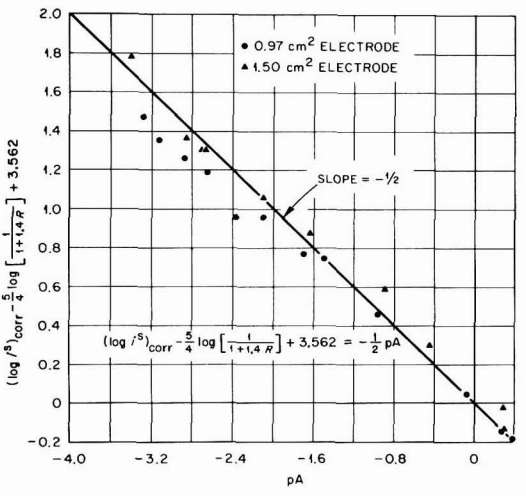

Fig. 7. The corrosion current for iron in H_2-saturated 0.50M H_2SO_4 EtOH-HOH as a function of pA at 30°C.

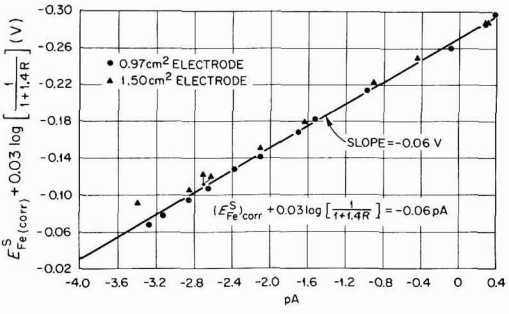

Fig. 8. The corrosion potential for iron in H_2-saturated 0.50M H_2SO_4-EtOH-HOH as a function of pA at 30°C.

Equation [46] can be written in terms of the experimentally measured cell potentials for Fe and Pt. In this form it is seen that the corrosion potential is independent of the liquid junction potential E^s_L

$$E^s_{(cell\ Fe)corr} = -0.270 + E^s_{(cell)Pt} - 0.03 \log\left[\frac{1}{1+\lambda R}\right] \qquad [47]$$

The value $\lambda = 1.4$ (obtained from Eq. [40]) does indeed give good agreement between the calculated and the observed corrosion potentials. Using Eq. [47] a better value would be $\lambda = 1.8$. Alternatively, with this value of λ (say, gotten now from Eq. [47], Eq. [41] and [45] are better satisfied using Grunwald's (1) or Aleksandrov's and Izmailov's (10, 11) set of junction potentials rather than Popovych's (12, 13).

Accepting this value for λ from Eq. [47], a set of liquid junction potentials can be generated from Eq. [41]. Proton activities calculated using these experimentally determined junction potentials are compared with those estimated using the junction potentials of Grunwald and Gutbezahl (1), Aleksandrov and Izmailov (10, 11), and Popovych and Dill (13). A plot of these proton activities as a function of R is shown in Fig. 9. In this form, it is seen that the proton activities of Popovych and Dill are unacceptable.

Summary

Values for the junction potentials (1) between acidic EtOH-HOH solutions and saturated aqueous KCl were used to interpret the electrochemical polarization behavior of the active iron electrode in acidic EtOH-HOH solutions. The junction potentials were obtained from a correlation of the pK^s of organic acids in EtOH-HOH solvents. The correlation was based on the validity of the "activity postulate" of Grunwald and co-workers (1, 8).

The mechanism suggested by Kelly (4) for iron dissolution in hydrogen saturated sodium benzoate solutions (referred to as the inhibited system) was accepted with a few additional assumptions: the surface coverage was mostly adsorbed water $(Fe \cdot (H_2O)_{ad})$ and alcohol $(Fe \cdot (EtOH)_{ad})$, *i.e.*, $\theta_1 + \theta_4 \sim 1$; there was a simultaneous dissolution by EtOH and HOH, with the dissolution rate by water much greater than by alcohol; and finally it was assumed that the ratio of the activity of alcohol to water was proportional to the weight per cent ratio. Thus, in a competition for active sites on the electrode surface, alcohol acts as a "relative" inhibitor. The decision to test this mechanism to the corrosion data was based primarily on the observation that the anodic Tafel slope, $(\partial E/\partial \log i_+)_{s,a+} = 2/3\ (2.303\ RT/\mathbf{F})$, and was unchanged for all solvent compositions. Thus a mechanism (2, 3)

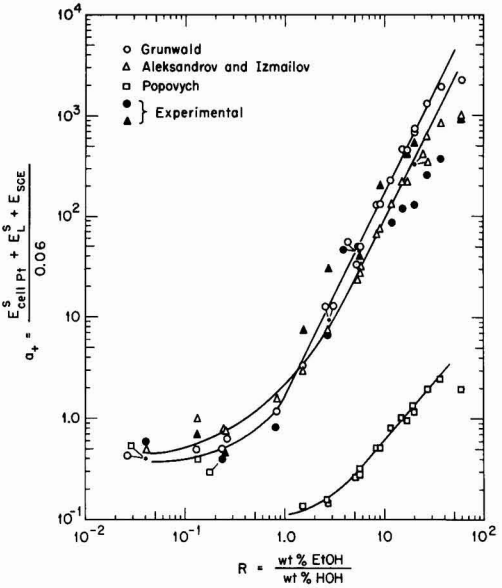

Fig. 9. The variation of proton activities, a_+, as a function of R = w/o EtOH/w/o HOH; proton activities calculated using several sets of liquid junction potentials, E^s_L.

similar to that accepted for dissolution in water solvent was suggested. The further choice of the mechanism suggested by Kelly (4) for the inhibited system was based primarily on the better fit to the results for the anodic polarization with a second order dependency on coverage.

The cathodic polarizations gave a Tafel slope ($\partial E/\partial \log i_-)_{s,a+} \sim 2$ (2.303 $RT/\mathbf{F}$), and was unchanged for all solvent compositions. On the basis of this observation, and to explain the observed variation of corrosion potential and corrosion current with solvent, it was postulated that the cathodic partial current was first order in both coverage, θ_1, and the activity of the protons, a_+.

Alternatively, accepting the corrosion mechanism, an "experimental" set of liquid junction potentials was generated. The proton activities, (a_+), calculated using these junction potentials were in much better agreement with those estimated using the values of E^s_L from Grunwald and Gutbezahl (1) or Aleksandrov and Izmailov (10, 11) than with the proton activities calculated using the junction potentials proposed by Popovych (12) and Popovych and Dill (13).

Acknowledgment

The authors would like to express their appreciation to Dr. Eugene J. Kelly of the ORNL Chemistry Division for the many hours spent in discussions of this work, particularly relating to the final form of the rate expression. We also would like to thank Dr. Robert E. Meyer of the ORNL Chemistry Division for his many constructive criticisms.

This research was sponsored by the U.S. Atomic Energy Commission under contract with the Union Carbide Corporation.

Manuscript submitted July 27, 1973; revised manuscript received Aug. 12, 1974.

Any discussion of this paper will appear in a Discussion Section to be published in the December 1975 JOURNAL. All discussion for the December 1975 Discussion Section should be submitted by Aug. 1, 1975.

Publication costs of this article were partially assisted by Oak Ridge National Laboratory.

REFERENCES

1. B. Gutbezahl and E. Grunwald, *J. Am. Chem. Soc.*, **75,** 565 (1953).
2. E. J. Kelly, *This Journal,* **112,** 124 (1965).
3. J. O'M. Bockris, D. Drazic, and A. R. Despic, *Electrochim. Acta,* **4,** 325 (1961).
4. E. J. Kelly, *This Journal,* **115,** 1111 (1968).
5. A. L. Bacarella, E. Grunwald, H. P. Marshall, and E. Lee Purlee, *J. Org. Chem.,* **20,** 747 (1955).
6. R. G. Bates, "Determination of pH," pp. 189 et seq., John Wiley & Sons, Inc., New York (1964).
7. R. A. Robinson and R. H. Stokes, "Electrolyte Solutions," pp. 351 et seq., Butterworth & Co., (Publishers) Ltd., London (1959).
8. E. Grunwald and B. J. Berkowitz, *J. Am. Chem. Soc.,* **73,** 4939 (1951).
9. E. Grunwald and S. Winstein, *ibid.,* **70,** 846 (1948).
10. V. A. Aleksandrov and N. A. Izmailov, *Zh. Fiz. Khim.,* **32,** 404 (1958).
11. N. A. Izmailov and V. A. Aleksandrov, *ibid.,* **31,** 2619 (1957).
12. O. Popovych, *Critical Rev. Anal. Chem.,* **1,** 73 (1970).
13. O. Popovych and A. J. Dill, *Anal. Chem.,* **41,** 456 (1969).
14. G. Bianchi, G. Faita, R. Galli, and T. Mussini, *Electrochim. Acta,* **12,** 439 (1967).
15. R. E. Meyer, *This Journal,* **106,** 930 (1959).
16. G. Eichkorn, W. J. Lorenz, L. Albert, and H. Fischer, *Electrochim. Acta,* **13,** 183 (1968).

Accelerated Life Testing of Lead-Acid Industrial Motive Power Cells

N. J. Maskalick*

Westinghouse Research Laboratories, Pittsburgh, Pennsylvania 15235

ABSTRACT

Depth of positive grid corrosion is a regular and precise indicator of cell degradation during life testing of the subject lead-acid cells. Average corrosion depth at constant temperature is directly proportional to (time on cycle test)$^{0.67}$ for Pb-5% Sb positive grids. The temperature dependence of the logarithm of the corrosion rate constant is employed to predict a room-temperature corrosion function. Lifetime at room temperature is then estimated to a predefined average depth of corrosion corresponding to actual failure in normal service. This test is capable of high precision predictions of cell lifetime in a period of 4-6 months, compared to 3-4 years in conventional testing.

The time required to test lead-acid cells is greatly shortened at high temperatures as was demonstrated by Willihnganz (1) in his work with cells on float service. He observed that the logarithm of the constant potential lifetime of lead-acid cells with lead-calcium positive grids increases linearly with the reciprocal absolute temperature, and that over-all positive plate growth can be plotted as a regular function of time on test. Cannone *et al.* (2) identified this functional dependence as parabolic for cells with pure lead, or lead-calcium positive grids, and as linear, for cells with lead-antimony positive grids. They extended and corroborated Willihnganz' work by demonstrating that the logarithm of the constant term in their derived positive plate growth functions is a linear function of the reciprocal absolute test temperature. They consequently specified a value of this constant for room temperature float service by log-linear extrapolation of high temperature results.

Cell life, and positive plate growth, in all of these prior experiments, must be considered to be directly related to over-all positive plate corrosion current and time. In the case of a constant voltage test, which was chosen to relate to the usage mode of cells in float service, over-all corrosion current does not remain constant but increases with surface roughness and decreases with the buildup of barrier (passivating) layers. This progress of corrosion with time (or the positive plate growth *vs.* time) is described by experimentally determined degradation functions employing a single temperature-dependent constant.

A test relating to the positive corrosion and lifetime expectancy of cells in cyclic charge-discharge service must differ from constant voltage operation as a matter of definition. The over-all positive grid corrosion in such cells varies with time in an even more complex manner.

This present work is a study of the temperature dependence of corrosion of lead-antimony alloy positive grids in cells in deep cycle service. As an investigation involved with direct and indirect measurements of corrosion depth as a function of time and temperature, it is designed to employ a testing cycle consisting of a constant-current, constant ampere-hour discharge, and a tapered-current, constant ampere-hour charge. This test routine, essentially a constant-coulombs per cycle (coulostatic) test, was chosen instead of a constant voltage schedule to reflect more faithfully the usage pattern of motive power cells.

The purpose of this paper is to describe experiments monitoring, directly and indirectly, the time and temperature dependence of the corrosion of lead-5% antimony positive grids in specific industrial motive power cells on this fixed charge-discharge cycle routine. The test specifications employed (maximum temperature, depth of discharge, extent of overcharge) are selected from a prior unpublished study of stress parameter combinations by the author. These parameter levels are one of many possible compatible sets reflecting different types of service. One objective of the subject experiments was to produce a near maximum in cell degradation rate leading to failure comparable to field service and room-temperature bench testing. These accelerated test results are further applied to predict charge-discharge cycle lifetime for cells operating at room temperature.

* Electrochemical Society Active Member.

Key words: anodic, statistics, batteries, corrosion, oxidation.

Experimental

Charge-discharge cycling was conducted on a uniform group of 48 series-connected 5-plate industrial motive power cells equally divided among constant-temperature baths held at 60.0°, 70.2°, and 82.2°C. A 4 hr constant current discharge was set at 72 A-hr (90% of nominal capacity at the 6 hr rate). A 4 hr taper charge for all cells at 101 A-hr (140% of amount withdrawn) completed the cycle. The initial charging current was 101A, tapering logarithmically to 1A at 4 hr. Continuous cycling was carried out 5 days per week. All cells were given an equalizing charge of 2.0A throughout each weekend.

The test cells employed 1.280 sp gr H_2SO_4. Positive grids consisted of an alloy containing 4.83% Sb, 0.40% Sn, 0.075% As, and 0.055% Cu. These grids were approximately 14.8 cm wide, 25.2 cm high, and 0.62 cm thick at the outside frame as cast. Cured positive paste content of these grids was maintained at 1.41 ± 0.01 lb average deviation by avoiding both overpasting and underpasting. All positive plates were wrapped horizontally with Fiberglas yarn followed by Fiberglas mat; finally with a perforated PVC outer envelope. Such plates normally fail due to grid corrosion and disintegration rather than via active material loss or degradation. Cell capacities at room temperature (6 hr rate = 13.3A) were determined at 50-100 cycle intervals. Three cells were removed from each constant temperature bath at 50-100 cycle intervals for measurement of antimony content in the active material, over-all grid growth, and grid corrosion depth. Antimony content of both the positive and negative active material was determined by atomic absorption spectrophotometry. Samples for these analyses were obtained by removing active material from the entire plate, blending with a mortar and pestle, washing with water, then oven-drying to constant weight.

The dimension chosen to describe grid growth was the change in width of the positive grid at one-half of

plate height. Mean depth of corrosion of the positive grid was estimated from direct micrometer measurements of residual grid thickness along the outside frame of the chemically cleaned grid. Oxide film removal was accomplished with an aqueous stripping solution of 12% KOH containing 10g hydrazine sulfate per liter.

The estimated mean value of residual grid thickness was subtracted from the estimated mean thickness value (0.614 cm) of formed grids from cells in the same production run, but with no accelerated life test charge-discharge cycles. The precision of the resulting estimated mean depth of corrosion for the test grids was specified by employing tabulated values of the t statistic (3)

$$\text{precision} = \pm t_{\nu,0.025}\sqrt{\frac{s^2}{n}}$$

where ν = degrees of freedom $(n-1)$, $t_{\nu,0.025}$ = tabulated values for 95% confidence limits, s^2 = estimate of the variance of the data

$$\sum_n (y_i - \bar{y})^2/(n-1),$$

n = total number of observations in a sample, and y = observed values for corrosion depth.

The t statistic was similarly employed to determine precision of the curve describing the slope (E/R) of the plot of ln k *vs.* 1/°K, where R is the gas constant, and E is expressed as an activation energy. Over-all precision for the prediction of room temperature lifetime was related to the precision with which E could be specified. Details of the calculations are given in the Appendix.

Results

Periodic capacity data.—Cell capacities at room temperature (6 hr rate = 13.3A), taken at intervals during cycle life, were distributed over a range which revealed only a general trend toward capacity decay (Fig. 1a). Both positive and negative limitations were observed, as determined by individual electrode measurements *vs.* a Hg/Hg_2SO_4 standard electrode. Treatment of the data to obtain 95% confidence level estimates of the mean cell capacity resulted in improvement in precision of the capacity decay curve. but not enough to allow characterization leading to a lifetime prediction (Fig. 1b). These data did show, however, a general trend toward more rapid capacity decay with increasing test temperature. End-of-life capacity limitation was due to disintegration of the positive plate grid, leading to abrupt failure. For the 60.0°C cells this occurred beyond 216 days on test; it was not included on the curves of Fig. 1 due to the much lower confidence levels with which mean capacity values could be estimated for cells near end of life.

Periodic plate expansion data.—The positive plate expansion displayed a similar trend, with most highly expanded plates found in the highest temperature test bath. However, the results (Fig. 2) were mixed, precluding interpretation to yield any lifetime prediction.

Antimony migration.—The corrosion of the lead-antimony positive grid, accompanied by subsequent migration of soluble antimony-containing species, can be accurately monitored by direct periodic analysis of antimony pickup in the active material under ideal circumstances. Figure 3 demonstrates that test conditions are less than ideal, however, yielding antimony pickup curves showing such irregularities as concentration crossovers between discrete test temperatures and concentration maxima at approximately half-cycle life. No quantitative interpretation of these data was possible in terms of the experimental goal: prediction of room temperature cycle life. Qualitative interpretation is included in the Discussion section.

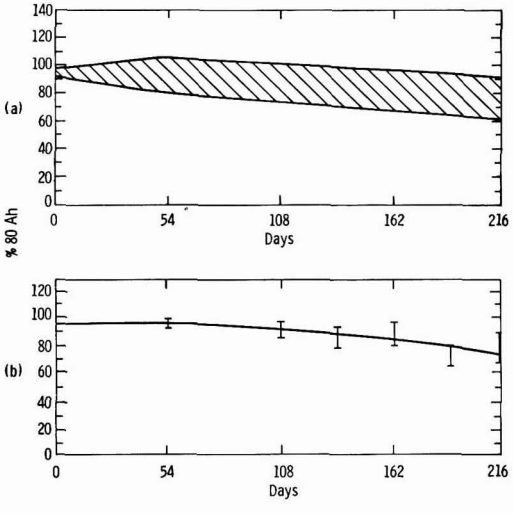

Fig. 1. Cell capacity *vs.* days on test at 60.0°C, room temperature capacity, 13.3A (nominal 6-hr rate).

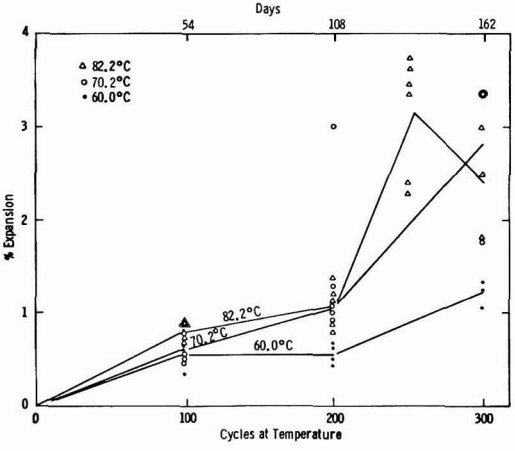

Fig. 2. Positive plate expansion during accelerated testing

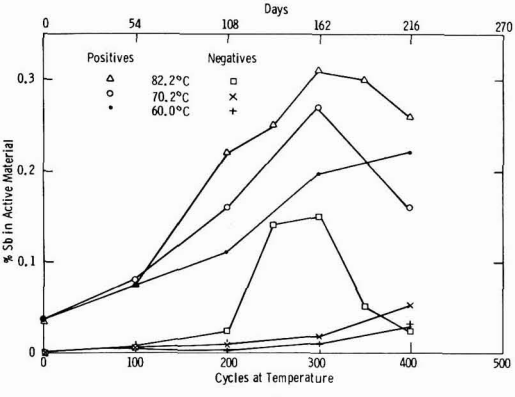

Fig. 3. Antimony absorption in PbO_2 (positive) and sponge Pb (negative).

Corrosion depth.—Residual grid thicknesses, after removal of corrosion layers, yielded estimates of mean corrosion depth. Initial measurements, involving a total of four measurements along the grid frame (Fig. 4), were insufficient to describe a precise corrosion depth *vs.* time curve. The average of 14 measurement points per grid improved precision of the estimated mean to ±0.001 cm at a 95% confidence level. These estimates of the mean corrosion depth were plotted as points for purposes of curve fitting (Fig. 5).

The function corresponding to these curves was of the type

$$\text{Corrosion depth} = kt^x$$

where t = time on test (days) and, k = a temperature-dependent constant, with a sensitive response to temperature change such that log k is a linearly decreasing function of the reciprocal test temperature in degrees Kelvin. The best fitting value of the temperature-independent constant x, as determined by least squares approximation, is $x = 0.67$. Figure 6 illustrates this result and also specifies the k values corresponding to each test temperature, using $x = 0.67$.

The log-linear extrapolation of these k values (Fig. 7; Appendix D) leads to an estimate of 4.42×10^{-4} cm days$^{-0.67}$ for k at 25°C. The 95% confidence interval for this estimate would span from $k = 4.30 \times 10^{-4}$ to $k = 4.52 \times 10^{-4}$ cm days$^{-0.67}$.

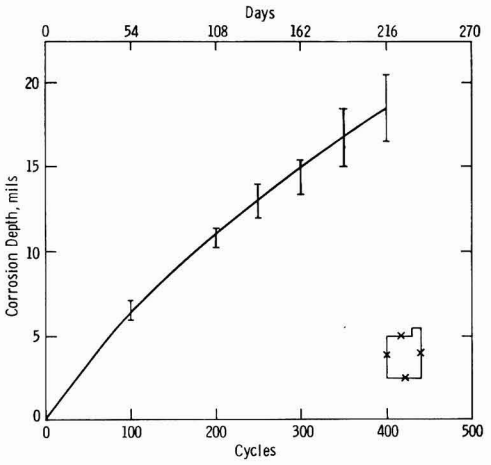

Fig. 4. Grid corrosion during accelerated testing, 82.2°C. Four-point grid thickness measurements, and 95% confidence limits for mean value corrosion depth.

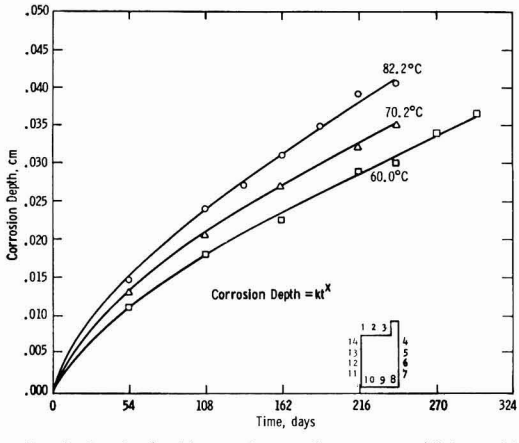

Fig. 5. Depth of grid corrosion *vs.* days on test. Minimum 14 points per grid.

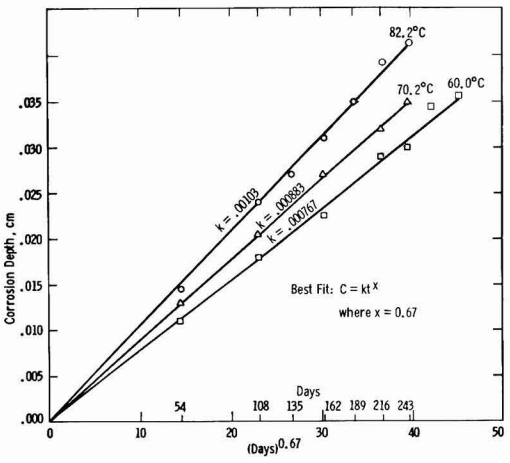

Fig. 6. Best fitting curve set at $C = kt^{0.67}$

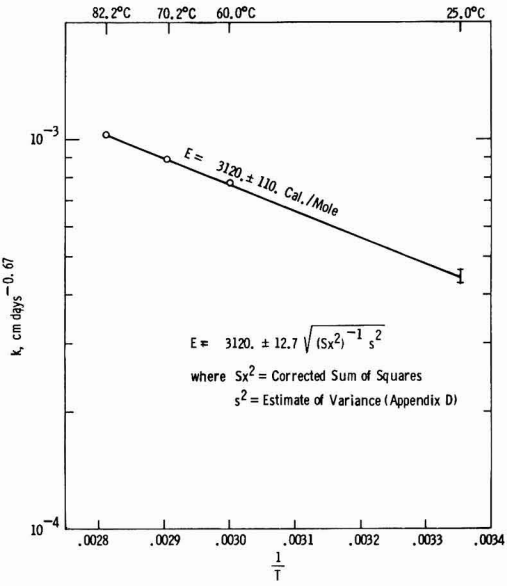

Fig. 7. Log-linear extrapolation of k

A solution was obtained for estimated time at room temperature to corrode to a target depth of 0.035 cm for the charge-discharge cycle routine employed (Fig. 8; Appendix D). The target corrosion depth was estimated from corrosion measurements of similar plates bench-tested at room temperature according to interim federal specification W-B-00133B (GSA-FSS), performance test No. 2. In this test, and in field service, lifetime end-point is characterized by disintegration of the positive grid, the life-limiting component of the lead-acid cell on normal duty. In the accelerated test, the positive grid fails in the same manner. The extent of positive grid disintegration and the microscopic and crystallographic structure of the PbO_2 corrosion layers are equivalent to those which are found in cells cycled on long-term bench tests and cells in field service.

The assumption was made that casting quality for the room temperature, reference grids was substan-

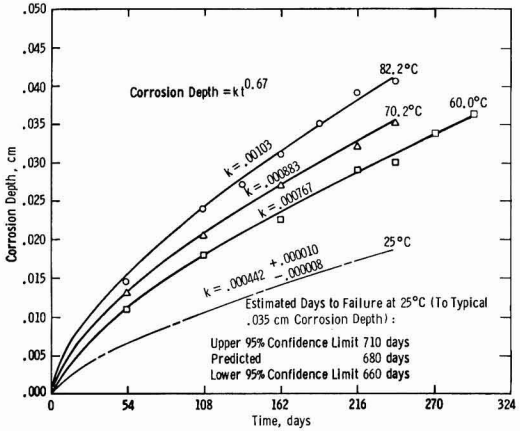

Fig. 8. Depth of corrosion vs. days on test

tially the same as for the group of positive castings employed in this accelerated test. This 0.035 cm depth of corrosion should, however, be viewed as a flexible target in a finalized life test, subject to changes reflecting casting quality, grid geometry, grid composition, etc. For this accelerated test, assuming practical equivalence with the reference grids, calculation yields a predicted lifetime of 680 days +4%, −3%. Converting to number of charge-discharge cycles, the corresponding 95% confidence statement is 1260 cycles +4%, −3%.

Discussion

Cell capacity vs. life.—During the test, some cells failed for reasons unrelated to the test objectives (shorts, loss of contact from lugs to posts, etc.). Also, progressive degradation evidence, specifically positive and negative plate voltages, did not consistently show that the positives were always failing preferentially. In cases of abrupt failure, such cells were removed, repaired, and returned to test if possible; if not, then removed permanently and disassembled to record temperature-dependent control parameter data (plate expansion, antimony migration, grid corrosion). In cases of gradual failure, lowest capacity cells were permanently removed and examined similarly at the programmed 50-100 cycle intervals. Although ultimate cell failure was due to sudden positive limitation, the capacity decline shown in Fig. 1 embodies substantial contributions from causes such as negative limitation, sediment and moss shorting, etc. Therefore, capacity curves, as taken on this test, are viewed as indicators of general cell performance, and not specific for the positive plate.

In all cases, however, the test was unaffected by these extraneous effects due to its inherent design, which called for exclusive monitoring of critical positive plate temperature-dependent control parameters. Thus, even if a cell had been abruptly removed for post failure, the critical data, *e.g.*, grid corrosion, could be taken and employed as valid for that particular point in cycle life. Therefore, the progress of, *e.g.*, grid corrosion during cycle life should be viewed as data collected on a partially selective, partially random basis.

Since the grids and plates were constructed as uniformly as possible, these data are considered to be representative of positive plate degradation for the entire group. Further, positive plate degradation is identified as the life-limiting mechanism in the lead-acid cell in deep discharge service. Consequently, the measured control parameters, particularly depth of corrosion, are viewed as related to critical normal service degradation, while cell capacity data is confused by extraneous and less significant failure modes. These extraneous modes, though extremely temperature sensitive in themselves, do not affect the temperature dependence of corrosion of the positive grid.

Plate expansion vs. life.—Prior work in the literature had indicated that simple plate growth could be correlated with plate lifetime. Lander (4) cycled strips of Pb-6% Sb and Pb-4.5% Sn about typical positive plate potentials twice a day in 30% H_2SO_4 at 49°C. He measured regular increases in strip length with testing time, reporting up to 3% elongation. Cannone *et al.* (2), working with cells for telephone service in an elevated temperature range of 60°-93°C, showed that pure lead grids on constant potential charge expanded regularly in width in a parabolic fashion and that lead-antimony grids expanded along a linear curve.

The behavior of our lead-antimony grids was analogous to these two prior studies. However, because of the tendency of our grids to corrode completely through along fault lines, then to spring open abruptly, no smooth growth curve could be measured. If grid castings showing more regular growth are tested, direct nondestructive growth measurements could provide a lifetime prediction test with a minimum of test samples. An analysis of precision would be required, however, to establish the merit of this approach relative to the depth of corrosion approach.

Antimony migration vs. life.—Corrosion of lead-antimony positive grids in the lead-acid storage cell produces either PbO_2 or $PbSO_4$, depending on state of charge. Both are essentially insoluble, and remain in place in the positive plate. The antimony component of the grid alloy is quite soluble in H_2SO_4, forming the anions $Sb(SO_4)_2^-$, $SbOSO_4^-$, and $Sb_3O_9^{3-}$, as proposed by Dawson *et al.* (5, 6). Adsorption of antimony on active material crystal surfaces is believed to occur, affecting crystalline growth habit on charge and discharge. Such adsorption is also viewed as the reason why antimony content of the positive active material increases so markedly with increased grid corrosion.

Anionic transfer to the sponge lead negative plate, and subsequent adsorption there leads to a lesser concentration buildup in the negative active material, compared with the positive, PbO_2 electrode. The well-known "poisoning" effect of Sb in the negative electrode is shown here to be associated with antimony accumulations well below antimony levels present in the positive plate. While positive plate voltages indicated that performance was virtually independent of antimony level, negatives showed decreasing voltages early in cycle life. Concentrations of antimony in the electrolyte itself are negligible, so that almost all antimony, though considered to be soluble, is associated with the solid phases of both electrodes.

If total antimony pickup in the active material can be determined, then, by direct analysis of the active material, a measure of grid corrosion would result. The irregularities found in the test are interpreted as being primarily due to inhomogeneous antimony levels in the cast grid alloy. Antimony-rich phases are known to be discrete entities in cast Pb-Sb alloys, existing in regions between the predominant, lower antimony grains. This work indicates, however, that a further change in composition occurs as corrosion strips away the outer surfaces of the cast grid, with significantly lower antimony concentrations found at levels approximately 0.025-0.030 cm below the surface. The peaks in the curves of antimony concentration *vs.* time on cycle life (Fig. 3) correspond to such a view.

In addition to these radial concentration gradients in the grid bar cross section and the concentration segregation inherent in the two-phase Pb-Sb alloy structure, a third effect is known to exist: the evolution of stibine gas, SbH_3, from the negative electrode while the cell is in the charge mode, could reduce the estimate of grid corrosion depending on the efficiency

of stibine synthesis. This effect, in combination with the radial concentration model, accounts for negative curve slopes beyond 300 cycles.

Corrosion depth vs. life.—Test precision.—As the data of Fig. 5-8 demonstrate, the precision of this accelerated life test is considerably better than typical precision in lifetime prediction currently achieved in standard, long-time industrial testing ($\sim \pm 20\%$ at 95% confidence level). It is possible to identify the factors chiefly affecting precision from the derived corrosion function

$$C = \text{mean depth of corrosion} = k_{25°C}t^x$$

when C is a targeted value, and being defined, does not limit precision. X, once derived, is employed as a constant which does not affect precision, only accuracy. This simplifying assumption is justified in the same way as other work, *e.g.*, when ideally linear ($x = 1$) or ideally parabolic ($x = 2$) functions are assumed to describe phenomena. Therefore, only $k_{25°C}$ has inherent limitations of precision when solving for t.

Examination of Eq. [A-9], Appendix D, shows that, if the temperatures are fixed, and precisely measured ($\pm$ 0.05°C) within the span of temperatures available in the test, then the estimate of the variance of the quantity $R \ln k$ (where $R = 1.9872$, the gas constant) and the degrees of freedom in the t statistic are the two factors influencing precision. In this three-temperature experiment (three degrees of freedom), two degrees of freedom are used up, due to the fact that, in solving for the least squares log-linear extrapolation of k, two unknowns, the slope E and the intercept $R \ln A$ are involved. Since this leaves only one degree of freedom to define the t statistic, the corresponding tabulated t statistic for 95% confidence limits is 12.7. Inspection of the t statistic tables shows that, for a four-temperature experiment, the term before the square root sign in the precision expression [A-9], is reduced to 4.3 since the t statistic can then be based on two degrees of freedom. For better precision, then, data should be grouped into four temperature groups. For industrial testing, which may involve only two temperatures, the cells should be grouped into equal samples of duplicate temperatures to yield at least four temperature groups, provided the variance of $R \ln k$ does not increase too rapidly.

The estimate of the variance of experimental values of $R \ln k$ with respect to the corresponding least squares values, $R \ln \hat{k}$

$$\frac{1}{n-2} \sum (R \ln k - R \ln \hat{k})^2$$

also decreases significantly as n, the total number of temperature groups, is increased from 3 to 4 or more. The difference term within the summation: (*i*) decreases with increasing accuracy in temperature measurement, (*ii*) decreases with increasing precision in temperature measurement, (*iii*) decreases with increasing uniformity of replication in the entire lot of positive plates employed in the test cell group, and (*iv*) decreases with increasing uniformity of replication of cell cycling parameters, *e.g.*, A-hr discharge, A-hr charge, shape of charge curve.

If means can be found to avoid rapid negative sulfation, and thereby extend the temperature range of this test, precision can be further improved.

The corrected sum of squares in Eq. [A-9]

$$\sum \left(\frac{1}{T}\right)^2 - \frac{1}{n}\left(\sum \frac{1}{T}\right)^2$$

increases with increasing temperature range. Since this term is a denominator, it therefore increases the precision as the range of temperature increases.

The question arises: Why not collect the experimental corrosion depth data at a single temperature, preferably at room temperature, and simply extrapolate the experimental room temperature curve to a targeted depth of corrosion? The answer is that this elevated temperature test magnifies the form of the corrosion function so that it can be identified and precisely specified at room temperature. Any room temperature experiment must be carried out nearly to end-of-life to achieve the same precision. Experience and analysis show that curves derived from direct room temperature measurements over the shorter period of time involved in this accelerated test lack the precision needed for satisfactory lifetime prediction. This is because, while the precision of the measurement data is constant, the actual values of corrosion depth decrease exponentially with decreasing absolute temperature.

Consequently, as an example, direct room temperature corrosion curves of differing grid alloys would be practically indistinguishable from each other; perhaps also even from a straight line over the first 200-300 charge-discharge cycles. Such room temperature curves are readily and precisely characterized with respect to k and x by extrapolation of high temperature experiments, thus revealing critical differences in calculated, room temperature, lifetime estimates.

It is appropriate to ask whether the predicted, room temperature, corrosion function has been experimentally demonstrated out to a point in cycle life where meaningful precision can be obtained. To make such a comparison it is assumed that the room temperature control cells will ultimately demonstrate the 0.035 cm mean depth of corrosion exhibited by the high temperature test groups and by prior bench testing of similar production cells. Three five-plate cells from the original test group, which were cycled at room temperature, obey the calculated corrosion function to within 0.001 cm at an estimated one-half cycle life to date, thus providing reasonable agreement of theory with experiment.

Testing time.—If subsequent test results on other types of cells and materials show that corrosion functions repeatedly turn out to be of the form

$$C = kt^x$$

then the taking of samples for corrosion depth measurements need not be conducted all along the curve, but merely at one point, sufficiently far along to permit acceptable precision in lifetime prediction. Given a test closely controlled as outlined above, with a group of cells all constituting faithful replicas of each other, excellent precision should be obtainable in 4-6 months testing time. However, any experiment with a different form of corrosion function would necessarily involve a full complement of cells being periodically extracted from test and measured to describe the exact form of the corrosion function until such time as actual failure occurs.

Number of specimens.—Five-plate cell variability is significant enough to require four or five such cells in each of four temperature groups for tests involving extraction from test and measurement at a single point in life ($c = kt^x$ assumed). As an alternative, the equivalent number of positive plates in fewer cells with more plates would serve the same purpose.

Asymmetrical upper and lower bounds in predicted life.—Adapting Eq. [A-8], Appendix D, to solve for k

$$\ln k = \frac{E\left(\frac{1}{T}\right) + R \ln A}{R}$$

it is evident that the upper and lower bounds obtained in the least squares estimate of E, at 95% confidence limits, yield a corresponding upper and lower bound expressed in $\ln k$; not k itself. As a consequence, translation of these derived limits, which are symmetrical

about ln k, results in asymmetrical limits about k itself.

The significance of this lies simply in the Arrhenius model which was originally assumed (Eq. [A-5], Appendix D)

$$k = A \exp\left(\frac{b}{T}\right)$$

where it can be seen that any symmetrical uncertainties in either temperature or Rb ("activation energy") result in logarithmically related uncertainties in k.

As a practical application of this, it can be pointed out, for example, that temperature overestimation is more damaging to accuracy than temperature underestimation. Conceptually, the range of values of predicted life may be visualized as a probability distribution skewed to the right with the mode located to the left of the predicted value of lifetime.

"Activation energy," E.—The slope in Fig. 7 is characterized as an activation energy to conform to established practice and to provide a preliminary criterion for the identification of the type of rate control which prevails. It should be noted that true charge transfer activation energies generally lie in a range above 5000 cal/mole. At 3120 cal/mole, it is difficult to distinguish from the case of diffusion limitation. However, it is evident that the over-all effect of cyclic operation of the positive plate of these lead-acid storage cells is to bring about progressive anodization of the lead alloy current collector with the corrosion depth curve tending toward a diffusion-limited value (Fig. 8). E, then, may alternatively be viewed as related to a characteristic concentration overpotential.

Conclusions

High temperature charge-discharge cycle testing of lead-acid cells can yield a prediction of room temperature cycle life in as quickly as 4 months. The logarithm of cell lifetime decreases linearly with the absolute temperature.

Measurement of positive grid corrosion depth as a function of temperature yields a corrosion function characterized by one temperature-dependent constant. The value of this constant at room temperature is specified by a log-linear extrapolation. An experimental design employing 16 five-plate 80 A-hr cells at each of three different temperatures permits a +4%, −3% precision in lifetime prediction at a 95% confidence level.

This technique of elevated-temperature corrosion function analysis permits charge-discharge cycle life prediction capability of unprecedented precision and speed.

Acknowledgments

A. M. DiCroce and C. A. Hager assisted in conducting the tests. W. N. Ritchie and B. Terzic, of KW Battery Company, prepared and supplied all cells used in this program and helped to examine selected cell components against the background of their field experience. G. M. Jouris was consulted with respect to the statistical treatment of the data. J. T. Brown provided many stimulating technical discussions of the problem, particularly with respect to extrapolation theory.

Manuscript submitted May 31, 1974; revised manuscript received Aug. 13, 1974.

Any discussion of this paper will appear in a Discussion Section to be published in the December 1975 JOURNAL. All discussions for the December 1975 Discussion Section should be submitted by Aug. 1, 1975.

Publications costs of this article were partially assisted by Westinghouse Electric Corporation.

APPENDIX

A. Estimation of Mean Depth of Corrosion

Grid corrosion depth during cycle life was estimated by subtracting the average residual grid thickness

$$\bar{y} = \frac{1}{n}\sum_{i}^{n} y_i \qquad [A\text{-}1]$$

from the average initial grid thickness ($\bar{y}_o$) after formation and initial capacity determination, then dividing by two. The mean value estimate of corrosion depth obtained in this way was characterized with respect to precision at a 95% confidence level by employing tabulated values of the t statistic (3) in the following expression

$$\frac{\bar{y}_o - \bar{y}}{2} \text{ estimates } \eta = \text{mean value} \pm t_{\nu,0.025}\sqrt{\frac{s^2}{n}}$$

where $t_{\nu,0.025}$ = tabulated values for 95% confidence limits, ν = degrees of freedom ($n - 1$), n = total number of observations in a sample of grids, s^2 = estimate of the variance of the data

$$\frac{1}{n-1}\sum_{i}^{n}(y_i - \bar{y})^2,$$

and y = observed values for corrosion depth.

The number of observations, n, was increased until the 95% confidence level precision of the estimate of the mean value of corrosion depth approached 0.001 cm, comparing with the precision of the micrometer (0.0005 cm). To do this, up to 30 individual residual thickness measurements were made per grid.

B. Estimation of Power of t in Corrosion Depth Function

It was observed that the estimated mean grid corrosion depth obeyed a time and temperature-dependent function of the form

$$C = \text{corrosion depth (cm)} = kt^x \qquad [A\text{-}2]$$

where k = a temperature-dependent constant, t = time (days), and x = a constant, with no apparent temperature dependence.

Taking logarithms

$$\log C = \log k + x \log t$$

In a least squares analysis of the data (7), x is given by

$$x = \frac{\Sigma \log t \log C - \frac{1}{n}(\Sigma \log t)(\Sigma \log C)}{\Sigma (\log t)^2 - \frac{1}{n}(\Sigma \log t)^2} \qquad [A\text{-}3]$$

where n = the number of t data points.

The best fitting value of x was taken as the average x over all three temperatures employed in the test

$$\begin{aligned} X_{82.2°C} &= 0.694 \\ X_{70.2°C} &= 0.635 \\ X_{60.0°C} &= 0.693 \\ \bar{X} &= 0.67 \end{aligned}$$

For purposes of precision analysis, this value, approximately 2/3, was considered to be a temperature-independent, constant exponent not affecting precision. A similar assumption is commonly employed in many curves which are arbitrarily fitted to strictly linear or quadratic models.

C. Estimation of "k" in Corrosion Depth Function

The constant k was then specified for each temperature by solving

$$\log k = \overline{\log C} - 0.67\,\overline{\log t} \qquad [A\text{-}4]$$

The results yielded three corrosion functions

82.2°C: C = corrosion depth (cm) = $0.00103\ t^{0.67}$
70.2°C: C = corrosion depth (cm) = $0.000883\ t^{0.67}$
60.0°C: C = corrosion depth (cm) = $0.000767\ t^{0.67}$

The adequacy of the model to represent the data is demonstrated by Fig. 6.

D. Determination of Precision of the Log-Linear Extrapolation of "k"

The decrease of k with respect to temperature conformed to an expression of the type

$$k = A \exp\left(\frac{b}{T}\right) \qquad [A\text{-}5]$$

where T = absolute temperature (°K) and A, b = constants.

The best fitting value of b was expressed as an activation energy, E cal/mol, by multiplying by the gas constant, $R = 1.9872$ cal °K^{-1} mole^{-1}.

Taking logarithms

$$R \ln k = R \ln A + E\left(\frac{1}{T}\right) \qquad [A\text{-}6]$$

Least squares analysis leads to the following expression

$$E = \frac{\left(\sum \frac{R \ln k}{T}\right) - \frac{1}{n}\left(\sum \frac{1}{T}\right)\left(\sum R \ln k\right)}{\sum\left(\frac{1}{T}\right)^2 - \frac{1}{n}\left(\sum \frac{1}{T}\right)^2} \qquad [A\text{-}7]$$

where $n = 3$ for this case involving three temperatures. ln A is obtained by straightforward substitution of average experimental data points, ($\bar{}$), in [A-6]

$$\ln A = \frac{\overline{R \ln k} - E\overline{\left(\frac{1}{T}\right)}}{R} \qquad [A\text{-}8]$$

permitting subsequent estimation of k at room temperature from [A-5].

The precision of the derived value of E is: 95% confidence level precision =

$$\pm t_{\nu,0.025} \sqrt{\frac{\Sigma(y - \hat{y})^2}{\left[\sum\left(\frac{1}{T}\right)^2 - \frac{1}{n}\left(\sum \frac{1}{T}\right)^2\right]} \frac{1}{n-2}} \qquad [A\text{-}9]$$

where y = experimental value of $R \ln k$, $\hat{y}$ = least squares predicted value of $R \ln k$, $\Sigma(y - \hat{y})^2$ = estimate of variance, and

$$\sum\left(\frac{1}{T}\right)^2 - \frac{1}{n}\left(\sum \frac{1}{T}\right)^2 = \text{corrected sum of squares.}$$

The maximum and minimum E values yield corresponding maximum and minimum predicted room temperature k values, from [A-5] and [A-8], in this case at a 95% confidence level.

E. Determination of the Precision of Room Temperature Lifetime Prediction

Maximum and minimum k values at room temperature are employed in [A-2], assuming 0.035 cm depth of corrosion, corresponding to field service and bench failure; solving for t. These room temperature, cycle lifetimes, therefore, represent the span of predicted values generated by 95% confidence level data.

REFERENCES

1. E. Willihnganz, *Electrochem. Technol.*, **6**, 338 (1968).
2. A. G. Cannone, D. O. Feder, and R. V. Biagetti, *Bell System Tech. J.*, **49**, 1279 (1970).
3. A. Hald, "Statistical Theory with Engineering Applications," pp. 388-397, John Wiley & Sons, Inc., New York (1960).
4. J. J. Lander, *This Journal*, **98**, 220 (1951).
5. J. L. Dawson, J. Wilkinson, and M. I. Gillibrand, *J. Inorg. Nucl. Chem.*, **32**, 501 (1970).
6. J. L. Dawson, M. I. Gillibrand, and J. Wilkinson, "The Chemical Role of Antimony in the Lead-Acid Battery," 7th International Power Sources Symposium, September 15-17, 1970, Brighton, England.
7. A. Hald, "Statistical Theory with Engineering Applications," pp. 528-549, 558-570, John Wiley & Sons, Inc., New York (1960).

The Existence of Multiple Steady States during Differential Aeration Corrosion

Richard Alkire* and George Nicolaides**

Department of Chemical Engineering, University of Illinois, Urbana, Illinois 61801

ABSTRACT

A method of calculation has been developed for predicting the multiple steady-state current distributions which may exist along a metal surface undergoing localized attack by differential aeration corrosion. The calculational method is capable of finding all such multiple steady-state solutions. A compilation of those regions of parameter space within which highly localized attack is likely has been carried out for the model system.

Owing to differential aeration the local rate of corrosion along a metal surface may be highly nonuniform, especially if the metal exhibits passivity. The problem of determining the location and the local rate of corrosion attack corresponds to elucidating the details of the current flow between the anodic and cathodic regions which occur simultaneously on the metal surface. That is, one needs to know the current distribution. Whereas electrochemical current distribution problems originated in attempts to predict the over-all current-voltage behavior of electrolysis cells, such studies have also been conducted on corrosion-like configurations of fixed anode/cathode geometry as briefly reviewed in Ref. (1). More recently, current distribution calculations have been conducted on corroding systems wherein multiple electrochemical reactions occur on localized net anodic and cathodic areas, which coexist on adjacent regions of a single conductive surface. For simple configurations, such "bipolar" current density distributions may be computed once the system parameters have been specified (*i.e.*, properties such as electrolyte conductivity, oxygen availability, electrode reaction kinetics, system geometry, etc.). Corrosion of rotating disks (2, 3) has been shown to occur with nonuniform rates wherein one portion of the disk is passive while another portion corrodes actively. The study of aeration corrosion under barrier films of variable thickness (1, 4, 5) has shown that more than one steady-state

* Electrochemical Society Active Member.
** Electrochemical Society Student Member.

Key words: corrosion, differential aeration, current distribution, mathematical model, bipolar electrode.

current distribution may be expected to exist for a single set of system parameters; some of these multiple steady-state corrosion distributions suggest the possibility of highly localized corrosion. However, the numerical methods employed in the foregoing studies were not well suited for determining how many such multiple solutions exist. Therefore the following investigation has been conducted with two goals in mind. First, a different computation method has been employed which is capable, for a given set of system parameters, of finding all possible steady-state current distributions. Second, a compilation has been carried out of all regions of parameter space within which highly localized corrosion may be anticipated for the model system under study. The results therefore contribute toward design of corrosion systems so as to avoid altogether those potentially hazardous situations where localized attack is likely.

Derivation of Model

The corrosion system to be investigated, shown in Fig. 1, is identical to that studied by other methods in Ref. (1). Readers may examine that reference for more extensive introductory remarks than are provided here. The metal is covered by an electrolyte-moistened barrier of locally variable thickness. Oxygen diffuses through the barrier layer to the metal surface, which corrodes. Both oxidation and reduction reactions occur everywhere along the corroding surface. In many cases, however, the local oxidation rate may exceed the local reduction rate, thus creating a local net anodic region. Similarly, local net cathodic regions may also arise. Electrical current flows in the barrier layer between the net anodic and the net cathodic regions which coexist along the metal surface. The buildup of corrosion products has not yet occurred to an appreciable extent. The simple situation shown in Fig. 1 has been modeled by a differential equation (1) subject to the following restrictions: (*i*) the corroding system is confined by two insulating planes as shown in Fig. 1; (*ii*) the potential within the corroding metal is uniform owing to the high conductivity of the metal phase; (*iii*) current flows in the barrier layer parallel to the corroding surface; (*iv*) oxygen diffuses through the barrier layer along paths which are perpendicular to the metal surface; (*v*) the barrier thickness varies with position in an exponential manner; and (*vi*) the concentration of ionic species is uniform.

Subject to these restrictions, the model system is assembled from Ohm's law (for flow of electrical current along the barrier layer), Fick's law (for diffusion of oxygen through the layer), a Tafel rate expression (for the oxygen reduction kinetics), and an active-passive rate expression (for the metal undergoing corrosive attack). Before proceeding it is suggested that interested readers review details concerning the derivation of the model as provided in Ref. (1). The equation of conservation of charge which models the system is

$$\frac{d^2\Phi}{dX^2} - (1 + \tanh X)\frac{d\Phi}{dX} = \frac{\xi}{(1 - \tanh X)}\left\{\left[\frac{1-\beta}{e^{\frac{(\Phi-\Phi_R)^2}{\sigma}}} + \beta\right] - \left[\frac{\zeta e^{-\alpha\Phi}}{\zeta\Gamma e^{-X}e^{-\alpha\Phi} + 1}\right]\right\} \quad [1]$$

with boundary conditions

$$\frac{d\Phi}{dX} = 0 \text{ at } X = -\lambda \quad [2]$$

$$\frac{d\Phi}{dX} = 0 \text{ at } X = +\lambda \quad [3]$$

where the dimensionless variables are

$$X = \frac{x}{l}$$

$$\Phi = (V - \Phi_s)\frac{\mathbf{F}}{RT}$$

$$C = \frac{c}{c^0}$$

$$\sigma = \left(\frac{\mathbf{F}}{RT}\right)^2 s$$

$$\Phi_R = \frac{V_R\mathbf{F}}{RT} \quad [4]$$

and the dimensionless system parameters are

$$\Gamma = \frac{a\delta_m}{4\mathbf{F}Dc^0}$$

$$\xi = \frac{\mathbf{F}l^2a}{RT\kappa\delta_R}$$

$$\zeta = \frac{k}{a} \quad [5]$$

The notation employed in the equation, boundary conditions, variables, and parameters, is the same as in Ref. (1) and is listed at the end of the text. Reading from left to right, the terms in Eq. [1] indicate that the electrical current flowing along the barrier layer suffers ohmic resistance (second derivative term) which varies locally with the film thickness (first derivative term). The bracketed term on the right side of Eq. [1] is the net local reaction rate, *i.e.*, the local rate at which current flows into or out of the barrier layer. The local net reaction rate may be anodic or cathodic, depending on which partial reaction proceeds at the greater rate. For conditions of uniform corrosion, the right side of Eq. [1] would have the value of zero everywhere along the surface. On physical grounds, Eq. [1] therefore indicates that current flows into the barrier in the net anodic regions, flows along the moist layer while experiencing ohmic

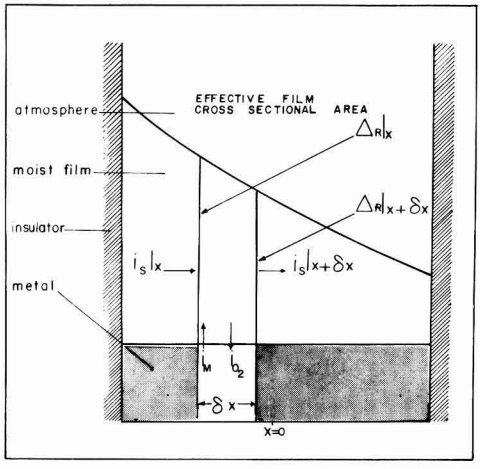

Fig. 1. System configuration for differential aeration corrosion study.

resistance and cross-sectional strictions, and flows out of the barrier into the net cathodic regions.

A detailed discussion of the physical significance of the dimensionless parameters has been given in Ref. (1). In brief, the parameter Γ is related to the ease with which oxygen diffuses to the corroding surface. Small values of Γ correspond to rapid diffusion of oxygen so that the concentration along the metal surface would be essentially uniform, near the saturated value; large values of Γ correspond to slow diffusion rates. The parameter ξ characterizes the resistivity of the barrier layer and takes on small values when the barrier layer is highly conductive. The parameter λ is a measure of the difference in oxygen availability between one end of the surface and the other end; large values of λ correspond to large differential aeration and thereby enhance tendencies toward localized corrosion. Once again, the reader is urged to consult Ref. (1) for a more complete discussion of the model.

Method of Solution

Equation [1], along with its boundary conditions, was solved numerically with use of IBM 1800 and IBM 360 digital computers. The boundary value system was transformed to an initial-value system by introducing a guessed condition at one end and adjusting this condition until the required relation was satisfied at the other end (6). That is, Eq. [1] was re-cast into a pair of first-order differential equations. Integration of an initial-value problem was then carried out such that the boundary condition at the far end of the spatial interval was satisfied by inspection. The method proceeds by writing

$$\frac{d\Phi}{dX} = Y \qquad [6]$$

hence Eq. [1] becomes

$$\frac{dY}{dX} - (1 + \tanh X)Y = \frac{\xi}{(1 - \tanh X)} \left\{ \left[\frac{1-\beta}{e^{\frac{(\Phi - \Phi_R)^2}{\sigma}}} + \beta \right] - \left[\frac{\zeta e^{-\alpha\Phi}}{\zeta\Gamma e^{-X} e^{-\alpha\Phi} + 1} \right] \right\} \qquad [7]$$

For initial conditions at $X = -\lambda$, Eq. [2] provides

$$Y = 0 \qquad [8]$$

For the second initial condition at $X = -\lambda$, guess

$$\Phi = A \qquad [9]$$

where A is a constant, which must be chosen with care. Equations [6] and [7] thus constitute two first-order equations having the unknown functions $\Phi(X)$ and $Y(X)$. The solution of this set, along with its initial conditions, is identical to the solution of Eq. [1], along with its boundary conditions, provided that the constant A is chosen such that

$$\frac{d\Phi}{dX} = 0 \text{ at } X = +\lambda \qquad [3]$$

The procedure for integration therefore consisted of arbitrarily choosing a value for the constant A, and then integrating Eq. [6] and [7] by means of Runge-Kutta fourth-order formulas (7). Every value of A which satisfies Eq. [3] corresponds to a different steady-state current distribution.

As a check against numerical errors, integration was also carried out beginning at the opposite end of the spatial interval, *i.e.*, beginning at $X = +\lambda$ and proceeding to $X = -\lambda$. Identical solutions were found for the current distribution regardless of direction of integration. In addition, the iterative method of solution employed in Ref. (1) was always found to converge upon any desired solution provided that a reasonable trial distribution was provided. That is, three methods of calculation provided identical numerical results.

The advantage of the "shooting" method of calculation described here is that all multiple solutions may be found for a given set of parameter values. In clear contrast, the iterative method used previously (1) had the disadvantage that one could not know how many solutions existed, except by finding them. That is, one could not determine whether a certain solution actually disappeared in some region of parameter space or whether it merely became difficult to converge upon.

Results and Discussion

Calculations have been conducted in order to clarify the nature of the multiple steady-state current distributions predicted by the model system. In addition, a compilation has been carried out in order to indicate those regions of parameter space in which at least one steady-state current distribution indicates the likelihood of highly localized corrosion. Because the model is somewhat preliminary in nature, and because it has been investigated primarily as an intuitive aid, an exhaustive compilation has not been attempted. Parameter values which were not varied in the investigation are $\alpha = 0.5$, $\beta = 0.01$, and $\sigma = 0.15$. Except where otherwise stated, the parameter ζ has the value 0.5.

It is important to make a clear distinction between the number of algebraic roots of the right side of Eq. [1], and the number of solutions to the differential equation. Although up to three algebraic roots may be found on the right side, such information bears no direct relation to the number of solutions which the differential equation may exhibit. Analyses of even simple distribution equations have demonstrated that an infinite number of solutions may be found (8, 9). In a similar manner, steady-state, nonisothermal behavior of porous, spherical, catalyst pellets has been shown to have an infinite number of multiple steady-state conditions (10). Therefore one should not go under the expectation that a maximum of only three solutions are to be expected of Eq. [1].

In certain regions of parameter space, several classes of independent solutions of Eq. [1]-[3] have been found. For one set of system parameters, for example, Fig. 2 illustrates that for many values of A [*i.e.*, the abscissa, $\Phi(-\lambda)$], the derivative at the far boundary [*i.e.*, the ordinate, $d\Phi/dX$ $(+\lambda)$] takes on values which may be nonzero. The model equations, however, are satisfied only for those situations for which the curve in Fig. 2 intersects the zero axis; each intersection point corresponds to a different steady-state current distribution. For the parameters used in Fig. 2, it is seen that thirteen multiple steady-state solutions are found. Some of the intersections are labeled (A, B, C, etc.) so that the solutions associated with them can be referred to in subsequent discussion.

It seems clear that all such solutions to the differential equation need not necessarily correspond to an observable steady-state condition of a physical system, even if that system is generally compatible with the approximations of the model. There are several reasons for which a mathematical solution may be regarded as physically unrealizable. First, a solution of the equation might predict a state of the system which is physically unstable to random disturbances. Although a stability analysis has not been conducted in this preliminary study, it should be mentioned that when multiple solutions exist as indicated in Fig. 2, it is frequently expected that the unstable solutions correspond to every other (*i.e.*, alternate) intersection. Second, a solution may be improbable in the sense that the sequence of events necessary for the attainment of the steady state may be difficult to achieve. An informal discussion of the possible transient conditions

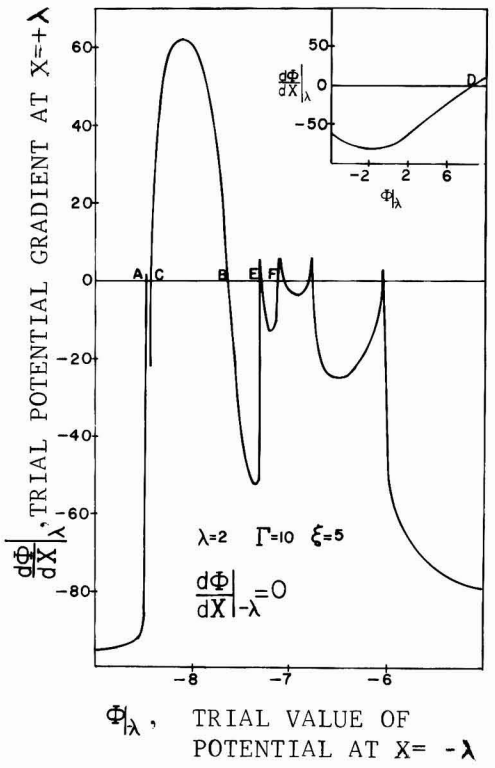

Fig. 2. Display of the existence of multiple solutions obtained by integrating Eq. [1] with a single set of system parameters. An independent solution exists at each intersection of the curve with the line.

that may lead to the various steady-state solutions is given below. Finally, a solution would be unrealistic if it depends strongly on one particularly weak approximation of the model. Such unrealistic solutions would be incompatible with data from a physical system, or with predictions of a more rigorous model.

The potential, current, and concentration distributions corresponding to the intersections A, B, C, and D of Fig. 2 are shown in Fig. 3. Figure 3 also corresponds to Fig. 3 of Ref. (1), and detailed discussion of the curves is contained therein. For Solution A, the metal is in the active potential range everywhere so that the local dissolution rate increases with decreasing layer thickness. Solution D represents a fully passive situation at a very positive potential. Solutions B and C exhibit intermediate behavior where one portion of the surface is passive while the rest is reactive. Solution B lies entirely on the decreasing branch of the anodic polarization curve whereas Solution C varies all the way from mildly reactive potentials to the passive potential region. One additional solution, denoted A', has general characteristics similar to the four solutions in Fig. 3 Solution A' is found at an intersection located between A and C in Fig. 2 (not drawn in for want of space) and yields distributions whose nature is in every respect intermediate between distributions corresponding to A and C. That is, the anodic rate distribution for A' usually includes a local maximum although the potential distribution has a smaller range than C.

The physical significance of the aforementioned five solutions will now be examined. The potential and anodic rate distributions of Solution A resemble closely the differential aeration corrosion of a nonpassivating

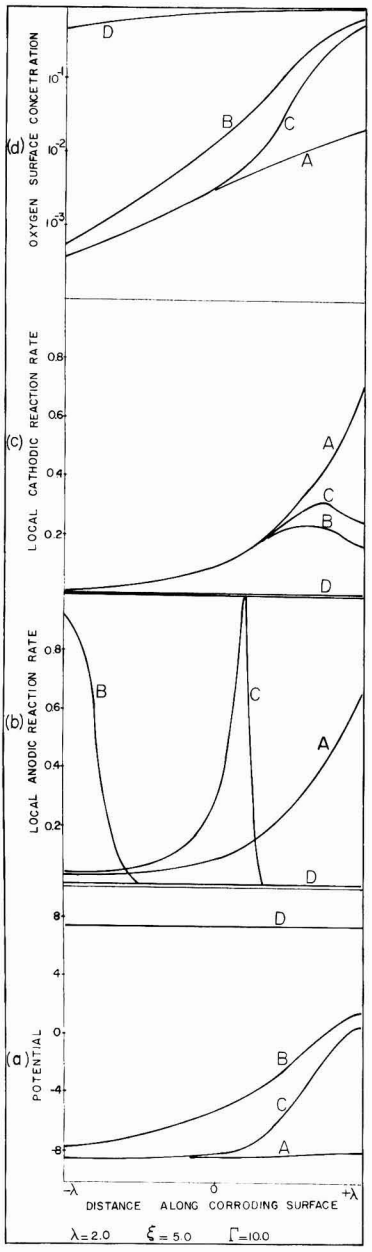

Fig. 3. Several distributions satisfying Eq. [1] were found for a single set of parameters. The curves labeled A, B, etc., comprise families of distributions which correspond to intersections A, B, etc., in Fig. 2. The distributions shown are: (a) potential of the metal relative to the solution, (b) anodic dissolution rate, (c) cathodic reduction rate, (d) oxygen concentration at the surface.

metal. Since range of potential is restricted to the active branch of the polarization curve, assumptions made in the model with regard to the passivating behavior of the metal have no influence. Therefore Solution A can be regarded as a stable and realistic situation which might be encountered in a physical system. For Solution D, the potential distribution is sufficiently removed from the active region that kinetic details

regarding active/passive transitions are inconsequential. The physical reasonableness of Solution D is clear, and fully passivated metal surfaces are commonly encountered.

If we assume that solutions corresponding to alternate intersections in Fig. 2 are unstable, then since A and D are clearly stable, A′ and B will be unstable while C will be stable. Solution C is especially interesting since it indicates the likelihood of highly localized corrosion at intermediate positions under the barrier layer. Solution B appears to be unstable, perhaps because the potential distribution lies entirely on the decreasing branch of the polarization curve, a region of negative charge-transfer resistance. Because the nature of Solution B depends strongly on the negative-resistance region of the passivation curve, these solutions may be regarded as unrealistic (in the narrow sense defined above) insofar as they depend strongly on a rather weak aspect of the model. It therefore seems unlikely that Solution B would be observed in actual physical systems.

It is useful to postulate in an informal manner the transient conditions which might lead to the various steady-state solutions encountered thus far. For example, if the electrolyte is saturated with oxygen prior to formation of the barrier layer, the entire surface will passivate and the steady-state condition captured by the system would be expected to be Solution D. On the other hand, if the electrolyte is deaerated so that oxygen diffusion proceeds with great difficulty, then the steady-state condition may be attained before any part of the surface undergoes passivation, as in Solution A. For intermediate initial oxygen concentrations in the electrolyte, the oxygen might passivate a part of the metal surface at the thin side of the layer before a steady state is achieved. Then Solutions C, B, or A′ might be exhibited, although the foregoing discussion has cast some doubt upon the attainment of B and A′.

We will now proceed to examine the remaining solutions encountered between B and D in Fig. 2. The number of such intersections was found to vary considerably with changes in the parameter values. In addition, these solutions are quite different from any solutions reported so far. Two such solutions, denoted E and F in Fig. 2, have been chosen for display. Figure 4(a) shows that the potential distributions for E and F exhibit maxima and minima, in clear contrast to Solution A′ which is also shown. As a consequence, anodic dissolution rate distributions, shown in Fig. 4(b), are highly nonuniform and indicate that localized attack may proceed at more than one location along the surface. Solution E has two strong anodic rate maxima, while F has two strong maxima and one weakly anodic region at $X = -\lambda$. The cathodic reaction rate distributions, shown in Fig. 4(c), are similar for all three solutions. By comparing Fig. 4(b) and 4(c), it is realized that Solutions E and F indicate that several anodic regions exist along the corroding metal, each separated by a cathodic region. The oxygen concentration distribution for each solution is shown in Fig. 4(d). For all cases, the oxygen concentration tends to be highest at $X = +\lambda$, where the barrier layer is thinnest, and lowest at $X = -\lambda$, where the thick barrier impedes oxygen diffusion. The remaining six solutions indicated in Fig. 2 exhibit behavior similar to E and F, but have not been illustrated since they do not appear to contribute additional information.

In accord with the informal rule that alternate intersections in Fig. 2 correspond to stable solutions, one may conclude tentatively that Solutions E and F are stable. On the other hand, one may inquire as to what transient events would be required to arrive at the steady states given by E or F. It seems reasonable that highly novel start-up conditions would be required in order to capture Solutions E or F, and their likelihood of existence may be regarded as highly improbable in comparison with Solutions A, C, or D.

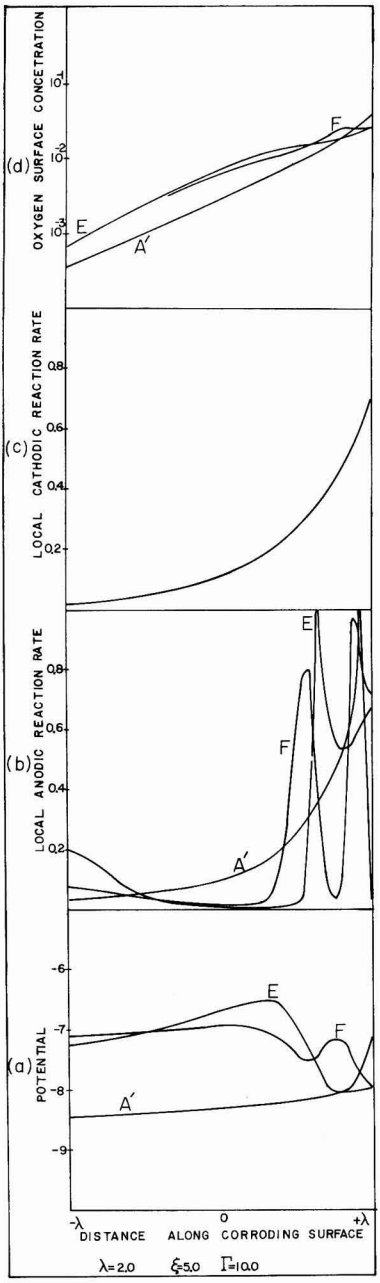

Fig. 4. Several distributions satisfying Eq. [1] were found for a single set of parameters. The curves labeled A′, E, and F correspond to the solutions indicated in the text and in Fig. 2. The distributions shown are: (a) potential of the metal relative to the solution, (b) anodic dissolution rate, (c) cathodic reduction rate, (d) oxygen concentration at the surface.

As the system parameters are changed, the curve given in Fig. 2 moves up and down and also changes shape. As a consequence, points of intersection which correspond to different classes of solutions (A, B, C, etc.) may pass out of existence. For example, as parameter Γ is decreased, Solution A eventually merges with

A′ and both disappear. As Γ is further decreased, Solutions B and C merge and disappear simultaneously. Such behavior also supports the contention that Solutions A′ and B are unstable whereas A and C are stable.

The foregoing discussion has been directed at evaluating the mathematical model and computational method as well as gaining an understanding of a somewhat complex phenomenon. In what follows, the model is employed to indicate the regions of parameter space over which solutions with an unacceptable maximum local corrosion rate exist. In principle, the approach promises to be of value to corrosion engineers since the physical conditions corresponding to unacceptable regions may thereby be avoided through proper design.

Parameter values were compiled for which Solutions A and C indicated localized corrosion. In Fig. 5, the region between any of the two matching coded lines corresponds to the region where Solution C exists. For example, when $\lambda = 3$ and $\xi = 0.1$, localized corrosion by steady-state Solution C would be expected over the range $3 < \Gamma < 20$; outside of this range of Γ, Solution C is not found. The influence of parameter λ on the existence of C is also shown in Fig. 5. A large value of λ corresponds to a large differential aeration and thereby enhances tendencies toward localized corrosion. The region of existence of C is therefore markedly increased by an increase in λ.

The region of existence of Solution C is also influenced by the value of the parameter ζ which is the ratio of the cathodic rate constant to the maximum anodic current density at the "tip" of the passivation hump. Figure 6 illustrates, for $\lambda = 2$, the influence of parameter ζ. An increase in ζ corresponds to an increase in oxygen reactivity so that the surface concentration of oxygen would thereby be decreased. As a consequence, the range of Γ over which C exists is shifted to larger values in order to increase the extent of differential aeration, which is the sole driving force for localized corrosion in this system.

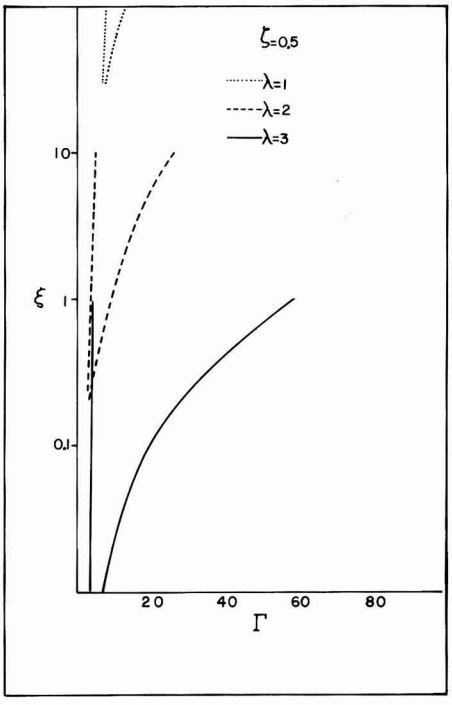

Fig. 5. Effect of differential aeration (parameter λ) on the existence of Solution C. The ξ-Γ region between any two matched coded lines is the region wherein Solution C exists.

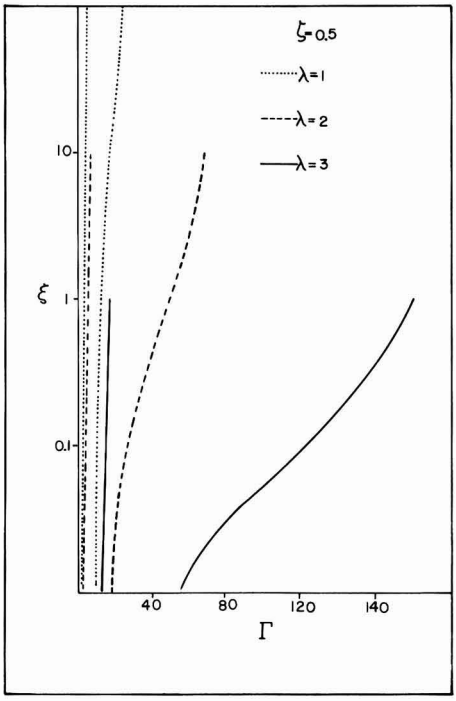

Fig. 6. Effect of differential aeration (parameter λ) on regions of parameters space where Solution A indicates highly localized attack.

Comparison of the influence of parameters λ and ζ as shown in Fig. 5 and 7 indicates clearly that approximations regarding the geometric form of the barrier layer have a far more drastic effect than approximations regarding the reaction kinetics which are applied to the model. Therefore applications of the results of this study to systems of different geometry would appear to risk introducing significant errors.

Solution A corresponds to the situation where the metal corrodes in the active region everywhere so that the local anodic dissolution rate increases steadily with decreasing barrier layer thickness (1). Although no passivation occurs, highly nonuniform dissolution may nevertheless occur. The regions shown between the matching coded lines in Fig. 6 correspond to situations where the maximum dissolution rate exceeds the value $0.1a$. It may be seen that the geometric parameter λ has a strong influence on the region of localized corrosion, similar to that shown in Fig. 5. On the other hand, the influence of the kinetic parameter ζ is essentially negligible and has not been displayed.

The existence of Solutions A′ and B has always been found to lie within the range of existence of A and C as given by Fig. 5-7. The range of parameter space over which the remaining multiple solutions exist (excluding the passive solution, D) have not been compiled. In some cases, multipolar solutions having characteristics similar to E and F have been found which lie outside the envelopes of existence for Solutions A and C provided by Fig. 5, 6, and 7. On the other hand, arguments have already been presented regarding the improbability of attainment of steady states corresponding to the E- and F-type solutions which exhibit multipolar behavior. That is, the regions of parameter space indicated by Fig. 5-7 include all likely regions wherein highly localized corrosion rates have been found in the model system under

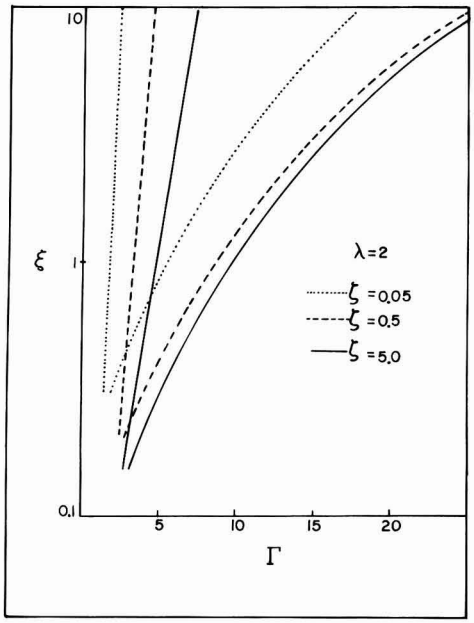

Fig. 7. Effect of the kinetic parameter ζ on regions of parameters space wherein Solution C exists.

study. Corrosion systems designed so as to lie outside these regions may therefore be expected to be unsusceptible to localized attack.

Conclusions

By determining the current distribution along a corroding surface, it has been possible to elucidate conditions under which highly localized corrosion is likely to occur in a simple model of differential aeration corrosion. Because the theoretical model is relatively straightforward, and because the underlying assumptions are relatively flexible, it is reasonable to expect that the foregoing transport phenomena approach may be extended to more complex situations of differential aeration corrosion as well as to other types of corrosion phenomena. The transport phenomena approach provides a route to predictive capabilities which has heretofore been lacking in corrosion design.

Owing to the active-passive behavior of the corroding metal incorporated in the model, multiple steady-state current distributions may exist for a single set of system parameters. The method of calculation employed above is capable of finding all of the multiple steady-state solutions. The method can therefore be used to seek out parameter regions where corroding systems would be susceptible to localized corrosion. The calculational method does not clarify the stability of the various multiple solutions in a rigorous manner but, by informal convention, suggests that Solutions A, C, and D are stable. Further, the method does not indicate which steady-state conditions would be attained following transient response from any given initial conditions; physical arguments, however, suggest that Solutions A , C, and D are most likely to be captured.

Several of the steady-state solutions exhibit multipolar behavior with up to three anodic and three cathodic regions distributed along the corroding surface. Current distributions of this type are not known to have been predicted in any previous investigation. However, the likelihood of observing such steady-state distributions in actual systems seems to be low in view of the unusual start-up conditions which would probably be required for their capture.

By developing dimensionless groups of system parameters, by investigating the response of the model to those parameters, and by developing a calculation method for finding all possible multiple solutions, the investigation provides a powerful intuitive grasp on the differential aeration corrosion phenomenon.

Acknowledgment

This study received partial support from the National Science Foundation via Grant NSF GK-36623.

Manuscript submitted Sept. 14, 1973; revised manuscript received July 19, 1974.

Any discussion of this paper will appear in a Discussion Section to be published in the December 1975 JOURNAL. All discussions for the December 1975 Discussion Section should be submitted by Aug. 1, 1975.

Publication costs of this article were partially assisted by the University of Illinois.

LIST OF SYMBOLS

a	maximum anodic current density, A/cm^2
c^o	oxygen concentration at barrier-atmosphere interface, g-mole/cm^3
D	oxygen diffusion coefficient, cm^2/sec
$\mathbf{F}$	Faraday constant, 96,500 coulombs/g-equiv
k	oxygen reaction rate constant, A/cm^2
l	characteristics length, cm
R	gas constant, 8.31 joules/g-mole °K
T	temperature, °K
X	distance along corroding surface, x/l, dimensionless

Greek characters

α	transfer coefficient
β	anodic current density on passive plateau
δ_m	mass transport layer thickness at $X = 0$, cm
δ_R	effective cross-sectional area at $X = 0$, cm
ζ	kinetic parameter, k/a, dimensionless
κ	barrier electrolytic conductivity, (ohm cm)$^{-1}$
λ	half-length of corroding surface, dimensionless
ξ	kinetic parameter, k/a, dimensionless
σ	characteristic width of passivation hump
Φ	potential, dimensionless

REFERENCES

1. R. Alkire and G. Nicolaides, *This Journal*, **121**, 183 (1974).
2. I. Epelboin, C. Gabrielli, M. Keddam, J. Lestrade, and H. Takenouti, *ibid.*, **119**, 1632 (1972).
3. N. Vahdat and J. Newman, *ibid.*, **120**, 1682 (1973).
4. R. Alkire and G. Nicolaides, Paper 101 presented at Electrochemical Society Meeting, Boston, Massachusetts, Oct. 7-11, 1973.
5. G. Nicolaides, M.S. Thesis, University of Illinois, Urbana, Illinois, September 1973.
6. L. Fox, "Numerical Solution of Ordinary and Partial Differential Equations," Chap. 5, Addison-Wesley Publishing Co., Reading, Massachusetts (1962).
7. L. Lapidus and J. Seinfeld, "Numerical Solution of Ordinary Differential Equations," p. 65, Academic Press, New York (1971).
8. I. M. Gel'Fand, *Am. Math. Soc. Translations*, **29**, 295 (1963).
9. H. Fujita, *Bull. Am. Math. Soc.*, **75**, 132 (1969).
10. I. Copelowitz and R. Aris, *Chem. Engr. Sci.*, **25**, 906 (1970).

Magnetic Properties of Anodic Oxide Coatings on Aluminum Containing Electrodeposited Co and Co-Ni

Satoshi Kawai

The Pilot Pen Company, Limited, Hiratsuka Works, Kanagawa, Japan

and Ryuzo Ueda

Department of Applied Physics, Waseda University, Tokyo, Japan

ABSTRACT

Cobalt and Co-Ni alloy were electrodeposited into the micropores of various kinds of anodic oxide films on aluminum. Fine granular metals precipitated on the barrier layer and formed columnar structures. Although the films of cobalt or nickel showed remarkable magnetic anisotropies perpendicular to the surface, the alloy films which consisted of approximately 50% cobalt showed a strong anisotropy along the horizontal direction. Coercive forces ranged from about 500 to about 1100 oe and the density of residual magnetization rose above 1000 gauss. The films may have applications in magnetic memories and recording devices.

When the surface of aluminum is anodized in some electrolytes, a film with micropores characteristic of the electrolytic conditions is formed (12). Asada (3) found that unsealed oxide coatings show peculiar colors when immersed in metal salt solutions after application of a.c. One of the authors (4) in a previous study observed that metallic nickel and nickel oxide were precipitated in the micropores when nickel sulfate was used as the electrolyte.

As cobalt has a larger saturation magnetization than nickel, deposits of cobalt and cobalt alloy are of particular interest for applications in magnetic devices. Zetner (5) reported that electrodeposited cobalt layers have a coercive force of 150-500 oe and a residual magnetization of 4000-8000 gauss, and that the coercive force could be increased to as high as 800 oe by the use of a.c. + d.c. during deposition. Morral (6) found that the magnetic properties of electrodeposited cobalt layers depend on bath temperature, current density, concentration of cobalt salt, ratio of a.c./d.c., and time of electrolysis.

Electrodeposited layers of Co-Ni alloy have a coercive force of 200-300 oe with remanence as high as 4000-8000 gauss. Zetner studied the relationship between the magnetic properties of Co-Ni alloy and electrolytic conditions and found that as *p*H varied from acid to neutral, the retentivity decreased, whereas the coercivity increased by about 50%. Furthermore, he indicated that a maximum coercivity and an excellent squareness ratio were obtained at about a 60% cobalt content in the deposited layer.

Endicott *et al.* (7) studied hardness and tensile strength of Co-Ni alloy deposits obtained from sulfamic acid baths under various conditions and found that the structure of the deposit affects the physical properties. In contrast to a columnar structure of the layers of pure cobalt and nickel, deposited layers of Co-Ni alloy have a lamellar structure with approximately 50% cobalt content, resulting in improved mechanical properties.

According to the phase diagram for Co-Ni alloys, the structures are β-phase at room temperature for a cobalt content of less than about 70%, and α-phase for the rest. Aotani (8) noted in his study of the structure of Co-Ni electrodeposits, using x-ray diffraction analysis, that the deposit obtained from an electrolyte solution of *p*H 1.2 showed fcc structure whereas those obtained from a bath of *p*H 6.3 included hcp at about 70% cobalt content.

Key words: anodizing, magnetic thin film, coercive force, remanence.

Experimental Procedures

Specimens were prepared by the following three methods, and the treatment conditions were as shown in Table I:

(*i*) Rolled aluminum sheets (99.99% in purity, 0.5 × 500 × 1000 mm^3 in size) were anodized in sulfuric acid, oxalic acid, chromic acid, phosphoric acid, sodium bisulfate, and sodium hydroxide [Table I (a)]. These oxide films were electrodeposited with cobalt in the sulfate solution [Table I (c)].

(*ii*) The oxide films made in sulfuric acid bath under various conditions [Table I (b)] were electrodeposited with cobalt in the sulfate solution [Table I (c)].

(*iii*) The anodic films formed in the sulfuric acid bath [Table I (d)] were electrodeposited with Co-Ni alloy for various ratios of cobalt and nickel in these sulfate solutions [Table I (e)].

Anodizing was carried out, with sufficient air stirring, either with a carbon plate as a counterelectrode for the oxalic acid and sodium hydroxide baths, or with a lead plate for the other electrolytes. When 15V

Table I. Bath compositions

Procedures	Remarks
Degreasing	5% NaOH, 80°C, 2 min
Desmut	5% HNO_3, 23°C, 1 min
(a) Anodizing	
Sulfuric acid	15% H_2SO_4, 0.1% Al, 1 A/dm^2, 21°C, 20 min
Oxalic acid	4% $(COOH)_2$, 0.1% Al, 1 A/dm^2, 35°C, 20 min
Chromic acid	5% CrO_2, 1 A/dm^2, 55°C, 40 min
Phosphoric acid	15% H_3PO_4, 1 A/dm^2, 30°C, 30 min
Sodium bisulfate	10% $NaHSO_4 \cdot H_2O$, 1.5 A/dm^2, 30°C, 20 min
Sodium hydroxide	0.5% NaOH, 2 A/dm^2, 15°C, 30 min
(b) Anodizing	
Sulfuric acid	5, 15, and 30% H_2SO_4, 0.1% Al 20° and 30°C 0.5, 1.0, and 2.0 A/dm^2 5, 10, 15, and 20 min
(c) Electrodeposition	
Cobalt	5% $CoSO_4 \cdot 7H_2O$, 2% H_3BO_3, *p*H 6.0 15V (50 Hz), 23°C, 10 min
(d) Anodizing	
Sulfuric acid	15% H_2SO_4, 0.1% Al, 1.5 A/dm^2, 21°C, 30 min
(e) Electrodeposition	
Co-Ni	4 ~ 0% $CoSO_4 \cdot 7H_2O$, 0 ~ 4% $NiSO_4 \cdot 7H_2O$, 2% H_3BO_3, 0.2% glycerine, 25°C, 20 min, 15V (50 Hz), *p*H 6.5
Sealing	1% $Ni(CH_3CO_2)_2 \cdot 4H_2O$, 90°C, 20 min

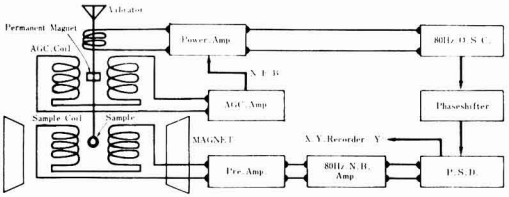

Fig. 1. Schematic diagram of sample vibrating magnetometer

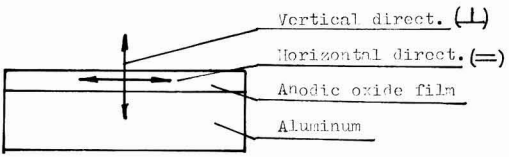

Fig. 2. Directions of magnetic anisotropies of anodic oxide film

a.c. was applied, about 5 A/dm^2 passed for a short time; after 5-10 sec a stationary current of about 1A/dm^2 was observed. The color of the oxide coating was brown at first, becoming black finally. After sealing, the specimens were wiped using a cotton cloth.

Specimens anodized in sulfuric and phosphoric acids were embedded in epoxy resin and sectioned to about 700Å using an ultrathin-film cutter. These sliced sections were then observed under an electron microscope.

For x-ray diffraction analysis, specimens anodized in sulfuric acid and electrodeposited with cobalt and Co-Ni alloy were immersed in 3% mercuric chloride solution and allowed to stand at room temperature for about 3 hr to strip the oxide. The stripped oxide films were washed, dried, and pulverized in an agar mortar.

The composition of the alloy deposited in the oxide films anodized in the sulfuric acid bath was determined by spectroscopic analysis. Specimens of 20 × 20 mm^2 were immersed in 5% sodium hydroxide solution at 30°C and the oxide films were stripped. The filtrate was boiled after adding hydrochloric acid, and the cobalt and nickel contents were determined using an atomic absorption spectrometer.

M-H hysteresis curves of the magnetic films were recorded with a vibrating magnetometer. A sample was vibrated along a direction vertical to the surface of the film; this made the measurement 50-500 times more sensitive than the usual automatic magnetometers. A schematic diagram of the apparatus is given in Fig. 1. Specimens in the form of a disk, 6 mm diameter were in sets of four on a quartz holder. The hysteresis loops along the horizontal and vertical direction were recorded to compare the magnetic anisotropies shown in Fig. 2.

Experimental Results

Figures 3 and 4 show electron micrographs of ultrathin sections of cobalt-deposited films anodized in sulfuric and phosphoric acids, respectively. The oxide film formed in sulfuric acid separated from the surface of the aluminum by a barrier layer. In the outer oxide film, columnar micropores about 100Å in diameter, about 400Å in distance from each other, and perpendicular to the surface were observed. These micropores were filled with fine granular deposits. In the phosphoric acid film, pillar-shaped deposits about 500Å in diameter were arranged nearly perpendicular to the surface at about 1000Å intervals.

From x-ray diffractometer analysis of the cobalt deposits, the structure was assigned as hcp α-Co (a = 2.507Å, c = 4.070Å) by reference to ASTM x-ray card 5-0727. In the case of Co-Ni alloy depositions, as the cobalt content decreased, the fcc crystal gradually appeared and the hcp structure disappeared. Figure 5 depicts the relationship between the calculated lattice constants and the cobalt content in the deposits.

The amount of cobalt and nickel deposited into the oxide film formed in the sulfuric acid bath is shown in Fig. 6.

The M-H hysteresis curves of the oxide films formed in various electrolytes and electrodeposited with the cobalt are shown in Fig. 7 (a)-(f). In these experiments, correction for the demagnetizing field of the quartz holder was made in advance.

With sulfuric acid, oxalic acid, and sodium bisulfate baths the cobalt-deposit layers showed strong magnetic anisotropies along the vertical direction with good squareness ratios but rather weak anisotropies along the horizontal direction. With chromic acid and sodium hydroxide baths, the anisotropies along the vertical direction were decreased. While with the phosphoric acid bath, this property along the horizontal direction was increased.

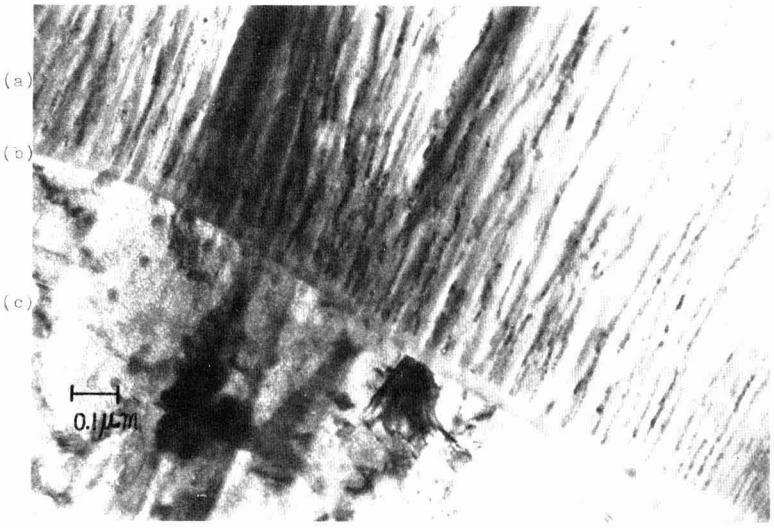

Fig. 3. Electron micrograph of ultrathin section film anodized in sulfuric acid and electrodeposited with cobalt. (a) Aluminum oxide film, (b) barrier layer, (c) aluminum.

Fig. 4. Electron micrograph of ultrathin section film anodized in phosphoric acid and electrodeposited with cobalt. (a) Aluminum oxide film, (b) barrier layer, (c) aluminum.

Coercive forces indicated are characteristic of each electrolyte. The values for the films anodized in sulfuric and oxalic acid baths were greater than 1000 oe, while low values of about 500 oe were obtained with the phosphoric acid bath.

In Fig. 8 coercivities of the films anodized in the sulfuric acid bath are given as a function of the anodizing time. The effects in various electrolytic conditions were also measured. Coercive forces along the horizontal direction varied little, while the vertical components increased with increasing electrolyte concentration and decreasing current density. However, these vertical coercive forces were reduced with anodizing time and converged to a definite value.

Similarly, the relation between the strength of the residual magnetizations and the anodizing time was measured. The strength along the horizontal direction increased with the anodizing time, this increase being more pronounced as the electrolyte concentration and current density increased. After calculating the film thickness using an empirical formula, the relationship between the residual induction and the film thickness was as shown in Fig. 9. Residual magnetization increased with film thickness, but approached a saturation value. A larger magnetization value was obtained for an electrolyte of 30% concentration than with one of 15%.

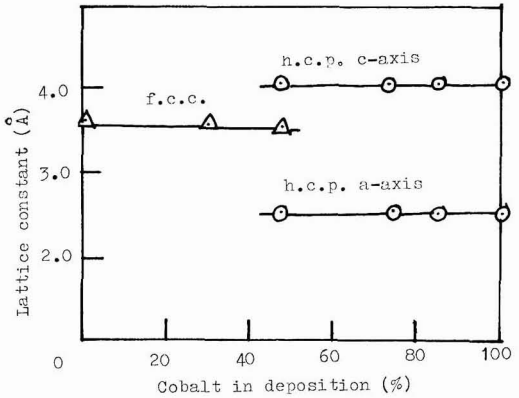

Fig. 5. Lattice constants of Co-Ni deposition onto anodic oxide films.

In general, the density of remanence, B, can be expressed as

$$B = 4\pi M/V$$

where M indicates the strength of remanence (emu) and V designates the volume of the magnetic film (cgs). Then, $0.01M$ for a disk 6 mm in diameter having a 10 μm film thickness gives a magnetic density of about 440 gauss, and $0.025M$ is calculated to be more than 1000 gauss.

From some typical hysteresis curves for Co-Ni alloy deposits in films anodized in the sulfuric acid bath, the relation between the cobalt contents in the deposit layers to the coercivities and retentivities are shown in Fig. 10 and 11, respectively.

The coercive forces along the vertical direction varied from about 750 oe at 100% nickel content to about 1100 oe at 100% cobalt content. On the other hand, the coercivities along the horizontal direction rapidly increased from a value of 300 oe for 100% nickel content to a maximum of about 1100 oe for

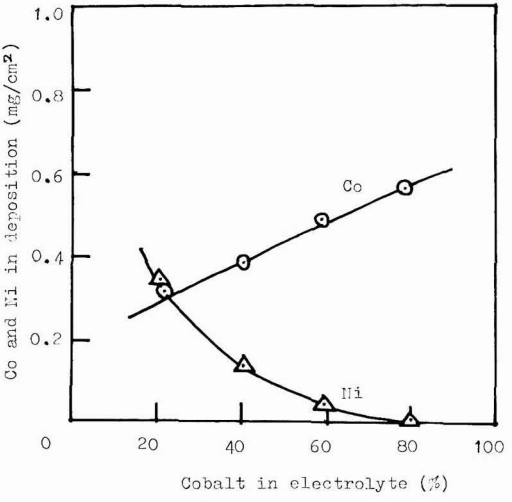

Fig. 6. Cobalt and nickel content between electrolyte and deposition.

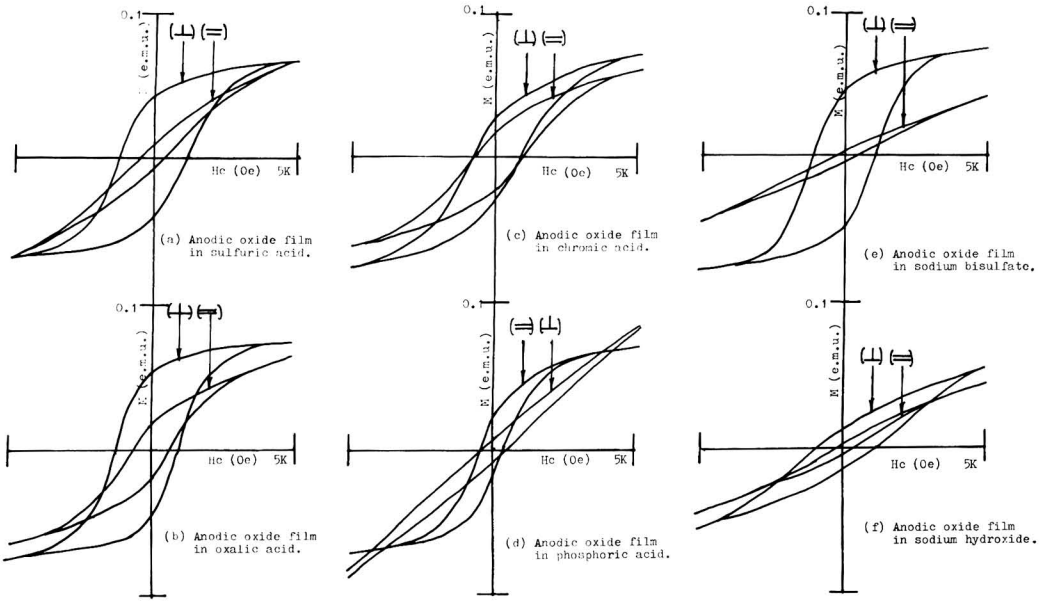

Fig. 7 (a)-(f). M-H hysteresis curves of oxide films anodized in various kinds of electrolytes and electrodeposited with cobalt

50% cobalt content, followed by a slight decrease to about 600 oe for 100% cobalt. The remanence strength along the vertical and horizontal directions showed a trend similar to that of the coercive forces, indicating a maximum value along the horizontal direction at about 50% cobalt content. The fact that the vertical and the horizontal magnetic properties reversed at around 50% content is considered to be an indication of some change in the structure of the deposited metal.

Magnetic Properties of Cobalt Deposits

The crystal orientation of the deposits has an influence on magnetic anisotropy. For α-Co with hcp structure, the axis of easiest magnetization has been measured to lie along the c-axis (9). Endicott and Knapp (7) demonstrated that electrolytic deposits obtained from cobalt salt solution show a columnar structure. Morral (6) indicated that the axis of easiest magnetization of cobalt obtained from an electrolyte near neutral pH was vertical to the surface. Thus, with the columnar structure, magnetic anisotropy along the vertical direction may be attributed to crystal growth in a direction which is parallel to the c-axis. From these facts, cobalt crystals deposited in the micropores of anodic oxide films may be presumed to have similar structures.

Assuming a film thickness of 1 μm, the ratio of the length to the diameter of the micropore will be 100:1. A needlelike structure of the metal deposit would result forming long unit magnetic domains. The magnetic anisotropy of the cobalt deposit may result not

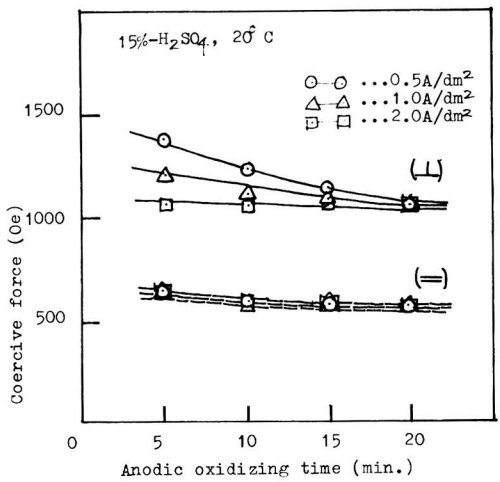

Fig. 8. Relations between remanences of electrodeposited layers and anodic oxidizing times.

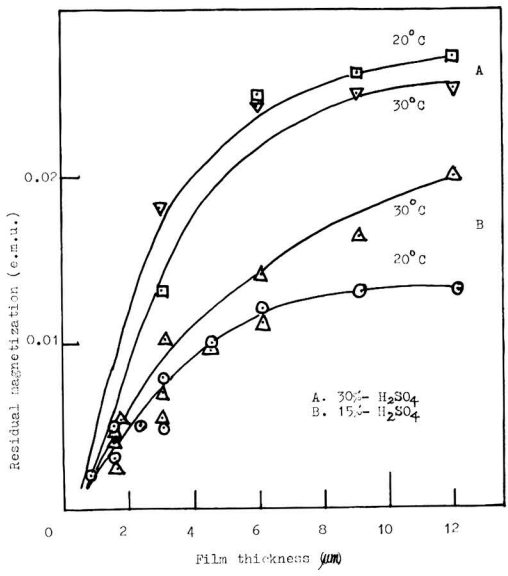

Fig. 9. Residual magnetizations vs. film thickness of anodic oxide films deposited with cobalt.

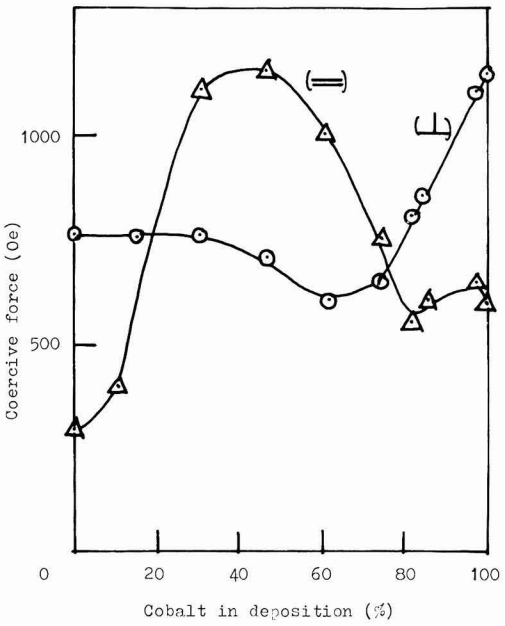

Fig. 10. Coercive forces of anodic oxide films electrodeposited with Co-Ni.

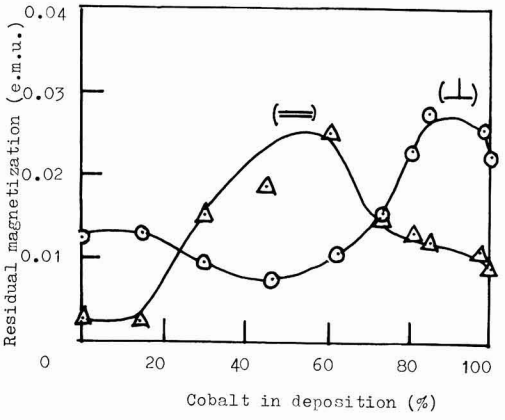

Fig. 11. Residual magnetizations of anodic oxide films electrodeposited with Co-Ni.

only from the orientation of the cobalt crystal particles but also by the effect of particle shape.

Anodic oxide films obtained from the chromic acid bath are reported to form zigzag micropores, which occurrence reduces the uniformity of deposition, resulting in a weaker magnetic anisotropy along the vertical direction than that obtained from the sulfuric acid bath. Magnetic films anodized in a sodium bisulfate bath are said to have properties similar to those in sulfuric acid, hence the identical hysteresis loop. Little is known about the film obtained from sodium hydroxide baths. Although the oxide film shows good adsorption of dyestuff, this indicates relatively large micropores in the film. From the magnetic properties of this film, the presence of an irregular pore structure similar to the chromic acid bath case can be expected.

The coercive forces of the films did not show any marked variation with electrolytic conditions, although the trend was observed that coercivities increased with concentration of the sulfuric solutions and decreasing current densities. According to Keller *et al.* (1), decreasing electrode potential has the effect of decreasing the cell diameter, and it may be accepted that variations in temperature and concentration of electrolyte influence the electrode potential. From these considerations, the diameter of micropores in this case should be reduced to a certain extent. The shorter the electrolysis time, the higher the coercivity obtained. This might be due to a greater uniformity of the micropore structure for thinner films.

The remanence strength became larger with increasing film thickness and electrolyte concentration. However, it reached a saturation value probably due to a definite amount of cobalt deposition in the micropores under the given operating conditions. On the other hand, the density of magnetization was smaller than the values obtained from the usual electrodeposition, and it is considered that there is some limitation of the amount of the density because the porosity of micropores is estimated to be about 10% of the whole volume of the oxide film.

Magnetic Properties of Co-Ni Alloy Deposits

An x-ray diffraction analysis of the Co-Ni alloy deposits revealed the presence of α-Co for the film having a cobalt content greater than about 50% and a fcc structure for the lower concentration. The magnetic anisotropy of these deposits rotated by 90° from the direction vertical to the horizontal at about 50% cobalt content.

The crystal orientation of metal grain in the films was not experimentally determined in this study, but the orientation of the metal deposit in the micropores should determine the magnetic anisotropy of the film. In the lamellar structure, as the direction of the crystal growth is parallel to the surface and the c-axis is easiest magnetization, the magnetic anisotropy of the oxide film develops to the horizontal direction of the surface, and this is regarded as crystal anisotropy.

The anodic oxide coatings deposited with magnetic metals provide not only a powerful means for study of the film structures, but also have potential applications for high bit density memories and recordings.

Acknowledgment

The authors thank Messrs. N. Shinohara and U. Sakai of the Pilot Pen Company, Limited for their help.

Manuscript submitted Feb. 11, 1974; revised manuscript received Aug. 7, 1974.

Any discussion of this paper will appear in a Discussion Section to be published in the December 1975 JOURNAL. All discussions for the December 1975 Discussion Section should be submitted by Aug. 1, 1975.

Publication costs of this article were partially assisted by The Pilot Pen Company, Limited.

REFERENCES

1. F. Keller, M. S. Hunter, and D. L. Robinson, *This Journal*, **100**, 411 (1953).
2. H. Akabori and T. Fukushima, *J. Electronmicroscopy (Tokyo)*, **13**, 162 (1964).
3. T. Asada, Jap. Pat. 310401 (1963).
4. S. Kawai and M. Mizusawa, *J. Metal Finishing Soc. Japan*, **20**, 272 (1969).
5. V. Zetner, *Plating*, **52**, 868 (1965).
6. F. Morral, *Metal Finishing*, **62**, 59 (1964).
7. D. W. Endicott and J. R. Knapp Jr., *Plating*, **53**, 43 (1966).
8. T. Aotani, *J. Inst. Metals Japan*, **B-14**, 55 (1950).
9. R. Bozorth, "Ferro-Magnetism," p. 555, D. Van Nostrand Co., Inc., Princeton, N.J. (1968).

Electrodeposition along the Air-Solution Interface

I. Experimental Investigation

R. A. Dilorio,[1] W. J. Newby,[2] and A. J. Sukava*

Chemistry Department, University of Western Ontario, London, Ontario, Canada

ABSTRACT

In the electrolysis of an acidified copper sulfate solution with a copper wire cathode located vertically along the axis of a cylindrical copper anode, addition of a small amount of norvaline to the solution causes a disklike deposit of copper to grow outwardly from the cathode and along the air-solution interface. Experiments show that this phenomenon is due mainly to a solid reaction product arising from air oxidation of the norvaline along the line of contact between the copper anode, air, and solution. This solid, presumably present in a highly subdivided state, migrates by surface diffusion from the anode to the cathode along the air-liquid interface, giving rise to nucleation sites that lead to the interfacial cathode growth. The mechanism is thought to involve a conductive surface film containing copper powder as a conducting medium. The rate of disk formation depends on the concentration of the norvaline, the area of anode surface along the air-solution interface, the acidity of the solution, the partial pressure of oxygen above the solution, and the rate of current flow. It does not depend very markedly on the concentration of the copper sulfate.

The results of preliminary experiments on the growth of a copper electrodeposit along the air-solution interface, caused by small concentrations of norvaline in the acid sulfate electrolyte, have been described in a previous publication (1). This unusual phenomenon was first noticed in this laboratory in the course of a study of excess deposit weights caused by various additives. It occurs when the acidified copper sulfate solution containing the norvaline is electrolyzed with a wire cathode positioned vertically along the axis of a cylindrical copper anode. The interfacial deposit consists of a disk-shaped growth of copper extending outwardly from the cathode along the liquid surface. The disk is sometimes radially asymmetric as a result of noncoincidence of the cathode position and the anode axis, with growth favored in the direction of greatest current flux.

As reported (1), the formation of the interfacial disk is always accompanied by a change in color of the copper sulfate solution to a blue-green, and by formation of a finely divided, black, suspended solid that settles on standing after electrolysis is stopped. Separation of the anolyte and catholyte by means of a porous thimble surrounding the wire cathode (Whatman cellulose extraction thimble as indicated by a- - -a in Fig. 1) prevents formation of the disk. Moreover, both the color change and the formation of black solid occur only in the electrode compartment outside the thimble, whether the outer cylindrical electrode is made the anode or the cathode. Obviously, these two effects are interdependent and not markedly affected by the electrode potential. They occur primarily at the electrode with the greater surface area.

Experiments showed that prior oxidation of the dissolved norvaline by air or oxygen in the presence of a copper surface (presumably as catalyst) is a primary requisite in giving rise to the interfacial disk. The color change and black solid are a result of this oxidation, and electrolysis of a solution containing these oxidation products produces the interfacial disk whether or not oxygen is excluded. If a freshly prepared norvaline-containing electrolyte is deaerated with nitrogen and then electrolyzed under a nitrogen atmosphere, none of these effects occur.

* Electrochemical Society Active Member.
[1] Present address: Colonel By Secondary School, Ottawa, Ontario, Canada.
[2] Present address: Alcan International Limited, Research Centre, Kingston, Ontario, Canada.
Key words: interfacial disk, anode effects, norvaline, copper powder, conductive film.

A more detailed study has now been made of this form of interfacial electrodeposition. The results of various experiments, some still preliminary in nature, are presented and discussed in this report.

Experimental Technique

The simple apparatus used in this study is illustrated in Fig. 1. The glass cell, fitted with a ground-glass cap as shown, had a total volume of about 100 mliters. A copper wire cathode, about 1 mm in diameter, was positioned approximately along the axis of a cylindrical copper anode with an inside diameter of about 3 cm. The cathode was immersed to a depth of about 4.9 cm when the cell contained 50 mliters of solution. An appropriate opening in the cell cap held the cathode in place and another opening provided access for the anode lead. Two other openings (not shown) provided for electrolysis under an atmosphere of nitrogen or oxygen as required.

Most of the anodes were made from ordinary commercial copper tubing. These anodes, as well as the wire cathodes, were heated to redness prior to use to destroy any possible organic contaminants that might have been present. They were then etched in nitric acid and washed and rinsed with distilled water. However, some of the anodes were prepared by electrodeposition of "pure" copper on cylindrical platinum gauze substrates, *i.e.*, using platinum electrodes and a copper sulfate electrolyte previously purified by passing through a column of activated charcoal. These anodes were not preheated since no organic additives were used in their formation.

The standard solution used in the disk-growth experiments contained 0.5M copper sulfate and 1.0M sulfuric acid, both reagent grade. The organic additives were also reagent grade, as obtained commercially. These were added without further purification to the freshly prepared standard electrolyte to give the desired concentration. The water used in the solutions was distilled twice with all-glass apparatus. It had a specific conductance of about 6×10^{-6} ohm^{-1}-cm^{-1}.

All experiments were carried out at a constant applied current, using a Harrison regulated power supply, Model 6201-A. In most of the experiments, several cells containing different concentrations of organic additive were connected in series so that the same amount of charge flow occurred in each. The cell assembly was immersed to the solution level in a temperature-regulated bath maintained at 25° ± 0.05°C.

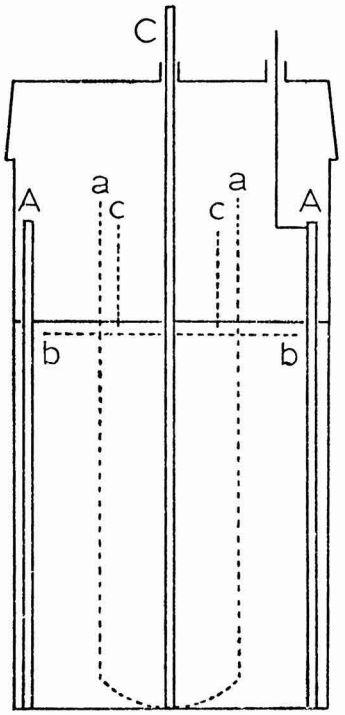

Fig. 1. Electrolysis cell. A, Cylindrical copper anode, about 3.0 cm ID; C, copper wire cathode, diameter about 1 mm; a - - - a, porous cellulose thimble to separate anolyte and catholyte; b - - - b, horizontal Parafilm or cellulose sheet to eliminate convection flow at the air-solution interface; c - - - c, cylindrical Parafilm barrier to isolate the cathode region of the air-solution interface from the anode. Length of the cathode immersed with 50 mliter solution, 4.9 cm.

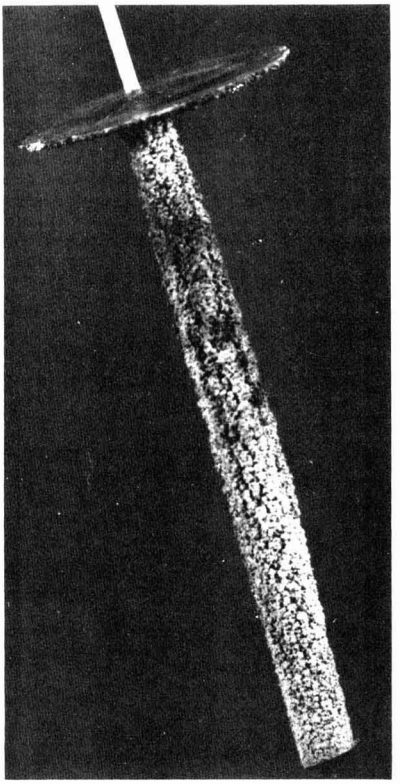

Fig. 2a. Copper cathode with interfacial disk. Top view. Diameter of disk, 2.0 cm

Results and Discussion

Figure 2 shows photographs of a typical cathode deposit obtained after prolonged electrolysis in the presence of a small amount of norvaline. The disklike deposit grew along the air-solution interface, during a given period of electrolysis and at a given current flow, to an extent dependent on the norvaline concentration. Typical data are shown in Fig. 3. At a constant current flow of about 45 mA, the optimum norvaline concentration was about 2.5×10^{-2} molar.[3] Experiments with freshly prepared solutions always showed that the disk growth did not begin until after several hours of initial electrolysis. Furthermore, the results were qualitatively the same whether the anodes were made from "impure" commercial copper tubing or whether they were made by prior electrolysis of a "purified" copper sulfate electrolyte with deposition on cylindrical platinum substrates. The indication here is that possible minor impurities in the anode metal are of no apparent consequence in the disk growth process. The cathode and anode current efficiencies were about 100 and 83%, respectively.

Besides formation of the surface disk, the following additional effects were observed:

1. The initial blue color of the copper sulfate solution changed to a blue-green with about 24 hr of electrolysis.

2. A small amount of finely divided black solid was found dispersed and suspended in the solution.

3. Finely divided copper powder was sometimes found at the bottom of the electrolysis cell, confirming Ibl's observation (2) that such powder forms at the cathode during electrolysis.

Inhibition of disk growth.—The decreased diameter of the copper disk with norvaline concentrations greater than 2.5×10^{-2}M (see Fig. 3) is probably due to some kind of inhibiting effect caused by the excess norvaline. This suggestion is based on the observation that the same effect was obtained by adding other structurally related organic compounds to the solution. For example, if the norvaline concentration was kept constant at 2.5×10^{-2}M, and if either N-acetyl norvaline or glycine was added, the effect was to decrease the disk growth. N-acetyl norvaline was found to cause a greater decrease in disk growth than glycine at the same concentration, indicating presumably that a large additional molecule has a greater inhibiting effect than a small one.

Disk growth and rate of current flow.—Figure 4 shows the effect of the rate of current flow on the size of the disk. In these experiments, the time of electrolysis was adjusted so that the same total charge passed through the solution in every case, with the initial concentration of norvaline being fixed at the optimum 2.5×10^{-2}M. The maximum rate of disk growth occurred under these conditions when the current, kept constant throughout, was about 60 mA.

Disk growth and convective flow.—In the cell shown in Fig. 1, the presence of the cellulose thimble a- - -a

[3] In one experiment, a paper-thin layer of copper metal formed across the surface of the solution, causing a direct short between cathode and anode. Attempts to reproduce this extreme form of interfacial deposition were not successful, indicating that the conditions for maximum rate of disk growth are probably rather critical.

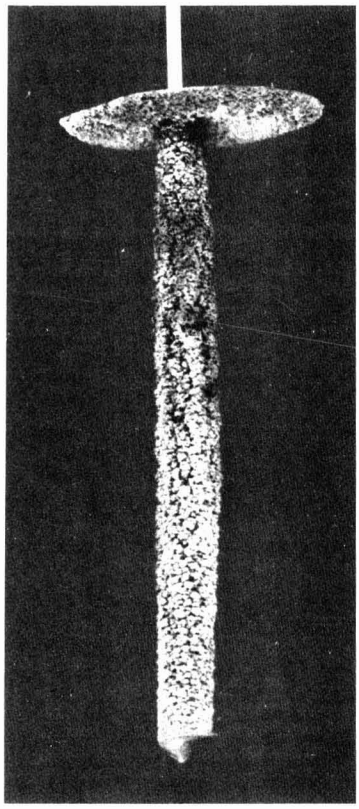

Fig. 2b. Copper cathode with interfacial disk. Bottom view

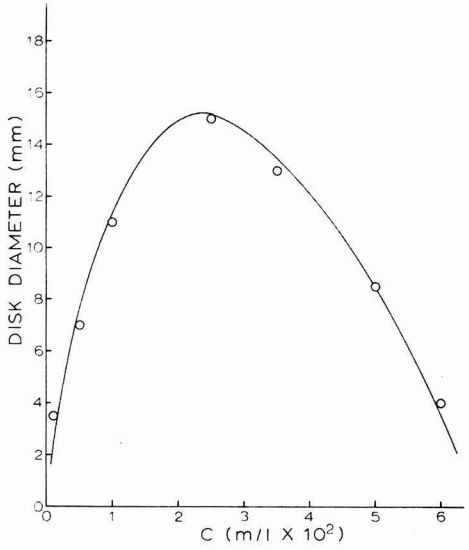

Fig. 3. Disk diameter *vs.* C, the initial molar concentration of norvaline. Time of electrolysis, 48 hr; current, 45 mA; temperature, 25°C.

can be expected to eliminate or at least substantially reduce the normal convective flow, which is upward

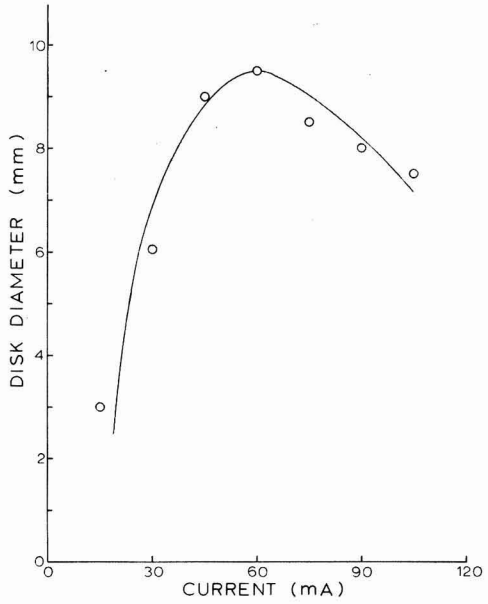

Fig. 4. Disk diameter *vs.* current. Norvaline concentration, 2.5 × 10^{-2}M; charge flow, 5200 coulombs; temperature, 25°C.

at the cathode and downward at the anode. Since this thimble prevents formation of the interfacial disk (1), experiments were designed to examine the role that convection might possibly play in the disk-growth mechanism. In some of these experiments, shortened, fully immersed thimbles were used such that they surrounded only the bottom 1-3 cm of the cathode. In others, pieces of cellulose cut from the thimbles were immersed in the solution in such a manner that they did not interfere with the convection stream. In every case, with the amount of cellulose being in excess of about 18 cm^2 of the thimble material, it was found that formation of the air-solution interfacial disk did not occur. Apparently the cellulose interferes with the disk-growth process by removing some soluble or colloidal active agent, possibly by adsorption.

Further evidence to support this view was obtained from experiments in which horizontal barriers were used to reduce or eliminate the normal convection (see b- - -b in Fig. 1). As was noted previously (1), formation of the interfacial disk is not prevented by a thin sheet of nonporous Parafilm (a waxy waterproof material obtained from the Fisher Scientific Company) attached to the cathode and located horizontally just below the solution line. However, similar horizontal barriers consisting of cellulose sheet (cut from Whatman extraction thimbles) do prevent the disk formation. Accordingly, since the convection stream cannot be affected very differently by these similar horizontal barriers, whether Parafilm or cellulose, then adsorption of a disk-growth agent by the cellulose is indicated. The convection stream as such is not an important factor in the disk-growth mechanism, except perhaps as an aid in keeping the disk-growth agent in suspension along the liquid surface.

Outgrowth at the bottom end of the cathode.—In the experiments with shortened cellulose thimbles, outgrowths sometimes appeared at the bottom end of the cathode and along the inner surface of the thimble (see Fig. 5). Evidence was found showing the presence of copper powder inside these fully immersed thimbles, indicating that decreased local turbulence due to reduced convection might be a factor in causing the powder to settle to the bottom. No copper powder

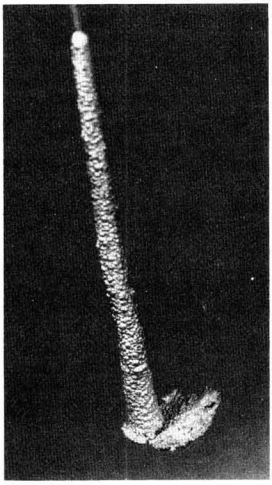

Fig. 5. Cathode growth with short, fully immersed, cellulose thimble, showing effect of settled solid and copper powder. Diameter of bottom outgrowth, 1.3 cm.

was found in any of the full-length thimbles that surrounded the cathode completely, and no such bottom-end growths occurred. Therefore, it seems evident and reasonable that copper powder is a factor in giving rise to the nucleation sites and conducting medium for the bottom outgrowth, if norvaline is present in the solution. It is also evident that a second factor required for the cathode outgrowths, whether at the bottom of a shortened thimble or at the air-solution interface, arises from an oxidation (1) of the norvaline at the anode.[4] This is indicated by the behavior of the full-length cellulose thimble apparently acting as a barrier against the transport of some active powder-forming and outgrowth-producing agent to the cathode. Moreover, the anode reaction product is probably particulate in form, against which the cellulose can act as an effective and adsorptive screen. More conclusive evidence to support this view follows.

Role of the air-solution interface.—Since the cathode outgrowth along the air-solution interface is caused by effects arising initially at the anode, and since the convection stream is not the means of transport of the active agent to the cathode, experiments were done to test the possibility of transport of particulate material from anode to cathode by a diffusion mechanism operating along the liquid surface. A vertical Parafilm cylinder was used as a surface barrier (see c---c in Fig. 1). Because this cylinder, about 1.5 cm in diameter, extended into the solution to a depth of less than a millimeter, it did not interfere with the normal convection in the cell. It isolated the cathode only along the air-solution interface, and it prevented formation of the interfacial disk. Apart from this there was no other observable effect. The color change to blue-green and the formation of black solid occurred as before.

Obviously, transport of some kind of particulate material occurs along the surface of the solution, from anode to cathode, when norvaline is present during the electrolysis. It seems reasonable that this material is involved in the formation of a conductive film along the air-solution interface such that deposit nucleation can occur, and it is suggested that the interfacial conductivity probably arises from the presence in this film of metallic copper in a highly subdivided state. Copper powder can be expected to form along the upper part of the cathode, as observed by Ibl (2), and to accumulate in the adjacent air-solution interface.

Material responsible for disk growth.—It was of interest to try to determine whether the color-change effects as well as the solid formed at the anode might be directly involved in the disk formation. Experiments with the cellulose thimbles and the Parafilm surface barriers, as already described, indicate that the material responsible is particulate in form.

It was found that if the suspended solid was removed from the electrolyzed solution by filtration through a fine sintered-glass funnel, and if the blue-green filtrate was then deaerated and electrolyzed under nitrogen, no disk formation occurred. Clearly, the disk-growth process requires the presence of the solid. (It was also found that if such a filtrate is electrolyzed in the presence of air, disk growth occurs after a few hours of such further electrolysis together with formation of more solid.) Other experiments then showed that if the solid obtained by filtering an electrolyzed norvaline solution is added to standard electrolyte containing no norvaline, and if this solution is deaerated and electrolyzed in the absence of oxygen, the interfacial disk is obtained and in a shorter period of time. The same result is obtained if the solid is first produced without electrolysis, that is, by sufficiently prolonged contact of the norvaline-containing electrolyte with air and a copper surface. (Copper turnings were used in these experiments.) Obviously, the dispersed solid is the only factor responsible for the disk growth, to the extent that the anode effects are concerned. The soluble color-affecting reaction products are not directly involved, indicating that the possible presence of dissolved copper-norvaline complexes is not important.

Particulate nature of the disk-forming agent.—A further indication that the material involved in the disk-growth mechanism is particulate in form came about in a different manner. An acid copper sulfate-norvaline solution was first electrolyzed for about 48 hr, during which the air-solution interfacial disk was formed. The electrolysis was then stopped and the system was left undisturbed for about 6 hr. After this period, during which the black solid settled to the bottom of the cell, the circuit was closed again for another 48 hr of electrolysis. The disk at the air-solution interface increased in size, but a second and larger disk now formed at the bottom along the glass-solution interface. A similar result was obtained if the solution was stirred by means of a steady stream of air flowing upward along the anode from a small capillary introduced into the cell. The effect was to decrease considerably the rate of disk formation at the air-solution interface, though not completely, and to cause a relatively rapid disk growth at the bottom end of the cathode (see Fig. 6). Obviously, the air stream causes coagulation and settling of the otherwise suspended solid to form a conducting medium along the bottom of the cell. [It should be noted at this point that a corresponding effect occurs in the disk growth along the upper surface of horizontal Parafilm sheets attached to the cathode at various depths, as observed previously (1), presumably because the solid then settles on these sheets during electrolysis due to reduced convection.]

Role of the anode.—Since the solid formed by air oxidation of norvaline is a primary cause of the disk growth at the cathode, and since this solid originates at the anode, experiments were done to examine the role of the anode in the oxidation mechanism. Variation in the area of anode surface in contact with the solution had no effect on the rate of growth of the interfacial disk, indicating that the oxidation of the norvaline does not occur on the immersed surface of the anode. Experiments were then done with a completely immersed anode, using a shortened copper cylinder such that the upper rim was immersed just below the

[4] Whatever the detailed nature of the anode reaction, the effects are not stereospecific with respect to the norvaline. Experiments with the D and L forms alone gave the same results as the DL-norvaline routinely employed.

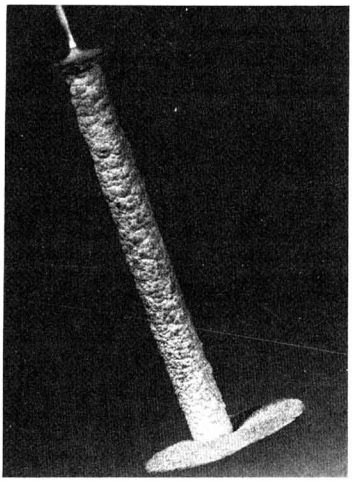

Fig. 6. Copper cathode with small interfacial disk, showing bottom outgrowth due to coagulation of solid by air flow past the anode. Diameter of bottom outgrowth, 1.9 cm.

solution line. No disk formation occurred and no color change or formation of black solid took place. Clearly, the air oxidation of norvaline at the anode occurs only along the line of contact between copper surface, air, and solution.

Dispersed solid and the oxidation reaction.—The results of preliminary and incomplete experiments indicate that a thorough study is required to examine the mechanism of air oxidation of norvaline at a copper surface, including in particular a detailed analysis of the solid and other possible products of the reaction. Roughly quantitative analyses showed that the composition of the solid material, which contains copper, varies from sample to sample. The solid is insoluble in ordinary organic solvents, indicating possibly a polymeric character. It is soluble in concentrated inorganic acids and, apart from a residue identified as copper powder, it dissolves also in dilute aqueous bases. (This evidence of copper powder in the dispersed solid reinforces our suggestion, or assumption, that conductivity of the interfacial film is probably due to metallic copper.) The base-soluble portion undergoes a nonreversible hydrolysis since a regenerated solid obtained on acidification no longer has the same organic composition as the original material. Nor does this regenerated solid have the disk-forming ability, presumably in part because it does not contain copper powder. However, analyses showed that about 30% by weight of the regenerated solid is copper, indicating that at least part of the copper in the original solid is present in combined or complexed form. This copper content, considerably greater than the amount found in the original material, about 5.5%, suggests strongly that the original solid is a mixture rather than a pure compound, with the combined copper presumably complexed in at least one component. Further study of the solid oxidation product was not attempted.

Formation of NH_3 and CO_2.—Takajama *et al.* (3) have reported that amino acids undergo electrodecomposition to yield an aldehyde of one carbon less together with evolution of NH_3 and CO_2. The oxidation of norvaline by air or oxygen in our experiments cannot be regarded as an electrodecomposition, since it occurs even in the absence of electrolysis, but it was nevertheless observed that NH_3 and CO_2 were produced, with the NH_3 appearing as ammonium ion in the acid solution. The results of various experiments are presented here primarily as observations, without attempt at interpretation.

Analyses were done to determine the NH_3 and CO_2 produced as air, and then pure oxygen, was passed slowly through the cell and over the norvaline-containing solution. The NH_3 was determined after electrolysis by a standard Kjeldahl method, and the CO_2 was found by passing the gas stream during electrolysis through a solution of $Ba(OH)_2$.

The rates of formation of NH_3 and CO_2, with a given amount of norvaline present, were found to depend on the partial pressure of oxygen above the interface as shown in Fig. 7, the amount of each gas formed being approximately linear with time. It was also found that the rates of formation of NH_3 and CO_2 do not depend on the concentration of $CuSO_4$, but that they do depend very markedly on the concentration of acid as shown in Fig. 8. Obviously, the rate of growth of the interfacial disk is correspondingly dependent on the acidity of the solution, and this in fact was observed. The maximum disk growth occurred with 2.5×10^{-2}M norvaline when the H_2SO_4 concentration was about 1.0M. It was found as well that the production of NH_3 and CO_2 does not depend on the current, which is consistent with the observation that formation of the black solid occurs with equal facility in the absence of electrolysis. The reaction requires only an acidified norvaline solution, a copper surface, and air or oxygen at the interface.

It is interesting to note in Fig. 7 that the formation of NH_3 and CO_2 in our experiments does not take place in a one-to-one ratio, as would be the case if Takajama's observation regarding formation of an aldehyde were applicable to our system (3). Our data show that NH_3 and CO_2 are produced in a mole ratio of about four to one when norvaline in acid solution is oxidized by air or oxygen on a copper surface.

Experiments with other compounds.—Numerous experiments were done to see whether compounds other than norvaline are similarly capable of causing formation of the interfacial disk. Compounds structurally

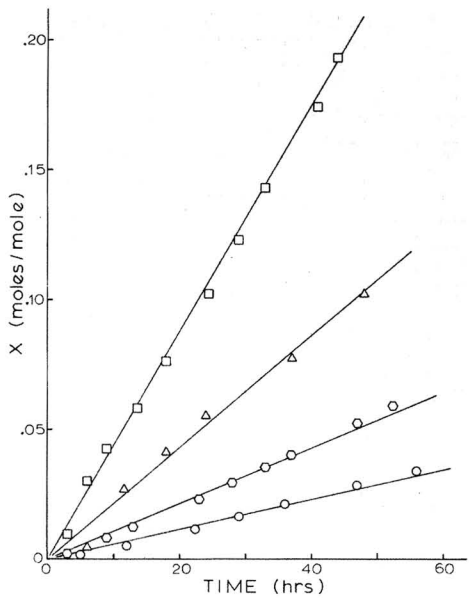

Fig. 7. *X* moles NH_3 and CO_2 produced per mole of norvaline present *vs.* time of electrolysis. Initial norvaline concentration, 2.5×10^{-2}M; current, 45 mA; temperature, 25°C. ○, CO_2 with air at the interface; ○, CO_2 with O_2 at the interface; △, NH_3 with air at the interface; □, NH_3 with O_2 at the interface.

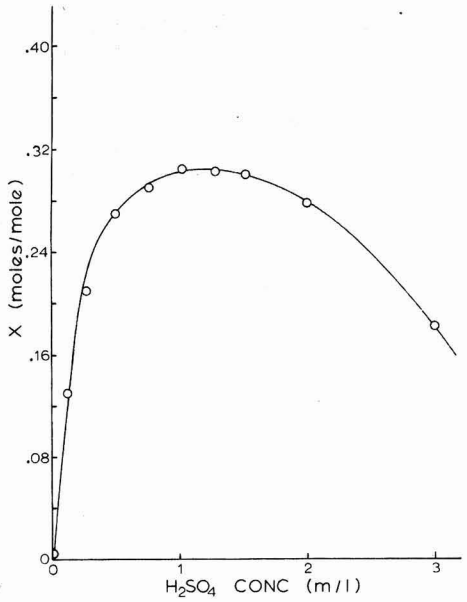

Fig. 8. X moles NH_3 produced per mole of norvaline present vs. molar concentration of H_2SO_4. Initial norvaline concentration, 2.5 × 10^{-2}M; time, 48 hr; temperature, 25°C.

and constitutionally related to norvaline were chosen. These were: norleucine, leucine, valine, α-aminobutyric acid, β-aminobutyric acid, α-aminooctanoic acid, and N-acetyl norvaline. The concentration of the additive, the acidity of the solution, and the time of electrolysis were all varied, but no condition was found such that disk formation occurred. Qualitative and quantitative tests showed that NH_3 was formed to a greater or lesser degree with all of these compounds, and a change in color of the solution was observed with some of them, particularly with norleucine and with α-aminooctanoic acid. However, unlike norvaline, none of them showed any formation of dispersed solid in observable amount. Obviously, the functional groups are not the only requirement for the formation of the solid and the interfacial disk. The length of the carbon chain appears to be a critical factor in the process.

Summary and Conclusions

1. In the electrolysis of an acid copper sulfate solution with a wire cathode surrounded by a cylindrical copper anode, addition of a small amount of norvaline causes a disk-shaped outgrowth to form on the cathode and along the air-solution interface.

2. The primary cause of this interfacial outgrowth is a solid oxidation product arising from reaction of the dissolved norvaline with air or oxygen at a copper surface, in this case the anode. Dissolved reaction products are not involved.

3. During the electrolysis, oxidation of the norvaline occurs only along the line of contact between copper anode, air, and solution.

4. Transport of the solid oxidation product from anode to cathode takes place by surface diffusion along the air-solution interface.

5. Cathode outgrowths can be produced along the bottom of the electrolysis cell by causing the otherwise suspended solid to settle.

6. Evidence of copper powder at the bottom of the cell in some experiments, and evidence of a copper-powder residue left on dissolving the solid reaction product in dilute bases, indicates that formation of the interfacial cathode outgrowths probably involves copper powder as a conducting medium.

7. In a group of eight structurally related amino acids, all examined under similar electrolytic conditions, only norvaline produced the interfacial cathode outgrowths.

Acknowledgments

Financial support from the National Research Council, Ottawa, in the form of a research grant, and also in the form of a scholarship to R.A.D., is gratefully acknowledged.

Manuscript submitted May 31, 1973; revised manuscript received July 29, 1974.

Any discussion of this paper will appear in a Discussion Section to be published in the December 1975 JOURNAL. All discussions for the December 1975 Discussion Section should be submitted by Aug. 1, 1975.

Publication costs of this article were partially assisted by the University of Western Ontario.

REFERENCES

1. A. J. Sukava, W. J. Newby, *et al.*, *Nature*, **220**, 574 (1968).
2. N. Ibl, *Helv. Chim. Acta.*, **37**, 1149 (1954).
3. Y. Takajama, T. Harada, and S. Miduno, *Bull. Chem. Soc. Japan*, **12**, 342 (1937).

Electrodeposition along the Air-Solution Interface

II. Metallographic Study

J. M. Trenouth,[1] R. A. Dilorio,[2] and A. J. Sukava*

Department of Chemistry, University of Western Ontario, London, Ontario, Canada

ABSTRACT

A metallographic examination was made of a cathode deposit formed along the air-solution interface of an acid copper sulfate electrolyte containing a small amount of norvaline. The photomicrographs indicate initial nucleation at the interface, presumably along a preexisting conductive film, followed by growth of the deposit downward toward the solution. No evidence was found of growth cones extending radially and horizontally from the cathode and along the interface.

The preceding paper (1) describes the results of some experiments on the mechanism by which a small amount of norvaline added to an acid copper sulfate electrolyte causes the cathode deposit to grow preferentially along the air-solution interface when electrolysis occurs with a wire cathode and a cylindrical copper anode. It is speculatively suggested that this particular form of electrodeposition occurs as a consequence of a conductive film formed along the surface of the solution. This film is thought to contain copper powder formed at the cathode, thus giving rise to initial deposit nucleation at or near the cathode but along the liquid surface.

The details of the growth habit of the interfacial disk are not revealed by the chemical investigation described in Part I (1). Moreover, it is not clear whether the assumed conductive film can be regarded as a preexisting condition followed by the observed downward thickening of the interfacial deposit, due to nucleation only along its lower face, or whether a preferred horizontal growth occurs outwardly and radially from the cathode, along the air-solution interface, prior to the downward growth. To attempt a further elucidation of the mechanism, a brief metallographic examination of the interfacial deposit was carried out as part of the investigation. For this purpose, photomicrographs of deposit cross sections were produced and examined by one of us (J.M.T.) at the Structures and Materials Laboratory, National Aeronautical Establishment, National Research Council, Ottawa. The results are reported in this paper.

Specimen Preparation

Typical cathode deposits with the interfacial outgrowth were prepared as described in Part I (1). Various cross sections were then made for metallographic study, using standard techniques. Referring to Fig. 1a and b, longitudinal sections were made of the wire cathode and deposit in the region at the solution line and at the bottom end. A transverse section, made approximately midway, is represented in Fig. 1c. For the specimen examined, the interfacial disk-shaped deposit was detached readily from the electrode intact, enabling a separate cross section to be made of it as indicated in Fig. 2.

After sectioning, all specimens were coated with electroless nickel plating to preserve specimen edges and to prevent their rounding during subsequent grinding and polishing. All specimens were etched after polishing with either of the solutions A or B (Table I).

Table I. Polishing solutions

Solution A	
H_2SO_4 (conc)	1 mliter
H_2O_2 (10%)	20 mliters
Followed by	
$SnCl_2 \cdot 2H_2O$	0.5g
$CuCl_2 \cdot 2H_2O$	1.0g
$FeCl_3 \cdot 6H_2O$	30.0g
HCl (conc)	42 mliters
C_2H_5OH	500 mliters
H_2O	500 mliters
Solution B	
H_2SO_4 (conc)	1 mliter
H_2O_2 (10%)	20 mliters
H_2O	21 mliters

Results and Discussion

Normal deposit.—The longitudinal and transverse sections of the electrode in Fig. 1, photographed under plane polarized light, show the wire with the copper deposit as it is normally formed. A variation in the structure of the deposit from the original substrate to the outer surface is evident, the deposit near the substrate having a columnar or conelike structure of the field-oriented type and that near the outer surface having an unoriented-dispersion type of structure. The crystallinity of the outermost deposit in this specimen is also considerably coarser than that near the original wire. These structural variations are presumably the result of a combination of factors including the gradu-

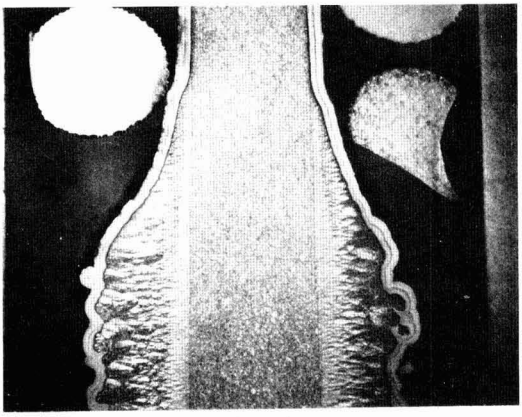

Fig. 1a. Longitudinal cross section of wire cathode and deposit at the solution line. Interfacial disk removed.

* Electrochemical Society Active Member.
[1] Present address: Structures and Materials Laboratory, National Aeronautical Establishment, National Research Council, Ottawa, Ontario, Canada.
[2] Present address: Colonel By Secondary School, Ottawa, Ontario, Canada.
Key words: interfacial disk, photomicrographs, growth cones, cone orientation.

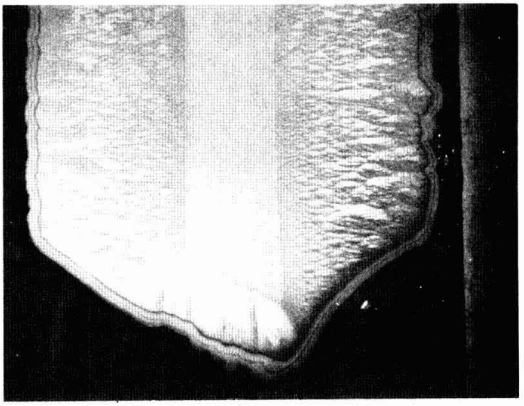

Fig. 1b. Longitudinal cross section of bottom end of wire cathode and deposit, showing vertical and horizontal growth cones.

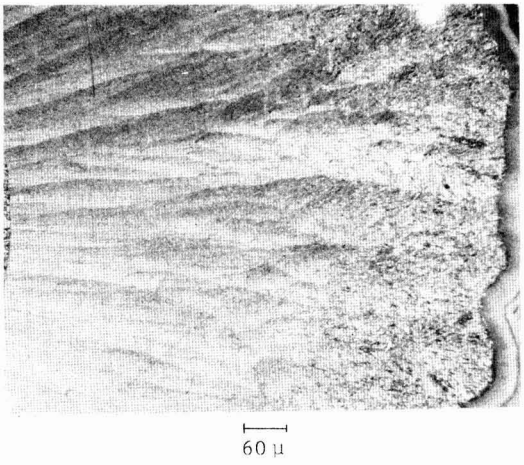

Fig. 1c. Transverse cross section of cathode deposit midway between solution line and bottom end. Part of the cathode wire substrate is visible on the left.

ally decreasing current density with increasing cathode area under constant current flow [see Part I (1)] and the presence of adsorbed components of the solution affecting the growth habit. These features were not always observed, however. In another specimen, the oriented columnar structure extended all the way to the outer surface, but only along the upper part of the cathode. The lower region showed a transition to the unoriented structure similar to Fig. 1. Examination showed that the oriented and unoriented internal structures are associated with relatively smooth and rough external surfaces, respectively.

The columnar structure evident in the longitudinal view in Fig. 1b is of particular interest in that it shows a discontinuity in direction of the growth cones at the bottom end of the electrode. The longitudinal section at the solution line where the interfacial disk was originally attached (Fig. 1a) showed only the horizontal columnar feature.

The conelike structure noted in all the sections of the deposit appears to be identical with that of vapor-deposited silicon carbide (2) and pyrolytic graphite (3, 4). The growth cones are all of the continuously nucleated type shown schematically in Fig. 12 of Ref. (3) and as an actual deposit in Fig. 2B of Ref. (2). In the case of pyrolytic graphite, such continuous nucleation has been attributed to relatively large agglomerations of carbon being deposited with much finer particles (3). However, unlike the vapor deposits, the growth cones at the bottom end of the copper electrode shown in Fig. 1b are parallel with the axis of the electrode rather than perpendicular to the surface of deposition, and in place of continuous radiation of deposit around the corners at the electrode tip, there is an abrupt change from horizontal to vertical growth. If the direction of growth of the cones in the electrodeposit follows current flow lines as indicated by the deposit in Fig. 1c and that along the axis of the electrode in Fig. 1a and b, then the deposit at the electrode tip implies a discontinuous pattern of current flow lines at the corners of the tip.

Deposit at the air-solution interface.—In several instances, the interfacial disk-shaped deposit was only loosely held to the wire cathode, as was evident in its easy detachment enabling it to be lifted off along the wire. This suggests a primarily mechanical contact between the disk and the electrode rather than the presence of actual chemical bonds of the normal metallic type, as might be expected if the disk growth occurs and originates from a preexisting conductive surface film. On the other hand, it might be possible, although it appears less likely, that a thin or brittle interfacial deposit actually bonded to the wire at the meniscus could also result in the observed easy detachment of the disk.

The cross section of the interfacial disk shown in Fig. 2 reveals a columnar or conelike structure in all regions. This is just visible in the low-power micrograph of Fig. 2a taken in ordinary illumination but more clearly revealed when examined in polarized light and under greater magnification as shown in Fig. 2b and c. An enlarged view of one of the wings is shown under ordinary illumination in Fig. 2d, slightly defocused to bring out the obvious laminar pattern in the deposit. The similarity of the structure of this copper deposit with those of silicon carbide (2) and pyrolytic graphite (3, 4) is apparent not only with respect to the growth cones perpendicular to the substrate surface but also with respect to the laminar pattern. The heavy line running midway through the deposit in Fig. 2d was probably caused by a current interruption leading to a discontinuity in the deposition process.

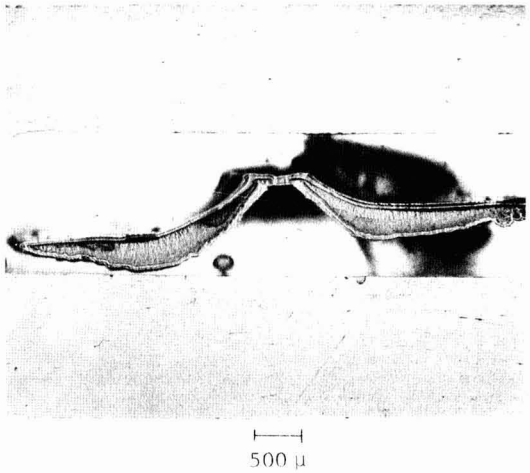

Fig. 2a. Vertical cross section of interfacial disk

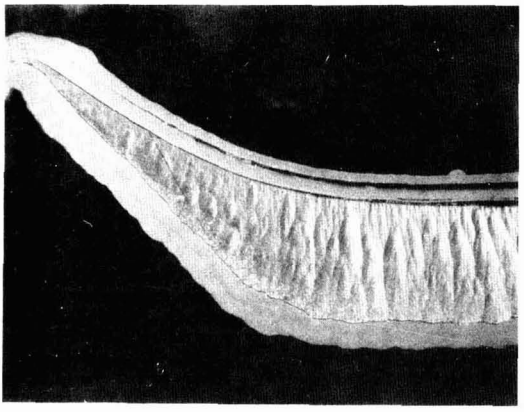

Fig. 2b. Vertical cross section of one wing of the interfacial disk under polarized light.

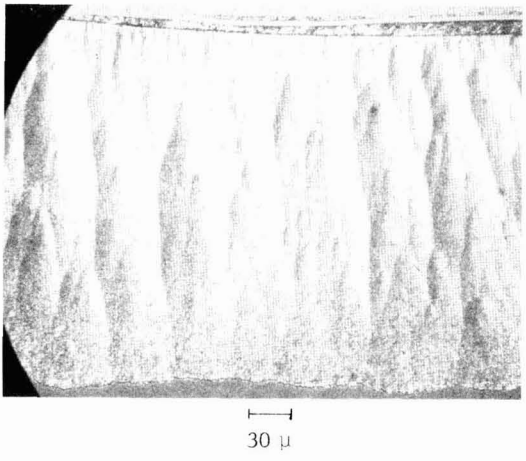

Fig. 2c. Vertical cross section of interfacial disk. Enlarged view under polarized light, showing columnar structure.

The orientation of the growth cones in the interfacial disk shown in Fig. 2 indicates that nucleation occurred at the surface of the electrolyte, along the air-solution interface. Growth perpendicular to this interface took place at all times, even within the meniscus. There is no evidence in the photomicrographs to indicate nucleation at the surface of the wire electrode with growth radiating out along the air-solution interface and perpendicular to the electrode axis. In fact, examination of Fig. 1a shows that the normal horizontal growth cones on the electrode just below the meniscus are prevented from continued growth by the downward-growing interfacial disk. Furthermore, the photomicrograph of the bottom end of the cathode in Fig. 1b seems to indicate that growth cones normally develop in a fixed orientation determined by the manner in which the growth begins, and that this orientation continues with the new cones as the deposit grows in a lateral direction. Presumably, the growth pattern of the interfacial disk is no exception.

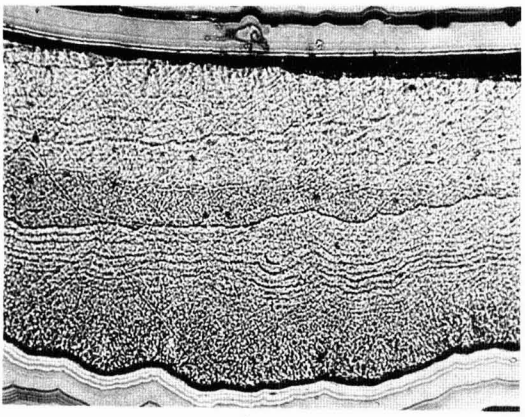

Fig. 2d. Vertical cross section of interfacial disk under ordinary illumination, showing laminar pattern.

Summary and Conclusions

1. Metallographic examination of cross sections of copper deposits formed at the cathode and along the air-solution interface, and caused by small amounts of norvaline in the acid copper sulfate electrolyte, shows growth cones extending downward from the interface into the solution.

2. The downward orientation of the growth cones, with no evidence of horizontal growth cones at the air-solution interface near the cathode, supports the view that deposit nucleation occurs at the liquid surface and that a conductive surface film is probably present as a preexisting condition for the nucleation.

3. The assumed conductivity of the interfacial film is considered to arise from the presence of copper powder formed at the cathode, in conjunction with reaction products arising from oxidation of the norvaline at the copper anode (1).

4. The disk-shaped deposit was sometimes easily detached from the cathode by lifting off along the wire, indicating mainly a mechanical contact with no particular metallic bond between the disk and the cathode wire. This is consistent with downward growth of the disk from a preexisting conductive surface film.

Acknowledgments

The financial support of the National Research Council, Ottawa, the use of the facilities of the Structures and Materials Laboratory, National Aeronautical Establishment, National Research Council, Ottawa, and, in particular, the preparation of the metallographic specimens by Mrs. Mary Grzedzielski, are all gratefully acknowledged.

Manuscript submitted May 31, 1973; revised manuscript received July 29, 1974.

Any discussion of this paper will appear in a Discussion Section to be published in the December 1975 JOURNAL. All discussions for the December 1975 Discussion Section should be submitted by Aug. 1, 1975.

Publication costs of this article were partially assisted by the University of Western Ontario.

REFERENCES

1. R. A. DiIorio, W. J. Newby, and A. J. Sukava, *This Journal*, **122**, 37 (1975).
2. T. D. Gulden, *J. Am. Ceram. Soc.*, **51** (8), 424 (1968).
3. L. F. Coffin, Jr., *ibid.*, **47** (10), 473 (1964).
4. S. Yajima and T. Hirai, *J. Mater. Sci.*, **4** (5), 416 (1969).

Electrode Kinetic Studies on Electro-organic Syntheses Involving Carbonium Ions

II. Anodic Oxidation of Acetate Ions in Presence of Dimethylformamide

G. Bélanger,* C. Lamarre,* and A. K. Vijh*

Hydro-Quebec Institute of Research, Varennes, Quebec, Canada

ABSTRACT

The anodic oxidation of acetate ions in (nominally nonaqueous) glacial acetic acid and in glacial acetic acid-dimethylformamide solutions has been examined on platinum at various temperatures between 25° and 75°C. Potentiostatic and potentiodynamic techniques were used in conjunction with reaction product analysis by infrared and NMR. The real heat of activation at the reversible potential for the Kolbe reaction in glacial acetic acid is 53 kcal $mole^{-1}$. Also, acetate ions can undergo oxidation at low potentials (*e.g.*, 0.45V *vs.* RHE) when the reaction is carried out at a high temperature (*ca.* 75°C). The oxidation of DMF is indicated around 1.1-1.5V at temperature above 55°C, both in potentiostatic and potentiodynamic profiles. The product analysis shows that oxidation of DMF also occurs at high potentials (*e.g.*, 2.37V) in parallel to the Kolbe reaction. The product of DMF oxidation at this potential is N-acetoxymethyl N'-methylformamide; the coulombic efficiency for the formation of this product at 2.37V is about 5%.

In the first report (1) in this series of publications, anodic oxidation of acetate ions to methyl acetate, on a graphite electrode, was examined from an electrode kinetic point of view. The purpose of the present work was to investigate some aspects of the anodic oxidation of acetate ions in acetic acid in the presence of dimethylformamide (DMF) on a smooth platinum electrode. This has already been examined from a synthetic point of view by Ross (2) who suggests that the following reactions can occur

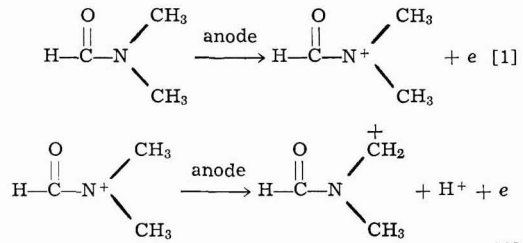

[1]

[2]

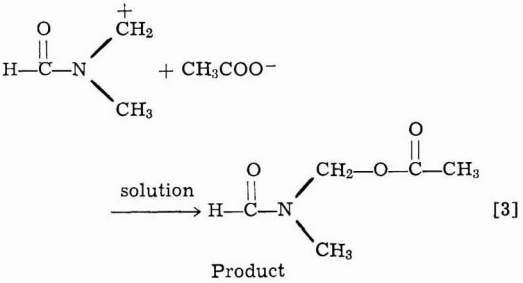

[3]

Product

Recently, Ross *et al.* (3) have also reported some current potential studies, both steady-state and cyclic voltammetric, on the above system. The present work explores these electrode kinetic aspects in somewhat more detail, especially with regard to the effect of temperature on the reaction. In order to obtain this information, it was necessary also to investigate the temperature effects on the oxidation of the acetate ions themselves, which has been examined previously only quite briefly (4).

*Electrochemical Society Active Member.

Key words: Kolbe reaction, carbonium ions, electrosyntheses, DMF electro-oxidation, heat of activation.

Experimental

All experimental details except the following have been described recently (1).

Smooth platinum wires, sealed into Pyrex in open flame with subsequent thorough cleaning were used as the working electrodes. The platinum wire was 99.999% pure and was supplied by the Engelhard Industries Ltd. The DMF was Baker analyzed reagent.

The steady-state current-potential relationships were recorded by the automatic procedure described previously (5). All potential values refer to the hydrogen electrode in the same solution and are designated by the symbol, E_H.

Although the usual precautions to eliminate moisture from the acetate/acetic acid solutions were taken, the solutions must be presumed to contain traces of water since the experiments were not conducted in a controlled-atmosphere chamber.

For the analysis of reaction products, a large smooth platinum foil (10 cm^2) was used for the galvanostatic electrolysis of a 1M DMF plus 1M potassium acetate in glacial acetic acid solutions. The current density used was 1.5 mA/cm^2 and the electrolysis was carried out for 5 days at 78°-79°C. The product was isolated and identified from its infrared and nuclear magnetic resonance (NMR) spectra by comparing with a known product synthesized chemically by the acetylation of N-hydroxymethyl N'-methylformamide, prepared as described previously (6).

Results and Discussion

Temperature effects in the anodic oxidation of acetate ions.—In Fig. 1, potentiostatic, steady-state current-potential curves for the anodic oxidation of 1M CH_3COOK in acetic acid at smooth platinum are presented for various temperatures. Although steady-state polarization curves were conducted at several temperatures for the determination of ΔH^* values (Fig. 2), the various Tafel plots shown in Fig. 1 and 4 depict only a few representative temperatures in order to avoid cluttering. These curves were corrected graphically for the iR drop. At the higher anodic potentials, there is little hysteresis between the ascending and descending curves. From these corrected current-

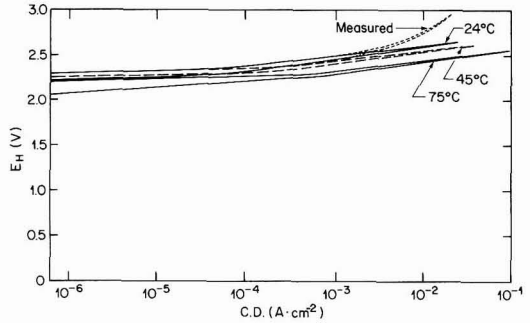

Fig. 1. Steady-state, potentiostatic current-potential relationships on smooth platinum in 1M CH_3COOK in CH_3COOH, at the shown temperatures. These curves were corrected for the ohmic drop in the solution. The 24°C curve illustrates the current-potential behavior with and without the ohmic corrections.

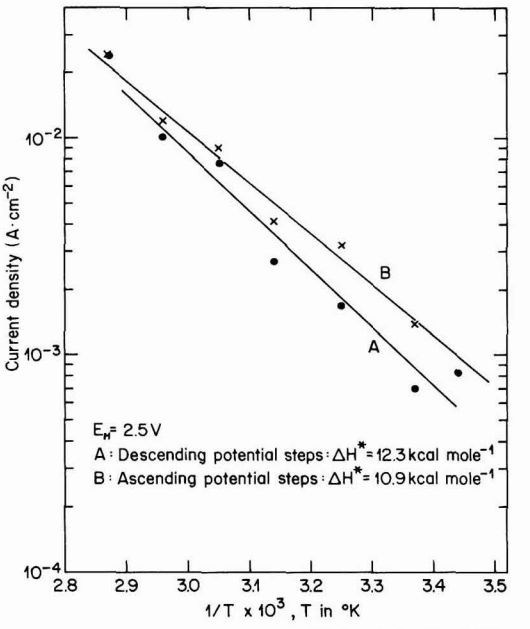

Fig. 2. Plots for the determination of ΔH^*, *i.e.*, $(\partial \log i/\partial (1/T))_{E_H}$ values as deduced from the data in Fig. 1.

potential relationships, a Tafel correlation can be observed for at least two decades. In Table I, we present the experimental values of Tafel slopes and the transfer coefficient β for various temperatures. The latter is constant within the experimental error. The b values

Table I. Tafel slopes in 1M CH_3COOK in glacial acetic acid solutions

Temp, °C	Ascending potential steps		Descending potential steps	
	b (exp), mV	β^*	b (exp), mV	β^*
24	150	0.39	125	0.47
35	140	0.44	105	0.58
45	135	0.47	113	0.55
55	150	0.43	118	0.55
65	150	0.45	133	0.50
75	137	0.50	125	0.55
		Avg: 0.45 ± 0.04		Avg: 0.53 ± 0.04

* $\beta = 2.303RT/b\mathbf{F}$.

for the ascending potential steps are greater than $2RT/\mathbf{F}$. This high value of the Tafel parameter has also been observed for the Kolbe reaction (7) at low temperatures (25°C) and was accounted for by a barrier-layer film mechanism (7).

The apparent heat of activation ΔH^* can be evaluated from the log current density *vs.* $1/T$ relationships for a given potential as illustrated in Fig. 2. The slopes as obtained from a least square deviation treatment of the data give value of 11-12 kcal mole^{-1} for the ΔH^*. This heat of activation does not, of course, refer to the value at the reversible potential for the over-all reaction of acetate oxidation

$$2CH_3COO^- \rightarrow C_2H_6 + 2CO_2 + 2e \qquad [4]$$

The apparent heat of activation at a given potential, ΔH^*, is related to the apparent heat of activation for the reaction at the reversible potential, ΔH^*_r, by the equation

$$\Delta H^*_r = \Delta H^* + \beta\eta\mathbf{F} \qquad [5]$$

where η is the value of the overpotential at which the ΔH^* value has been determined. The reversible potential for the acetate oxidation (*i.e.*, Eq. [4]) in glacial acetic acid is −1.05V (with reference to the reversible hydrogen electrode) (7). If the anodic oxidation of acetate, and hence the determination of ΔH^* is done at 2.5V (*vs.* RHE), as in Fig. 2, the value of the overpotential, η, becomes 3.55V for this case. By using this value of η and the experimental values of ΔH^* (at 2.5V) and β in Eq. [5], one obtains the value of $\Delta H^*_r \simeq 47$ kcal mole^{-1}. This is the value of the heat of activation which is relevant to the process in reaction [4] since it refers to the reversible potential. Alternatively, one could have obtained the same value by determining the exchange current density, i_o, values at various temperatures and then plotting log i_o *vs.* $1/T$; however, extremely long extrapolations needed to obtain i_o values for the present case would make the values thus determined meaningless. The only approximation involved in our determination of ΔH^*_r value, as outlined above, is that the value of β is constant at various temperatures studied. Although the values of β in Table I are not exactly constant, they do not show a systematic variation with temperature and hence must be attributed to a normal scatter of experimental data within a fairly narrow range from which a mean constant value of β may be deduced, as in our calculation.

It is interesting to point out that from the value of the apparent heat of activation at the reversible potential, ΔH^*_r, one can estimate the real heat of activation, ΔH^*_R, for the Kolbe reaction in nonaqueous medium, *i.e.*, for the reaction in Eq. [4]. This real heat of activation is given as (10)

$$\Delta H^*_R = \Delta H^*_r + \beta\,\Delta H^\circ$$

where ΔH° is the heat of the Kolbe reaction (Eq. [4]). This latter thermodynamic quantity has to be estimated from the heats of formation of $CH_3COO^-{}_{solvated}$, C_2H_{6gas}, and CO_{2gas}. The last two quantities are available in standard handbooks. The value of the heat of formation of acetate ion in acetic acid has to be approximated to its value in aqueous solution which is −116.84 kcal mole^{-1} (11). The validity of this approximation can be based on the near equality of free energy of formation of acetic acid in aqueous solution and its value in glacial acetic acid (7): the difference between these values is less than 4 kcal mole^{-1}. Since the heat of formation of the proton is defined as zero, one feels that the approximation for the ΔH° is sound. The ΔH° so obtained is equal to 13 kcal mole^{-1} with an uncertainty of ±5 kcal mole^{-1} arising from the above assumption. Using the experimentally determined β(0.45), the real heat of activation at the reversible potential, ΔH^*_R is estimated at 53 kcal mole^{-1} with an estimated error of ±3 kcal mole^{-1}.

It should be pointed out that the extremely high (53 kcal mole^{-1}) value of ΔH^*_R for the Kolbe reaction (*i.e.*, Eq. [4]) is consistent with other features of this reaction (7, 8) such as: very low exchange current densities, extremely high overpotentials needed to obtain a given rate of reaction, filming of the electrode and hence increase in the reaction resistance during the course of the reaction. No previous data, it is believed, are available for comparing the magnitude of our ΔH^*_R values.

An interesting temperature effect arises in the potentiodynamic profiles (Fig. 3). At a comparable sweep rate, the potentiodynamic profile at 75°C shows an additional anodic peak around 0.45V, which is not observed in the experiments carried out at a much lower temperature (24°C).

The appearance of the new anodic peak indicates that at high temperatures, a noticeable surface reaction between the surface oxides and the adsorbed organic (or its intermediates) occurs giving rise to the new anodic peak at 0.45V. This peak is similar to the one observed in the electrooxidation to CO_2 of other organic fuels, *e.g.*, $HCOO^-$ (9). This assignment of the peak would be consistent with the fact that at high temperatures, complete oxidation of the acetate ions to CO_2 does indeed occur at potentials below *ca.* 0.7V (4).

It has been observed that the peak at 0.45V appears only at low sweep rates (*e.g.*, 50 mV sec^{-1}) whereas it tends to disappear at higher sweep speeds (*e.g.*, 343 mV sec^{-1}). This would suggest that at faster sweep rates, the surface reaction between the oxide and the adsorbed organic does not have sufficiently long opportunity to pass enough charge needed to give rise to a pronounced anodic current peak.

Temperature effects in the anodic oxidation of acetate ions and DMF.—In the potentiostatic, steady-state current-potential curves (Fig. 4) obtained at various temperatures, it is observed that at potentials above 2.1V (*i.e.*, at which the Kolbe reaction commences), there is little difference in the behavior in the presence or absence (Fig. 1) of DMF. At lower potentials, however, at temperature above *ca.* 55°C, new features appear which are presumably associated with the oxidation of DMF. The oxidation of DMF between 1.1 to 2.0V approximately, at 55°C and above, is suggested by

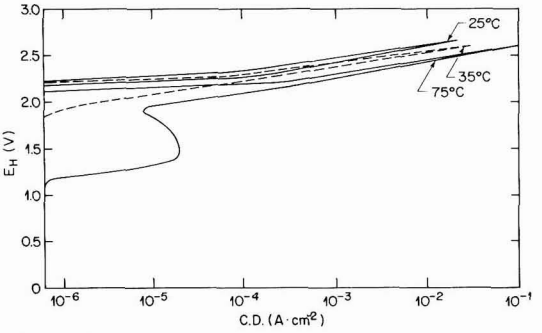

Fig. 4. Same as in Fig. 1 but now the solution made 1M in DMF

the new current inhibition regions appearing in Fig. 4. This type of inhibition inflections are not uncommon for electro-organic oxidations and have been discussed previously by Bagotskii (12), Conway and Gilroy (13), and others (14). The ΔH^* values for the DMF oxidation cannot be determined because of the absence of well-defined Tafel lines, at several temperatures, pertaining to the DMF oxidation (*i.e.*, at potential below 2.0V). The ΔH^* values deduced from the Tafel lines (above 2.1V) in Fig. 4 are comparable to those obtained from Fig. 1 suggesting thereby that at high anodic potentials oxidation of the acetate is the predominant reaction even in the presence of DMF.

There are some pronounced effects of temperature on the potentiodynamic profiles obtained in solutions containing DMF (Fig. 5). At 25°C there is virtually no difference between this solution containing DMF and the profile obtained for potassium acetate in acetic acid. At 75°C, one clearly observes detailed structure in the profile, including the anodic peak around 0.5V. The

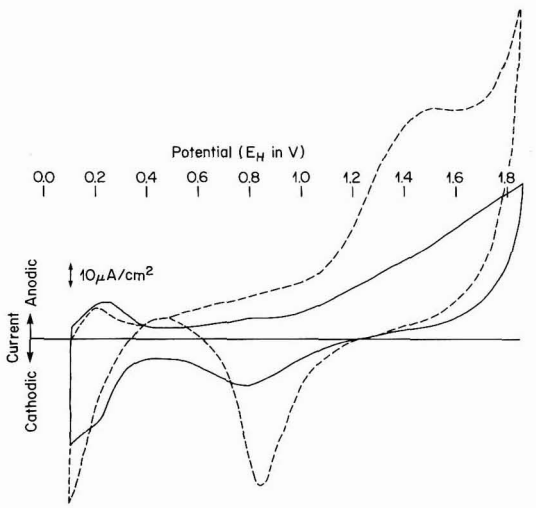

Fig. 3. Potentiodynamic profiles on smooth platinum in 1M CH_3COOK in CH_3COOH (also containing, presumably, traces of water). The solid line refers to the profile at 25°C whereas the dashed line is for 75°C. The new anodic peak around 0.45V may be noted at 75°C (sweep rate, 50 mV sec^{-1}).

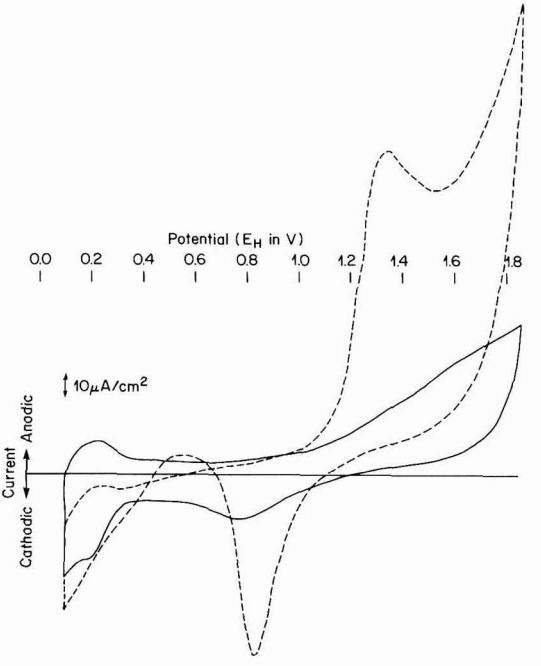

Fig. 5. Potentiodynamic profiles on smooth platinum in 1M CH_3COOK in CH_3COOH to which 1M DMF has been added. The solid profile is for 25°C whereas the dashed one is at 75°C (sweep rate, 50 mV sec^{-1}.

Table II. Tafel slopes in 1M CH_3COOK + 1M DMF in glacial acetic acid solutions

Temp, °C	Ascending potential steps		Descending potential steps	
	b (exp), mV	β	b (exp), mV	β
25	157	0.38	165	0.36
35	163	0.37	125	0.49
45	163	0.39	125	0.50
55	163	0.40	130	0.50
65	175	0.38	150	0.45
75	175	0.39	163	0.42
		Avg: 0.38 ± 0.01		Avg: 0.45 ± 0.06

peak at 1.35V is perhaps associated with the oxidation of DMF and the one at 0.55V may be attributed to the oxidation of acetate and of a product of the DMF oxidation.

This last hypothesis is confirmed by the fact that the peak at 0.5V increases in magnitude as the number of scans increases, and, as a function of time as shown in Fig. 6. This time effect is more pronounced in the presence of DMF than in the acetate-acetic acid solution. The increase in the anodic current at 0.5V, 1.3V, and higher potentials is concomitant with the diminution in the size of the oxide reduction peak at 0.85V; this oxide peak presumably originates from the presence of traces of water in the solution. The nature of the oxidized species at 0.5V cannot be ascertained but it could be an oxidation current of a byproduct of the DMF oxidation. The increase in current with time could indicate an accumulation of this byproduct in the solution. As the temperature is decreased to 25°C, after several potentiodynamic scanning experiments at 75°C, the peak at 0.5V is still observed which would confirm the suggestion of byproduct accumulation. Such evidence for the formation of this byproduct was not observed in the absence of DMF. For the acetate-acetic acid solution containing no DMF, the profiles at 25°C were identical in fresh solutions and in solutions in which experiments had already been conducted at 75°C.

The Tafel parameters determined from the upper (above 2.0V) part of the steady-state polarization curves are shown in Table II. The Tafel slopes are somewhat larger than those in the absence of DMF. In the potential range in which the reaction products can be practicably determined (*i.e.*, the Tafel region), the Kolbe reaction proceeds with the simultaneous oxidation of DMF that could perhaps influence the Tafel slopes (see below).

The product isolated from the reaction solution after the galvanostatic electrolysis, was identified as N-acetoxymethyl N'-methylformamide

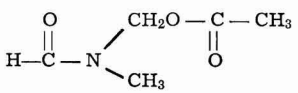

The refractive index, the infrared spectrum (2), and the NMR spectrum were identical with those for the same product synthesized by the acetylation of N-hydroxymethyl-N' methylformamide. The coulombic efficiency, assuming a two-electron process was found to be 5.2%. The main reaction at the potential of electrolysis (2.37V) is the Kolbe reaction. This confirms the results obtained by Ross *et al.* (3) where similar results were obtained at 25°C.

It may be added that in the anodic or cathodic charging curves triggered from the rest potentials (around 1.0V), in solutions containing DMF, no arrests were observed. This would indicate an absence of electroactive (*i.e.*, which can be deposited on, or stripped off from, the electrode in a transient) adsorbed species. Similarly, no arrests or inflections were observed in the fast (time of decay less than 1 sec) open-circuit potential decay profiles taken from various anodic potentials. In the slow (time of decay of the order of 1 min) open-circuit decay profiles, an "arrest" characteristic of the presence of a "depolarizer" was, however, observed in solutions with or without DMF. The "depolarization" effect must be associated with the relatively slow adsorption (or desorption) of intermediates (*e.g.*, traces of CH_3OH) that might be produced in an electro-oxidation such as the present one. It is obvious that open-circuit profiles such as these cannot be subjected to a meaningful analysis and are hence not shown here.

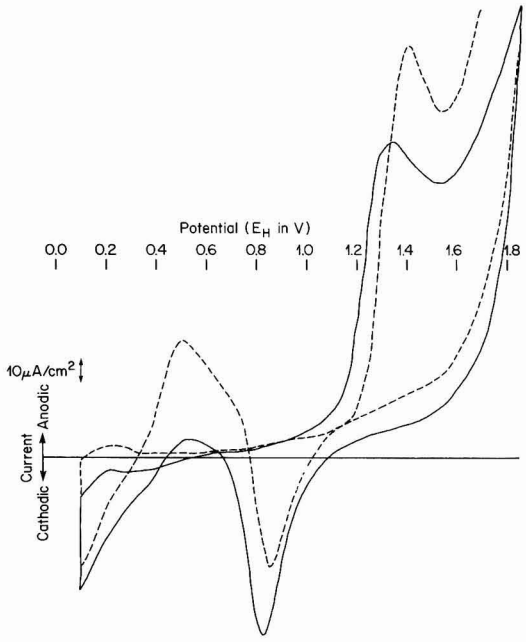

Fig. 6. Time effect for a 1M DMF and 1M CH_3COOK in CH_3COOH (T = 75°C; sweep rate = 50 mV sec^{-1}). Curve B, (dashed profile), 5 single sweeps after curve A (solid profile) and 1 hr interval between these two curves.

Conclusions

1. The apparent and the estimated real heats of activation (at the reversible potential) for the Kolbe reaction in acetate-glacial acetic acid solutions are 47 and 53 kcal $mole^{-1}$, respectively.

2. At temperatures above 55°C, the acetate ions tend to undergo anodic oxidation at potentials as low as 0.45V (RHE).

3. In the steady-state polarization curves of acetate-acetic acid-DMF solutions at smooth platinum, DMF undergoes oxidation between 1.1 and 1.5V at high temperatures (*e.g.*, 75°C). This behavior is also confirmed in the potentiodynamic profiles.

4. From the product analyses (which had to be carried out at high potentials in order to obtain reasonably high rates) at 2.37V, it is indicated that the oxidation of DMF proceeds parallel to the Kolbe reaction with a coulombic efficiency of the former equal to about 5%.

Acknowledgments

Thanks are due to Mr. Réal Jacques for his skillful contributions to the experimental manipulations, Mr. Yves Giguère for infrared analyses, Dr. Yvon Pépin, Chemistry Department, Université du Québec, at Montreal, for NMR analysis, and Mr. A. Bélanger for helpful discussions.

Manuscript submitted April 11, 1973; revised manuscript received Aug. 26, 1974.

Any discussion of this paper will appear in a Discussion Section to be published in the December 1975 JOURNAL. All discussions for the December 1975 Discussion Section should be submitted by Aug. 1, 1975.

Publication costs of this article were partially assisted by Hydro-Quebec Institute of Research.

REFERENCES

1. A. K. Vijh, *This Journal*, **119**, 679 (1972).
2. S. D. Ross, *Trans. N. Y. Acad. Sci., Series II*, **30**, 901 (1968); S. D. Ross, M. Finkelstein, and R. C. Petersen, *J. Am. Chem. Soc.*, **86**, 2745 (1964); **88**, 4657 (1966); *J. Org. Chem.*, **31**, 128 (1966).
3. E. J. Rudd, M. Finkelstein, and S. D. Ross, *J. Org. Chem.*, **37**, 1763 (1972).
4. D. F. A. Koch and R. Woods, *Electrochim. Acta*, **13**, 2101 (1968).
5. G. Bélanger, *This Journal*, **118**, 583 (1971).
6. C. H. Bramford and E. F. T. White, *J. Chem. Soc.*, **1959**, 1860.
7. A. K. Vijh and B. E. Conway, *Chem. Rev.*, **67**, 623 (1967).
8. B. E. Conway and A. K. Vijh, *Z. Anal. Chem.*, **224**, 149 (1967).
9. B. E. Conway, in "Progress in Reaction Kinetics," Vol. 4, G. Porter, Editor, Pergamon Press, Elmsford, N.Y. (1967).
10. B. E. Conway, "Theory and Principles of Electrode Processes," p. 108, The Ronald Press Co., New York (1965).
11. K. B. Harvey and B. Porter, "Introduction to Physical Inorganic Chemistry," p. 322, Addison-Wesley Publishing Co. Inc., Reading, Mass. (1963).
12. V. G. Bagotskii and Y. B. Vasile'v, *Electrochim. Acta*, **9**, 869 (1964).
13. D. Gilroy and B. E. Conway, *J. Phys. Chem.*, **69**, 1259 (1965).
14. A. K. Vijh, *Can. J. Chem.*, **49**, 79 (1971); A. K. Vijh, "Electrochemistry of Metals and Semiconductors," p. 183, Marcel Dekker, New York (1973).

On the Electrochemical Nucleation of Silver on Different Crystal Orientations of Graphite

Ikram Morcos*

Hydro-Quebec Institute of Research, Varennes, Quebec, Canada

ABSTRACT

An attempt was made to determine experimentally the nucleation overpotential of silver on high-pressure, stress-annealed pyrolytic graphite as a function of crystal orientation, surface oxidation state, and solution composition using both galvanostatic and potentiostatic pseudo-steady-state current-potential relationships. Silver deposits on the edge orientation from silver perchlorate with a nucleation overpotential of about 30 mV but does not adhere to cleavage orientation at the conditions of the study. The deposition of silver takes place on both cleavage and edge orientations from silver cyanide solution and is accompanied with a nucleation overpotential of about 200 and 250 mV, respectively.

A knowledge of the magnitude of nucleation overpotentials of metals on graphite and carbon substrates is useful for both fundamental and applied aspects of electrodeposition. In spite of the progress made in understanding the kinetics of electronucleation (1-5), there is a lack of reliable data on the values of nucleation overpotentials of metals on graphite. Available information (1) appears to have been obtained under poorly defined experimental conditions and on carbon substrates with poorly defined surface structure and oxidation state. The present availability of high-pressure, stress-annealed pyrolytic graphite with well-oriented structure similar to that of single crystal material permits a more reliable determination of nucleation overpotentials. The results recently reported (7-8) on the electrochemical nucleation of mercury on the latter type of graphite are strongly in conflict with both theoretically predicted (6) and experimentally determined values on carbon samples used in previous work (9).

In the present work an attempt has been made to obtain some reliable values for the nucleation overpotential of silver on well-oriented (ZYH type) pyrolytic graphite. The effect of crystal orientation, surface oxide films, and solution composition has also been explored using both galvanostatic and potentiostatic pseudo-steady-state current-potential scanning methods. The effect of solution composition was explored by performing the study in solutions containing either simple salt (silver perchlorate in perchloric acid) or complex salt (0.19*N* silver cyanide). Possible variations in the oxidation state of the graphite surface were examined by obtaining cathodic voltammograms in oxygen-free perchloric acid solutions.

Experimental Procedure

Galvanostatically controlled current-potential relationships were obtained by applying the circuit diagram shown in Fig. 1. A Tacussel function generator was used as a source of scanning voltage with a linear scanning rate of 1 $\mu A/sec^{-1}$. A Wenking potentiostat (Type 68FR 0.5) was used to convert the scanning

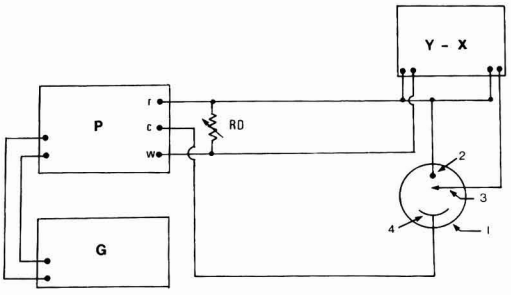

Fig. 1. Schematic diagram for the galvanostatic variation of current with potential. X-Y, X-Y recorder; G, function generator; P, potentiostat; RD, variable resistor; 1, electrochemical cell; 2, working electrode; 3, reference electrode; 4, counterelectrode.

* Electrochemical Society Active Member.

Key words: nucleation of silver, nucleation on graphite, graphite orientation and nucleation.

voltage into the applied galvanostatic current by connecting it (10) in the manner shown in Fig. 1. A Honeywell X-Y recorder was used to record the potential as a function of the current. Potentiostatically controlled current-potential relationships were obtained by connecting the potentiostat in the more conventional manner. The same potentiostatic method was applied to produce the cathodic voltammograms in perchloric acid solutions. All potentiostatic experiments were performed at a scan rate of 0.2 V/min^{-1}.

The electrochemical cell consisted of two compartments, one for the reference electrode and the other for both the working and counterelectrode. As a reference electrode a silver wire was used in silver perchlorate solution and a saturated calomel in both perchloric acid and silver cyanide solutions. The former reference electrode exhibited a potential of 0.666V (NHE). In solutions containing silver ions two silver plates were used as a counterelectrode. In voltammetric experiments in perchloric acid the counterelectrode was a spectroscopic graphite rod to avoid contamination of the solution with silver ions. The rotating disk was applied throughout the work at a speed of 1600 rpm. Electrodes of both cleavage and edge orientations were machined and fitted to the Teflon coated steel shaft of the rotating disk assembly as described elsewhere (11). Solutions were prepared from AR quality salts and water triply distilled twice from a permanganate solution. All experiments were carried out in helium saturated solutions.

Results and Discussion

The electrodeposition of a metal on a foreign substrate with which it does not form mixed crystals involves the formation of a new phase, which, therefore, requires an energy of nucleation. The latter is provided by a nucleation overpotential which is necessary to bring the concentration in the double layer (12) to a certain supersaturation value.

Nucleation overpotential is experimentally well defined in galvanostatically controlled current-potential relationships. When the current is slowly increased, the overpotential with respect to a reference of the same metal in the test solution, will first increase rapidly at a low current density until the first layer of metal nuclei is deposited on the inert substrate. A further increase in the current density will cause a decrease in the overpotential as the deposition of the metal takes place on the same metallic surface and therefore results in a well-defined maximum. If, as in many cases, the reduction of the metal ion on the same metal substrate occurs reversibly, the increase in current density following the formation of the first layer of metal nuclei, in the absence of concentration polarization, will take place at an almost constant potential. Nucleation overpotential can then be defined as the difference between the maximum potential and that corresponding to the reduction of the metal ion at constant potential.

Figure 2 shows galvanostatically controlled current-overpotential relationships for the reduction of Ag^+ ion from helium-saturated silver perchlorate solution (0.05*N* silver perchlorate in 1*N* perchloric acid) on both cleavage and edge graphite orientations. No electrode pretreatment was applied after exposing the new surface. Both plots of Fig. 2 show well-defined maxima at overpotentials of −52 and −46 mV for cleavage and edge graphites, respectively. In the case of edge graphite the increase in current following the maximum occurs at a constant potential. The difference of 14 mV between that constant potential and the reversible reference is a slight activation polarization because of the high current density caused by the small true area of formed silver nuclei. Such is not the case with cleavage graphite where it is observed that the potential shows a linear increase with the increase in current. Figure 2 then clearly indicates that the nucleation and deposition of silver from a silver perchlorate solution occurs only on edge but not on

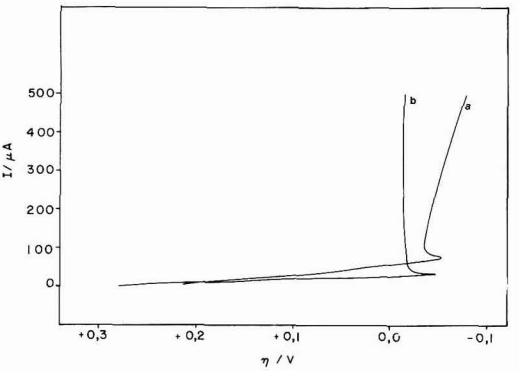

Fig. 2. Galvanostatic current-overpotential relationships for the reduction of Ag^+ ion from silver perchlorate on both cleavage and edge orientation of high-pressure, stress-annealed pyrolytic graphite. a, Cleavage graphite; b, edge graphite.

cleavage graphite. The appearance of the maximum in the case of cleavage graphite indicates that nucleation actually starts to take place on the surface, but, because of the lack of sufficient adhesion forces between the graphite surface and the formed nuclei, the process of nucleation is discontinued, the formed nuclei are removed, and the further reduction of silver ions continues to take place on the graphite surface. On the basis of the previously stated definition, nucleation overpotential, according to Fig. 2, is 32 mV in the case of edge graphite and 16 mV at the initial stage of nucleation in the case of cleavage graphite. These values are considerably smaller than a value of 100 mV reported in Ref. (1).

The observed difference in the activity of cleavage and edge orientations toward nucleation is consistent with the known differences in the chemical and electrocatalytic activity of both surfaces. Studies on the electroreduction of oxygen (11) on both surfaces have shown that edge graphite is much more electrocatalytically active than cleavage graphite. Furthermore the determination of cleavage graphite's surface tension (about 35 dynes/cm) (13) and the electrocapillary data obtained on the cleavage surface/electrolyte interface (14) indicates that ionic adsorption is strongly inhibited on that surface from aqueous solutions. The chemical and electrochemical inertness of cleavage orientation results from the lack of any unsatisfied valencies or polar surface structures. The atoms at the cleavage surface have satisfied valencies and are symmetrically arranged in rings parallel to the surface which are separated from successive carbon layers by only weak van der Waals forces. On the other hand, the edge orientation exposes different organic functional groups which can exist in different oxidation states.

Figure 2 indicates that the open-circuit potential of graphite in silver perchlorate solution is strongly shifted to more anodic values as compared with the corresponding reversible Ag/Ag^+ couple. The observed potential is probably a mixed one which consists of both the Ag/Ag^+ couple and the potential established between the surface organic functional groups and the hydrogen ions of the solution. Although only a very small number of these groups exists on the cleavage surface at sites of crystal defects, they can still have a similar effect on the open-circuit potential. Because these organic functional groups may exist in different oxidation states, it may be suggested that the maxima of Fig. 2 result from the reduction of a surface oxide rather than from the nucleation of silver on graphite.

The reduction of graphite's surface oxide can be identified with the appearance of peaks in cathodic voltammograms obtained in inert solutions. In two different studies (15-16), carried out on ordinary

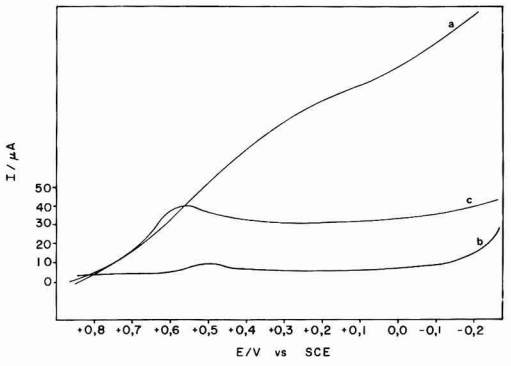

Fig. 3. Cathodic voltammograms on both cleavage and edge graphites in 1*N* $HClO_4$. a, Cleavage graphite; b, edge graphite without pretreatment; c, edge graphite pretreatment in conc. HNO_3.

pyrolytic graphite in 1M H_2SO_4, it was reported that the oxide film formed by either chemical or electrochemical treatment is reduced at 0.5V (*vs.* SCE). The latter value is considerably more anodic than the potentials at which the maxima of Fig. 2 occur, and accordingly these maxima result from nucleation and not from the reduction of surface oxides. However, in order to confirm this latter conclusion it was considered necessary to obtain the cathodic voltammograms on the same graphite samples used in the present study and in perchloric acid rather than in sulfuric acid. Figure 3 shows the result of such experiments and it is seen that a small peak appears only in the case of edge graphite at 0.5V (*vs.* SCE). The absence of organic functional groups on cleavage graphite explains the absence of a well-defined peak in its voltammogram. The relatively large current observed on cleavage graphite probably results from charging of the double layer. When edge graphite is pretreated in concentrated nitric acid the peak becomes more prominent but still takes place at approximately the same potential. As a further confirmation, the galvanostatic current potential relationships for the reduction of Ag^+ ion were obtained on both graphite orientations which were pretreated in concentrated nitric acid. Figure 4 shows that the section of the plots which is related to nucleation for both types of graphite is almost the same as that shown in Fig. 2. From this it is concluded that even when an oxide film is deliberately formed before the study of electrochemical nucleation, reduction occurs at a potential more anodic than that corresponding to nucleation. The higher currents observed in Fig. 4 as compared to Fig. 2 at potentials more positive than that corresponding to nucleation are probably due to surface oxide reduction. Pretreatment in concentrated nitric acid oxidizes the cleavage surface and exposes the organic functional groups. Such formation and subsequent reduction of the organic functional groups on cleavage surface has probably resulted in the observed shift of the maximum overpotential into more negative potentials (compare Fig. 2a with Fig. 4a). It is probable that the reduction of such film activates the surface towards nucleation.

Figure 5 shows that nucleation overpotential of silver under potentiostatic conditions on both cleavage and edge graphite at the initial stage of deposition is 30 mV. This value is approximately the same as that determined by galvanostatic experiments on edge graphite. With the increase in current, the latter value shows only a slight increase because of the activation overpotential caused by the small true area but soon reaches a constant value. One observes, however, from Fig. 5 that this initial nucleation overvoltage in the case of cleavage graphite shows a linear increase with the increase in current for the reasons already mentioned in discussing the galvanostatic experiments.

The study of electrochemical nucleation on foreign substrates (particularly on an organic substrate such as graphite) is important in applied aspects of electrodeposition. This is because the important property of adhesion can be related to the magnitude of nucleation overpotential. It is known that conditions which favor microcrystalline deposits also favor the formation of new nuclei and better adhesion properties (17). The higher the nucleation overpotential the smaller is the grain size and therefore the stronger will be the adhesion between the deposited metal and the foreign substrate.

Such correlations between nucleation overpotential, adhesion, and grain size explain the common use of complex salts in industrial electrodeposition. Silver, for example, is deposited from alkaline silver cyanide solution. The much higher stability constant (5.6×10^{18}) of silver cyanide $[Ag(CN)_2]^-$ results in a much less concentration of silver ions. Consequently a higher magnitude of nucleation overpotential is required to break the strong bonding forces and bring the ionic concentration into the required supersaturation value. Figure 6 compares the galvanostatic current-potential plots for the reduction of silver cyanide on both cleavage and edge orientations. The nucleation overpotential is well defined and is 0.2 and 0.25V on cleavage and edge, respectively. It is obvious that the silver nuclei under these conditions can adhere to the inert cleavage surface. The accompanying overvoltage provides the silver atoms with the required energy to form the metal-graphite bonding.

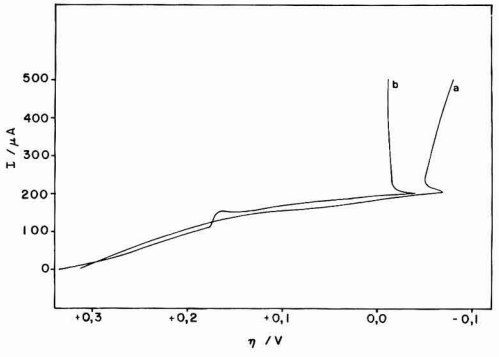

Fig. 4. Galvanostatic current-overpotential relationships for the reduction of Ag^+ ion from silver perchlorate on both cleavage and edge graphites which have been pretreated in conc. HNO_3. a, Cleavage graphite; b, edge graphite.

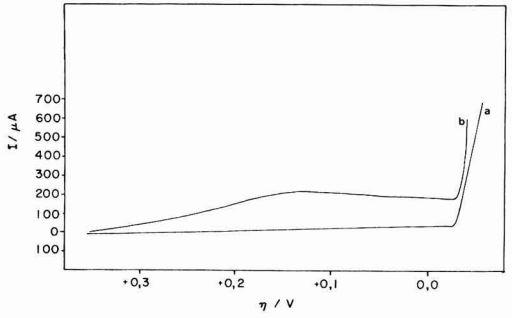

Fig. 5. Potentiostatic current-overpotential relationships for the reduction of Ag^+ ion from silver perchlorate on both cleavage and edge graphite. a, Cleavage graphite; b, edge graphite.

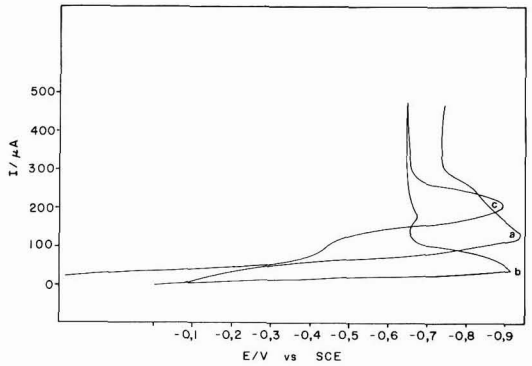

Fig. 6. Galvanostatic current-potential relationships for the reduction of $[Ag(CN)_2]^-$ from silver cyanide solution on both cleavage and edge graphites. a, Cleavage graphite; b, edge graphite; c, edge graphite pretreated in conc. HNO_3.

Acknowledgments

The author is grateful to Union Carbide Research Center, Parma, Ohio, for providing him with the graphite samples used in the present work and to Mr. G. Larochelle for his assistance in the physical realization of the investigation.

Manuscript submitted May 29, 1974; revised manuscript received July 30, 1974.

Any discussion of this paper will appear in a Discussion Section to be published in the December 1975 JOURNAL. All discussions for the December 1975 Discussion Section should be submitted by Aug. 1, 1975.

Publication costs of this article were partially assisted by Hydro-Quebec Institute of Research.

REFERENCES

1. M. Fleischmann and H. R. Thirsk, in "Advances in Electrochemistry and Electrochemical Engineering," Vol. III, P. Delahay and C. W. Tobias, Editors, Chap. 3, John Wiley & Sons, Inc., New York (1963).
2. D. J. Astley, J. A. Harrison, and H. R. Thirsk, *Trans. Faraday Soc.*, **64**, 192 (1968).
3. J. A. Harrison, *J. Electroanal. Chem.*, **36**, 71 (1972).
4. I. Markov, A. Boynov, and S. Toschev, *Electrochim. Acta*, **18**, 377 (1973).
5. P. Bindra, M. Fleischmann, J. W. Oldfield, and D. Singleton, *Discussions Faraday Soc.*, **56** (1973). (1973).
6. T. Erdey-Crüz and M. Volmer, *Z. Physik. Chem.*, **A157**, 182 (1931).
7. I. Morcos, *J. Electroanal. Chem.*, **50**, 373 (1974).
8. I. Morcos, *ibid.*, **54**, 87 (1974).
9. T. Erdey-Crüz and H. Wick, *Z. Physik. Chem.*, **162**, 63 (1937).
10. Operating Manual "121," Wenking Electronic Potentiostats, Brinkmann Instruments, Westbury, N.Y.
11. I. Morcos and E. Yeager, *Electrochim. Acta*, **15**, 953 (1970).
12. T. Erdey-Crüz, "Kinetics of Electrode Processes," p. 260, Wiley-Interscience, New York (1970).
13. I. Morcos, *J. Chem. Phys.*, **57**, 1801 (1972).
14. I. Morcos, *J. Phys. Chem.*, **76**, 2750 (1972).
15. G. Mamantov, D. B. Freeman, F. J. Miller, and H. E. Zittel, *J. Electroanal. Chem.*, **9**, 305 (1965).
16. K. F. Blurton, *Electrochim. Acta*, **18**, 869 (1973).
17. G. Milazzo, "Electrochemistry," p. 435 (English Edition) Elsevier Publishing Company, Amsterdam (1973).

Photoeffects at Polycrystalline Tin Oxide Electrodes

Hasuck Kim and H. A. Laitinen*

School of Chemical Sciences, University of Illinois at Urbana-Champaign, Urbana, Illinois 61801

ABSTRACT

The electrochemical behavior of thin-film polycrystalline tin oxide electrodes under subbandgap energy photoexcitation has been investigated. Photocurrents were dependent on the intensity of the light, wavelength, and the applied potential. The photocurrent spectrum showed a sharp decrease near the bandgap energy. This photocurrent is due to the oxidation of water in the electrolyte by holes at the permitted energy levels in the bandgap region. These energy states are formed by the presence of impurities, which are largely halides remaining from the preparation steps, grain boundaries, and adsorbed foreign molecules. A superficial hydrogen bonding interaction between oxide layers of SnO_2 and water molecules is proposed for the hydrated surface of tin oxide.

Long after the first photovoltaic effect was noticed by Becquerel, many investigators observed photocurrents at various electrode materials; such as mercury (1-3), elemental germanium (4), CdS (5), ZnO (6, 7), GaP (8), GaAs (9), and CuO (10). In all the semiconductor studies, single crystals were used. It was found that the bandgap energy illumination produced electron hole pairs which participated in the electrochemical process, *i.e.*, electrons for the cathodic photocurrent in p-type electrodes, and holes for the anodic reaction in n-type materials. It was also found that the extra currents were due to the electrochemical decomposition of the electrode material under illumination.

One of the advantages of the use of a semiconductor electrode in the study of electrochemical reactions is the fact that the charge transfer processes occur only via the energy bands. Therefore, in the presence of organic dye in the electrolyte, charge transfer processes involving the excited states can be studied by observing dye sensitized photocurrents (11).

A semiconducting thin film of tin oxide on glass or quartz has shown some distinctive advantages over metals as an electrode in electrochemical investigations. Nearly metallic conductivity, optical transparency, high oxygen overvoltage, low background current, absence of any electrochemically active oxide layer, chemical durability, and excellent mechanical stability of the film made it possible to study many special electrochemical applications. Detailed applica-

* Electrochemical Society Active Member.
Key words: semiconductor, thin-film electrode, transparent electrode, photocurrent, tin oxide electrode.

tion of polycrystalline tin oxide material as an electrode can be found in Ref. (12).

Even though there are many applications and advantages in the use of tin oxide electrode, little attention has been paid to the nature and to the physical properties of the surface. Accordingly, this study of photoexcitation with radiation of energy less than the bandgap energy is one of a series (13, 14) to characterize the electrode surface.

Experimental

Reagents.—Chemicals used in this study were reagent grade and were used without further purification except where specifically noted. Stannic chloride, stannic bromide, hydrobromic acid, and tetrabutyltin were purified by vacuum distillation. Rhodamine B was recrystallized from ethanol. Solutions were made using laboratory distilled water which had been distilled twice.

Preparation of tin oxide electrodes.—The procedure in Mochel's patent (15) was generally followed. In addition to stannic chloride-hydrochloric acid, a stannic bromide-hydrobromic acid mixture was also used. The coating of tin oxide was obtained by blowing the spray mixture onto a hot quartz or glass substrate using a conventional all-glass atomizer. Each spray lasted for about 5 sec followed by a 3 min waiting period to prevent excessive cooling of the hot substrate. After each spray, the substrate was rotated clockwise by 90° to get a uniform thickness over the surface. The surface of the tin oxide film was then polished with Gamma polishing alumina[1] and Selvyt polishing cloth.[1] The commercial tin oxide coated glass (IRR) was used as substrate instead in the case of double coated electrodes. More details about the coating, polishing, and the cleaning, are given in Ref. (16).

The thickness of the coating was determined by measuring interference fringes (17) obtained by scanning the spectral region from 250-700 nm.

Construction of electrolyte cell.—The cell used for the photoexcitation studies on tin oxide is shown in Fig. 1. Its design was similar to that reported earlier (13), but it had a side flange and a side conical end as shown. The end of this side branch was polished flat. The electrical contact to the semiconductor electrode surface was made by a flat, highly polished copper "O" ring tightened firmly onto the electrode by three 4/40 machine screws and a Plexiglas support. A Teflon washer which provided both a tight seal between the cell and the electrode and defined the area of the electrode was placed tightly inside the metal "O" ring. To insure a good seal it was necessary to polish the Teflon washer on a plate of ground Lucite until a completely smooth surface was obtained. The area of the electrode was 0.124 cm^2.

[1] Buehler product, Evanston, Illinois.

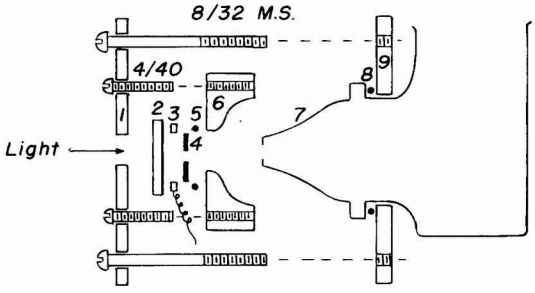

Fig. 1. Diagram of electrolytic cell. 1 and 9, Brass plates; 2, tin oxide electrode; 3, metal "O" ring with copper wire; 4, Teflon washer; 5 and 8, rubber "O" rings; 6, Plexiglas support; 7, all-glass electrolytic cell.

Photocurrent and photovoltage measurements.—The experimental setup is shown in Fig. 2. A saturated potassium chloride calomel electrode (SCE) with a porous Vycor junction was used as a reference electrode. A Luggin capillary filled with saturated potassium nitrate solution was placed between the reference Vycor junction and near the working electrode.

Under a constant applied potential, the SnO_2 electrode in contact with electrolyte was illuminated from the backside for a while; then the light path was interrupted manually with a metal sheet for the photocurrent measurement. The net change of current or voltage after it reached a steady-state value was taken as the photocurrent or photovoltage. The light source was a 100W xenon arc lamp with a Bausch and Lomb High Intensity Grating Monochromator (33-86-25-02).

Since the light intensity of the lamp was not uniform throughout the spectral region, the photocurrent was normalized to unit light intensity after the absolute intensity at each wavelength had been measured using a Hewlett-Packard Model 8334A Radiant Flux Detector with a Model 8330A Radiant Flux Meter.

Adsorption of rhodamine B.—C-14 labeled rhodamine B was prepared by condensation between m-diethylaminophenol and C-14-phthalic anhydride (18). A double coated tin oxide electrode was prepared by the same procedure as the electrodes used in the photoexcitation experiments. The electrode was first placed in a known concentration of labeled dye in 1*M* KNO_3 solution for a given time with or without applied potential, then was taken out. The electrode was washed thoroughly with distilled water using a wash bottle. Absolute ethanol (35 drops) was used to dissolve any adsorbed rhodamine B molecules from the electrode surface. Fifteen milliliters of scintillation liquid was then added to a counting vial in which 35 drops of ethanol had already been collected. Disintegration rates were counted using 2003 Packard Tri-Carb Liquid Scintillation Spectrometer seven times for 10 min each to achieve the desired S/N ratio.

Results and Discussion

Photocurrent measurements.—An increase of anodic residual current was observed by illumination with photoenergies which are less than the energy gap between the conduction and valence bands. The profile of photocurrent was dependent upon wavelength and applied potential. It decayed to a steady value after a sharp increase. Since the time constant of the electrode/electrolyte system was found to be 0.17-0.18 sec, while the photocurrent-time curve provided 0.3-1 sec, a simple charging-discharging of the double layer capacitance cannot be the total rate-determining process. It was also found that the photocurrent was directly related to the intensity of the light.

In order to find the most suitable surface for this study several different types of tin oxide material were examined. Since minority carriers, as mentioned before, play an important role in the photocurrent process (6), use of a poorly conductive electrode material is

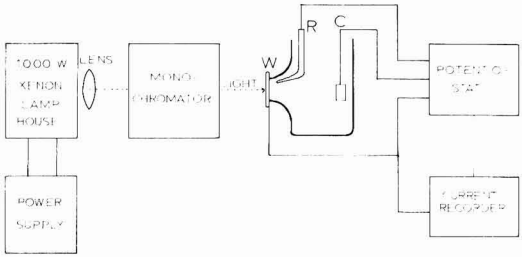

Fig. 2. Block diagram of experimental setup. W, Working electrode; R, reference electrode; C, counterelectrode.

desired. The source and nature of conductivity of "undoped" tin oxide film has been studied (16). Although the main source of conductivity is attributable to halides remaining after hydrolysis, the nonstoichiometry of tin oxide also contributes appreciably. A poorly conductive electrode can give a higher value of the ratio of the excess holes produced by photoenergy to major carrier concentration than a highly conductive electrode under the same light intensity. It also offers an electrode material with fewer impurities to cause additional complexities. But a large *IR* drop has to be considered when a highly resistive electrode is used. In order to eliminate this *IR* drop, a double coating technique was developed. The second layer of a highly resistive tin oxide film was obtained by use of nondoped stannic bromide on a commerical antimony-doped tin oxide surface. The thickness of the second layer was determined indirectly by measuring the thickness of another film obtained simultaneously on Pyrex substrate and was found to be about 0.4 μm. It is quite possible that antimony in the first layer may diffuse to some extent into the second layer during the preparation step. This electrode, however, behaves like a highly resistive one at the electrode-electrolyte interface yet has a high conductivity to facilitate passage of electricity.

The double coated electrode prepared from stannic bromide, which has the most resistive surface among the electrodes, does give a higher photocurrent and a sharper slope than any other electrode. The sharper slope indicates a clear band separation, *i.e.*, fewer impurities or energy states present between bands in the crystal structure. Therefore, double coated electrodes prepared with stannic bromide were used throughout this investigation.

Figure 3 shows a series of photocurrent spectra at different applied potentials obtained in 1*M* KNO_3. The shapes of the spectra are similar. With an ideal tin oxide single crystal, the photocurrent would be noticeable only with bandgap energy illumination, corresponding to the energy at which electrons in the valance band would be promoted to the conduction band, leaving holes behind. No electron hole pairs would be produced by illumination of energies less than the bandgap energy.

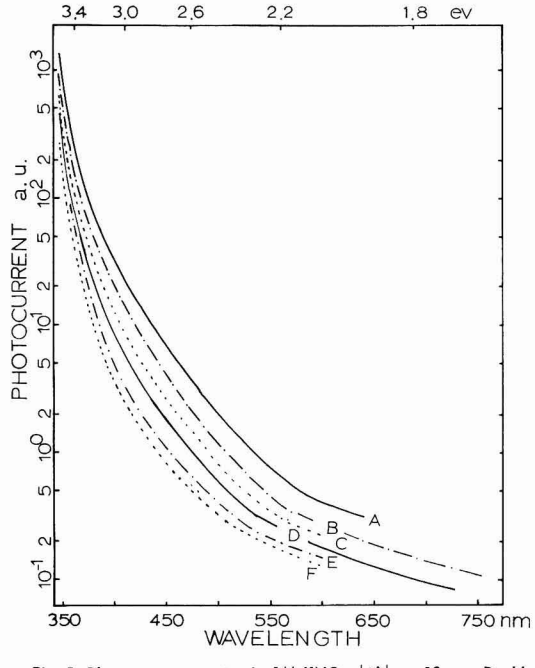

Fig. 3. Photocurrent spectra in 1M KNO_3. $|\Delta\lambda| = 10$ nm. Double coated electrode with $SnBr_4$. a.u., Arbitrary units; A, at 1.3V *vs.* SCE; B, 1.1V; C, 0.9V; D, 0.7V; E, 0.5V; F, 0.4V.

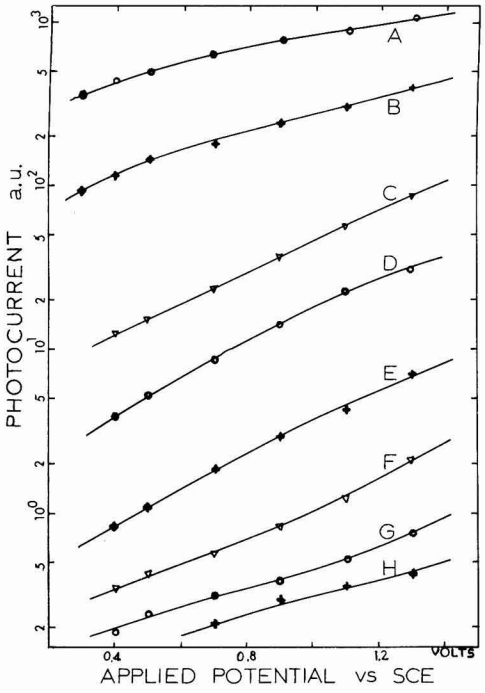

Fig. 4. Effect of applied potential on photocurrent in 1M KNO_3 A, 350 nm; B, 360 nm; C, 380 nm; D, 400 nm; E, 450 nm; F, 500 nm; G, 550 nm; H, 600 nm.

However, as shown in Fig. 3, the polycrystalline tin oxide electrode shows an appreciable photocurrent in wavelengths longer than 335 nm which corresponds to the bandgap energy of 3.7 eV. Therefore, there must be a number of energy states between bands. It is known that physical imperfections of a crystal, chemical impurities, grain boundaries (19), adsorbed foreign molecules, and surface states can introduce discrete energy levels into the forbidden gap much as donor and acceptor ions do in the case of a doped semiconductor.

We know there are "unintentionally added" bromides in the tin oxide electrode (16) which can be easily ionized at room temperature. These ionized donors introduce energy levels which are distributed according to Fermi-Dirac statistics. Therefore, the observed photocurrent near 350 nm decreases sharply.

As Fig. 4 shows, there is no saturation phenomenon as observed in single crystals of ZnO (6), SnO_2 (20), and CdS (1) with bandgap energy illumination in which the photocurrent is determined only by the diffusion rate of holes to the surface. In a polycrystalline material, holes produced by photoenergy could be recombined through the adjacent energy states before they reach the surface to participate in electrochemical processes.

The potential dependence of the charge transfer rate could be another reason for polycrystalline tin oxide electrodes not having a saturation phenomenon. The tunneling probability of an electron into the bulk of the electrode is governed by the shape of the energy barrier (14) and thickness of the space charge layer, which in turn primarily depends upon the density of charge carriers in the bulk and on the applied potential, since applying a different potential to a semiconductor electrode results only in a variation of the electrical potential difference in the space charge layer

without a major change in the Helmholtz double layer structure (21). Figure 5 reveals schematically the effect of applied potential on the potential energy diagram of semiconducting tin oxide. The tunneling probability or electron transfer coefficient would be much higher at the higher anodic potential than at a low anodic potential.

A change of the pH of the electrolyte, on the other hand, is believed to influence the Helmholtz layer, flatband potential, and surface hydroxyl groups. These changes occur at or near the electrode-electrolyte interface while the applied potential or electrode material can change the internal properties of the electrode.

HNO_3 and KOH were used to adjust pH values in order to eliminate any possible specific adsorption of buffer systems on the electrode surface. As shown in Fig. 6, a steady increase of the photocurrent in the range of pH from 3 to 10 can be explained by a continuous change of the flatband potential at a rate of 60 mV/pH unit (20).

A simple shift of the flatband potential by 60 mV/pH unit, however, cannot explain large changes of the photocurrent below pH = 3 and above pH = 10. In addition to the shift of the flatband potential, change of the charge transfer rate seems to take place due to the protonation and the formation of surface hydroxyl groups, respectively (see below). Even though this experiment had been done at a fixed applied potential, the shape of the potential energy curve, and thereby the space charge layer thickness, can be changed drastically by such surface changes.

Sensitized photocurrent.—In the presence of rhodamine B, an additional anodic photocurrent was observed and the photocurrent spectra were very similar to the absorption spectra of the dye as shown in Fig. 7. A similar phenomenon using various semiconducting electrodes has been observed (11, 22). The dye is electrochemically inactive in the dark in the region of the applied potentials. This additional photocurrent can be interpreted as a considerable increase of the number of carriers in the electronic energy states due to the adsorption of the dye molecules (23). A maximum conductivity has been observed in the course of photoconductivity measurements on ZnO single crystal (24) in the presence of adsorbed organic dye under absorption band illumination. Since the photocurrent is directly proportional to the rate of formation of carriers, there is a maximum population of carriers in the energy state corresponding to the absorption band of the dye.

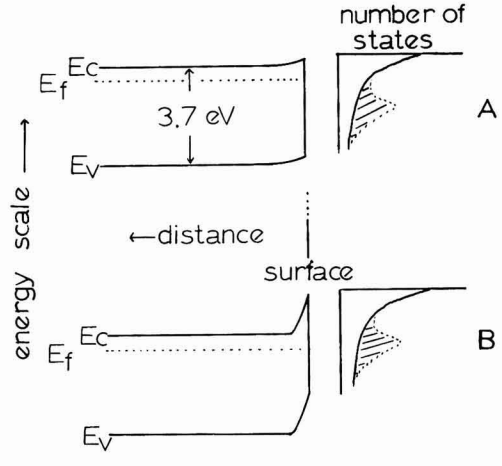

Fig. 5. Potential energy diagram of SnO_2 at the interface. A, Low anodic potential; B, high anodic potential; E_c, conduction band; E_f, Fermi energy level; E_v, valence band. Shaded areas are the energy states due to the presence of adsorption.

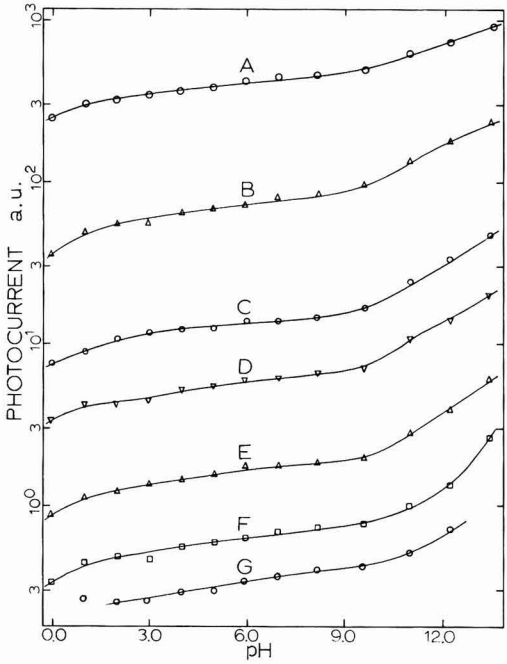

Fig. 6. Effect of pH on photocurrent at 0.7V vs. SCE. A, 360 nm; B, 380 nm; C, 400 nm; D, 450 nm; E, 500 nm; F, 550 nm; G, 610 nm.

The effect of applied potential on the sensitized photocurrent was very similar to the effect of applied potential on the photocurrent shown in Fig. 4. Again, no saturation was observed.

The sigmoid shape in Fig. 8 reveals a typical adsorption isotherm, and further evidence for the adsorption of rhodamine B at the tin oxide electrode surface has been provided by the radioactive carbon-14 labeling technique. The specific activity of C-14-rhodamine B was determined by relating the spectrophotometrically determined concentration to the counting rate.

The theoretical amount of a monolayer coverage was calculated, assuming 18Å as the diameter of rhodamine B molecule, to correspond to 3.93×10^{13} molecules/cm^2 or 6.53×10^{-11} mole/cm^2.

It was noticed that up to 99.5% of the adsorbed dye can be dissolved from the surface into ethanol in three successive washings, but water washings did not disturb the adsorbed dye. Adsorption of the dye appears to be very rapid because 4.2×10^{-11} moles/cm^2 (about two-thirds of theoretical monolayer coverage) of dye was observed after only 1 sec of immersion in $1.46 \times 10^{-4}M$ solution. Values between 5.8 and 6.9×10^{-11} moles/cm^2 were obtained after 2 and 10 min of immersion with or without polarization at applied potentials of 1.21 and −1.0V *vs.* SCE. About a monolayer coverage (5.9×10^{-11} moles/cm^2) was also observed in the following way. The electrode was dipped into a $4.53 \times 10^{-6}M$ dye solution for 5 min, then it was taken out very slowly. There was no washing with water. This was done on the basis that the tin oxide was not easily wettable and that uniformly distributed solution layer 1 μm thick contained an amount of dye corresponding to less than 1% of a monolayer coverage. Actually there was only a little wetted area and the solution was efficiently taken away by an absorbing paper towel.

Photovoltage measurements.—A shift of rest potential by the bandgap energy illumination is due to the generation of excess hole electron pairs. The separation of photogenerated charge carriers of the different

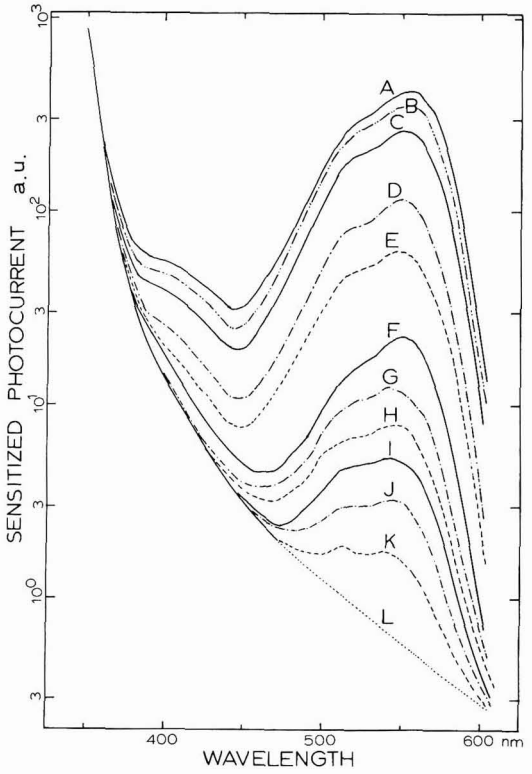

Fig. 7. Sensitized photocurrent by rhodamine B at 0.7V vs. SCE. $|\Delta\lambda|$ = 10 nm. A, 2.434 × 10^{-5}M; B, 1/2A; C, 1/4A; D, 1/10A; E, 1/20A; F, 1/40A; G, 1/100A; H, 1/200A; I, 1/400A; J, 1/1000A; K, 1/2000A; L, 1M KNO_3 only.

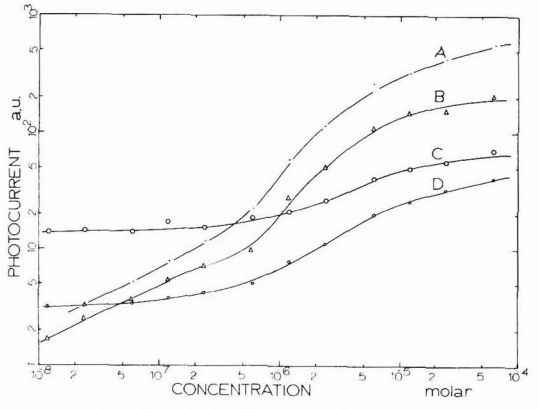

Fig. 8. Effect of rhodamine B concentration on sensitized photocurrent at 0.7V vs. SCE. A, At 550 nm; B, at 500 nm; C, at 400 nm; D, at 450 nm.

mobilities can also produce a photopotential (25). Both responses are known to be instantaneous because they are caused only by a nonequilibrium charge distribution.

When photoenergies of less than the energy gap were introduced on SnO_2, a long rise and decay time was observed in an open circuit as shown in Fig. 9. The measured photovoltage depends very much on the previous history of the electrode and does not give reproducible values.

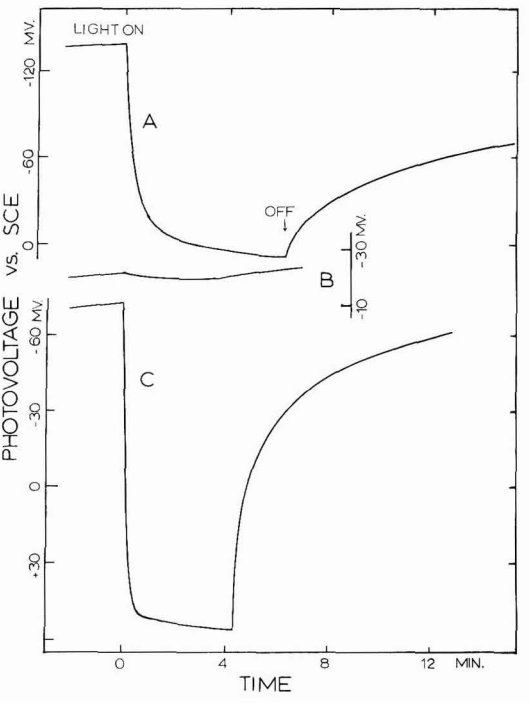

Fig. 9. Time dependence of photovoltage. A, 1M KNO_3 with 350 nm; B, 1M KNO_3 with 550 nm; C, 1.217 × 10^{-5}M rhodamine B in 1M KNO_3.

The slow response of photovoltage due to chemical process at the electrode surface was discussed in Ref. (6). In the open circuit measurement, there is no net current flow between the electrode and the electrolyte interface. But we already know that holes in the case of an n-type semiconductor are responsible for the anodic photocurrent. Therefore, electrons have to be consumed by means of a cathodic reaction at the reference electrode at the same rate as holes in the anodic reaction in order to get a quasi-steady-state response. The slow photovoltage response, therefore, is limited by the charge transfer rate at the electrode surface. It cannot simply be due to a pH change in solution, because the quantities of electricity are entirely inadequate for such changes at steady states. Moreover, the photovoltage was found to be insensitive to stirring.

The photovoltage spectrum which was obtained by measuring the photovoltages at each wavelength was very similar to the photocurrent spectrum. In the presence of rhodamine B, the photovoltage spectrum revealed a big hump corresponding to the absorption band around 550 nm. Therefore, the photovoltage measurement can also be used to determine the position of energy levels and the relative number of states in the surface level just as the photocurrent measurement can.

Surface hydroxyl groups.—The presence of hydroxyl groups on natural crystals of Bolivian cassiterite SnO_2 was first determined by infrared absorption near 3.07 μm (26). The electrochemical behavior of the tin oxide which had been immersed in 1M KNO_3 for 3 days after photoexcitation work is shown in Fig. 10, curve B. The cyclic voltammogram shows not only high background and photocurrent but also a decrease in oxygen overvoltage by as much as 0.5V. Polishing the electrode with alumina made only a small change; however, heating at 90°C for 3 hr (curve C) did improve its behavior. After further heating at 115°C for 24 hr (curve D), the electrode showed about the same volt-

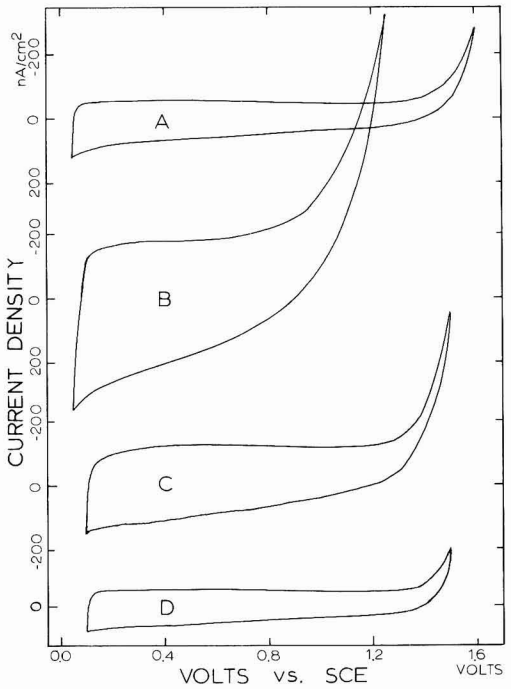

Fig. 10. Cyclic voltammograms of tin oxide electrode. Sweep rate = 20 mV/sec. A, Newly prepared electrode; B, 3 days old in 1M KNO_3 after photoexcitation work; C, dried at 90°C for 3 hr; D, dried at 115°C for 24 hr.

ammogram as shown by a newly prepared electrode. It is interesting that the wetting of the electrode surface is noticed even after polishing with alumina but not after heat-treatment. A new electrode is not wettable. Compared to the surface hydroxyl groups on silica or alumina which required much higher temperature and vacuum drying for complete removal, it seems very unlikely that such a gentle heat-treatment dehydrates a Sn-OH bond. A superficial hydrogen bonding interaction between oxide layers of SnO_2 and water molecules instead is proposed for the aging in the electrolyte. Presumably such an interaction is preserved under wet polishing conditions.

Proposed mechanism.—To determine whether the anodic decomposition of water or of the cassiterite lattice is energetically favorable we may compare the free energy changes of the reaction

$$2H_2O(l) + 4h^+(\text{holes}) \rightarrow 4H^+aq + O_2\ 113.38\ \text{kcal} \quad [1]$$

obtained from $\Delta G^\circ(H_2O) = -56.69$ kcal//mole, and

$$SnO_2(s) + 4h^+ + 4H_2O \rightarrow SnO_2 \cdot 2H_2O(s) + 4H^+aq + O_2\ 123.46\ \text{kcal} \quad [2]$$

obtained from $\Delta G^\circ(SnO_2(s)) = -124.2$ kcal mole, $\Delta G^\circ(SnO_2 \cdot 2H_2O(s)) = -227.5$ kcal/mole, and $\Delta G^\circ(H_2O)$ of reaction [2] requires more energy than reaction [1] by 10.08 kcal. Therefore, the decomposition of water is energetically favored. A prolonged experiment did not show any sign of decomposition of the electrode surface. The oxidation of water by photogenerated holes at TiO_2 electrodes also has been proposed (27).

Finally, the following scheme for the anodic photoprocess at the tin oxide polycrystalline electrode is proposed

$$(ES) + h\nu \rightarrow (ES)^+ + e^- \text{ (conduction band)}$$

$$(ES)^+ \rightarrow (ES) + h^+ \text{ (intermediate band)}$$

$$e^- \text{ (conduction band)} \rightarrow \text{move to interior}$$

$$H_2O(l) + 2h^+ \text{ (intermediate band)} \rightarrow 1/2\ O_2 + 2H^+$$

where (ES) represents the surface energy states due to the presence of impurities, defects, grain boundaries, and adsorbed molecules.

Acknowledgment

This research was supported by the National Science Foundation under grant GP 32847X.

Manuscript submitted Feb. 20, 1974; revised manuscript received Aug. 13, 1974. This was Paper 105 presented at the Houston, Texas, Meeting of the Society, May 7-11, 1972.

Any discussion of this paper will appear in a Discussion Section to be published in the December 1975 JOURNAL. All discussions for the December 1975 Discussion Section should be submitted by Aug. 1, 1975.

Publication costs of this article were partially assisted by the University of Illinois at Urbana-Champaign.

REFERENCES

1. R. Williams, *J. Chem. Phys.*, **32,** 1505 (1960).
2. H. Berg, *Naturwissenschaften*, **47,** 320 (1960).
3. M. Heyrovsky, *Nature*, **200,** 880 (1966).
4. G. C. Barker, A. W. Gardner, and D. C. Sammon, *This Journal*, **113,** 1182 (1966).
5. W. H. Brattain and C. G. B. Garrett, *Bell System Tech. J.*, **34,** 129 (1955).
6. H. Gerischer, *This Journal*, **113,** 1174 (1966).
7. F. Lohmann, *Ber. Bunsenges. Phys. Chem.*, **70,** 87 (1966).
8. R. Memming and H. Tributsch, *J. Phys. Chem.*, **75,** 562 (1971).
9. H. Gerischer, *Ber. Bunsenges. Phys. Chem.*, **69,** 578 (1965).
10. H. R. Schöppel and H. Gerischer, *ibid.*, **75,** 1237 (1971).
11. H. Gerischer and H. Tributsch, *ibid.*, **72,** 437 (1968); **73,** 850 (1969).
12. H. Kim, Ph.D. Thesis, University of Illinois, 1973.
13. H. A. Laitinen, C. A. Vincent, and T. M. Bednarski, *This Journal*, **115,** 1025 (1968).
14. D. Elliott, D. L. Zellmer, and H. A. Laitinen, *ibid.*, **117,** 1343 (1970).
15. J. M. Mochel, U.S. Pat. 2,564,707 (1951).
16. H. Kim and H. A. Laitinen, To be published.
17. E. A. Corl and H. Wimpfheimer, *Solid State Electron.*, **7,** 755 (1964).
18. P. Friedlaender, "Fortschritte der Teerfarbrikation and Verwandter Industriezweige," Vol. 2, pp. 68-72, Julius Springer, Berlin (1891).
19. R. G. Rhodes, "Imperfections and Active Centers in Semiconductors," pp. 259-270, Pergamon Press Oxford (1964).
20. F. Mollers and R. Memming, *Ber. Bunsenges. Phys. Chem.*, **76,** 469 (1972).
21. H. Gerischer, "Physical Chemistry an Advanced Treatise," H. Eyring, D. Henderson, and W. Jost, Editors, Academic Press, New York (1970).
22. R. Memming, *Photochem. Photobiol.*, **16,** 325 (1972).
23. D. R. Frankl, "Electrical Properties of Semiconductor Surface," pp. 186-194, Pergamon Press, Oxford (1967).
24. G. Heiland, W. Bauer, and M. Neuhaus, *Photochem. Photobiol.*, **16,** 315 (1972).
25. V. A. Myamlin and Yu. V. Pleskov, "Electrochemistry of Semiconductors," pp. 100-110, Plenum Publishing Corp., Inc., New York (1967).
26. E. E. Kohnke, *J. Phys. Chem. Solids*, **23,** 1557 (1962).
27. A. Fujishima and K. Honda, *Nature*, **238,** 37 (1972).

Light-Deflection Errors in the Interferometry of Electrochemical Mass Transfer Boundary Layers

F. R. McLarnon,* R. H. Muller,* and C. W. Tobias*

Inorganic Materials Research Division, Lawrence Berkeley Laboratory, and Department of Chemical Engineering, University of California, Berkeley, California 94720

ABSTRACT

The effect of light deflection on interferograms of electrochemical mass transfer boundary layers can result in substantial errors if interferograms are interpreted in the conventional way. Corrections in boundary layer thickness, interfacial concentration, and interfacial concentration gradient for the convection-free electrodeposition of Cu from aqueous $CuSO_4$ have been calculated to provide estimates for a wide range of experimental conditions.

Concentration profiles of single solutes in electrolytes near working electrodes can, in principle, be quantitatively observed by interferometric techniques. Such observations are useful in the study of transport processes and in the analysis of different measures designed to provide uniform accessibility and increased reaction rates at electrodes. Some of the advantages of interferometry compared to other means of observing boundary layers and local transport rates are: high resolution for concentration changes (typically 10^{-5}M) and, the possibility of continuous observation without disturbance (*e.g.*, of flow), not restricted to conditions of limiting current.

In the conventional interpretation of interferograms, local changes in the phase depicted by the interferogram are taken as a direct measure of local refractive index variations in the object. Such an interpretation is often not valid because it assumes that light travels along a straight line through the specimen. Refractive index variations normal to the propagation direction of the light beam produce a deflection of the beam (refraction, Schlieren effect) that results in two types of distortions in the interferogram: (*i*) Geometrical distortion due to displacement of the beam normal to its propagation direction. This effect falsifies conventional interpretation of distance on the interferogram and causes displacement of the apparent electrode/electrolyte interface. (*ii*) Phase distortion due to increased geometrical path length and passage of the beam through regions of varying refractive index. Quantitative concentration profiles, therefore, often cannot be derived by the conventional interpretation of interferograms.

Figure 1 schematically shows the trajectories of two light rays traversing a cathodic concentration boundary layer. Ray ABC is only slightly deflected and stays within the boundary layer over its path AB because it propagates near the edge of the boundary layer where the refractive index gradient is small. Ray DEF, which enters the electrolyte where the refractive index gradient is high, is deflected so much that it leaves the boundary layer at the intersection with line GH (and then travels along a straight line) before leaving the electrolyte at point E. A deflected ray will contribute to the interferogram only if it passes through the aperture of the objective lens. For instance, if ray DEF were to be deflected at any higher angle, it would not pass through the objective lens and, therefore, would not contribute to the interferogram. The corresponding part of the boundary layer would then not be visible on the interferogram.

Details of computational techniques, that have been developed to account for the effect of light deflection on interferograms of one-dimensional boundary layers, have been described elsewhere (1, 2). Suffice it to say that for any concentration profile, the shapes of (double beam) interference fringes can now be calculated taking into account effects of light deflection. It has been found that distortions in the interferogram depend strongly on the position of the plane of focus of the imaging objective lens. Although for each concentration profile a plane of focus can be found (3) for which the location of the electrode surface is not distorted on the interferogram, it is preferable to use a more easily defined plane of focus at a fixed location and accept the resulting displacement of the electrode shadow. For the observation of cathodic boundary layers (to be considered here) we recommend (2) focusing on the inside of the cell wall on the light-entrance side of the cell, where suitable targets can be inscribed. (For anodic boundary layers, it would be preferable to focus on the inside of the cell wall on the light-exit side.)

It is the purpose of this paper to present calculations of light-deflection errors for the interferometric observation of boundary layers so that investigators may estimate errors to be expected under a wide range of experimental conditions.

Light-Deflection Errors

Figure 2 shows the experimental interferogram of a concentration boundary layer formed by constant-current electrolysis. Superimposed are the theoretical concentration profile, AE, derived by use of the Sand (4) equation, and an interference fringe, BF, computed from the concentration profile by taking light-deflection effects into account.

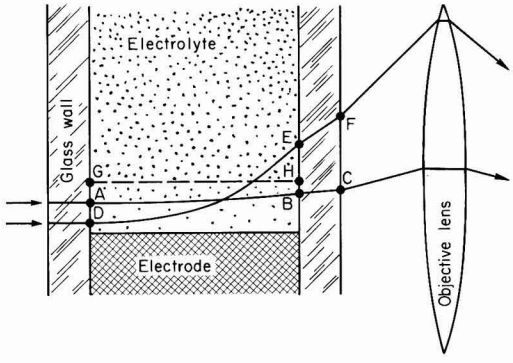

Fig. 1. Schematic of light ray trajectories in a cathodic concentration boundary layer: refractive index increases in the direction away fom the electrode surface. ABC, trajectory of a ray that remains inside the boundary layer. DEF, trajectory of a ray that is deflected out of the boundary layer. GH, edge of the boundary layer.

* Electrochemical Society Active Member.

Key words: interferometry, refraction, diffusion, mass transfer.

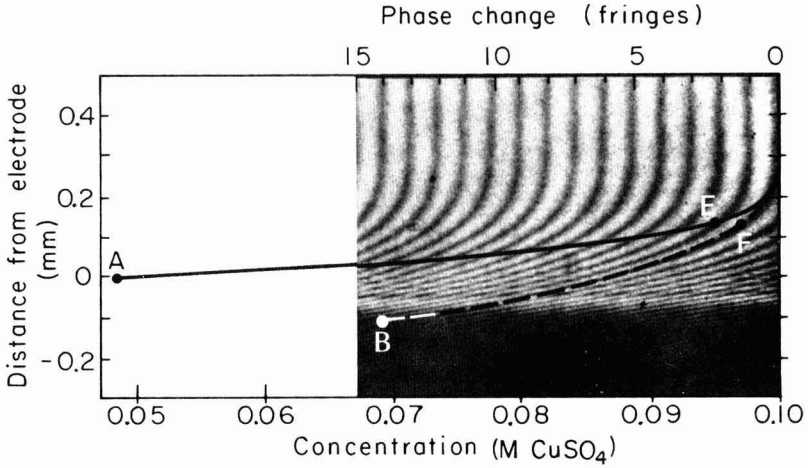

Fig. 2. Experimental interferogram of a concentration boundary layer during galvanostatic deposition of copper on a 10 mm wide electrode. i = 10.0 mA/cm², C_b = 0.1M $CuSO_4$, and t = 10.0 sec. —— Theoretical concentration profile AE corresponding to experimental conditions (calculated from Eq. [13]). - - - - - Computed interference fringe BF corresponding to theoretical concentration profile. A, true interfacial concentration and position. B, apparent interfacial concentration and position. E, true (90%) boundary layer edge (position where θ = 0.9). F, apparent boundary layer edge.

The ordinate on Fig. 2 denotes distance from the true (undistorted) image of the electrode surface. Local changes in the phase of transmitted light, visible as displacements of originally straight interference fringes, have been related to local concentration changes, as shown on the abscissa. The relationship has been based on the conventional interpretation of interferograms that assumes straight-line light propagation. Thus, local changes in phase have been linearly related to changes in concentration (or refractive index) at the corresponding point in the image.

If the interferogram was free of light-deflection effects, the interference fringes would follow the theoretical concentration profile AE. The figure illustrates that the apparent location B of the interface on the interferogram has receded from its original position A, identified by $y = 0$. Also, the apparent concentration change over the boundary layer is smaller than the true change.

Conventional interpretation of the interferogram in Fig. 2 would therefore lead to a boundary layer thickness that is too large. If we define the extent of the boundary layer as the region containing 90% of the concentration variation, the error e_t in boundary layer thickness can be defined in terms of the ordinates of the points shown in Fig. 2 as

$$e_t = (y_F - y_B) - (y_E - y_A)$$

Similarly, the apparent interfacial concentration is too high and the error can be formulated as a difference of abscissas

$$e_c = C_B - C_A$$

The interfacial concentration (refractive index) gradient is too low. The error can be represented by the difference in slope of the two curves at the interface

$$e_g = \left.\frac{dC}{dy}\right|_B - \left.\frac{dC}{dy}\right|_A$$

In addition to the above absolute errors in the interferometry of boundary layers, it is often desirable to estimate the relative errors. Such relative errors in boundary layer thickness, interfacial concentration, and interfacial concentration gradient, as shown in Fig. 8-13, are defined here as

$$\epsilon_t = \frac{e_t}{y_E}$$

$$\epsilon_c = \frac{e_c}{C_b - C_A}$$

$$\epsilon_g = \frac{e_g}{\left.\frac{dC}{dy}\right|_A}$$

Convection-Free Boundary Layers

Diffusion boundary layers free of convection effects offer a useful model for optical investigation since the concentration profiles are easily derived, and experimental results can serve to test the optical calculations. Convection-free transport conditions are common in electrochemical studies, and results can be used as a basis for convective transport studies.

The convectionless electrodeposition of a metal cation from a stagnant layer of an aqueous binary salt electrolyte is described by the time-dependent diffusion equation in one dimension[1]

$$\frac{\partial C}{\partial t} = D\frac{\partial^2 C}{\partial y^2} \qquad [1]$$

The current density is related to the interfacial concentration gradient by

$$i = \frac{z\mathbf{F}D}{1 - t_+}\left.\frac{\partial C}{\partial y}\right|_{y=0} \qquad [2]$$

For potentiostatic electrodeposition, the boundary conditions are

$$C = C_s \text{ at } y = 0,\ t > 0 \qquad [3]$$

$$C = C_b \text{ at } t = 0, \text{ all } y \qquad [4]$$

$$C = C_b \text{ as } y \to \infty \qquad [5]$$

The solution, first obtained by Cottrell (5), is

$$\theta = \text{erf}\,\zeta \qquad [6]$$

$$i = \frac{z\mathbf{F}(\Delta C)}{1 - t_+}\sqrt{\frac{D}{\pi t}} \qquad [7]$$

where erf ζ is the error function of dimensionless distance

$$\zeta = \frac{y}{2\sqrt{Dt}} \qquad [8]$$

$\Delta C = C_b - C_s$ and the dimensionless concentration

$$\theta = \frac{C - C_s}{\Delta C} \qquad [9]$$

For galvanostatic electrodeposition, the boundary conditions to Eq [1] are

$$\frac{\partial C}{\partial y} = \text{constant at } y = 0,\ t > 0 \qquad [10]$$

[1] Concentration-independent diffusivity will be assumed. Solutions for variable diffusivity can also be obtained, although not in a convenient closed form.

$$C = C_b \text{ at } t = 0, \text{ all } y \quad [11]$$

$$C = C_b \text{ as } y \to \infty \quad [12]$$

The solution, first obtained by Sand (4), is

$$\theta = 1 + \sqrt{\pi}\,\zeta(1 - \text{erf}\,\zeta) - e^{-\zeta^2} \quad [13]$$

$$\Delta C = \frac{2i(1 - t_+)}{z\mathbf{F}}\sqrt{\frac{t}{\pi D}} \quad [14]$$

Concentration profiles for use in the light-deflection analysis, with electrodeposition of Cu from aqueous $CuSO_4$ serving as a model, have been calculated. Equations [6] and [7] and Eq. [13] and [14] have been used in this computation. The interfacial concentration has been set $C_s = 0$, and the values of the bulk concentration were $C_b = 0.01$, 0.10, and 0.20M $CuSO_4$ ($\Delta C = 0.01$, 0.10, or 0.20). For constant potential calculations, time t is varied to give different concentration profiles and interfacial mass flux rates. For constant current calculations, various current densities are used (substituting Eq. [2] into Eq. [10]) to give different concentration profiles and interfacial mass flux rates. (Note that specification of i and ΔC fixes t through Eq. [14].) A diffusion coefficient (6) $D = 6 \times 10^{-6}$ cm^2/sec and Cu^{++} transference number (7) $t_+ = 0.36$ (typical values for 0.1M $CuSO_4$ at 25°C) are used in all calculations. Representative concentration profiles employed in the optical analysis are shown in Fig. 3 and 4.

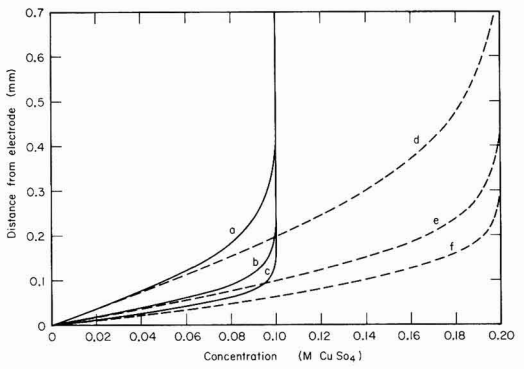

Fig. 3. Concentration profiles for potentiostatic conditions. —— ΔC = 0.1M $CuSO_4$; - - - - - ΔC = 0.2M $CuSO_4$; a, i = 10.0 mA/cm^2, t = 17.5 sec; b, i = 20.0, t = 4.4 sec; c, i = 30.0, t = 1.9 sec; d, i = 10.0, t = 70.0 sec; e, i = 20.0, t = 17.5 sec; f, i = 30.0, t = 7.8 sec.

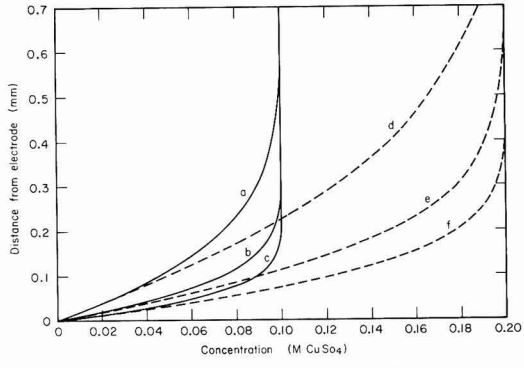

Fig. 4. Concentration profiles for galvanostatic conditions. ΔC and i designation as in Fig. 3. a, t = 43.2 sec; b, t = 10.8 sec; c, t = 4.8 sec; d, t = 172.7 sec; e, t = 43.2 sec; f, t = 19.2 sec.

Error Calculations

Cell dimensions and optical constants must be specified in order to compute interferograms from concentration profiles. The electrode, which is assumed here to fully occupy the space between the glass sidewalls, was assigned widths of 1.0, 2.5, 5.0, 10.0, and 20.0 mm. In order to model our experimental cell, the glass sidewalls were assumed to be 12.7 mm wide with a refractive index of 1.5231. However, refraction in the glass sidewalls has a negligible effect on light-deflection errors (3). Light of 632.8 nm wavelength is assumed incident parallel to the planar electrode surface and perpendicular to the glass sidewalls. The plane of focus is chosen as the plane where light enters the electrolyte. Electrolyte refractive index was experimentally found to be a linear function of $CuSO_4$ concentration at 632.8 nm wavelength and 25°C

$$n = 1.3311 + 0.029C \quad [15]$$

Interferograms similar to the dashed line in Fig. 2 are now calculated from concentration profiles using the above-mentioned computational technique (1).

Absolute errors in boundary layer thickness, interfacial concentration, and interfacial concentration gradient are shown in Fig. 5, 6, and 7, respectively, for a 10 mm wide electrode. Current density (interfacial refractive-index gradient) was chosen as abscissa because it is an easily measured variable. Note that a positive error means that the value of a variable on the interferogram is larger than the true value.

Relative errors in boundary layer thickness, interfacial concentration, and interfacial concentration gradient are shown in Fig. 8-13. Figures 8-10 also demonstrate the dependence of errors on concentration difference ΔC. The effect of electrode width is illustrated in Fig. 11-13.

Discussion

Figures 5-7 show that for a 10 mm wide electrode, the light-deflection errors depend strongly on current density and concentration difference ΔC and only weakly on the specific boundary condition (potentio-

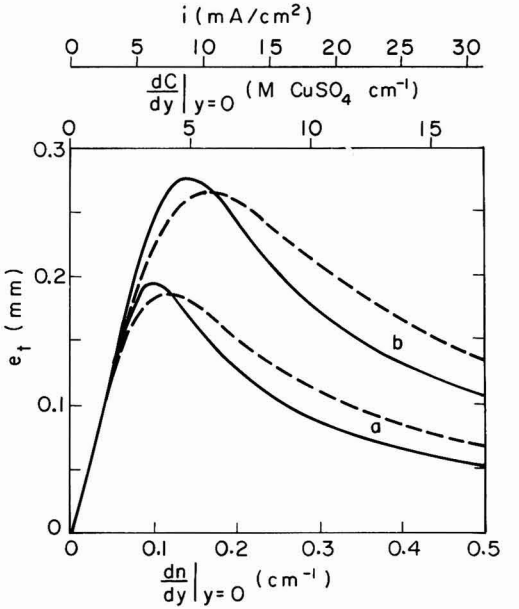

Fig. 5. Absolute error in boundary layer thickness. Electrode width = 10.0 mm. —— potentiostatic boundary condition; - - - - - - galvanostatic boundary condition; a, ΔC = 0.01M $CuSO_4$; b, ΔC = 0.10M $CuSO_4$; c, ΔC = 0.20M $CuSO_4$.

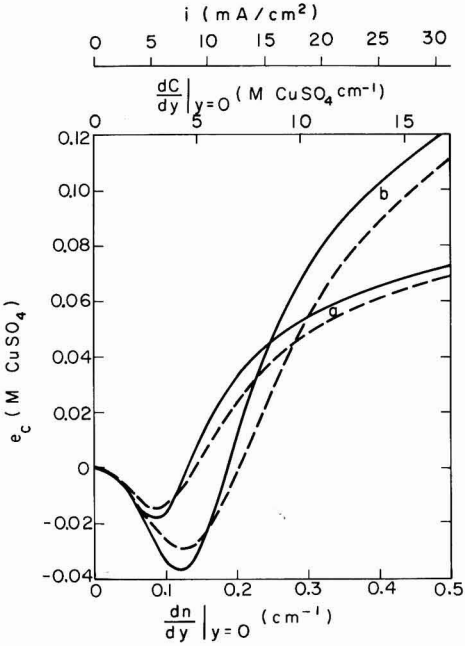

Fig. 6. Absolute error in interfacial concentration. Designations as in Fig. 5.

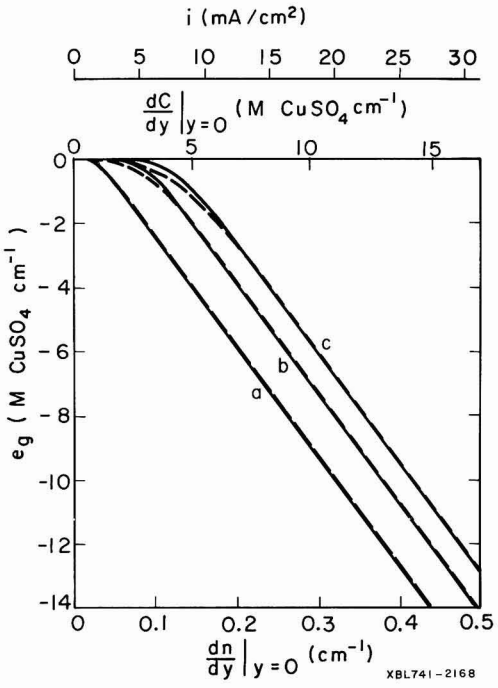

Fig. 7. Absolute error in interfacial concentration gradient. Designations as in Fig. 5.

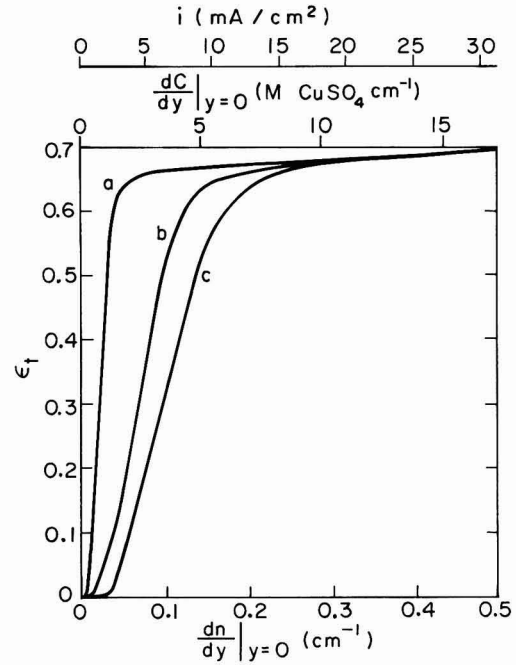

Fig 8. Relative error in boundary layer thickness for various concentration differences. Electrode width = 10.0 mm, potentiostatic boundary condition. a, ΔC = 0.01M $CuSO_4$; b, ΔC = 0.10M $CuSO_4$; c, ΔC = 0.20M $CuSO_4$.

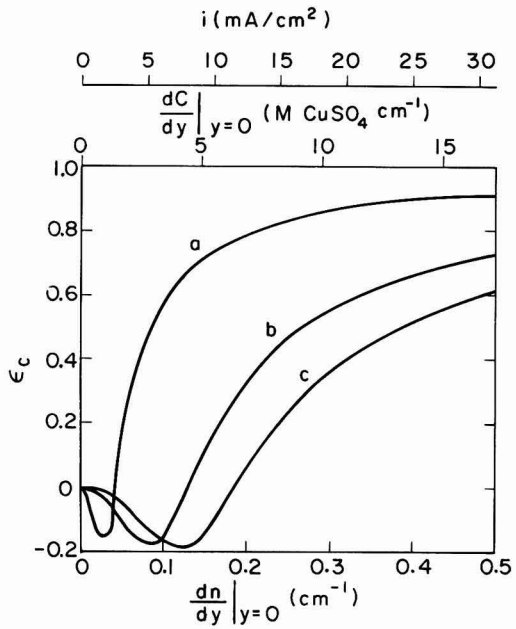

Fig. 9. Relative error in interfacial concentration for various concentration differences. Designations as in Fig. 8.

static or galvanostatic). For current densities in the order of 1 mA/cm², the errors are independent of ΔC and boundary condition. The weak dependence on boundary condition can be ascribed to the similarity between the respective concentration profiles; compare Fig. 3 and 4. Above about 2 mA/cm² for ΔC = 0.01M $CuSO_4$, about 7 mA/cm² for ΔC = 0.1M, and about 10 mA/cm² for ΔC = 0.2M, the light rays entering the boundary layer at the electrode surface are

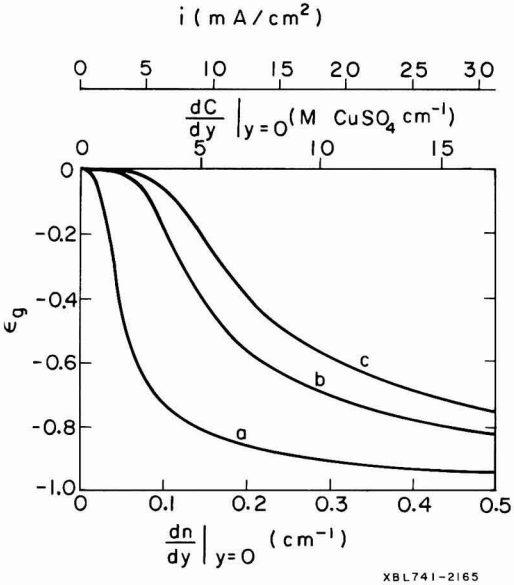

Fig. 10. Relative error in interfacial concentration gradient for various concentration differences. Designations as in Fig. 8.

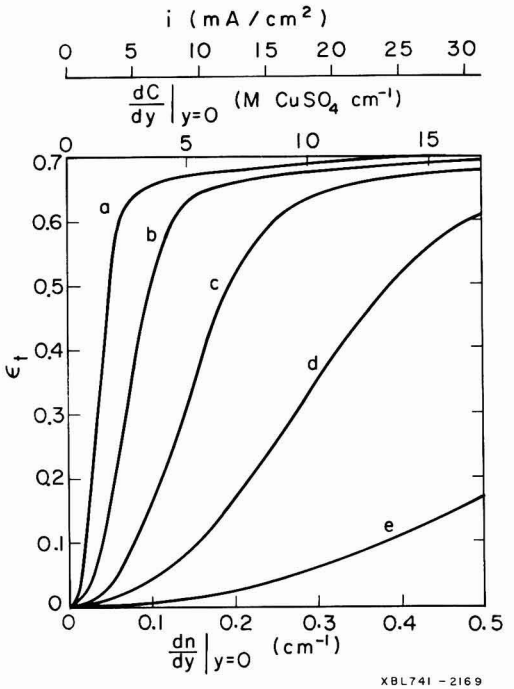

Fig. 11. Relative error in boundary layer thickness for different electrode widths. ΔC = 0.1M $CuSO_4$, potentiostatic boundary condition. a, electrode width = 20.0 mm; b, 10.0 mm; c, 5.0 mm; d, 2.5 mm; e, 1.0 mm.

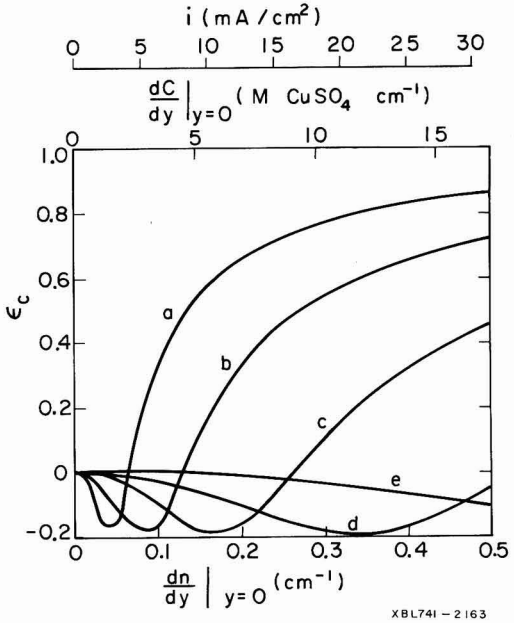

Fig. 12. Relative error in interfacial concentration for different electrode widths. Designations as in Fig. 11.

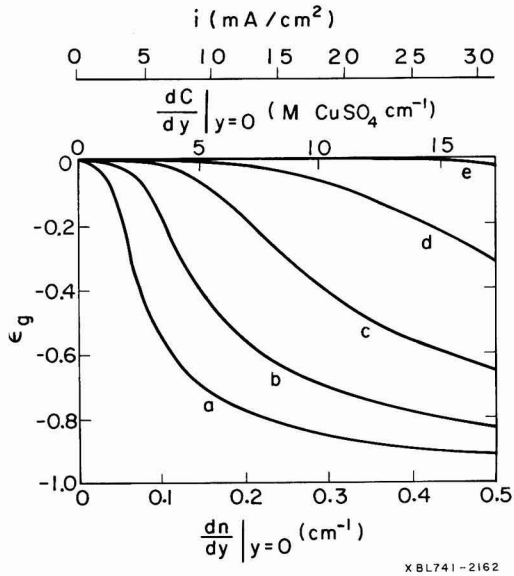

Fig. 13. Relative error in interfacial concentration gradient for different electrode widths. Designations as in Fig. 11.

deflected so much that they leave the boundary layer before they leave the electrolyte (as ray DEF in Fig. 1). This effect causes an error extremum in the curves of Fig. 5 and 6 and a knee in the curves of Fig. 7. The abrupt changes in the character of the error curves are due to the straight paths traversed by the deflected rays once they leave the boundary layer; at lower current densities the rays are continuously changing direction within the boundary layer. (Fig. 2 illustrates an interferogram in which rays entering the cell near the electrode surface are deflected out of the boundary layer.) As infinite current density is approached, the error in boundary layer thickness approaches zero, the error in interfacial concentration approaches ΔC, and the error in interfacial concentration gradient approaches negative infinity.

The trend toward apparent negative concentrations (*i.e.*, on the interferogram) seen in Fig. 6, 9, and 12 is a result of the choice of focal plane position. For focus in the center of the cell, for instance, no such negative errors would occur.

Figures 8-10 show that, contrary to what one might expect, relative errors are generally smaller for larger concentration difference ΔC. However, for large concentration differences, interferogram interpretation can be impeded by crowding of the fringes near the interface.

Figures 11-13 show that similar to absolute errors derived analytically for constant concentration gradients of unlimited extent (3), relative errors strongly diminish with decreasing cell width, but are negligible only for electrodes thinner than a few millimeters.

Figures 5-13 can be used to estimate light-deflection errors in experimental interferograms if all deflected portions of the test beam are accepted by the objective lens. The maximum angle ϕ_{max} of light deflection within a boundary layer is given by (2, 3)

$$\tan \phi_{max} = \sqrt{\left(\frac{n_b}{n_s}\right)^2 - 1} \qquad [16]$$

and the maximum angle of deflected light emanating from the specimen cell can be calculated by substituting numerical values of refractive index (*e.g.*, Eq. [15] into Eq. [16]) and accounting for refraction in the glass sidewall. For example, the objective lens aperture must accept illumination at angles up to 1.59° for $\Delta C = 0.01$M $CuSO_4$, up to 4.65° for $\Delta C = 0.10$M, and up to 7.14° for $\Delta C = 0.20$M.

Conclusions

Light-deflection effects in the interferometry of electrochemical mass transfer boundary layers can lead to serious errors in the derivation of concentration profiles unless appropriate corrections in the interpretation of interferograms are employed. The magnitude of errors encountered may be estimated from the data presented in Fig. 5-13, but the accurate interpretation of interferograms with significant light-deflection effects requires individual optical analysis (2). Light-deflection errors are small (<10%) for small current densities (below 2.5 mA/cm² for a 1 cm wide electrode) or narrow electrodes (less than 2.5 mm for up to 10 mA/cm²).

Acknowledgment

This work was conducted under the auspices of the U. S. Atomic Energy Commission.

Manuscript submitted March 19, 1974; revised manuscript received Aug. 12, 1974. This was Paper 352 presented at the San Francisco, California, Meeting of the Society, May 12-17, 1974.

Any discussion of this paper will appear in a Discussion Section to be published in the December 1975 JOURNAL. All discussions for the December 1975 Discussion Section should be submitted by Aug. 1, 1975.

Publication costs of this article were partially assisted by the Lawrence Berkeley Laboratory, University of California.

NOMENCLATURE

C	concentration (mole/liter)
C_b	bulk concentration (mole/liter)
C_s	interfacial concentration (mole/liter)
D	diffusion coefficient (cm²/sec)
e_t	absolute error in boundary layer thickness (mm)
e_c	absolute error in interfacial concentration (M $CuSO_4$)
e_g	absolute error in interfacial concentration gradient (M $CuSO_4$ cm^{-1})
$\mathbf{F}$	Faraday constant (coul/equiv)
i	current density (A/cm²)
n	refractive index
n_b	bulk refractive index
n_s	interfacial refractive index
t	time after current (voltage) switch-on (sec)
t_+	cation transference number
y	distance from electrode (mm)
z	cation valence
ΔC	$C_b - C_s$ (mole/liter)
ϵ_t	relative error in boundary layer thickness
ϵ_c	relative error in interfacial concentration
ϵ_g	relative error in interfacial concentration gradient
ζ	dimensionless distance (Eq. [8])
θ	dimensionless concentration (Eq. [9])
ϕ_{max}	maximum angle of deflection within a boundary layer

REFERENCES

1. K. W. Beach, R. H. Muller, and C. W. Tobias, *J. Opt. Soc. Am.*, **63**, 559 (1973).
2. K. W. Beach, Ph.D. Thesis, University of California at Berkeley (1971).
3. R. H. Muller in "Advances in Electrochemistry and Electrochemical Engineering," R. H. Muller, Editor, Vol. 9, pp. 326-353, Wiley-Interscience, New York (1973).
4. H. J. S. Sand, *Phil. Mag.*, **1**, 45 (1901).
5. F. G. Cottrell, *Z. Physikal. Chem.*, **42**, 385 (1903).
6. W. G. Eversole, H. M. Kindsvater, and J. D. Peterson, *J. Phys. Chem.*, **46**, 370 (1942).
7. J. J. Fritz and C. R. Fuget, *ibid.*, **62**, 303 (1958).

Electrochemical Behavior of Rotating Iron Disks

Effect of Fe(III)

R. F. Tobias* and Ken Nobe*

School of Engineering and Applied Science, University of California, Los Angeles, California 90024

ABSTRACT

The electrochemical behavior of iron in deaerated H_2SO_4 containing ferric ions has been investigated with rotating disk electrodes. The rest potential and corrosion current of iron in 1*N* H_2SO_4 were not affected by variation in the angular velocity. On the other hand, the rest potential, E_m, and corrosion current of iron in 1*N* H_2SO_4 containing ferric ions varied with the ferric ion concentration, C, and the angular velocity of the iron disk, ω. E_m followed the relation

$$E_m = \text{constant} + 0.040 \log C + 0.020 \log \omega, \text{ volts}$$

The corrosion current of iron increased in the presence of ferric ions and was controlled by the diffusion of ferric ions. Diffusion coefficients of ferric and ferrous ions were determined: $D_{Fe(III)} = 5.2 \pm 0.3 \times 10^{-6}$ and $D_{Fe(II)} = 6.5 \pm 0.4 \times 10^{-6}$ cm²/sec.

Metallic corrosion which is controlled by the diffusion of an electroreducible species in the solution can be studied conveniently with the rotating disk electrode technique. Previously, Makrides (1) examined the electrochemical behavior of rotating iron cylinders in H_2SO_4-$Fe_2(SO_4)_3$ solutions. He developed relationships between the rest potential (corrosion potential) and the ferric iron concentration and the rotation rate. In addition, he constructed anodic polarization curves from the rest potential-limiting diffusion current (ferric ion reduction) data, which was in good agreement with the experimental anodic polarization curve.

In this study the rotating disk electrode has been utilized to investigate the electrochemical behavior of iron in H_2SO_4. The polarization and open-circuit characteristics of rotating iron disks in H_2SO_4 containing ferric sulfate at various rotation rates have been determined. In addition, the diffusion coefficients of ferric and ferrous ions have been determined from the limiting diffusion current densities for ferric and ferrous ion reduction, respectively. In contrast to the turbulent flow conditions in Makrides' studies with rotating cylinders (1), the rotating disk experiments were conducted within the laminar flow regime.

Experimental

The test electrodes were prepared from Ferrovac E iron rod stock which was turned down on a lathe to a diameter of either 1.25 or 0.65 cm. The rod was cut into 0.64 cm lengths with an Al_2O_3 abrasive cutoff wheel using water as a cutting lubricant. A Teflon sleeve was pressure-fitted about the cylindrical part of the electrode so that only the lower cross-sectional surface was exposed to the electrolyte. The outer diameter of the Teflon sleeve was 1.73 cm.

Before the test electrodes were mounted in the electrode assembly they were hand-polished with waterproof Al_2O_3 paper. Grit 240 was used initially to smooth out the rough surface. followed by 600 grit. After the polishing procedure the electrodes had a mirrorlike finish. The electrodes were then rinsed in water, wiped dry, placed in a Soxhlet column, and degreased with hot benzene for 4 hr. The degreased electrodes were annealed for 1 hr at 650°C and slowly cooled to room temperature under vacuum (pressure $<10^{-4}$ mm Hg). The finished electrodes were then stored in a desiccator until used.

The cell consisted of three parts: a separate compartment for the auxiliary electrode, the Pyrex jar, and the Teflon top. The Pyrex jar contained a ground glass joint, through which small amounts of a concentrated solution of $Fe_2(SO_4)_3$ or $FeSO_4$ were added to the solution from a precision burette equipped with a greaseless Teflon stopcock. The Teflon cell top had entry ports which provided space for the test electrode assembly, a Luggin capillary, a thermometer, a bubbler, and an entry to pass N_2 gas through the bottom and above the solution. The volume of electrolyte used was 1200 ml.

Analytical reagent grade chemicals and doubly distilled water were used to prepare the solutions. For the electrochemical studies of iron in the absence and presence of ferric sulfate, 1*N* H_2SO_4 was used for the supporting electrolyte. The ferric ion concentration was varied from 1.26 to 25.2 mM.[1] To determine limiting diffusion current densities for the reduction of ferrous ions, 0.5M sodium sulfate was used for the supporting electrolyte with the pH adjusted to 3.0 by addition of an appropriate amount of H_2SO_4. The ferrous ion concentration was varied from 5.03 to 13.2 mM. After the electrolyte was placed in the cell, deaeration was accomplishd by passing prepurified N_2 through the solution for at least 8 hr. All experiments were conducted at room temperature, 23° ± 1°C. All potentials are given with respect to a saturated calomel reference electrode (SCE).

The kinematic viscosity of the supporting electrolytes was measured with a Cannon-Ubbelohde semimicro viscometer. For 1*N* H_2SO_4, the kinematic viscosity was 0.973×10^{-2} cm²/sec, while for the 0.5M sodium sulfate the kinematic viscosity was 1.088×10^{-2} cm²/sec.

An Exact function generator Type 255 was used to drive a Wenking potentiostat for the potential sweep experiments. The potential-current data were recorded on a semilogarithmic scale by use of a Moseley Model 7561A logarithmic converter connected to a Moseley Model 7035AX-Y recorder.

The test sample was mounted in the electrode assembly. The iron electrode was washed with distilled water and then activated in 5*N* H_2SO_4 for 10 min. After activation, the sample was washed thoroughly with distilled water and then immersed in the cell solution. Then, cathodic potential sweeps were applied to the rotating disk electrode. In the preliminary experimental tests, sweep rates of 1, 10, and 100 mV/sec were investigated. Since the results of the two slower sweep rates were in good agreement, 10 mV/sec was selected for the experiments. After the hydrogen evolution reaction was determined by the first sweep, a known amount of ferric or ferrous sulfate was added to the cell from the burette. After the angular velocity

* Electrochemical Society Active Member.
Key words: corrosion, polarization, diffusion coefficients.

[1] Milligram ion.

was set to a specific value, the steady-state rest potential was recorded. Then, electroreduction experiments at one concentration were performed over the entire range of angular velocities selected before the concentration was increased to a new value.

A schematic diagram of the apparatus and the complete set of the experimental data are given elsewhere (2).

Results and Discussion

Fe-1N H_2SO_4 system.—In deaerated 1*N* H_2SO_4 solutions the steady-state rest potential (corrosion potential) of iron is -498 ± 8 mV and is not a function of the rotational velocity. The corrosion potential of iron is in reasonable agreement with Kelly (3) and with iron exhibiting Makrides' type i behavior (1) which exhibited an increase in corrosion potential with time from -550 mV to about a steady-state value of -515 mV.

The Tafel slope for hydrogen evolution, b_c, is 116 $\pm$ 8 mV/decade and is in good agreement with the values obtained by others (3-5). Makrides (1), on the other hand, reported lower values of the Tafel slope for the HER. The anodic Tafel slope, b_a, of 41 mV was also in good agreement with other workers (3, 4). Makrides (1), on the other hand, obtained values of about 60 mV for his type i electrodes.

The corrosion current, $I_{m,o}$, determined by extrapolation of the anodic and cathodic Tafel lines to the corrosion potential is 1.8×10^{-4} and 1.6×10^{-4} A/cm^2, respectively. $I_{m,o}$ can also be determined from the slope of the polarization, ϵ, *vs.* current density, I, plot in the region $\epsilon = 0$ as shown in Eq. [1].

$$I_{m,o} = \frac{b_a b_c}{2.303(b_a + b_c)} \left(\frac{dI}{d\epsilon}\right)_{\epsilon=0} \qquad [1]$$

Equation [1], which was derived by Stern (6), is the basis of the polarization resistance method for the determination of the corrosion current. The $I_{m,o}$ value calculated from the polarization resistance plot for iron in 1*N* H_2SO_4 is 1.2×10^{-4} A/cm^2. The corrosion currents obtained in this study are in good agreement with those reported by Kelly (3) and Greene (7). Makrides (1) reports that the corrosion current obtained for his type i iron was 4.1×10^{-4} A/cm^2 by extrapolation of the cathodic Tafel line and the polarization resistance method and 5.6×10^{-4} A/cm^2 by extrapolation of the anodic Tafel line.

The electrochemical parameters of iron in 1*N* H_2SO_4 are summarized in Table I. These results are based on experiments with at least eight different electrodes.

Limiting diffusion currents for Fe(III) and Fe(II) reduction.—Typical cathodic polarization behavior of iron in 1*N* H_2SO_4 containing ferric ions at angular velocities varying from 625-4225 rpm is shown in Fig. 1. For this system at sufficiently large cathodic polarization the total cathodic current, I_c, consisted of the partial currents for the hydrogen evolution, I_H, and ferric ion reduction, $I_{Fe(III)}$, reactions. Makrides' results (1) indicate that the rate of ferric ion reduction on iron in acidic solutions is diffusion controlled. Thus

$$I_c = I_H + I_{Fe(III)} = I_H + I_L \qquad [2]$$

where I_L is the limiting diffusion current.

Figure 2 represents a graphical description of the system. The cathodic polarization curves are given for four different situations: first, in the absence of ferric ions; second, with ferric ion concentration, C_1, and rotational velocity, ω_1; third, concentration. C_1, and angular velocity, ω_2; fourth, concentration C_2, and angular velocity, ω_1. For the case shown, $C_2 > C_1$ and $\omega_2 > \omega_1$. If the hydrogen evolution reaction is subtracted from the total cathodic current, the limiting diffusion current for the reduction of ferric ions is obtained. The square and triangle points shown in Fig. 2 represent cathodic polarization data constructed from the iron dissolution and the HER Tafel lines and the limiting diffusion currents for the reduction of ferric ions. The circle points represent cathodic polarization data constructed from the iron dissolution and the HER Tafel lines.

Table I. Electrochemical parameters of iron in 1*N* H_2SO_4

Rest potential (E_m)	-498 ± 8 mV (*vs.* SCE)
Corrosion current ($I_{m,o}$) (polarization resistance)	$1.2 \pm 0.3 \times 10^{-4}$ A/cm^2
Corrosion current ($I_{m,o}$) (anodic Tafel line extrapolation)	$1.8 \pm 0.3 \times 10^{-4}$ A/cm^2
Corrosion current ($I_{m,o}$) (cathodic Tafel line extrapolation)	$1.6 \pm 0.4 \times 10^{-4}$ A/cm^2
Anodic Tafel slope (b_a)	41 $\pm$ 3 mV/decade
Cathodic Tafel slope (b_a)	116 $\pm$ 8 mV/decade
Initial differential capacitance	42 $\pm$ 2 μf/cm^2

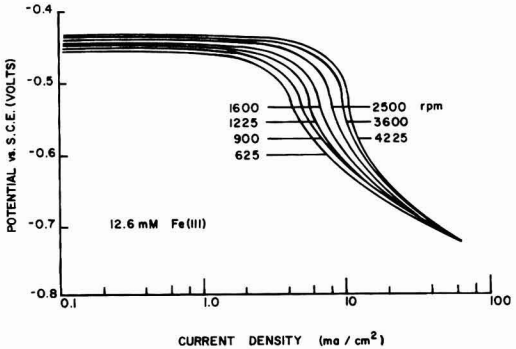

Fig. 1. Cathodic polarization of iron in 1*N* H_2SO_4 containing ferric ions.

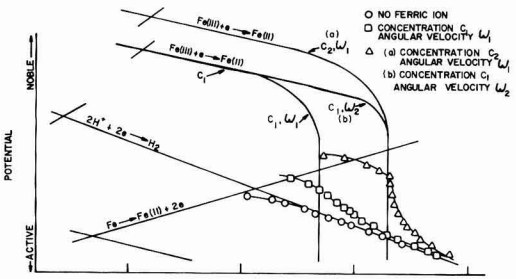

Fig. 2. Cathodic polarization of iron in absence and presence of ferric ions. Points represent calculated cathodic polarization data.

Figure 3 shows some typical results of the limiting current density for the reduction of ferric ions. These limiting currents were obtained in the following manner. First, before ferric ions were added to the sulfuric acid solution, the rate of hydrogen evolution on iron in 1*N* H_2SO_4 was determined. Then, with Eq. [2], the limiting diffusion currents for the reduction of ferric ions were obtained by subtracting the rate of the HER from the total measured current density obtained from the cathodic polarization curves of iron in solutions containing ferric ions as shown in Fig. 1.

The limiting current densities for the reduction of ferric ions *vs.* the square root of angular velocity are plotted in Fig. 4. A linear relationship is obtained in accord with the Levich equation for the limiting current density at a rotating disk electrode

$$i_L = 0.62\, nFD^{2/3}\nu^{-1/6}\omega^{1/2}C \qquad [3]$$

where the letters have their usual meaning.

Cathodic polarization measurements of iron in Na_2SO_4 (pH = 3) were conducted at various angular velocities in the absence (Fig. 5) and in the presence (Fig. 6) of ferrous ions. The observed limiting diffusion currents in Fig. 6 are the sum of the limiting dif-

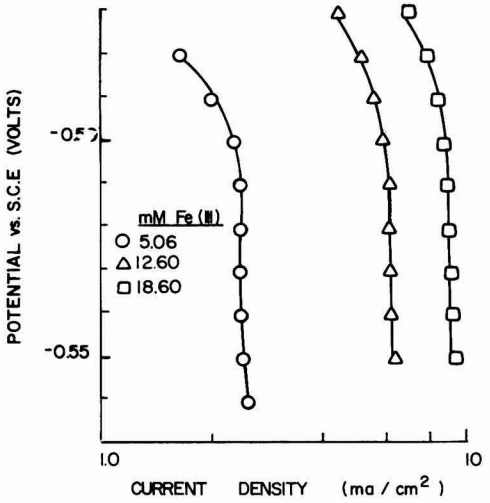

Fig. 3. Limiting diffusion currents for ferric ion reduction; $\omega = 1225$ rpm.

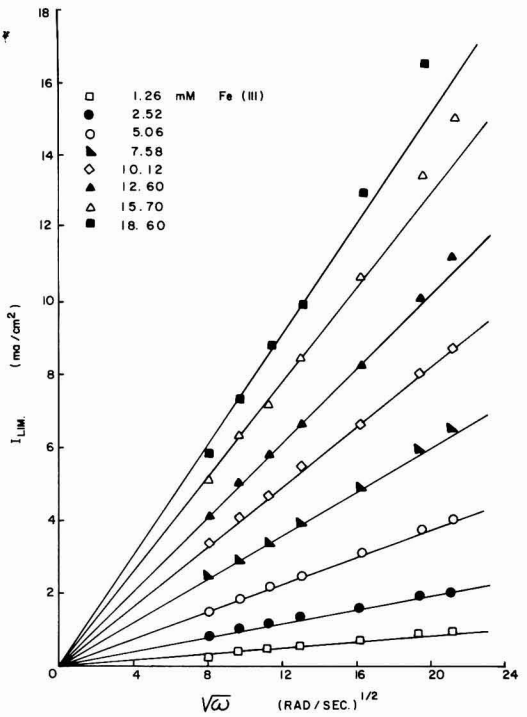

Fig. 4. I_L vs. $\sqrt{\omega}$ for ferric ion reduction

fusion currents for hydrogen ion and ferrous ion reduction. The limiting diffusion currents for ferrous ion reduction are readily determined by subtracting the I_L for hydrogen ion reduction (Fig. 5) from the total diffusion current (Fig. 6). Figures 7 and 8 show the limiting diffusion current for the reduction of ferrous ions *vs.* the square root of the angular velocity and the concentration of the ferrous ions, respectively. In both plots Levich behavior is obtained.

Fe-1N H_2SO_4-$Fe_2(SO_4)_3$ system.—The rest potential behavior of iron in the presence of ferric ions showed

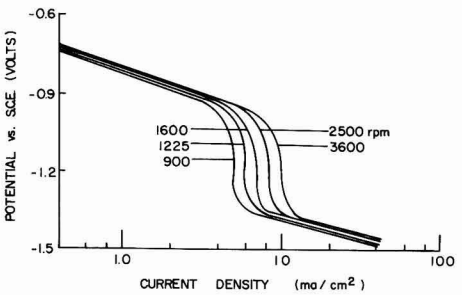

Fig. 5. Cathodic polarization of iron in 0.5M Na_2SO_4 (pH = 3)

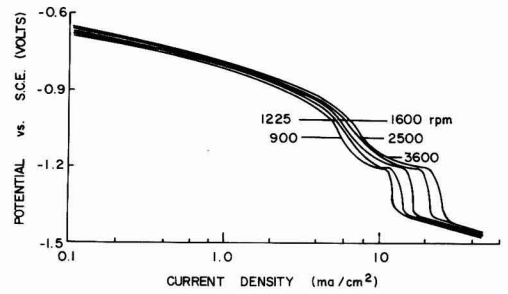

Fig. 6. Cathodic polarization of iron in 0.5M Na_2SO_4 (pH = 3) containing ferrous ions (6.68 mM).

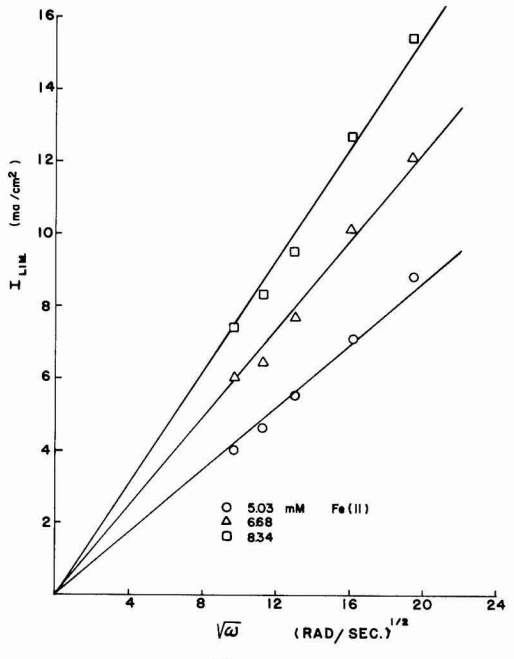

Fig. 7. I_L vs. $\sqrt{\omega}$ for ferrous ion reduction

a marked dependence on both the concentration of ferric ions and the angular velocity of the iron disk. The data presented in Fig. 9 show the dependence of the rest potential on the concentration of the ferric ions over the range of angular velocities, 625-4225 rpm. ΔE_o is defined as the rest potential of iron in the presence of ferric ions and at an angular velocity, ω, rela-

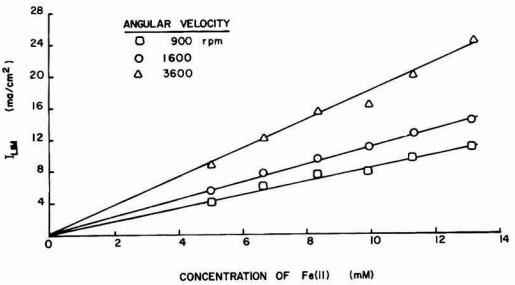

Fig. 8. I_L *vs.* concentration of Fe(II) for ferrous ion reduction

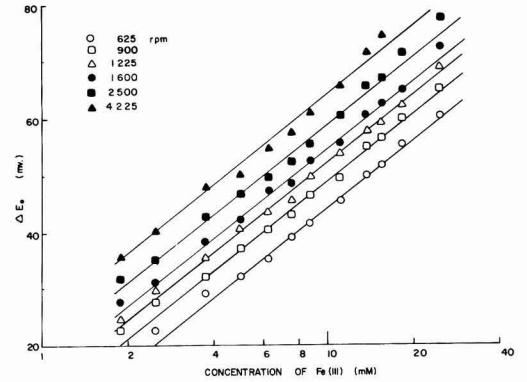

Fig. 9. ΔE_o *vs.* concentration of Fe(III)

tive to the rest potential of iron in the absence of ferric ions.

For iron in an acidic media containing only reducible species, H^+ and H_2O, the corrosion current $I_{m,o}$, is

$$I_{m,o} = I_a = I_c \qquad [4]$$

where I_a is the partial anodic process corresponding to iron dissolution and I_c is the partial cathodic process corresponding to the reduction of hydrogen ions.

For activation-controlled iron dissolution and HER, the total measured current for iron in H_2SO_4 can be represented by

$$I = I_{m,o}\left[\exp\left(\frac{\alpha_a n_a \mathbf{F}\epsilon}{RT}\right) - \exp\left(\frac{-(1-\alpha_c)n_c\mathbf{F}\epsilon}{RT}\right)\right] \qquad [5]$$

where the electrode kinetic parameters have their usual meaning. The first term on the right-hand side of Eq. [5] represents the rate of anodic dissolution of iron and the last term represents the rate of hydrogen evolution. The anodic dissolution term can be rearranged to obtain the Tafel equation

$$\epsilon_a = A + b_a \log I_a \qquad [6]$$

If another easily reducible species is introduced into the solution (*e.g.*, Fe^{+3}), the total cathodic current would consist of the sum of the rate of hydrogen evolution and the rate of reduction of the added oxidized species, *i.e.*

$$I_c = I_H + I_{ox} \qquad [7]$$

When ferric ions are added to the iron-sulfuric acid system, the rate of ferric ion reduction is diffusion controlled as mentioned above. For this situation, $I_{ox} = I_L$, and the cathodic current can be expressed by Eq. [2]. For the conditions studied in this work

$$I_L >> I_H \qquad [8]$$

Thus

$$I_c \simeq I_L \qquad [9]$$

and at the rest potential, E_m

$$I_m = I_a = I_L \qquad [10]$$

where I_m is the corrosion current of iron in H_2SO_4 containing ferric ions. Since the limiting diffusion current is independent of potential, the rest potential, E_m, is determined by the intersection of the anodic polarization curve and I_L.

The rate of iron dissolution in the absence of ferric ions at the rest potential, $E_{m,o}$, can be expressed as

$$I_{m,o} = I_a = i_{o,a}\left[\exp\frac{\alpha_a n_a \mathbf{F}}{RT}(E_{m,o} - E^e{}_a)\right] \qquad [11]$$

where $E^e{}_a$ is the equilibrium potential of the Fe/Fe^{+2} reaction.

When ferric ions are added to the solution, the corrosion current can be expressed as

$$I_m = I_L = I_a = i_{o,a}\exp\left[\frac{\alpha_a n_a \mathbf{F}}{RT}(E_m - E^e{}_a)\right] \qquad [12]$$

where E_m is the rest potential of iron in the presence of ferric ions. The quantity, $(E_m - E^e{}_a)$, can be rearranged to

$$E_m - E^e{}_a = (E_m - E_{m,o}) + (E_{m,o} - E^e{}_a) = \Delta E_o + (E_{m,o} - E^e{}_a) \qquad [13]$$

where ΔE_o is defined as the change in the rest potential with the addition of ferric ions to the H_2SO_4 solution. Equations [11] and [13] can be used to express Eq. [12] in the following form

$$I_m = I_L = I_{m,o}\exp\left[\frac{\alpha_a n_a \mathbf{F}}{RT}\Delta E_o\right] \qquad [14]$$

or rearrange Eq. [14]

$$\Delta E_o = a' + b_a \log I_L \qquad [15]$$

ΔE_o can be expressed as a function of both the ferric ion concentration and the angular velocity by utilizing the Levich equation for I_L, Eq. [3]. Then, Eq. [15] becomes

$$\Delta E_o = a + b_a \log C_{Fe(III)} + \frac{b_a}{2}\log\omega \qquad [16]$$

Thus, ΔE_o is shown to be a linear function of the logarithm of the ferric ion concentration with proportionality constant equal to the anodic Tafel slope obtained from anodic polarization experiments. The continuous lines in Fig. 9 have slopes of 40 mV/decade. Thus, the experimental data are consistent with Eq. [16], since a value of 41 mV for b_a was determined directly from anodic polarization measurements.

Figure 10 shows a plot of ΔE_o *vs.* log ω at constant ferric ion concentration. The experimental data fit the continuous lines well. The slopes of these lines are 20 mV/ decade which is consistent with the ½ b_a slopes predicted by Eq. [16].

Figure 2 indicates that a plot of ΔE_o *vs.* I_L should give the anodic polarization curve for anodic dissolution of iron in H_2SO_4. The effect of ferric ions on iron dissolution should be evident by comparing the anodic polarization curves obtained from the ΔE_o *vs.* I_L plots and curves obtained by direct anodic polarization. Figure 11 provides such a comparison. The data points obtained by the two methods are in reasonable agreement indicating that the anodic polarization of iron in H_2SO_4 is not affected appreciably by the addition of ferric ions. These results are in accord with those obtained by Makrides (1) who showed that ferric ions had no specific effect on the anodic polarization of rotating cylindrical iron electrodes.

Since the corrosion rate is controlled by the limiting diffusion current for ferric ion reduction when ferric ions are introduced into the Fe-H_2SO_4 system, the cathodic Tafel slope is infinity ($b_c = \infty$). Then, Eq. [1]

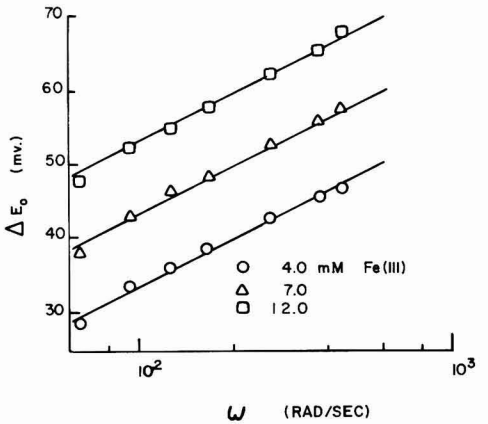

Fig. 10. ΔE_o *vs.* log ω plot

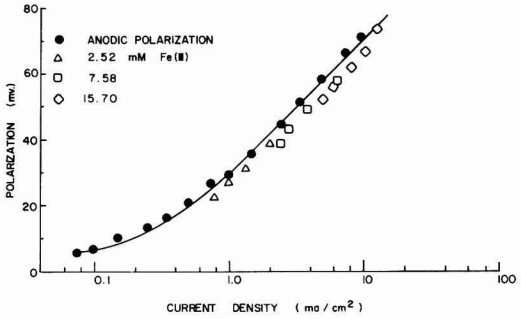

Fig. 11. Anodic dissolution of iron. Closed points represent anodic polarization data. Open points represent rest potential *vs.* I_L plots at various concentrations of Fe(III).

becomes

$$I_m = I_L = \frac{b_a}{2.303}\left(\frac{dI}{d\epsilon}\right)_{\epsilon=0} \qquad [17]$$

Figure 12 shows typical linear plots of ϵ *vs.* I for small values of ϵ at a constant concentration of ferric ions. The corrosion current of iron at various angular velocities can be calculated from Eq. [17] and the slopes of these lines. Table II compares the corrosion currents obtained by the polarization resistance method and by the cathodic polarization method. In general, the corrosion currents obtained by cathodic polarization are larger than the corrosion currents obtained by the polarization resistance method. However, for the lower ferric ion concentrations the corrosion currents of iron determined by the two methods are in good agreement.

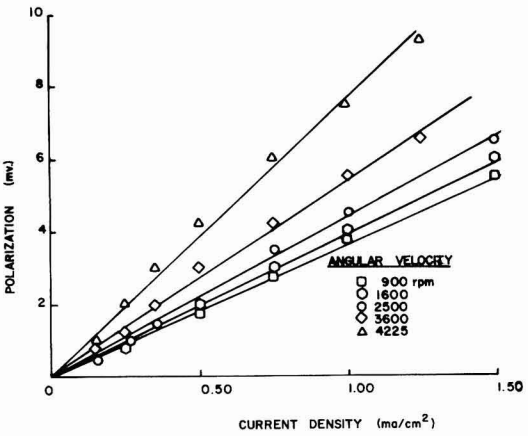

Fig. 12. Polarization resistance plot of iron in 1*N* H_2SO_4 and 7.5 mM Fe(III).

Table II. Corrosion currents of iron in acidic ferric sulfate solutions

Fe(III) conc, mM	Angular velocity, rpm	$\left(\frac{d\epsilon}{dI}\right)_{\epsilon=0}$	I_m (polarization), resistance), mA/cm²	I_m (polarization), mA/cm²
2.52	900	13.6	1.3	1.1
	1,600	11.6	1.5	1.5
	2,500	9.6	1.9	1.8
	3,600	8.2	2.2	2.2
	4,225	7.2	2.5	2.4
5.06	900	9.8	1.8	2.1
	1,600	7.0	2.6	2.7
	2,500	5.9	3.0	3.4
	3,600	5.0	3.6	4.0
	4,225	4.5	4.0	4.4
7.58	900	7.6	2.4	3.1
	1,600	5.4	3.3	4.1
	2,500	4.4	4.1	5.2
	3,600	3.9	4.6	6.1
	4,225	3.6	5.0	6.6
10.12	900	5.0	3.6	4.2
	1,600	3.8	4.7	5.2
	2,500	3.4	5.2	6.7
	3,600	3.0	6.0	8.2
	4,225	2.6	6.9	8.8
12.60	900	4.8	3.7	5.3
	1,600	3.1	5.8	6.7
	2,500	2.8	6.3	8.4
	3,600	2.2	8.3	10.2
	4,225	2.0	9.2	11.1

Table III. Diffusion coefficients of ferrous and ferric ions

Diffusion coefficient × 10^6 (cm²/sec)		Supporting electrolyte	Temp, °C	Reference
Ferric ion	Ferrous ion			
5.2 ± 0.3		1*N* H_2SO_4	23	This work
	6.5 ± 0.4	0.5M Na_2SO_4	23	This work
4.5 ± 0.1	5.6 ± 0.2	1M H_2SO_4	25	8
3.92	4.21	0.1M $HClO_4$	23	9
6.5	5.7	1M $HClO_4$	25	10

Diffusion coefficients of Fe(III) and Fe(II).—Diffusion coefficients of electroactive species can be readily determined from limiting diffusion current plots of rotating disk electrode experiments. The diffusion coefficients of ferric and ferrous ions were determined from the I_L *vs.* $\sqrt{\omega}$ and concentration plots as in Fig. 4, 7, and 8. These values are presented in Table III. For comparison, diffusion coefficients reported by several other workers (8-10) are also given in Table III.

Acknowledgments

This work was supported by the University of California sea water desalination program. One of us (R. F. T.) was a NASA predoctoral trainee during a part of this investigation.

Manuscript submitted March 21, 1974; revised manuscript received July 27, 1974.

Any discussion of this paper will appear in a Discussion Section to be published in the December 1975 JOURNAL. All discussions for the December 1975 Discussion Section should be submitted by Aug. 1, 1975.

REFERENCES

1. A. C. Makrides *This Journal*, **107,** 869 (1960).
2. R. F. Tobias, Ph.D. Dissertation, UCLA, March 1968.
3. E. J. Kelly, *This Journal*, **112,** 124 (1965).
4. J. O'M. Bockris and D. Drazic, *Electrochim. Acta*, **7,** 293 (1962).
5. T. Hurlen, *Acta Chem. Scand.*, **14**, 1533 (1960).
6. M. Stern and A. L. Geary, *This Journal*, **109,** 56 (1957).

7. N. D. Greene and G. A. Saltzman, *Corrosion*, **20**, 292t (1964).
8. A. M. Baticle, F. Perdu, and P. Vennereau, *Compt. Rend. Acad. Sci. Paris*, **t264**, 12 (1967).
9. L. B. Anderson and C. N. Reilley, *J. Electroanal. Chem.*, **10**, 295 (1965).
10. D. Jahn and W. Vielstich, *This Journal*, **109**, 849 (1962).

Double-Layer Capacity Determination of Porous Electrodes

William Tiedemann*

Globe-Union, Incorporated, Corporate Applied Research Group, Milwaukee, Wisconsin 53201

and John Newman*

Inorganic Materials Research Division, Lawrence Berkeley Laboratory, and Department of Chemical Engineering, University of California, Berkeley, California 94720

ABSTRACT

A method is presented for evaluating double-layer charging of porous electrodes. The maximum in the curve of $i\sqrt{t}$ *vs.* $\sqrt{t}$ lends itself readily to experimental evaluation. Values of the double-layer capacity determined for the Pb and PbO_2 electrodes in sulfuric acid are in agreement with those reported in the literature.

A number of models have been developed for analyzing the behavior of porous electrodes, and various degrees of complexity have been taken into account. The transient charging of the double-layer capacity (1-5) is of interest first of all because it provides a comparison between experimental and theoretical results. The transient charging can also be used to advantage to measure the capacity per unit volume of the electrode. A measurement of the double-layer capacity reflects most directly the active surface area coherently connected electrically and therefore accessible for electrochemical consumption. Such results should be useful for the characterization of battery electrodes and may be especially valuable since the electrode is not destroyed and indeed need not be removed from the cell in which it is cycled.

Transient measurement of the double-layer capacity of porous electrodes, as opposed to integration of the current passed following a potential step, has the advantage of emphasizing the charging current relative to the faradaic current, which interferes with the measurement. Furthermore, the resistance-capacity time constant will be large for an electrode with a large surface area, and the transient measurement will then reduce the experiment time substantially.

Johnson and Newman (4) have shown that the current response of a porous electrode to a step change in the potential yields, under certain circumstances, a nearly constant value of $i\sqrt{t}$, the product of the current density and the square root of time. A plot of $i\sqrt{t}$ *vs.* $\sqrt{t}$ yields a curve with a plateau. The curve is below this plateau value at short times because the ohmic resistance of the system prevents an infinite current density. At long times the curve again drops below the plateau value because the total capacity of the electrode begins to become saturated. The plateau value on a graph of this type is directly related to aC, the product of the specific interfacial area of the electrode and the double-layer capacity per unit area, and is independent of the thickness of the electrode. In this manner, Johnson and Newman inferred a value of $aC = 83.5$ farads/cm^3 for their porous carbon electrode.

However, most battery electrodes (for example, Pb and PbO_2 electrodes in sulfuric acid) are so thin that the ohmic limitation at short times overlaps with the approach to saturation at long times, and the plateau on the plot of $i\sqrt{t}$ *vs.* $\sqrt{t}$ is reduced to a maximum whose magnitude now depends on the electrode thickness or an equivalent parameter. This maximum still deserves the focus of our attention in a simple method for inferring the double-layer capacity aC from the measured transient current response. The earlier part of the curve is governed by the ohmic resistance, not the capacity, and the latter part is subject to interference from faradaic reactions. (This difference between thick porous carbon electrodes and thin battery electrodes can be visualized graphically by referring below to Fig. 2, where basically $i\sqrt{t}$ is plotted against $\sqrt{t}$, although dimensionless variables are used. The parameter λ is inversely proportional to the electrode thickness, if the matrix conductivity is very high.)

Analysis

Figure 1 is a diagram of the equivalent circuit of the system. R_2 represents the resistance of the solution in the pores of the electrode; R_1 that of the electrode matrix. C is the double-layer capacity between the electrode matrix and the pore solution. R_s corresponds to the resistance in the solution between the porous electrode and the reference electrode while R_L

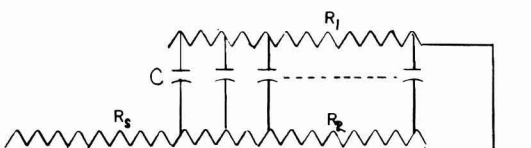

Fig. 1. Equivalent circuit of a porous electrode. The right side of the resistors represents a plane of symmetry in the center of the electrode.

* Electrochemical Society Active Member.
Key words: double-layer capacity, porous electrodes, lead-acid battery.

corresponds to the resistance in the leads and the current collector. For this system, Johnson and Newman (4) have related the Laplace transform of the current response to the Laplace transform of the applied potential. We make the following re-interpretation of their Eq. [20] (4) by including the resistance of the leads and that between the porous electrode and the reference electrode

$$R = \frac{L_s}{\kappa_s} + \frac{L}{\sigma + \kappa} + R_L \qquad [1]$$

where L_s is the distance between the reference electrode and the porous electrode (κ_s being the conductivity of the medium between the two), L is the half thickness of a porous electrode with a counterelectrode opposite each face, σ is the effective conductivity of the matrix of the porous electrode, and κ is the effective conductivity of the pore solution. The terms in Eq. [1] have units of ohm-cm^2; consequently, R_L is the lead resistance multiplied by twice the apparent cross-sectional area of a porous electrode with a counterelectrode opposite each face.

Thus, R is the effective resistance of the composite system and is subject to direct experimental determination as we shall discuss briefly. At zero time, the current cannot be infinite; it is limited by the effective resistance of the system

$$i|_{t=0} = \Delta V/R \qquad [2]$$

where $i|_{t=0}$ is the peak current density at time zero and ΔV the applied potential step between the reference and working electrodes. Thus, R can be directly obtained from the initial current surge measured on an oscilloscope.

Let us consider the case of a highly conducting matrix, $\sigma >> \kappa$ (for Pb and PbO_2 electrodes, $\sigma \approx 10^2$ and $\kappa \approx 0.1$ mho/cm). Posey and Morozumi (1) were the first to treat extensively double-layer charging of porous electrodes of finite thickness. They used a straight pore model and a highly conducting matrix. In an example involving the resistance between the working and reference electrodes, they inverted the Laplace transforms which are applicable to the system discussed in this paper. After some rearrangement the solution is

$$\frac{i\sqrt{\pi T}}{\Delta V}\frac{L}{\kappa} = 2\sqrt{\pi T}\sum_{n=1}^{\infty}\frac{\exp(-TX_n^2)}{1+\lambda+\lambda^2X_n^2} \qquad [3]$$

where

$$T = \frac{t}{aCL}\frac{\kappa}{L} \text{ and } \lambda = \frac{R\kappa}{L} \qquad [4]$$

aC is the double-layer capacity per unit volume of the electrode, and X_n is the positive root of cotangent $X_n = \lambda X_n$ [tabulated by Abramowitz and Stegun (6)]. In this result, no attempt has been made to account for faradaic reaction or concentration variations in the pore solution.

Since in our interpretation of the charging current we seek to emphasize the maximum in the curve of $i\sqrt{t}$ *vs.* $\sqrt{t}$, we plot in Fig. 2 the left side of Eq. [3] against $\sqrt{T}$. For $\lambda = 0$ the ordinate is a constant for short times. This corresponds to the plateau value discussed earlier, where

$$i\sqrt{t} = \Delta V\sqrt{aC\kappa/\pi} \qquad [5]$$

At longer times, the value of $i\sqrt{t}$ begins to decrease as the charging wave penetrates to the center of the electrode. For $\lambda = 0$ the ohmic limitation at short times is not seen on this scale.

As the effective resistance in the circuit is increased ($\lambda > 0$), the instantaneous charging current is reduced, and the ordinate is initially zero. Providing the effective resistance is small enough, the ordinate may rise to the plateau predicted for $\lambda = 0$ after an initial transient period. As λ increases further, the value of the plateau (or maximum of the ordinate) decreases.

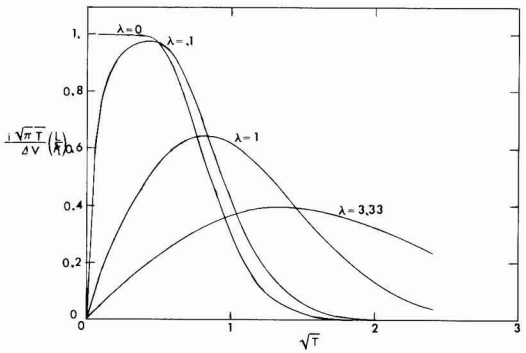

Fig. 2. Effect of the resistance-thickness parameter λ on the double-layer charging of a porous electrode.

The lower initial charging currents postpone the time at which the electrode capacity begins to become saturated and the value of $i\sqrt{t}$ begins to decrease. Consequently, the time at which the plateau or maximum occurs increases with increasing λ. This maximum readily lends itself to experimental determination.

For interpretation of the charging current we need only the coordinates of the maxima shown in Fig. 2. This information is summarized in Fig. 3 by plotting against $1/\lambda$ the following three quantities: the ratio of the coordinates of the maximum (this quantity being independent of the value of the double-layer capacity), $1/T_{max}$ (the time at which the maximum occurs, and a dimensionless value of $i\sqrt{t}$ at the maximum.

Interpretation and Evaluation of Charging Curves

Utilization of the information contained in Fig. 3 requires prior knowledge of the effective conductivity, κ, of the solution contained in the porous electrode. De la Rue and Tobias (7) found that the effective conductivity of a dispersion of glass beads in electrolytes can be represented by

$$\kappa = \kappa_0 p^{1.5} \qquad [6]$$

where κ_0 is the conductivity and p is the volume fraction of the continuous phase. The effective conductivity of a solution contained in a porous medium can be estimated with this equation by using the porosity for p. Alternatively, the conductivity can be measured directly. Romanova and Selitskii (8) have employed the porous electrode as an inert separator. The ohmic potential drop through the electrode is then equal to $i2L/\kappa$. The value of κ needs to be re-estimated or redetermined if the electrode structure changes sig-

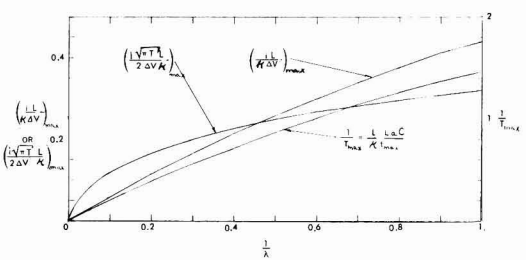

Fig. 3. Dependence of the coordinates of the maximum on the resistance-thickness parameter λ. Maximum refers to the maximum when $i\sqrt{t}$ is plotted against $\sqrt{t}$ for the double-layer charging of a porous electrode with a step change in the applied potential.

nificantly on repeated cycling. However, it is possible to determine κ by replotting the information in Fig. 3. Multiplying the ordinate of Fig. 3, $\left(\frac{i}{\Delta V}\frac{L}{\kappa}\right)_{max}$, by λ, we obtain $i_{max}/i|_{t=0}$ (where i_{max} refers to the value of the current density at the maximum in Fig. 2) which is plotted *vs.* $1/\lambda$ in Fig. 4. An oscilloscope trace of the current response to a voltage step will yield $i|_{t=0}$ directly, and a plot of $i\sqrt{t}$ *vs.* $\sqrt{t}$ will give i_{max}. The ratio of these two numbers will then yield a value of λ (which contains κ) as shown in Fig. 4. The measured value of the double-layer capacity is relatively insensitive to the value of κ when the resistance-thickness parameter λ is large.

An interesting sidelight of the results shown in Fig. 4 is that the value of κ determined in this manner can then be used to estimate the porosity of the electrode through the use of Eq. [6]. In this manner one may determine *in situ* the porosity of an electrode and follow its change through extended cycling tests.

The procedure used to extract the double-layer capacity per unit volume of electrode from the current response to a potential step can be stated as follows: (*i*) An oscilloscope trace of the current response of a porous electrode to a voltage step is obtained. (*ii*) The value of the current at time zero, $i|_{t=0}$, is recorded and a plot of $i\sqrt{t}$ *vs.* $\sqrt{t}$ is made. The coordinates of the plateau or maximum of the resulting curve are recorded and yield i_{max} and t_{max}. (*iii*) If information is available concerning κ, one then uses the left-hand ordinate of Fig. 3 to obtain $1/\lambda$ which in turn is used to obtain T_{max}, from the right-hand ordinate of Fig. 3. Using the definition of T_{max} and the experimentally determined t_{max}, one can calculate aC, the double-layer capacity per unit volume of electrode. (*iv*) If no information is available concerning κ, one first calculates $i_{max}/i|_{t=0}$ and then obtains λ from the ordinate of Fig. 4. The value of aC can then be obtained as mentioned in (*iii*).

This value of aC is regarded to be a measure of the electrochemically accessible surface area of a macro-homogeneous porous electrode. A further division of the aC product requires either specific knowledge about the total interfacial surface area of the electrode or a measurement of C on a flat surface. An approximate value of a can be obtained from a BET surface area determination and then a value of C calculated. This type of calculation should only be considered qualitative due to the uncertainty of the type of microstructure existing at any given site in a porous electrode. Also the measured BET surface area does not distinguish between electrochemically active and inactive areas. One may also question whether alterations in the specific surface area might not occur during the preparation of the electrode for the BET measurement.

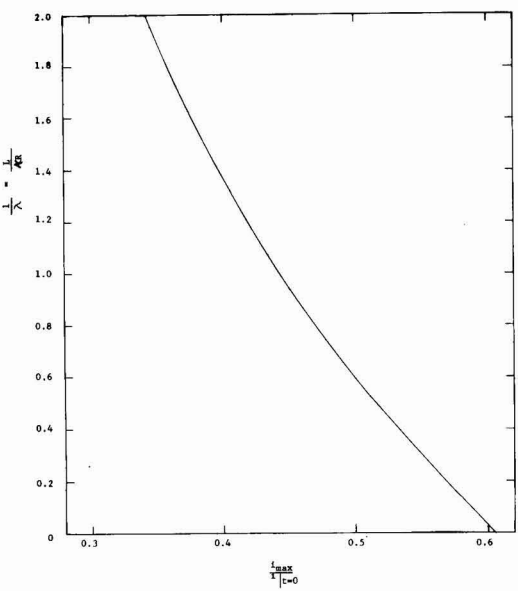

Fig. 4. Determination of the resistance-thickness parameter λ for a given set of i_{max} and $i|_{t=0}$.

Errors in Double-Layer Measurements

Geometric surface area.—A real porous electrode (*e.g.*, a Pb or PbO_2 plate in the lead-acid battery) usually includes a grid support structure which, for practical purposes, does not contribute to the electrochemical capacity of the electrode but may occupy a significant portion of the electrode volume and geometric surface area. For many porous electrodes the active material is held in the grid support in the form of rectangular pellets, and it is the geometric area of these pellets which should be used in calculating the current density to be used in the treatment of the double-layer data. As grid support structures become more complicated, the specific area correction becomes more difficult leading to errors in the interpretation of the double-layer charging curves.

Electrode response time.—Most potentiostats have characteristic rise times of 1-10 μsec; however, it is the electrical analog of the electrochemical system in question which usually is the limiting factor in determining the rise time for the system as a whole. Real porous electrodes contain specific surface areas of the order of 10^4 cm^2/cm^3 and thus unavoidably present a large RC time constant. When the rise time of the potentiostat becomes significant compared to 0.1 t_{max}, one can expect errors to occur in the evaluation of the charging curves and the subsequent determination of aC. (We have examined the effect of the nonzero rise time of the potentiostat-electrode system by inverting the governing Laplace transform for an applied potential with an exponential approach to a constant value. While this is awkward for routine analysis of charging curves, it does provide an inexpensive alternative to the development of sophisticated electronics.)

Changes in electrode porosity.—For porous electrodes which undergo significant gassing, the effective conductivity of the solution within the electrode, κ, may change as a function of time (8). Also, the effective porosity of the electrode matrix may be altered by extended cycling. Therefore, it may be necessary to determine κ prior to performing a double-layer measurement.

Symmetry of the electrode.—Due to the manner in which real porous electrodes are fabricated (*e.g.*, the Pb and PbO_2 electrodes), there may exist a lack of symmetry about the center line of the electrode. Therefore, one should measure the double-layer capacity with the reference electrode at several locations and on both sides of the porous electrode in question to determine what uncertainty is associated with the measurement.

Faradaic reactions.—The electrode has been assumed to be ideally polarizable. Small departures from this requirement will result in a charging current which does not decay to zero. In a plot of $i\sqrt{t}$ *vs.* $\sqrt{t}$ the departure from a theoretical curve increases with time because the charging current is decreasing while the faradaic current is increasing. If the displacement is minor at large times, the effect on the coordinates of the maximum can safely be ignored. For battery electrodes which are selected to be highly reversible, one should minimize faradaic reactions by polarizing a fully charged electrode in the direction of further charge. (Actually, fully charged Pb and PbO_2 plates

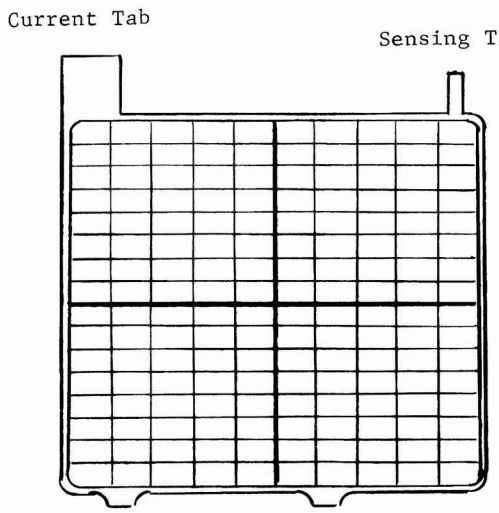

Fig. 5. Porous electrode with a lead grid.

can be polarized in the discharge direction because of the slow nucleation of $PbSO_4$.)

Experimental

The electrodes investigated in this study were positive and negative plates manufactured for use in automobile batteries. These electrodes contained grids of a lead alloy (6% antimony) as current collectors (Fig. 5). Sensing leads were attached to the top of the grid opposite the electrode tab. The solution employed was 4.5M sulfuric acid. The physical parameters for each type of electrode are given in Table I. The total current, I, is divided by the geometric electrode area to obtain the current density, i. L is half of the electrode thickness given in Table I.

The cell (a polypropylene case, filled with 4.5M H_2SO_4) used for these measurements contained the electrode in question located symmetrically between two counterelectrodes. A $Hg/HgSO_4$ reference electrode was used for both the Pb and PbO_2 electrodes. A small capillary from the reference electrode compartment was positioned adjacent to each electrode.

Controlled potential measurements were made with a Wenking Model 6BTS1 potentiostat which was programmed with a Hewlett-Packard 3300A Function Generator. An input voltage divider was required for reproducible 1-4 mV square wave signals. The current response was recorded with a Tektronix 564 storage oscilloscope and/or a recorder fitted with a function converter which would automatically plot $i\sqrt{t}$ *vs.* $\sqrt{t}$.

The PbO_2 and Pb electrodes were held at 1.17 and -0.972V *vs.* a $Hg/HgSO_4$ reference electrode, respectively, for 12 hr after they had been electrochemically cycled. This time was provided to accommodate surface modifications which have been reported to occur within the first few hours after cycling (9-12). All double-layer measurements were performed at the above-mentioned potentials.

Table I. Physical parameters of the PbO_2 and Pb electrodes

Electrode	BET surface area[1] (10^4 cm²/cm³)	Porosity[1]	Electrode thickness (cm)	Geometric electrode area[2] (cm²)
PbO_2	20.5	0.56	0.2	241
Pb	2.5	0.63	0.15	241

[1] Determinations made at Globe-Union, Incorporated.
[2] Total geometric electrode area (both sides) minus grid area.

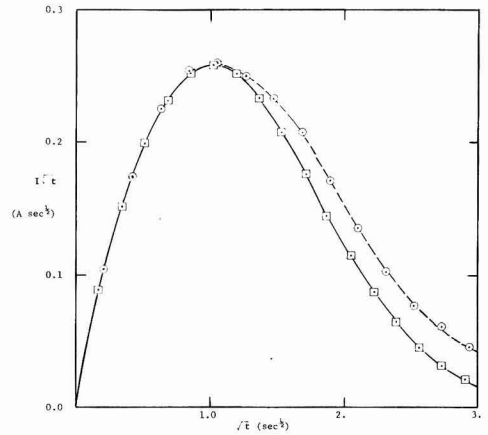

Fig. 6. Comparison of experimental and theoretical results for potentiostatic double-layer charging of a porous PbO_2 electrode. ⊙, Experimental; ⊡, theoretical, Eq. [3]. L = 0.095 cm, ΔV = 1.52 mV, area = 241 cm², λ = 0.768, aC = 26 farads/cm³, temperature = 28°C.

Results and Discussion

Figure 6 shows a typical current response of a PbO_2 electrode to a voltage step and a subsequent display of $i\sqrt{t}$ *vs.* $\sqrt{t}$. Similar curves are obtained for the Pb electrode, only the time scale is two orders of magnitude smaller. The accuracy associated with the determination of aC for a given electrode is strongly dependent on the shape of the maximum in the $i\sqrt{t}$ *vs.* $\sqrt{t}$ curve, a broad maximum implying a larger error. We therefore sought to make λ as small as possible by minimizing the effective resistance in the system (*i.e.*, reference electrode placed as close to the working electrode as possible, separate sensing leads). The magnitude of ΔV was selected more for its convenience (as long as faradaic currents and the potential dependence of the double-layer capacity were small) since the value of T_{max} is independent of the value of ΔV. The effective conductivity of the solution inside the porous electrode was determined using Fig. 4.

Entrapped gases were observed to increase the effective resistance of the electrode which prolonged the charging period. As a consequence, both electrodes were placed in a vacuum chamber and degassed before the measurements were performed. Since the PbO_2 electrode is continually gassing, there will always be some entrapped gases which are unavoidably included in the measurement. One might then consider the real value of aC to be higher than that found experimentally.

Since the electrodes being examined are commercial plates, there exists a certain degree of nonuniformity over the electrodes. The extent to which the position of the reference electrode reflects these nonuniformities was observed by determining aC at three locations on each electrode. As shown in Table II, the position of the reference electrode does reflect somewhat the nonuniformities of the electrodes; also, within the potential difference applied to each electrode, the double-layer capacity appears to be a constant. However, the difference between these values is of the same order of magnitude as the error associated with the double-layer measurement (~5%). One may conclude that the assumption of a macrohomogeneous electrode is valid within experimental error.

Using the information contained in Tables I and II, the double-layer capacity per unit area for the PbO_2 and Pb electrodes is 143 and 10 μfarads/cm², respec-

Table II. Double-layer capacity as a function of reference electrode position and applied potential

	Reference electrode position			Applied potential, mV		
	1	2	3	2	3	4
Electrode	aC (farads/cm³)	aC (farads/cm³)	aC (farads/cm³)	aC (farads/cm³)	aC (farads/cm³)	aC (farads/cm³)
PbO_2	30.2	28.4	29.2	30.2	30.4	30.7
Pb	0.254	0.238	0.248	0.252	0.246	0.250

Position 1, First quadrant, right side of electrode.
Position 2, First quadrant, left side of electrode.
Position 3, Second quadrant, right side of electrode.

tively. These values are in agreement with those reported in the literature (9-14) for electrochemically deposited PbO_2 and Pb on flat surfaces. However, it is realized that BET areas are a measure of the entire area available for gas adsorption and not the electrochemically active area. Therefore, the true double-layer capacity per unit area is higher than that calculated using areas determined by gas adsorption. The high observed value for PbO_2 may be due, in part, to a pseudocapacity. The term double-layer capacity has been used to mean interfacial capacity in a macroscopic sense and would include any capacity associated with the adsorption of charged species at the solution-matrix interface. It would exclude faradaic reactions which can be carried out in a steady state.

Conclusions

An interpretation of potentiostatic double-layer charging of porous electrodes has been presented. The emphasis on the maximum in the $i\sqrt{t}$ *vs.* $\sqrt{t}$ curve results in experimental curves which lend themselves readily to the evaluation of the double-layer capacitance, and it is this quantity which directly reflects the active electrochemical connected area. It has been demonstrated that the values for the double-layer capacity determined on commercial-size battery electrodes are in agreement with that determined on small, flat experimental electrodes. This result is encouraging since one wishes to apply fundamental techniques in the study of large electrodes. We may also note that this procedure was used on two electrodes whose aC values differed by two orders of magnitude.

One application of this type of measurement will be in the determination of changes occurring in the active electrochemical surface area with cycling. Also, the effects of additives which alter surface morphology may be detected by their effect on the double-layer capacity.

The possibility of determining the effective conductivity of the solution inside the porous electrode, and thereby inferring something about the electrode porosity, may require carefully designed experiments.

Manuscript submitted April 25, 1974; revised manuscript received July 29, 1947.

Any discussion of this paper will appear in a Discussion Section to be published in the December 1975 JOURNAL. All discussions for the December 1975 Discussion Section should be submitted by Aug. 1, 1975.

Publication costs of this article were partially assisted by Globe-Union, Incorporated.

LIST OF SYMBOLS

- a specific interfacial area, cm²/cm³
- C double-layer capacity, farads/cm²
- i current density, A/cm²
- $i|_{t=0}$ peak current density at time zero given by Eq. [2], A/cm²
- i_{max} current density at the maximum of $i\sqrt{t}$ *vs.* $\sqrt{t}$ given in Fig. 2, A/cm²
- L half-thickness of electrode, cm
- L_s separation distance between reference and working electrodes, cm
- p porosity
- R effective resistance given by Eq. [1], ohm-cm²
- R_L resistance of leads and current collector, ohm-cm²
- t time, sec
- t_{max} time of the maximum in the curve shown in Fig. 2b, sec
- T dimensionless time given by Eq. [4]
- T_{max} dimensionless time at the maximum shown in Fig. 2
- ΔV applied potential step, V
- κ conductivity of solution in porous matrix, mho/cm
- κ_0 conductivity of bulk solution, mho/cm
- λ effective resistance-thickness parameter given by Eq. [4]
- σ conductivity of the porous electrode matrix, mho/cm
- π 3.14159

REFERENCES

1. F. A. Posey and T. Morozumi, *This Journal*, **113**, 176 (1966).
2. R. de Levie, *Electrochim. Acta*, **8**, 751 (1963).
3. Robert de Levie, in "Advances in Electrochemistry and Electrochemical Engineering," Vol. 6, P. Delahay and C. W. Tobias, Editors, pp. 329-397, Interscience Publishers, Inc., New York (1967).
4. A. M. Johnson and John Newman, *This Journal*, **118**, 510 (1971).
5. L. G. Austin and E. G. Gagnon, *ibid.*, **120**, 251 (1973).
6. Milton Abramowitz and Irene A. Stegun, "Handbook of Mathematical Functions," NBS, p. 225, Dept. of Commerce, Washington, D.C. p. 225, (1964).
7. R. E. De La Rue and C. W. Tobias, *This Journal*, **106**, 827 (1959).
8. I. L. Romanova and I. A. Selitskii, *Elektrokhimiya*, **6**, 1776 (1970).
9. J. Burbank, A. C. Simon, and E. Willihnganz, in "Advances in Electrochemistry and Electrochemical Engineering, Vol. 8, P. Delahay and C. W. Tobias, Editors, pp. 157-252, Interscience Publishers, Inc., New York (1971).
10. J. P. Carr and N. A. Hampson, *Chem. Rev.*, **72**, 679 (1972).
11. J. P. Carr, N. A. Hampson, and R. Taylor, *J. Electroanal. Chem.*, **27**, 466 (1970).
12. J. P. Carr, N. A. Hampson, and R. Taylor, *ibid.*, **27**, 201 (1970).
13. P. Rüetschi, J. B. Ockerman, and R. Amlie, *This Journal*, **107**, 325 (1960).
14. E. Willihnganz, *ibid.*, **102**, 99 (1955).

Unified Approach to Cell EMF Calculations

David Gray*

Math/Science Division, Golden West College, Huntington Beach, California 92647

General Discussion

In calculating the emf of an electrochemical cell composed of two half-cell reactions, the usual procedure is to take the algebraic sum or difference (depending on convention) of the electrode potentials of the half-cells. In mathematical terms, this is expressed as

$$E_{cell} = E_{ox} \pm E_r \qquad [1]$$

where E is the reversible or Nernst potential and the subscripts ox and r stand for oxidation and reduction half-cell, respectively. It will be shown in this paper that, while Eq. [1] is correct for most cases, it is not the general equation for cell emf calculations.

The only thermodynamic formula that will be necessary for this discussion is the well-known equation at constant temperature and pressure

$$\Delta G = -n\mathbf{F}E \qquad [2]$$

where ΔG is the change in the Gibbs free energy, n is the change in the number of electrons, and $\mathbf{F}$ is the Faraday.

In general, if we consider two half-cell reactions, such as

$$A^{n_1} = n_{ox}e + A^{n_1+n_{ox}} \qquad [3]$$

$$B^{n_2+n_r} + n_r e = B^{n_2} \qquad [4]$$

they may be combined to form a cell by the following procedure

$$n_r(A^{n_1} = n_{ox}e + A^{n_1+n_{ox}}) \qquad \Delta G_{ox} = -n_{ox}\mathbf{F}E_{ox} \qquad [5]$$

$$n_{ox}(B^{n_2+n_r} + n_r e = B^{n_2}) \qquad \Delta G_r = -n_r\mathbf{F}E_r \qquad [6]$$

$$n_r A^{n_1} + n_{ox}B^{n_2+n_r} = n_r A^{n_1+n_{ox}} + n_{ox}B^{n_2} \qquad \Delta G_{cell} = -n_{cell}\mathbf{F}E_{cell} \qquad [7]$$

From thermodynamics, we can write that

$$\Delta G_{cell} = n_r\Delta G_{ox} + n_{ox}\Delta G_r \qquad [8]$$

so that, from Eq. [2]

$$E_{cell} = \frac{n_r n_{ox}E_{ox} + n_{ox}n_r E_r}{n_{cell}} \qquad [9]$$

Note that n_{cell} is the net cell electron change. It is obvious that

$$n_r n_{ox} = n_{ox}n_r \qquad [10]$$

is true for all cases of cell formation. Thus, Eq. [9] may be written as

$$E_{cell} = \frac{n_r n_{ox}}{n_{cell}}(E_{ox} + E_r) \qquad [11]$$

For cell calculations (case I, $A \neq B$) other than disproportionation reactions

$$n_{cell} = n_r n_{ox} \qquad [12]$$

will be true, and Eq. [11] will reduce to Eq. [1].

Now, in disproportionation systems ($A = B$) there are two cases which will result in Eq. [12] and, therefore, Eq. [1] not being valid. If we set (case II)

$$n_1 = n_2 \qquad [13]$$

$$n_r \neq n_{ox} \qquad [14]$$

then we can rewrite Eq. [5], [6], and [7] as

$$n_r A^{n_1} = n_{ox}e + A^{n_1+n_{ox}} \qquad n_r\Delta G_{ox} = -n_r n_{ox}\mathbf{F}E_{ox} \qquad [15]$$

$$n_{ox}(A^{n_1+n_r} + n_r e = A^{n_1}) \qquad n_{ox}\Delta G_r = -n_{ox}n_r\mathbf{F}E_r \qquad [16]$$

$$n_{ox}A^{n_1+n_r} = n_r A^{n_1+n_{ox}} + (n_{ox} - n_r)A^{n_1} \qquad (n_{ox} > n_r) \qquad [17a]$$

or

$$\Delta G_{cell} = -n_{cell}\mathbf{F}E_{cell}$$

$$(n_r - n_{ox})A^{n_1} + n_{ox}A^{n_1+n_r} = n_r A^{n_1+n_{ox}} \qquad (n_r > n_{ox}) \qquad [17b]$$

It is obvious that for this particular case there exists no general relationship between n_{cell} and $n_r n_{ox}$.

Or if we set (case III)

$$n_1 + n_{ox} = n_2 + n_r \qquad [18]$$

$$n_r \neq n_{ox} \qquad [14]$$

then we can rewrite Eq. [5], [6], and [7] as

$$n_r A^{n_1} = n_{ox}e + A^{n_1+n_{ox}} \qquad n_r\Delta G_{ox} = -n_r n_{ox}\mathbf{F}E_{ox} \qquad [19]$$

$$n_{ox}(A^{n_1+n_{ox}} + n_r e = A^{n_2}) \qquad n_{ox}\Delta G_r = -n_{ox}n_r\mathbf{F}E_r \qquad [20]$$

$$n_r A^{n_1} + (n_{ox} - n_r)A^{n_1+n_{ox}} = n_{ox}A^{n_2} \qquad (n_{ox} > n_r) \qquad [21a]$$

or

$$\Delta G_{cell} = -n_{cell}\mathbf{F}E_{cell}$$

$$n_r A^{n_1} = (n_r - n_{ox})A^{n_1+n_{ox}} + n_{ox}A^{n_2} \qquad (n_r > n_{ox}) \qquad [21b]$$

Once again, it is obvious that for this case there exists no general relationship between n_{cell} and $n_r n_{ox}$.

* Electrochemical Society Active Member.

Key words: cells, emf, potential.

Further, it should be noted that in cases II and III Eq. [1] will result in erroneous cell potentials (see examples). Thus, these generalized examples demonstrate that Eq. [11] and not [1] is the general equation for cell emf calculations. It is essential to remember

path 1
$$2(Cu^+ = e + Cu^{++})$$
$$Cu^{++} + 2e = Cu$$
$$\overline{2Cu^+ = Cu + Cu^{++}}$$

path 2
$$Cu^+ = e + Cu^{++}$$
$$Cu^+ + e = Cu$$
$$\overline{2Cu^+ = Cu + Cu^{++}}$$

path 3
$$Cu = 2e + Cu^{++}$$
$$2(Cu^+ + e = Cu)$$
$$\overline{2Cu^+ = Cu + Cu^{++}}$$

that addition of half-cell reactions, even to obtain a complete cell, means addition of ΔG or nE, but not of E alone (1). But as case I illustrates, most cell combinations are such that Eq. [12] can be used. For other disproportionation systems (*i.e.*, $n_r = n_{ox}$), Eq. [12] and Eq. [1] will be valid.

For completeness, the method of combining half-cell reactions to form a new half-cell reaction will be included in this discussion. If we consider the following half-cell reactions

$$A^n = A^{n+n_1} + n_1e \qquad \Delta G_1 = -n_1\mathbf{F}E_1 \qquad [22]$$

$$A^{n+n_1} = A^{n+n_1+n_2} + n_2e \qquad \Delta G_2 = -n_2\mathbf{F}E_2 \qquad [23]$$

$$A^n = A^{n+n_1+n_2} + (n_1 + n_2)e \qquad \Delta G_{12} = -(n_1 + n_2)\mathbf{F}E_{12} \qquad [24]$$

and since

$$\Delta G_{12} = \Delta G_1 + \Delta G_2 \qquad [25]$$

we can write

$$E_{12} = \frac{n_1E_1 + n_2E_2}{n_1 + n_2} \qquad [26]$$

Specific Example

There are numerous examples which can be given to show that Eq. [1] is not always valid. Here one example will be assumed to be sufficient to show the general validity of Eq. [11].

If we take the following three half-cells (example 1) and their respective half-cell standard potentials (2)

$$Cu^{++} + 2e = Cu \qquad E^\circ_r = 0.337V \qquad [27]$$

$$Cu^+ + e = Cu \qquad E^\circ_r = 0.521V \qquad [28]$$

$$Cu^{++} + e = Cu^+ \qquad E^\circ_r = 0.153V \qquad [29]$$

we can form the cell

$$2Cu^+ = Cu + Cu^{++} \qquad E^\circ_{cell} = -\frac{\Delta G}{n\mathbf{F}} = 0.368 \qquad [30]$$

by three different paths:

$$E^\circ_{path\ 1} = \frac{2(-0.153) + 2(0.337)}{1} = 0.368V$$

(case III)

$$E^\circ_{path\ 2} = \frac{(-0.153) + 0.521}{1} = 0.368V$$

$$E^\circ_{path\ 3} = \frac{2(-0.337) + 2(0.521)}{1} = 0.368V$$

(case II)

If we had calculated these values by Eq. [1], E°_{cell} would have been 0.184V for paths 1 and 3, and 0.368V for path 2. This, in effect, would make E°_{cell} dependent on path, which it obviously is not. The important thing to note in this example is that n_{cell} has a definite and specific value which is determined by the over-all cell reaction and not by the half-cell reactions which make up the cell. In this example $n_{cell} = 1$ for all three paths

This example has been considered by Laitinen (3). However, he maintains the general validity of Eq. [1], which has been disproved in this discussion. Laitinen's book has been cited here because it is the only major textbook which discusses this problem at length.

One can now see that general use of Eq. [1] can make certain disproportionation systems path dependent, while Eq. [11] preserves the path independence of all cell emf calculations.

Manuscript submitted March 11, 1974; revised manuscript received *ca.* May 10, 1974.

Any discussion of this paper will appear in a Discussion Section to be published in the December 1975 JOURNAL. All discussions for the December 1975 Discussion Section should be submitted by Aug. 1, 1975.

REFERENCES

1. R. G. Bates, in "Treatise on Analytical Chemistry," Part 1, Vol. 1, I. M. Kolthoff and P. J. Elving, Editors, Chap. 9, Interscience Publishers, New York (1959).
2. W. M. Latimer, "Oxidation Potentials," 2nd ed., Prentice-Hall, Inc., Englewood Cliffs, N.J. (1952).
3. H. A. Laitinen, "Chemical Analysis," pp. 283-286, McGraw-Hill Book Company, New York (1960). See also W. H. Eberhardt, *J. Chem. Educ.*, **48,** 829 (1971); and D. A. Jenkins and D. J. Marks, *Educ. Chem.*, **2,** 213 (1965).

Relating Structural Variables of Porous Electrodes

T. Katan* and H. F. Bauman*

Materials and Structures, Lockheed Palo Alto Research Laboratory, Palo Alto, California 94304

The continued development of principles for electrode design [*e.g.*, Ref. (1-3)] and the improvement of fabrication methods [*e.g.*, Ref. (4-6)] must ultimately involve some specification of porous electrode structure. Yet, porous structures tend to elude physical description and relation of their electrochemically important (1-3) and geometrically derived variables such as specific surface area and porosity (7). Frequently, these variables are suspected to have mutual dependence, but it is not clear how a change in one variable will affect another.

It is our purpose here to show how the structural variables of battery and fuel cell electrodes can be specified and related by adapting a filamentary analog for porous structures. We also present practical values of these structural variables for typical electrodes.

The filamentary analog has been previously used by Everett and others in the study of adsorption processes (8). More complex models have been developed in other technical fields (9-13), but none of these appear to yield practical information of geometrical value so directly from a set of elementary equations.

Theoretical

In this approach a porous electrode is represented by a series of filaments, extending from one face of the mass to the other, which are assigned shapes and positions closely resembling the solid portions of an actual electrode. The filaments are assumed to have their ends situated at the centers of oppositely aligned unit squares in the electrode's facial planes and to individually occupy only the volumes contained between the squares. The unit squares have a side dimension x and comprise the grids of two matching Cartesian coordinate systems. As shown in Fig. 1, the pore parameter,[1] r, is defined as the radius of an imaginary pore with a circular cross-sectional fitting between, and touching only at the ends of, any four adjacent, parallel filaments, each with an over-all solid radius, R, and tortuosity factor, τ. For shapes consisting of regular particles, each particle is assigned a volume, v, area, a, and length, L, along the filament through the electrode of thickness t and fractional void volume θ.

From the Pythagorean theorem, R and r are related with the side of the unit square, and, considering a single filament, an expression is written for the solid volume fraction $(1 - \theta)$. These two equations are then used together with the definition of specific surface area, A, *i.e.*, the area of the particles per unit volume of electrode, to obtain a set of two equations relating r, R, τ, θ, A, a, v, and L

$$\frac{\tau}{(1-\theta)} = \frac{(R+r)^2}{v/2L} \qquad [1]$$

$$A = \frac{a(1-\theta)}{v} \qquad [2]$$

A third equation resulting from Eq. [1] and [2] also is useful

$$A = \frac{a\tau}{2(R+r)^2 L} \qquad [3]$$

For some structures, it is more accurate to treat the filaments as pores; the forms of the equations are then unchanged but the meanings of the symbols become reversed. For such filamentary pores the dimensionless group $\tau/(1 - \theta)$ of Eq. [1] is directly related to the so-called effective diffusion coefficient (14). Unless otherwise noted, filaments will be considered in analyses as the solid portion of the structure.

The equations can be generalized if it is understood that $v = k_1 R^2 L$ and $a = k_2 RL$ for a given particle shape, where k_1 and k_2 are the applicable constants. Substitution into Eq. [1]-[3] yields, respectively, three corresponding equations relating the variables r, R, τ, θ, and A

$$\frac{\tau}{(1-\theta)} = \frac{2}{k_1}\left(\frac{r}{R}+1\right)^2 \qquad [4]$$

$$A = \frac{k_2}{k_1}\frac{(1-\theta)}{R} \qquad [5]$$

$$A = \frac{k_2}{2}\frac{R\tau}{(R+r)^2} \qquad [6]$$

The constants k_1 and k_2 are altered only by a constant factor when particle shape is changed but are unchanged for all sizes of a given particle shape.

Results and Discussion

The set of three general equations suggests a natural division of structural variables into those which may be classified as either general, r, R, θ, τ, and A, or particulate, v, a, and L, and also suggests the use of certain groups of general variables, namely, $(R + r)$, r/R, $R/(R + r)^2$, and $(1 - \theta)$ which have practical significance. The variables $(R + r)$ and r/R are monotonically dependent on the defined pore parameter and hence, for typical τ and $(1 - \theta)$, on the effective pore radius for constant R; $(R + r)$ and R/r are similarly dependent on filament (solid) size for constant r; and $(1 - \theta)$ is the fractional solid volume. With the use of the general variables, the over-all effect on structure of suggested changes in design or fabrication becomes evident by considering, first, the relation of the general variables, and, second, the influence of particulate variables on the relation of the general variables.

General structural variables.—It is advantageous to examine plots of the general variables in some detail because the same dependences are found for all structures which can be represented by the filamentary analog. We may plot either R/r or $(r + R)$ *vs.* $(1 - \theta)$ for various τ from Eq. [1] or [4], A *vs.* R for various θ from Eq. [5], and A *vs.* τ for various $R/(R + r)^2$

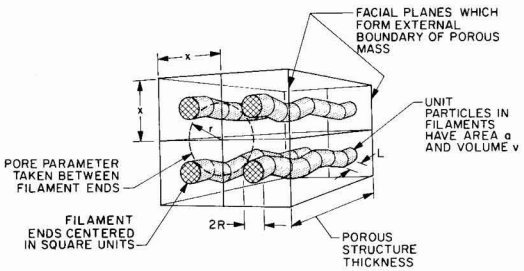

Fig. 1. Four volumetric units of electrode matrix with filaments showing effective dimensions.

* Electrochemical Society Active Member.

Key words: porous electrodes, porous structures, electrode design, batteries.

[1] The pore parameter, r, is also useful because it is essentially equivalent to an "effective" pore radius excepting when τ and $1 - \theta$ become large i.e., when the average filament spacing at the interior differs appreciably from the assigned spacing of the ends.

from Eq. [6]. As a guide, we select Fig. 2 through 4 for electrodes constructed of uniform spheres, bonded together, where the filamentary analog is taken to consist of rows of touching spheres. Here, $v = 4/3\pi R^3 = k_1R^2L$, $a = 4\pi R^2 = k_2RL$, and $L = 2R$, hence $k_1 = 2/3\pi$ and $k_2 = 2\pi$ in Eq. [4]-[6].

Particulate structural variables.—From Eq. [2] and [3], it can be seen that for a given set of general variables, A is increased linearly with increases in a/v or a/L. In fabrication this increase is usually accomplished by increasing surface roughness or by using filamentary particles having micropores. Ultimately, such increases in particle area become of limited practical use because of the onset of transport process limitations within the micropores (15). From Eq. [1] we see that the ratio v/L has the same influence as τ in shifting the curves of Fig. 2. The relation of particulate to general variables of porous structures is thus evident by Eq. [1]-[3]; the form of the relations of general variables always holds while these relations are changed by a proportionality constant with changes in the particulate variables as indicated above.

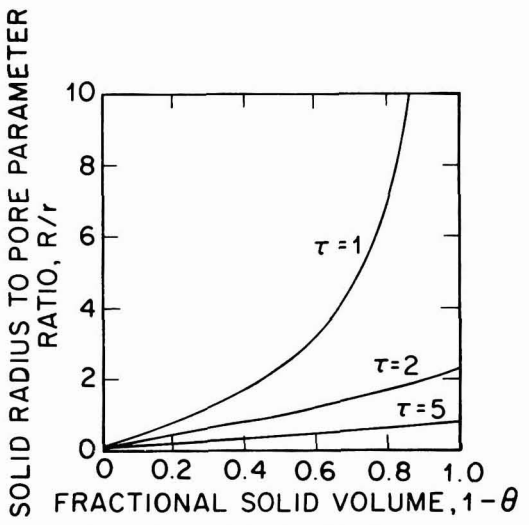

Fig. 2. Variation in ratio of effective solid radius to pore parameter for changes in fractional solid volume.

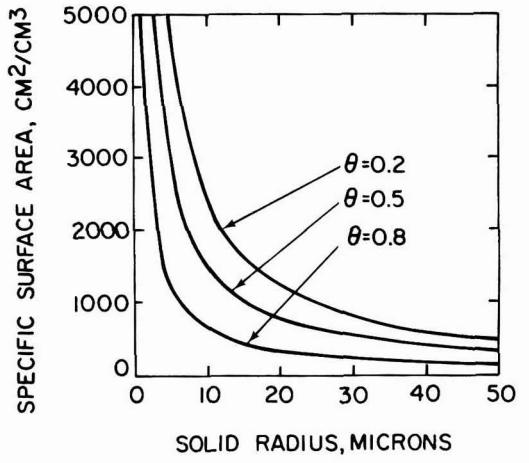

Fig. 3. Variation in specific surface area for changes in filament radius.

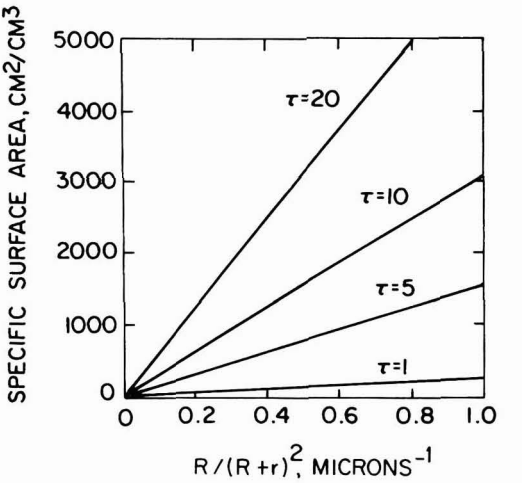

Fig. 4. Variation in specific surface area for changes in $R/(R + r)^2$.

Some applications.—Accuracy of the given equations is best for those structures whose void or solid portions are simply shaped or for those which closely resemble a filamentary network. For example, accurate relations should be obtained with many known practical structures which are structurally ordered, such as stacks of woven wire meshes or screens, bundles of parallel, uniform metal fibers (16), compacted short lengths of uniform metal fibers,[2] structures of sieved, bonded particles (5), metallized paper fiber structures (17), or uniform sphere beds (18). The latter three structures have been reported as experimental fuel cell and battery electrodes.

The filamentary analog for electrode structures should be selected so that the best correspondence in the representation is made, *i.e.*, so that variables can be easily assigned. For example, with stacks of plain square weave screens, the wires in one direction could be taken as the principal filaments while wires perpendicular to these filaments should be considered as segments with specified area, divided and attached to the principal filaments at regular intervals. With more complex structures, it is useful to consider the porous mass to be divided into smaller, identical volume elements, equivalent to x^2t volumes, taken so that each volume element contains essentially the same geometrical configuration of filaments throughout the mass. In practice, we have found that some accuracy is retained with this method even with typical electrodes.

We have summarized in Table I the structural variables of four typical, more complex, electrode structures, giving the representations selected for the filamentary analog. For the given structures, r and R were determined by averaging several values measured from photomicrographs of polished metallographic cross sections taken with an optical microscope of the porous masses after impregnation with epoxy under vacuum, *e.g.*, see Fig. 5a. Circles were fitted between the assumed filaments at a large number of randomly selected locations to obtain the average radius, r. Thickness of the assumed filaments, $2R$, was measured perpendicular to the filament direction, also at several randomly selected locations, as indicated in Fig. 5a. Photographs of a calibrated scale at the same magnification were used to ascertain distance.

Scanning electron microscopy, as shown in Fig. 5b, helped in selection of assumed filament shapes and direction. In Fig. 5b, the solid portions are visualized as approaching an ordered shape of interconnected

[2] "Feltmetal," prepared by Armour Research Foundation, Chicago, Illinois.

Table I. Structural variables of some porous electrodes

Material	Assumed structure of filament	Measured θ	Measured R (μm)	Measured r (μm)	Calc. A (cm^2/cm^3)	Calc. τ
Silver spheres[a]	Rows of spheres	0.373	18.6	6.30	1,010	1.1
Silver membrane[b]	Cylindrical	0.571	1.82	1.21	4,720	2.4
Porous nickel[c]	Cylindrical	0.823	0.979	4.48	3,470	3.4
Silver oxide[d]	Square pores	0.420	0.922	1.81	35,600	14.1

[a] Silver spheres obtained in classified size from Metz Refining Company, Newark, New Jersey.
[b] 0.002 in. thick porous silver plaques, Cat. No. FM-13-5, Selas Flotronic 5, Spring House, Pennsylvania.
[c] Clevite nickel battery plaque, nickel screen not considered in 0.056 in. thick sheets, Clevite Corporation, Cleveland, Ohio.
[d] Silver oxide electrodes, silver screen not considered in 0.040 in. thick sheets, Order No. 16-24587, The Eagle-Picher Company, Cincinnati, Ohio.

Table II. Surface areas obtained by different methods

Material*	Specific surface area (cm^2/cm^3)		
	Calc. from filamentary analog	BET	Stereometric analysis
Silver spheres	1,010	(1,260)	(695)
Silver membrane	4,720	4,690	4,700
Porous nickel	3,470	3,460	3,270
Silver oxide	35,600	31,100	—

* See Table I for material descriptions.

cylindrical filaments. For all of the complex structures, enough order could be detected to allow application of the filamentary analog method. Porosities were calculated from the measure weights of predetermined volumes of the specimens free of any supporting screen material and from the known densities of the void-free substances.

After the selection of a filamentary analog shape, A is calculated by Eq. [2], using the measured θ and R, and τ is calculated from Eq. [1] using the measured θ, R, and r. The average deviation in determined R and r values was less than $\pm$ 6%.

In Table II values are given of specific surface areas for the electrode materials determined by the filamentary analog representation (Table I), by the BET method (19), and by a stereometric method (20). The area of the specimen of silver spheres was too low to yield accurate analysis by the BET method to better than $\pm$ 50%. The stereometric analysis with the spheres also failed to yield accurate analysis because of the inability of the used method of scanning to distinguish touching spheres from single spheres. On the other hand, for those cases where BET and stereometric methods are accurate, agreement with the filamentary analog values is to within $\pm$ 15%, which thus appears to be the limit of accuracy of the filament method for complex shapes. With simple shapes, accuracy is limited only by the accuracy in measurements of R and r as applied to Eq. [4]-[6].

Summary and Conclusions

A filamentary analog of a porous mass is mathematically developed to show how structural variables can be mutually related and act as a guide in evaluations of porous electrodes. Specific surface area, porosity, solid tortuosity, solid radius, and a pore parameter are related, and the influence of changes in solid filamentary particle volume, length, and area on these relations is shown. Accuracy of the filament method in estimating specific surface area was found to be within $\pm$ 15% for complex electrode structures.

Acknowledgments

This work was supported in part by the Office of Naval Research. The work is a continuation of an earlier effort under National Aeronautics and Space Administration Contract NAS 3-11833.

Manuscript submitted March 29, 1974; revised manuscript received Aug. 12, 1974. This was Paper 353 presented at the San Francisco, California, Meeting of the Society, May 12-17, 1974.

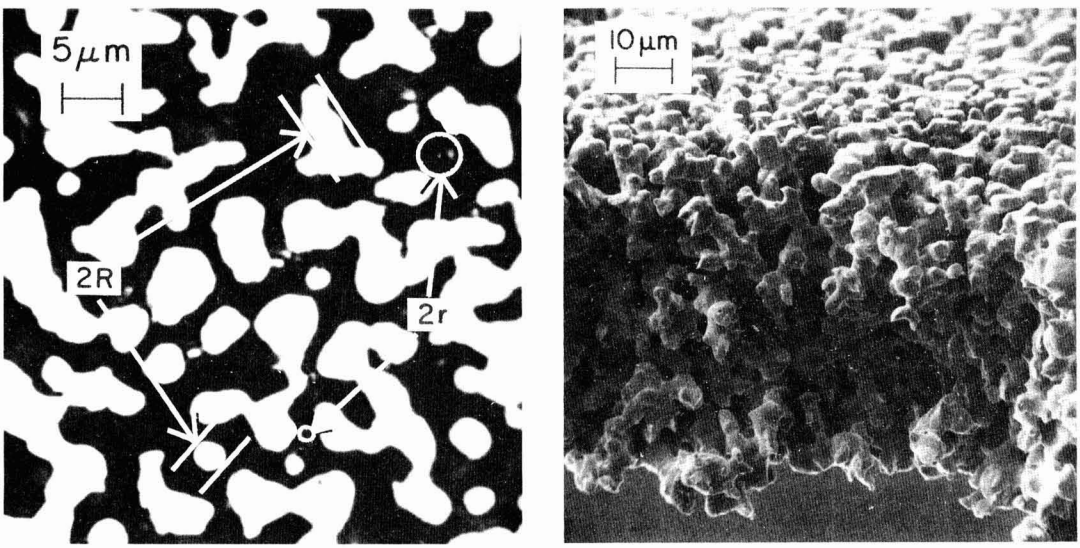

Fig. 5. Typical photomicrographs used for determining filament shape and size. a (left), Optical photomicrograph of polished, sectioned specimen of porous Flotronics silver membrane. Method of selecting r and R indicated. b (right), SEM photomicrograph of broken specimen of porous Flotronics silver membrane.

Any discussion of this paper will appear in a Discussion Section to be published in the December 1975 JOURNAL. All discussions for the December 1975 Discussion Section should be submitted by Aug. 1, 1975.

Publication costs of this article were partially assisted by Lockheed Palo Alto Research Laboratory.

LIST OF SYMBOLS

a	area of unit particle, cm^2
k_1, k_2	dimensionless constants depending only on particle shape
r	pore parameter, cm
t	electrode thickness, cm
v	unit particle volume, cm^3
x	side of square grid, cm
A	specific surface area, cm^2/cm^3
L	length of unit particle, cm
R	over-all radius of unit particle (filament), cm
τ	filament tortuosity or ratio of filament length to electrode thickness
θ	fractional void volume

REFERENCES

1. E. A. Grens *Ind. Eng. Chem., Fundamentals,* **5,** 542 (1966).
2. J. S. Dunning, D. N. Bennion, and J. Newman, *This Journal,* **118,** 1251 (1971).
3. D. Gidaspow and B. Baker, *ibid.,* **120,** 1005 (1973).
4. F. T. Bacon, *Electrochim. Acta,* **14,** 569 (1969).
5. E. Justi and A. Winsel, "Kalte Verbrennung," F. Steiner, Wiesbaden, Germany (1962).
6. D. J. Gordy, E. Luksha, and C. J. Menard, *This Journal,* **120,** 1447 (1973).
7. S. D. Holdsworth, *Chem. Process Eng.,* **44,** 184 (1963).
8. D. H. Everett, in "The Structure and Properties of Porous Materials," D. H. Everett and F. S. Stone, Editors, p. 95, Butterworth's Scientific Publications, London (1958).
9. A. J. De Bethune and R. L. Rowell, *J. Phys. Chem.,* **67,** 2065 (1963).
10. R. N. Foster and J. B. Butt, *A.I.Ch.E. J.* **12,** 180 (1966).
11. M. F. Johnson and W. E. Stewart, *J. Catalysis,* **4,** 248 (1965).
12. N. Wakao and J. M. Smith, *Chem. Eng. Sci.,* **17,** 825 (1962).
13. E. A. Mason, A. P. Malinauskas, and R. B. Evans III, *J. Chem. Phys.,* **46,** 3199 (1967).
14. C. N. Satterfield and T. K. Sherwood, "The Role of Diffusion in Catalysis," p. 15, Addison-Wesley Publishing Company, Inc., London (1963).
15. E. W. Thiele, *Ind. Eng. Chem.,* **31,** 916 (1939).
16. J. Sherfey, NASA TN D-6259, National Aeronautics and Space Administration, Washington, D.C., April 1971.
17. R. A. Botosan and T. Katan, *Electrochem. Technol.,* **5,** 315 (1967).
18. T. Katan, S. Szpak, D. N. Bennion, *This Journal,* **121,** 757 (1974).
19. S. Brunauer, P. H. Emmett, and E. Teller, *J. Am. Chem. Soc.,* **60,** 309 (1938).
20. E. E. Underwood, "Quantitative Stereology," p. 31, Addison-Wesley Publishing Company, Inc., London (1970).

Brief Communication

The Kinetics of Nickel Passivation

Adolf Pigeaud*

Department of Materials Science and Metallurgical Engineering, University of Cincinnati, Cincinnati, Ohio 45221

Passive surface conditions may be produced on metals and alloys by electrochemical polarization in the anodic region. The passive condition occurs as the result of a series of surface reactions which culminate in the deposition of a highly protective film. Such films usually consist of several very thin oxide phases parallel to, and in intimate contact with, the surface. Potentiostatic experiments are often performed to study the formation of these layers on sample metal electrodes in an electrochemical cell. Current is measured while potential is generally varied according to a controlled schedule of specified values. Unfortunately, this controlled variation in most potentiostatic experiments is selected without adequate regard for the reaction kinetics of the individual film formation processes. This is evident because the normal procedure usually is to vary the applied potential in stepwise fashion or to increase it monotonically during polarization even though individual reactions obviously still have not yet run their course.

In a recent study of pure Ni-polarization in 15*N* sulfuric acid, very fast and very slow current changes were investigated while potential across the total cell was maintained at a constant value throughout each experimental run. Oxide layers left on the surface from previous experiments were removed before each new run by a kind of electropolishing technique in which vigorous oxygen evolution is enforced for about ½ min. The sample is then allowed to come to its equilibrium rest potential in a fresh quantity of solution. A new run begins the moment a particular desired potential is applied across the total cell (*i.e.*, from counterelectrode to working electrode without reference to any solution potential). Current data were obtained by means of two types of recorders: a light-beam oscillograph for the very fast initial changes and an $X(\log t) = Y$ recorder for the medium and very slow, long term changes. The current variable also extended over a wide range of values from about 100 $\mu A/cm^2$ to over 1000 mA/cm^2. Hence "instantaneous" log converted values of current were the actually recorded variables for obtaining high frequency, wide band response. A large number of such isopotential experiments were run and in each case current behavior was followed for a considerable length of time, from 10 msec after startup to at least 17 min (1000 sec). Thus an enormous body of data was accumulated which proved too large and cumbersome to be handled by ordinary means of curve comparison. A powerful new method of analysis, using 3D-computer graphics, was then applied and a very revealing picture of the kinetics of nickel passivation resulted. Figure 1 illustrates this total kinetic

* Electrochemical Society Active Member.

Key words: polarization, kinetics, nickel, passivity.

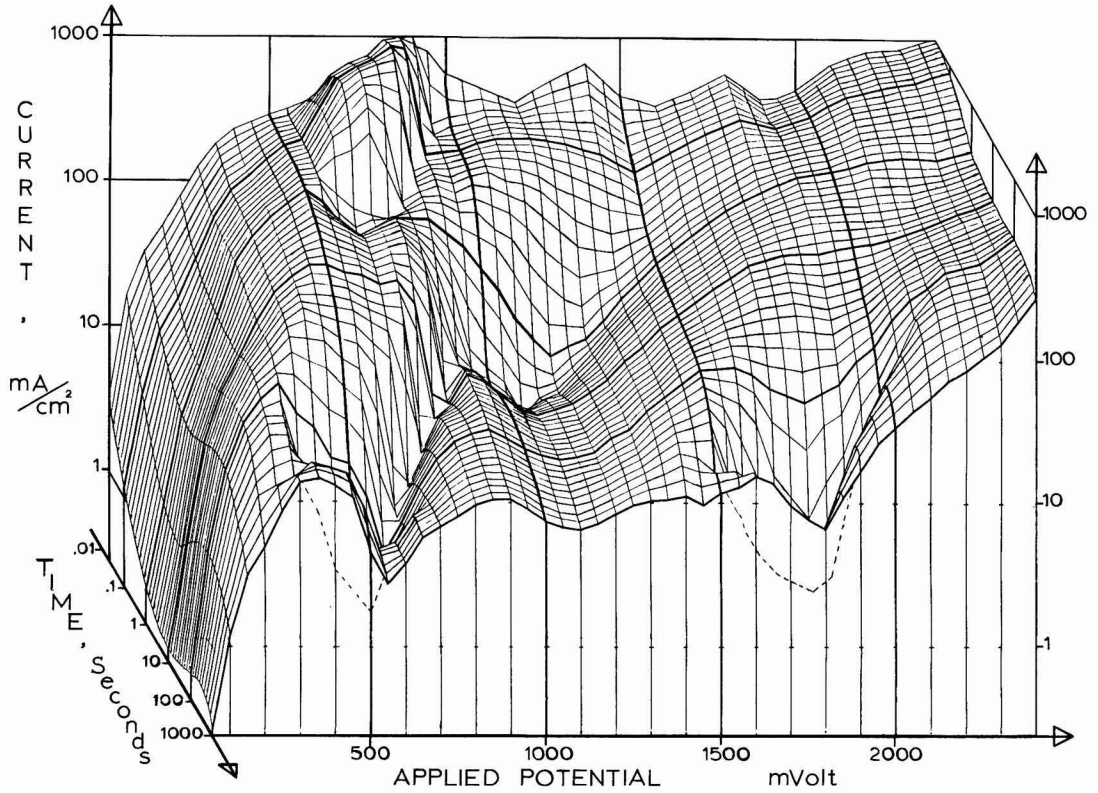

Fig. 1. Complete electrokinetic response in current-time-potential space of pure nickel polarized in 15*N* sulfuric acid

behavior as a complex surface in current-time-potential space. The surface was generated by manually converting the (*I-t*) analog data of each isopotential curve into digital form (*e.g.*, some 2304 points were read) and these were then plotted as a three-dimensional perspective view from the side of the orthogonal current-potential plane. One should note that the (*I-E*) curves so obtained can never be directly generated in a real experiment since potential, of course, cannot be increased from 0 to 2400 mV in zero time.

To our knowledge this method of obtaining the complete "electrokinetic" response of a system while it polarizes is unique. The data were obtained both by a greatly improved instrumental method and a somewhat different operating procedure. Analysis of these data, in the form of a complex current-time-potential surface, moreover has proven powerful indeed. Originally the minima and maxima in the isopotential curves seemed to bear little relationship to known equilibria or to familiar reaction processes. After plotting in three dimensions, however, the extremes and inflections in these curves can be recognized as part of a larger system of ridges, saddle points, and valleys which have real meaning in terms of the various reactions that are likely to occur on the surface. Thus it has been possible, with the help of other visual and analytical evidence obtained during the experimental part of this program, to identify most of these features as being due to the formation on the surface of a number of colloidal hydroxides (1) and multiphase oxide layers.

Additional support for these conclusions came when it was realized that these data, which are basically kinetic in nature, can also be used to supply evidence of the momentary existence of thermodynamic equilibria during polarization. Namely when the saddle points and valleys of the complex surface are projected onto the (*E-t*) base plane of Fig. 1 a kind of pseudo-Pourbaix diagram results which is illustrated in Fig. 2. This projection of the diffuse features of the complex surface in a different dimension suddenly allows one to fit rather precise straight-line boundaries to what were seemingly only vaguely defined regions of electrochemical stability. Single and dual phase layers which previously could only be inferred have also been added to this diagram which, it must be emphasized, shows stability with respect to a "time" frame of reference. When Fig. 2 is compared to a partial ver-

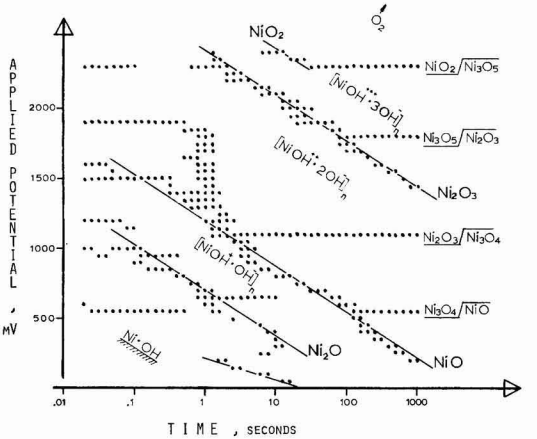

Fig. 2. Pseudo-Pourbaix diagram obtained directly from nickel polarization data.

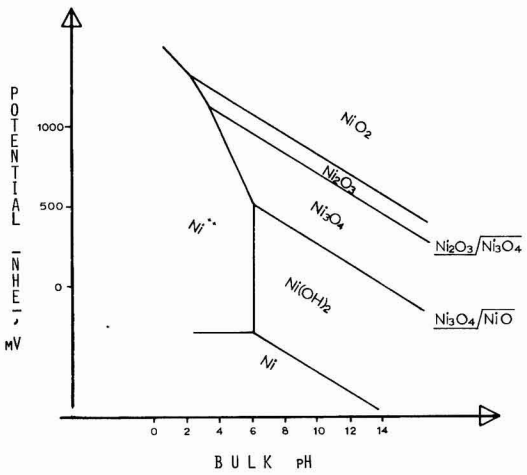

Fig. 3. Partial Pourbaix diagram of Ni-H_2O system

sion of the Pourbaix diagram for nickel, such as is shown in Fig. 3, the remarkable similarity between these two modes of expressing thermodynamic equilibria becomes apparent. In fact the almost 1:1 analogy between the phase boundaries in these two diagrams suggests that a simple inverse relationship must exist between polarization time and H^+-ion concentration in the immediate vicinity of the polarizing metal surface (*e.g.*, as compared to the bulk concentration). Such a relationship is not difficult to justify on theoretical grounds if one can assume a polarization model in which proton removal from the interface occurs at a constant electrophoretic rate of migration due to a constant electric field.

This means that a Pourbaix diagram, such as shown in Fig. 3 which is actually a composite of free energy data obtained from many different sources, can now be obtained all at once by means of a single experimental procedure and also with respect to a more realistic time frame of reference. Furthermore, when completely developed, this procedure holds the promise of being able to yield detailed information on the various spinellike phases and multilayer combinations which may occur in protective films (*e.g.*, on alloys) formed in real environments (*e.g.*, in aqueous or organic solutions containing other cationic and anionic species).

Conclusion

An improved polarization and data analysis technique applicable to most metal/electrolyte systems has been developed which shows considerable promise as a new tool for the direct, time-dependent characterization of anodically deposited films.

Acknowledgment

The author wishes to thank Professor Clair M. Hulley, the developer of the generalized computer program, and Mr. Bob Hsieh for their assistance in running his data program on the IBM-1130 computer slaved to the Calcomp-718 curve plotter of the Electrical Engineering Department at the University of Cincinnati. The present communication will be followed by a more detailed theoretical and experimental paper on a new theory of metal/electrolyte polarization after the author has submitted it to the faculty of his Department in partial fulfillment of the requirements for the Ph.D. degree (1974).

Manuscript submitted May 16, 1974; revised manuscript received July 22, 1974.

Any discussion of this paper will appear in a Discussion Section to be published in the December 1975 JOURNAL. All discussions for the December 1975 Discussion Section should be submitted by Aug. 1, 1975.

REFERENCE

1. A. Pigeaud and H. B. Kirkpatrick, *Corrosion*, **25**, 209 (1969).

Erratum

In the paper "Additive Ternary Molten Salt Systems—Calculation of Phase Diagrams from Thermodynamic Data of Lower Order Systems" by Marie-Louise Saboungi and Pierre Cerisier which appeared on pp. 1258-1263 in the October 1974 JOURNAL, Vol. 121, No. 10, Eq. [11] should read as follows

$$-\frac{A_m}{kT} = \ln Z_m = \ln Z_o + \sum_{i=1}^{3} (g_i - 1)\left(\frac{\partial \ln Z_m}{\partial g_i}\right)_{g=1} + \frac{1}{2}\sum_{i=1}^{3}\sum_{j=1}^{3}(g_i - 1)(g_j - 1)\left(\frac{\partial^2 \ln Z_m}{\partial g_i \partial g_j}\right)_{g=1} + \sum_{i=1}^{3} x_i \ln x_i + \dots$$

JOURNAL OF THE ELECTROCHEMICAL SOCIETY

SOLID-STATE SCIENCE AND TECHNOLOGY

JANUARY 1975

Solid-State Ionics: High-Conductivity Solid Copper Ion Conductors: N,N'-Dialkyl (or Dihydro)-Triethylenediamine Dihalide-Copper(I) Halide Double Salts

Takehiko Takahashi* and Osamu Yamamoto

Department of Applied Chemistry, Faculty of Engineering, Nagoya University, Nagoya, Japan

ABSTRACT

New solid electrolytes with high copper ion conductivity at ambient temperature have been found in the system N,N'-dialkyl (or dihydro)-triethylenediamine dihalide-copper(I) halide in the composition range of 94-80 mole per cent (m/o) copper(I) halide. For example, the solid-state reaction product between copper(I) bromide 94 m/o and N,N'-dimethyl-triethylenediamine dibromide 6 m/o exhibited the conductivity of 0.035 $(ohm\text{-}cm)^{-1}$ at 20°C, which was essentially ionic. X-ray diffraction investigations indicated that these new solid electrolytes are unique and not the mixtures of their constituents.

During the past decade, the electrical properties of high-conductivity solid electrolytes and their applications to electrochemical devices have been described by many authors (1). However, the high-conductivity materials reported previously have been mainly the silver ion or alkali ion conductors. Recently, promising results have been found by Takahashi, Yamamoto, and Ikeda (2), that N-alkyl (or hydro)-hexamethylenetetramine halide-copper(I) halide double salts exhibited high copper ion conductivities of 4×10^{-4} to 1.7×10^{-2} $(ohm\text{-}cm)^{-1}$ at 20°C and their electronic conductivities were less than 10^{-10} $(ohm\text{-}cm)^{-1}$ at 100°C. Further investigations on copper ion conductors in our laboratory have revealed that the N,N'-dialkyl (or dihydro)-triethylenediamine dihalide-copper(I) halide double salts have the ionic conductivities of 2×10^{-3} to 4×10^{-2} $(ohm\text{-}cm)^{-1}$ at 20° C.

Experimental

N,N'-dialkyl (or dihydro)-triethylenediamine dihalides, $C_6H_{12}N_22RX$ (R = H, CH_3, C_2H_5, X = Cl, Br, I), were prepared by mixing the ethanol solution of triethylenediamine (1,4-diazabicyclo 2,2,2 octane), $C_6H_{12}N_2$, and alkyl halides or hydrohalogenic acids. Triethylenediamine and alkyl halides used were manufactured by Tokyo Chemical Industry Company, and they were used without further purification. For example, to a solution containing 5g (0.045 mole) of triethylenediamine in 50 mliters of ethanol were slowly added 21g of a 50% methyl bromide (0.11 mole) solution in ethanol and the mixture was allowed to stand overnight at room temperature. After being filtered, the precipitate was dried in vacuo on P_2O_5. By this method, five kinds of N,N'-dialkyl (or dihydro)-triethylenediamine dihalides, $C_6H_{12}N_22HCl$, $C_6H_{12}N_22HBr$, $C_6H_{12}N_22C_2H_5Br$, $C_6H_{12}N_22HI$, and $C_6H_{12}N_22CH_3I$ were prepared. For the preparation of all these precipitates, the mole ratio of alkyl halides (or hydro halogenic acids) to triethylenediamine was made larger than the stoichiometric ratio (2:1 mole ratio). N,N'-dimethyl-triethylenediamine dichloride was prepared as follows: triethylenediamine (25.5g) was added to a 7.3% ethanol solution of methyl chloride (422g). After standing for two days, methyl chloride gas was blown into the solution. The mixture was allowed to stand for seven days at room temperature, and after being filtered, the precipitate was dried in vacuo on P_2O_5. The crystals obtained were recrystallized from ethanol.

Triethylenediamine has two nitrogen atoms in a molecule, and the following two types of quarternary alkyl triethylenediamine halide (a) and (b) may exist

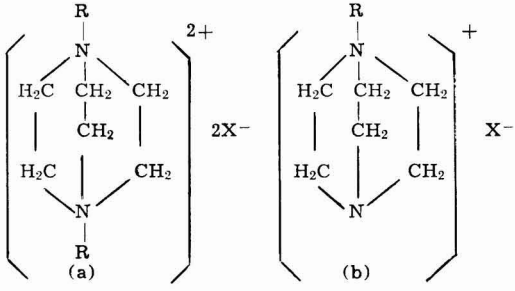

where R is H, CH_3, or C_2H_5, and X is halogen. In this study, as the quarternary alkyl triethylenediamine halides were obtained using an excess amount of alkyl halide or hydrohalogenic acid, the chemical formulas of the obtained compounds were type (a) which are certificated by the analytical data shown in Table I. The analytical data agree well with the values calculated from the molecular form of $C_6H_{12}N_22RX$. The decomposition temperature of these compounds are

* Electrochemical Society Active Member.

Key words: solid electrolyte; copper ion conductor; copper(I) halide; N,N'-dialkyl-triethylenediamine dihalide.

Table I. Analytical data of N,N'-dialkyl(or hydro)-triethylenediamine dihalides

Compound	Analysis Calculated C	H	N	Found C	H	N	Decomposition temperature, °C
$C_6H_{12}N_22HCl$	38.9	7.6	15.1	39.1	7.4	15.2	167
$C_6H_{12}N_22CH_3Cl$	45.1	8.4	13.1	40.5	8.9	12.3	201
$C_6H_{12}N_22HBr$	26.3	5.1	10.2	26.1	4.9	10.1	232
$C_6H_{12}N_22CH_3Br$	31.8	6.0	9.3	31.6	6.0	9.6	218
$C_6H_{12}N_22C_2H_5Br$	36.4	6.7	8.5	36.8	6.6	8.5	216
$C_6H_{12}N_22HI$	19.6	3.8	7.5	19.2	3.7	7.3	247
$C_6H_{12}N_22CH_3I$	24.3	4.5	7.1	24.2	4.5	6.9	176

also shown in the table. Copper(I) halides were purified by recrystallizing in the corresponding hydrohalogenic acid.

The materials used for the conductivity and x-ray experiments were prepared by combining CuX with $C_6H_{12}N_22RX$. The appropriate quantities of both compounds were mixed with a small amount of ethanol and dried completely at about 80°C before being pressed to form a pellet under a pressure of 4000 kg/cm², and then heated in a sealed evacuated Pyrex vessel for 17 hr. The reactions were carried out below the decomposition temperatures of the corresponding $C_6H_{12}N_22RX$ shown in Table I, that is, at 160°C for the CuCl-$C_6H_{12}N_22HCl$ system, at 170°C for the CuI-$C_6H_{12}N_22CH_3I$ system, and at 190°C for the other systems. The resulting materials did not melt at these reaction temperatures, except for the $C_6H_{12}N_22HCl$-CuCl system.

The electrical conductivity was measured by using a cell, Cu, sample/sample/Cu, sample. The sample of about 0.8g was stacked between the mixture of powdered copper (325 mesh) and the sample (2:1 weight ratio), and pressed into a pellet of 13 mm diameter under a pressure of 4000 kg/cm². The pressed samples with copper electrodes were annealed for several hours at 100°-200°C, corresponding to the kind of sample, in oxygen-free nitrogen gas flow before being slowly cooled to room temperature in an oven. This treatment provides for removal of the excess halogen in the sample, thus avoiding a deficit of copper which will give hole conduction in addition to ionic (3). The resistance of the conductivity cell was measured by means of the Ando Denki conductance bridge using 1000 Hz. The frequency dependence of resistance was not observed for all samples investigated.

The method for determining the electronic conductivity was described previously in some detail (2). It was determined from the relation of the current density and the cell voltage for the cell, Cu/sample/graphite, upon passing a direct current.

The transport number of copper ion was measured by Tubandt's method. In order to reduce the electrode polarization, a mixture of powdered copper and the sample was used for the electrode, and the weight changes of the electrode and the sample of the cell of the type

Cu, sample/sample/sample/Cu, sample [I]

were measured.

The x-ray diffraction patterns of the powdered samples were obtained at room temperature using conventional techniques with CuKα radiation.

Differential thermal analysis (DTA) was carried out for the sample which was sealed in a Vycor tube under vacuum. The heating rate was 3.5°/min. The decomposition temperature of samples was measured by thermogravimetric analysis (TGA), the heating rate of which was 3.3°C/min.

Results and Discussion

Electrical conductivity.—The effect of composition on the conductivity at room temperature was determined for the systems $C_6H_{12}N_22HCl$-CuCl, $C_6H_{12}N_22CH_3Cl$-CuCl, $C_6H_{12}N_22HBr$-CuBr, $C_6H_{12}N_22CH_3Br$-CuBr, $C_6H_{12}N_22C_2H_5Br$-CuBr, $C_6H_{12}N_22HI$-CuI, and $C_6H_{12}N_22CH_3I$. Of these systems, the conductivity of the thermal reaction products of the $C_6H_{12}N_22HI$-CuI system was comparable to or less than that of CuI. The other systems showed conductivities of 10^{-4}-10^{-2} (ohm-cm)$^{-1}$ at room temperature in the composition range of 95-80 mole per cent (m/o) CuX. Figure 1 shows the electrical conductivities of the systems studied at 20°C as a function of the mole per cent of copper(I) halide. These curves show that the conductivity has a maximum at a certain content of copper(I) halide and decreases rapidly with decreasing the content of copper(I) halide. The maximum values of conductivity were obtained at 85 m/o CuCl for the system $C_6H_{12}N_22HCl$-CuCl, at 80 m/o CuCl for $C_6H_{12}N_22CH_3Cl$-CuCl, at 87.5 m/o CuBr for $C_6H_{12}N_22HBr$-CuBr, at 94 m/o CuBr for $C_6H_{12}N_22CH_3Br$-CuBr, at 85 m/o CuBr for $C_6H_{12}N_22C_2H_5Br$-CuBr, and at 85 m/o CuI for $C_6H_{12}N_22CH_3I$-CuI. The highest conductivity of 4.9×10^{-2} (ohm-cm)$^{-1}$ at 20°C was found in the system $C_6H_{12}N_22HBr$-CuBr at 87.5 m/o CuBr. This value of conductivity is about three times larger than that reported in our previous paper (2), in which the conductivity of 1.7×10^{-2} (ohm-cm)$^{-1}$ at 20°C was obtained in the system N-methyl-hexamethylenetetramine bromide-copper(I) bromide at 87.5 m/o CuBr. Further, the conductivity value is comparable to that of silver ion conductors which are obtained by combining silver iodide with organic ammonium iodides (4-6).

From the above results, it is recognized that in the systems $C_6H_{12}N_22RBr$-CuBr, the conductivity decreases successively with R being H, CH_3, or C_2H_5. This result suggests that the symmetry of organic ammonium halide may play a role to give the high conductivity compound. Triethylenediamine is known as a bicyclic cage compound, the stereo structure of which shows somewhat spherical symmetry, and the symmetry of the quarternary alkyl triethylenediamine ion gets worse with increasing the volume of R from H to C_2H_5.

The temperature dependence of the electrical conductivities was determined for the samples in the

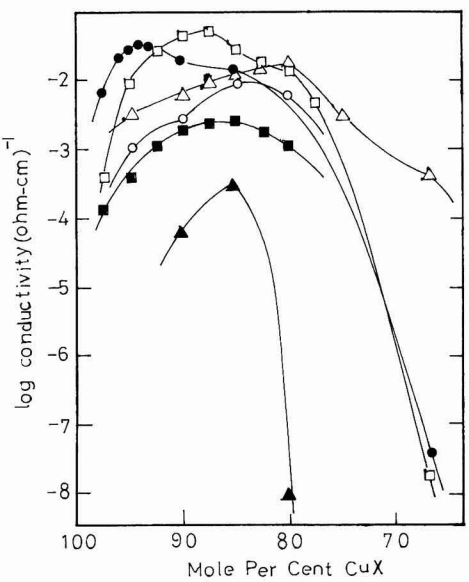

Fig. 1. Composition dependence of the electrical conductivity of the binary solid electrolyte systems $C_6H_{12}N_22HCl$-CuCl (○), $C_6H_{12}N_22CH_3Cl$-CuCl (△), $C_6H_{12}N_22HBr$-CuBr (□), $C_6H_{12}N_22CH_3Br$-CuBr (●), $C_6H_{12}N_22C_2H_5Br$-CuBr (▲), and $C_6H_{12}N_22CH_3I$-CuI (■) at 20°C.

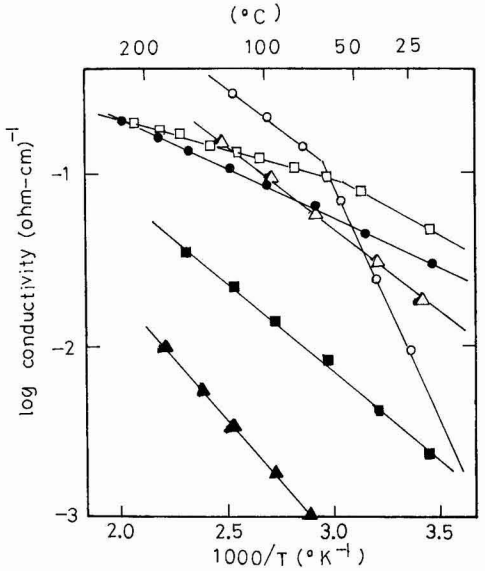

Fig. 2. Temperature dependence of the electrical conductivity of 17CuCl·3$C_6H_{12}N_2$2HCl (○), 4CuCl·$C_6H_{12}N_2$2CH_3Cl (△), 7CuBr·$C_6H_{12}N_2$2HBr (□), 47CuBr·3$C_6H_{12}N_2$2CH_3Br (●), 17CuBr·3$C_6H_{12}N_2$2C_2H_5Br (▲), and 17CuI·3$C_6H_{12}N_2$2CH_3I (■).

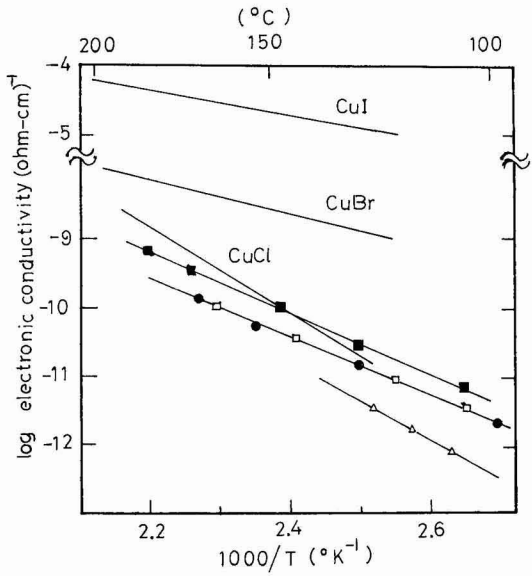

Fig. 3. Temperature dependence of the electronic conductivity of copper(I) halides, 4CuCl·$C_6H_{12}N_2$2CH_3Cl (△), 7CuBr·$C_6H_{12}N_2$2HBr (□), 47CuBr·3$C_6H_{12}N_2$2CH_3Br (●), and 17CuI·3$C_6H_{12}N_2$2CH_3I (■).

$C_6H_{12}N_2$2RX-CuX system. The results of several temperature cycles are shown in Fig. 2. The log conductivity *vs.* the reciprocal of the absolute temperature curves for 4CuCl·$C_6H_{12}N_2$2CH_3Cl, 47 CuBr·3$C_6H_{12}N_2$2CH_3Br, 17 CuBr·3$C_6H_{12}N_2$2C_2H_5Br, and 17 CuI·3$C_6H_{12}N_2$2CH_3I indicate that no phase transition occurs in the range of the temperature investigated. The activation energies calculated from these curves are 4.2 kcal/mole for 4CuCl·$C_6H_{12}N_2$2CH_3Cl, 2.7 kcal/mole for 47 CuBr·3$C_6H_{12}N_2$2CH_3Br, 5.6 kcal/mole for 17CuBr·3$C_6H_{12}N_2$2C_2H_5Br, and 4.8 kcal/mole for 17CuI·3$C_6H_{12}N_2$2CH_3I. The results for 17CuCl·3$C_6H_{12}N_2$2HCl and 7CuBr·$C_6H_{12}N_2$2HBr exhibit an increasing activation energy at low temperature, which suggests that phase transitions occur near 65°C for 17CuCl·3$C_6H_{12}N_2$2HCl and 50°C for 7CuBr·$C_6H_{12}N_2$2HBr. However, 7CuBr·$C_6H_{12}N_2$2HBr is conductive at room temperature and has a low activation energy of 3.3 kcal/mole at 20°C. On the other hand, 17CuCl·3$C_6H_{12}N_2$2HCl has a high activation energy of 13.5 kcal/mole at 20°C, and it indicates that the conductive phase transfers to a nonconductive phase below 65°C.

Electronic conductivity.—Though stoichiometric copper(I) halides exhibit ionic conduction predominantly, the existence of excess halogen or oxygen which corresponds to a deficit of copper causes hole conduction (3). Therefore, it is important to measure the electronic conductivity of the solid electrolyte containing copper(I) halides. The electronic conductivity of the $C_6H_{12}N_2$2RX-CuX system was measured by Wagner's polarization method. The current *vs.* cell voltage curves for the cell, Cu/sample/graphite, showed a quasi-exponential increase of current in the temperature range of 100°-200°C for all samples investigated. Therefore, according to Wagner's theory, the hole conduction may be assumed to be dominant under this experimental condition. The electronic conductivities were calculated with the help of this theory. The temperature dependence of the electronic conductivity of 4CuCl·$C_6H_{12}N_2$2CH_3Cl, 7CuBr·$C_6H_{12}N_2$2HBr, 47CuBr·3$C_6H_{12}N_2$2CH_3Br, and 17CuI·3$C_6H_{12}N_2$2CH_3I is shown in Fig. 3, compared to those of the copper(I) halides. The electronic conductivities of these new high conductivity materials are smaller than those of the corresponding copper(I) halides. At room temperature, the electronic conductivities of these materials were too small to measure with this method. Thus, it is concluded that the conduction in these new compounds is essentially ionic in nature.

Transport number measurements.—The ionic transport number in 47 CuBr·3$C_6H_{12}N_2$2CH_3Br was determined with the help of Tubandt's method. In order to reduce the electrode polarization, the measurement was carried out at 100°C. The direct current at the current density of 500 $\mu A/cm^2$ was passed through cell [I] over 21 hr. The total charge passed through the cell corresponded to the quantity of copper deposited at the cathode and dissolved at the anode; that is, the efficiencies of 102% at the anode and 100.5% at the cathode were obtained. This result indicates that the transport number of copper(I) ion is unity within the experimental error.

TGA and DTA.—The decomposition temperatures of these new, high copper ion conductivity materials were measured with the help of TGA, and the results are shown in Table II. All samples, except 17CuCl·3$C_6H_{12}N_2$2HCl, are stable up to 200°C. The N,N'-dialkyl (or hydro)-triethylenediamine dihalide-copper(I) halide double salts are thermally more stable than the previously reported N-alkyl (or hydro)-hexamethylenetetramine-copper(I) halide double salts, which decomposed below 150°C.

Table II. Thermal data for N,N'-dialkyl(or dihydro)-triethylenediamine dihalide-copper(I) halide double salts

Compound	Decomposition temperature, °C	Melting point, °C
17CuCl · 3$C_6H_{12}N_2$2HCl	120	112
4CuCl · $C_6H_{12}N_2$2CH_3Cl	222	199
7CuBr · $C_6H_{12}N_2$2HBr	206	300
47CuBr · 3$C_6H_{12}N_2$2CH_3Br	223	314
17CuBr · 3$C_6H_{12}N_2$2C_2H_5Br	234	196
17CuI · 3$C_6H_{12}N_2$2CH_3I	210	295

Further, DTA was carried out for these samples sealed in a Vycor tube. Each sample presented an endothermic peak which may be due to the melting of the sample. The melting points are also shown in Table II.

X-ray diffraction analysis.—The x-ray diffraction patterns were obtained at room temperature for the samples containing 95-50 m/o copper(I) halide in the system $C_6H_{12}N_22RX$-CuX. In the systems $C_6H_{12}N_22HCl$-CuCl and $C_6H_{12}N_22CH_3Cl$-CuCl, the samples containing 90 and 85 m/o CuCl showed the mixed patterns of CuCl and a new compound. Samples containing 80 m/o CuCl gave a pattern for a new single phase. In the $C_6H_{12}N_22HBr$-CuBr system, the high-conductivity solid containing nearly 87.5 m/o CuBr gave a single-phase pattern. Another two intermediate compounds were found at the composition of 66.7 and 50 m/o CuBr, which were poor conductors. In the $C_6H_{12}N_22CH_3Br$-CuBr system, the sample containing 94 m/o CuBr, which exhibits the highest conductivity in this system, did not give a single-phase pattern but gave the patterns of two phases corresponding to a new compound and CuBr. However, a single-phase pattern was observed at the composition of 90 m/o CuBr, 66.7 m/o CuBr, and 50 m/o CuBr. In the $C_6H_{12}N_22HI$-CuI system, only the peaks due to the starting materials were observed in the composition range of 90-50 m/o CuI. In the $C_6H_{12}N_22CH_3I$-CuI system, three intermediate compounds were found at the composition of 85 m/o CuI, 66.7 m/o CuI, and 50 m/o CuI. The compound containing 85 m/o CuI is a high conductive solid electrolyte and the other compounds are poor conductors.

It was found from the x-ray investigation that the highest conductivity material in each system did not always give a single-phase pattern. This may be due to the fact that the conductivity measurement is not precise enough to determine the exact formula of the compounds (4). However, it is concluded that the high-conductivity materials found in the $C_6H_{12}N_22RX$-CuX systems are new compounds and not the mixtures of their constituents. The x-ray diffraction patterns of the new compounds were too complex to determine their crystal structures.

Conclusion

The high, copper ion conductivity and the low electronic conductivity were found in the N,N'-dialkyl (or dihydro)-triethylenediamine-dihalide-copper(I) halide double salts. The values of the conductivity are comparable to that of the previously reported quaternary ammonium iodide-silver iodide compounds.

Manuscript submitted May 20, 1974; revised manuscript received Aug. 7, 1974.

Any discussion of this paper will appear in a Discussion Section to be published in the December 1975 JOURNAL. All discussions for the December 1975 Discussion Section should be submitted by Aug. 1, 1975.

Publication costs of this article were partially assisted by the authors.

REFERENCES

1. "Physics of Electrolyte," J. Hladik, Editor, Academic Press, New York (1972).
2. T. Takahashi, O. Yamamoto, and S. Ikeda, *This Journal*, **120**, 1431 (1973).
3. J. B. Wagner and C. Wagner, *J. Chem. Phys.*, **26**, 1597 (1957).
4. B. B. Owens, *This Journal*, **117**, 1536 (1970).
5. B. B. Owens, J. H. Christie, and G. T. Tiedeman, *ibid.*, **118**, 1145 (1971).
6. M. L. Berardelli, C. Biondi, M. De Rossi, G. Fonseca, and M. Giomini, *ibid.*, **119**, 115 (1972).

Interface States and Fixed Charge as a Function of Small Changes in Orientation of (111) Silicon Wafers

Sigurd Wagner

Bell Laboratories, Holmdel, New Jersey 07733

and Edward I. Povilonis

Bell Laboratories, Murray Hill, New Jersey 07974

ABSTRACT

The orientation of a silicon substrate for integrated circuits frequently deviates from its nominal value. In this study the densities of the interface states (N_{SS}) and of the fixed charge (Q_{FC}) were determined as a function of small changes of the orientation. Metal-silicon dioxide-silicon capacitors were made on eleven silicon wafers oriented from -25 to $+173$ min of arc off the [111] direction toward the [011] direction. N_{SS} and Q_{FC} were derived from the high frequency and quasi-static capacitance-voltage characteristics. Both are independent of the orientation over the range examined with $N_{SS} = (4.4 \pm 1.3) \times 10^{10}$ cm^{-2} V^{-1}, and $Q_{FC} = + (6.7 \pm 1.2) \times 10^{10}$ cm^{-2}.

Two types of electronic states, the interface states (N_{SS}) and the fixed charge (Q_{FC}) are located at the interface between silicon and silicon dioxide. The interface states exchange charge with the bulk of the semiconductor. Their equilibrium population depends on the position of the Fermi level at the interface. The fixed charge states do not alter their population when the Fermi level scans the bandgap. Because of their contribution to the threshold voltage the densities of both types of states are important characteristics of insulated gate field effect devices.

One question about N_{SS} and Q_{FC} is whether they vary when the orientation of the silicon wafer deviates slightly from its nominal value. Silicon wafers for MOS integrated circuits may deviate by as much as one degree of arc from their nominal orientation (1).

Key words: interface, orientation, silicon.

Substrates for epitaxy are intentionally oriented off low index orientations by angles of the order of one degree (1). This is done to obtain epitaxial layers of good quality free of pyramidal growth. It is known that the "offset" in orientation is retained at the surface of the epitaxial layer. Another case where the effect of a small change in orientation is of interest is found in experiments on the effects of strain on the interface characteristics (2). Neither the existing theories about the origin of these states nor the published experiments on their orientation dependence answer the question.

No theory relates N_{SS} or Q_{FC} directly to the orientation of the interface. N_{SS} has been associated with unpaired localized electrons which could result from incomplete oxidation (3) or which may exist at misfit dislocations in the interface (4). N_{SS} has also been ascribed to lateral fluctuations of the interface potential due to charges distributed in the silicon dioxide (5), and to impurity atoms located at the interface (6, 7). Q_{FC} is believed to result from charges attached to incompletely oxidized silicon on the oxide side of the interface (8), or to strained regions at the interface (9). The fixed charge may be identical with charge in interface states located outside of the bandgap where net charging or discharging cannot take place.

One important aspect of both types of states is the dependence of their density on the crystallographic orientation of the SiO_2/Si interface. Maxima of N_{SS} [Ref. (10)] and of Q_{FC} [Ref. (8, 9, 11)] exist in the vicinity of {111} interfaces, and minima near {110} and {100}. Qualitatively these extrema can be correlated with the density of atoms in the first layer of a free surface of silicon. The existing data cannot be used for conclusions about the dependence of N_{SS} and Q_{FC} on small ($\sim 1°$) changes in orientation. First, the densities of N_{SS} and Q_{FC} obtained in the previous studies (9, 10) are about five and ten times, respectively, higher than the lowest obtainable values. Second, in the published studies the spacing between experimental points ranges from 5 to 30 degrees of arc, and therefore does not offer sufficient resolution. We have measured N_{SS} and Q_{FC} of eleven samples oriented between -25 and $+173$ min of arc off the [111] direction toward the [01$\bar{1}$] direction, *i.e.*, with the "zone axis" parallel to [01$\bar{1}$]. The (111) interface was selected to obtain comparatively large values of N_{SS} and Q_{FC} and concurrent low relative experimental errors. However, we did employ processing procedures to minimize these densities to the lowest values which can be attained for this orientation.

Experimental

One float zone grown [111] oriented 1¼ in. diameter p-type boron-doped ingot with a nominal resistivity of 0.46-0.55 ohm-cm was sawed into oriented wafers with successively increasing tilt off [111]. After a chemical etch and a Syton polish the orientation of the 14 mils (0.35 mm) thick wafers was determined by x-ray goniometry. After cleaning by a sequence of organic solvents, aqueous detergent solutions, acidic and oxidizing solutions, and by scrubbing, the wafers were prepared for oxidation by rinsing in deionized water and in dilute HF. All eleven wafers were then immediately brought into the very clean oxidation furnace. This furnace is made up of a double-walled, fused quartz tube within a silicon carbide liner. Gases enter the furnace through the inner quartz tube and flow back out through the annulus between the inner and the outer tube. All wafers were oxidized simultaneously for 100 min at 1000°C in a pure oxygen flux of 30 cm sec^{-1}, and subsequently annealed *in situ* in pure nitrogen at a flux of 30 cm sec^{-1} for 30 min at 1000°C. After rapid cooling to room temperature, the SiO_2 film was etched to 0.0925 μm in HF:H_2O = 1:15. Then high purity aluminum was evaporated from a sodium-free tungsten coil onto the wafers. A 30 mil (0.076 cm) diameter dot and guard ring pattern was etched into the aluminum by standard photolithographic techniques. After a cleaning procedure, the back sides were aluminized, and the samples were annealed for 30 min at 400°C in pure hydrogen with a flux of 20 cm sec^{-1}.

The experimental setup used for the high frequency (1 MHz) and quasi-static (0.048 Vsec^{-1}) capacitance-voltage measurements is similar to that described by Lopez (12). The mobile charge in the SiO_2 was determined by the triangular voltage sweep technique (13) at 300°C with 0.048 Vsec^{-1}. In all measurements the guard ring was held at the voltage of the field plate.

The high frequency and quasi-static C-V curves were first evaluated for the doping profile, correcting for surface states (14)

$$N_A(x) = \left[\frac{2}{q\kappa_S\epsilon_0}\right]\left[\frac{1 - C_Q/C_{ox}}{1 - C_H/C_{ox}}\right]\left[\frac{d(1/C_H)^2}{dV}\right]^{-1}$$

where $N_A(x)$ is the net concentration of acceptors as a function of the distance x from the SiO_2/Si interface; q is the electronic charge, κ_S the relative dielectric constant of silicon, ϵ_0 is the permittivity of free space; C_Q, C_H, and C_{ox} are the quasi-static, the high frequency, and the maximum (oxide) capacitance, respectively; V is the voltage. For the numerical evaluation, points were taken off the C-V curves at 0.1V intervals.

The normalized flatband capacitance C_{FB}/C_{ox} was then calculated using the dopant concentration measured at $x = 0.1$ μm, N_A (0.1)

$$\frac{C_{FB}}{C_{ox}} = \left[1 + \left[\frac{\kappa_{ox}^2\epsilon_0 kT}{\kappa_S q^2}\right]^{1/2}\left[\frac{1}{t_{ox}N_A(0.1)^{1/2}}\right]\right]^{-1}$$

where κ_{ox} is the relative dielectric constant of SiO_2, k is the Boltzmann constant, T the absolute temperature, and t_{ox} the thickness of SiO_2.

The density of fixed charge, Q_{FC}, was determined from the difference between the ideal (ϕ_{MS}) and measured flatband voltage (V_{FB})

$$Q_{FC} = C_{ox}(\phi_{MS} - V_{FB})$$

(C_{ox} is the capacitance of the unit area of the SiO_2 layer.) It should be noted that this is a net charge made up of all ionized donor and acceptor states at the interface regardless of their location within or without the bandgap.

The density of interface states N_{SS} as a function of the interface potential ψ_S was derived from the difference between the quasi-static and the high frequency capacitance (15)

$$N_{SS}(\psi_S) = \frac{C_{ox}}{q}\left[\left[\frac{C_{ox}}{C_Q} - 1\right]^{-1} - \left[\frac{C_{ox}}{C_{HF}} - 1\right]^{-1}\right]$$

ψ_S was calculated by integration of the quasi-static capacitance with respect to applied voltage (16). The flatband voltage was taken as the lower limit

$$\psi_S(V) = \int_{V_{FB}}^{V}\left[1 - \frac{C_Q}{C_{ox}}\right]dV$$

Results

The mobile ionic charge in the SiO_2 films was uniformly low and ranged from 2 to 3 $\times$ 10^{10} cm^{-2}. It was too small to be determined by the bias-temperature stress technique which showed only the non-ionic "slow trapping" instability. A typical acceptor concentration *vs.* depth is shown in Fig. 1. The 5% accuracy limits (14) are denoted by $3L_B$ and $2L_B\sqrt{u_B}$. L_B is the extrinsic Debye length and u_B is the bulk Fermi potential in units of kT/q. N_A drops from the bulk toward the interface as a consequence of the depletion of boron during the oxidation. N_A at $x = 0.1$ μm is plotted against the orientation of the interface in Fig. 3c. This plot corresponds roughly to one of N_A *vs.* the position

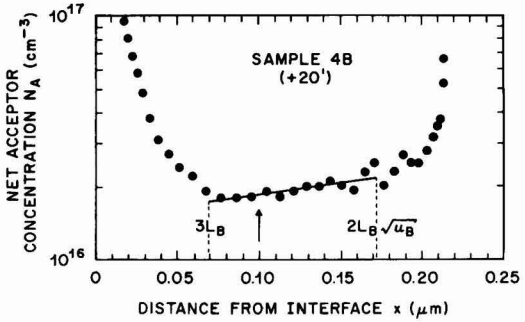

Fig. 1. Typical concentration profile of acceptors vs. distance from the SiO_2/Si interface. $3L_B$ and $2L_B\sqrt{u_B}$ denote the 5% error limits. The high values of N_A at $x < 3L_B$ and $x > 2L_B\sqrt{u_B}$ are artifacts of the capacitance-voltage technique.

in the original silicon ingot. $N_A(x = 0.1)$ is virtually constant at $(1.97 \pm 0.14) \times 10^{16}$ cm^{-3}.

Figure 2 shows a typical plot of the density of interface states *vs.* interface potential. The average of N_{SS} within ±0.20V of the midgap potential is used to construct the plot of N_{SS} *vs.* the angle Φ, Fig. 3a. A least squares treatment of N_{SS} *vs.* Φ gives

$$N_{SS} = 4.60 \times 10^{10} - 0.0032 \times 10^{10} \times \Phi(\text{min}) \pm 1.31 \times 10^{10}\ \text{cm}^{-2}\ \text{V}^{-1}$$

The standard deviation corresponds to an uncertainty in the determination of $(C_Q - C_{HF})/C_{ox}$, at midgap potential, of $\pm 5 \times 10^{-3}$. An uncertainty of this order is usually encountered as a consequence of errors in the normalization of C_Q to C_{HF} in accumulation. Therefore we consider N_{SS} as constant within the experimental error

$$N_{SS} = (4.4 \pm 1.3) \times 10^{10}\ \text{cm}^{-2}\text{V}^{-1}$$

A least squares treatment of Q_{FC} *vs.* Φ (Fig. 3b) results in

$$Q_{FC} = 6.66 \times 10^{10} + 0.0002 \times 10^{10} \times \Phi(\text{min}) \pm 1.20 \times 10^{10}\ \text{cm}^{-2}$$

Here the standard deviation corresponds to an uncertainty of 0.06V in the determination of the flatband voltage. Q_{FC} is thus virtually constant at $Q_{FC} = (6.7 \pm 1.2) \times 10^{10}$ cm^{-2}.

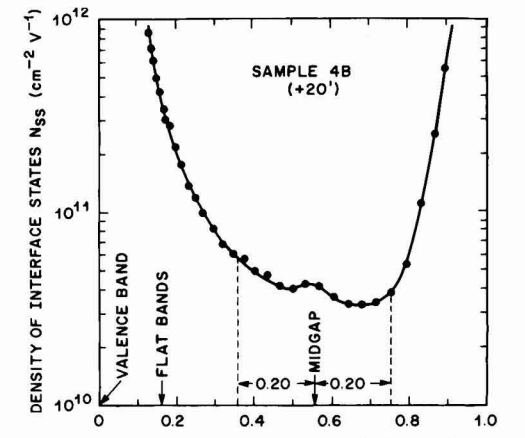

Fig. 2. Typical profile of the density of interface states vs. the interface potential. The average density within 0.20V of the midgap potential was used for further evaluation.

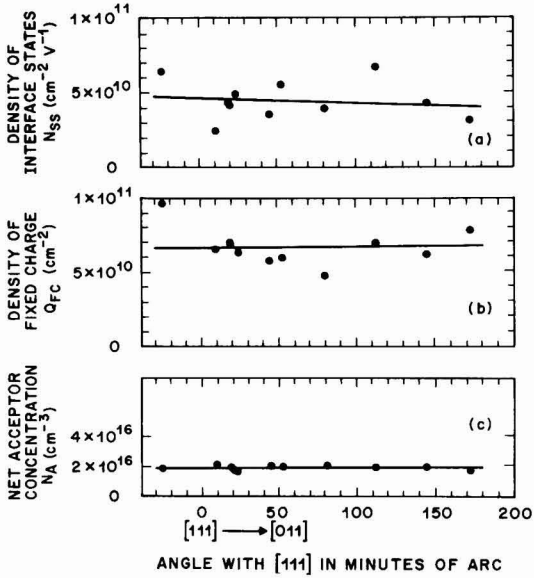

Fig. 3. (a) Density of interface states, (b) density of fixed charge, (c) acceptor concentration, all as a function of orientation.

Conclusion

The SiO_2/Si interfaces of eleven wafers, oriented within about 3° of the [111] direction, were characterized. These orientations are typical for device material. The densities of the interface states and of the fixed charge were constant with $N_{SS} = (4.4 \pm 1.3) \times 10^{10}$ cm^{-2} V^{-1} and $Q_{FC} = +(6.7 \pm 1.2) \times 10^{10}$ cm^{-2}.

Acknowledgments

The authors wish to thank R. O. Miller and W. A. Sachs for slicing, polishing, and orienting the silicon wafers. They are indebted to D. V. McCaughan, B. C. Wonsiewicz, and J. R. Brews for valuable discussions.

Manuscript received March 7, 1974.

Any discussion of this paper will appear in a Discussion Section to be published in the December 1975 JOURNAL. All discussions for the December 1975 Discussion Section should be submitted by Aug. 1, 1975.

Publication costs of this article were partially assisted by Bell Laboratories.

REFERENCES

1. J. W. Carlson, *Solid State Technol.*, **16**, (11), 49 (1973).
2. D. V. McCaughan and B. C. Wonsiewicz, *J. Appl. Phys.*, **45**, 4982 (1974).
3. E. Kooi, "The Surface Properties of Oxidized Silicon," Springer, New York (1967).
4. G. F. Neumark, *Phys. Rev. Letters*, **21**, 1253 (1968).
5. A. Goetzberger, V. Heine, and E. H. Nicollian, *Appl. Phys. Letters*, **12**, 95 (1968).
6. S. Kar and W. E. Dahlke, *ibid.*, **18**, 401 (1971).
7. W. Fahrner and A. Goetzberger, *J. Appl. Phys.*, **44**, 725 (1973).
8. Y. Miura, *Japan. J. Appl. Phys.*, **4**, 958 (1965).
9. G. Abowitz, E. Arnold, and J. Ladell, *Phys. Rev. Letters*, **14**, 543 (1967).
10. E. Arnold, J. Ladell, and G. Abowitz, *Appl. Phys. Letters*, **13**, 413 (1968).
11. J. F. Delord, D. G. Hoffmann, and G. Stringer, *Bull. Am. Phys. Soc., Ser. 2*, **10**, 546 (1965).
12. A. D. Lopez, *Rev. Sci. Instr.*, **44**, 200 (1973).
13. N. T. Chou, *This Journal*, **118**, 601 (1971).
14. J. R. Brews, *J. Appl. Phys.*, **44**, 3228 (1973).
15. R. Castagné and A. Vapaille, *Surface Sci.*, **28**, 157 (1971).
16. C. N. Berglund, *IEEE Trans. Electron. Devices*, **ED-13**, 701 (1966).

Improved Dielectric Reliability of SiO_2 Films with Polycrystalline Silicon Electrodes

C. M. Osburn* and E. Bassous*

IBM Thomas J. Watson Research Center, Yorktown Heights, New York 10598

ABSTRACT

Time dependent dielectric breakdown of SiO_2 films in MOS structures is shown to be strongly dependent on the electrode material used. Polycrystalline silicon electrodes give substantially longer times to failure than do aluminum electrodes. The improvement is 3-4 decades at 300°C; and, because of the larger activation energy for wearout with poly-Si (2.4 eV) compared to Al (1.4 eV), the relative advantage would be 8-16 decades at room temperature. Although time to breakdown is a strong function of SiO_2 thickness when the electrode is Al, it is nearly independent of thickness for structures having poly-Si electrodes.

Increasing reliability requirements for MOSFET devices makes it desirable to optimize the selections of dielectric and electrode materials as well as processing conditions used to fabricate the gate region. Device failure due to gate oxide dielectric breakdown has been reported (1) as one failure mode. Because of its importance to over-all device reliability, several recent studies (2-9) have focused on the causes of time-dependent, dielectric degradation and breakdown in SiO_2 films. The electrode metal has been shown (6, 9) to be an important factor in determining the rate of dielectric deterioration.

MOS capacitor structures having polycrystalline silicon electrodes have previously been shown to exhibit (6) a more substantial resistance to dielectric degradation at high temperature than those utilizing reactive metals like Al or Mo. However, the earlier work only considered degradation during various post-metallization annealing treatments when no bias was applied; this study specifically extends that work to determine the influence of an electric field on wearout. Data are presented to show a thousandfold improvement of SiO_2 dielectric reliability due to breakdown, as a result of using positively biased poly-Si electrodes rather than aluminum. As such, it is the most reliable MOS system reported in studies to date, including those utilizing SiO_2 films grown in HCl-O_2 ambients (7). When stressed negatively, the poly-Si was only slightly more reliable than aluminum.

Experimental

The metal-oxide-semiconductor capacitors used here were fabricated on both n- and p-type silicon wafers (2 ohm-cm); oxide films were grown in oxygen at 1000°C. To avoid electrical shorts originating at the electrode perimeter due to definition of the electrodes using chemical etching processes, a thick, supporting oxide layer was first grown; 25 mil diameter holes were opened photolithographically; and the desired thin (200-700Å) oxide film was grown. The electrodes were fabricated by: chemical vapor depositing (CVD) 3000Å of poly-Si at 650°C using a mixture of SiH_4 and N_2; doping the poly-Si surface by reaction with $POCl_3$ vapor at high temperature; and, diffusing the phosphorus throughout the electrode at 1000°C using alternate dry-wet-dry oxygen ambients. Capacitance measurements were used to determine the optimal doping parameters: a high capacitance value indicated inadequately doped poly-Si while the appearance of a high flatband voltage signaled that the phosphorus had been driven too far into the oxide.

Two different dielectric breakdown measurements were made: voltage ramp breakdown (10) and accelerated bias-temperature breakdown (6). With the former technique, many (typically 200) MOS capacitors on a wafer are stressed with a voltage ramp and the breakdown voltages (or fields) are recorded. In the second measurement, capacitors are stressed at constant electric field at elevated temperature (100°-400°C) and the times at which capacitor breakdown occurs are recorded: the largest value (t_{max}) has been shown (6) to be a good measure of the wearout time of an initially defect-free SiO_2 film.

Results and Discussion

Measurements of the breakdown voltages of MOS structures, having either poly-silicon or aluminum electrodes, by the ramping technique yielded statistically equivalent values: histograms of breakdown voltages were the same for both materials. Before reproducible silicon deposition and phosphorus-doping procedures were established, both abnormally high and low breakdown voltages were often observed using poly-Si structures. The high voltages were attributed to inadequate homogenization of the dopant in the electrode with attendant loss of voltage in this material due to the appearance of a depletion region. The low voltage values were probably caused by the large number of process steps involved and the subsequent higher chance of contamination, mask misalignment, and thermal stressing. Measurements on boron-doped poly-Si electrodes (11) also revealed carrier depletion unless the electrode homogenization was done at sufficiently high temperatures. Once the fabrication process was well controlled, it was repeatedly verified that ramp breakdown voltage values are the same for both contact electrodes. The high temperatures required to fabricate poly-Si electrodes does not degrade oxide quality once a reproducible Si deposition and doping procedure has been established.

During accelerated testing, however, the electrodes were found to play an important role. Compare the results for poly-Si and Al in Fig. 1, for stressing at 5 and 6 MV/cm at 300°C. The 300Å SiO_2 capacitors having poly-Si electrodes lasted 3 to 4 decades longer than the others. The wearout times (t_{max}) for the positive electrode bias case confirms that the ten-thousandfold improvement occurs over a wide range of applied electric fields (see Fig. 2). The maximum time to failure decreases almost exponentially with applied field; this dependence can be contrasted to a Peek's law behavior ($E \propto t^{-1/4}$) which was observed in other MOS samples (3, 4) which were intentionally contaminated with large amounts of mobile sodium. In contrast with the electrode biased negatively, t_{max} for poly-Si is only a factor of three larger than that for Al. For both polarities, the conduction current increases (often by several decades) prior to breakdown as shown earlier

* Electrochemical Society Active Member.

Key words: dielectric breakdown, silicon dioxide, silicon gates, reliability.

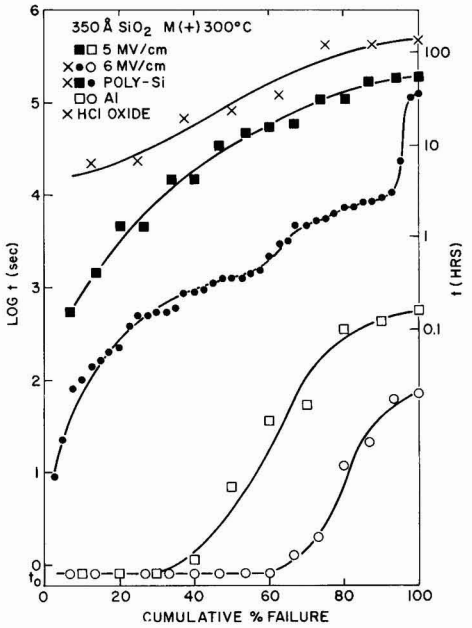

Fig. 1. Statistical failure times of 350Å SiO_2 films having either poly-Si or Al electrodes as measured at 300°C with positive electrode bias.

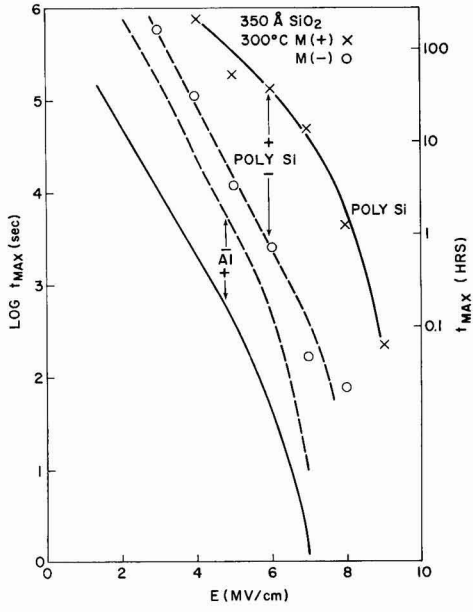

Fig. 2. Maximum time to failure as a function of applied field at 300°C for poly-Si and Al electrodes.

(6). The only difference between samples having poly-Si electrodes and those with Al is the time at which the current increases. The fact that with negative electrode bias Al and poly-Si have nearly equal wearout times, further shows that the wearout time depends on the anode material.

By plotting log t_{max} *vs.* temperature^{-1}, it was determined that the wearout times in both aluminum and poly-Si structures had a thermal activation energy of 1.4 eV for negative bias. With positive electrode bias, activation energies of 2.4 eV were observed with the poly-Si electrodes and 1.4 eV for aluminum (6) (see Fig. 3). The activation energy with poly-Si was so high that most of the points in Fig. 3 had to be extrapolated from plots of t_{max} *vs.* E at each temperature. In the absence of alternate wearout mechanisms, the activation energies coupled with the data of Fig. 2 would predict that poly-Si devices should last 10^8-10^{16} times longer than Al ones at 25°C.

Other processing conditions were then varied in order to further enhance the dielectric reliability. For example, improved reliability has been previously demonstrated (7) for aluminum-electroded structures when the SiO_2 was exposed to hydrogen at high temperatures. During standard processing of poly-Si structures here, hydrogen is present at two stages: (*i*) during CVD deposition of Si at 650°C, and (*ii*) during the phosphorus drive-in done in steam at 1000°C. An alternate phosphorus drive-in process, using dry oxygen alone, was tested and did not give significantly different breakdown characteristics than samples receiving the dry-wet-dry sequence. Formation of the SiO_2 in a 3% HCl/97% O_2 ambient was found to further enhance the dielectric integrity of poly-Si structures. The statistical occurrence of low field breakdown events (<0.8 MV/cm) in HCl oxides was less than half that for standard oxides. The wearout time improvement attributable to the HCl oxidation step was only apparent at moderate (~6 MV/cm) to low applied fields and could not be extensively studied because of the prohibitively long times to failure. At the higher fields, no substantial difference was noted for the two types of oxides.

Limiting failure times were measured as a function of oxide thickness (from 100-1500Å) and are com-

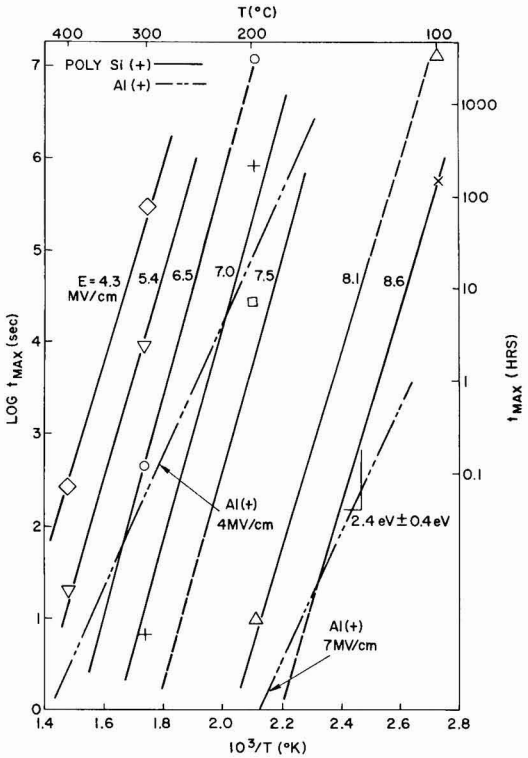

Fig. 3. Temperature dependence of wearout with positively biased poly-Si electrodes. The dashed lines go to points extrapolated from t_{max} *vs.* E plots at constant temperature.

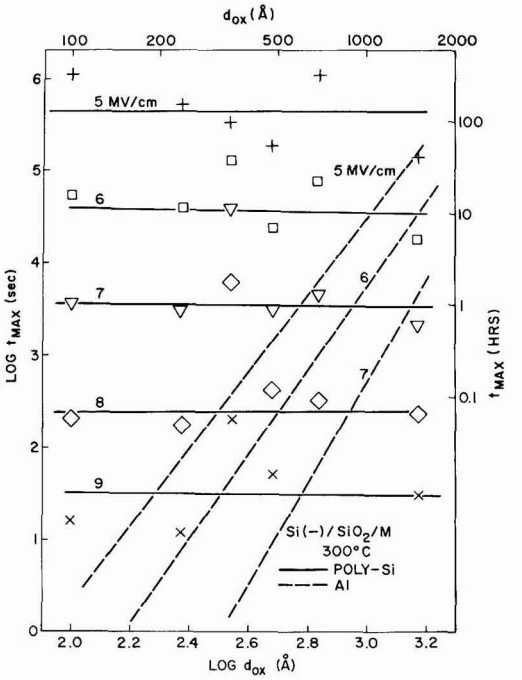

Fig. 4. Maximum time to failure as a function of oxide thickness for poly-Si electrodes biased positively at 300°C for different applied fields. The dotted lines represent the Al electrode data of Osburn and Chou (6).

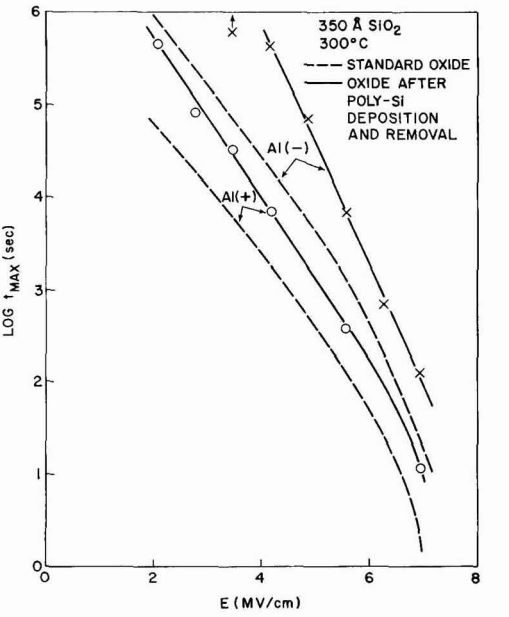

Fig. 5. Maximum time to failure as a function of applied field at 300°C for Al electrodes on standard oxides and on oxides from which doped poly-Si had been removed.

pared to those using Al electrodes in Fig. 4. For some, as yet, unknown reason the scatter in the poly-Si results was greater than that for aluminum; nevertheless, it is apparent that wearout in poly-Si structures is nearly independent of oxide thickness. Thus poly-Si gates have three reliability advantages over aluminum: (*i*) under accelerated conditions, they are substantially longer lived, (*ii*) the activation energy for wearout is higher and hence they are comparatively more reliable at lower operating temperatures, and (*iii*) they are comparatively more reliable as the thickness of the dielectric is reduced.

Experiments were conducted to determine the source of the improved reliability of poly-Si devices. In one test, poly-Si was deposited on an oxide, doped and then stripped off with ethylene diamine-pyrocatechol solution (12); aluminum electrode dots were evaporated onto the oxide, and the wearout properties were characterized (see Fig. 5.) Even though the electrode was aluminum, the maximum time to failure was 2-20 times longer than with standard samples. Clearly, the silicon deposition and/or doping processes yield a longer lasting SiO_2 layer, regardless of electrode material. Nevertheless, for the positive bias case, the oxide improvement is only a small fraction of that seen with poly-Si electrodes; with a negative bias, on the other hand, the oxide improvement alone is often greater than the net improvement with poly-Si. Both electron microprobe and oxide etch rate measurements were made after doped silicon electrodes were stripped from SiO_2; phosphorus or a phosphosilicate glass (PSG) layer was not observed although neither technique is well-suited to detect a thin (10-20Å), dilute (1-3%) phosphorus-containing layer. In several instances, large flatband voltages (−1.5V) and hysteresis in C-V curves were observed. This might be attributed to phosphorus in the oxide (13, 14) as a result of overdoping the poly-Si. Dielectric wearout measurements on SiO_2 films having different PSG layers suggest that a 50-100Å layer of 3-4% P_2O_5 would be required to give the oxide improvement that is seen after poly-Si removal.

Although several models can be proposed to account for the superior properties of poly-Si electrodes, they must all be considered speculative at this time. Poly-Si is much less reactive with SiO_2 than Al: poly-Si on SiO_2 has been shown (6) to withstand high temperature annealing better than Al on SiO_2; and aluminum injection and diffusion into SiO_2 were seen at relatively low temperature (15). Hydrogen introduced during silicon deposition or dopant drive-in contributes to the oxide integrity. A thin PSG layer or phosphorus-rich layer could also increase wearout time. Each individual model has serious drawbacks and a more complete knowledge of the mechanism of dielectric deterioration is needed to fully understand the source of the improvement seen here. Nevertheless, poly-Si electrodes can be used to fabricate MOS structures that have superior dielectric reliability.

Acknowledgments

The authors would like to thank J. Eldridge, H. Yu, and N. Chou for stimulating conversations during the course of this work. Sample preparation and measurement were aided by J. Kucza, M. Smyth, H. Lazzari, V. Maniscalco, and D. Ormond.

Manuscript submitted April 30, 1974; revised manuscript received July 11, 1974.

Any discussion of this paper will appear in a Discussion Section to be published in the June 1975 JOURNAL. All discussions for the June 1975 Discussion Section should be submitted by Feb. 1, 1975.

The publication costs of this article have been assisted by IBM Corporation.

REFERENCES

1. G. L. Schnable, H. J. Ewald, and E. S. Schlegel, *IEEE Trans. Reliability*, **R21**, 12 (1972).
2. F. L. Worthing, *This Journal*, **115**, 88 (1968).

3. S. I. Raider, *Appl. Phys. Letters*, **23**, 24 (1973).
4. C. M. Osburn and S. I. Raider, *This Journal*, **120**, 1369 (1973).
5. T. H. DiStefano, *J. Appl. Phys.*, **44**, 527 (1973).
6. C. M. Osburn and N. J. Chou, *This Journal*, **120**, 1377 (1973).
7. C. M. Osburn, *ibid.*, **121**, 809 (1974).
8. N. Klein, *IEEE Trans. Electron Devices*, **ED-11**, 788 (1966).
9. N. J. Chou and J. M. Eldridge, *This Journal*, **117**, 1287 (1970).
10. C. M. Osburn and D. W. Ormond, *ibid.*, **119**, 591 (1972).
11. C. A. Neugebauer, J. F. Burgess, R. E. Joynson, and J. L. Mundy, *J. Appl. Phys.*, **43**, 5041 (1972).
12. R. M. Finne and D. L. Klein, *This Journal*, **114**, 965 (1967).
13. E. H. Snow and B. E. Deal, *ibid.*, **113**, 263 (1966).
14. J. M. Eldridge, R. B. Laibowitz, and P. Balk, *J. Appl. Phys.*, **40**, 1922 (1969).
15. H. L. Hughes, R. D. Baxter, and B. Phillips, *IEEE Trans. Nuc. Sci.*, **NS-19**, 256 (1972).

Curie Points of Electrodeposited Nickel Films

M. Ya. Popereka

Graduate School of Applied Science, The Hebrew University of Jerusalem, Israel

ABSTRACT

An abnormally low Curie temperature was observed in nickel films up to 50 μm thick, which were electrodeposited from sulfate solutions containing saccharin. In several cases this abnormal Curie point was 100° or more below that of pyrometallurgical bulk nickel. The phenomenon is explained by the formation of solid solutions of sulfur and carbon in nickel, saccharin being the main source of the sulfur and carbon.

It has been shown (1-5) that in very thin nickel films the Curie temperature is lower than it is in bulk samples of that metal (in the latter $\theta_K \cong 354$°C). According to Neugebauer (4), this phenomenon is observed only up to thicknesses of 27Å, but Goureaux and Colombani (5) observed it in films as thick as 1000Å. The lowering of the Curie temperature in such thin films has been explained by the "thin film" state theories (7-9). Films of a thickness over 10^3Å are considered theoretically as bulk samples; also, measurements have shown that the Curie points in such films do not differ from those measured in bulk samples (6).

This paper describes nickel films of thicknesses up to ~50 μm possessing abnormally low Curie temperatures. This property is not connected with the thin film state, since the films are too thick, but is, as is shown later, connected with the technology used for preparation of the films.

Experimental

Nickel films were electrolytically deposited from a solution of composition (in grams/liter): $NiSO_4 \cdot 7H_2O$, 294; H_3BO_3, 30; and Rochelle salt, 25. Saccharin was added to the solution (1 g/liter unless otherwise indicated). Except in specified cases, the electrodeposition current density was 2 A/dm^2, the temperature of the solution 22°C, and *p*H 2.3. Polished copper rods of 2.2 mm diameter served as substrates.

The Curie points were measured by three methods. The first involved measurement of the dependence on temperature of the electric resistance by means of the automatically recording bridge-circuit. The second method was determination of the temperature at which the maximum differential magnetic permeability became zero (as observed by differential hysteresis loops displayed on the screen of an oscilloscope). The third method was based on the drop in value of the initial permeability near the Curie point; the initial permeability was measured using a device the main features of which are described in Ref. (11). In all cases, the rate of heating of the oven containing the sample was 5 deg/min and was held strictly constant. The temperature of the sample was, in all cases, controlled by a Chromel-Alumel thermocouple, graduated according to the melting points of gallium (99.999%), lead and tin (both 99.99%). The results obtained by the three methods (of which the third was the most reliable and accurate) are shown in Fig. 1-3. No measurement exceeded the margin of errors indicated.

Key words: ferromagnetic properties, magnetic films, incorporation of organic substances, solid solutions.

Results

As can be seen from the graphs, the Curie point in the films studied was, in a number of cases, lower than that in pyrometallurgical nickel (control measurements of the Curie point on the latter are represented by the dashed line in Fig. 2). In some cases, the Curie point dropped to 240°-250°C, *i.e.*, to more than 100° below the "normal" value. Increasing the electrodeposition current density (Fig. 1) elevated the Curie temperature somewhat, bringing it nearer to its normal value. A similar effect could be obtained by superimposing a magnetic field along the substrate axis (Fig. 2) during the deposition of the film, and also by

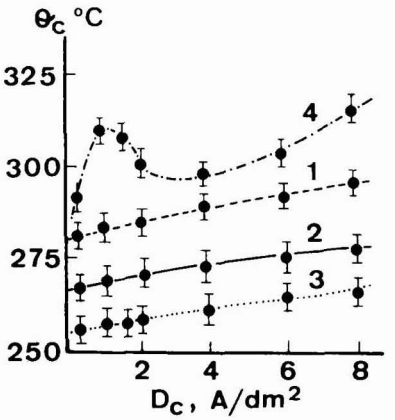

Fig. 1. Dependence of the Curie temperature of nickel films on the cathode current density. Curves 1, 2, 3: films deposited without the superposition of a magnetic field; curve 4: in field 975 Oe parallel to the substrate axis. The saccharin concentration in the solution (grams/liter) is: curve 1, 0.1; curve 2, 0.5; curves 3 and 4, 1.0. Film thickness, 10 $\pm$ 0.2μ.

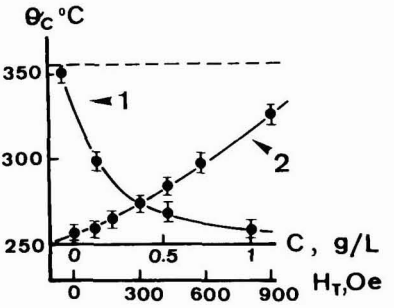

Fig. 2. Dependence of the Curie temperature of nickel films on the saccharin concentration in the solution (curve 1) and on the intensity of the technological magnetic field (curve 2). For curve 1, $H_T = 0$; for curve 2, $c = 1$ g/liter. The film thickness is $10 \pm 0.2\mu$.

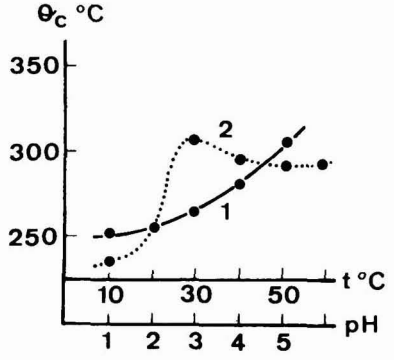

Fig. 3. Dependence of Curie temperatures of nickel film on the solution temperatures (curve 1) and on pH of the solution (curve 2). For curve 1, pH = 2.3; for curve 2, $t = 22°$. The film thickness is $10 \pm 0.2\mu$.

raising the solution temperature (Fig. 3). On the other hand, an increase in the concentration of saccharin in the plating solution (Fig. 2) moved the Curie point away from that of a pyrometallurgical nickel. In the absence of saccharin, the Curie point of the nickel film electrodeposited from a sulfate bath was ~352°C, *i.e.*, differing little from the value measured on a sample of pyrometallurgical nickel, of ~354°C. The Curie point of a nickel film deposited from a solution containing $NiCl_2 \cdot 6H_2O$, 150 g/liter and H_3BO_3, 30 g/liter, but containing no organic compounds, coincided with that of the sample of pyrometallurgical origin.

The results shown on the graphs can be supplemented by the following data. In the range of thicknesses from ~2 to ~50 μm, no substantial dependence has been discovered between the Curie points of the films and their thickness. The annealing of the films at 100°C (in a vacuum of $\sim 10^{-5}$ Torr for 3 hr) changed the Curie point very little (for example, for films deposited at 2 A/dm^2 in the presence of 1 g/liter saccharin, the change is from ~260° to ~265°C), but an identical annealing at 500°C increased the Curie temperature to as great as 354°C, *i.e.*, to the normal value.

Discussion

The Curie temperature is a magnitude which is structure-sensitive only to a small degree. Factors such as difference in internal stresses, in concentration of defects, in grain size, etc., cannot account for such a large range of measured Curie points. The results described above enable us to assume that the anomalously low values of the Curie temperatures observed are due to the codeposition of an alien material with the nickel, the main source of which is saccharin.

The assumption that the cause of the observed anomaly is the formation of a solid solution of the cathode hydrogen in the nickel (12) is contrary to the observed facts. Indeed, as shown in Ref. (13), with an increase in the saccharin concentration in the solution, the occlusion of hydrogen in the nickel film decreases; at the same time, the Curie point decreases from its normal value (Fig. 2, curve 1). Moreover, the nickel deposited from a chloride solution contains an amount of hydrogen approximately equal to that deposited from a sulfate solution, but in the first, the Curie point does not differ from its normal value, while in the second, it does. Thus, it is not hydrogen but other impurities that are responsible for the lowering of the Curie point.

As shown in Ref. (14) and (15), nickel films electrodeposited in the presence of a series of organic compounds, including saccharin, contain carbon (up to 0.2% by weight) and sulfur, the sulfur content generally exceeding that of the carbon. Formation of solid solutions of the elements in the nickel could be the cause of the observed phenomena.

It has been found in Ref. (16) that the Curie point of the solid solution of carbon in nickel decreases linearly with the increase in carbon content by ~30°/atom per cent (~0.2% by weight). Hence, the presence of carbon in the films studied can account for a large part of the drop in the Curie point.

We have not found any mention of the influence of sulfur on the Curie point of nickel in the literature. It can be expected that the influence of sulfur is qualitatively identical to that of other nonferromagnetic elements [they all lower the Curie point of nickel by different degrees (4)]. Hence, we can ascribe the observed phenomenon to the joint effect of sulfur and carbon.

The above explanation falls in with the facts. With an increase in current density, the amount of sulfur and carbon in the film decreases (15), since metal grows at a higher speed while sulfur and carbon are being included into the growing layers of the metal at a constant speed. At the same time, the Curie point approaches its normal value (Fig. 1). Increasing the concentration of saccharin causes the amount of sulfur and carbon in the film to increase (15), and the Curie point is lowered from that of pure nickel (Fig. 2). The same correlation is observed for the other dependencies.

Some differences between the Curie points of films deposited without saccharin from a sulfate bath and those of pure nickel are probably due, as well, to the fact that a definite amount of sulfur from the sulfate, or carbon from the Rochelle salt, is incorporated into the film. Indeed, when the film is deposited from a chloride solution containing no sulfur or organic additives, it has a normal Curie point.

Annealing at a sufficiently high temperature (in our case ~500°C) must lead to the disintegration of the solid solutions of sulfur and carbon in the nickel, hence the Curie acquires a normal value.

If the suggested explanation is correct, the conclusion may be drawn from curve 1, Fig. 2 that the superposition of a magnetic field during deposition of the film leads to a substantial decrease in the amount of alien material in the film.

Acknowledgment

The author wishes to express his gratitude to N. Suponyev and A. Ivanov who took an active part in the described experiments, and to Dr. I. Fried for her invaluable help in the preparation of the manuscript.

Manuscript received March 15, 1974.

Any discussion of this paper will appear in a Discussion Section to be published in the December 1975 JOURNAL. All discussions for the December 1975 Discussion Section should be submitted by Aug. 1, 1975.

REFERENCES

1. A. Colombani, G. Goureaux, and P. Huet, *J. Phys. Radium*, **20**, 303 (1959).
2. A. Colombani and G. Goureaux, *Compt. Rend.*, **248**, 380 (1959).
3. K. Kuwahara, *J. Phys. Soc. Japan*, **14**, 1247 (1959).
4. C. A. Neugebauer, *Phys. Rev.*, **116**, 1441 (1959).
5. G. Goureaux and A. Colombani, *Compt. Rend.*, **246**, 1979 (1958).
6. S. V. Vonsovskii, Magnetizm, Publ. "Nauka," Moscow (1971) (Russian).
7. M. J. Klein and R. S. Smith, *Phys Rev.*, **81**, 378 (1952).
8. L. Valenta, *Izv. Akad. Nauk SSSR, Ser. Fiz.*, **21**, 879 (1957) (Russian; English *Transl., Bull. Acad. Sci. USSR, Phys. Ser.*).
9. A. Corciovei, *J. Phys. Chem. Solids*, **20**, 162 (1961).
10. M. Prutton, "Thin Ferromagnetic Films,' Butterworths, London (1961).
11. V. I. Berzhanski, G. A. Petrakovski, and V. N. Seleznev, Coll. "Tonkie magnitniye plionki, vychyslitelnaya tekhnika i radiotekhnika," Vol. 2, p. 140, Krasnoyarsk Institut Fiziki (1970) (Russian).
12. H. Bauer and E. Shmidbauer, *Z. Phys.*, **164**, 307 (1961).
13. V. V. Reklite and Yu. Matulis, Coll. "Navodorozhivanie metallov i borba s vodorodnoy khrupkostyu," p. 158, Publ. Moskoviskii Dom nautchno tekhnicheskoy propagandy, Moscow (1968) (Russian).
14. A. I. Bodnevas, A. V. Petrauskas, Yu. K. Viagis, and Yu. Yu. Matulis, Coll. "Issledovaniya v oblasti elektroosazhdeniya metallov," p. 9, Publ. Rintip, Vilnius (1968) (Russian).
15. D. S. Zheimite, A. I. Bodnevas, and Yu. Yu. Matulis, *ibid.*, p. 22.
16. F. C. Schwerer, *J. Appl. Phys.*, **40**, 2205 (1969).

Wavelength Dependence of PVA-Phosphor-Dot Photohardening

P. B. Branin and W. H. Fonger

RCA Laboratories, Princeton, New Jersey 08540

ABSTRACT

Dichromate-sensitized PVA coatings were exposed through 23V dot-aperture masks and several different absorption filters in order to study the dependence of dot growth and adherence upon exposure wavelength. For clear-resist coatings exposed under weak-absorption conditions, the hardening spectrum was proportional to the dichromate absorption spectrum. For coatings containing phosphor, the hardening spectrum was fairly flat and insensitive to the dichromate absorption spectrum; this different spectrum resulted because scattering increased the pathlengths of exposure light and led to strong-absorption conditions. With regard to phosphor-dot adherence, except at wavelengths below 350 mμ where phosphor bandgap absorption was strong, adherence was insensitive to the exposure wavelength, that is, to dichromate strong or weak absorption.

The photohardening of dichromate-sensitized polyvinyl alcohol (PVA) coatings, both with and without phosphor, was studied as a function of exposure wavelength. See Kosar (1) for a general review of dichromated colloids. Dichromate absorption spectra are shown in Fig. 1. These spectra were taken for $(NH_4)_2Cr_2O_7$-PVA aqueous solutions but are similar to $K_2Cr_2O_7$ solution spectra reported by Kortüm (2) and Davies and Prue (3). The spectra show strong, broad, u.v. absorption bands peaking near 270 and 370 mμ plus a weak, blue-green absorption tail extending to 530 mμ. For acid solutions which emphasize $Cr_2O_7^{-2}$ over CrO_4^{-2} ions, the u.v. bands are displaced to slightly shorter wavelength, the resolution between the bands is reduced, and the blue-green absorption tail is larger relatively.

O'Brien (4) and Koana (5) have reported photohardening rates of some dichromated colloids to be proportional to the rates at which photons are absorbed in dichromate ions, and this behavior is indicated for the PVA coatings studied here. However, this behavior does not make the hardening spectrum unique. Effective hardening spectra for coatings with and without phosphor were found to be different. The differences had to do with absorption conditions. For weak absorption, the hardening spectrum is proportional to the dichromate absorption spectrum; for strong absorption, it is flat and insensitive to the dichromate absorption spectrum.

Experimental

The phosphor used in these studies was $Zn_{0.92}Cd_{0.08}S$:Cu green phosphor (Z-910D). Slurries for the phosphor coatings were prepared by ball-milling a stock of phosphor, PVA, and water from which final coating formulations were made by adding PVA, water, $(NH_4)_2Cr_2O_7$ sensitizer (1:10 relative to PVA), an acrylic resin, and a surfactant. For clear-resist coatings, the phosphor was eliminated and the water content adjusted, but the ratios of the remaining constituents were maintained the same.

The coatings were applied to 23V television faceplates using a stationary single-head slurry machine in a conventional rotating-tilting and final-spinout mode. Coating weight and uniformity were controlled by adjusting spinout speed and duration.

Key words: phosphor-dot screening, photochemistry, PVA-hardening spectrum.

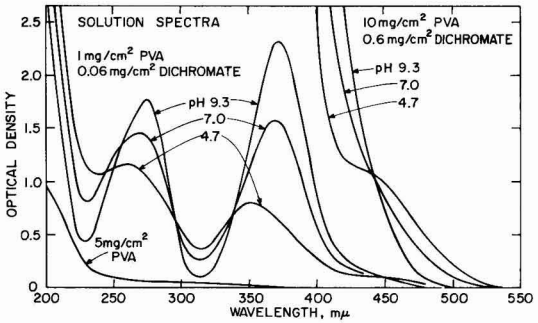

Fig. 1. Absorption spectra of $(NH_4)_2Cr_2O_7$-PVA aqueous solutions. The pH was adjusted with NH_4OH. These spectra were taken with a Cary Model 14 spectrophotometer.

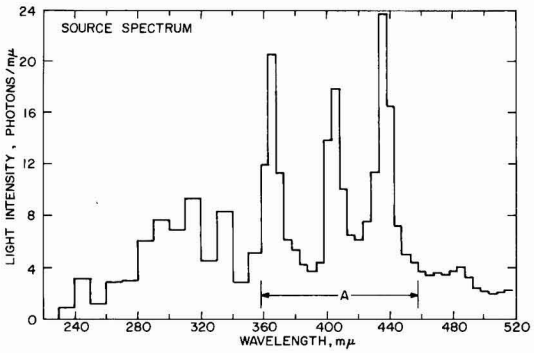

Fig. 2. Spectrum of the BH6-1 Hg capillary lamps used for the dot exposures. This spectrum contains strong Hg lines at 365, 404, and 436 mμ plus an underlying continuum. Normalization was made such that the 100 mμ interval labeled A contains 1000 photons.

The coatings were exposed in a single-position lighthouse equipped with a BH6-1 Hg capillary lamp and 100 mil quartz collimator. The spectrum of this source is shown in Fig. 2. The spectrum above 360 mμ was measured with a calibrated spectrometer. The spectrum below 360 mμ was adapted from vendor data (6) but was also roughly verified using some u.v. filters and the quantum counter liumogen (7). The coatings were exposed through a 23V dot-aperture mask plus several 2 × 2 in. absorption filters positioned below the mask as illustrated in Fig. 3. Exposures were made with the lighthouse lens package removed to provide high enough light intensity to offset low transmissions of the filters, to avoid center-to-edge variations in the spectrum caused by the lens coating, and to preserve the source spectrum down to 230 mμ.

The transmissions of the absorption filters are shown in Fig. 4. Apart from a $NiSO_4$-solution cell used in the short u.v. region (240-350 mμ), the filters were Corning glass color filters of the 3, 7, and 0 series. The 3-series filters divide up the blue-green region of the spectrum. The remaining filters involved 7-series filters and divide up the u.v. region. The transmission of the 23V panel glass is also shown because it was an added filter for some exposures made through the panel.

After exposure, the dot patterns were developed on a rotating head in a water spray at 104°F and 17 psi for 30 sec.

Dot Growth with Exposure Time

The observed growth of dot diameters with exposure time is shown in Fig. 5 for 4.5 mg/cm² phosphor coat-

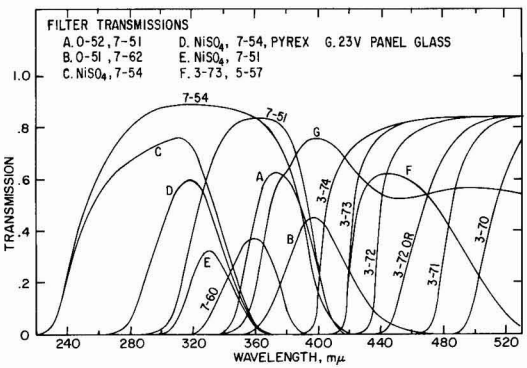

Fig. 4. Transmissions of the $NiSO_4$ and Corning filters used for filtered dot exposures; 3-72 OR was a particularly orange 3-72 filter.

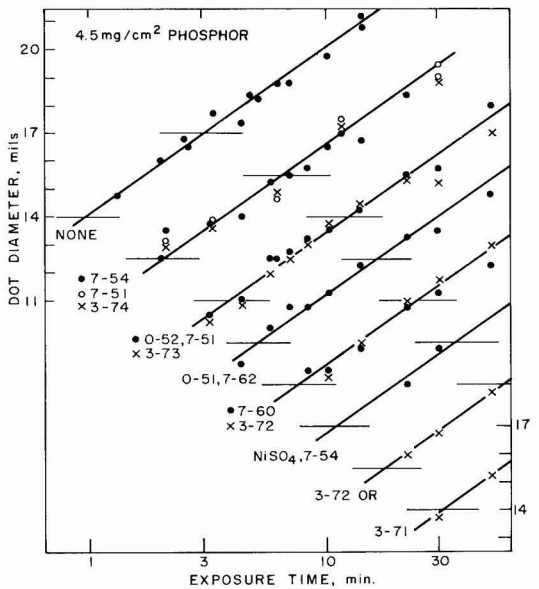

Fig. 5. Observed dot diameters vs. exposure time for 4.5 mg/cm² phosphor coatings exposed through various absorption filters. For the various sets of data, the two short horizontal lines mark the levels of 14- and 17-mil dot diameters. Exposure times have been corrected to constant light intensity.

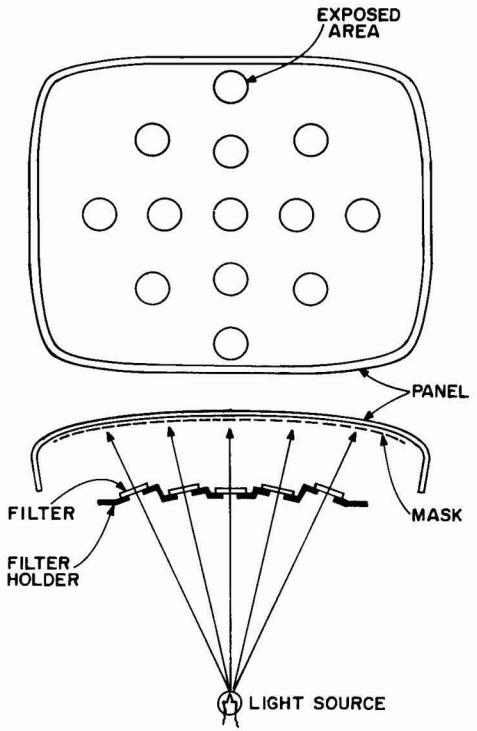

Fig. 3. Lighthouse arrangement used to make thirteen filtered exposures on 23V panels. The spacing between the mask and panel was 0.60 in.

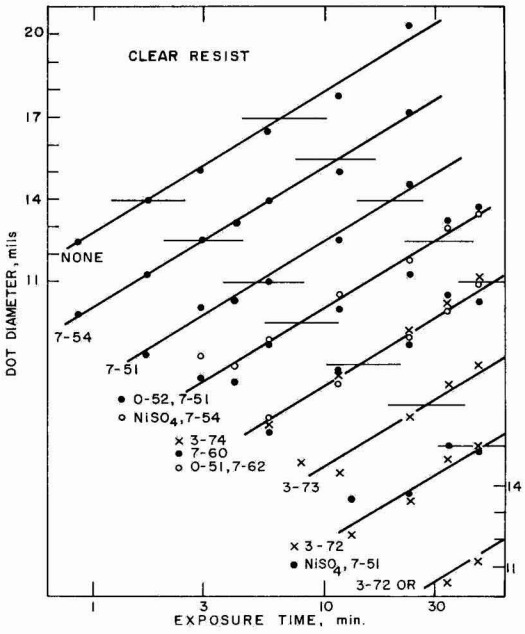

Fig. 6. Observed dot diameters vs. exposure time for clear-resist coatings.

ings. Exposures in the blue-green region through 3-series filters are shown by crosses and in the u.v. region through 7-series filters by dots. To avoid overlapping of data points, the ordinate scale is offset for the various sets of data, and the short horizontal lines show the 14-mil and 17-mil diameter levels. Dot diameters measured at the various filter positions (see Fig. 3) were corrected to center-panel values empirically. For the 23V panel mask used, 14 mils was the image size of center-panel mask holes projected from a point source, and 17 mils was the diameter of tangent tricolor dots.

For all exposures, dot diameter growth was approximately proportional to the log of the exposure time. Assuming that a fixed exposure level is needed for threshold photohardening, this behavior indicates that light intensity in the penumbra region decreased radially approximately exponentially. The slope of the D *vs.* log t lines shown in Fig. 5 corresponds to a radial $1/e$ distance of 1.30 mils.

Similar dot growth data for clear-resist coatings without phosphor are shown in Fig. 6.

Exposure times for the various filters were in different proportions for the phosphor and clear-resist coatings. That is, the hardening spectra for these coatings were different. Relative to exposure times in the near-u.v. region (most 7-series filters) as a base, the phosphor coatings required longer exposure times in the short-u.v. region with the $NiSO_4$, 7-54 filter and the 7-54 filter and shorter exposure times in the blue-green region (3-series filters). For example, exposure times for the short-u.v. $NiSO_4$, 7-54, near-u.v. 7-60, and blue-green 3-73 filters were in that order for phosphor coatings but were in the reverse order for clear-resist coatings.

Since the slopes of the D *vs.* log t lines are fairly close in all cases, we will characterize hardening rates simply by the exposure times required to produce dots of a particular size, namely, 14 mils. These exposure times, T_{CR}, and $T_{4.5}$, and their ratios, $T_{CR}/T_{4.5}$, are listed in Table I. The ratios $T_{CR}/T_{4.5}$ are ≈ 6 in the blue-green region, ≈ 2 in the near-u.v. region, and ≈ 0.7 in the short-u.v. region where light is strongly absorbed in the phosphor bandgap.

The exposure times in Table I have been compared with simple, limiting hardening rates. Following behaviors reported for some other dichromated colloids (4, 5), we assume that, following absorption in dichromate ions at wavelength λ, the quantum efficiency for hardening $\eta(\lambda)$ is insensitive to λ. Hardening rates H_i are then proportional to the rates at which photons are absorbed in dichromate ions

$$H_i \propto \int d\lambda L(\lambda) t_i(\lambda) a(\lambda)$$

where $L(\lambda)$ is the source spectrum in photons per unit wavelength (Fig. 2), $t_i(\lambda)$ is the transmission of filter i (Fig. 4), and $a(\lambda)$ is the fraction of incident light absorbed in dichromate ions. For weak absorption $a(\lambda) << 1$, $a(\lambda)$ is proportional to the dichromate absorption constant $k(\lambda)$. For strong absorption $a(\lambda) \approx 1$, $a(\lambda)$ is insensitive to λ and can be omitted from the integrals.

The clear-resist dot exposures were made under weak-absorption conditions. Layer transmissions were ≈ 0.70 at the dichromate 370 mμ absorption peak. Thus, in the table, the clear-resist exposure times T_{CR} have been compared with the weak-absorption hardening rates $\int d\lambda L(\lambda) t_i(\lambda) k(\lambda)$. The products $T_{CR} \int d\lambda L t_i k$ decrease somewhat from shorter to longer wavelengths (from top to bottom in the table) but are relatively constant compared to the strong wavelength variation of the dichromate absorption constant $k(\lambda)$. Thus, the quantum efficiency $\eta(\lambda)$ was relatively constant, and the clear-resist hardening spectrum was approximately the dichromate absorption spectrum $k(\lambda)$.

In the integrals, $k(\lambda)$ was taken proportional to the dried-layer absorption spectrum shown in Fig. 7. This spectrum was taken for fresh, dried, clear-resist coatings deposited on 23V panels (transmission measurements possible down to 360 mμ) and on 2 × 2 in. quartz slides. The resist had the same component ratios as the resist used in the clear-resist dot exposures, but the water content was reduced to give thicker coatings with absorption increased sixfold, as convenient for absorption measurements. The dried-

Table I. Observed exposure times T_{CR} and $T_{4.5}$ to make 14-mil dots for clear-resist and 4.5 mg/cm^2 phosphor coatings exposed through various absorption filters. These times are compared with weak- and strong-absorption hardening rates $\int d\lambda\, Lt_i k$ and $\int d\lambda\, Lt_i$, respectively. The source spectrum $L(\lambda)$ and the dichromate absorption spectrum $k(\lambda)$ are expressed in the arbitrary units used in Fig. 2 and 7, respectively.

Filter	T_{CR}, min	$T_{4.5}$, min	$T_{CR}/T_{4.5}$	$\int d\lambda\, Lt_i k$	$T_{CR} \int d\lambda\, Lt_i k$	$\int d\lambda\, Lt_i$	$T_{4.5} \int d\lambda\, Lt_i$
$NiSO_4$, 7-54	7.8	11.0	0.71	325.0	2540.0	362.0	3980.0
$NiSO_4$, 7-51	42.0			39.4	1650.0	64.0	
7-54	2.9	2.1	1.4	703.0	2040.0	770.0	1620.0
7-51	5.1	2.1	2.4	403.0	2060.0	470.0	990.0
None	1.7	0.95	1.8	1095.0	1860.0	1800.0	1710.0
7-60	14.0	7.8	1.8	115.0	1610.0	117.0	910.0
0-52, 7-51	8.2	3.9	2.1	219.0	1800.0	234.0	910.0
0-51, 7-62	14.0	5.2	2.7	93.0	1300.0	190.0	990.0
3-74	14.0	2.1	6.7	98.0	1370.0	581.0	1220.0
3-73	27.0	4.0	6.8	54.0	1460.0	446.0	1780.0
3-72	48.0	7.8	6.2	24.5	1180.0	261.0	2040.0
3-72 OR	≈140.0	18.0	≈8.0	7.7	≈1100.0	128.0	2300.0
3-71	>200.0	≈30.0	>6.0	2.5	>500.0	69.0	≈2100.0

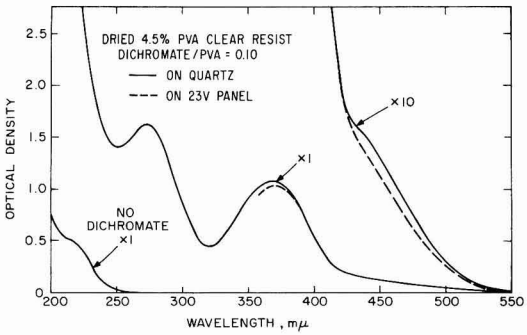

Fig. 7. Absorption spectra of dried, clear-resist coatings on a 23V panel and a 2 × 2 in. quartz slide. Substrate absorption has been subtracted out. Without dichromate sensitizer, absorption was negligible down to 250 mμ. For the thinner clear-resist coatings used in the dot exposures, the optical densities were 1/6 times the values in this figure.

layer spectrum is similar to the dichromate solution spectra shown in Fig. 1 but is not identical to any one of these spectra. The position of the 370 mμ peak is typical of the neutral solution, but the relative size of the blue-green absorption tail is typical of the acid solution.

The phosphor exposure times $T_{4.5}$ in the table have been compared with the strong-absorption hardening rates $\int d\lambda L(\lambda) t_i(\lambda)$.[1] For the phosphor exposures, light scattering increased light pathlengths in the coatings and thereby enhanced absorption and hardening. In addition, dichromate absorption competed with phosphor absorption. For $\lambda < 350$ mμ (strong phosphor bandgap absorption), hardening was inefficient, and the product $T_{4.5}\int d\lambda L t_i$ was larger ($NiSO_4$, 7-54 filter). For $\lambda > 350$ mμ (phosphor Cu-impurity absorption), the products $T_{4.5}\int d\lambda L t_i$ were smaller and increased somewhat from shorter to longer wavelengths. Nevertheless, at these wavelengths, these products were relatively constant compared to the strong wavelength variation of the dichromate absorption constant, and the hardening spectrum of the phosphor coatings can be described as fairly constant and insensitive to the dichromate absorption constant.

For 4.5 mg/cm² phosphor coatings, one-half of the hardening capacity of BH6 light is contained in wavelengths above 400 mμ, that is, in the region of dichromate weak, blue-green absorption. This result is evident from Fig. 5 where the hardening rates using the 7-54 and 3-74 filters were the same. The 7-54 and 3-74 filters are low-pass and high-pass filters, respectively, about the wavelength point 400 mμ. See the filter profiles in Fig. 4.

Dot-growth curves similar to those shown in Fig. 5 and 6 were also obtained for 2 mg/cm² phosphor layers and for 4.5 mg/cm² phosphor layers exposed through the panel glass. In the latter cases, the penumbra shape at panel center was maintained as in normal exposures by using the same source-to-mask distance and the same effective mask-to-coating distance.[2] After correction for the panel-glass transmission at the exposure wavelength, these exposure times were the same as for 4.5 mg/cm² phosphor coatings exposed in the normal way. That is, exposure times were the same for exposures from either side. For the 2 mg/cm² phosphor coatings, the wavelength dependence of the hardening rate was intermediate between the two wavelength dependences described above for clear-resist and 4.5 mg/cm² phosphor coatings.

[1] For exposures with 3-series filters, the integrals $\int d\lambda\, Lt_i$ were arbitrarily terminated at 518 mμ near the end of dichromate absorption. For a different termination point, these integrals would be somewhat different.

[2] For exposures through the panel, the light source and filters were maintained as in Fig. 3, and the coated panel was inverted. A formed mask cut from its frame was attached to the bottom (convex) side of the panel via standoffs of length $q_2 = 0.30$ in. The effective mask-to-coating distance was then $q_{eff.} = q_1/n_1 + q_2$, where q_1 was the thickness of the panel glass and n_1 its index of refraction.

Dot Adherence

Except for exposures in the short-u.v. region ($\lambda <$ 350 mμ) where phosphor bandgap absorption was strong and adherence poor, dot adherence was insensitive to exposure wavelength. Exposure with any filter above 350 mμ always led to adherence failure at exposures corresponding to 11-11½ mils dot diameter for clear-resist coatings, to 12-12½ and 15-16 mils for 2 and 4.5 mg/cm² phosphor coatings, respectively, and to 12-12½ mils for 4.5 mg/cm² phosphor coatings exposed through the panel.

The better phosphor-dot adherence for 2 mg/cm² coatings and for 4.5 mg/cm² coatings exposed through the panel is qualitatively explained by obvious gradings of exposure light intensity across the coatings. However, the insensitivity of dot adherence to dichromate strong 370 mμ or weak blue-green absorption seems surprising. We believe that, for the phosphor layers, gradings of light intensity across the layers were determined primarily by the scattering paths of the light and only secondarily by light absorption. In this way, the adherence could become insensitive to the dichromate absorption constant.

Conclusions

Relative to the photohardening rate in the dichromate strong 370 mμ absorption region, hardening in the dichromate weak blue-green absorption region was three times greater for 4.5 mg/cm² phosphor coatings than for clear-resist coatings. For the clear-resist coatings, exposures approximated weak-absorption conditions, and the hardening spectrum was proportional to the dichromate absorption spectrum. For the 4.5 mg/cm² phosphor coatings, exposures more nearly approximated strong-absorption conditions, and the hardening spectrum was fairly flat and insensitive to the dichromate absorption spectrum. For 4.5 mg/cm² phosphor coatings, one-half of the hardening capacity of BH6 light resides in blue-green wavelengths above 400 mμ. Except at wavelengths below 350 mμ where phosphor bandgap absorption was strong, phosphor-dot adherence was insensitive to exposure wavelength, that is, to dichromate strong or weak absorption.

Manuscript received Aug. 23, 1974. This was Paper 122 presented at the San Francisco, California, Meeting of the Society, May 12-17, 1974.

Any discussion of this paper will appear in a Discussion Section to be published in the December 1975 JOURNAL. All discussions for the December 1975 Discussion Section should be submitted by Aug. 1, 1975.

Publication costs of this article were partially assisted by RCA Corporation.

REFERENCES

1. J. Kosar, "Light-Sensitive Systems," Chap. 2, John Wiley & Sons, Inc., New York (1965).
2. G. F. Kortüm, *Z. physik. Chem.* (*B*), **33**, 243 (1936).
3. W. G. Davis and J. E. Prue, *Trans. Faraday Soc.*, **51**, 1045 (1955).
4. B. O'Brien, Jr., *J. Optical Soc. Am.*, **42**, 101 (1952).
5. Z. Koana, Intern. Congress of Photographic Science, Sect V, Sept. 1967.
6. Illumination Industries, Inc., Sunnyvale, Calif. 94086.
7. N. Kristianpoller and D. Dutton, *Appl. Optics*, **3**, 287 (1964).

Luminescence Properties of Thiogallate Phosphors

III. Red and White Emitting Phosphors for Flying Spot Scanner Applications

T. E. Peters

GTE Laboratories Incorporated, Waltham, Massachusetts 02154

ABSTRACT

Ions with the ns^2 electronic configuration were investigated as activators in the $SrGa_2S_4$ host lattice. Phosphors activated with Sn^{2+} or Pb^{2+} were found to cathodoluminesce in the red spectral region and exhibit relative efficiencies (η_{cr} Rel.) of 1.1 and 4.6%, respectively. The Pb^{2+} phosphor has a short fluorescent decay time ($I_o/100 \sim 10^{-6}$ sec) and was found suitable for use as the red screen component in a flying spot scanner tube (FSST) employed as the transducer in color video playback. Coactivation of $SrGa_2S_4$ by Ce^{3+} and Pb^{2+} was found to result in a white-emitting phosphor that exhibits lower noise in FSST screens than is usually found when phosphor blends are employed.

The cathodoluminescence emission and decay properties of the Ce^{3+} activated alkaline earth thiogallates were reported earlier (1) with particular emphasis on factors governing the use of these materials in flying spot cathode-ray tubes. Phosphors activated with ions possessing the ns^2 electronic configuration (Tl^{1+}, Sn^{2+}, Pb^{2+}, Sb^{3+}, Bi^{3+}) are also of interest for use in this type of device because their fluorescence lifetime should be very short. As a consequence, these ions were also evaluated as activators in the $SrGa_2S_4$ host lattice, and this paper describes the cathodoluminescence emission and decay characteristics of the Pb^{2+} and Sn^{2+} activated, and Ce^{3+}-Pb^{2+} coactivated $SrGa_2S_4$ phosphors and discusses their application in flying spot scanner tubes (FSST) designed for use in color video playback systems.

Experimental

Phosphor preparation.—The phosphors described herein were synthesized according to the general formulas

$$Sr_{1-x}M_xGa_2S_4 (M = Tl^{1+}, Sn^{2+}, Pb^{2+})$$

$$Sr_{1-2x}M_xNa_xGa_2S_4 (M = Sb^{3+}, Bi^{3+})$$

$$Sr_{1-(2x+y)}Ce_xNa_xPb_yGa_2S_4$$

by reacting mixtures of the previously prepared, high purity sulfides at 900°-950°C in a stream of H_2S. The activators were generally introduced at sufficiently high concentration to assure stoichiometry, and lower doping levels were achieved by dry dilution. Monovalent sodium was added as Na_2SO_4, usually in excess of the stoichiometric amount, to serve as a mineralizer and provide charge compensation for the trivalent activators. Any sodium not incorporated in the $SrGa_2S_4$ host lattice was subsequently removed from the phosphor by washing with demineralized water. The Pb^{2+} and Sn^{2+} activated phosphors did not require valence compensation; consequently, the Na_2SO_4 was usually omitted and the higher reaction temperature was employed. In the case of Tl^{1+}, charge compensation was allowed to occur through a vacancy mechanism.

Measurements.—Standard analytical techniques were employed to monitor the purity and stoichiometry of the sulfide reagents and finished phosphors. X-ray powder diffraction was used to ascertain formation of the $SrGa_2S_4$ compound.

Emission spectra were recorded in terms of relative energy, and the relative cathode-ray efficiency values (η_{cr} Rel.) were obtained by comparing the integrated area under the spectral energy distribution curves to that of selected thiogallate and NBS-1021 phosphors of known absolute efficiency.

Cathodoluminescence brightness levels of $SrGa_2S_4$:Pb were measured under conditions simulating those found in a color video playback system employing flying spot scanners (3). Phosphor-coated conducting glass slides were placed in a demountable CRT and excited with a 25 kV-100 μA electron beam which was scanned at the normal TV rate over a 5.7 cm × 7.6 cm raster. The emission was detected by a Gamma photometer equipped with a Wratten No. 25 filter.

Cathodoluminescence decay times were measured by pulsing a 20 kV electron beam of a 12.7 cm diameter FSST at a rate of 60 Hz with a pulse duration of 100 nsec. The fluorescence was detected by a photomultiplier tube equipped with a Wratten No. 25 or 47B filter and displayed on an oscilloscope. Screen noise measurements were obtained by monitoring the change in emission intensity of the flying spot of light as it was scanned across the screen of a 12.7 cm FSST.

Results and Discussion

Of the ns^2 ions evaluated as activators only Sn^{2+} and Pb^{2+} produced visible emission at room temperature. The cathodoluminescence emission and decay characteristics of these materials are given in Table I, together with similar data for $Y_3Al_5O_{12}$:Ce (YAG:Ce) (2). The latter material is a fast decay phosphor that has been advanced as a replacement for the ZnO:Zn (P-24) screen in a version of the FSST employed as a playback transducer for color television. The radiant efficiency under cathode-ray excitation (η_{cr} Rel.) of the $SrGa_2S_4$:Pb (2 atom per cent [a/o]) is slightly higher than that of YAG:Ce while the $SrGa_2S_4$:Sn (1 a/o) phosphor has a lower efficiency.

The decay time (β) given in the last column of Table I is the time required for the fluorescence to decrease to $I_o/100$. This value has been found to be more significant for FSST phosphor evaluation than the fluorescence lifetime, τ-(decay to I_o/e), because it includes even the low level, long persistence components of the decay. The fluorescence intensity *vs.* time curve for the $SrGa_2S_4$:Sn phosphor exhibits a power law dependence ($I_o \propto t^{-n}$), and its decay time is longer than that of the other phosphors which have essentially exponential decay curves (Fig. 1). The per-

Table I. Cathodoluminescence emission and decay characteristics of Sn^{2+} and Pb^{2+} activators

Phosphor	η_{cr} (%)	λ_{max} (nm)	Decay time, β (μsec)
$SrGa_2S_4$:Pb	4.6	595	1.24
$SrGa_2S_4$:Sn	1.1	680	>10.0
$Y_3Al_5O_{12}$:Ce	3.5	550	0.54

* Electrochemical Society Active Member.
Key words: video playback, fast decay phosphors, cathodoluminescent phosphors.

Table II. Decay time quenching in $SrGa_2S_4$:Pb

Pb (atom per cent)	Co (weight per cent)	Decay β (μsec)	Relative red brightness	Mechanism used to increase decay rate
2	—	1.24	125	Concentration quenching
4	—	1.16	113	Concentration quenching
8	—	1.0	100	Concentration quenching
8	0.01	1.0	100	Transition metal quenching
8	0.1	0.98	98	Transition metal quenching

sistence of the $SrGa_2S_4$:Sn phosphor is long enough to eliminate it as a candidate for use in FSST screens; however, the decay of the Pb^{2+} activated phosphor is of a magnitude which would permit its use in systems employing electronic compensation (3).

The data in Table II shows that the decay time of $SrGa_2S_4$:Pb can be reduced slightly by concentration quenching. Although the reduction is slight, the effect appears to be real, with phosphors containing 8-10 a/o Pb consistently having decay times of 1 μsec and those with lower Pb^{2+} concentrations having longer decay times. The reduction in decay attributed to concentration quenching is accompanied by a reduction in emission intensity (Table II) and a shift of λ_{max} to lower energy.

Transition metal quenching, which produced a dramatic reduction in the decay time of the Ce^{3+} fluorescence in $SrGa_2S_4$:Ce, Na (1), is seen (Table II) to exert little influence on the fluorescence decay time of Pb^{2+} in the same host compound. This result is in agreement with that of other workers (4) who have shown that transition metal quenching does not alter the persistence of a phosphor whose fluorescence decays exponentially.

The efficiency and spectral energy distribution of the $SrGa_2S_4$:Pb phosphor make it particularly attractive for use in FSST's for color TV playback. This is shown in Fig. 2 which depicts the spectral energy distribution curves for YAG:Ce and $SrGa_2S_4$:Pb together with a spectral sensitivity curve (shaded) for a simulated red detector of a video playback system. The detector sensitivity curve was generated from a convolution of the transmission curve for a Kodak No. 25 Wratten filter and the S-4 response curve of an RCA 931A phototube. The convoluted data was then normalized by setting the optimum detector output at 100. It is evident that the $SrGa_2S_4$:Pb emission is better matched to the detector's response than is the emission of YAG:Ce. This is important because most phototubes are relatively insensitive in the red spectral region and, as a consequence, the photocurrent generated by the red detector must be amplified to a much greater extent than that of the corresponding green and blue detectors.

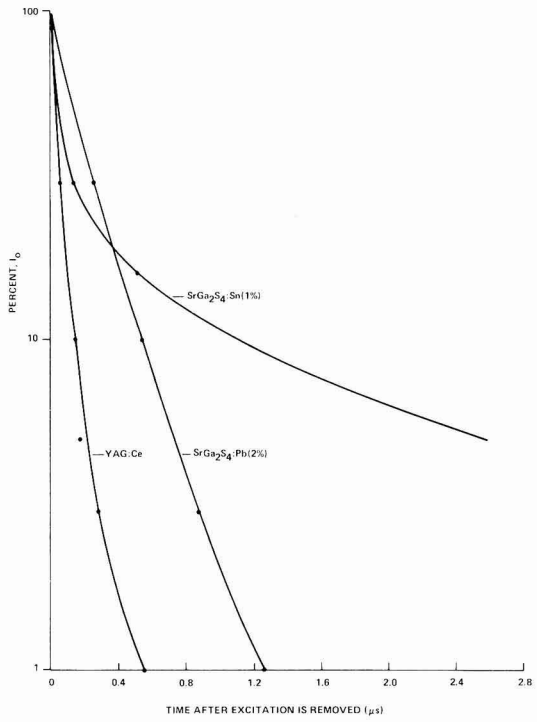

Fig. 1. Decay of fluorescence of red emitting phosphors

For color video playback applications, FSST's that exhibit a uniform emission in the visible region of the spectrum are desirable. This effect can be achieved by blending the $SrGa_2S_4$:Pb wtih a blue-emitting phosphor such as $SrGa_2S_4$:Ce,Na (1), or by activating the $SrGa_2S_4$ host compound with both Ce^{3+} and Pb^{2+}. The spectral energy distribution of the emission of FSST's prepared with the blended and single component thiogallate screens are compared to that of a commercial FSST (3) in Fig. 3. The tubes containing the thiogallate phosphors are seen to have a fairly uniform emission over the entire visible spectrum, while the commercial tube is deficient in the blue-green and red spectral regions.

The emission spectrum of the blended phosphor screen [Fig. 3(a)] can be altered to some extent by changing the ratio of its blue-to red-emitting components. Similar modifications in the spectral distribution of the single component screen [Fig. 3(b)] are best affected by altering the Ce^{3+} and/or Pb^{2+} concentration of the phosphor. This is illustrated in Fig. 4, where the trichromatic coefficients and blue (~450 nm)/red (~605 nm) peak intensity ratios (B/R) are given for $SrGa_2S_4$:Ce,Pb,Na phosphors activated with 4 or 8 a/o Pb and 0.03-0.5 a/o Ce. For materials with spectral distributions similar to that in Fig. 3(b) (viz., $B/R \cong 1$, $x \cong 0.35$, $y \cong 0.33$), the $[Ce^{3+}]$ should be in the vicinity of 0.1 a/o. When $[Ce^{3+}]$ increases much beyond this value, the blue emission band begins to dominate the fluorescence spectrum.

FSST's having the spectral distributions shown in Fig. 3 were evaluated in a color video playback system, and relevant data is reported in Table III. The data show the response of all three of the playback system's photodetectors to be significantly greater for the FSST's employing thiogallate screens. The fluorescence decay times for the thiogallate screens are somewhat longer than those exhibited by the blended phosphor screen of the commercial tube, but the longer decay times did not result in a noticeable deterioration in the televised picture. Screen noise for the blended thiogallate phosphor screen is equivalent to that of the $Ca_2Al_2SiO_7$:Ce-$Y_3Al_5O_{12}$:Ce screen, but the single component thiogallate screen is noticeably better in this respect.

Summary

Ions with the ns^2 electronic configuration were evaluated as activators in the $SrGa_2S_4$ host lattice. Under cathode-ray excitation, phosphors activated with Sn^{2+} or Pb^{2+} were found to fluoresce in the red spectral region with relative efficiencies (η_{cr} Rel.) of 1.1 and 4.6%, respectively. The Pb^{2+} activated phosphor was found to have a short fluorescence decay time

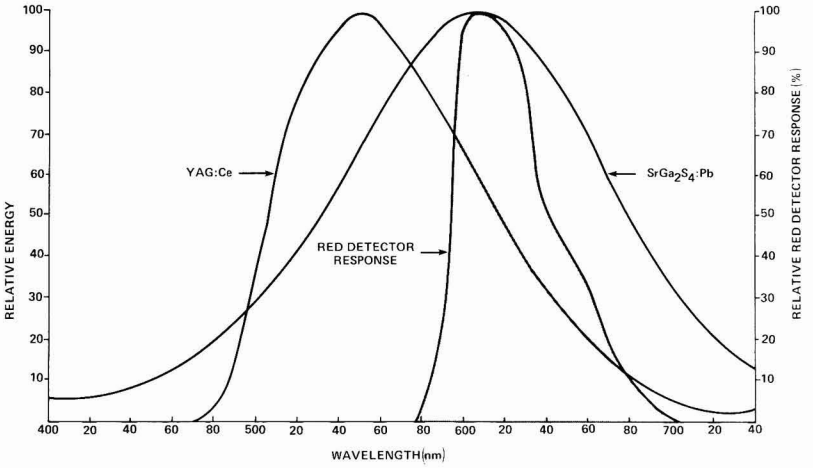

Fig. 2. Red detector response and spectral energy distribution of $SrGa_2S_4$:Pb and YAG:Ce.

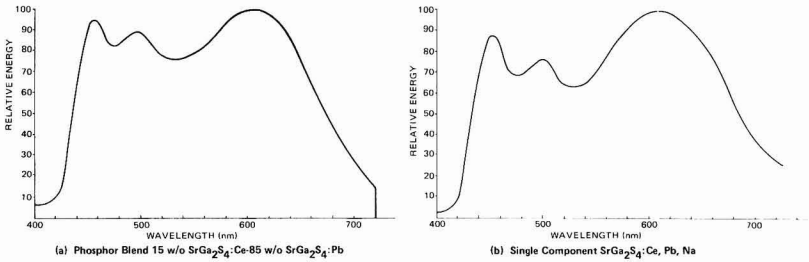

(a) Phosphor Blend 15 w/o $SrGa_2S_4$:Ce-85 w/o $SrGa_2S_4$:Pb

(b) Single Component $SrGa_2S_4$:Ce, Pb, Na

Fig. 3. Spectral energy distribution of FSST screens.

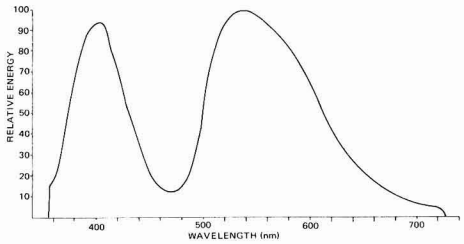

(c) Commercial Blend 25 w/o $Ca_2Al_2SiO_7$:Ce-75 w/o YAG:Ce

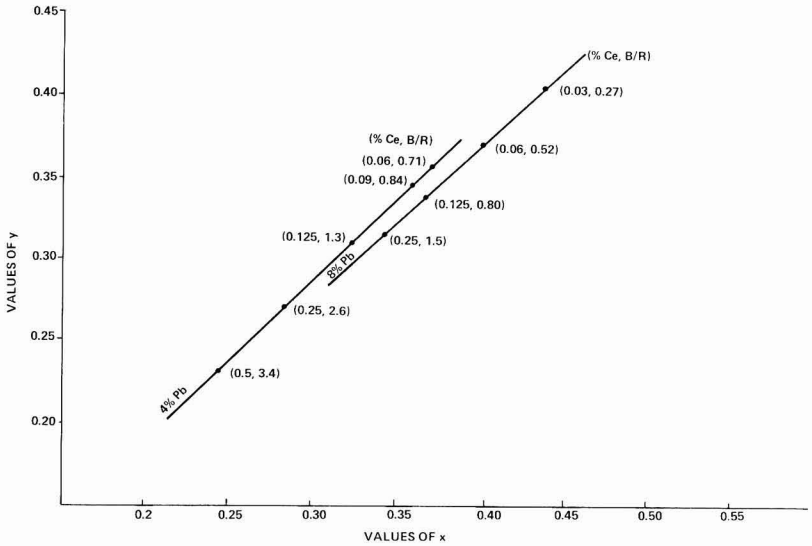

Fig. 4. Trichromatic coefficients and B/R ratios for $SrGa_2S_4$: Ce, Pb, Na phosphors.

Table III. FSST's evaluation in color video playback system

Type tube	Screen composition	Relative photodetector response			Decay time, β (μsec)		Screen noise (%)
		Blue	Green	Red	Blue	Red	
Experimental blended screen	15 w/o $SrGa_2S_4$:Ce,Na* 85 w/o $SrGa_2S_4$:Pb**	280	125	230	1.48	1.18	8
Experimental single component screen	100 w/o $SrGa_2S_4$:Ce,Pb,Na†	255	130	230	1.26	1.35	4
Commercial†† blended screen	25 w/o $Ca_2Al_2SiO_7$ 75 w/o $Y_3Al_5O_{12}$:Ce	100	100	100	0.52	0.54	8

* 4 a/o Ce.
** 8 a/o Pb.
† 0.125 a/o Ce, 8 a/o Pb.
†† Ref. (5).

($I_o/100 \sim 10^{-6}$ sec) and was judged suitable for use as the red screen component in a FSST employed as a playback transducer for color television.

For color video playback applications, FSST's that exhibit a uniform emission in the visible region of the spectrum are desirable. This was achieved by blending the $SrGa_2S_4$:Pb phosphor with a blue emitting $SrGa_2S_4$:Ce,Na or by activating the $SrGa_2S_4$ host compound with both Ce^{3+} and Pb^{2+}.

FSST's with screens containing the blended or single component thiogallate screens were found to elicit a substantially higher output from a playback system's photodetectors than a commercial tube with a screen composed of a $Ca_2Al_2SiO_7$:Ce-$Y_3Al_5O_{12}$:Ce phosphor blend. The single component thiogallate screen also exhibited lower screen noise than those of the thiogallate blend or the commercial phosphor mixture.

Acknowledgments

The author wishes to express his appreciation to T. Sisneros for brightness measurements, and to J. Ragusin for technical assistance. Thanks are also due to K. Speigel, of GTE Sylvania Electronic Tube Division, who provided much of the decay data, and to F. Palilla and S. Natansohn for manuscript review.

Manuscript submitted May 13, 1974; revised manuscript received July 26, 1974.

Any discussion of this paper will appear in a Discussion Section to be published in the December 1975 JOURNAL. All discussions for the December 1975 Discussion Section should be submitted by Aug. 1, 1975.

Publication costs of this article were partially assisted by GTE Laboratories.

REFERENCES

1. T. E. Peters, *This Journal*, **119**, 1720 (1972).
2. G. Blasse and A. Bril, *Appl. Phys. Letters*, **11**, 53 (1967).
3. C. B. Neal and H. E. Smithgall, *IEEE Trans.*, **BTR-16**, 56 (1970).
4. W. Lehmann and F. M. Ryan, *This Journal*, **119**, 275 (1972).
5. H. Smithgall and K. Speigel, U.S. Pat. 3,566,012 (1971).

Rare Earth Doped Vitroceramics: New, Efficient, Blue and Green Emitting Materials for Infrared Up-Conversion

F. Auzel, D. Pecile, and D. Morin

Centre National d'Etudes des Télécommunications, 92220 Bagneux, France

ABSTRACT

New, efficient, vitroceramic hosts for rare earth luminescence are discussed. Their applications to infrared up-conversion are emphasized. Optimized compositions lead to an efficiency nearly twice as high as commercially available LaF_3:Yb:Er. As for infrared to blue efficiency, these vitroceramics are among the best compounds obtained so far. The easy preparation in air atmosphere is described. The excitation spectra have the advantage of being broader than usual for up-conversion phosphors. Kinetic studies present some puzzling behavior with respect to sample geometry; *e.g.*, the rise time increases fourfold with sample thickness between 0.1 and 4.5 mm. Segregation of rare earths in the microcrystalline phase rather than in the glassy one is clearly shown which explains the high efficiencies.

Although the up-conversion processes by energy transfer between Yb^{3+} and Tm^{3+} or Er^{3+} were first discovered in a glass matrix (1), all the hosts reported to date are pure crystalline compounds (1-3). The main reason is that the fluorescence of rare earth ions is generally less efficient in a glass. Yet Auzel has shown that in the case of Er^{3+}, the fluorescence emission at 0.54μ is strongly enhanced with respect to glass inside the devitrified glass matrix (4); one then deals with a vitroceramic since large amounts of microcrystals are embedded in an amorphous structure.

The preparation, preliminary results about the structure, as well as up-conversion properties, of such vitroceramics are discussed. The general formula of these new materials is (Ln_2O_3, Yb_2O_3, PbF_2, M_nO_m) doped with oxides of erbium, thulium, holmium, or terbium with Ln = Y, La, Gd, or Lu and M being one of the following glass forming elements B, Si, P, Ge, or Te. According to the doping ion choice, either sequential or cooperative sensitization may be obtained.

Key words: glass ceramics, up-conversion, rare earths, infrared, energy transfer.

Several glasses of different forming elements have been examined, but emphasis is given to the following example: (Yb_2O_3, PbF_2, GeO_2) doped either with Er_2O_3 or Tm_2O_3.

From an efficiency point of view, such ceramics can be favorably compared with crystalline hosts. Furthermore, their shorter time response and their easy preparation make them particularly suitable for pulsed GaAs:Si diode excitation for LED applications. The fact that such materials can be cast, cut, and polished just as glasses may be also a further advantage over crystalline phosphors when large displays are considered.

On the other hand, several fundamental interesting aspects are shown. These matrices contain a large amount of oxygen, yet their green emission yield is as high as those obtained from the best oxygen-free YF_3 hosts. This fact is in contrast with what has been generally found in crystalline hosts (3). The trapping effect and radiative energy transfer between Yb^{3+} ions before nonradiative energy transfers take place, as recently evidenced (5), are particularly strong.

Experimental

Vitroceramics composition and preparation.—The vitroceramics are obtained by simply mixing together one or several of the following glass-forming oxides SiO_2, GeO_2, B_2O_3, P_2O_5, TeO_2 with lead fluoride and high purity rare earth oxides (99.999%). The mixture, contained in a platinum crucible with a cover, is heated and melted inside a muffle furnace at 1000°C for about 1 hr. The sample is then obtained by pouring the melt, in air, into a graphite mold of the desired form, the mold is maintained at about 300°-400°C for 4 hr for annealing purposes. A white compound with a glassy aspect is finally obtained.

The compositions (GeO_2-PbF_2):Yb, Er and (GeO_2-PbF_2):Yb, Tm are mainly discussed in this paper. These compositions have been optimized for infrared up-conversion under CW excitation. Under pulsed excitation, the optimization may be somewhat different since time constants vary with composition differently from efficiencies.

Spectroscopy and optical measurements.—Absorption and fluorescence spectra as well as excitation spectra are obtained with a Cary 17 spectrophotometer. The spectrometer has been modified, when used for fluorescence and excitation, by laboratory-made attachments. Only one beam is used with external excitation for fluorescence, and with internal excitation for excitation spectra.

The vitroceramic samples are either optically polished plates of 50μ thickness or powders obtained by crushing the ceramics in a mortar and sieving to various sizes.

Efficiency comparison with other phosphors and fluorescence spectra are performed on powdered samples, whereas excitation spectra and absorption spectra are obtained from plate samples which are then compared with phosphor samples in forms of platelets of 80 mg/cm^2 sizes. This size is the optimum for relative up-conversion efficiency for an excitation through the phosphor samples. The details of the efficiency measurements have already been reported elsewhere (6).

Time constants are measured using a Texas Instruments TIXLI6 infrared emitting diode pulsed at 2A peak current with a 40 Hz repetition rate, the pulse width being usually 10 msec. The visible signal is collected from the same side as excitation, filtered by KG3, BG18 Shott glasses, detected by a photomultiplier, and fed directly to a storage oscilloscope.

The scanning electron microscope analysis has been obtained with a Cameca MEB 07 microscope to which has been added a cathodoluminescence attachment (7).

Results and Discussion

Comparative results for up-conversion efficiencies.—Several types of vitroceramics with different glass-forming elements have been prepared each having the same molar composition: M_nO_m = 27.18%; PbF_2 = 67.57%; Yb_2O_3 = 4.85%; Er_2O_3 = 0.39%. The relative efficiency is given in Table I. Except for B_2O_3 and TeO_2, about the same results are obtained for the other glass-forming oxides: P_2O_5, SiO_2, and GeO_2.

Table I. Relative infrared green conversion efficiency for different glass-forming elements in vitroceramics of the general formula (not optimized):

M_nO_m = 27.18%; PbF_2 = 67.57%; Yb_2O_3 = 4.85%; Er_2O_3 = 0.39%; (molar per cent)

Composition: M_nO_m	Efficiency relative to YF_3:Yb:Er (= 100))
B_2O_3	10
TeO_2	30
P_2O_5	70
SiO_2	65
GeO_2	70

The compositions involving GeO_2 and SiO_2 were more thoroughly investigated. The relative ratios of GeO_2 and PbF_2 were systematically varied between 5 and 36% by weight leading to the results presented in Fig. 1, where the optimum $GeO_2/PbF_2 + GeO_2$ ratio is around 20%.

Optimization of Yb_2O_3, Er_2O_3, or Tm_2O_3 in the GeO_2-PbF_2 matrix are presented in Fig. 2 and 3 for the blue and green emissions, respectively. The optimum rare earth concentrations for blue are 25% Yb_2O_3 and 0.062% Tm_2O_3; the best ones for green are 10% Yb_2O_3 and 2% Er_2O_3 (weight per cent).

In Tables II and III, comparisons are made between our best vitroceramics obtained so far, with RE fluoride phosphors. Comparison is made between powdered samples of the same particle size (about 50μ). But it should be noted that reducing vitroceramics to powder of 50μ grain size decreases their efficiency by 75% with respect to the uncrushed ceramics or crushed ceramics with grains longer than 200μ. This effect of reduction of efficiency for powdered ceramics is not yet fully understood. It does not appear to be a lack of refractive index matching but seems closely linked to the effect of photon trapping as is shown below.

Comparisons are made under CW as well as pulsed excitation by using a figure of merit defined (8) as

$$M = \eta_n(\tfrac{1}{2}\pi\tau_1)$$

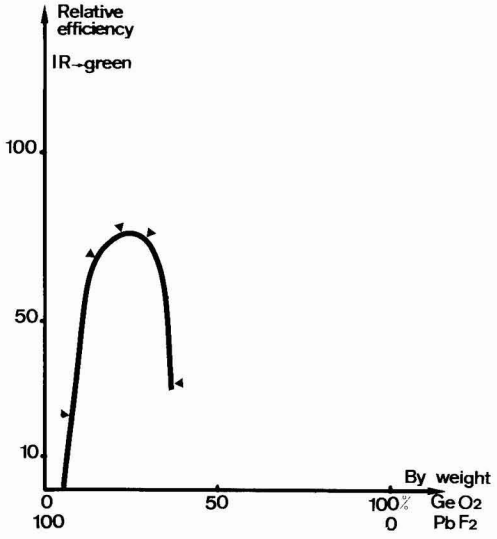

Fig. 1. Relative efficiency for infrared → green conversion vs. $GeO_2/(PbF_2)$ ratio.

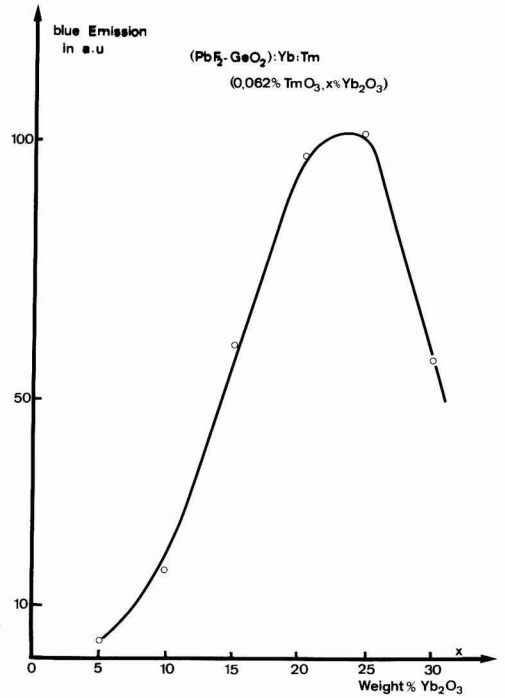

Fig. 2. Relative blue conversion efficiency vs. Yb^{3+} concentration for a $(PbF_2\text{-}GeO_2)$:Yb:Tm vitroceramic doped with 0.062% Tm_2O_3.

where η_n is the efficiency as defined by the emitted power per square centimeter when 1 mW power per cm^2 at 0.97μ is falling on the sample; τ is the rise time of the emission as measured on the powder on the same side as excitation.

It is necessary to define the frame work of the time constant measurements for excitation and emission since the infrared photon trapping effect (5) due to Yb^{3+} ($^2F_{5/2} \rightarrow {}^2F_{7/2}$) $\Longrightarrow$ Yb^{3+} ($^2F_{7/2} \rightarrow {}^2F_{5/2}$) radiative transfer is particularly strong in this type of matrix. For example Fig. 4 presents the rise and fall times for the GeO_2-PbF_2 optimized-type vitroceramic; the measurements are made through samples of various thicknesses. A fourfold increase in rise time is found for thicknesses varying between 0.1 and 4.5 mm, and an increase of 3.4 times in decay time is found for the same thickness range. For larger thicknesses a time constant saturation takes place. This increase is due to the Yb^{3+} lifetime increase by resonance since the relation (9) $\tau_2 = Yb/2$ is found constant for any thickness: at 0.1 mm we have $\tau_{Yb} = 1.6$ msec or $\tau_{Yb}/2 = 0.8$ msec and τ_2 is found to be 0.9 msec; at 4.5 mm $\tau_{Yb} = 7$ msec or $\tau_{Yb}/2 = 3.5$ msec and τ_2 is found to be 3.4 msec. This effect has to be taken into account if one wishes to calculate transfer efficiencies from lifetime measurements.

This explains the reduction in efficiency when the vitroceramics are reduced to a powder. This hypothesis is based on the fact that τ_{Yb} is found to be lower for two samples of given thickness joined together, than for one of double thickness even if the two samples are bound by an index matching medium. In the same way, the efficiency cannot be restored for a powder using such a medium. If a space limited excitation is produced using a diaphragm, light emission of a ceramic wafer is obtained at a distance of about several millimeters from the diaphragm. This is the same average distance through which energy can migrate radiatively as indicated from lifetime curves in Fig. 4.

Table II. Comparison of efficiency and transient times for Yb^{3+}-Er^{3+} doped materials

Sample Chemical formula powdered samples (ϕ 50μ)	Infrared → 0.55μ conversion			
	Rise time, τ_1 (msec)	Fall time, τ_2 (msec)	Efficiency† × 10^6	Figure of merit × 10^8 Hz
Vitroceramic No. 776 (CNET 1974) $(PbF_2\text{-}GeO_2)$:Yb-Er PbF_2 78%, GeO_2 22%, + 10% Yb_2O_3 + 0.75% Er_2O_3 (per cent by weight)	2	0.65	285	22.8
YF_3:Yb:Er (CNET 1972)†† $Y_{0.80}Yb_{0.19}Er_{0.01}F_3$	3.2	1.2	285	15
YF_3:Yb:Er (BTL 1970)†† $Y_{0.84}Yb_{0.15}Er_{0.01}F_3$	3.5	1.3	185	8.8
LaF_3:Yb:Er (GE 1970)†† $La_{0.86}Yb_{0.12}Er_{0.02}F_3$	4.25	1.6	165	7

† Definitions are given in Ref. (8).
†† The samples are discussed in Table X of Ref. (8) where a comparison between different samples from different origins at one point in their development is reported.

Table III. Comparison of efficiency and transient times for Yb^{3+}-Tm^{3+} doped materials

Sample Chemical formula powdered samples (ϕ 50μ)	Infrared → 0.475μ conversion			
	Rise time, τ_1 (msec)	Fall time, τ_2 (msec)	Relative efficiency	Relative figure of merit × 10^2
Vitroceramic No. 774 (CNET 74) $(PbF_2\text{-}GeO_2)$:Yb-Tm PbF_2 78%, GeO_2 22% + 25% Yb_2O_3 + 0.062% Tm_2O_3	2.25	0.8	100	7
YF:Yb:Tm (CNET 1973) $Y_{0.65}Yb_{0.349}Tm_{0.001}F_3$	3.25	1.4	100	4
YF:Yb:Tm ($Tm_{0.003}$ Philips USA 1971) $Y_{0.647}Yb_{0.35}Tm_{0.003}F_3$	3.25	1.7	37	1.4

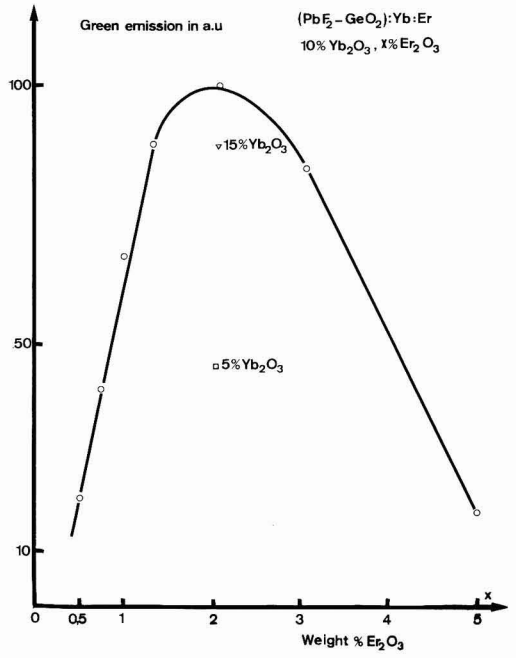

Fig. 3. Relative green conversion efficiency vs. Er^{3+} concentration for a $(PbF_2\text{-}GeO_3)$:Yb:Er vitroceramic.

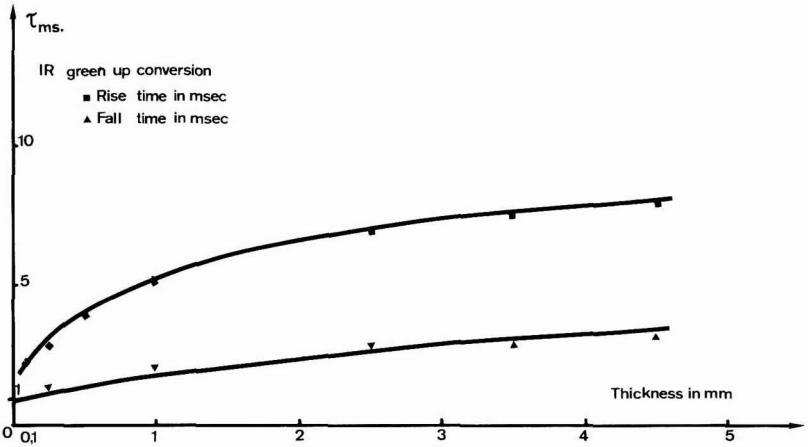

Fig. 4. Rise time and fall time vs. sample thickness for a (PbF_2-GeO_2):Yb:Er vitroceramic.

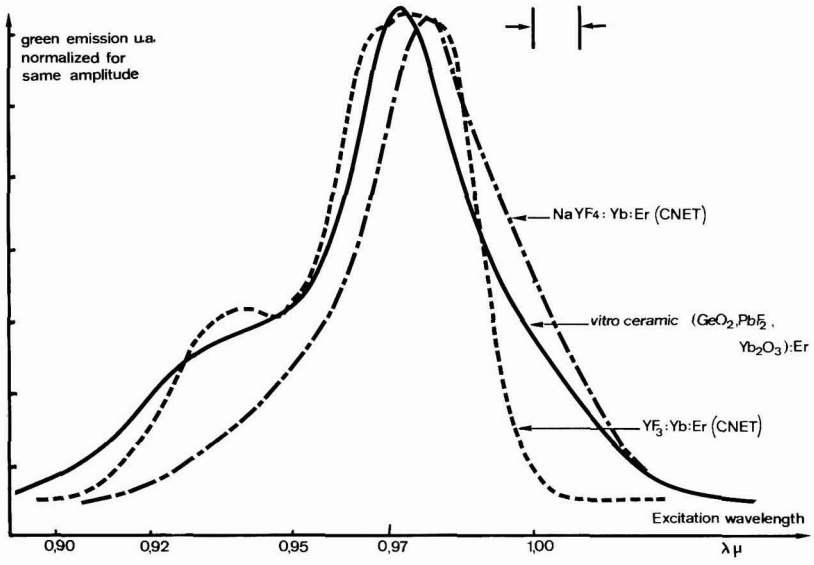

Fig. 5. Comparative excitation spectra for YF_3:Yb:Er, $NaYF_4$: Yb:Er, and (GeO_2, PbF_2, Yb_2O_3): Er normalized to have same maximum.

These results, in our view, indicate that the radiative transfer of Yb^{3+} energy is a necessary link for the efficiency of the up-conversion process and that the structure of the material plays a determinant role in that transfer. But we feel more work is necessary to assess these hypotheses. For LED applications, the optimum sample thickness was found to be around 300μ.

Comparative spectral results.—In order to compare the vitroceramics with classical up-conversion phosphors, excitation spectra are given in Fig. 5. The GeO_2-PbF_2 vitroceramic spectrum extends as far as the $NaYF_4$ one at longer wavelengths and somewhat farther than the YF_3 one at shorter wavelengths. Therefore excitation is possible with a GaAs laser at 0.9μ or a YAG:Nd laser at 1.06μ. As far as line width is concerned the general aspects of the excitation spectra are different; the vitroceramic shows fewer and broader lines. For instance, in Fig. 6, for the strongest line, the width is 20Å as compared to 6Å for YF_3:Yb:Er. Using the same excitation and detection conditions, the spectral peak intensity is stronger for YF_3, which confirms the direct results of Table I. Similar results are presented in Fig. 7 for the blue emission. Approximately the same line width is found but the over-all splitting is stronger in ceramics.

The line widths of vitroceramics are much smaller than that usually found for the same emission in glass, 20Å against 200Å for a germanate glass. On the other hand the up-conversion efficiency is more than two orders of magnitude better than in a germanate glass (8). These two facts imply that the rare earths concentrate in the crystal phase rather than in the glass phase during the precipitation process; this segregation effect is evidenced below by the scanning electron microscope study. The Yb^{3+} concentration in the microcrystals is then higher than the one given by the bulk formula. This enhances the trapping effect found in these materials.

Another point of interest is the high efficiency and the high green/red emission ratio for hosts with such high oxygen concentration. The green/red energetic ratio for the vitroceramic is about 7 while for our best YF_3, this ratio is 10, yet it is well known that the presence of oxygen in fluorides usually gives a lower green/red ratio and lower green efficiency (4). One hypothesis is that during the microcrystal precipitation process most of the oxygen of the melt is concentrated in the glassy phase rather than in the crystalline one; most of the oxygen present is necessary for the glassy phase to exist. Also as is well known, PbF_2 may act as a

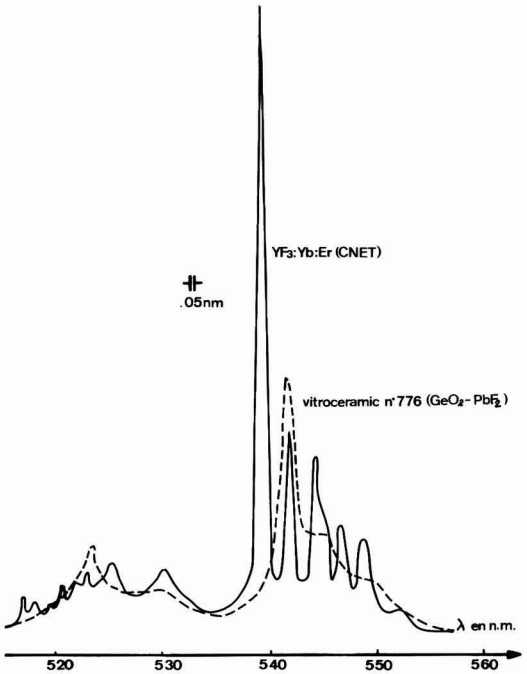

Fig. 6. Comparative green emission spectra of YF_3:Yb:Er (CNET) and (GeO_2, PbF_2, Yb_2O_3):Er vitroceramics.

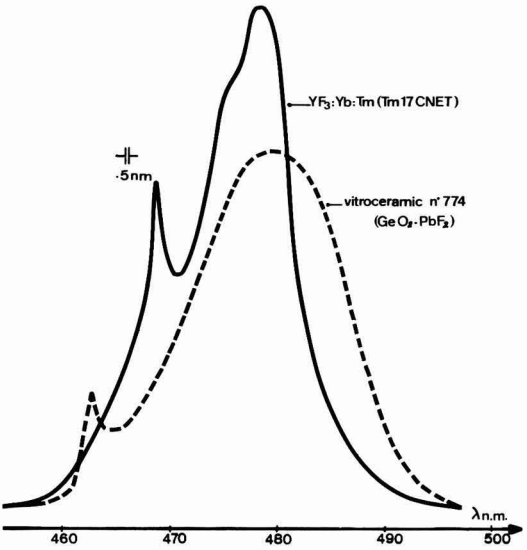

Fig. 7. Comparative blue emission spectra of Yb_3:Yb:Tm (CNET) and (GeO_2, PbF_2, Yb_2O_3):Er vitroceramics.

scavenger for oxygen; this effect can also play a role to eliminate oxygen from the microcrystals. Yet this oxygen segregation hypothesis is not necessary if one considers a homogeneous distribution of constituents since the calculated Debye cutoff frequency is then 320 cm^{-1}, which according to Matsubara (10) predicts a green emission.

Relationship between spectroscopic results and microstructure.—The hypothesis that the rare earths (Yb, Er, or Tm) concentrate mainly in the microcrystal phase and germanium only in the glassy phase has been confirmed by the scanning electron microscope. Figure 8a presents the microcrystals (white) inside the glassy phase (dark) as obtained by back scattering of electrons. Figure 8b gives the same picture obtained by x-ray fluorescence of germanium (white) which shows that Ge is the main constituent of the glassy phase; on the other hand, when looking at x-ray fluorescence of ytterbium one obtains Fig. 8c which shows that Yb is essentially in the microcrystalline phase. The same results are obtained for the cathodoluminescence of erbium at 0.65μ as shown in Fig. 8d. When analyzing for lead by x-ray fluorescence, Fig. 8e is obtained which indicates that Pb is uniformly distributed.

Hence the glassy phase is probably a lead germanate whereas the microcrystalline phase (which is found to be homogeneous as shown on Fig. 9 by electron absorption) could be a fluoride of lead, ytterbium, and erbium. Attempts at producing good up-conversion efficiency by direct preparation of PbF_2-YbF_3:Er microcrystals lead to an output of only 2% of the best vitroceramics sample. The role played by the microstructure may be an explanation. Figure 10 shows a cathodoluminescence picture of the 0.65μ Er^{3+} emission at a lower magnification than the previous one. A long distance order ($\simeq 200\mu$) is found for the microcrystalline structure; such long order cannot be obtained by a direct preparation of lead-ytterbium fluoride.

On the other hand, the decrease in up-conversion efficiency observed when crushing the ceramics into grains smaller than 200μ can be explained by the long distance order which is then destroyed and if one assumes that the radiative energy transfer migrates preferably along the microcrystal in the same way as in light-pipes, the behavior of these vitroceramics could be understood.

Conclusions

We have presented here a new class of efficient materials for infrared up-conversion which has the advantages of easy preparation and good efficiencies. However their puzzling behavior requires more experiments for a clearer understanding.

In the vitroceramics described. we have clearly demonstrated by up-conversion results as well as x-ray fluorescence and cathodoluminescence scanning microscopy that rare earth ions concentrate mainly in the precipitated microcrystals, which accounts for the high up-conversion efficiency.

Recently glass ceramics of quite different compositions have been demonstrated as replacements for glass laser materials (11, 12). But their lower fluorescence efficiency (12) and their broader emission line width (11) with respect to the glass of the same bulk composition is an indication that rare earth ions stay mainly in the glassy phase. The new high efficiency vitroceramics presented here with the rare earth segregation in the microcrystals, should be a better prospect for glass ceramic laser materials than the previous ones, provided the microcrystal size could be reduced.

For display applications, the fact that such vitroceramics can be cast, polished, and cut as glass, could lead to new ways to couple these solid phosphors to infrared sources. Seven segment displays, using the vitroceramics as a substrate coupled with discrete diodes can be encompassed. Another advantage over powder phosphors is that multidielectric coatings (8) can be used easily with a glass substrate to capture the infrared radiation.

Acknowledgments

We are much indebted to J. Semo who performed the scanning microscope analysis, and to Dr. Mürau

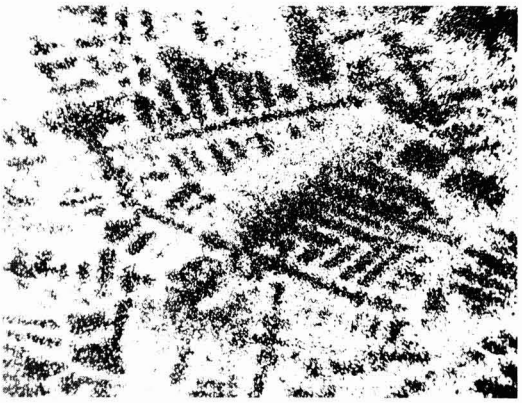

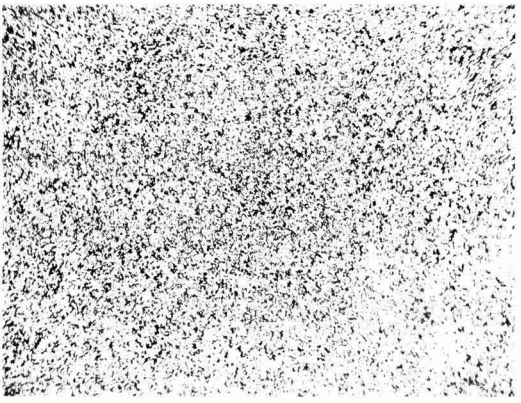

Fig. 8. Microscopic study of a (GeO_2, PbF_2, Yb_2P_3):Er vitroceramic. (a, upper left) White microcrystals inside the black glassy phase as revealed by electron back scattering. (b, upper right) X-ray emission from Ge (white). (c, center left) X-ray emission from Yb (white). (d, center right) Cathodoluminescence from Er^{3+} at 0.65μm (white). (e, lower left) X-ray emission from Pb (white).

from North American Philips for kindly supplying the YF_3:Yb:Tm sample for comparison. This work has been partially supported by D. G. R. S. T.

Manuscript submitted April 22, 1974; revised manuscript received Aug. 20, 1974. This was Paper 105 presented at the San Francisco, California, Meeting of the Society, May 12-17, 1974.

Any discussion of this paper will appear in a Discussion Section to be published in the December 1975 JOURNAL. All discussions for the December 1975 Discussion Section should be submitted by Aug. 1, 1975.

10 μ

Fig. 9. Microcrystals (dark) inside the glassy phase for a (GeO_2, PbF_2, Yb_2O_3):Er^{3+} vitroceramic as revealed by electron absorption.

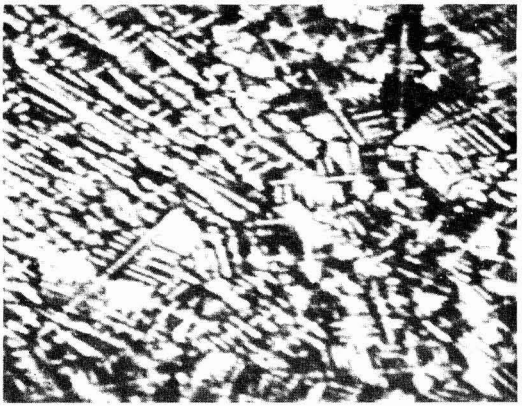

30 μ

Fig. 10. Long distance order inside a (GeO_2, PbF_2, Yb_2O_3):Er^{3+} vitroceramic as revealed by Er^{3+} cathodoluminescence at 0.65μ.

REFERENCES

1. F. Auzel, *C. R. Acad. Sci. (Paris)*, **262,** 1016 (1966); *ibid.*, **263,** 819 (1966).
2. V. V. Ovsyankin and P. P. Feofilov, *Sov. Phys. JETP Letters*, **4,** 317 (1966); L. Esterowitz, J. Noonan, and J. Bahler, *Appl. Phys. Letters*, **10,** 126 (1967); R. A. Hewes and J. F. Sarver, *Phys. Rev.*, **182,** 427 (1969); R. L. Sommerdijk, *J. Luminescence*, **6,** 61 (1973); N. Menyuk, K. Dwight, and J. W. Pierce, *Appl. Phys. Letters*, **21,** 159 (1972); H. J. Guggenheim and L. F. Johnson, *Appl. Phys. Letters*, **15,** 51 (1969); J. E. Geusic, *et al., J. Appl. Phys.*, **42,** 1958 (1971); F. W. Ostermayer, *Met. Trans.*, **2,** 747 (1971); L. G. Van Uitert, L. Pictroski, and W. H. Grodkiewicz, *Mater. Res. Bull.*, **4,** 777 (1969); N. M. P. Low and A. L. Major, *Mater. Res. Bull.*, **7,** 203 (1972); S. G. Parker and R. E. Johnson, *This Journal*, **119,** 610 (1972); T. Matsubara, *Japan. J. Appl. Phys.*, **10,** 1647 (1971); T. Kano, H. Yamamoto, and Y. Otomo, *This Journal*, **119,** 1561 (1972); J. P. Wittke, I. Ladany, and P. N. Yocom, *Proc. IEEE*, **58,** 1283 (1970).
3. P. C. Mürau and Z. Szilagyi, Paper 161 presented at Electrochemical Society Meeting, Cleveland, Ohio, Oct. 3-7, 1971.
4. F. Auzel, Thèse, Paris (1968).
5. F. Auzel and D. Pecile, *C. R. Acad. Sci. (Paris)*, **277,** 155 (1973).
6. F. Auzel and D. Pecile, *J. Luminescence*, **8,** 32 (1973).
7. J. Semo, Brevet Français BF 73-35044.
8. F. Auzel, *Proc. IEEE*, **61,** 758 (1973).
9. J. D. Kingsley, *J. Appl. Phys.*, **41,** 175 (1970).
10. T. Matsubara, *Japan. J. Appl. Phys.*, **11,** 1579 (1972).
11. C. F. Rapp and J. Chrysochoos, *J. Mater. Sci.*, **7,** 1090 (1972).
12. G. Muller and N. Neuroth, *J. Appl. Phys.*, **44,** 2135 (1973).

Poly(Vinylferrocene)—Conversion to an Oxidized Iron System Suitable for Use as a Semitransparent Hard Photomask

L. F. Thompson

Bell Laboratories, Murray Hill, New Jersey 07974

ABSTRACT

A novel technique for the production of iron oxide films from a polymer precursor is described. Films of poly(vinylferrocene) (PVFc) can be converted to iron oxide films in either a 200W oxygen plasma at room temperature or thermally in oxygen at 380°C. The thermal decomposition appears to be more suitable for routine use, and process parameters for this technique have been optimized. The thermal conversion has been studied using infrared, visible, and u.v. spectroscopy and a decomposition reaction proposed. The iron oxide films prepared from PVFc have chemical and physical properties similar to the iron oxide films prepared using the iron pentacarbonyl process. Films prepared from PVFc are presently being evaluated for use as semitransparent photolithographic masks.

The use of iron oxide for the fabrication of hard, semitransparent masks for use in the manufacture of integrated circuits is gaining rapid acceptance (1). Although the film material is primarily Fe_2O_3, the exact structure is far more complicated than a pure Fe_2O_3 system. Iron oxide was chosen from a large group of transition metal oxides and mixed oxides as having the best combination of chemical and physical properties required for use as a transparent mask material (2). The relevant properties are given by Peters *et al.* (3) as: (*i*) <1% transmission in the 360-400 nm spectral region; (*ii*) >30% transmission at the sodium D line (589 nm); (*iii*) an etching rate compatible with conventional photolithographic processes and materials; (*iv*) in addition, the physical integrity of the film (hardness, abrasion resistance, etc.) must be sufficient to sustain the abuses of routine handling.

Three techniques are presently available for the deposition of thin films of iron oxide. The first is a chemical vapor deposition scheme using $Fe(CO)_5$ developed by MacChesney *et al.* (4). Iron pentacarbonyl is thermally decomposed at temperatures in the 130°-200°C range in an oxidizing atmosphere ($CO_2 + O_2$) on glass substrates. Films prepared by this technique have excellent mask properties, and this is presently the technique of choice for mask film manufacture. The only substantial disadvantage of the procedure is using a poisonous compound, $Fe(CO)_5$. A second deposition technique involving sputtering has been devised by Sinclair *et al.* (2, 3) for depositing Fe_2O_3 films. The sputtering techniques used were conventional with the exception that it was found necessary to introduce $CO_2 + O_2$ as a discharge gas in order to increase the solubility of the deposited Fe_2O_3 films to an acceptable level for etching. The exact role that CO_2 plays is not clear, but it appears likely that the presence of iron carbonate in films leads to increased solubility (3). The sputtering technique produces films which meet all mask requirements with the only disadvantage being that the process is slow and requires expensive vacuum equipment. The third general procedure, one similar to the process described in this paper, involves the decomposition of an organometallic compound in an oxidizing atmosphere resulting in the deposition of a metal oxide film. Reid and Cukor (5) suggested that organo-iron compounds could be thermally decomposed in O_2 to Fe_2O_3. Shelby and Cukor (6) decomposed nickel tetradecanoate and iron dodecanoate to Fe-Ni alloys at 500°C in a H_2 ambient. These films were subsequently used as x-ray standards and could be deposited with good reproducibility.

Key words: iron oxide, photomasks, semitransparent masks, photolithography.

This paper describes a method for the deposition of an oxidized iron film using a high molecular weight, organometallic polymer as a precursor. This technique offers the advantage of being able to deposit uniform films of sufficient thickness to yield a useful mask material in one application. However, two or more thinner films may be applied if necessary to reduce defect densities.

Poly(vinylferrocene) (PVFc) has been synthesized by a number of workers (7-9). It has been shown that PVFc can be converted to Fe_2O_3 in an oxygen plasma and subsequently to Fe° capable of serving as a catalytic tract for selective electroless deposition of Cu, Au, and Ni (10). The disadvantage of plasma conversion lies in the time required to convert a 400 nm film to Fe_2O_3. In preliminary studies it was found that in O_2 at 400°C, PVFc could be thermally converted in <30 min to an oxidized iron film possessing useful mask properties.

It should be noted that exact chemical composition of these films is difficult to ascertain. They are complex mixtures of Fe_2O_3, Fe_3O_4, $Fe(CO_3)_2$, and other inorganic iron compounds. Since any attempt to produce larger samples of material for subsequent analysis would significantly alter the physics and chemistry of the thin-film system and possibly yield a different conversion process and material, the exact structure remains undetermined.

The reaction scheme is shown in Fig. 1. The object of this study was to evaluate the oxidation of PVFc.

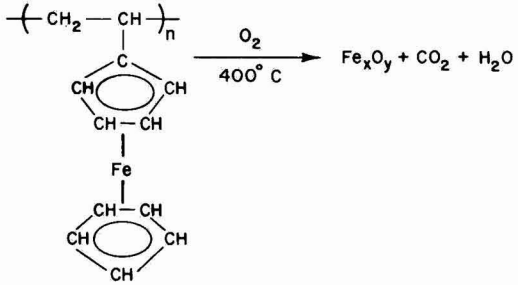

Fig. 1. Reaction scheme of the thermal oxidation of PVFc to Fe_2O_3.

Experimental

PVFc deposition.—The PVFc used in this work was prepared by free radical bulk polymerization of vinyl ferrocene at 80°C (7, 8). The monomer, vinyl ferrocene, was purchased from Research Organics, Incorporated (ROC/FIC) and purified by vacuum sublimation (mp 50°-50.5°C). Azobisisobutyronitrile (AIBN) was used as a catalyst and was purified by recrystallization from methanol (mp 102°-103°C with slow decomposition). Vinyl ferrocene and 0.08% AIBN (by weight) were sealed in a glass tube under N_2. The vinyl ferrocene was melted and AIBN allowed to dissolve in it. The sealed tube was placed in a bath at 80° ± 0.5°C, and the polymerization was allowed to continue for 72 hr. The mixture solidified after about 12 hr. The tube was cooled in ice water, broken open, and the polymer dissolved in chlorobenzene. The PVFc was precipitated in cold methanol, recovered by filtration, and dried in a vacuum at 80°C for 24 hr. The polymer was dissolved in chlorobenzene (6-7% solids) and filtered to remove particulates by multiple passes through a 0.2μ sintered silver filter prior to use. The substrates were spin coated with PVFc using standard photoresist techniques (11). All substrates used in this study were 1 in. diameter by ⅛ in. thick quartz disks which facilitated direct quantitative visible and ultraviolet (u.v.) absorption studies.

The visible-ultraviolet absorption spectra for Fe_2O_3 suitable for use as a photomask is well established (2) and is shown in Fig. 2 (dashed curve). The spectrum from 300 to 700 nm obtained with a Cary Model 14 spectrophotometer was used to follow the conversion of PVFc to Fe_2O_3.

Infrared studies were carried out using attenuated total reflection (ATR) with a Perkin-Elmer Model 631 spectrophotometer. The samples were coated on 5 mil aluminum foil and mounted against a KRS-5 plate for ATR studies. Spectrum assignments were made with the aid of known spectra.

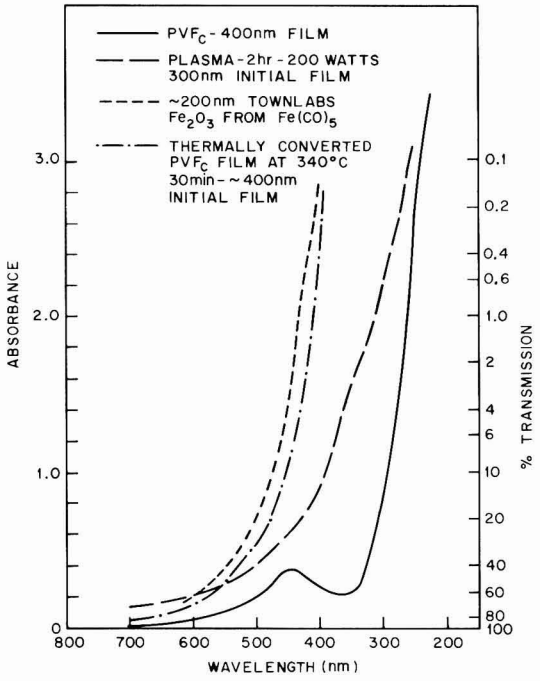

Fig. 2. 700-200 nm absorption spectra for PVFc and oxidized iron films.

Plasma conversion.—A 200W, 4 MHz radio frequency plasma was used to study plasma conversion of PVFc to Fe_2O_3. The degree of conversion was followed using visible u.v. spectroscopy to determine changes in absorption in the 360-400 nm region of interest. Although this does not yield precise information regarding structural changes, it does measure the primary parameter of interest for a semitransparent mask material.

Thermal conversion.—Thermal conversions were carried out in a 2 in. diameter tube furnace regulated to ±10°C with an O_2 flow rate maintained at ≈5 liters/min^{-1}. Infrared analysis and ultraviolet visible spectroscopy were then used to study the thermal conversion of PVFc.

Results and Discussion

The free-radical bulk polymerization of vinyl ferrocene as described yielded about 70% polymer in the 72 hr reaction time. The molecular weight of the polymer as determined by dilute solution viscosity was found to be ~80,000. Several separate batches of polymer were prepared with good reproducibility, although molecular weight varied by as much as ±20%. The yield never varied by more than 10%. A detailed study of the reaction parameter is presently underway. The polymer yielded uniform, defect-free films from a chlorobenzene solution.

Plasma oxidation.—It was found that in a 200W oxygen plasma, PVFc oxidized to an iron compound with a visible u.v. spectrum similar to that of Fe_2O_3 films prepared by the $Fe(CO)_5$ process. For complete conversion 3 hr or more were required. Figure 2 illustrates the spectrum of a 300 nm PVFc film which was oxidized in a plasma to an inorganic iron film. It is noted that the absorption is not adequate for mask purposes in the 300-400 nm region; however, if 400 nm of polymer is used, the absorption increases to an adequate level. This thickness can be achieved either by a single 400 nm coating or two sequential 200 nm coatings. The double coating technique has the advantage of reducing defects in the film at the expense of additional processing steps and time.

Plasma exposure time as a function of absorption (and per cent transmission) is shown in Fig. 3 at wavelengths of 600, 500, 400, and 350 nm. Note that the absorption in the 350 and 400 nm region increases rapidly as the oxidation proceeds, while in the 500 and 600 nm region absorption remains relatively unaffected. The plasma oxidation is complete after 3 hr. A slight decrease in absorption is noted after long exposures, probably due to sputter removal of material from the oxidized material. The oxidized films were soluble in cold 6-8M HCl and etched at about 1 μmin^{-1} after

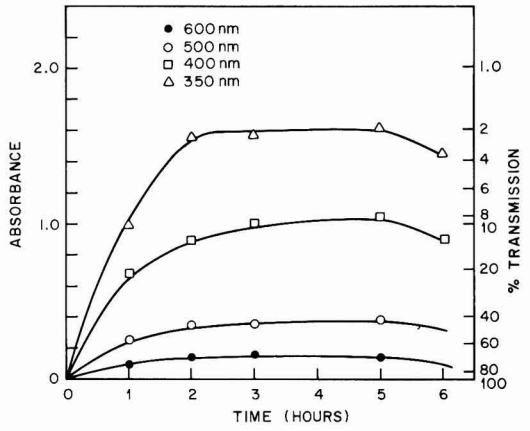

Fig. 3. Absorption as a function of time for the plasma conversion of PVFc with a 200W O_2 plasma.

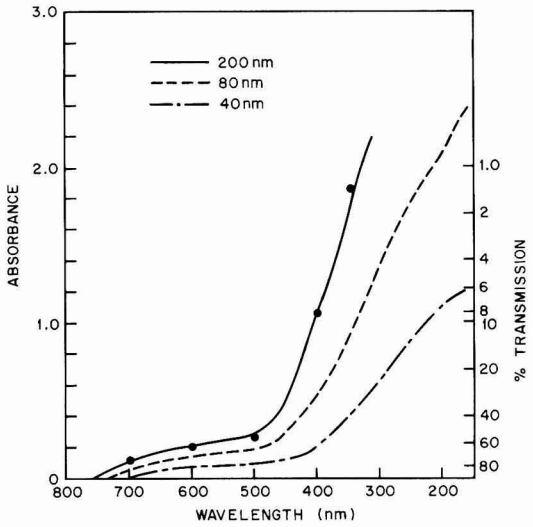

Fig. 4. 200-700 nm absorption spectra for the thermal conversion at 280°C of PVFc of three thicknesses.

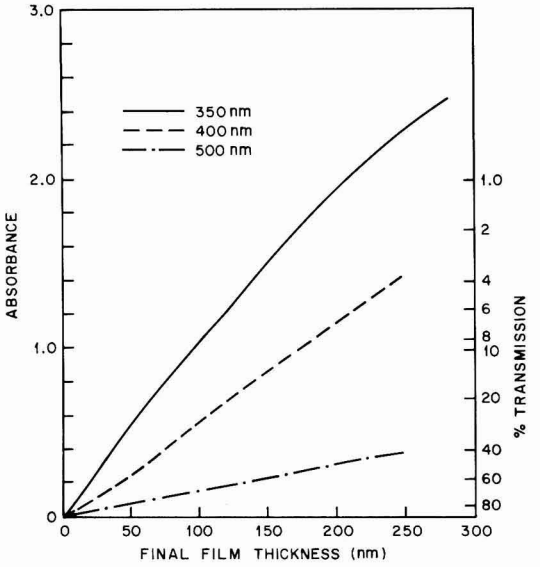

Fig. 6. Absorption as a function of thickness for PVFc films oxidized at 300°C for 30 min.

complete plasma conversion. They became insoluble after a 450°C heat-treatment, although there were no noticeable absorption changes. Scanning electron microscopy (SEM) studies revealed no defects in the oxidized films that were not attributable to particulate inclusions in the precursor polymer film.

Thermal conversion.—It was found that thermal oxidation treatments at 400°C for 20-30 min in an oxygen atmosphere was sufficient to convert PVFc to a stable oxidized iron material. The optimum oxygen flow for the furnace used was ~5 liters/min^{-1}. However, flow rates are expected to be system dependent, they are not a critical parameter. Again the energy absorption in the visible u.v. region was used to optimize the conversion process since this is the primary property of concern in mask materials. Figure 4 shows the absorption spectra for three final film thicknesses. It should be noted that the thermal conversion is accompanied by a 50-60% decrease in film thickness.[1] It was found that to minimize the detrimental effects of film shrinkage, a programmed baking schedule was necessary. Figure 5A is a (SEM) micrograph of a 200 nm film which was baked in a preheated 400°C furnace. The broken areas shown were common on films treated in this way. However, when the baking schedule was started at room temperature and increased at ~10°C/min^{-1} rates, this catastrophic crazing effect was eliminated, and uniform films were then obtained (Fig. 5B).

It was found that ~200 nm of final film was necessary to give the desired absorption properties using thermal conversion. Figure 6 shows absorption as a function of film thickness for three wavelengths: 350, 400, and 500 nm. This film was converted with a 400° ± 10°C, 30 min baking schedule in which the temperature was increased from 22° to 400°C at ~10°C/min^{-1} and then held at 400° ± 10°C for 30 min. The 200 nm final film thickness was achieved by converting a single coating of PVFc of an initial thickness of ~470 nm. As before, there are advantages in using two thin (~240 nm) coatings each followed by a bake, since the defect density will be less and the film should be more homogeneous throughout its thickness.

Both scratch resistance and adhesion were qualitatively compared to films deposited from $Fe(CO)_5$. The adhesion (as per "scotch tape" test and epoxy pull

[1] The thickness referred to in this study is final film thickness unless otherwise stated.

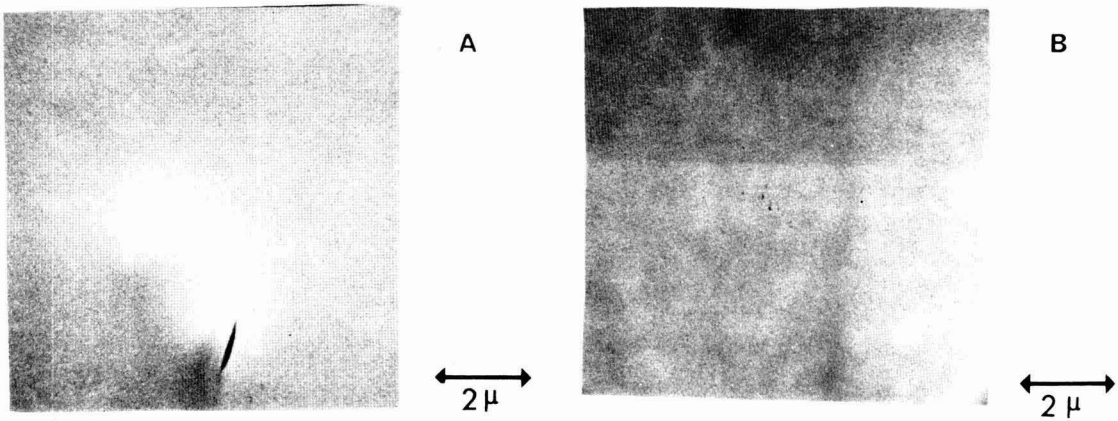

Fig. 5. SEM of thermally converted oxidized iron films

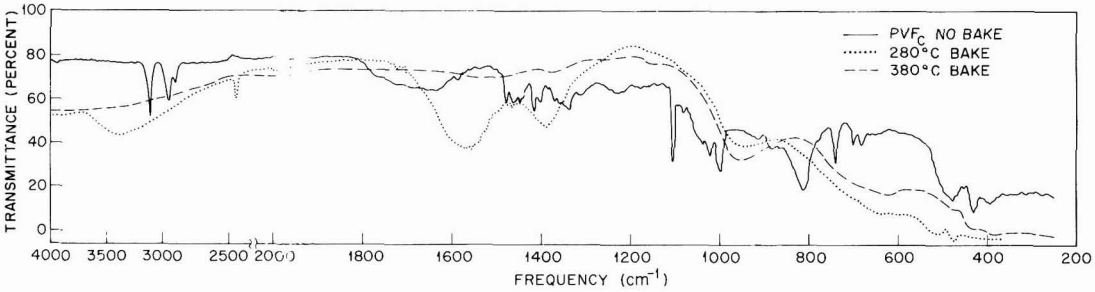

Fig. 7. Infrared spectra of a 400 nm polyvinylferrocene film baked at two temperatures, 200° and 400°C, for 30 min each

test) was in no case worse than the standard sample and exceeded that of the carbonyl film in most samples. The scratch resistance was comparable to the carbonyl standard. Precise defect density measurements are presently underway.

The conversion of PVFc to oxidized iron compounds involves considerable chemical changes in the film. Attenuated total reflectance (ATR) infrared spectroscopy was used to study the thermal oxidation of PVFc. A possible reaction spectra scheme is given in Fig. 1. Figure 7 shows three ATR spectra obtained using a 400 nm PVFc film. The spectrum of the film prior to baking is identical to those reported (8) for pure PVFc. The 250°C bake was sufficient to eliminate the general hydrocarbon structure of the original film. The C-H stretching bands in the 3225-2777 cm^{-1} region are probably the most sensitive and have completely disappeared. A broad peak centered about 3333 cm^{-1} is suggestive of bonded water, one of the decomposition products from the thermal oxidation of PVFc. The associated band at 1612 cm^{-1} also is suggestive of water. A large band at 1390 cm^{-1} has been assigned to the iron carbonate structure. The remainder of the spectrum is characteristic of Fe_2O_3. After baking at 370°C for 30 min all traces of water and iron carbonate have disappeared and normal Fe_2O_3 spectrum remains. It should be noted that carbonate free material is still soluble in dilute HCl.

If these materials are fired above 450°C, the solubility in cold acids decreases until it becomes essentially zero. This has generally been attributed to crystallization of the iron oxide. It was found that the addition of 3% $SnCl_2$ to the 6M HCl increased the dissolution rate; however, this failed to facilitate solubility of normally insoluble material.

It should be emphasized that although results of the present investigation are internally self-consistent for this system, they deviate from results reported on other iron oxide systems (2, 3). It is likely that in none of the three investigations was pure Fe_2O_3 being studied, and it is likely that complex mixtures of several iron compounds and possibly residual cyclic carbon skeletons were involved. Since in all of the studies it was the final properties, such as u.v. visible absorption, defect density, and solubility (etch rate), which were of primary consideration, it is not surprising that details of the fundamental chemistry have remained obscure. Care should be exercised in comparing the films made by the three techniques: $Fe(CO)_5$, sputtered, and the polymer precursor system.

Conclusions

1. Poly(vinylferrocene) can be converted to an oxidized iron compound with properties similar to the films presently used to make semitransparent masks.

2. The PVFc may be oxidized with a 200W rf, oxygen plasma in 3 hr yielding a film with good mask properties. The disadvantages of this procedure are the long times and expensive equipment necessary.

3. PVFc may alternatively be thermally converted in 30 min to a suitable mask material in an O_2 ambient at 400°C.

4. Infrared analyses indicates that conversion below ~280°C yields a product which contains appreciable amounts of carbonate and water.

5. Baking above 400°C removes all traces of CO_3^{++} and H_2O; however, if 400°C is not exceeded, the films remain soluble in cold acids.

6. Scratch resistance and adhesion appear to be similar to the iron oxide films prepared by the pentacarbonyl process.

Acknowledgments

The author would like to acknowledge helpful conversations with W. Robert Sinclair, P. A. Turner, R. D. Heidenreich, and Gene Feit. He also thanks Betty Prescott for the spectroscopic studies and G. W. Kammlott for the x-ray diffraction studies. The plasma apparatus was used with the assistance of Frank Ryan. D. D. Bacon carried out the filtration and some thermal conversions, and E. P. Otocka provided the molecular weight data.

Manuscript submitted May 21, 1974; revised manuscript received Aug. 20, 1974.

Any discussion of this paper will appear in a Discussion Section to be published in the December 1975 JOURNAL. All discussions for the December 1975 Discussion Section should be submitted by Aug. 1, 1975.

Publication costs of this article were partially assisted by Bell Laboratories.

REFERENCES

1. M. V. Sullivan, *This Journal*, **120**, 545 (1973).
2. W. R. Sinclair, M. V. Sullivan, and R. A. Fastnacht, *ibid.*, **118**, 341 (1971).
3. F. G. Peters, W. R. Sinclair, and M. W. Sullivan, *ibid.*, **119**, 305 (1972).
4. J. B. MacChesney, P. B. O'Connor, and M. V. Sullivan, *ibid.*, **118**, 776 (1971).
5. F. J. Reid and P. Cukor, Abstract 127, p. 326, Electrochemical Society Extended Abstracts, Spring Meeting, Los Ange.es, Calif., May 10-15, 1970.
6. W. B. Shelby and P. Cukor, *Anal. Chim. Acta*, **49**, 275 (1970).
7. J. C. Lai, T. Rounsfell, and C. U. Pittman, *J. Polymer Sci.*, **9**, 651 (1972).
8. M. G. Baldwin and K. E. Johnson, *ibid.*, **5**, 2091 (1967).
9. C. Aso, T. Kunitake, and T. Nakashima, *Makromol. Chem.*, **124**, 232 (1969).
10. L. F. Thompson and R. D. Heidenreich, Unpublished results (1971).
11. L. I. Maissel and R. Glang, "Handbook of Thin Film Technology," McGraw-Hill Book Co., New York (1970).

Optical Characterization of GaAs Layers Grown on Ge Substrates

Hiroyuki Kasano and Sigeyuki Hosoki

Central Research Laboratory, Hitachi Limited, Kokubunji, Tokyo, Japan

ABSTRACT

The structural quality of GaAs layers grown on Ge substrates has been optically characterized as a function of the distance d from GaAs-Ge interface along the growth axis, supported by electrical measurement and also by x-ray measurement. It is found that the degradation of the structural quality due to interface alloying and autodoping of Ge can be detected in the grown layers only within $\sim 3\mu$ from the interface, where the concentration of Ge involved would exceed 1×10^{17} atoms/cm^3. However, the degradation caused by misfit dislocations extends as far as 80μ from the interface, in spite of the fact that the dislocation density decreases exponentially with increasing d. These misfit dislocations introduce quite effective nonradiative recombination centers in GaAs, which quench the luminescence intensity, L, in a form of $L = A \log (1 \times 10^6/N)$, where N is the density of these nonradiative recombination centers and A is a constant. If the GaAs layers are contaminated with Cu during the growth process, it is found that L is reduced in such a way that the constant A in the above equation is decreased.

In the commercial production of epitaxial layers of III-V compound semiconductors, such as GaAs and $GaAs_{1-x}P_x$, it is profitable to use Ge wafers as substrates. This is because Ge is superior to GaAs in wafer area and also in cost. However, heteroepitaxial growth of III-V compounds on Ge substrates causes degradation of the structural quality of the grown layers at the interface. This problem has been investigated in detail in the case of a GaAs-Ge system. The degradation includes misfit dislocations (1), interface alloying (2), autodoping of Ge (3), and the cross diffusions of Ge, Ga, and As (4). The structural quality of these GaAs layers has also been characterized by measurements on electron mobility (5) and the width of an x-ray rocking curve (6), but optical characterization has not yet been reported. Since crystal imperfections in GaAs crystals, such as dislocations (7) and precipitates (8), form deep levels and act as nonradiative recombination centers, structural quality can be studied by photoluminescence (PL) or cathodoluminescence (CL). Some works (5, 6) suggested that structural quality of these GaAs layers was rather improved in the bulk region of the epitaxial layer, more than 10μ from the heterojunction. It seems obvious that some portion of these improvements was due to an accommodation of the misfit by dislocation lines (9). However, little experimental work has been done to clarify the layer thickness dependence of the structural quality, which is an important factor for the practical use of Ge substrates.

The purposes of this study are: (*i*) to measure the distribution of crystal imperfections in these GaAs layers along the growth axis, (*ii*) to examine the influence of Ge involved in the GaAs epitaxial layers on the electrical and optical properties of the layers, and (*iii*) to examine the influence of other residual impurities on the optical properties of these GaAs layers. In order to achieve these purposes, the luminescence properties were observed at ~ 80°K under constant excitation level as a function of the distance, d, from Ge substrates. This conventional optical characterization, supported by x-ray topography, leads to the conclusion that degradation of structural quality due to misfit dislocations and residual impurity Cu (10) are important for the bulk properties of these GaAs layers. The concentration of Ge involved is estimated to be less than 1×10^{17} atoms/cm^3 except for the interface region, which is different from the case of $GaAs_{1-x}P_x$ layers (11).

Key words: misfit dislocations, cathodoluminescence, degradation of luminescence, nonradiative recombination, GaAs.

Experimental

GaAs was epitaxially grown on a (311) surface of a Ge substrate in the growth apparatus reported elsewhere (12) by using a GaAs-$AsCl_3$-H_2 system. The substrate, Ge, was doped with arsenic ($\rho = 3 \sim 5 \times 10^{-3}$ ohm-cm). The front face of the substrate was polished to a mirror surface and chemically etched with a solution of $1HF:1H_2O_2:1H_2SO_4$ prior to use, whereas the back and side faces of the substrate were coated with a Si polycrytalline film (11). Unintentionally doped GaAs crystals ($n = 1 \sim 3 \times 10^{17}$ cm^{-3}) and Te-doped ones ($n = 1 \times 10^{18}$ cm^{-3}) were used as source materials for the epitaxy. The source and substrate temperatures adopted empirically were in the range of $750° \sim 950$°C and $680° \sim 720$°C, respectively. Pd-diffused hydrogen and 7-nines pure $AsCl_3$ were used. The partial pressure of $AsCl_3$ was $0.5 \sim 3 \times 10^{-3}$ atm. GaAs layers, with a thickness of $20 \sim 180\mu$, were grown for 2-8 hr. All the grown layers had mirror-smooth surfaces except when the surface of the substrate was contaminated.

The doping profile in the grown layers was measured electrically along the growth axis, using both the point-contact breakdown (PCB) method and the d-c Van der Pauw technique (13) at a magnetic field of 4500 gauss. The measurement of PCB voltages, V_B, was carried out on a one-degree angle-lapped surface of the sample. The relation between the carrier concentration and V_B was calibrated beforehand by the C-V measurement on Schottky barriers formed on the as-grown surface. The PCB method is excellent for obtaining the profile of the carrier concentration near the interface. Electron mobility, as well as carrier concentration in the bulk region of GaAs layers was measured against the distance, d, from the interface by the d-c. Van der Pauw technique. Prior to the Van der Pauw measurement, both the Ge substrate and the GaAs layer of $\sim 10\mu$ in thickness adjacent to the interface were removed by lapping. Indium alloys were used as ohmic contacts. In these cases, electrical measurement and chemical etching of the GaAs layer for only the as-grown surface side were alternatively repeated on the same sample. Fluctuation of layer thickness by etching was controlled within 10μ.

Photoluminescence (PL) was measured at 80°K to examine the optical influence of Ge on GaAs layers, using the Hg 3650Å line as an excitation source and a

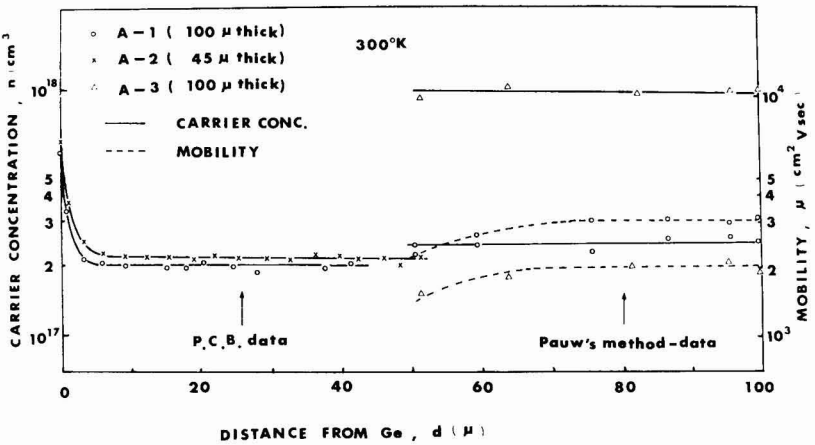

Fig. 1. Electrical properties of GaAs layers grown on Ge substrate, measured as a function of distance from the GaAs-Ge interface, *d*, at 300°K. The influence of Ge incorporated into GaAs layers is only observed in a region within ~3μ from the interface. The concentration of Ge involved is of the order of magnitude of 10^{16} atoms/cm^3 or less beyond the interface region. The gradual decrease in mobility with decreasing *d* is caused by the crystal imperfections due to lattice mismatch.

33-86-40 Type spectrometer (Bausch and Lomb) coupled with a 7102 photomultiplier (Hamamatsu TV) as a detector. The excitation level of PL was kept constant for all samples. Since the PL intensity was observed to decrease drastically with reduction of the layer thickness, the intensity variation against *d* was further investigated using cathodoluminescence (CL) at 77°K. Operating conditions of CL were: accelerating voltage 30 kV, primary beam current 10^{-7}A, and beam spot diameter 1 ~ 3μ for all samples. These conditions result in a quite high excitation level of luminescence, which is higher than that of the above-mentioned PL by several orders of magnitude. In this case, an EPU-2A Type spectrometer (Hitachi) coupled with a 7102 Type photomultipler (Hamamatsu TV) was used as a detector. A step-etching technique was applied to each sample to vary *d*.

The dislocation density in GaAs layers, *N*, was measured against *d* by a transmission x-ray topograph using an Ag target. Prior to the measurement, the Ge substrates were removed by lapping, and GaAs layers with the desired thickness were obtained by using mechanical polishing and chemical etching. Samples with a different doping level and a different thickness were examined. Precipitates were observed in the GaAs layers near the interface using a transmission electron microscope. In this case, a hot H_2O_2 solution (5) was used as an etchant of the Ge substrate. After the Ge substrate was removed, the GaAs layer was carefully etched with a solution of $4H_2SO_4$: $1H_2O_2$: $1H_2O$ from only the as-grown surface side, in order to obtain the thin layer with a thickness of about 1000Å at the peripheral. These thin layers were bombarded with a 100 kV electron beam under a vacuum of 10^{-5} Torr.

In order to ascertain the origin of the acceptor-like residual impurities, a Cu-diffused GaAs sample was also prepared.

Results and Discussion

Influence of Ge incorporated into GaAs layers by autodoping process.—In this section, the influence of Ge incorporated into GaAs layers by the autodoping process is discussed.

Profiles of the carrier concentration, as well as those of mobility, were electrically measured and are shown in Fig. 1 as a function of *d*. The GaAs source crystals used for the epitaxial growth were an undoped one ($n = 2 \times 10^{17}$cm^{-3}, $\mu = 3000$ cm^2/V·sec) for samples A-1 and A-2, and a Te-doped one ($n = 1 \times 10^{18}$cm^{-3}, $\mu = 2000$ cm^2/V·sec) for sample A-3. It is found from Fig. 1 that the carrier concentrations in these layers are kept constant along the growth axis and are consistent with those in the GaAs source, except for the regions within 2 ~ 3μ from the interface, where they are significantly high. These high carrier concentrations are believed to be caused by Ge incorporated by the autodoping process, because the samples examined in this section were carefully prepared in an atmosphere kept as clean as possible to minimize the influence of residual impurities. This is supported by the following results obtained using a transmission electron microscope. A high density (10^5 ~ 10^6 cm^{-2}) of precipitates with a diameter of ~1μ in the interface region was observed, and a typical example is shown in Fig. 2. Stacking faults were also observed to originate from some precipitates. However, no precipitate could be detected in layers a few microns apart from the interface. These results suggest that the Ga-Ge-As alloy (2) was partially produced only in regions within 2 ~ 3μ from the interface as a result of relatively heavy incorporation of Ge by the autodoping process. The profiles of the carrier con-

Fig. 2. A micrograph of the GaAs layer within 1 ~ 2μ from the interface, obtained by using a transmission electron microscope. A high density (10^5 ~ 10^6 cm^{-2}) of precipitates probably due to alloying are shown to exist. Prior to measurements, the Ge substrate was completely removed from the GaAs layer by chemical etching with hot H_2O_2 solution (5).

centration in Fig. 1 suggest that the Ge concentration in the GaAs layers is of the order of magnitude of 10^{16} atoms/cm^3 or less except for the interface region, and that the impurity doping from the source materials is kept constant during the whole growth process.

The relatively low concentration of Ge in the bulk region of the GaAs layers was ascertained by the following thermodynamical consideration for the vapor etching process of Ge substrates and also by the results of photoluminescence measurement.

At the substrate temperatures adopted in this experiment, 680° ~ 720°C, the predominant reaction between Ge and HCl is expressed as (14)

$$Ge + 3HCl \rightleftarrows GeHCl_3 + H_2 \qquad [1]$$

with the equilibrium constant, K_{P1}, which was given by Miller *et al.* (14) as a function of temperature. In this case, the partial pressure of $GeHCl_3$ can be expressed by

$$P_{GeHCl_3} = \frac{1}{3}\left\{ P_{HCl(GaAs)} - \left[\frac{P_{HCl(GaAs)}}{6K_{P1}} + \frac{\sqrt{\frac{P^2_{HCl(GaAs)}}{K^2_{P1}} + \frac{4}{81K^3_{P1}}}}{6} \right]^{1/3} + \left[-\frac{P_{HCl(GaAs)}}{6K_{P1}} + \frac{\sqrt{\frac{P^2_{HCl(GaAs)}}{K^2_{P1}} + \frac{4}{81K^3_{P1}}}}{6} \right]^{1/3} \right\} \qquad [2]$$

where $P_{HCl(GaAs)}$ is the equilibrium partial pressure of HCl over the GaAs source and equals $3P_{AsCl_3}/(1 + \sqrt[4]{K_P/P_{As_4}})$. The equilibrium constant of the GaAs-$AsCl_3$-H_2 system, K_P, has been calculated (11). By inserting the values of the growth parameters (the source temperature, the substrate temperature, and the partial pressure of $AsCl_3$) adopted in this experiment into the above equations, we get $P_{GeHCl_3} \lesssim 1 \times 10^{-6}$ atm. This value corresponds to a Ge concentration of 3×10^{18} atoms/cm^3 in GaAs if the back-deposition rate of Ge is assumed to be 50%. Once the front face of the Ge substrate is covered with a GaAs layer, P_{GeHCl_3} may immediately drop by a few orders of magnitude. The net weight loss of Ge was measured after the grown layer was removed by chemical etching. None of the Ge was lost during the chemical etching process. The amount of the weight loss due to vapor etching was 0.05 ± 0.02 mg after a 5 hr run for a sample with an exposed surface area of 4 cm^2. This value is reasonable when compared with the calculated result, *i.e.*, the vapor etching of the Ge substrate with $AsCl_3$ is not so serious that the resultant incorporation of Ge will be reduced to less than 10^{17} atoms/cm^3 in the bulk region of GaAs more than a few microns apart from the interface.

Photoluminescence spectra from the epitaxial layers are shown in Fig. 3. The data of a Ge-free sample (sample B) is included for comparison. Sample B was grown on a GaAs substrate in a different growth apparatus using a Ga source. There exist broad and intense low energy emission bands in addition to the near-gap emission band in every sample. The origin of these low energy bands is not well understood but is considered to be complexes associated with vacancies, such as a Ga vacancy-donor complex (15), because they appear in any bulk GaAs crystal containing various kinds of donors. Emission peaks due to Ge in n-GaAs are known to locate at 8380Å for the first acceptor level (16, 17), 8890Å for the second acceptor level (18), and ~ 10,100Å for the donor level (16) at 77°K. Kressel *et al.* (18) reported

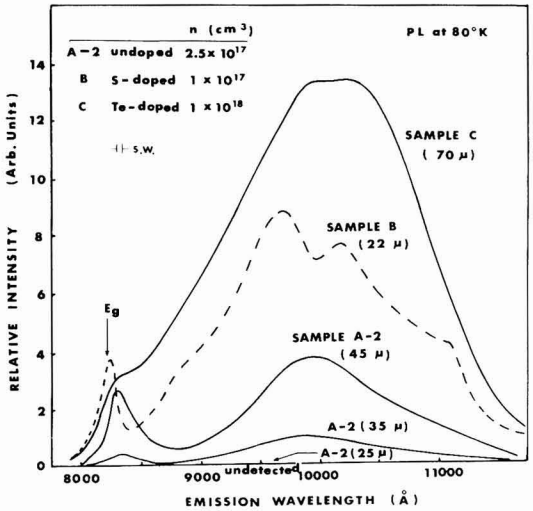

Fig. 3. Photoluminescence spectra at 80°K under constant excitation level. Samples A-2 and C were grown on Ge substrates, whereas sample B was grown on a GaAs substrate using a Ga-$AsCl_3$-H_2 system. The decrease of luminescence intensity is found in the case of A-2 as the layer thickness is reduced.

that the emission bands due to Ge could be detected in the PL spectra of GaAs if the Ge concentration exceeded 1×10^{17} atoms/cm^3. However, none of them is observed in the PL spectra on the present samples. So, there is no evidence that samples A-2 and C are doped with Ge, although they are doped more heavily than sample B.

It is found in Fig. 1 that the electron mobility of the GaAs layers grown on the Ge substrates decreases gradually as d is reduced to less than 70μ, though the carrier concentration is invariant in this region. It is also found in Fig. 3 that luminescence intensity of sample A-2 decreases drastically with reducing d, whereas the spectrum is unchanged. The other samples grown on Ge substrates also showed similar results. Therefore, it is believed that these reductions in mobility and luminescence intensity were caused by the inhomogeneous distribution of crystal imperfections, and not by that of impurities. This problem is discussed in detail in the next section.

Influence of misfit dislocations.—In addition to the autodoping of Ge and interface alloying, lattice mismatch at the GaAs-Ge interface also causes the degradation of the structural quality of the GaAs layers. In this experiment, the distribution of dislocations was investigated as a function of d, using a transmission x-ray topograph. Topographs were taken at different thicknesses of the GaAs layers as they were lapped and chemically etched from only their substrate sides. The result is shown in Fig. 4. It is found in Fig. 4 that the dislocation density, N, increases exponentially with decreasing d, which is similar to the case of GaP layers grown on GaAs substrates (19). Such a high density of dislocations and their exponential distribution could not be observed in GaAs layers grown on GaAs substrates. The value of N at the interface, 1×10^6 cm^{-2}, obtained from Fig. 4 by extrapolation is consistent with that reported by Holloway *et al.* (1), 2×10^6 cm^{-2}, for the sample grown at 750°C. As was suggested by Meieran (20), these dislocations are considered to have originated from the lattice constant mismatch between Ge and GaAs. These misfit dislocations, as is shown in Fig. 3, act as quite effective nonradiative recombination centers. On the other hand, the dislocations introduced by a four-point bending are less active recom-

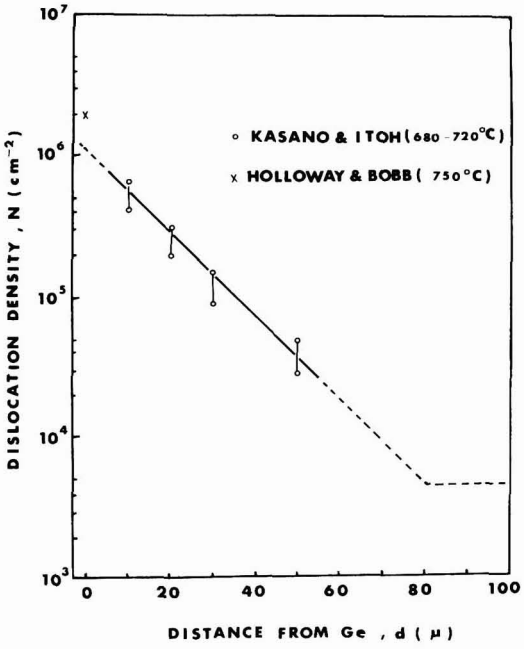

Fig. 4. Dislocation density of GaAs layers grown on Ge substrates, measured by using an x-ray topograph technique as a function of d. The dotted line is estimated from the result of the CL data shown in Fig. 5.

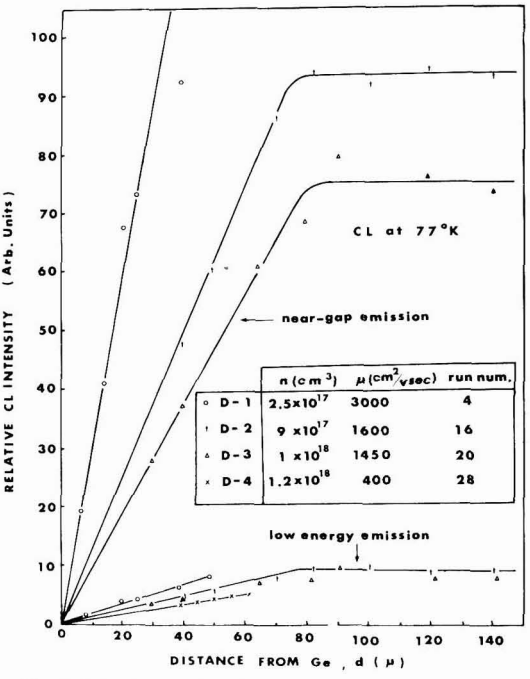

Fig. 5. Intensity variation of the cathodoluminescence from the GaAs layers grown on Ge substrates, measured as a function of d at 77°K. There are only two emission bands in the CL spectra, one of which is the near-gap emission with stronger intensity and the other is the low energy subband peaked at 9200Å with weaker intensity.

bination centers; Esquivel *et al.* (21) showed in the CL measurement for GaAs that only half of the initial intensity was quenched when high 10^6 cm^{-2} dislocations were introduced by bending. The decreasing rate of intensity is smaller than that observed in Fig. 3 by an order of magnitude. These differences in the decreasing rate may be caused by the impurity effect for dislocations; *i.e.*, grown-in dislocations associated with impurities act as effective nonradiative recombination centers (7, 22), whereas dislocations without impurity association do not do so (22). Therefore, a predominant part of the misfit dislocations in this experiment is considered to be associated with impurities, Ge, and other residual impurities.

In order to clarify the dependence of luminescence intensity, L, on the misfit-dislocation density, cathodoluminescence was measured at 77°K (23) as a function of d on several samples with different doping levels. The observed CL spectra consisted of only two emission bands as are shown in Fig. 6. They were the near-gap emission band peaked at 8230 ~ 8290Å and the lower energy subband peaked at ~ 9200Å. The intensity of both the bands varied with d as was shown in Fig. 5, though the spectra were unchanged as in the case of the above-mentioned PL. Figure 5 shows that L is nearly constant in a region of $d \geqq 80\mu$, but it decreases linearly with decreasing d in a region of $d < 80\mu$ in any sample and in any emission band. At the interface ($d = 0$), L converges to zero. As the excitation level increased, L generally increased until saturation occurred, whereas L at the interface remained zero. From Fig. 4 and 5, L is given as a function of N by

$$L = L_s \log\left(\frac{N_0}{N}\right) / \log\left(\frac{N_0}{N_s}\right) = A \log\left(\frac{N_0}{N}\right), \quad (N_s \leqq N \leqq N_0) \quad [3]$$

where L_s is the saturated intensity at ~ 80μ, N_0 is the density corresponding to $L = 0$, N_s is the density which gives L_s, and A is $L_s/\log(N_0/N_s)$. In this case, $N_0 = 1 \times 10^6$ cm^{-2}, and $N_s \simeq 5 \times 10^3$ cm^{-2}. The excited pairs which are within a diffusion length, l, of the edge of the recombination center with the effective radius, r, will be drawn to this center, where they recombine nonradiatively via the continuum of states (24). It is noteworthy that the decrease of L is proportional to log N, and not to N in the empirical Eq. [3]. The logarithmic dependence of L on N may be caused by the decrease of l as N increases. It has been established (25) that the lifetime of minority carriers, τ, in plastically deformed pure Ge is proportional to $1/N$. If l is simply defined as $\sqrt{D\tau}$, and the decrease of L is assumed to be proportional to l^2N, the decrease of L becomes independent of N in pure Ge as suggested in the case of dislocations without impurity association in $GaAs_{1-x}P_x$ (22). However, the N dependence of τ becomes a more complicated form in the case where the dislocations are associated with impurities (25). The $D\tau$ is in this case proportional to $(1/N)$ ln N based on Eq [3], though the mechanism is not clarified. The intensity saturation at $d \simeq 80\mu$ in Fig. 5 is probably caused by the "background" crystal imperfections, whose density is determined by the growth conditions. The dislocation density corresponding to this intensity saturation is estimated to be ~ 5×10^3 cm^{-2} from Fig. 4. The results of Fig. 1, 3, and 5 indicate that the profile of misfit dislocations is explicitly obtained by measuring luminescence intensity under the constant excitation conditions along the growth axis. This results from the fact that the intentionally doped and/or unintentionally doped impurities are uniformly distributed except for the interface region.

As briefly mentioned above, the constant A in Eq. [3] can drastically vary from sample to sample. A

typical case is shown in Fig. 5. The D-series samples in Fig. 5 were grown using the same lot of $AsCl_3$ but a small amount of leakage existed in the gas line of the growth apparatus between the Pd diffuser and the $AsCl_3$ reservoir. By comparing the electrical properties of the D-series samples included in Fig. 5, it is found that the constant A becomes smaller in the sample with lower electron mobility, and that electron mobility becomes lower with the run number for the same lot of $AsCl_3$. It was also observed that the emission bandwidth became broader for the samples with a smaller value of A. Sample D-4 is the extreme case, were no near-gap emission band but only the broad and weak subband peaked at $\sim$ 9200Å was observed. This sample showed n-type conduction with the carrier concentration of 1.2×10^{18} cm^{-3}, but mobility was only 400 cm^2/V·sec. The growth conditions of D-4 were similar to those of other D-series samples except that the Pd diffuser was broken. The degradation of luminescence due to the decrease of A is obviously different from the degradation due to the misfit dislocations mentioned above. Both the bandwidth broadening and the relative increase of intensity of the low energy subband happen in this case. Hence, the origin of the decrease of A is deduced to be the contamination that occurred during the growth process. It should be emphasized that these contaminants also act as the origin of the low-energy subband. The details are discussed in the next section.

Influence of Cu on cathodoluminescence properties. —The CL properties of GaAs containing Cu are dealt with in this section, being correlated with the results obtained in the above section.

In the previous section, we have pointed out that the reduction of L due to the decrease of A is caused by contamination. The low electron mobility and the bandwidth broadening of the D-series samples suggest that the contaminants increase the compensation ratio of GaAs. It means that the contaminants act as acceptors in GaAs. We observed in this CL measurement at 77°K that the low energy subband was located at ~9800Å in Si-doped GaAs crystals and that luminescence intensity was not quenched in oxygen-doped semi-insulating GaAs crystals. They indicate that neither silicon nor oxygen is the contaminant in the present case. The peak position of the subband in this case, ~9200Å (1.35eV) at 77°K, is consistent with that of Cu-doped GaAs crystals, reported by Alferov *et al.* (26) using a photoluminescence technique. Hence, we can speculate the contaminant to be Cu, which can be easily introduced into III-V compounds during the growth process and degrades the radiative efficiency (27).

In order to make sure of this assignment, a Cu-diffused GaAs sample was prepared, and the CL properties of this sample were measured. A Te-doped GaAs wafer ($n = 1 \times 10^{18}$ cm^{-3}) with a mirror-smooth surface (sample E) was dipped into a Cu_2SO_4 solution for 1 min and sealed in a quartz ampule at 1×10^{-5} Torr. The diffusion was carried out at 960°C for 20 min. Then, sample E was angle-lapped at 5° and its CL properties were measured as a function of the distance from the front surface along the wafer thickness, d. Figure 6 shows the CL spectra of samples D-2 and E (before and after Cu diffusion, respectively) near the front surface of the wafer. In sample E, the intensity of the near-gap band, L_G, became very weak and the relative intensity of the low energy subband against L_G,L_{Cu}/L_G, increased as a result of Cu diffusion. This result supports the above assignment that the degradation of luminescence with reduction of A was caused by Cu contamination. The reduction of luminescence intensity, as well as the enhancement of the relative intensity of the 1.35 eV band, was also reported for Cu-doped GaAs samples (28). As was predicted by Batavin *et al.* (28), the concentration of Cu involved can be estimated by measuring L_{Cu}/L_G. Figure 7 shows the variations of L_G and L_{Cu}/L_G along the wafer thickness in the sample E before and after Cu diffusion. The values of L_G and L_{Cu}/L_G are constant with d before Cu diffusion and it indicates a uniform distribution of unintentionally doped Cu impurity in the sample E. After Cu diffusion, both of them vary with d. It is found that the concentration of Cu dips near the center of depth, $d \simeq 450\mu$ as a result of Cu diffusion from both sides of the wafer surface. It is noticeable that the anomalous diffusion coefficient of Cu in GaAs (29) resulted in a rather high concentration of Cu even at the center of depth.

Next, the excitation current (I_B) dependence of L_G and L_{Cu} was observed. Figure 8 shows the I_B dependence of the CL intensities, L_G and L_{Cu}, of a GaAs layer near the front face of the Cu-diffused sample E. It is found that L_G is proportional to I_B^2, whereas L_{Cu} is proportional to I_B. Rao-Sahib *et al.* (30) reported that CL intensity in p-GaAs was proportional to I_B^m ($1 \leq m \leq 2$) under the constant accelerating voltage, where $m = 1$ for low current region and $m > 1$ for high current region. A linear dependence of L on I_B was also observed by Casey *et al.* (31) in the Zn-O doped GaP, which was measured using an unfocused beam. These current dependences are reasonably ex-

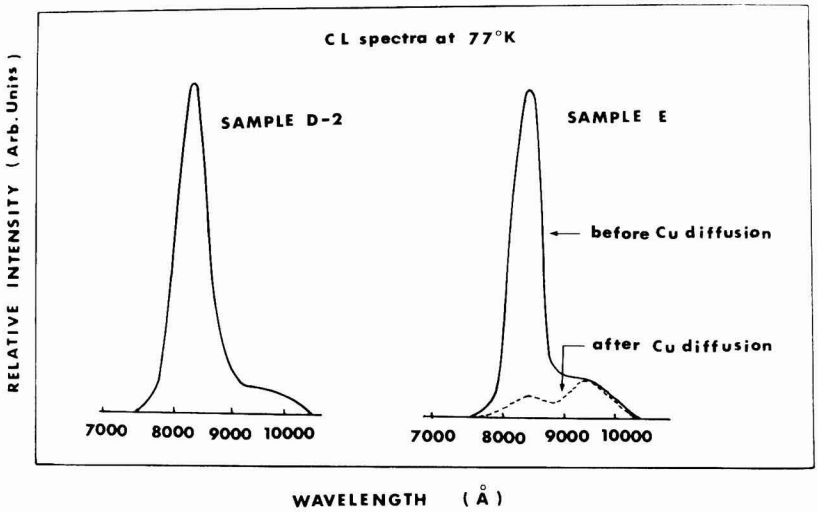

Fig. 6. Cathodoluminescent spectra of GaAs at 77°K, indicating the optical influence of Cu contaminants.

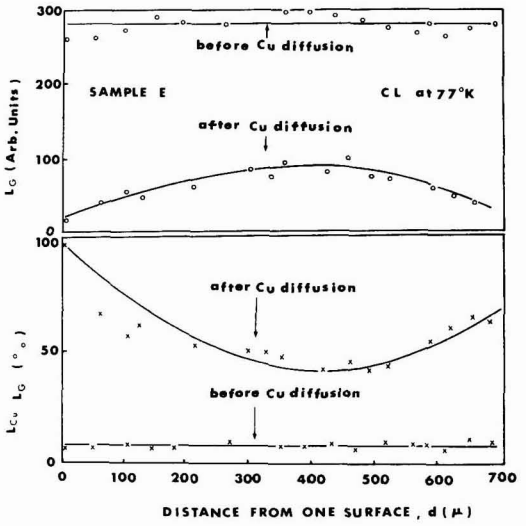

Fig. 7. Intensity variation of the cathodoluminescence of sample E before and after Cu diffusion along the wafer thickness, measured at 77°K. The figure shows that the concentration of Cu varies along the wafer thickness after Cu diffusion.

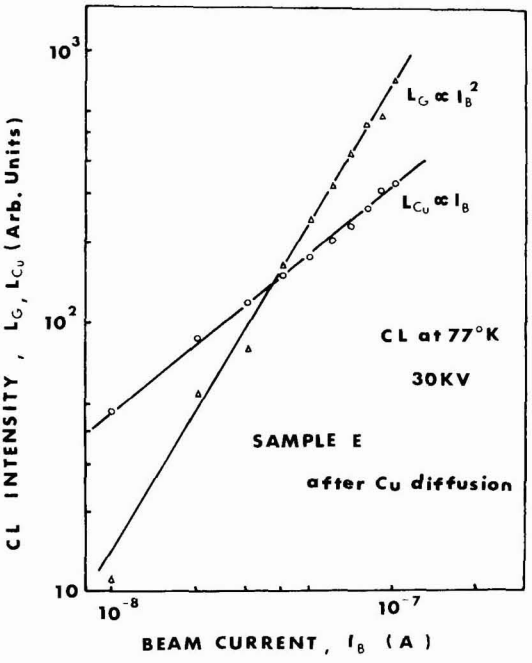

Fig 8. Beam current dependence of the two emission bands at 77°K, measured under the constant accelerating voltage of 30 kV.

plained as follows. The density of free hole-free electron pairs, N_{pair}, created by electron beam excitation is given by (24)

$$N_{pair} = K\left(\frac{I_B}{S}\right)\left(\frac{E_P}{E_o}\right)F(\gamma, d) \qquad [4]$$

where E_P/E_o is the number of pairs created per incident electron, S the excited area, γ the back-scattering rate of the incident electron, d the effective penetration depth of the incident electron, and K the constant. Though F is given as the complicated form (32) because of the nonuniform distribution of carrier generation with depth, it is considered that γ, d, and also F are kept nearly constant if the material, the accelerating voltage, and the flatness of the beam-incident plane are kept constant. As is well known, the radiative recombination rate of free electron-hole pairs under a constant excitation condition is given by the following equations

$$R_{exc} = \frac{np}{n_i^2} = \frac{(n_o + \Delta n)(p_o + \Delta p)}{n_i^2}R \qquad [5]$$

where R is the radiative recombination rate at thermal equilibrium which was derived by van Roosbroeck and Shockley (33), n_i the intrinsic carrier concentration, $\Delta n(\Delta p)$ a deviation of electron (hole) concentration from a thermal equilibrium value of $n_o(p_o)$ caused by the excitation, or N_{pair}. Since p_o is much greater than n_o in uncompensated p-type materials or vice versa in n-type ones, the following relation is approximately derived for p-GaAs from Eq. [4] and [5] under a constant accelerating voltage

$$R_{exc} \propto \Delta n(p_o + \Delta p) \propto p_o I_B + \alpha I_B^2 \qquad [6]$$

where α is the constant. Equation [6] indicates that R_{exc} is proportional to I_B at low excitation levels where $p_o >> \Delta p$, whereas R_{exc} proportional to I_B^2 at high excitation levels or in a lightly doped p-type material where $\Delta p >> p_o$ holds. This is the case of Rao-Sahib *et al.*

If GaAs is highly compensated, which is the case of sample E, a relation $p_o \simeq n_o$ holds and

$$R_{exc} \simeq \frac{(p_o + \Delta p)^2}{p_o^2}R = \left(1 + \frac{\Delta p}{p_o}\right)^2 R \qquad [7]$$

At the excitation levels used in this experiment, $\Delta p >> p_o$ holds in sample E. Hence, R_{exc} is proportional to I_B^2 in the case of near-gap emission, namely $L_G \propto I_B^2$.

The 1.35 eV subband was reported (26) to be due to the recombination between a free electron and a hole bound to the first acceptor level of Cu. In this case, the radiative recombination rate would be limited by the concentration of Cu in the first acceptor state, N^A_{Cu}, because of p, $n >> N^A_{Cu}$, namely, the recombination rate is proportional to the product of $n \cdot N^A_{Cu}$. Hence, a relation $L_{Cu} \propto N_{pair} \propto I_B$ is obtained if $\Delta p >> p_o$, which is the case shown in Fig. 8.

Summary

In this work the structural quality of the GaAs layers grown on the Ge substrates has been investigated as a function of distance from the GaAs-Ge interface, by measuring the photo- and cathodoluminescence properties at 77°K, as well as electrical properties at 300°K. The measurements using an x-ray topography and a transmission electron microscope were also carried out. At the interface, the structural quality of these GaAs layers was heavily degraded by misfit dislocations, interface alloying, and also by autodoping of Ge from the substrate, though the backside faces of the substrate were coated with a Si polycrystalline film during the epitaxy. It is found that the influences of interface alloying and also autodoping of Ge on the electrical and optical properties of these GaAs layers are substantially neutralized in the regions more than a few microns apart from the interface. However, it is also found that structural quality of these GaAs layers less than ~80μ in thickness is affected by the misfit dislocations, though the dislocation density decreases exponentially with d. These misfit dislocations introduce quite effective nonradiative recombination centers in GaAs. It is noteworthy that luminescence intensity, L, is reduced by these nonradiative recombination centers according to the following experimental equation

$$L = A \log(N_0/N) + L_{min}$$

where N is the density of these centers and $N \leq N_0$. In the case of the GaAs-Ge system, $N_0 \simeq 1 \times 10^6$ cm^{-2} $L_{min} = 0$. Hence, by measuring the variation of L under the constant excitation conditions, the distribution of these centers can be easily estimated. The other factor which drastically reduces L is the residual impurities, especially Cu incorporated into GaAs during the growth process. The reduction of L due to Cu is found to occur as the decrease of A in the above equation. The distribution of Cu was estimated by measuring the distribution of the relative intensity of the 1.35 eV subband against the near-gap emission band, L_{Cu}/L_G, under the constant excitation conditions at 77°K. The dependence of the intensities of these two bands on the excitation level was also examined.

Acknowledgments

The authors are grateful to M. Tamura for his measurements using a transmission electron microscope, to Dr. S. Kishino for measurements using an x-ray topograph technique, to A. Doi for photoluminescence measurements, to S. Fukuhara for his technical assistance for cathodoluminescence measurements, and to K. Itoh for providing a part of the data of misfit-dislocation density. They would also like to thank Dr. J. Umeda, K. Kurata, and S. Tanimizu for their stimulating discussions and advice. They also wish to voice their appreciation of the support and encouragement given by Dr. H. Okano during the course of this experiment.

Manuscript submitted March 15, 1974; revised manuscript received July 29, 1974.

Any discussion of this paper will appear in a Discussion Section to be published in the December 1975 JOURNAL. All discussions for the December 1975 Discussion Section should be submitted by Aug. 1, 1975.

Publication costs of this article were partially assisted by Hitachi, Limited.

REFERENCES

1. H. Holloway and L. B. Bobb, *J. Appl. Phys.*, **39,** 2467 (1968).
2. H. Kasano and S. Iida, *Japan. J. Appl. Phys.*, **6**, 1038 (1967).
3. J. Grossman, *This Journal,* **110,** 1065 (1963).
4. W. Rice, *Proc. IEEE,* **52,** 284 (1964).
5. G. O. Radd, Jr. and D. L. Feucht, *Met. Trans.*, **1,** 609 (1970).
6. L. C. Bobb, H. Holloway, and K. H. Maxwell, *J. Appl. Phys.*, **37,** 4687 (1966).
7. K. H. Zschauer, *Solid-State Commun.*, **7,** 385 (1969).
8. H. Kressel, H. Nelson, S. H. McFarlane, M. S. Abrahams, P. LeFur, and C. J. Buiocchi, *J. Appl. Phys.*, **40,** 3587 (1969).
9. J. W. Matthews, S. Mader, and T. B. Light, *ibid.*, **41,** 3800 (1970).
10. T. N. Morgan, M. Pilkuhn, and H. Rupprecht, *Phys. Rev.*, **138,** A 1551 (1965).
11. H. Kasano, *Solid-State Electron.*, **16,** 913 (1973).
12. M. Aoki and H. Kasano, *Japan. J. Appl. Phys. Suppl.*, **39,** 234 (1970).
13. L. J. Van der Pauw, *Philips Res. Rept.*, **13,** 1 (1958).
14. K. J. Miller and M. J. Grieco, *This Journal,* **111,** 1099 (1964).
15. E. W. Williams, *Phys. Rev.*, **168**, 922 (1968).
16. H. Kressel, *J. Appl. Phys.*, **38**, 4383 (1967).
17. W. Schairer and W. Graman, *J. Phys. Chem. Solids,* **30,** 225 (1969).
18. H. Kressel, F. Z. Hawrylo, and P. LeFur, *J. Appl. Phys.*, **39,** 4059 (1968).
19. L. C. Luther, *Met. Trans.*, **1,** 593 (1970).
20. E. S. Meieran, *This Journal,* **114,** 292 (1967).
21. A. L. Esquivel, W. N. Lin, and D. B. Wittry, *Appl. Phys. Letters,* **22,** 414 (1973).
22. G. B. Stringfellow and P. E. Greene, *J. Appl. Phys.*, **40,** 502 (1969).
23. S. Hosoki and H. Okano, 6th Int. Conf. on X-ray Optics and Microanalysis, Osaka, 1972.
24. J. I. Pankove, "Optical Processes in Semiconductors," Prentice-Hall Inc., Englewood Cliffs, N. J. (1971).
25. G. K. Wertheim and G. L. Pearson, *Phys. Rev.*, **107,** 694 (1957).
26. Zh. I. Alferov, D. Z. Garbuzov, and E. P. Morozov, *Soviet Phys. Solid-State,* **8,** 2589 (1967).
27. A. A. Bergh, *IEEE Trans. Electron Devices,* **ED-18,** 166 (1971).
28. V. V. Batavin, V. M. Mikhaélyan, and G. V. Popava, *Soviet Phys. Semicond.*, **6,** 1616 (1973).
29. C. S. Fuller and J. M. Whelan, *J. Phys. Chem. Solids,* **6,** 173 (1958).
30. T. S. Rao-Sahib and D. B. Wittry, *J. Appl. Phys.*, **40,** 3745 (1969).
31. H. C. Casey, Jr. and J. S. Jayson, *ibid.*, **42,** 2774 (1971).
32. D. F. Kyser and D. B. Wittry, *Proc. IEEE,* **55,** 733 (1967).
33. W. van Roosebroeck and W. Shockley, *Phys. Rev.*, **94,** 1558 (1954).

Chemisorption Reactions on High Index ZnS Surfaces

W. R. Bottoms and D. B. Lidow

Princeton University, Princeton, New Jersey 08540

ABSTRACT

An attempt is made to determine the relative strength of interaction with an ambient for ZnS surfaces which differ only in the crystallographic perfection of the surface. Chemisorption reactions for a (110) crystal and a stepped high index ZnS surface with oxygen and carbon monoxide were monitored with low energy electron diffraction (LEED) and Auger electron spectroscopy (AES). The correlation of the dissociation and chemisorption activity with the disorder on these ZnS surfaces exhibits the importance of active sites in surface chemical reaction.

Various investigators have suggested that there exist certain "active sites" which are responsible for the chemical activity of catalysts (1). These "active sites" have generally been attributed to lattice defects and/or the topographic structure of a catalyst surface (2). Experimental investigations undertaken to determine the role of surface irregularities in the catalytic activity support an important role for surface imperfections in the chemical activity of these surfaces (2-4). In the present investigation an attempt is made to determine the relative strength of interactions with an ambient for ZnS crystal surfaces which differ only in the crystallographic perfection of the surface.

A (110) surface and a stepped high index face were prepared from a single ZnS crystal to insure identical bulk properties. Two independent experiments were performed upon these crystal faces to characterize the chemical activity of the edge states present upon the high index face using the nonreconstructed (110) surface as a control. In the first experiment, the two crystal faces were introduced separately into a 4-grid LEED-Auger device with a base pressure of 2×10^{-10} Torr. The surface composition and surface symmetries were then monitored with low energy electron diffraction (LEED) and Auger electron spectroscopy (AES). After cleaning the surfaces by argon ion bombardment and annealing, the crystal faces were subjected to various oxygen containing atmospheres and the chemical interaction was observed with LEED and AES. The second experiment exposed the same crystals, both faces mounted simultaneously in the system, to carbon dioxide containing atmospheres and similar LEED and AES observations were made. The results support the dominance of active sites in surface based chemical reactions.

Sample Preparation

The (110) surface, prepared by cleaving in air, exhibited a diffraction pattern upon room temperature pumpdown before any in vacuum processing. Auger spectra taken on these crystals before processing indicated the presence of oxygen, carbon, and chlorine in that order of abundance in addition to sulfur and zinc. These surface contaminants resulted in a poorly developed diffraction pattern and a sequence of annealing steps was undertaken to determine the desorption temperature for chemisorbed gases. The quality of the diffraction pattern showed no significant change until 580°C at which time there was a relatively abrupt change to a well-developed diffraction pattern. The development of the LEED pattern with annealing, illustrated in Fig. 1, indicates a relatively low binding energy for chemisorbed gases on the cleaved (110) surface of ZnS. Auger spectra taken after this high vacuum annealing confirm that the surface is relatively clean since no elements other than zinc, sulfur, and small amounts of carbon were detected. This carbon was almost completely removed by the argon ion bombardment and annealing sequence indicated in Table I before the dosing experiments.

Key words: chemisorption, defect states, zinc sulfide.

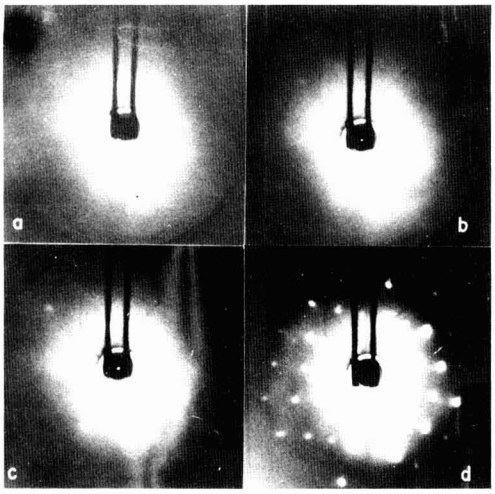

Fig. 1. Diffraction pattern of a (110) ZnS surface after cleaving in air, (a) no vacuum annealing, (b) 200°C for 10 min, (c) 500°C for 20 min, (d) 580°C for 10 min.

Numerous experimentors have founnd that a high index crystal surface will, if given sufficient energy to initiate mass transfer, reorder itself into a surface of low index steps. These stepped or terraced surfaces have been observed by LEED for copper, germanium, gallium arsenide, uranium dioxide, and platinum (6). In the present study, a ZnS crystal was cut at a low angle to the (110) and chemically polished to provide such a stepped surface. This surface did not exhibit a diffraction pattern upon its first introduction into the vacuum system, and the argon ion bombardment

Table I. Preparation of the crystal faces

Random high index	(110)
Sawed at a low angle to the (110)	Cleaved
Chemically polished	Argon bombarded 41 hr
Annealed 30 min at 400°C*	Annealed 10 min at 1000°C*
Argon bombarded 20 hr	Annealed 10 hr at 600°C*
Annealed 45 min at 650°C*	Oxygen exposure of 1×10^{-4} Torr-sec
Oxygen exposure of 1×10^{-2} Torr-sec	Oxygen exposure of 10^{-2} Torr-sec
Oxygen exposure of 20 min at 1 atm	Oxygen exposure of 20 min at 1 atm
Annealed 30 min at 650°C*	Annealed 60 min at 600°C*

* Vacuum during annealing was maintained in the 10^{-9} Torr range.

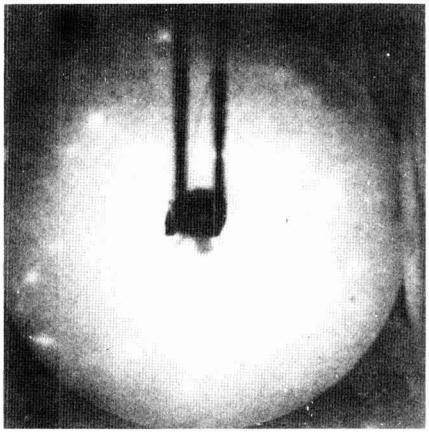

Fig. 2. Diffraction pattern of high index surface after cleaning by argon ion bombardment and annealing.

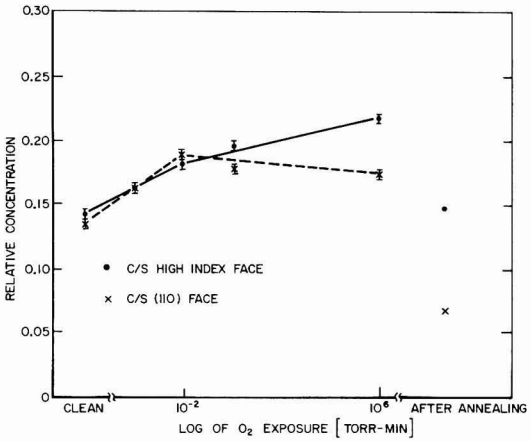

Fig. 3. Relative surface concentration of carbon on the (110) and high index surfaces of ZnS as a function of oxygen exposure.

and annealing steps listed in Table I were necessary to obtain a diffraction pattern and a clean Auger spectrum. The LEED pattern observed on this surface (Fig. 2) was not characteristic of any major crystal plane, and there was evidence of small scale faceting. Streaking in the pattern due to an ordered array of steps is minimal, indicating the steps in the surface were not ordered over large areas (7). Auger spectra confirmed that this surface, after the in vacuum processing, was essentially atomically clean.

Experimental Results

The high index face, after in vacuum cleaning, was subjected to oxygen dosings ranging from 1×10^{-4} Torr-sec to 20 min at 1 atm. Auger data obtained after these oxygen exposures indicated substantial changes in the carbon concentration. The relative magnitude of the carbon Auger signal increased after each oxygen exposure with no indication of saturation as illustrated by Fig. 3. The source of this carbon is attributed to the high CO partial pressure (on the order of 20%) observed in this VacIon pumped system in the presence of oxygen. In addition to the increase in the carbon signal amplitude, there was a broadening of the peak. This broadening is attributed to chemical shifts due to the distribution of bonding configurations for the carbon atoms contributing to the spectra. Subsequent annealing caused the carbon Auger peak to decrease in width, indicating that the carbon remaining on the surface was predominantly in one valence state. The relative amplitude of carbon *vs.* oxygen Auger peaks increases with gas exposure indicating that the carbon on this surface is partially dissociated from the oxygen and the oxygen partially desorbed. This was also supported by the annealing behavior since the net result of the oxygen exposure on this surface after annealing was to increase rather than decrease the relative abundance of surface carbon.

Identical experiments were conducted on the cleaved (110) ZnS surface as a control. The entire ion cleaning, oxygen exposure, and annealing sequences were repeated as in the high index surface dosing experiment. It has been demonstrated (4, 5) that surfaces of some II-VI compound semiconductors can be rendered virtually inert to chemisorption by careful processing to remove surface imperfections. The ZnS (110) surface followed this pattern in the LEED, and AES data gave little evidence for chemisorption of CO or O_2 on the cleaved surface after that surface had been cleaned and ordered by the ion bombardment and annealing sequence in Table I. An increase in the carbon Auger signal was observed. However, the changes were reversible with annealing and the slight buildup observed was found to saturate after dosings of 10^{-2} Torr-sec of oxygen. Both the slight carbon amplitude change and saturation in the Auger signal upon oxygen exposure indicates that a low density of chemisorption sites were present upon the (110) face. These sites can be attributed to imperfections left in the surface by cleaving.

The high index face was introduced into the vacuum system for CO_2 exposures, mounted on the same sample holder with the low index crystal. Concentrations of carbon found upon the surface were removed by argon bombardment and gentle annealing to produce LEED patterns similar to that of Fig. 1d. Auger spectra confirmed a clean surface. After dosings in steps from 10^{-4} Torr-sec to 45 min at 1 atm of carbon dioxide, the high index face exhibited considerably higher carbon concentration than was observed on the (110) face. The carbon peak increase was not accompanied by an increase in the oxygen peak indicating dissociation as in the oxygen dosings. As before, this additional carbon was not loosely bound to the surface since upon annealing no decrease in the carbon Auger signal was observed (Table II). These results directly contrasted those obtained from the low index face. The CO_2 that adsorbed upon the (110) surface during the dosings was found to be loosely bound and both the oxygen and carbon Auger signals virtually disappeared during subsequent gentle annealing. Little ele-

Table II. Auger data/CO_2 dosings

	Random high index				110			
	$\frac{S}{Zn}$	$\frac{C}{S}$	$\frac{C}{Zn}$	$\Delta\frac{C}{S}$ (%)	$\frac{S}{Zn}$	$\frac{C}{S}$	$\frac{C}{Zn}$	$\Delta\frac{C}{S}$ (%)
Clean surface	11.6	0.059	0.667	—	14.1	0.078	1.11	—
After 45 min at 1 atm of CO_2	10.2	0.052	0.526	−12	5.4	0.059	0.319	−24
After 24 hr anneal at 200°C*	2.4	0.093	0.222	+79	1.7	0.030	0.050	−51

* Vacuum during anneal was maintained in the 10^{-9} Torr range.

mental carbon was present since the carbon to oxygen peak ratio remained relatively constant throughout the dosings, indicating adsorption of a carbon-oxygen compound without surface dissociation.

Summary

The exposure to oxygen with a high partial pressure of carbon monoxide showed that chemisorption on the stepped surface was much faster than on the (110) surface. In addition, the stepped surface showed evidence of dissociation of the carbon monoxide which was never observed for the (110) face. Similar results were observed for carbon dioxide exposure in that a strong chemisorption and evidence of dissociation at the surface was observed for the stepped high index surface and not for the (110). This increased chemical activity can be explained in terms of active sites associated with edge states on the surface. The edges and corners present on the high index surface provide sites where the number of nearest neighbor and next nearest neighbor atoms is greater than on the clean and ordered low index surface. This results in an increase of the effective binding energy for chemisorption at certain "active sites." The correlation of the dissociation and chemisorption activity with the order of these ZnS surfaces exhibits the importance of "active site" in surface chemical reactions on II-VI compounds.

Manuscript submitted Nov. 2, 1972; revised manuscript received *ca.* Jan. 15, 1974. This was Paper 287 presented at the Miami Beach, Florida, Meeting of the Society, Oct. 8-13, 1972.

Any discussion of this paper will appear in a Discussion Section to be published in the December 1975 JOURNAL. All discussions for the December 1975 Discussion Section should be submitted by Aug. 1, 1975.

REFERENCES

1. H. E. Grenga and K. R. Lawless, *J. Appl. Phys.*, **43,** 1508 (1972); W. S. Taylor, *Proc. Phys. Soc. (London)*, **A108,** 105 (1925).
2. B. Lang, R. W. Joyner, and G. A. Somorjai, *Surface Sci.*, **30,** 454 (1972).
3. A. Spilners and R. Smoluchowski, "Reactivity of Solids," p. 475, Elsevier, New York (1961).
4. S. Baidyaroy, W. R. Bottoms, and P. Mark, *Surface Sci.*, **29,** 165 (1972).
5. J. D. Levine, A. Willis, W. R. Bottoms, and P. Mark, *ibid.*, **29,** 144 (1972).
6. W. P. Ellis and R. L. Schwoebel, *ibid.*, **11,** 82 (1968); M. Henzler, *ibid.*, **19,** 159 (1970); G. E. Rhead and J. Perdereau, *ibid.*, **24,** 555 (1971); B. Lang, R. W. Joyner, and G. A. Somorjai, *ibid.*, **30,** 440 (1972).
7. J. E. Houston and R. L. Park, *ibid.*, **26,** 269 (1971).

Doping Profiles by MOSFET Deep Depletion *C(V)*

D. M. Brown,* R. J. Connery, and P. V. Gray

General Electric Company, Corporate Research and Development, Schenectady, New York 12301

ABSTRACT

Deep depletion MOS $C(V)$ curves obtained by reverse biasing the junctions of MOSFET's are analyzed to produce $N(X)$ doping profiles. Analytical techniques and possible errors are discussed together with experimental results obtained from samples on bulk, ion-implanted, and epitaxial Si wafers. Experimental results are compared with spreading resistance measurements. The simplicity of the method makes it suitable for rapid impurity profile research and process control applications.

Measurements of impurity profiles utilizing reverse biased capacitance $C(V)$ measurements of diffused junction and Schottky barrier diodes have been described previously by many authors. Little use, however, has been made of MOS devices to provide doping profiles even though, as discussed by Nicollian *et al.* (1), information on the profile can be obtained closer to the surface by this method than by any other. The reasons for this, we believe, are based on a belief that the measurement techniques and required apparatus are complicated and there has been considerable concern about interface state errors in MOS doping profile determinations. Some of the techniques utilized in the past for Si profiling using MOS structures are discussed briefly below.

Because of minority carrier surface inversion, deep depletion is not easily obtainable using MOS capacitors at room temperature, and so specialized equipment and techniques have been required. Short pulses are usually used to measure the capacitance because the lifetime is usually too short to maintain the depleted state long enough to make a static measurement. Van Gelder and Nicollian (2) have used the pulsed high frequency technique to examine redistribution of impurities during thermal oxidation of Si. Slow voltage ramps can be applied to deplete the surface if the minority carrier lifetime is sufficiently long. Long lifetimes resulting in low minority carrier generation rates can be obtained by cooling the samples to 78°K and this has been utilized advantageously in the past. In fact, the analytical studies presented here indicate that accurate profile information can be obtained closer to the interface for low impurity concentrations by cooling the samples to 78°K. This has also been pointed out by Le Blanc *et al.* (3). A graphical analysis of low temperature (78°K) MOS deep depletion $C(V)$ curves was used by Brown *et al.* (4) to detect B compensation in n-type Si. This method has also been more recently used by Adda and Clemens (5). A high frequency second harmonic technique has been described as a method of obtaining profiles with minimal interface state errors (1). Also, since the second harmonic technique directly measures the slope of the $1/C^2$ *vs.* V curve used to determine N, one can use slower ramp voltages without introducing errors caused by minority carrier depletion "fill up." That is to say, only the second harmonic signal and total capacitance information are required to obtain $N(X)$. Deep depletion information at large X may still require rather long lifetimes, however, if slow voltage ramps are used. This is also true of the technique utilized by Brews where the maximum depletion width was that occurring for minority carrier inversion at thermal equilibrium (6).

Method and Purpose

MOS deep depletion caused by minority carrier removal using an adjacent reversed biased diode in MOS

* Electrochemical Society Active Member.
Key words: $N(X)$, MOS deep depletion, impurity profiles.

gate controlled diodes has been discussed by Grove and Fitzgerald (7). The purpose of this paper is to examine in detail the technique and possible errors and limitations of using deeply depleted MOS devices for impurity profiles.

This method has the advantage of the fact that static measurements can be made for a wide range of temperatures because the minority carrier depletion state is maintained as long as the depletion potential "well" produced by the reverse voltage, V_R, applied to the drain is "deeper" than that which can be produced by the gate bias. However, if the diode "well" potential, V_R, is "shallower," minority carriers will fill the gate bias well up to the bottom of the diode well. The maximum attainable depletion distance in this instance is therefore determined by the diode bias and for a uniform doping profile is given by (7)

$$X_{VR} \cong (2\epsilon_0 K_s V_R/qN)^{1/2} \quad [1]$$

Resultant $N(X)$ profiles for gate voltages which could produce "deeper" depletion wells than the adjacent diode well will therefore be incorrect. The surface potential produced by the MOS gate voltage on uniformly doped samples can be found from Eq. [5] below. For lightly doped samples ($N \leq 4 \times 10^{15}/cm^3$) and gate oxides about 1000Å thick the deep depletion surface potentials are only a few volts less than the applied gate voltages.

Within the limitations discussed above, and subsequently within this paper, the impurity profile $N(X)$ can be obtained by using the familiar equations (2)

$$N = 2 \Big/ \left(q\epsilon_0 K_s \frac{d}{dV} \left(\frac{1}{C^2} \right) \right) \quad [2]$$

with X being obtained from

$$C_S = C_0 C/(C_0 - C) = \left(\frac{\epsilon_0 K_s}{X} \right) A \quad [3]$$

$$C_0 = (\epsilon_0 K_{ox}/X_{ox}) A \quad [4]$$

where C is the measured capacitance, C_s the semiconductor space charge capacitance, C_0 the oxide capacitance, X the depletion distance into the silicon, X_{ox} the oxide thickness, K_s and K_{ox} the dielectric constants of silicon and silicon dioxide, respectively, ϵ_0 the free space permittivity, and A the metal gate area. N is determined by finding ΔV and $\Delta(1/C^2)$ from the $C(V)$ data using a series of point-to-point evaluations. C_0 is the measured majority carrier surface accumulation capacity. Combining C_0 with the measurement of C in Eq. [3] gives X.

Errors in $N(X)$ caused by interface state densities of 1×10^{12} cm^{-2} have been examined previously (1, 6). Errors caused by interface states decrease for increasing measurement frequencies. However, for H_2 annealed samples, interface state densities are $\leq 10^{10}$/cm^2 and in these instances MOS profile measurements are valid for frequencies $\geq 10^6$ Hz.

Analytical Study

Figures 1 through 4 represent analytical studies of the $N(X)$ analysis using computer simulated $C(V)$ sample data. This was done in order to test the data processing program and to examine the validity of the system under a wide variety of circumstances; theoretical "data" were calculated using equations given in the Appendix of Ref. (8). In all cases, a model using uniform phosphorous doping was assumed.

The salient feature of all these curves is the rapid rise in apparent $N(X)$ caused by majority carrier accumulation leading to the eventual flattening of the $C(V)$ curve as C_0 is approached. This basic limitation of the MOS analysis is caused by the fact that the method is sensitive only to the rate of change of C *vs.* V and as such cannot determine the sign or nature of the space charge. This limitation, called the extrinsic Debye length limit, has been previously discussed in

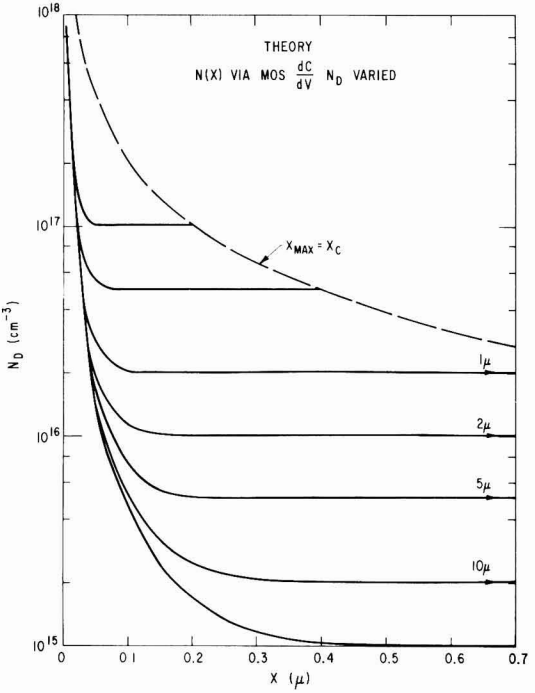

Fig. 1. Analytical $N(X)$ for uniform profiles for various donor concentrations. $X = X_c$ curve is limited by critical breakdown field $E_c = 3 \times 10^5$ V/cm.

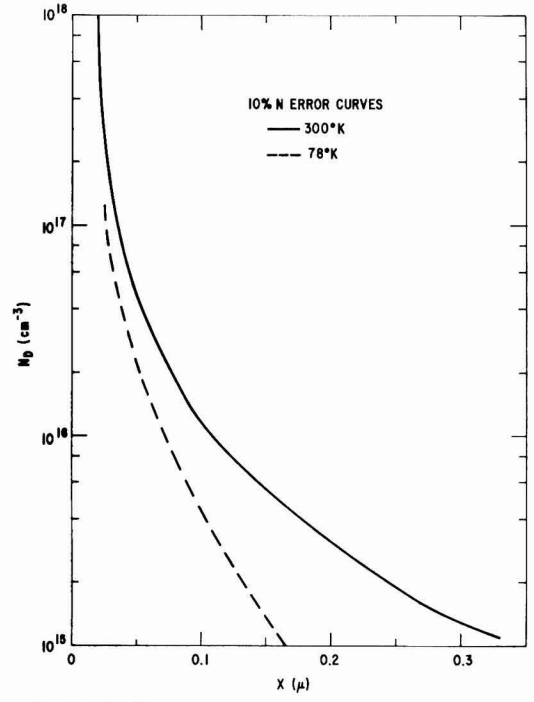

Fig. 2. 10% N error line blocking off valid analytical region to right of error line.

Ref. (1) and (3). Experimental errors caused by fixed value stray capacitances and errors in C_0 are also con-

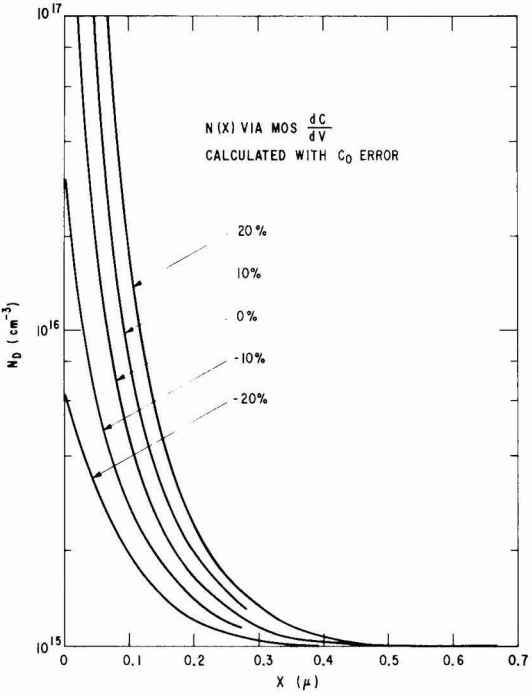

Fig. 3. *N(X)* lines showing effects of errors in oxide capacitance C_o.

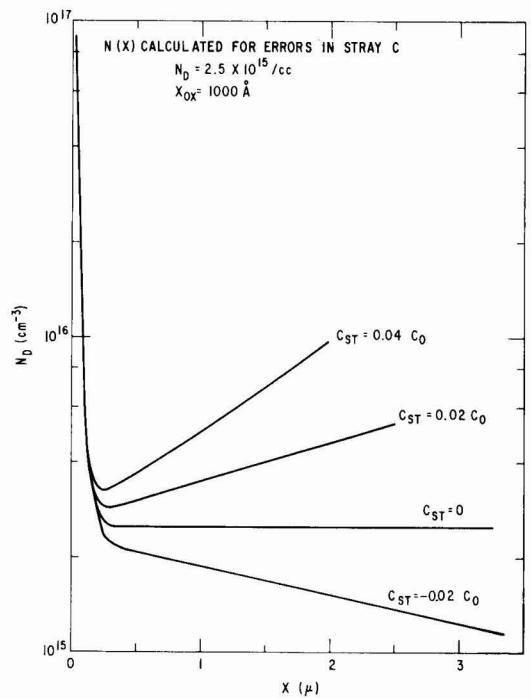

Fig. 4. *N(X)* lines showing effects of errors in estimated stray capacitance, C_{ST}.

sidered below. Stray capacitances are all fixed value capacitances in parallel with the MOS gate caused by any cable capacitances and MOS chip capacitances which are not part of the active thin oxide gate region.

The $C(V)$ equations for MOS structures on uniformly doped n-type Si from accumulation through deep depletion (no minority carrier inversion) are given by

$$V(U_S) = (kT/q)(U_S - U_B) - Q_S/C_o + \phi_{MS} \quad [5]$$

$$C_S(U_S) = \frac{q}{E_S}[A_c T^{3/2}\mathbf{F}_{1/2}(U_S - E_g) - N_D(1 + 2\exp(U_S + E_D - E_G))^{-1}] \quad [6]$$

where the surface field E_S is given by

$$E_S^2 = \frac{8\pi}{\epsilon_o K_s} kT\left[A_c T^{3/2}\{\mathbf{F}_{3/2}(U_S - E_G) - \mathbf{F}_{3/2}(U_B - E_G)\} + N_D \ln\left|\frac{2 + \exp(E_G - E_D - U_S)}{2 + \exp(E_G - E_D - U_B)}\right|\right] \quad [7]$$

These equations have been described in detail previously (8). U_S is the surface potential in kT units. The $N(X)$ analysis on these analytical $C(V)$ curves was carried out by the computer using Eq. [2] and [3].

The limitations caused by the surface accumulation of electrons can be estimated from Fig. 1 where the results for seven different uniform densities from 10^{15} to 10^{17}/cm^3 are given. Clearly the method is valid only for depleted surfaces and since the depletion width depends on N_D, the region of validity can be blocked off with an error curve. A 10% N_D error curve generated by picking points at approximate X values where the measured $N(X)$ would be 10% above the flat profile concentration is shown in Fig. 2. $N(X)$ data to the right of this line have an accuracy better than 10%. Figure 2 shows that accurate profile information can be obtained closer to the surface of lightly doped samples by cooling the samples to 78°K.

Errors in C_o can occur if, for instance, the gate is diode protected and C_o has to be estimated from the shape of the experimental $C(V)$ curve near $V = 0$. In this instance, C was set as $C = (C_o \pm\% \ C_o)C_S/((C_o \pm\% \ C_o) + C_S)$ and the analytical curves, Fig. 3, show that the errors in C_o have to be relatively large to produce noticeable effects for small X. Errors in C_o shift X values but do not change N because knowledge of N is independent of oxide thickness as seen in Eq. [2].

The errors introduced by unknown stray capacitances, however, are surprisingly large and have a large influence when the sample is in deep depletion and the total C is small. In this case, the error curves were calculated at a fixed donor density of 2.5 × 10^{15}/cm^3 assuming

$$C = \left(\frac{C_o C_S}{C_o + C_S}\right) \pm C_{ST}$$

where the positive and negative signs in front of the stray capacitance, C_{ST}, represent an over- and underestimation of the stray capacitance, respectively. Experimentally the stray must be subtracted to obtain an errorless $N(X)$ analysis as represented by the curve labeled $C_{ST} = 0$ in Fig. 4. Small percentage errors in any assumed stray can cause considerable errors in $N(X)$ profiles as indicated. The best way to check on the estimated stray is to experimentally determine $N(X)$ for bulk samples where the profile is known to be flat. Once this is done, samples with unknown profiles can be measured using the same FET device geometry.

Experimental Techniques

Test samples.—P-channel MOSFET structures with minimum size source and drain diffusions were fabricated using the p-channel Mo gate (RMOS) technique described previously (9) using phosphorous doped 4

ohm-cm bulk Si or approximately 2 ohm-cm epitaxial Si on (111) surfaces. Field oxides, 1.4μ thick, were grown in steam, and gate oxides, 1000Å thick, were grown in dry oxygen. The processing sequence will not be described in detail. H_2 annealing using 10% H_2 in N_2 for 1 hr at 500°C was carried out near the end of the process to reduce the fast interface state density to $<10^{10}/cm^2$. Ti-Au was evaporated on the backside of the wafers to ensure a low resistance contact. Arsenic ion implants at dose levels of approximately $1 \times 10^{12}/cm^2$ using implant energies of 300 keV were included in some samples at a processing stage between gate oxidation and Mo gate deposition. Ion implanted Al gate MOSFET's with large area diffused source and drain junctions have also been successfully studied.

All the planar junctions of the devices studied here were about 1μ deep with resultant reverse breakdowns of about −30V.

The junctions of the MOSFET device were connected to a large negative voltage (approximately −30V) and gate capacitance data *vs.* gate voltage were obtained by applying a slow ramp voltage to the gate in conjunction with the a-c measurement frequency. This arrangement transforms the MOSFET into a surface depletion MOS gate controlled diode structure and the $C(V)$ curves are accordingly those of a deep depletion MOS structure.

Method I ($f = 1$ *MHz*).—$C(V)$ data were obtained using a Boonton Electronics Model 71A capacitance meter which operates at a frequency of 1 MHz. These data were logged using two digital voltmeters connected to an online data logging computer terminal. $N(X)$ was obtained using the dC^{-2}/dV equations and plotted on site using an X-Y recorder and digital point plotter. The experimental data were obtained using a simple probe station, and all equipmental stray capacitance was balanced out with the gate probe lifted. Any stray capacitance was, therefore, limited to that present in the chip caused by landing pads and Al runs over thick (approximately 1.4μ) field oxide.

All the results shown in Fig. 5-8 were obtained in this manner.

Method II ($f > 1$ *MHz*).—In order to verify the assumption that any small residual number of fast interface states in properly annealed samples does not introduce errors for a 1 MHz measurement frequency, a digital capacitance bridge capable of utilizing measurement frequencies ≧ 1 MHz was constructed. Because of the higher frequencies, the profiling was done utilizing packaged devices in order to eliminate lead inductance and ground loop effects. Careful measurements of stray capacitances contributed by the package, instrument probes, and test jig were carried out using empty packages. This stray capacitance was subtracted from each capacitance measurement through the use of an appropriate computer program which subsequently reduced the corrected $C(V)$ data to $N(X)$ data. Measurements at 1 and 10 MHz produced identical $N(X)$ profiles. Residual numbers of fast interface states are therefore deemed to be insignificant for 1 MHz profile measurements of properly annealed samples.

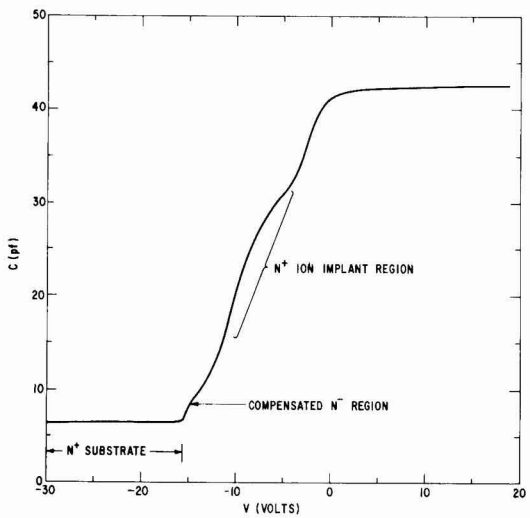

Fig. 5. Illustrative deep depletion $C(V)$ curve

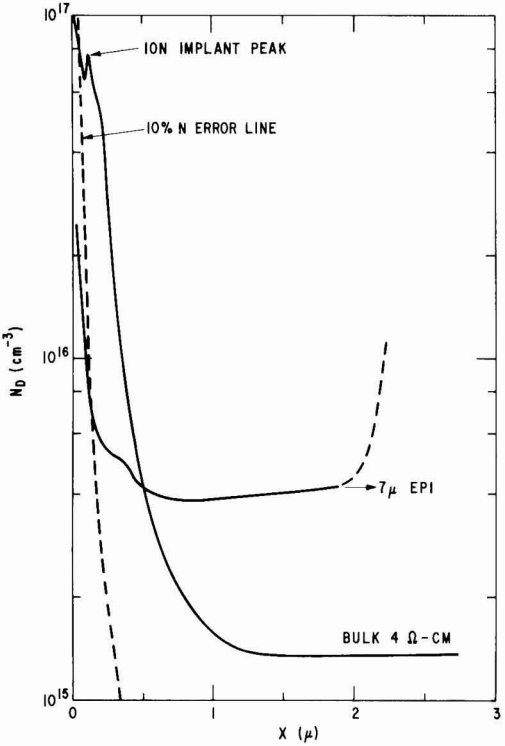

Fig. 6. $N(X)$ for bulk 4 ohm-cm ion implanted sample and $N(X)$ for lower resistivity epitaxial sample with ion implant. The sudden upward swing in the curve at large X is an indication of incomplete minority carrier removal occurring whenever the diode reverse bias is too small.

Device geometry.—Except for the expected parasitic effects discussed previously, device geometry did not appear to be a major factor. These effects were especially severe for the small Al gate FET's ($A = 6 \times 10^{-4}$ cm²) which therefore required a stray capacitance subtraction as discussed in Method II above. Ideally the areas should be large ($A > 10^{-3}$ cm²) and the junction gate overlap small. This was true of the self-aligned Mo gate structures ($A = 1.2 \times 10^{-3}$ cm²) whose diffused junction regions were furthermore limited to a very small fraction of the gate's periphery.

Experimental Results

Some illustrative features of a specific ion implanted device constructed on a thin (approximately 2μ) epitaxial layer are illustrated in Fig. 5. Several features are significantly different from the usual exponentially shaped depletion curve: the ion implant region is observed as a rather large bulge at moderate voltages and the presence of the N^+ substrate is observed at

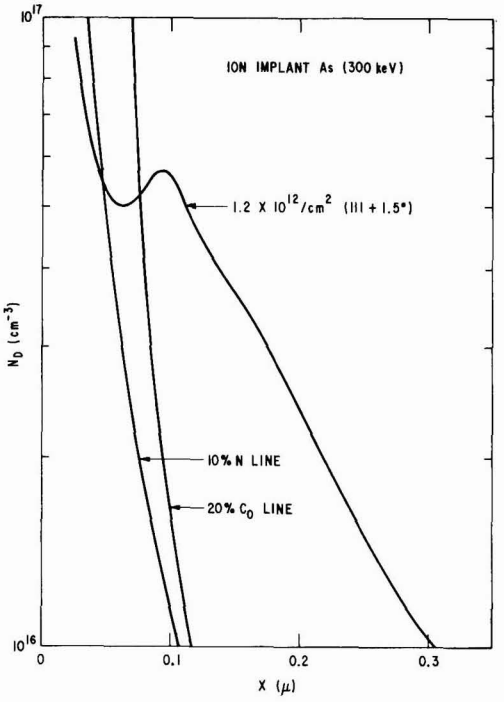

Fig. 7. As ion implant profile detail showing As ion implant peak and long tail.

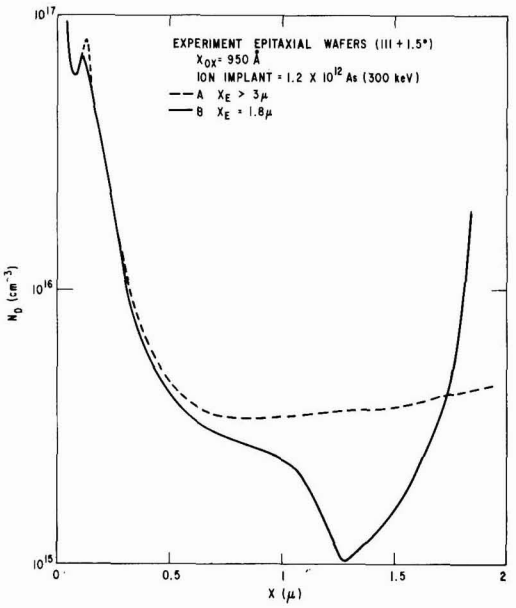

Fig. 8. N(X) profiles for epitaxial layer samples. Profile B is for a complex sample whose C(V) curve is given in Fig. 5. Profile shows ion implant peak, spurious high resistivity region at substrate interface, and epitaxial layer thickness. X_E means epitaxial layer thickness.

the highest voltages by the region where capacitance is independent of voltage. This particular sample contained a high resistivity region at the interface between the epitaxial layer and the N^+ substrate.

As indicated previously, the stray capacitance for the masks must be estimated with considerable accuracy and should be checked using samples where the profile and resistivity are known to be flat. A $N_D(X)$ profile of a 4 ohm-cm bulk sample is shown in Fig. 6. The measured donor concentration of $1.35 \times 10^{15}/cm^3$ for $1.5 \leq x \leq 3\mu$ is within 10% of the bulk carrier concentration obtained from four-point probe measurements. The fact that this sample received a shallow As ion implant is unimportant for the calibration check of stray capacitance errors since these errors are maximum at large depletion distances.

The data for the lower resistivity epitaxial sample in Fig. 6 indicate an important feature of this profiling technique. As discussed earlier, data taken when the surface field produced by the gate voltage approaches and exceeds that produced by the diode bias give anomalous results because the surface is not then completely depleted. This feature is observed in a flattening out of the $C(V)$ curve at high gate voltages which produces the apparent rapid increase in $N(X)$. In some cases like this it was found that the maximum depth of accurate profiling was limited by the reverse breakdown voltage of the diode rather than by the critical field condition shown in Fig. 1. Nevertheless, this sample shows the phosphorous surface pileup produced by the field and gate oxidation sequences as indicated by the data for $x \leq 0.5\mu$.

Figure 7 shows a more detailed As ion implant profile on a slightly off axis (111) surface. The concentration peak correlates well with the curves given by Gibbons (10) for an implant energy of 300 keV. The long As tail or shoulder is also apparent and has been described by others using the incremental sheet resistance technique or neutron activation analysis (11). The simplicity of our technique makes possible rapid analysis of such effects and provides useful information even though accurate analysis for very small X is limited by the N error line. It is also interesting to note that the As dose shown here is one order of magnitude less than the lowest dose in Ref. (11).

Figures 8 and 9 correlate the information obtained from our profiling technique and spreading resistance profiles of the same samples.[1] The electrical measurements on sample A indicate a nearly flat profile beyond the ion implant tail to a depth $> 2\mu$ as verified by spreading resistance profiling. Sample B whose $C(V)$ curve is shown in Fig. 5 indicates an anomalous dip in donor concentration between 0.5 and 1.5μ. This was verified by the spreading resistance profile of this sample as shown in Fig. 9. It is interesting to note that before processing, the spreading resistance data on both these epitaxial layers indicated a flat profile. The anomalous dip for sample B was caused by boron acceptor level compensation produced by an outdiffusion of boron from the 0.01 ohm-cm Sb doped substrate during high temperature processing. Higher than normal B concentrations in these substrates were verified by the substrate crystal vendor. This identical B compensation phenomenon in n-type epitaxial layers grown on n-type substrates has been studied analytically by Langer and Goldstein (12). The information presented in Fig. 8 and 9 appears to represent the first published experimental observation of this effect.

Sample A of Fig. 8 shows a slight upward tilt of a supposedly flat profile. As indicated in Fig. 4 this usually is an indication of unaccounted for stray capacitances which adversely affect the shape of the curve for large depletion distances, because the depletion capacitances are becoming increasingly small for these samples. Larger samples or slight adjustments in the stray estimates using Method II are required for high accuracy in this region. This was carried out as shown in Fig. 10 and was compared with the spreading resistance profile data of this wafer. The spreading re-

[1] All spreading resistance profiles were obtained using the Automatic Spreading Resistance Probe Model ASR-100 manufactured by Solid State Measurements Incorporated.

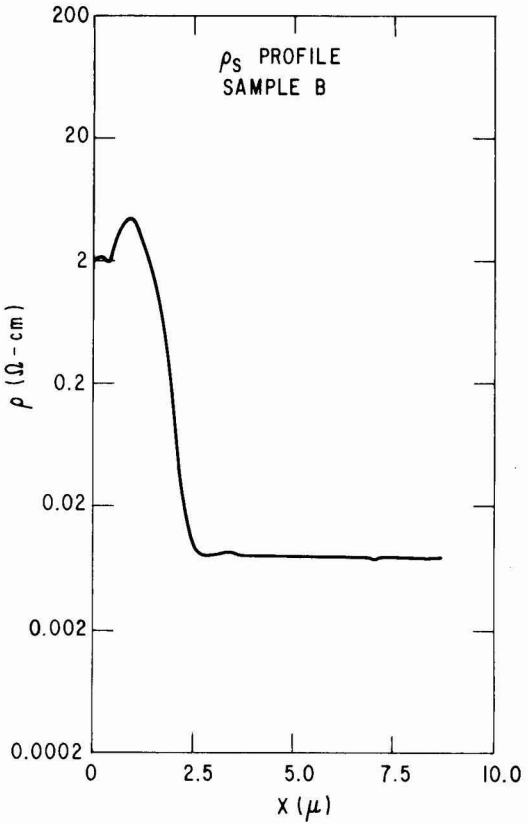

Fig. 9. Spreading resistance profile of sample verifying N(X) results in Fig. 8 on sample B.

sistance data indicated a uniform epitaxial base concentration of $\leq 2.5 \times 10^{15}/cm^3$ ($\rho \geq 2$ ohm-cm) whereas the $N(X)$ profile in Fig. 10 indicates a base concentration of $3.5 \times 10^{15}/cm^3$ corresponding to a resistivity of 1.4 ohm-cm. The calibration of the automatic spreading resistance probe was subsequently found to be in error (13).

Discussion and Summary

An impurity profiling technique using minority carrier depleted MOS samples has been examined analytically and experimentally.

Minority carrier removal was accomplished by reverse biasing adjacent junction diodes. The resultant deep depletion $C(V)$ curves are easily analyzed to give $N(X)$. One advantage of the method is that simple $C(V)$ equipment employing slow voltage ramps can be used, since the deeply depleted state is maintained as long as the diode potential is larger than the surface potential produced by the MOS gate bias. This feature makes static measurements of the semiconductor space charge capacitance possible over a wide range of temperatures, since sample lifetime and minority carrier generation rates are unimportant.

Furthermore, it has been shown, as expected, that fast interface state errors are unimportant at measurement frequencies of 1-10 MHz in properly annealed samples, because no dispersive effects were observed over this range of frequencies.

The extrinsic Debye length limitation caused by majority carrier accumulation is shown by error plots as a function of concentration and temperature giving the minimum depth at which the technique is accurate. Profiling errors caused by stray capacitance effects and

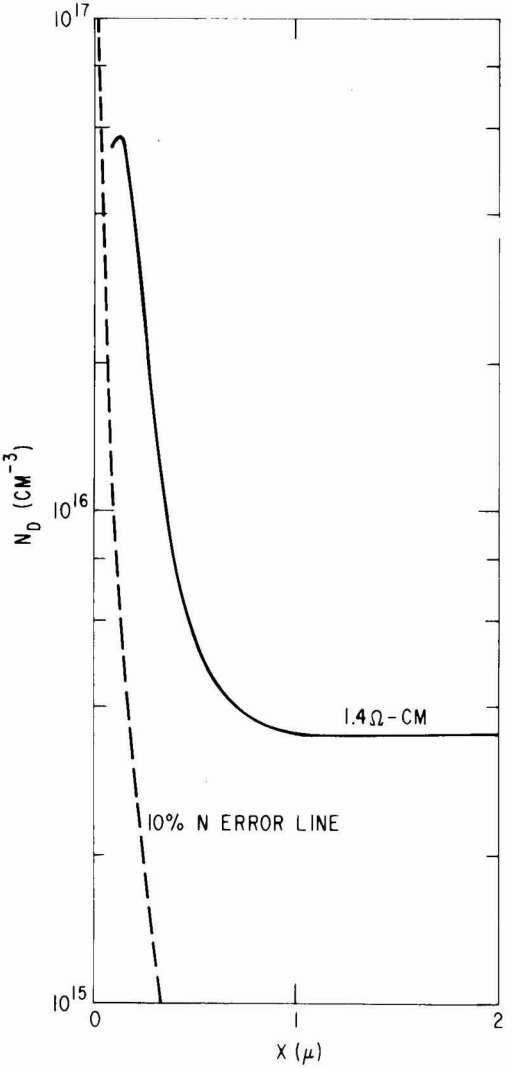

Fig. 10. Profile of sample using Method II in which small corrections for unknown stray were carried out.

errors in the MOS oxide capacitance have been detailed.

Experimental profiles obtained on different types of samples with ion implanted surfaces and using bulk and epitaxial wafers on compensated substrates have been presented showing the easy usefulness of the technique. The limitation in maximum depth caused by an insufficiently large drain bias, which results in minority carrier inversion at large gate voltages, has been pointed out. Some of the experimental results have been critically compared with spreading resistance profile measurements. The spreading resistance measurement is well suited to deeper profiles at even heavier impurity concentrations, whereas the major strength of this MOS profiling technique is its ability to measure profiles at shallower depths. The two methods, therefore, are good complements to one another especially when they have overlapping ranges of validity.

It is obvious that the MOS profiling technique presented here can be widely used for the study of diffusion phenomena, epitaxial layers, and ion implant pro-

files. Furthermore, it is a useful method to use for the measurement and control of the impurity profiles called for by certain types of MOS charge transfer devices.

Acknowledgments

The authors wish to thank L. F. Cordes for the use of his computer program for Method I and G. J. Charney for help with sample fabrication. M. Garfinkel's suggestions were most helpful, especially in indicating the proper use of the $C(V)$ equations for MOS $N(X)$ profiles. The ion implanted Al gate MOSFET's were supplied by D. Meyer.

Manuscript submitted April 8, 1974; revised manuscript received Aug. 22, 1974. This was Paper 270 RNP presented at the New York, New York, Meeting of the Society, Oct. 13-17, 1974.

Any discussion of this paper will appear in a Discussion Section to be published in the December 1975 JOURNAL. All discussions for the December 1975 Discussion Section should be submitted by Aug. 1, 1975.

Publication costs of this article were partially assisted by General Electric Company.

REFERENCES

1. E. H. Nicollian, M. H. Hanes, and J. R. Brews, *IEEE Trans. Electron Devices*, **ED 20**, 380 (1973).
2. W. Van Gelder and E. H. Nicollian, *This Journal*, **118**, 138 (1971).
3. A. R. LeBlanc, D. D. Kleppinger, and J. P. Walsh, *ibid.*, **119**, 1068 (1972).
4. D. M. Brown, P. V. Gray, P. R. Kennicott, and D. K. Hartman, Paper 338 RNP presented at Electrochemical Society Meeting, New York, N.Y., May 4-9, 1969; General Electric Report No. 69-C-168 (1969).
5. L. P. Adda and J. T. Clemens, Paper 52 presented at Electrochemical Society Meeting, San Francisco, Calif., May 12-17, 1974.
6. J. R. Brews, *J. Appl. Phys.*, **44**, 3228 (1973).
7. A. S. Grove and D. J. Fitzgerald, *Solid State Electron.*, **9**, 783 (1966).
8. D. M. Brown and P. V. Gray, *This Journal*, **115**, 760 (1968).
9. D. M. Brown, W. R. Cady, J. W. Sprague, and P. J. Salvagni, *IEEE Trans. Electron Devices*, **ED 18**, 931 (1971).
10. J. F. Gibbons, *IEEE Proc.*, **56**, 295 (1968).
11. F. N. Schwettman, *Appl. Phys. Letters*, **22**, 570 (1973).
12. P. H. Langer and J. I. Goldstein, *This Journal*, **121**, 563 (1974).
13. E. A. Taft, Private communication.

Electron-Beam Evaporated Al_2O_3 on Si

Philip C. Munro[1] and H. W. Thompson, Jr.

Purdue University, West Lafayette, Indiana 47907

ABSTRACT

Al_2O_3 is electron-beam evaporated onto n- and p-type silicon in an ion-pumped, high-vacuum environment. Fabrication parameters of substrate temperature, evaporation rate, and O_2 partial pressure are varied for optimization. The deposited films are annealed in several gas/temperature environment combinations for varying times. The resulting MOS structures are evaluated and an optimum process schedule is obtained. The deposited Al_2O_3 films have a relative dielectric constant of 8.0, a refractive index of 1.61, and breakdown field strengths exceeding 3×10^6 V/cm. Deposition rates of 100-500 Å/min onto substrates at 100°-200°C in an O_2 ambient of 2×10^{-5} Torr, followed by a 5-20 min anneal in N_2 at 550°C yield optimum insulator/interface characteristics. MOS devices so fabricated have surface-state densities in low 10^{11} states/cm^2-eV range, hysteresis in the C-V characteristic of 0.1-0.2V, and flatband voltages in the range of ±1V.

Thin films of Al_2O_3 are being investigated for use with Si and other semiconductors in device and surface passivation applications. When compared to SiO_2, Al_2O_3 has several advantages: (*i*) it has a higher density and therefore gives better hermetic sealing; (*ii*) it has shown superior radiation resistance (1, 2); (*iii*) its dielectric constant is twice that of SiO_2; (*iv*) it has shown better resistance to ion motion; and (*v*) p-type semiconductor surfaces (positive flatband voltage) have been obtained.

Films of Al_2O_3 have been deposited by pyrolysis (3, 4), plasma anodization (2, 5), RF sputtering (6, 7), and reactive sputtering (8, 9). Although several reports of vacuum-evaporated Al_2O_3 on Si have been published (10-14), no attempt to optimize the evaporation process or postdeposition anneals has been reported. It has been suggested that an added O_2 ambient during evaporation of Al_2O_3 improves the stoichiometry of the resulting films (13). This work provides data from Al-Al_2O_3-Si samples fabricated by E-beam evaporation of Al_2O_3 in an O_2 ambient onto Si substrates from which such an optimization can be made. High frequency capacitance-voltage (CV) and quasistatic current-voltage (IV) data are used to obtain insulator and insulator-semiconductor interface electrical characteristics including surface-state density, N_{ss}, flatband voltage, V_{FB}, and hysteresis.

[1] Present address: Youngstown State University, Youngstown, Ohio 44500.

Key words: Al_2O_3, E-beam, MOS devices, oxide anneal, vacuum evaporation.

Sample Fabrication

Substrate preparation.—Ten to fifteen ohm-centimeters (111) p- and n-type Si were used. Substrates were ultrasonically rinsed in trichloroethylene, acetone, methyl alcohol, and DI water. After cleaning in hot sulfuric and nitric acids, they were rinsed in dilute hydrofluoric acid. [Further details of sample fabrication and testing are given elsewhere (16).]

Square chips, 200 mils on a side, were coated for evaporation process optimization; whole wafers were coated for anneal optimization.

Al_2O_3 deposition.—The 99.998% pure Al_2O_3 tablets used for vacuum evaporation were obtained from Electronic Space Products, Incorporated. They were 10 mm in diameter and 7 mm thick and were contained in a water-cooled copper hearth during evaporation. Electron-beam spot sizes of about 5 mm were used during evaporations. O_2 was injected into the vacuum system at the base of a 5½ in. high by 2¾ in. diameter stainless steel chimney which was used to confine the evap-

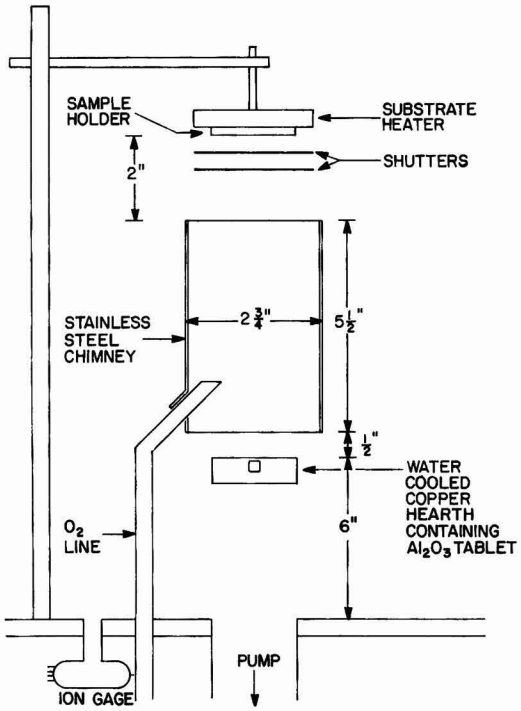

Fig. 1. Schematic layout of evaporation system

orant. System pressure was monitored at the base plate using an ion gauge. Figure 1 gives a diagram of the system showing relative placement of the substrate and the ion gauge.

The evaporations were carried out in a vac-ion system which included titanium sublimation onto a liquid-nitrogen cooled surface. Roughing was accomplished with an oil-free mechanical pump followed by sorption pumping. A 90° deflection electron gun was used to heat and evaporate the Al_2O_3. An automatic pressure controller, driven by the ion gauge unit, controlled the O_2 leak into the system. The source of O_2 was J. T. Baker Zero-Gas oxygen with a stated hydrocarbon content of less than 0.5 ppm. No attempt was made to dry or otherwise further purify the O_2 gas.

The parameters which may affect the nature of the deposited Al_2O_3 films are substrate temperature, source-to-substrate distance, deposition rate, E-beam accelerating voltage, and system pressure. Two of these parameters were fixed while the other three were purposely varied.

The E-beam accelerating voltage was held essentially constant near 5.5 kV except for minor changes needed to obtain the required E-gun power variation. Source-to-substrate distance was set at 8 in. At this distance, deposition rates as low as 100-150 Å/min were possible.

The three deposition parameters varied were (*i*) system pressure, which was varied upward from the attainable base pressure to a maximum of 2×10^{-5} Torr with the controlled O_2 leak; (*ii*) substrate temperature, which was varied upward from room temperature with a resistive heater; and (*iii*) deposition rate, which was varied by changing the E-beam power.

The optimum deposition parameters were used to obtain Al_2O_3-coated wafers for the study of postdeposition anneals. The significant anneal parameters are temperature, time, and ambient gas. Temperatures up to 800°C, times up to several hours, and N_2, O_2, and H_2 ambient gases were tested.

For the evaporation process study four pairs of n- and p-type Si chips were prepared simultaneously and then coated during a single vacuum system cycle. Each pair was coated separately by appropriately positioning two shutters.

For the anneal study, single wafers were coated and then scribed and broken into individual chips which were given different anneals.

Postdeposition processing.—Ohmic contacts consisted of plated electroless Ni for the n-type Si chips and evaporated Al for the p-type Si chips. The chips used for the evaporation optimization study were annealed for 5 min at 580°C in N_2. This anneal also produced the Al-Si alloy necessary for the p-type Si ohmic contacts. After annealing, circular aluminum gate electrodes about 7 mils in diameter were evaporated through Cu-Be dot masks onto the Al_2O_3 film in a small diffusion pumped vacuum system. The samples were not annealed after the gate electrode deposition.

CV Measurements for Process Optimizations

The numerous high-frequency CV measurements required to evaluate the results were obtained with a semiautomatic measurement system which included a Boonton 71A Capacitance Meter, a triangular-wave generator (15), and an XY recorder. Where greater accuracy was required for detailed surface-state analyses, or where higher signal frequencies were desired, point-by-point measurements were obtained with a Boonton 33A Admittance Bridge. Semiautomatic sweep-voltage amplitudes were 8-10V peak-to-peak and the CV curves were recorded beginning at accumulation bias with typical sweep rates of 100-200 mV/sec. Three or more different gate electrodes were probed on each chip. A typical CV curve is shown in Fig. 2.

CV slope was measured graphically at flatband capacitance and was normalized with respect to accumulation capacitance (approximately equal to C_i). This normalization removed the effects of differences in electrode areas and small differences in insulator thicknesses. The normalized slope is expressed algebraically as $1/C_i \cdot dC_g/dV_g$. If one writes $C = C_g/C_i$ then the relation between CV slope and surface-state density in states/cm²-eV at flatband bias can be seen to be (17)

$$N_{ss} = \frac{C_i}{Aq}\left(\frac{q\ (1-C)C}{3kT\ \partial C/\partial V_g} - \frac{1}{1-C}\right)\Bigg|_{C_g = C_{FB}}$$

V_{FB} is the gate voltage at flatband capacitance and was measured on the more negative leg of a complete

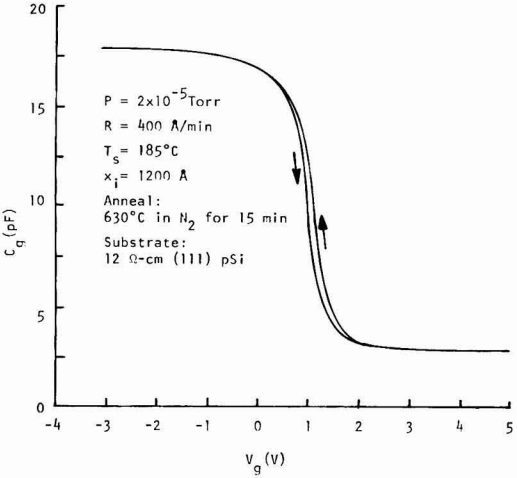

Fig. 2. A typical 1 MHz CV curve obtained with the semiautomatic measurement system.

CV curve for both n- and p-type Si samples. The ideal values of $V_{FB} = \frac{1}{q}\phi_{ms}$ are -0.05V for the n-type Si and -0.65V for the p-type Si samples. These values are calculated using an electron affinity of 4.0 eV for Si, work function of 4.2 eV for Al, and the appropriate fermi level positions for the Si used.

Hysteresis is the voltage difference between the two legs of a complete CV curve and was measured at flat-band capacitance.

Insulator Characteristics

The appearance of the deposited Al_2O_3 films was clear and of a color appropriate to the film thickness and refractive index. Only very slight nonuniformities in color were ever detected across a sample surface, and then only on large wafers with films of at least 3000Å thickness.

No cracking or peeling occurred on any of the samples fabricated, even for film thicknesses to 6000Å. The Al_2O_3 films showed no tendency to flake or peel away from the Si either before or after postdeposition anneals. Coated wafers of Si could be scribed on the coated surface with a diamond scribe and then broken into chips with no damage to the Al_2O_3 layer away from the scribe line. It was also observed that individual MIS capacitors which were destroyed by exceeding their breakdown field strengths had only local damage and no propagation of insulator damage away from the particular capacitor in question. Insulator breakdown field strength exceeded 3×10^6 V/cm.

Several Si samples with 3000Å depositions of Al_2O_3 were evaluated by ellipsometry (courtesy of Delco Electronics). From these measurements, the refractive index of the evaporated Al_2O_3 was found to be 1.61. Si samples with 3000Å films of Al_2O_3 were also used to obtain approximate values of the relative dielectric constant, k_i. Values of $k_i \approx 8.0$ were obtained. Similar values were obtained on several samples, some with no postdeposition anneals and others with a 15 min, 560°C anneal in N_2. A somewhat higher value of $k_i \approx 8.5$ was obtained on another sample which had an additional anneal at 800°C in N_2. These results for k_i parallel a similar and more detailed study of refractive index made by Woulbourn (18) on evaporated Al_2O_3.

Results

Deposition parameter variations.—The results of bell jar pressure variations are presented in Fig. 3. For these samples, the directions of hystereses were consistent with an Al_2O_3-Si interface trapping mechanism. The hysteresis was clockwise for n-type Si chips and counterclockwise for p-type Si chips. In addition to the data of Fig. 3, it was also noted that flatband voltage, V_{FB}, and CV hysteresis were more dependent on sweep voltage amplitude and rate for samples fabricated at the lower O_2 partial pressures. In fact, for Al_2O_3 deposited with zero O_2 leak, the hysteresis was about equal to the peak-to-peak sweep voltage, and the CV curves were very distorted. The dependence of V_{FB} and hysteresis on sweep rate and amplitude decreased considerably as the O_2 partial pressure during Al_2O_3 deposition increased.

Though results obtained at one value of a variable, such as O_2 pressure, generally differed from the results at another value of that variable, data for the best samples, fabricated under optimum conditions, were remarkably consistent. In almost all cases, C-V data from sample-to-sample within a group varied by less than 0.1V. Similarly, on samples fabricated using the optimum procedures hysteresis and flatband voltage show virtually no dependence on sweep voltage magnitude or rate.

Figure 4 presents deposition rate data. The directions of hystereses were again consistent with charge trapping at the Al_2O_3-Si interface.

Figure 5 presents substrate temperature data. It was noted that Al_2O_3 deposited on 25°C chips showed more

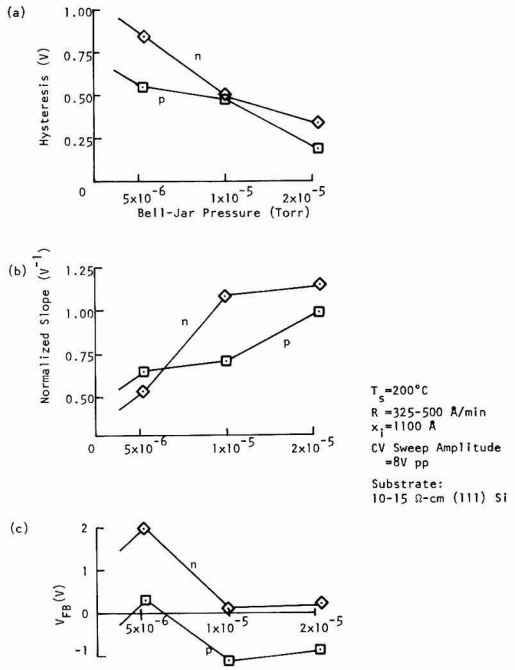

Fig. 3. CV results *vs.* the bell jar pressure during Al_2O_3 deposition on n- and p-type Si. The bell jar pressure was controlled with an O_2 leak.

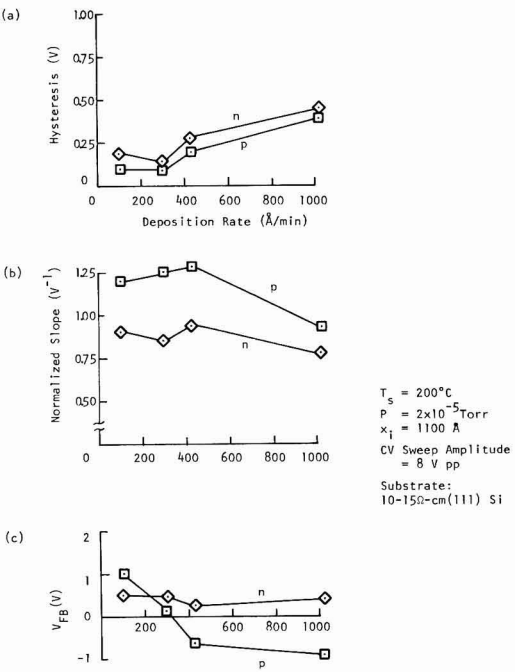

Fig. 4. CV results *vs.* the deposition rate during Al_2O_3 deposition on n- and p-type Si.

leakage and lower breakdown field strengths than those deposited at 100°C and higher. Except for the p-type Si chip coated at 25°C, directions of hystereses were consistent with charge trapping at the Al_2O_3-Si interface.

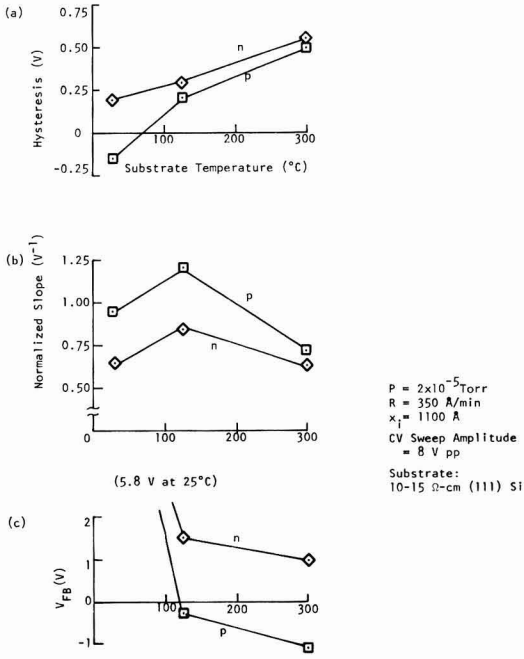

Fig. 5. CV results *vs.* the substrate temperature during Al_2O_3 deposition on n- and p-type Si.

Postdeposition anneal variations.—Different postdeposition anneals were tested on chips obtained from an Al_2O_3-coated wafer. Several control chips were given no anneal whatever in order to establish the zero-time point in the anneal data. Most of the chips were annealed in N_2 for different times and at temperatures which are shown on the graphs of the resulting data (Fig. 6-8). They were processed in groups of four chips each. The chips within a given group were annealed at the same temperature but for different lengths of time.

Two chips were annealed in H_2, and two in O_2, at 550°C, and the results of those anneals are also shown in the figures. Each H_2 anneal time includes 30 sec N_2 flushes at the beginning and end of the anneal.

Surface-state density.—Figure 9 shows surface-state density, N_{ss}, *vs.* energy measured from the center of the semiconductor bandgap for the sample whose semi-automatic 1 MHz CV curve is shown in Fig. 2. N_{ss}, as shown, was obtained from quasistatic IV measurements (19). An analysis of point-by-point high frequency CV measurements gave very similar results and is not shown here.

Discussion

The most favorable deposition and anneal parameters are chosen primarily to obtain minimum hysteresis, maximum normalized slope, and small or process controllable flatband voltage. In addition, deposition system constraints are considered, and observations of insulator leakage and breakdown influence the choice in some cases.

CV hysteresis is not always reported or denied in the literature, but it is a common occurrence where an insulating film is deposited, in contrast to those which are thermally grown (20). The mechanism of charge trapping and its relation to CV hysteresis has been discussed in the literature (21) and in particular for Al_2O_3 on Si (22, 23). Since the magnitude of hysteresis is an indication of trap density in the insulator (and of charge transport into and out of those traps), minimum hysteresis would be expected to coincide with the most favorable MIS conditions. It was also observed experimentally that smaller hysteresis coincided with a more stable surface potential to gate voltage relationship as the maximum sweep voltage magnitude was varied.

Deposition parameters.—Figure 3 shows the results of using different O_2 partial pressures during Al_2O_3 deposition. From these graphs and other similar experiments (24), it is evident that the higher values of bell jar pressure obtained with the controlled O_2 leak produce the most favorable CV results. Both hysteresis and slope have their best values at the highest bell jar pressure of 2×10^{-5} Torr, and the values of $|V_{FB}|$ are less than 1V at that pressure. Bell jar pressure was limited to 2×10^{-5} Torr due to increased difficulties when using an E-gun and a vac-ion system at much higher pressures. It should also be noted that the results in Fig. 3, and of previous experiments (24), show a similarity at the two higher pressures of 1 and 2×10^{-5} Torr, and therefore the improvement appears to saturate.

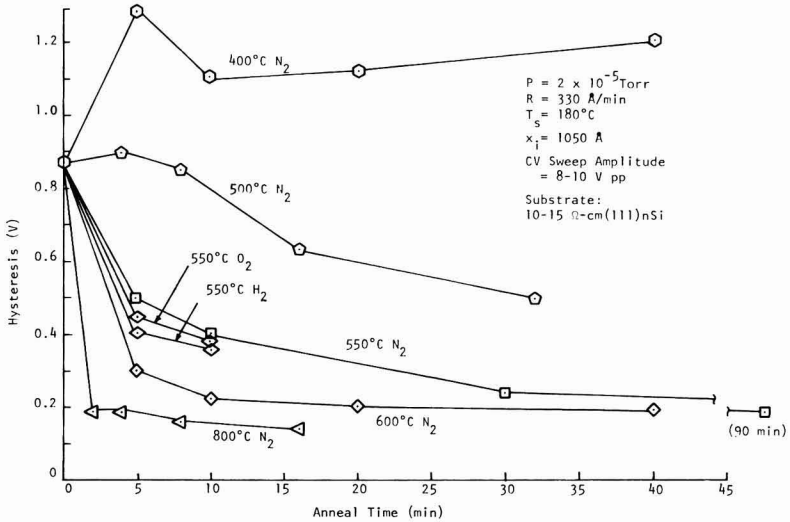

Fig. 6. CV hysteresis *vs.* postdeposition anneals.

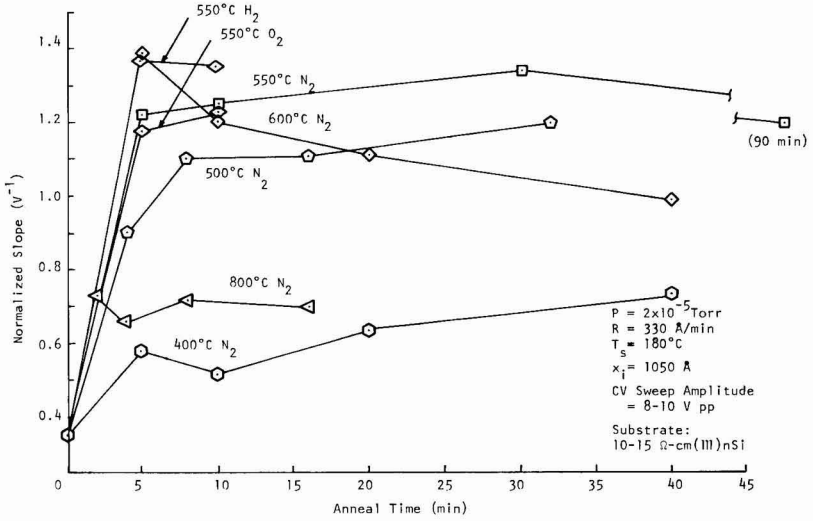

Fig. 7. CV normalized slope vs. postdeposition anneals.

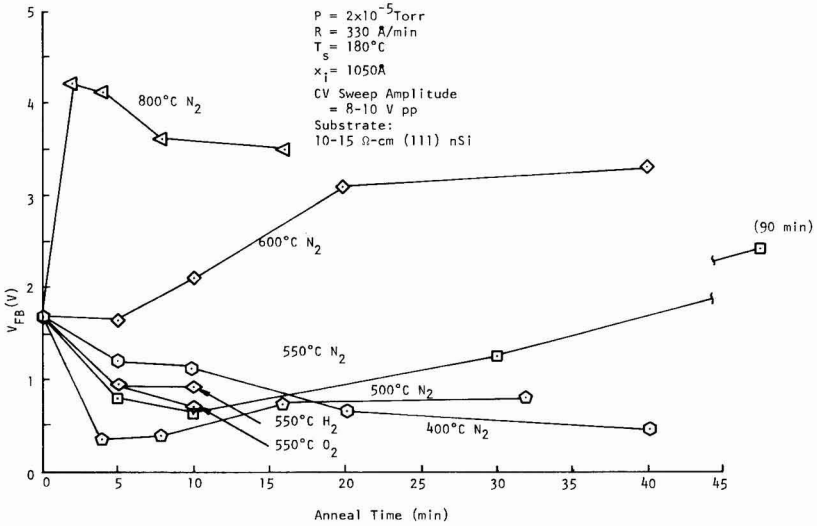

Fig. 8. CV flatband voltage vs. postdeposition anneals.

Figure 4 shows the results for different deposition rates and indicates that lower deposition rates give better results. Hysteresis of 0.1-0.2V is attainable and, more importantly, is smallest at the lower deposition rates. Normalized slope is also at its preferred higher values at the lower rates. $|V_{FB}|$ is less than 1V at all of the deposition rates tested. Deposition rate is constrained at its lower values by the total time required to obtain a given film thickness. Because of this and the favorable results obtained at both of the two lowest rates tested, it is concluded that the preferred deposition rate is in the range of 300 ± 200 Å/min.

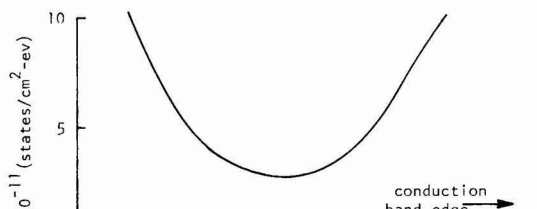

Fig. 9. Surface-state density vs. semiconductor bandgap energy measured from the center of the bandgap for the same sample whose 1 MHz CV curve is shown in Fig. 2.

Figure 5 gives results for different substrate temperatures. The increased leakage and much lower breakdown field strengths noted at 25°C may explain the "reverse" hysteresis obtained on the p-type Si chip. Such a reverse hysteresis could be due to charge injection from the metal gate, insulator polarization, or charge motion in the insulator. It is concluded that a substrate temperature in the range of 100°-200°C gives the best over-all results. CV slope is high, hysteresis low, and $|V_{FB}|$ is also low in that temperature range.

Summarizing these conclusions, the most favorable results with evaporated Al_2O_3 on Si are obtained by using an O_2 leak to hold the bell jar pressure near 2 ×

10^{-5} Torr, a deposition rate of about 300 Å/min, and a substrate temperature near 150°C.

In addition to the conclusions drawn from each of the three Fig. 3-5, comparisons can also be made among the figures. These comparisons bring together the results of samples which did not have common predeposition, deposition, or postdeposition processings, in contrast to a set of samples whose results are given within each of the three figures. This comparison reveals excellent consistency in almost every case. Best values of hysteresis are in the 0.1-0.2V range with the p-type Si chips having slightly smaller hysteresis than the n-type Si chips. Best values of normalized slope are near 1.2/V for p-type Si chips and 0.9/V for n-type Si chips. Values of V_{FB} are near the range of -1 to $+1$V for chips which had the preferred deposition parameters. Furthermore, V_{FB} for p-type Si chips is more negative than for n-type Si chips (only Fig. 4c contains an exception), which is the proper tendency for the work function differences involved. However, the value of the difference is somewhat higher than the 0.6V work function difference expected for the doping levels used.

Postdeposition anneals.—Several researchers (18, 25-27) have suggested that amorphous Al_2O_3 transforms to polycrystalline Al_2O_3 at processing temperatures above 700°C. The decrease in slope and the increase in V_{FB} seen in Fig. 7 and 8, respectively, for anneals at 600° and 800°C may be related to such a transformation. The hysteresis, as shown in Fig. 6, continues to decrease as temperature is raised. This effect, too, is consistent with previous studies of Al_2O_3 reported in the literature. Hysteresis is apparently not affected by the amorphous-to-polycrystalline transformation.

From an examination of these figures, the optimum anneal appears to be 550°C for 5-20 min. In agreement with this research, Iwauchi and Tanaka (28) reported a favorable range of anneal temperatures (500°-600°C) above which surface-state densities increase. This may indicate a similarity between their O_2-sputtered films and the present E-beam evaporated films. H_2 may offer some improvement over N_2 or O_2, but the effect of the anneal appears to be due primarily to temperature and time, and not to the gas used. This suggests that evaporated Al_2O_3 may offer a good hermetic seal for semiconductor surfaces.

Summary and Conclusion

Al_2O_3 films produced by E-beam evaporation as described in this work have a relative dielectric constant of about 8.0, a refractive index of 1.61, and breakdown field strengths exceeding 3×10^6 V/cm. The Al_2O_3 films are clear, hard, and adherent. Coated samples can be scribed and broken with no propagation of damage in the Al_2O_3 coating. Optimum interface and insulator results require Al_2O_3 evaporation in an O_2 ambient with bell jar pressure near 2×10^{-5} Torr, a substrate temperature of 100°-200°C, and deposition rates below 500 Å/min. A postdeposition anneal of 5-20 min in N_2 at 550°C is also required. Such evaporations onto Si give interface-state densities in the low 10^{11} states/cm^2-eV over the middle third of the Si energy bandgap, C-V hysteresis of 0.1-0.2V, and flatband voltages in the range of -1-$+1$V.

It is concluded that Al_2O_3 deposited by E-beam evaporation as described is comparable to and therefore competitive with Al_2O_3 films produced by other methods such as pyrolysis or sputtering. Furthermore, vacuum deposition of Al_2O_3 is truly a low temperature process (100°-200°C, or in general any temperature) compared to pyrolytic depositions (400°C and up). The absence of gaseous ambients (except O_2) during vacuum depositions should result in purer Al_2O_3 films. The lack of excited plasmas near the sample and in the deposition system (*cf.* the case of sputtering) provides a cleaner environment for the deposition and minimizes the possibility of semiconductor surface damage.

Acknowledgments

This work was supported in part by the National Science Foundation (MRL Program GH33574) and the Advanced Research Projects Agency (IDL Program DAHC-0213).

Manuscript submitted April 10, 1974; revised manuscript received Aug. 6, 1974.

Any discussion of this paper will appear in a Discussion Section to be published in the December 1975 JOURNAL. All discussions for the December 1975 Discussion Section should be submitted by Aug. 1, 1975.

Publication costs of this article were partially assisted by Purdue University.

LIST OF SYMBOLS

C_i	insulator capacitance
C_g	gate capacitance
V_g	gate voltage
ϕ_{ms}	metal-semiconductor work-function difference
T_s	substrate temperature during Al_2O_3 deposition
R	Al_2O_3 deposition rate
x_i	insulator (Al_2O_3) thickness
P	bell jar pressure during Al_2O_3 deposition

REFERENCES

1. W. J. Dennehy, A. G. Holmes-Siedle, and K. H. Zaininger, *RCA Rev.*, **30,** 668 (1969).
2. K. H. Zaininger and A. S. Waxman, *IEEE Trans. Electron. Devices,* **ED 16,** 333 (1969).
3. M. T. Duffy and W. Kern, *RCA Rev.*, **31,** 754 (1970).
4. L. H. Hall and W. C. Robinette, *This Journal,* **118,** 1624 (1971).
5. F. B. Micheletti, P. E. Norris, and K. H. Zaininger, *RCA Eng.*, **16,** 48 (1970).
6. C. A. T. Salama, *This Journal,* **117,** 913 (1970).
7. P. K. Ajmera, M. A. Littlejohn, and J. R. Hauser, *ibid.,* **119,** 1421 (1972).
8. T. Tanaka and S. Iwauchi, *Jap. J. Appl. Phys.*, **7,** 1420 (1968).
9. T. Tanaka and S. Iwauchi, *ibid.*, **8,** 730 (1969).
10. F. E. Cariou, V. A. Cajal, and M. M. Gajary, *IEEE Proc. Electron. Components Conf.*, 60 (**1967**).
11. N. Mandani and K. G. Nichols, *J. Phys. D Appl. Phys.*, **3,** L7 (1970).
12. R. A. Abbott and T. I. Kamins, *Solid State Electron.*, **13,** 565 (1970).
13. D. Hoffman and D. Leibowitz, *J. Vacuum Sci. Technol.* **8,** 107 (1971).
14. C. C. Cheng, T. W. Kim, V. D. Deokar, and W. W. Granneman, *Bull. Am. Phys. Soc. Series, II,* **18,** 555 (1973).
15. P. C. Munro and H. W. Thompson, Jr., *Rev. Sci. Instr.*, **43,** 1755 (1972).
16. P. C. Munro, Ph.D. thesis, Purdue University, Dec. 1973.
17. K. Lehovec, *Solid State Electron.*, **11,** 135 (1968).
18. J. M. Woulbroun, Ph.D. thesis, Massachusetts Institute of Technology, Aug. 1963.
19. M. Kuhn, *Solid State Electron.*, **13,** 873 (1970).
20. D. R. Kerr, *8th Annual Proc. Reliability Phys.*, 1 **(1970).**
21. F. P. Heiman and G. Warfield, *IEEE Trans. Electron Devices,* **ED 12,** 167 (1965).
22. T. Tsujide, S. Nakanuma, and Y. Ikushima, *This Journal,* **117,** 703 (1970).
23. S. Nakanuma, T. Tsujide, R. Igarashi, K. Onoda, T. Wada, and M. Nakagiri, *IEEE J. Solid-State Circuits,* **5,** 203 (1970).
24. P. C. Munro, K. Sandgren, and H. W. Thompson, Jr., Presented at the Am. Vac. Soc. Great Lakes Regional Symposium, May 1971.
25. M. T. Duffy and A. G. Revesz, *This Journal,* **117,** 372 (1970).
26. K. Iida and T. Tsujide, *Jap. J. Appl. Phys.*, **11,** 840 (1972).
27. J. A. Aboaf, *This Journal,* **114,** 948 (1967).
28. S. Iwauchi and T. Tanaka, *Jap. J. Appl. Phys.*, **10,** 260 (1971).

Four-Point Probe Measurements on N-Type Silicon with Mercury Probes

P. J. Severin and H. Bulle

Philips Research Laboratories, Eindhoven, The Netherlands

ABSTRACT

With an instrument consisting of four mercury probes, simple, rapid, and nondestructive four-point probe measurements can be done on freshly etched n-type silicon samples. Measurements on bulk material and on thin layers with a conventional and with a mercury four-point probe are compared. The ratio of two current-voltage configurations is used as a figure of merit of the instruments. The precision is found to be about 2% and the systematic deviation from theory, which is supposed to be satisfied by a conventional four-point probe, amounts to about 8% for thin layers and much less on bulk material. A number of aspects which may affect the performance are discussed. Because the instrument has no penetrating probes it is particularly useful for very thin heterotype epitaxial layers and for shallow, ion implanted samples. Experiments have also been done on polycrystalline silicon, metallic glass, and conductive plastic layers.

It is generally felt that the economy of semiconductor device processing improves with increasing slice diameter, particularly for larger devices. However, this requires the pertinent slice properties to be uniform and deficient slices to be rejected at the earliest stage. These considerations form the basis for an ever increasing effort in material properties evaluation and characterization. In order to avoid losing material, thus adding to the cost, and to ensure measuring at the relevant spot, it is highly desirable for the methods to be nondestructive. They should also be rapid and simple in application. The purpose of this paper is to show how the peculiar properties of mercury on n-type Si can be used most efficiently for evaluation purposes with the four-point probe method. In this sense the present paper is a continuation of an earlier one on capacitance-voltage measurements (1), where it was stated also that a mercury contact is ohmic to well-cleaned, n-type Si. It will be followed by a paper on spreading resistance measurements, also with mercury probes (2).

The use and experimental results of mercury four-point probe measurements on bulk and thin layers of n-type Si are described below. The sources of error and the limits of applicability of the theory are also discussed. Practical conclusions are drawn and the perspectives for the mercury four-point probe are illustrated with more advanced results.

Mercury Four-Point Probe Measurements

A mercury probe with a single channel used for capacitance-voltage measurements has been described earlier (1). The mercury four-point probe (Hg-fpp) consists of four such holes and channels of identical construction at identical center-to-center distances $s = 3000$ μm. Details of the instrument are shown in Fig. 1. With the interchangeable lid (C, Fig. 1) various contact diameters can be used; the experiments described have been done with contact diameter $2A = 1020$ μm. The embodiment shown is one of the many possibilities. The four platinum wires (B, Fig. 1) should penetrate far enough into the channels to reduce contact resistance and should not be short circuited by mercury in the reservoir (D, Fig. 1). The channels are filled as follows. When the channels have been closed by a sample, the block is tilted and air pressure is applied. The surface of the Perspex block should not be too well polished so that air can escape and mercury can contact the sample. Thereupon the block is put into the horizontal position again. After removing the air pressure enough mercury remains in the channels because they have been made slightly sloping. Now the instrument is ready to be used for four-point probe measurements.

To make an ohmic contact of mercury to silicon the surface should be carefully prepared. It should be freshly etched in HF, rinsed in deionized water, spin-dried, and subsequently left, until immediately before it is measured, top-side down closing a bottle filled with HF. As strictly speaking an ohmic contact is not required for fpp measurements, the storage stage can sometimes be skipped. The complete procedure is essential for mercury probe spreading resistance measurements (3), which will be discussed at length in a subsequent paper (2).

In the expression for the fpp resistance of a sample of resistivity ρ, thickness $d >> s$, and infinite in lateral extent, the distance s figures with $R_{2314} = V_{23}/i_{14}$

$$R_{2314} = \frac{\rho}{2\pi s} \qquad [1]$$

Hence the resistance R^{H}_{2314} measured with a Hg-fpp should be proportional to the resistance R^{D}_{2314} measured with any other, *e.g.*, a Dumas fpp, with proportionality constant s_D/s_H. In Fig. 2 these two four-point probe resistance values are compared, and it is clear that this ratio does not depend on ρ over four decades of resistivity between 10^{-3} and 10 cm n-type

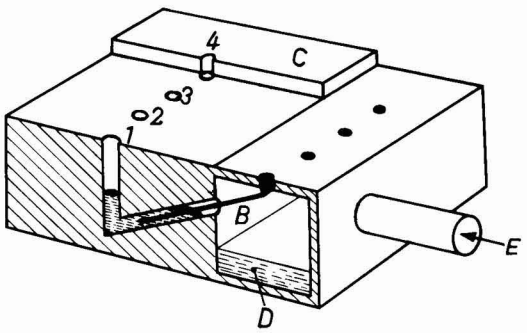

Fig. 1. The mercury four-point probe embodiment, shown schematically, cut through channel 1. Pressure is applied through E; the contact to the mercury is made with platinum wire B. Different contact diameters can be used with interchangeable cover C, shown cut through contact 4.

Key words: four-point probe, sheet resistance, silicon, mercury, epitaxy, polycrystalline, conductive layer, ion implanted layer.

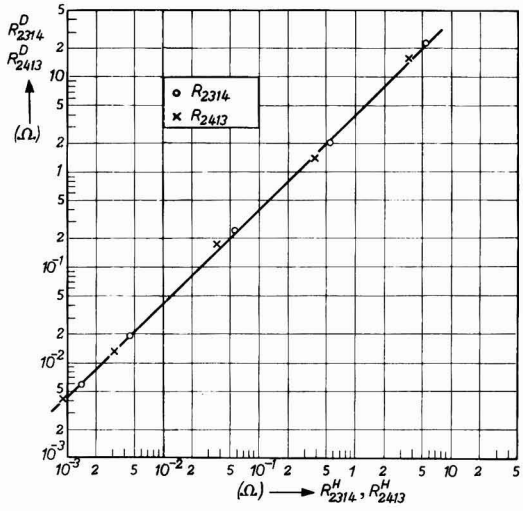

Fig. 2. The resistances R_{2314}(○) and R_{2413}(×) as measured with the mercury four-point probe plotted vs. the same parameters measured with a Dumas four-point probe, labeled H and D, respectively. The bulk sample data are given in Table I.

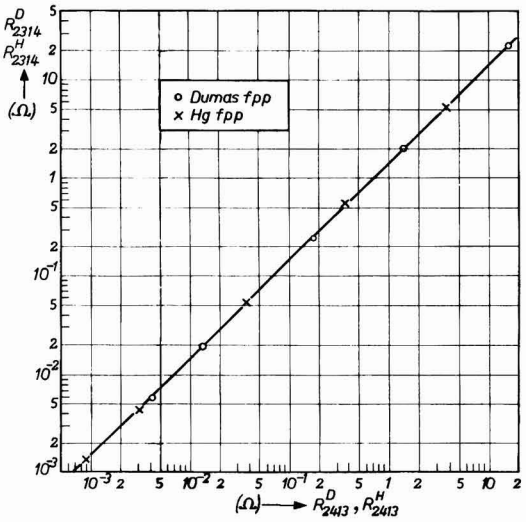

Fig. 3. The resistances R_{2314}, as measured with the mercury (×) four-point probe and with a Dumas (○) four-point probe, plotted vs. R_{2413} measured in the same way for the same samples as used in Fig. 2.

Si. As it has been explained elsewhere (4), two independent four-point probe measurements can be done by changing the probe order, the other one being for instance

$$R_{2413} = \frac{\rho}{2\pi s} 1.500 \qquad [2]$$

This resistance has also been plotted in Fig. 2 for both probes because they should have the same proportionality constant and the measurement points should be on the same line. The ratio s_D/s_H has been calculated and it is found that for both sets the ratios are equal: 0.235 ± 0.022 for R_{2314} and 0.236 ± 0.020 for R_{2413}. This error is rather large, but, as shown in Table I, the two ratios correspond more closely by an order of magnitude on the same slice. It should be borne in mind that the slices are nonuniform and that the two probes measure at different spots and integrate over widely different surface areas. This difference is typical for each slice.

Because the ratio of the two independent four-point probe resistances depends on resistivity only to second order, it mainly characterizes the instrument. In Fig. 3 these two four-point probe resistance values are compared and plotted for both instruments. The ratio R_{2314}/R_{2413} should be equal to 1.500 for both types of fpp. Calculation of this ratio for all data points yields 1.461 ± 0.026 for the Hg- and 1.464 ± 0.034 for the Dumas-fpp. The departures from the average values are found to be statistically distributed over all samples, independent of resistivity. Hence the errors may be attributed to irreproducibilities in the performance of the instruments.

The fpp resistance of a thin layer of resistivity ρ, thickness $d << s$, and infinite in lateral extent

Table I. Ratios of R_{2314} and R_{2413} for Hg- and Dumas-fpp measured on bulk samples

ρ (mohm-cm)	$\left(\frac{R^H}{R^D}\right)_{2314}$	$\left(\frac{R^H}{R^D}\right)_{2413}$	$\left(\frac{R_{2314}}{R_{2413}}\right)^H$	$\left(\frac{R_{2314}}{R_{2413}}\right)^D$
9370	0.235	0.247	1.445	1.521
832	0.271	0.263	1.491	1.448
102	0.216	0.213	1.439	1.445
7.79	0.232	0.231	1.440	1.437
2.9	0.222	0.219	1.488	1.471

$$R_{2314} = \frac{\rho}{2\pi d} \ln 4 \qquad [3]$$

is, to a first order, independent of the dimensions of the fpp. Hence the resistance as measured with a Dumas- and a Hg-fpp should be the same. In Fig. 4 the four-point probe resistances as measured with a Dumas- and a Hg-fpp are compared and are shown to be the same over four decades of substrate resistivities between 10^{-3} and 10 ohm-cm n-type Si. The ratio R_{2314}/R_{2413} has been measured twice with the two types of fpp on substrate slices. Typical results for a number of resistivities are presented in Table II. It is found that the reproducibility for both types of fpp is about equal; the two sets of data for both probes yield the same values which can be combined to 1.244 ± 0.015 for the Dumas- and 1.170 ± 0.029 for the Hg-fpp. The precision as measured on thin layers agrees closely

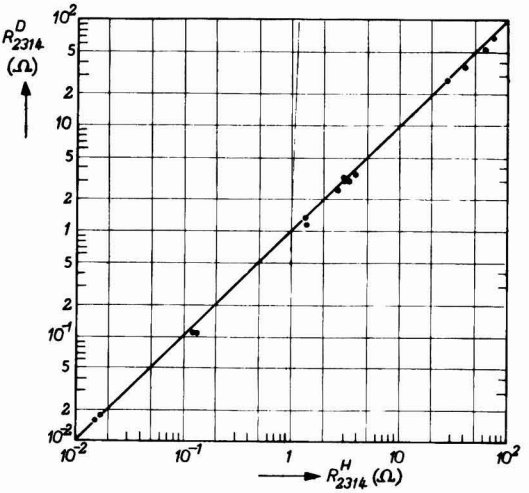

Fig. 4. The resistance R^H_{2314} as measured with mercury four-point probe plotted vs. R^D_{2314} as measured with a Dumas four-point probe for thin layers.

Table II. The ratio R_{2314}/R_{2413} for Hg- and Dumas-fpp measured twice on thin layers for a number of resistivities

ρ (ohm-cm)	$\left(\frac{R_{2314}}{R_{2413}}\right)^{H}$		$\left(\frac{R_{2314}}{R_{2413}}\right)^{D}$	
10^{-3}	1.173	1.153	1.237	1.237
10^{-2}	1.187	1.191	1.227	1.225
5×10^{-1}	1.119	1.115	1.231	1.260
3	1.205	1.199	1.241	1.243
7	1.164	1.164	1.248	1.270
10	1.176	1.182	1.270	1.243

with the precision obtained on bulk material for both probes.

The value of the ratio R_{2314}/R_{2413} has been introduced as a figure of merit of the instrument. The fpp resistance is directly affected both by nonuniformities in the sample and deficiencies of the instrument. The ratio is independent of the resistivity and the error in determining the ratio is due to the instrument deficiencies only. Because the two fpp resistances are about equally sensitive to the mainly mechanical irreproducibilities, the percentage of error of the ratio is about twice the percentage of error of the two fpp resistances.

The reproducibility of the Hg-fpp is excellent: removing and reapplying the Hg contact without displacing the slice produces identical readings, and when replacing it as well as possible on the same spot the error is within 1%. With the Dumas-fpp the reproducibility is about the same. The data presented in Fig. 2-4 are typically measured data and do not represent averages. Though, as will be shown below, the contact diameter, A, does not occur in the four-point probe formula, it is interesting to know its reproducibility. It turns out that A as measured under a microscope by pressing the mercury against a glass slide depends weakly on the applied pressure. At a controlled excess pressure of 150 Torr the diameter is reproducibly found to be 1020 μm. Work has been done with contacts 500 μm across, and smaller diameters down to 200 μm have been tried successfully.

From the measured data presented in the preceding section, referring to different spots on the same slice and on slices with different resistivities, it can be concluded that fpp measurements can be done with a precision of about 1% with the Dumas- and of about 2% with the Hg-fpp. There is no consistent indication of any influence of the resistivity of the sample.

Sources of Measurement Errors

The fpp method is probably the most familiar method in semiconductor evaluation. Generally, it is assumed that within the measurement precision the measured data are accurate with respect to the reference level set by the model and the ensuing theory. However, the data presented above show discrepancies with the theory worth discussing in greater detail.

In the model by which the mode of operation of an fpp is described, identical, nondamaging, circular contacts of diameter $2A$ are assumed, which can be neglected with respect to the identical probe center-to-center distances, s. The dependence of voltage, V, on distance, r, from the center of the current-carrying contact on a thin slice is given by

$$V_o - V(r) = \frac{\rho i}{2\pi d} \ln \frac{r}{A} \qquad [4]$$

where V_o is the potential of the contact, and on bulk material by

$$V = \frac{\rho i}{2\pi A} arcsin \frac{A}{r} \approx \frac{\rho i}{2\pi r} \qquad [5]$$

Equation [4] is evidently valid only for $r \geq A$ and the resistance R_m under the probe on a thin layer has been discussed (5) showing a complicated dependence on the contact resistance R_c and the sheet resistance R_s. Strictly speaking, this is valid only for a layer which is thin with respect to the probe diameter, whereas for fpp measurements the thickness is referred to the probe distance. In case $A < d$ in the direct vicinity of the probe, the potential drops according to Eq [5]. Because this is not of great importance with $r >> A$, Eq [4] may be considered applicable from $r = A$ onwards. Allowing for the different probe center-to-center distances, s_{ij}, Eq. [3] and related resistances should read

$$R_{2314} = \frac{\rho}{2\pi d} \ln \frac{s_{13}s_{24}}{s_{12}s_{34}}$$

$$R_{2413} = \frac{\rho}{2\pi d} \ln \frac{s_{14}s_{23}}{s_{12}s_{34}}$$

$$R_{3412} = \frac{\rho}{2\pi d} \ln \frac{s_{13}s_{24}}{s_{14}s_{23}} \qquad [6]$$

These equations have been derived, as usual, by adding the potential differences of the two probes due to currents flowing through each probe to infinity in opposite directions. This is not permitted when the potential is probed near the current source. For the mercury probe this could limit the applicability of Eq. [6].

It can easily be seen from Eq. [6] that whatever the probe contact diameters are, the three essentially different resistances on a uniform sample are always related by

$$R_{2314} = R_{2413} + R_{3412} \qquad [7]$$

and that there is one independent ratio which, when all s are equal yields

$$\frac{R_{2314}}{R_{2413}} = 1.2619 \qquad [8]$$

For bulk material the expressions corresponding to Eq. [6] are

$$R_{2314} = \frac{\rho}{2\pi}\left(\frac{1}{s_{13}} - \frac{1}{s_{12}} + \frac{1}{s_{24}} - \frac{1}{s_{34}}\right)$$

$$R_{2413} = \frac{\rho}{2\pi}\left(\frac{1}{s_{14}} - \frac{1}{s_{12}} + \frac{1}{s_{23}} - \frac{1}{s_{34}}\right)$$

$$R_{3412} = \frac{\rho}{2\pi}\left(\frac{1}{s_{13}} - \frac{1}{s_{14}} + \frac{1}{s_{24}} - \frac{1}{s_{23}}\right) \qquad [9]$$

Equation [7] holds under all conditions and the ratio given in Eq. [8] equals 1.500. In real life with a mechanical fpp all values of s are never equal.

In the above considerations it has been assumed that the voltage probes reflect the potential directly below the center of the contact, i.e., they act as point contacts. It is worth considering under what conditions this simplification holds, particularly as the mercury probe contacts are 1000 μm across with s = 3000 μm. Any current drawn by the voltage probes can be neglected because voltmeters of 100 megohms input resistance are used. So the potential of the voltage probe is such that over the contact cross-section as much current flows into as out of the mercury. If the probe diameter is small with respect to the distance, this potential can be assumed to be the potential below the center of the probe. This would apply exactly when the sample has a rectangular shape and contacts take the form of strips; it could be easily calculated with the contacts on concentric circles, but an analysis for on-line circular contacts is virtually impossible. As long as no more detailed

theory is available, the voltage probes will be considered as point contacts.

This effect arises whatever the nature or magnitude of the resistance of the probe sample contact. A second effect is due to the finite value of the specific contact resistance R_c (ohm-cm^2) or its voltage dependence. Because current flows through the contact, the same sample draws more current with a low contact resistance probe than with a high contact resistance probe; in other words the sample appears as lower resistivity material. A similar relation has been analyzed earlier for square and circular contacts used as spreading resistance probes (5). Because the main current then flows through these contacts, the theory cannot be directly applied, but the condition for negligible bypass, apart from a numerical factor of order unity, is roughly given by $R_s << R_c/A^2$ for thin layers and by $\rho << R_c/A$ for bulk samples. From mercury probe spreading resistance measurements on substrate material, to be reported in a subsequent paper (2), is follows that R_c is so low that these conditions are not met. Because, roughly, $R_c \sim \rho$, this applies equally over the resistivity range. When R_c is not very high and depends nonlinearly on ρ, the contacts may bypass the current through the sample to a different degree for various resistivity materials. A further complication may originate from a nonohmic characteristic of the voltage probe contact. When so high a potential is applied that the voltage drop over the diameter of a nonohmic contact in the material exceeds 25 mV, then the contact assumes a potential such that most of the contact draws reverse current. Moreover, the fpp resistance, as measured, turns out then to depend on the current. However, the current has, unless stated otherwise, been kept so low that the measured voltage is well below 25 mV, as advocated earlier (4).

In summary, the assumptions made in the theory are not completely met, firstly because current and probe contacts are not far enough apart to allow separation of the two current sources, secondly because the fairly large contact may partly short circuit the sample, and thirdly because R_c may depend on ρ and on the local voltage.

Discussion of Measurement Errors

From the data obtained from the experiments discussed above, conclusions could be drawn as to the precision of fpp measurements. The reproducibility on the same slices and on samples of different resistivity was tested particularly by using the ratio which depends on the uniformity of the slice to second order only. The data were arranged so as to be theoretically independent of any nonstatistically distributed influence. As the ratios did not show the expected values the theory was more carefully considered and some refinements were mentioned above. In this section the measurements related to these errors with respect to the true or theoretical value are discussed and some practical conclusions are drawn.

By way of example in Table III, the distances, s_{ij}, and probe radii, A_i, as measured under the microscope from a probes print of a Dumas-fpp are presented. From these data the ratio R_{2314}/R_{2413} is found to be 1.254 for thin layers and 1.486 for bulk material. When the two resistances are measured on two slices of widely different resistivity (10^{-2} and 10 ohm-cm n-type Si) and at two current levels, the results presented in Table IV are obtained. The ratios depend slightly on the resistivity and on the current. In actual practice the ratio is calculated regularly in this way and compared to the experimental value.

Table III. The probe center-to-center distances s_{ij} and probe radii A_i in micrometers as a practical example for a Dumas-fpp

$s_{12} = 629.2$	$s_{13} = 1259.0$	$A_1 = 19.2$	$A_3 = 25.0$
$s_{23} = 643.7$	$s_{24} = 1287.0$	$A_2 = 19.7$	$A_4 = 22.2$
$s_{34} = 653.4$	$s_{14} = 1907.8$		

Table IV. The ratios R_{2314}/R_{2413} for Hg- and Dumas-fpp on thin layers

	$\rho = 10^{-2}$ ohm-cm (10 mA)	$\rho = 10$ ohm-cm (22 μA)	$\rho = 10$ ohm-cm (220 μA)
$\left(\frac{R_{2314}}{R_{2413}}\right)^D$	1.246	1.270	1.243
$\left(\frac{R_{2314}}{R_{2413}}\right)^H$	1.195	1.176	1.182

Disagreement is always less than 2% of either sign, so systematic bias error, which affects the accuracy, is not found. Therefore, the true value which is the reference with respect to which the accuracy is to be discussed, can be considered to be given in the theory above and as measured with a Dumas-fpp.

The Hg-fpp with identical probe center-to-center distance, s, satisfies the ideal conditions, and the ratio R_{2314}/R_{2413} for thin layers should be equal to 1.2619, which exceeds the experimental values given in Tables II and IV by about 8%. It is not clear to what extent this bias error (it has always been found to have the same sign) is due to R_{2314} or to R_{2413}. It is worth noting that in R_{2413} the potential difference V_{24} caused by current through probe 3 is always zero due to symmetry, whatever theoretical assumption is made. Supposing now that this bias error has the same influence on the voltage difference between two probes for each current probe, the value of R_{2314} as measured with a Hg-fpp should be increased by 12% to reach the true value measured with Dumas-fpp. From Fig. 4 it can be seen that this semiquantitative conclusion is substantiated by experiments.

The ratio s_D/s_H as measured on bulk samples hardly exceeds the theoretical value with $s_D = 630$ μm and $S_H = 3000$ μm. The dependence on resistivity shown equally in $(R^H/R^D)_{2314}$ and $(R^H/R^D)_{2413}$ suggests some physical influence of the large area probes as discussed in the preceding section. It turns out to be an advantage of the ratio R_{2314}/R_{2413} that this resistivity-dependent effect also disappears. The experimental values of the ratio disagree with theory for both types of probe by equal amounts, not large enough with respect to the precision to be of any significance.

It would be worth investigating the influence of the ratio A/s on fpp measurements. In this paper it has been shown that the quite extreme ratio 1/6 produces results which can be interpreted in the same way and with the same amount of caution as conventional fpp measurements.

In conclusion a number of more advanced applications of the Hg-fpp are mentioned. The Hg-fpp is extremely useful for the assessment of very thin epitaxially grown heterotype silicon layers or shallow ion implanted samples, where conventional pointed probes cause substrate short circuit or even penetrate. It is found possible to measure silicon polycrystalline layers between 1000 and 2000Å thick with resistivities between 0.06 and 2 ohm-cm. These layers are increasingly used as diffusion sources, vertical resistors, and MOS gate electrodes. Layers of Au Rd-oxide about 200Å thick have been measured to yield a resistivity of about 1.6 mohm-cm. A reliable assessment of conductive plastic has also been made.

Manuscript submitted Jan. 22, 1974; revised manuscript received July 3, 1974. This was Paper 75 presented at the Chicago, Illinois, Meeting of the Society, May 13-18, 1973.

Any discussion of this paper will appear in a Discussion Section to be published in the December 1975 JOURNAL. All discussions for the December 1975 Discussion Section should be submitted by Aug. 1, 1975.

Publication costs of this article were partially assisted by Philips Research Laboratories.

REFERENCES
1. P. J. Severin and G. Poodt, *This Journal*, **119**, 1384 (1972).
2. P. J. Severin and H. Bulle, *ibid.*, **122**, 137 (1975).
3. P. J. Severin, Paper 75 presented at Electrochemical Society Meeting, Chicago, Illinois, May 13-18, 1973.
4. P. J. Severin, *Philips Res. Repts.*, **26**, 279 (1971).
5. P. J. Severin, *ibid.*, **26**, 359 (1971).

Spreading Resistance Measurements on N-Type Silicon Using Mercury Probes

P. J. Severin and H. Bulle

Philips Research Laboratories, Eindhoven, The Netherlands

ABSTRACT

With an instrument consisting of four mercury probes spreading resistance has been measured on n-type silicon bulk samples and thin layers without leaving any damage. With bulk samples the spreading resistance measured in a three-probe arrangement is found to be proportional to the resistivity without any indication of resistivity dependence of the proportionality constant between 10^{-3} and 10 ohm-cm. From repeated measurements it is concluded that the precision depends on the mechanical finish of the contact edge and can be as good as 3%. Upon comparison with the resistivity as measured with a conventional four-point probe, the mercury probe spreading resistance is found to be accurate within that error. The resistivity measured represents the average over about 1 mm^3, so that the resolving power of this instrument is intermediate between the resolving powers of conventional four-point and spreading resistance probes.

With thin layers a theory is used, in which the Hg-Si contact resistance is incorporated which is found to be almost proportional to the resistivity over the same four decades. It turns out to be small compared to the bulk spreading resistance, thus confirming the experiments on bulk material. Considering the cylinder resistance of an epitaxial n on n^+ layer as an extra contribution to the contact resistance, with a mercury four-point probe and spreading resistance measurement the product ρd can be found.

A mercury probe has been applied successfully for capacitance-voltage measurements on n- and p-type silicon and various other semiconductors (1). The procedure which should be followed to prepare a silicon surface so that the contact to mercury is ohmic has been described earlier (2, 3). An instrument consisting of four mercury probes has been used for four-point probe measurements on n-type silicon and the attainable precision and accuracy have been discussed at length (3). It is the purpose of this paper to show how with mercury probes in a three-point probe arrangement spreading resistance measurements may be carried out.

This study is a continuation of Ref. (3) in the sense that the same mercury four-point probe accessory and the same bulk and substrate samples are used. Because a spreading resistance measurement is more exacting than a four-point probe measurement, the sample preparation should be more carefully executed.

The next section is devoted to the results on bulk samples. The results on thin layers, for which 230 μm thick substrates for epitaxy have been used, are also presented in this paper. The theory needed to find the resistivity ρ and the contact resistance R_c from the measured data is recapitulated in the Appendix. In another section of this paper, a new method is outlined by which the product ρd for the top layer of thickness d of an n on n^+ epitaxial structure can be determined. In the final section the use of the same mercury four-point probe accessory for four different purposes is summarized.

This paper will be followed by a fourth paper on rapid and simple pulsed MIS capacitance lifetime measurements with the same accessory.

Key words: silicon, epitaxial layer, thickness, resistivity, contact resistance, mercury, spreading resistance, four-point probe resistance.

It is worth stressing that this paper deals with n-type silicon only. Though the contact resistance of mercury to p-type silicon may be reduced by the use of suitable etches, it is not yet small enough for spreading resistance measurements.

Mercury Spreading Resistance Measurements on Bulk Samples

In a few years' time the spreading resistance technique has become an accepted and widely used tool in semiconductor evaluation. However, the theoretical value of the spreading resistance on a semi-infinite sample of resistivity with a probe of contact radius A

$$R_s = \frac{\rho}{4A} \qquad [1]$$

is rarely found.

With hard metal probes, as discussed by Mazur and Dickey (4) and Keenan *et al.* (5), a contact resistance R_c is always found which generally is incorporated into the expression for spreading resistance as

$$R_s = k(\rho)\,\frac{\rho}{4A} \qquad [2]$$

The factor $k(\rho) = 1 + 4A\,R_c/\rho$ is experimentally determined and Eq. [2] can be used only after calibration because $k(\rho)$ depends also on the particular probe properties.

One of the present authors (6) solved the same problem in a slightly different manner by using a softer steel probe. Then the contact can be described by a series spreading resistance due to a number, n, of microcontacts with average contact radius, a, acting in parallel as

$$R_s = \frac{\rho}{4A} + \frac{\rho}{4na} \qquad [3]$$

It has been verified that R_s over four decades of resistivity is proportional to ρ. The magnitudes of the contributions of macro- and microcontacts are of the same order, which has an important bearing on the resolving power. In both approaches the precision and reproducibility of k and na are key conditions, the latter being the more relaxed one because only geometry is involved rather than ρ-dependent contact physics.

The main advantage of the spreading resistance method is the unparalleled resolving power, the information sampling depth being about equal to A which amounts to a few microns. Apart from the arguments given above an important drawback is that it is a destructive method. Furthermore, sophisticated vibration-free equipment is needed. In the experiments presented in this paper $A = 500$ μm, but it could easily be made 5 times smaller. The ensuing drop in resolving power is compensated by the fact that it is nondestructive, and that it can be done by simply switching the probe order after a mercury four-point probe measurement. Effectively, it offers a tool with resolving power intermediate between a metal spreading resistance probe and a four-point probe.

The same five bulk samples as used in the preceding paper (3) have been measured with mercury probes and the spreading resistance R_{2113} is plotted *vs.* the four-point probe resistance R_{2314} in Fig. 1. In the three-point probe arrangement chosen with center voltage-probe each of the four probes can be used as the common probe. No systematic difference turned out to exist. The spread arises from inhomogeneity of the sample and irreproducibility of the contacting process.

Working out the potential difference, V_{12}, measured due to current flow through probes 1 and 3, with the dependence on horizontal distance, r, from the probe center as

$$V(r) = \frac{\rho i}{2\pi A} \arcsin \frac{A}{r} \approx \frac{\rho i}{2\pi r} \qquad [4]$$

it is found that

$$R_{2314} = \frac{\rho}{2\pi s}$$

and that

$$R_{2113} = \frac{\rho}{4A}\left(1 - \frac{A}{\pi s}\right) \qquad [5]$$

With probe center-to-center distance $s = 3$ mm and $A = 0.5$ mm the term $A/\pi s$ equals 0.053 and the line in Fig. 1 is drawn so that $R_{2113}/R_{2314} = \pi s/2A = 9.42$.

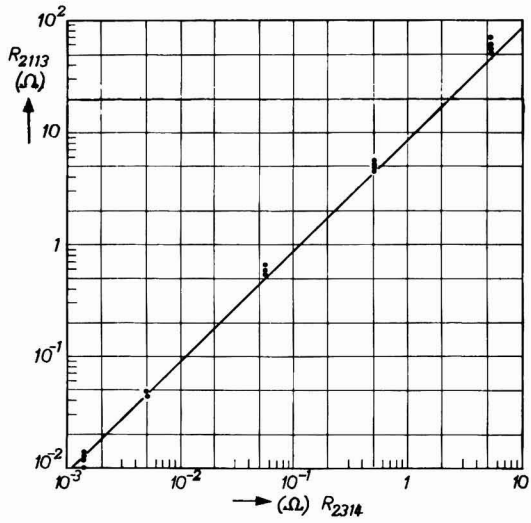

Fig. 1. The spreading resistance R_{2113} plotted *vs.* the four-point probe resistance R_{2314}, both measured with mercury probes, on bulk samples. The solid line represents $R_s = \rho/4A$, where 1 ohm corresponds to $\rho = 0.2$ ohm-cm.

It has been tacitly assumed above that any contact resistance is negligible. With specific contact resistance R_c' (ohm-cm^2), Eq. [2] should in fact be written as

$$R_s = \frac{\rho}{4A} + \frac{R_c'}{\pi A^2} \qquad [2a]$$

Anticipating the results of the next section where R_c' is determined, it can be verified that for $R_{2314} = 5.3$ and 1.4×10^{-3} ohms the corrections to R_{2113} would be 5 and 2×10^{-3} ohms, respectively, hence negligible on the logarithmic scale. Therefore, the spread of the measurement points cannot be due to differences in contact resistance.

In the experimental embodiment it turns out that the series resistance due to platinum lead, the platinum-mercury transition resistance, and the mercury channel resistance cannot be neglected for low resistivity specimens. The accurate value for each of the four channel series resistances, R_{ai}, can be determined with a platinum-coated, very low resistance specimen. The resistance R_{a1} which amounts to 65 ± 2 mohms, should be considered as a series resistance in the external circuit. It is evident from Fig. 1 that it seriously adds to the error for the low resistivity specimens.

It has been found that with removing and reapplying the mercury probes the measurement does not reproduce very well. Therefore, in order to test the reproducibility, the slice was removed, prepared again, and positioned at the same spot. The results of six measurements repeated in this way are presented in Fig. 2 for each of the four probes. It was found that the averages for each of the four probes are different by a few per cent and that each of these averages is subject to an error ranging from $\pm$ 3.1% for probe 1 to $\pm$ 9.1% for probe 2. From this experiment and further experience it should be concluded that repeated etching with HF does not affect the results. The performance of the probes probably depends on the quality of the mechanical finish of the hole and particularly on the absence of burrs at the contact edge. Upon averaging the 24 results of all four probes a value of 5.17 ohms is found with an error of $\pm$7%. With a Dumas four-point probe the area of measurement has been tested for nonuniformity, and it was found that measuring with a precision better than 1%, the resistivity ρ varied around the average value $\rho = 1.08$ ohm-cm by $\pm$ 4.4%. This value corresponds with Eq. [5] where a mercury probe measured $R_{2113} = 5.13$ ohms, hence well within the experimental error of the best probe.

In this way it has been proved that with a mercury probe it is possible to carry out spreading resistance measurements with a precision and accuracy of better than 3%.

Of course the value of the contact diameter $2A$ should be reproducible and precisely known: it is measured with a microscope by pressing the mercury against a glass slide. It has turned out that with increasing pressure the contact diameter first increases until the diameter of the hole has been reached then remains constant over a certain pressure range and finally increases again with increasing mercury pressure due to mercury penetrating between the Perspex and the sample. At a controlled pressure of 150 Torr the diameter is found to be reproducible and equal to the hole diameter within 1%. With a narrower channel the diameter of the contact increases with pressure over a longer range up to the hole diameter so that spreading resistance, contact resistance, and capacitance-voltage can be measured with the surface area as a continuous variable over about a factor of two.

Mercury Spreading Resistance Measurements on Thin Samples

The same measurement as described in the preceding section has been carried out on 230 μm thick substrate slices as used for epitaxy. A spreading resistance cor-

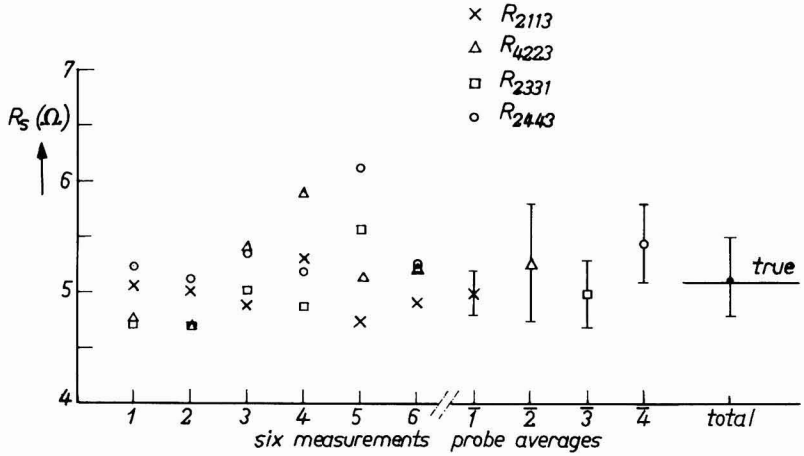

Fig. 2. The spreading resistance measurement on the same position on a 1.08 ohm-cm n-type Si bulk sample repeated 6 times. Each time data for four different common probes are obtained. The four averages and the total average are given separately; the true value $\rho = 1.08$ ohm-cm yields with Eq. [5] $R_{2113} = 5.13$ ohms, indicated by the horizontal bar.

rection formula for a thin layer on an insulating substrate based on a transmission-line model has been derived (7) and compared (10) to other models earlier. As recapitulated in the Appendix, the spreading resistance of the common probe (probe 1), with current probe (probe 4) and voltage probe (probe 2) is given by

$$R_{2114} = R_m + \frac{\rho}{2\pi d} \ln \frac{3s}{2A} \qquad [6a]$$

with a four-point probe resistance

$$R_{2314} = \frac{\rho}{2\pi d} \ln 4 \qquad [6b]$$

The resistance R_m is defined for a thin layer, $d << A$, as the difference between the contact potential V_0 and the potential $V(A)$ at $r = A$ in the thin layer, divided by the current i_0. It is found to be equal to

$$R_m = \frac{\rho}{2\pi d} \mathbf{F}(z) \qquad [7]$$

with $\mathbf{F}(z)$ plotted in Fig. 3, R_c' specific contact resistance in ohm-cm^2, $R_c = R_c'/\pi A^2$ and

$$z^2 = \frac{\rho A^2}{R_c' d} = \frac{\rho}{\pi d R_c} \qquad [8]$$

For $s/A = 6$ the logarithmic factor in Eq. [6a] equals 2.197 and Eq. [6] and [7] can be recast into a form more suitable for calculation

$$\mathbf{F}(z) = \frac{R_{2114}}{R_{2314}} 1.386 - 2.197 \qquad [9a]$$

and

$$R_c = \frac{R_{2314}}{z^2} 1.443 \qquad [9b]$$

The resistance R_m is plotted *vs.* R_{2314} in Fig. 4 and found to be almost proportional to ρ from 10 to 10^{-3} ohm-cm. This suggests, from Eq. [7], that z must be independent of ρ, hence that $R_c = R_c'/\pi A^2$ is proportional to ρ, as also shown qualitatively in Fig. 4.

It has been neglected in Eq. [9a] that in fact R_{2114} includes a term which refers to the local resistivity at probe 1 and a term which refers to the average value ρ between probes 1 and 4. The latter is represented adequately by the resistance R_{2314}.

In order to get the feel of the precision and accuracy involved let us consider a measurement of an 0.03 ohm-cm slice. We then find $R_{2114} = 4614$ mohms, $R_{2314} = 2702$ mohms, so that $R_m = 330$ mohms, $\mathbf{F}(z) = 0.169$, $z = 6.45$, hence $R_c = 93.6$ mohms. It is clear that with these values of $\mathbf{F}(z)$ and $\ln(3A/2s)$, the measurement conditions are very unfavorable: in order to find precise R_m within 10%, the values of R_{2114} and R_{2314} should be known within 1%. Because z hardly depends on ρ, this example is typical for the experiments described in this section. Because in this range $z >> 1$, Eq. [9a] and [9b] can be simplified by the relation $\mathbf{F}(z) = 1/z$.

As it is clear from Eq. [9a] and [9b], the measurement result is the contact resistance R_c. Usually quite some processing is involved in making an ohmic metal semiconductor contact, and R_c', though not very reproducible, is considered as a figure of merit of the process. As long as R_c is small with respect to the bulk resistance of the device concerned, this is an unimportant aspect. However, the instrument described and the spreading resistance method are intended to serve evaluation purposes, *viz.*, to measure the resistivity locally. From Eq. [9a] and [9b] it can be seen that $R_c(\rho)$ is finally the discriminating parameter which turns out not to be sufficiently precise and reproducible to yield ρ.

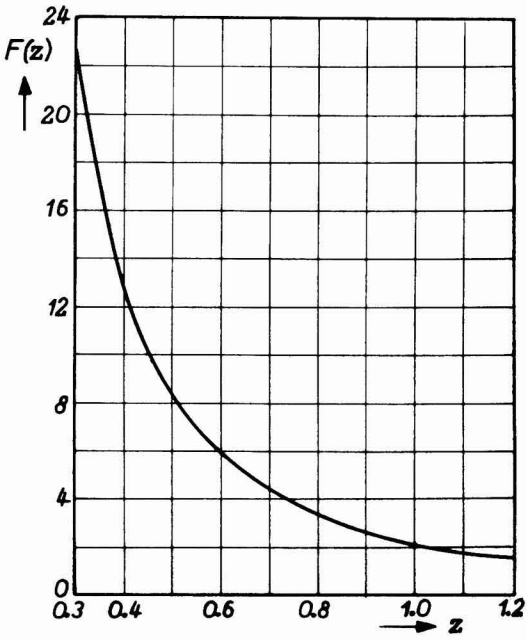

Fig. 3. The function F(z) as used in Eq. [7] and defined in Eq. [A-8]

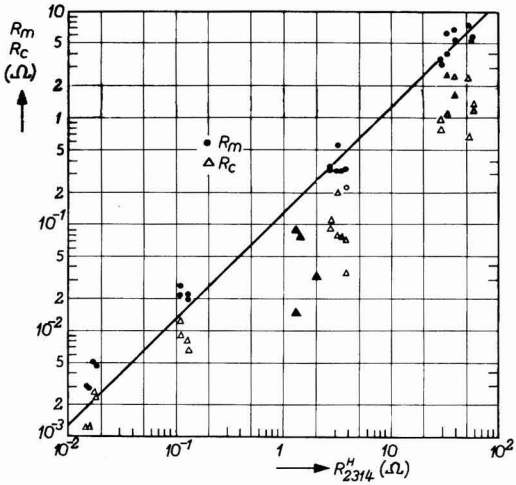

Fig. 4. The spreading resistance R_m (●) and the ensuing contact resistance $R_c = R_c'/\pi A^2$ (△) on chem-mechanically polished silicon substrate slices vs. the Hg fpp resistance R_{2314}. For a 230 μm thick slice, 9.59 ohms corresponds to 1 ohm-cm; thickness variations ± 5% are irrelevant on this scale. The contact resistance R_c (▲) on epitaxial layers agrees with R_c measured on substrate material within the measurement error.

Spreading Resistance Measurement of an N on N$^+$ Silicon Epitaxial Structure

The spreading resistance measurement discussed above can also easily be applied to measure the cylinder resistance R_y of an n-type silicon epitaxial layer on an n$^+$ substrate

$$R_y = \frac{\rho d}{\pi A^2} \qquad [10]$$

For a fpp measurement such a structure can be considered as being a single isolated n$^+$ layer; with a 10 μm thick, 1 ohm-cm n layer on a 250 μm thick, 10^{-2} ohm-cm n$^+$ substrate the sheet resistances are $\rho_e/d_e = 10^3$ ohms and $\rho_s/d_s = 0.4$ ohms, respectively. The thin resistance layer is of interest only for the spreading resistance probe because the real contact resistance R_c in series with the cylinder resistance R_y can be considered as an effective contact resistance R_{ce} in the sense as defined in the preceding section

$$R_{ce} = R_c + R_y \qquad [11]$$

In using this formalism with R_m the contact radius, A, should be much larger than the layer thickness, d. This eliminates the use, without additional and doubtful correction, of the steel probes with $A = 10$ μm, applied for conventional spreading resistance measurements (6, 7). For the above example, $R_y = 127$ mohms which, with the value $R_c \approx 60$ mohms to be found experimentally according to Fig. 4, should yield $R_{ce} \approx 200$ mohms.

It should be emphasized for this application of Eq. [9a] and [9b], that R_{2314} refers to the n$^+$ substrate, that R_m is influenced by both the epitaxial layer R_{ce} and the substrate ρ/d, and that R_y refers to the epitaxial layer only. The meaning of the various parameters introduced is illustrated in Fig. 5.

It turns out that for conventional epitaxial structures the function $\mathbf{F}(z)$ is near unity. Then $\mathbf{F}(z)$ can be approximated for $z < 1.2$ within 1% and for $1.5 < z < 2$ within less than 4%, by

$$\mathbf{F}(z) = \frac{2}{z^2} + 0.25 \qquad [12]$$

whence Eq. [9a] and [9b] can be written as

$$R_{ce} = R_{2114} - 1.77\ R_{2314} \qquad [9c]$$

Physically this means that due to the epitaxial layer cylinder resistance the contact is dominated by the contact resistance R_{ce}, whereas the substrate sheet resistance is so small that there is a horizontal equipotential surface under the probe.

In order to show simply the feasibility of this technique, R_{ce} was first determined from the measured values R_{2314} and R_{2114} for a number of $SiCl_4$-grown n on n$^+$ structures. Thereupon the resistivity ρ was determined using Sze's and Irvin's curves (8); from the CV measured (1) dope concentration at a fixed depth of 4 μm, and with the IMI measured (9) thickness d, the value of R_y was calculated. It turned out then that R_y exceeded R_{ce} so that R_c was negative. Then a few structures were selected which were low doped and thin enough to be probed by the CV method (1) over the full depth of the epitaxial layer and the integral

$$R_y = \frac{1}{\pi A^2} \int_0^d \rho(x)\, dx \qquad [13]$$

was determined. It was found that the IMI measured d includes a part of the transition layer which does not contribute at all to the cylinder resistance, and also that particularly for $SiCl_4$ grown slices, the dope concentration varies strongly with depth. Figures 6a and 6b show some typical profiles. Taking into account this real, reduced value of R_y a positive contribution due to contact resistance R_c was found. Some experimental data on the contact resistance of epitaxial layers measured in this way are presented in Table I and in Fig. 4. It is clear that the method can be used for evaluation purposes as described in the preceding section only when it is surely known that the dope atom concentration does not change with depth. This is the one restriction which hampers the use of the spreading resistance method for the evaluation of epitaxial layers, both with metal and mercury probes.

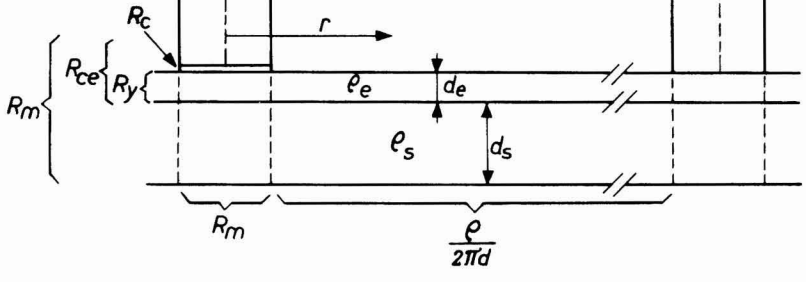

Fig. 5. The various parameters introduced for the measurement of the cylinder resistance on an n on n$^+$ structure presented schematically.

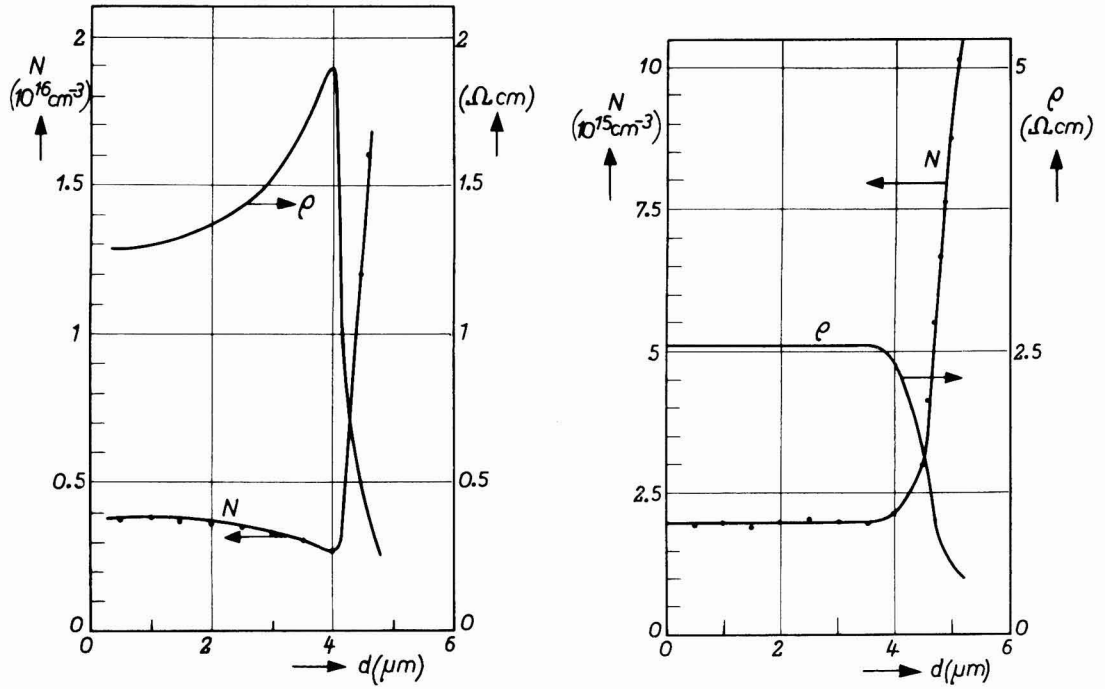

Fig. 6. The dope concentration N and ensuing resistivity ρ as a function of depth below the surface of an epitaxial n on n^+ structure. a, left: E2490-3, $SiCl_4$-grown; b, right: Ril 1345, SiH_4-grown. The IMI measured appropriately corrected thickness for a, left, 5.79 μm; and b, right, 5.96 μm.

Summary and Conclusions

An instrument with four identical mercury probes can be used most efficiently for at least four kinds of measurements. First with one probe connected to a high frequency capacitance bridge, immediate, precise, and accurate capacitance-voltage measurements can be done on substrates and epitaxial layers. An n-type silicon specimen should be slightly oxidized; p-type silicon can be measured without special preparations (1). For routine measurements the bridge can be an automated instrument of which several types are commercially available. Agreement of fpp with CV measurement data, converted with Sze's and Irvin's curves (8) to resistivity, has been obtained for substrates to within a few per cent.

Second, a freshly etched n-type silicon sample can be fpp measured with this instrument without leaving any damage. Agreement with conventional fpp instruments is within a few per cent (3).

Third, a structure prepared as above can be spreading resistance measured with this instrument, and on bulk samples the resistivity agrees within a few per cent with the four-point probe data. The resolving power of about 1 mm makes the mercury spreading resistance probe an interesting instrument, where the fpp would be too coarse and the conventional spreading resistance would be too fine. In addition it leaves no damage. The spreading resistance measured on layers of thickness $d \lesssim A$ should be corrected. A theory is used which integrates the effects of the contact resistance, R_c, into the final expression for the spreading resistance (7, 10). The parameters ρ/d and R_c are found in this way. When, as with conventional spreading resistance probe measurements, d has been obtained otherwise, the local value of ρ is found.

For an epitaxial n on n^+ structure tested in this way, the contact resistance consists of the cylinder resistance proportional to ρd and the real contact resistance in series.

It would be highly desirable to increase the precision of the method so that the contact resistance may be known from calibration, if necessary dependent on the surface preparation, in order to use the method for the determination of ρd of epitaxial layers.

Fourth, with the mercury probe a MIS diode can be made and pulse measured in order to evaluate simply and immediately the dope concentration directly below the surface and the bulk lifetime and surface recombination velocity. This will be the subject of a future paper.

Table I. The contact resistance R_c of mercury to n-type epitaxial silicon

Slice	ρ (ohm-cm) on surface	R_T (mohms)	R_c (mohms)
E 2490-3	1.31	76	31
Ril 1345	2.55	149	76
Ril 1286	1.20	55	13
Ril 1280	1.18	58	90

Manuscript submitted Jan. 22, 1974; revised manuscript received July 3, 1974. This was Paper 75 presented at the Chicago, Illinois, Meeting of the Society, May 13-18, 1973.

Any discussion of this paper will appear in a Discussion Section to be published in the December 1975 JOURNAL. All discussions for the December 1975 Discussion Section should be submitted by Aug. 1, 1975.

Publication costs of this article were partially assisted by Philips Research Laboratories.

APPENDIX

A current i_o enters a circular contact of radius A at potential V_o on a thin layer of infinite extent, of thickness $d << A$ and resistivity ρ, shown in Fig. 5. The current i_o leaves the structure through a contact at infinity at zero potential. The potential drops with r according to

$$\frac{\partial V(r)}{\partial r} = -\frac{\rho}{2\pi d}\frac{1}{r} \quad \text{for} \quad r \leqq A \qquad [A\text{-}1]$$

and the current $i(r)$ which passes through a cylinder increases below the contact as

$$\frac{\partial i(r)}{\partial r} = 2\pi r J(r) \qquad [A\text{-}2]$$

because of the local voltage drop over the specific resistance R_c' given by

$$R_c' J(r) = V_o - V(r) \qquad [A\text{-}3]$$

Writing $R_s = \rho/d$ and $\Lambda^2 = R_c'/R_s$, Eq. [A-1]-[A-3] can be combined to yield the differential equation

$$\frac{\partial^2 V}{\partial r^2} + \frac{1}{r}\frac{\partial V}{\partial r} - \frac{V - V_o}{\Lambda^2} = 0 \qquad [A\text{-}4]$$

with solution in terms of the modified Bessel function of the first kind

$$V - V_o = aI_o\left(\frac{r}{\Lambda}\right) \qquad [A\text{-}5]$$

and hence

$$i = -\frac{2\pi d}{\rho}\frac{ra}{\Lambda} I_1\left(\frac{r}{\Lambda}\right) \qquad [A\text{-}6]$$

From the boundary condition $i = i_o$ at $r = A$ follows that with $z = A/\Lambda$ the potential drop over R_c at $z = 0$ equals

$$a = -\frac{\rho i_o}{2\pi d}\frac{1}{zI_1(z)} \qquad [A\text{-}7]$$

and that the resistance R_m measured between the contact and a point very near $r = A$ given by

$$R_m = \frac{\rho}{2\pi d}\frac{I_o(z)}{zI_1(z)} = \frac{\rho}{2\pi d}\mathbf{F}(z) \qquad [A\text{-}8]$$

The solution for $r > A$, where $J(r) = 0$ and $i = i_o$, follows from Eq. [A-1] as

$$V - V_o = \frac{\rho i_o}{2\pi d}\ln\frac{r_1}{r} \qquad [A\text{-}9]$$

The solutions of Eq. [A-5] and [A-9] should be matched; it can easily be verified that

$$V_o - V = \frac{\rho i_o}{2\pi d}\left(\mathbf{F}(z) - \ln\frac{r}{A}\right) \qquad [A\text{-}10]$$

In this way both the potential and its derivative, proportional to the current, are matched at $r = A$. A discrepancy which cannot be overcome is due to the fact that at $r = A$ the current density is maximum under the contact but vanishes at $r > A$. No doubt the approximation of J only perpendicular to the contact does not hold at the edge $r = A$, which affects the applicability of the theory less if $A >> d$. The equation actually used in the measurement arrangement can be obtained from Eq. [A-10] by superposition of the two potential systems: current i_o enters through probe 1 and leaves at infinity and current i_o enters at infinity and leaves through probe 4. The ensuing logarithmic potential drop has experimentally been found to exist precisely.

REFERENCES

1. P. J. Severin and G. Poodt, *This Journal*, **119**, 1384 (1972).
2. P. J. Severin, Paper 75 presented at Electrochemical Society Meeting, Chicago, Ill., May 13-18, 1973.
3. P. J. Severin and H. Bulle, *This Journal*, **122**, 133 (1975).
4. R. G. Mazur and D. H. Dickey, *ibid.*, **113**, 255 (1966).
5. W. A. Keenan, P. A. Schumann, A. H. Tong, and R. P. Phillips, in "Ohmic Contacts to Semiconductors," B. Schwartz, Editor, p. 263, The Electrochemical Society Softbound Symposium Series, New York (1969).
6. P. J. Severin, *Solid State Electron.*, **14**, 247 (1971); NBS Special Publication 337, p. 224, 1970.
7. P. J. Severin, *Philips Res. Repts.*, **26**, 359 (1971).
8. S. M. Sze and J. C. Irvin, *Solid State Electron.*, **11**, 599 (1968).
9. P. J. Severin, *Appl. Opt.*, **9**, 2381 (1970); **11**, 691 (1972).
10. P. J. Severin, Symposium on Spreading Resistance Measurements, National Bureau of Standards, Gaithersburg, 1974.

Oxygen Ion Conduction of the Fluorite-Type $Ce_{1-x}Ln_xO_{2-x/2}$ (Ln = Lanthanoid Element)

Tetsuichi Kudo and Hidehito Obayashi

Central Research Laboratory, Hitachi, Limited, Higashi-koigakubo, Kokubunji, Tokyo, 185, Japan

ABSTRACT

The compounds $Ce_{1-x}Ln_xO_{2-x/2}$ (Ln = lanthanoid element) have been synthesized and the emf and resistivity measurements have been carried out between 400° and 1000°C. It is found that charge carriers of conduction in these compounds are oxygen ions above 600°C; the oxygen transference number being above 0.95 for all measured compounds. The resistivity value for $Ce_{0.77}Gd_{0.23}O_{1.885}$ is 15 ohm-cm at 750°C which compares with that of calcia stabilized zirconia at 1000°C. It is found that the dependence of the resistivity on temperature is described by

$$\rho = (\rho_o)_L \exp(\Delta E_L/kT) + (\rho_o)_H \exp(\Delta E_H/kT)$$

for most of the compounds, where the (ρ_o)'s and ΔE's are empirically determined parameters. The activation energies of conduction are determined by the compounds' lattice constant so long as the dopant concentration is held constant. The activation energies increase as the dopant concentration x increases and ΔE_L and ΔE_H coincide at $x \geqq 0.4$.

There have thus far been numerous studies on the ZrO_2 family oxygen ion conductive solid electrolytes (1-3). However, it seems that systems other than the ZrO_2 family have attracted less interest and that a systematic approach is lacking. Several compounds having oxygen ionic conduction have been reported by Singman (4), Mazelsky (5), and Iwahara (6). These solid electrolytes, however, exhibit poorer char-

Key words: ionic conductor, solid electrolyte, cerium/lanthanoid oxide, solid solution.

acteristics both in resistivity and transference number compared with the ZrO_2 family.

Etsell and Flengas (7) published an excellent review on CeO_2-base solid electrolytes as well as ZrO_2-, ThO_2-base and other solid electrolytes.

The CeO_2 family oxygen ion conductive solid electrolytes have been widely and systematically synthesized and their properties investigated in this paper. The compounds are represented in a general formula $Ce_{1-x}Ln_xO_{2-x/2}$ where Ln stands for the trivalent lanthanoid element ranging from Y, La, to Yb.

Experimental

Sample preparation.—The oxides CeO_2 (99.99% up, Shinetsu Kagaku K.K.) and Ln_2O_3 (99.9% up, Shinetsu Kagaku K.K.) were precisely weighed and mixed in an agar mortar. The mixture was pressed softly (0.5 t/cm^2) in a die and placed in an alumina boat. It was heated to 1300°C and kept at this temperature for 8 hr. The presintered sample did not show any foreign peaks other than fluorite-type compound $Ce_{1-x}Ln_xO_{2-x/2}$ in an x-ray diffraction pattern. The sample was then ground in an agar mortar to −325 mesh. When needed, 3 mole per cent (m/o) magnesium was added as $Mg(NO_3)_2$. As a binder 1 weight per cent (w/o) methyl cellulose was added and ground again to −40 to −60 mesh. The powder was pressed in a die at 3 t/cm^2, then placed in a Pt-40% Rh basket and sintered at 1800° ± 20°C for 2-3 hr in air. The sintered samples showed a porosity of less than 4% in all cases.

Oxygen ion transference number measurement.—The average oxygen ion transference number $\bar{t}_{O-2}$ is given by

$$\bar{t}_{O-2} = \frac{E}{\frac{RT}{4F} \ln (p''_{O_2}/p'_{O_2})} \quad [1]$$

where symbol E stands for the observed emf of the cell

$$O_2(p'_{O_2}), \text{ Pt/Solid Electrolyte/Pt, } O_2(p''_{O_2}) \quad [2]$$

In the experiments reported here, $p''_{O_2} = 1$ atm and $p'_{O_2} = 0.21$ atm.

For measurement of emf, a vertical type gas flow apparatus was made, whose schematic profile is shown in Fig. 1. A 20 mm diameter and 1-2 mm thick disk sample was sandwiched between silver packings to which ceramic tubes were attached. The silver packings ensure the gas tightness of the cell at elevated temperatures. The gas tightness was further ensured by a spring placed at the upper end of the ceramic tube. A rotary pump vacuum test was carried out before each run to test for gas tightness. An inner gas guide pipe was placed in both the upper and lower rooms so that both electrodes were exposed to fresh gas throughout each run. Oxygen gas was introduced into the upper room and air was introduced into the lower room.

Income gas flow rates were between 50 and 100 ml/min, and the gas was not preheated. Calculated linear flow rates for these conditions were around 0.5-1.0 cm/sec assuring that the gas is well heated to the equilibrium temperature of the furnace. The temperature of the sample was measured by a Pt-(Pt-Rh13) thermocouple and a cooling effect of incoming gas was proved to be negligibly small in the employed experimental conditions.

Resistivity measurement.—The electrical contacts were made using platinum paste electrodes to both sides of a disk sample. An a-c impedance bridge method was employed usually. An RC701 (Matsushita Electric) type frequency generator was used, and the bridge was an BV-Z-1 (Yokogawa Electric) type direct reading impedance bridge. The frequency used was 1 kHz. In the a-c measurements, the resistance of the platinum lead wire was compensated. In some cases, d-c four-probe method was employed. In the d-c measurements, 30 × 10 × 5 mm rod samples were used. Two platinum wires (0.3 mmϕ) which work as the potential drop measurement probes were spanned on a flat and smooth alumina plate. The current flowing porous platinum paint electrodes were attached to far ends of the rod sample. This rod was placed on that plate and on the sample was another alumina plate on which a 100g platinum rod was placed. This rod was used to ensure the contacts between the sample and the spanned platinum probes. The potential drop between two probes during the constant current flow was measured by a potentiometric Hitachi QPD54 recorder. At the initial stage of this work, platinum wire probes were placed in 0.3 mm wide and 0.3 mm deep ditches surrounding the sample separated by 10 mm. However, it was assured that the above method gives the same result, therefore, we have changed to the easier method.

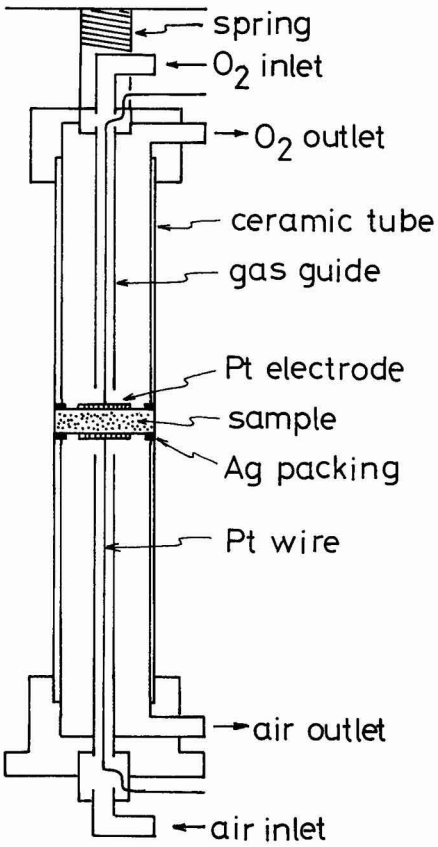

Fig. 1. Schematic drawing of emf measurement cell. The cell is placed in a vertical type furnace and the temperature is controlled within ±2°C. EMF was measured by a potentiometer.

The uniformity of the temperature in the furnace was increased by covering a quartz tube with 1 mm thick nickel tube. At the same time, one end of the nickel tube was grounded so as to eliminate electric noises from the external field.

X-ray diffraction.—Usually, Cu K_α or Fe K_α radiation were used. The scanning speed was 2θ/min = 1°/min. For the determination of lattice constants, diffractions from (620) and (533) planes were used when Cu K_α was employed while (422) and (511) planes were used when Fe K_α was employed. For some samples, high temperature x-ray diffraction measurements

were carried out at temperatures between room temperature and 1000°C.

DTA measurement.—DTA measurements were carried out using a Type M8006 macro DTA and a Type M8076 micro DTA apparatus (Rigaku-denki K.K.). Sample weights were 1.7-1.9g for macro and 10-50 mg for micro DTA measurements, respectively. The differential thermocouple used was Pt-(Pt-Rh13)-Pt thermocouple and one junction attached to reference (α-Al_2O_3) worked as temperature detecting thermocouple. Measurements were carried out between room temperature and 800°C and the speed of temperature rise was fixed to 20°C/min throughout all the measurements.

Result and Discussion

Crystal structure.—The compound CeO_2 has a fluorite-type cubic crystal structure. When trivalent lanthanoid ions Ln (Ln = Y, La, to Yb) replace the Ce ion sites of the fluorite lattice, the modified formula is generally expressed as

$$Ce^{+4}{}_{1-x}Ln^{+3}{}_xO^{-2}{}_{2-x/2}(V_{O-2})_{x/2} \qquad [3]$$

where V_{O-2} stands for the oxygen ion vacancy generated to compensate charges in the crystal.

The CeO_2-Ln_2O_3 system has a wide solid solution region of fluorite-type lattice and the compounds $Ce_{1-x}Ln_xO_{2-x/2}$ show the pure fluorite lattice pattern up to *ca.* $x = 0.5$. The lattice constants of $Ce_{1-x}Ln_xO_{2-x/2}$ ($x = 0.3$) are summarized in Table I. This table also contains several three component compounds, where the sum of the substituting components is $x = 0.3$. As seen from this table, the lattice constants decrease as the ionic radii of the substituting ions become smaller. When the system contains two kinds of substituting ions, the lattice constants fall into the intermediate values of two respective single-substituting ion cases. Thus it appeared that the lattice constant additivity rule holds in the system $Ce_{1-x}Ln_xO_{2-x/2}$.

Figure 2 shows the lattice constant change when the amount of Gd substitution was changed. Magnesia, like Ln_2O_3, dissolves into the lattice to form a solid solution. This was proven by the fact that the lattice constants of MgO-free compounds were larger than those of MgO-added compounds and the fact that there were no x-ray diffraction peaks comprising MgO. The saturation of lattice constant at $x \geqq 0.4$ does not necessarily mean that the solubility limit exists at $x = 0.4$.

Bevan, Barker, and Martin (8) interpreted that this saturation is due to the Gd^{3+} ions and oxygen vacancies' strong interaction and that point defects are complexed. A similar phenomenon was observed by Brauer and Gradiger (9), and they also observed a sharp decrease of lattice constant at $x \geqq 0.5$. As the fluorite lattice and the c-type Gd_2O_3 give quite similar x-ray diffraction patterns, it is difficult to determine the solubility limit precisely by this method. In our measurements, diffraction lines caused by the existence of superlattice in the compounds which could appear for c-type oxide, were not observed up to $x = 0.5$. Above this value, weak lines from superlattices were observed. Thus, it is reasonable to conclude that the system CeO_2-Gd_2O_3 keeps the fluorite lattice up to $x = 0.5$.

Figure 3 shows the lattice constant increase of the compounds $Ce_{1-x}Gd_xO_{2-x/2}$ as the temperature is raised. The change of the lattice constant is almost linear regardless of composition, in the temperature range between room temperature and 1000°C. The average linear expansion coefficient of these compounds as calculated from Fig. 3 is $\beta = 12.6 \times 10^{-6}$ °C^{-1} for the three compounds measured. The compounds $Ce_{1-x}Gd_xO_{2-x/2}$ do not have any transitions

Table I. Lattice constants, ΔE_L and ΔE_H, and $(\rho_0)_L$ and $(\rho_0)_H$ of conduction for the compounds $Ce_{1-x}Ln_xO_{2-x/2}$ ($x = 0.3$)

Ln[a]	Lattice[c] const (A)	ΔE_L[d] (eV)	ΔE_H[d] (eV)	$(\rho_0)_L$[d] (ohm-cm)	$(\rho_0)_H$[d] (ohm-cm)
Y	5.398	1.12	0.91	8.5×10^{-5}	1.4×10^{-3}
La	5.503	0.94	0.81	7.3×10^{-4}	4.0×10^{-3}
Nd	5.460	0.96	0.81	3.0×10^{-4}	2.7×10^{-3}
Sm	5.442	0.98	0.78	2.5×10^{-4}	4.4×10^{-3}
Eu	5.433	1.03	0.81	8.3×10^{-5}	2.5×10^{-3}
Gd	5.428	1.05	0.84	1.6×10^{-4}	2.0×10^{-3}
Dy	5.406	1.12	0.88	5.8×10^{-5}	3.1×10^{-3}
Ho	5.398	1.13	0.93	6.5×10^{-5}	9.3×10^{-4}
Er	5.391	1.14	0.93	6.8×10^{-5}	1.0×10^{-3}
Yb	5.379	1.08	0.89	1.8×10^{-4}	2.1×10^{-3}
1Sm-4Ho[b]	5.408	1.11	0.89	9.6×10^{-5}	1.7×10^{-3}
4Sm-1Ho	5.434	0.99	0.81	2.2×10^{-4}	2.5×10^{-3}
1Sm-4Y	5.407	1.11	0.87	7.8×10^{-5}	1.8×10^{-3}
4Sm-1Y	5.434	1.00	0.80	2.4×10^{-4}	3.8×10^{-3}
1Dy-1Gd	5.417	1.03	0.87	1.6×10^{-4}	1.5×10^{-3}

[a] Scandium does not form fluorite lattice with cerium.
[b] Notations like 1Sm-4Ho mean the atomic ratio of Ln, thus, the exact formula for 1Sm-4Ho is $Ce_{0.7}Sm_{0.06}Ho_{0.24}O_{1.85}$.
[c] Lattice constant values are valid to the final digits.
[d] Activation energies and (ρ_0)'s are valid within ±0.5 of the final digits.

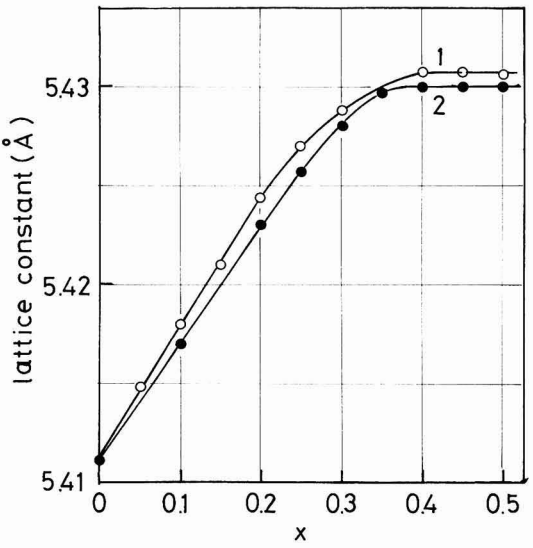

Fig. 2. Lattice constant change of $Ce_{1-x}Gd_xO_{2-x/2}$ as Gd content is changed. Curves 1 and 2 represent data for MgO free and 3% MgO added samples, respectively.

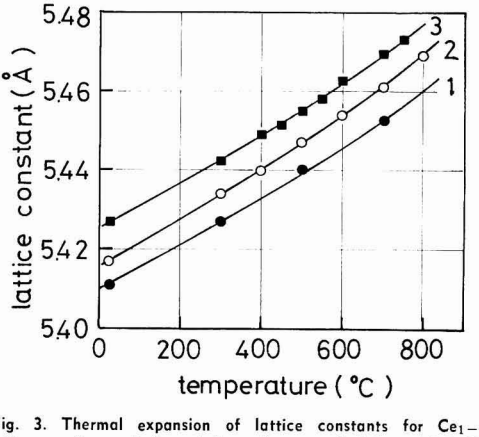

Fig. 3. Thermal expansion of lattice constants for $Ce_{1-x}Gd_xO_{2-x/2}$. Curves 1, 2, and 3 are for $x = 0$, 0.1, and 0.2. The average linear thermal expansion coefficient for these compounds are 12.6×10^{-6} °C^{-1}.

observable by x-ray diffraction in this temperature range.

Oxygen ion transference number.—The charge carrier of the conduction is considered to be O^{-2} ion. In this section, results of oxygen ion transference number measurements are presented.

Figure 4 is the change of oxygen ion transference number as the temperature is changed. The emf measurement cell setup was expressed in Eq. [2].

At temperatures lower than 400°C, the resistivity is so high that it prohibits the emf measurements. The emf value deviated from the theoretical one at temperatures below 600°-700°C for all samples. The reasons were considered to be as follows. The porous platinum paste electrode does not function as a reversible oxygen electrode at lower temperatures, suggesting a reaction polarization becomes critical at these temperatures. In this sense, Fig. 4 does not show the correct transference numbers for these samples at temperatures below 600°-700°C. Silver electrodes would have been better at lower temperatures as reversible oxygen electrodes. Above these temperatures, however, all the investigated compounds showed stable and reproducible emf values. The transference number for $Ce_{1-x}Ln_xO_{2-x/2}$ (Ln = Sm and Dy) saturates at 0.95-0.96, whereas the other compounds containing Nd, Gd, and Er gave unity as their transference number. The reason of deviation of transference number from unity in the cases of the compounds containing Sm and Dy is not known yet, however, the porosities of the two samples were measured to be a little larger than the other samples suggesting there existed some open pores in these samples.

From these data and in view of the analogy of crystal structure with ZrO_2, it was concluded that the charge carrier of conduction in Ce_{1-x}-$Ln_xO_{2-x/2}$ in air is the oxygen ion.

Resistivity measurement.—Figures 5 and 6 show the relation between log resistivity and the reciprocal temperature for the compounds $Ce_{0.7}Ln_{0.3}O_{1.85}$ (Ln = Y, La, Eu, Sm, Gd, Dy, Ho, Er, and Yb). All plots show the two differing slope lines. Around the intersection of two lines, however, data deviated from linear lines toward the high resistivity side. The resistivity values of these compounds are very small (1/10 to 1/1000) compared with those listed by Etsell and Flengas (7). However, the resistivity measurements by a-c and d-c methods gave good agreement and they are quite reproducible as shown by the plots in Fig. 5 and 6, it is believed that our data represent true resistivities for these compounds.

Figure 7 shows the resistivity isotherms against lattice constant. In these plots, resistivity values ρ were

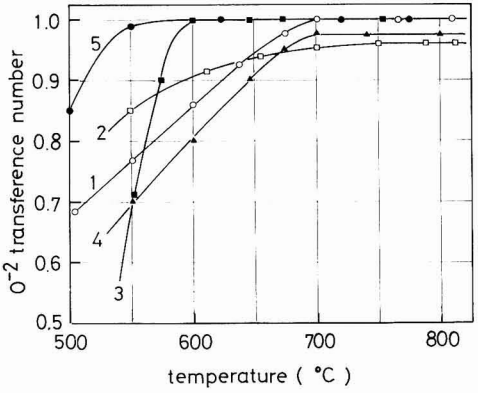

Fig. 4. Oxygen ion transference number of the compounds $Ce_{1-x}Ln_xO_{2-x/2}$ (x = 0.3). Curves 1-5 are for Ln = Nd, Sm, Gd, Dy, and Er.

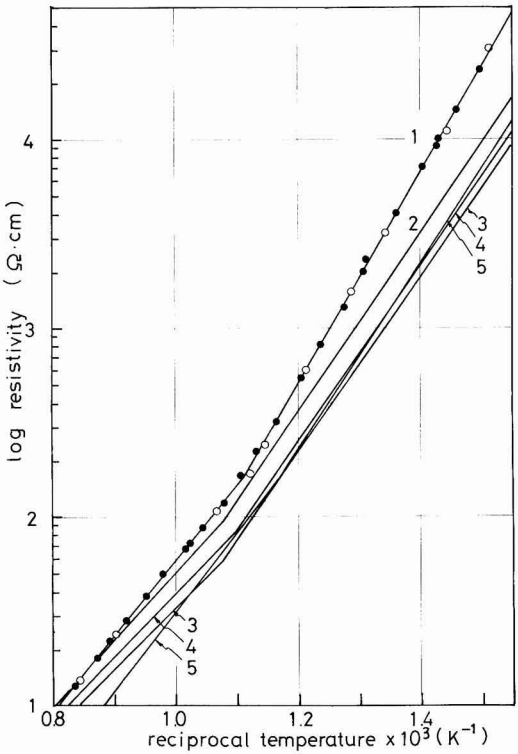

Fig. 5. Arrhenius plot of resistivity for the compounds $Ce_{1-x}Ln_xO_{2-x/2}$ (x = 0.3). Lines 1-5 are for Ln = Y, La, Nd, Sm, and Er. Filled circles are for rising temperature, and open circles are for lowering temperature measurements.

corrected in consideration of samples' porosity according to Juretschuke's formula (10)

$$\rho = \frac{1-\epsilon}{1+\frac{\epsilon}{2}}\rho_{obs} \qquad [4]$$

where symbol ϵ stands for the porosity of samples. Each isotherm has its minimum resistivity value at a certain lattice constant. This provides a guideline for the minimization of the resistivity at various temperatures. For example, in order to get a low resistivity solid electrolyte at 800°C, it would be advisable to investigate the compositions whose lattice constants range from 5.43 to 5.44Å. The fact that there exists a minimum resistivity value in the resistivity and lattice constant plot suggests the existence of a certain compensation rule between pre-exponential term ρ_o and the activation energy ΔE in the Arrhenius-type formula.

The resistivity change of the compounds $Ce_{1-x}Gd_xO_{2-x/2}$ *vs.* temperature is shown in Fig. 8. At temperatures lower than 350°C, some samples showed small ΔE of conduction which suggested the onset of an electronic conduction; however, the data were lacking in reproducibility.

In the temperature range where the oxygen ionic conduction is predominant, the plot of resistivity *vs.* the reciprocal temperature could well be approximated by two linear lines. Similar results were obtained by Bauerle and Hrizo (11) for $(ZrO_2)_{0.90}(Y_2O_3)_{0.10}$. They proposed two hypotheses which yield such a temperature dependence; one being the vacancy trapping by yttrium ions, and the other, the grain boundary effect.

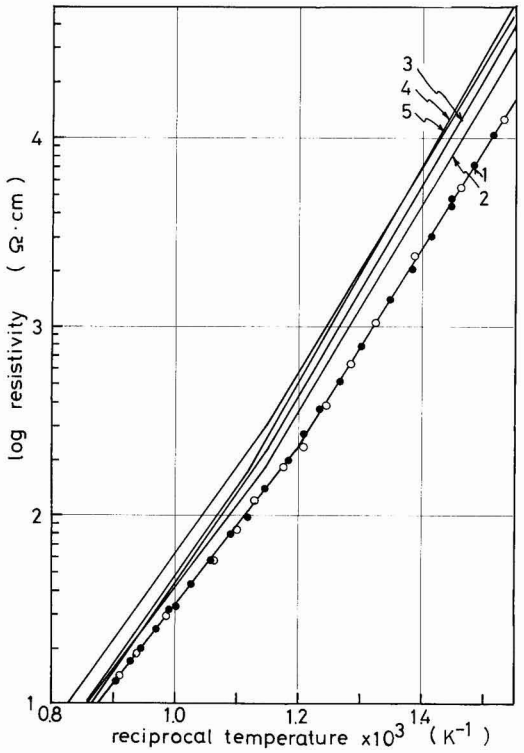

Fig. 6. Arrhenius plot of resistivity for the compounds $Ce_{1-x}Ln_xO_{2-x/2}$ ($x = 0.3$). Lines 1-5 are for Ln = Gd, Dy, Ho, Er, and Yb. Filled circles are for rising temperature, and open circles are for lowering temperature measurements.

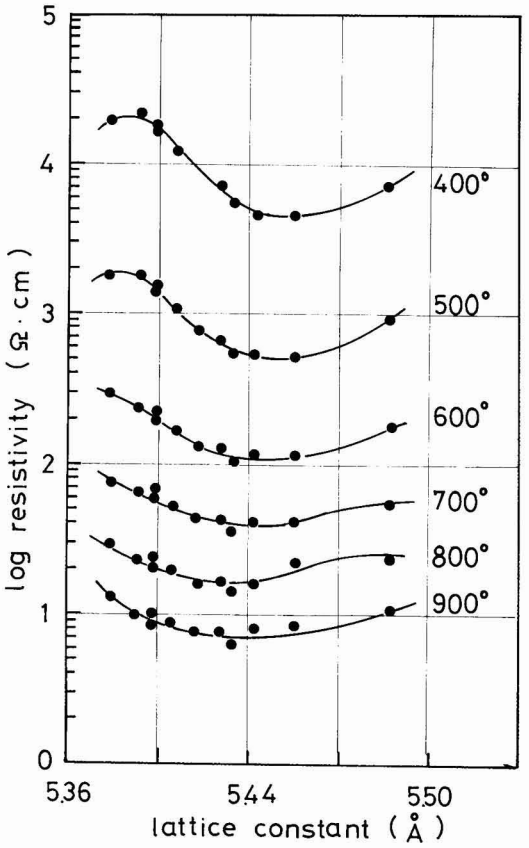

Fig. 7. Resistivity isotherms as summarized vs. lattice constant for the compounds $Ce_{1-x}Ln_xO_{2-x/2}$ ($x = 0.3$).

These hypotheses are open to discussion, however, if the log ρ *vs.* T^{-1} relation was approximated by the two linear lines, it means that we assumed two Arrhenius-type formulas

$$\rho = (\rho_0)_L \exp(\Delta E_L/kT) \quad \text{lower temp region}$$
$$\rho = (\rho_0)_H \exp(\Delta E_H/kT) \quad \text{higher temp region} \qquad [5]$$

Then the temperature range could appropriately be divided into two regions, the boundary being the intersection point of the Arrhenius plot. The calculated (ρ_0)'s and ΔE's are listed in Table I. The lower temperature region has a larger activation energy and the higher temperature region has a lower activation energy. The activation energy of CeO_2-15% La_2O_3 as given by other workers are 14.7 (12) or 21.0 (4) kcal/mol (0.64 or 0.91 eV). Our results of activation energy for Ln doped compounds fall in the range of 0.77-0.93 eV for high temperature region conduction. Thus, data by Croatto and Mayer (12) seem to be too small. The calculated activation energies of conduction were interpreted in terms of lattice constant. The result is shown in Fig. 9.

The lattice constant a_o of $Ce_{0.7}Ln_{0.3}O_{1.85}$ changes in the range from 5.38Å (Ln = Yb) to 5.50Å (Ln = La). The activation energies of conduction ΔE_L and ΔE_H pass the maximum values at $a_o = 5.39$Å, then they decrease as the lattice constant becomes larger. In the range where $a_o \geqq 5.45$Å, both activation energies ΔE_L and ΔE_H seem to be determined not by the kind of lanthanoid elements but by the value of lattice constant.

If the dopant concentration x is varied, the above discussion no longer holds. Figure 10 shows the activation energy change when the dopant concentration x is varied for the compounds $Ce_{1-x}Gd_xO_{2-x/2}$ ($0 \leq x \leq 0.5$). As seen from this figure, the activation energy remains comparably constant in the range $x \leq 0.2$. The values increase rapidly as x is increased in the range where $0.3 \leq x \leq 0.4$. The sharp increase of activation energies in this range is paralleled by the saturation range of lattice constants. We suggested that interaction between vacancy-vacancy and vacancy-doped ion begins to start. Here, again this sharp increase could be attributed to this effect reducing the mobility of oxygen ion vacancies. Above $x = 0.4$, the activation energies of lower and higher temperature regions coincide and the value increases gradually as x is increased. Heyne (13) argues that in stabilized ZrO_2, the conductivity increase cannot be interpreted by the simple concept of a conductivity proportional to the vacancy concentration. In CeO_2 base compounds, however, this concept can explain the increase of conductivity at least in the range $x \leq 0.2$.

As mentioned before, the cause of the existence of two activation energies of O^{-2} conduction is not known at present, however, it was observed by DTA measurements that the base line of the DTA curve deviates to the endothermic side at temperatures near 500°C for the compounds $Ce_{1-x}Gd_xO_{2-x/2}$ ($0 \leq x \leq 0.5$) suggesting an increase of the specific heat of the compounds. This increase does not necessarily mean the existence of transition in the crystal lattice as x-ray measurement revealed no pattern change between lower and higher temperatures. However, it seems likely that some higher order transition other than lattice type change occurs around 500°C and that this is the reason for the existence of kinks in the Arrhenius plots of

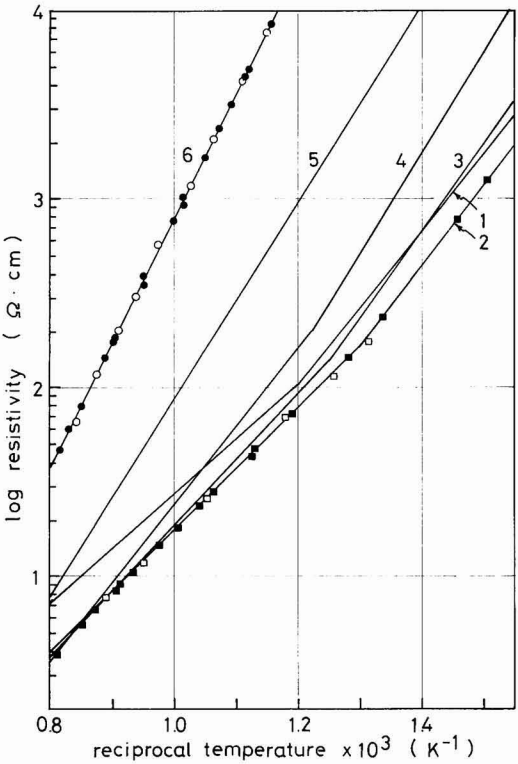

Fig. 8. Arrhenius plot of resistivity for the compounds $Ce_{1-x}Gd_xO_{2-x/2}$. Lines 1-6 are for x = 0.1, 0.2, 0.25, 0.3, 0.4, and 0.5. Filled plots are for rising temperature, and open plots are for lowering temperature measurements.

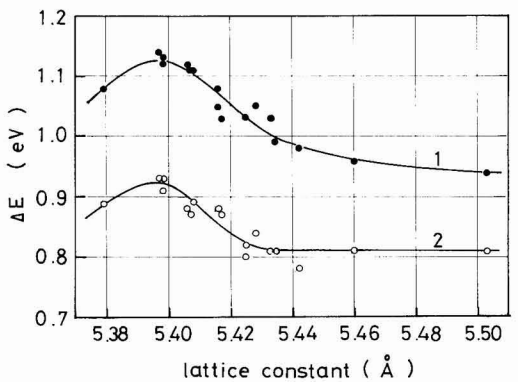

Fig. 9. Activation energy of oxygen ion conduction for the compounds $Ce_{1-x}Ln_xO_{2-x/2}$. Curves 1 and 2 are for low and high temperature regions.

resistivity. Further study is underway and the results will be published elsewhere.

Conclusion

The CeO_2 base fluorite-type solid solution $Ce_{1-x}Ln_xO_{2-x/2}$ (Ln = lanthanoid element) can be characterized as a family of good conductive oxygen ion solid electrolytes. The following are the conclusions derived from this study.

1. The transference number of the oxygen ion as measured by an emf cell method using the oxygen concentration cell is greater than 0.95 at temperatures above 600°C for $Ce_{1-x}Ln_xO_{2-x/2}$ (Ln = Nd, Sm, Gd, Dy, and Er).

2. The compounds $Ce_{1-x}Ln_xO_{2-x/2}$ (x — 0.5; Ln = Y, La, Nd, Sm, Eu, Ho, Er, and Yb) are single phase fluorite-type solid solutions. The compounds containing Sc do not form a solid solution in the same range.

3. The Arrhenius type plot of resistivity is well approximated by two linear lines in the temperature range $T \geqq 400$°C. At lower temperatures electronic conduction is observed in some compounds. The resistivity of $Ce_{1-x}Ge_xO_{2-x/2}$ (x = 0.23) at 750°C is 15 ohm-cm which rivals the value of calcia stabilized zirconia at 1000°C. The slope of the Arrhenius plot gives the activation energy of oxygen ion conduction, the value of which is determined by the dimension of the crystal lattice so long as dopant concentration x is kept constant. For x = 0.3, ΔE's pass the maximum values at a_o = 5.39Å.

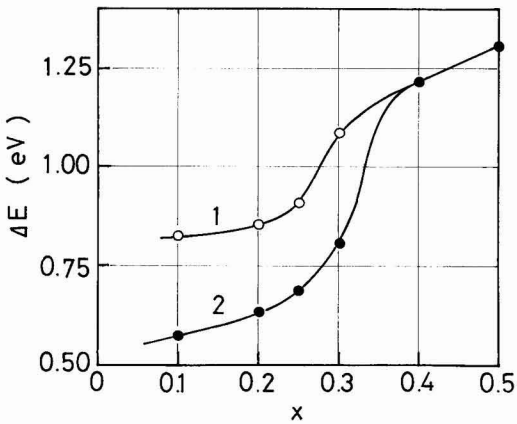

Fig. 10. Activation energy of oxygen ion conduction for the compounds $Ce_{1-x}Gd_xO_{2-x/2}$. Curves 1 and 2 are for low and high temperature regions. Above x = 0.4, both activation energies coincide.

Acknowledgments

The authors wish to thank Dr. Y. Maki for his continuous encouragement and helpful discussions throughout this work.

Manuscript submitted Jan. 30, 1974; revised manuscript received June 24, 1974.

Any discussion of this paper will appear in a Discussion Section to be published in the December 1975 JOURNAL. All discussions for the December 1975 Discussion Section should be submitted by Aug. 1, 1975.

Publication costs of this article were partially assisted by Hitachi, Limited.

REFERENCES

1. C. Wagner, Naturwissenschaften, **31**, 265 (1943).
2. F. Z. Hund, *Z. Phys. Chem.*, **199**, 142 (1952).
3. H. Tannenberger, *Proc. Int. Etude Pile Comb.*, **III**, 19 (1965).
4. D. Singman, *This Journal*, **113**, 502 (1966).
5. R. Mazelsky, *ibid.*, **111**, 528 (1964).
6. H. Iwahara, *Denki Kagaku (Japan)*, **34**, 254 (1966).
7. T. H. Etsell and S. N. Flengas, *Chem. Rev.*, **70**, 339 (1970).
8. D. J. M. Bevan, W. W. Barker, and R. L. Martin, in "Proceedings of the 4th Conference on Rare Earth Research, Phoenix, Ariz. 1964," L. Eyring, Editor, p. 441, Gordon and Breach, New York (1965).
9. G. Brauer and H. Gradiger, *Z. Anorg. Allgem. Chem.*, **276**, 209 (1954).
10. H. J. Juretschuke, *J. Appl. Phys.*, **27**, 838 (1956).
11. J. E. Bauerle and J. Hrizo, *J. Phys. Chem. Solids*, **30**, 565 (1969).
12. U. Croatto and A. Mayer, *Gazz. Chim. Ital.*, **73**, 199 (1943).
13. L. Heyne, *Electrochim. Acta*, **15**, 1251 (1970).

Charge Storage and Stoichiometry in Electron Beam Evaporated Alumina

Konrad M. Eisele

Institut fuer Angewandte Festkoerperphysik, Freiburg, Germany

ABSTRACT

Alumina films have been evaporated by means of an electron beam onto metal electrodes on ceramic substrates. A metal-oxide-metal structure has been subjected to an electric field and the resulting charge storage measured by recording the short circuit current. The charge storage has been related to the stoichiometry of the alumina film which in turn has been influenced by the beam power or by postdeposition treatment. The effect of electric field and temperature on the charge stored has been studied.

In a recent publication (1) aluminum oxide films have been examined for their ability to act as a barrier against alkali ion migration. This property makes such films useful as a passivation layer for integrated circuits. In these applications a low temperature process to generate the Al_2O_3 film is desirable. For this reason electron beam evaporation was considered.

It is known that this method yields Al_2O_3 films which are nonstoichiometric to various degrees. Hoffman and Leibowitz (2) showed that the stoichiometry can be regulated by controlling the potential of the substrate in such a way that secondary or reflected primary electrons coming from the hearth cannot build up charge which repels arriving oxygen ions. Whenever oxygen atoms emanate from Al_2O_3 under electron bombardment, part of these will be pumped away by the vacuum system and necessarily a certain lack of stoichiometry must result.

To study the electrical properties, especially charge storage as related to the stoichiometry of the oxide, we manufactured Al-Al_2O_3-Al sandwiches by means of an electron gun.

The Metal-Alumina-Metal Capacitor

The active area of the device (Fig. 1) was 0.185 cm^2, and the oxide thickness varied between 4,200 and 28,000Å resulting in capacities from 150 to 24 pf/mm^2. The substrate was glazed ceramic. The structure was obtained by evaporating through nickel masks; no etching was employed. Four different metals were used as electrodes. The deposition rates of the aluminum oxide varied from 10 to 400 Å/min. The power of the electron beam determined the deposition rate but also the decomposition of the source material.

In view of Ref. (2) the quantity of stray electrons responsible for charge buildup increases with the power of the primary beam. In our arrangement the masking device as well as the bottom electrode was grounded, so that secondary or reflected primary electrons moved between points of equal potential, *i.e.*, between the grounded hearth and the substrate.

At a power level of about 320W (4 kV, 80 mA) a blue glow appeared over the source material. The pressure in the vacuum system, usually in the low 10^{-6} Torr range, increased at this point indicating the liberation of oxygen from the aluminum oxide. With greater beam power the resulting Al_2O_3 film became increasingly darker in color. In addition the source material turned dark indicating loss of oxygen.

The influence of the electron beam acceleration voltage on the film composition was established by electron microprobe analysis and then correlated with the charge storage measurements. The index of refraction was derived from ellipsometer readings as being 1.762 compared to 1.765 for the bulk material and was the same for all samples. Electron diffraction analysis revealed no crystallinity. The electrical measurements could not distinguish between films deposited at various substrate temperatures in the range from 670° to 77°K. The best films were able to withstand fields as high as 5×10^6 V/cm.

Comparative measurements will be presented of two samples designated D_2 and D_4 representing the typical properties obtained with low and high beam power, respectively. For plate D_2 the evaporation of the Al_2O_3 was performed with low beam voltage (2.9 kV; 125 mA) and correspondingly low deposition rate (110 Å/min). The film was clear, of very low conductivity, and exhibited low charge storage. In contrast D_4 was deposited with high beam voltage (8 kV, 170 mA) at a rate of 410 Å/min which resulted in a dark film with a relatively high conductivity and charge storage. Between these extremes, various degrees of oxygen deficiency were produced.

Charge Storage in the Aluminum Oxide

Trap states have been encountered in various experiments with insulating films. They can store charge to change the space charge distribution in the insulator (3). Because the number of free electrons in an insulator is very small, a relatively small number of electrons getting trapped will suffice to change the charge distribution markedly.

One can assume that at a given temperature an equilibrium situation is established whereby a certain number of the traps are charged. If the metal-oxide-metal sandwich is now connected to a battery (Fig. 2), electrons will fill traps at the negative electrode and will leave them at the positive electrode. After the sample is disconnected the charge distribution is no longer in equilibrium. If the two metal electrodes are then

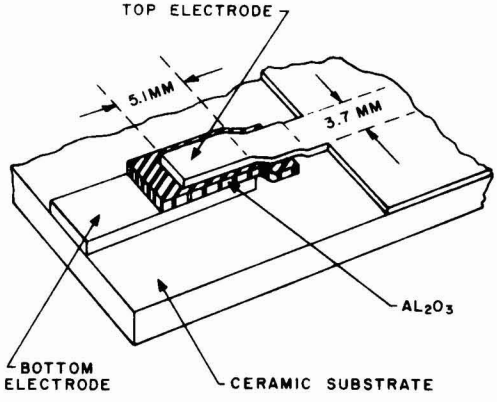

Fig. 1. Sample structure

Key words: Al_2O_3 films, stoichiometry, charge storage.

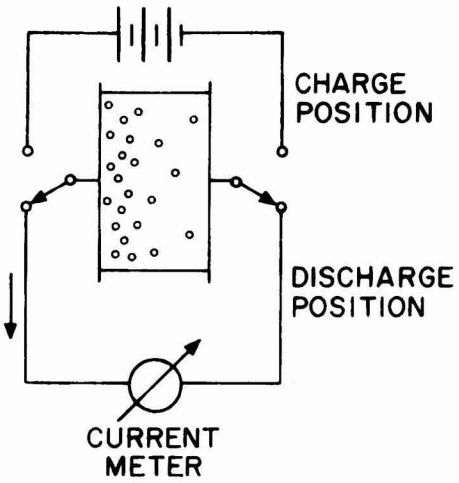

Fig. 2. Principle of charge storage measurement

shorted by an external conducting loop the electrons will flow in such a way as to restore equilibrium. This current was measured to investigate the number and the behavior of the trap states.

It is necessary to note that if the trapped charge was uniformly distributed in the oxide, no current would be measured in the outside loop. For this reason it is not entirely obvious that the measured current is proportional to the charge stored.

The following observation induced us to use this current as a representative quantity for investigating the alumina film. The stored charge increased measurably with the time the capacitor was connected to the voltage source but only during the first 30 min and stayed constant thereafter. Charging times of several hours did not equalize the charge distribution which would have resulted in a reduced or vanishing discharge current. There was also no saturation observed with increasing fields. In several attempts the voltage was increased to produce fields of 6×10^6 V/cm until breakdown occurred without the measured charge leveling off. In films that had low leakage up to high voltages, the increase of charge storage with voltage was close to linear. An example is presented in Fig. 3.

There have been cases (4) reported in which the charge distribution was opposite to the situation described here. But the reproducibility and the consistency with which we found the electron-injecting electrode always next to the volume of higher charge storage lead us to accept the current as a measure of the number of chargeable traps present.

For comparative measurements the voltage applied was 48V, the charging time was chosen to be 1 hr and so was the discharge time over which the current was integrated to determine the charge stored, although the discharge continued for several hours more. The contribution of the capacitive discharge to the recorded charge was not measurable because the RC product of the circuit was always $< 10^{-3}$ sec, too small to appear on the graph.

Four methods are available to influence the oxygen content of the film: (*i*) to evaporate at various oxygen pressures, (*ii*) to use different acceleration voltages on the electron beam, (*iii*) to control the substrate potential, and (*iv*) to heat the film in an oxidizing atmosphere. Table I lists the results of an experiment on three plates each with several capacitors. The film subjected to the most intensive oxidation process showed the least charge storage. Even more conclusive evidence is obtained when the same film is successively subjected to various degrees of oxidation. To this end the charge storage of a device was measured before and

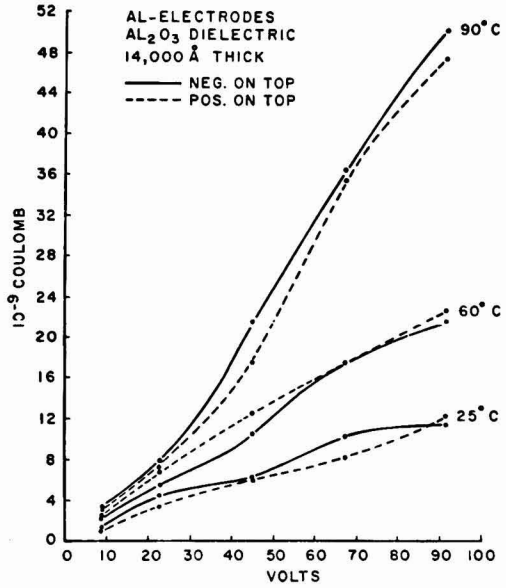

Fig. 3. Charge stored in dependence on voltage and temperature

after heating to 350°C in air for 6 hr. The average charge storage changed from 1440.8 to 165 nC. This change in storage capability supports the argument that the traps are associated with missing oxygen atoms.

To exclude the possibility of the heat-treatment alone reducing the traps, a plate was prepared on which the film was measured after manufacture, then fired at 380°C for 7 hr in dry hydrogen, and finally fired at 380°C for 7 hr in oxygen. The results for two samples are listed in Table II. No appreciable change was observed after the hydrogen firing, but the oxygen firing did reduce the trap density.

The dependence of the charge storage on temperature is shown in Fig. 3, which is typical of the many graphs plotted. When the dielectric is heated it stores considerably more charge than when cold. Conversely, when the film is cooled to liquid nitrogen temperature, charging or discharging of traps stops immediately. Discharge will continue after warm-up at the rate obtained prior to immersing the plate in the coolant. While

Table I. Effect of exposure to oxygen during and after deposition

	Thickness, Å	Charge stored $\times 10^9$ coulombs
Hot substrate High beam power Vacuum 10^{-5} Torr	6890	2393 2335
Hot substrate High beam power O_2 pressure 10^{-4} Torr	5400	1151 889 851
Plate fired at 400°C in oxygen	6860	12 48

Table II. Test slide with aluminum electrodes and alumina dielectric 15,000 Å thick

Treatment after deposition of Al_2O_3	Charge stored $\times 10^9$ coulombs
None	986 776
Fired in dry H_2 380°C, 7 hr	870 793
Fired in O_2 380°C, 7 hr	270 268

the substrate is at liquid nitrogen temperature, no charge can be stored.

In many samples the charge storage was not symmetric with respect to polarity even though both electrodes were of the same material. Almost invariably the larger amount was stored when the negative electrode was on top, that is, near the oxide that had been deposited last. The source material has been subjected to electron bombardment for a longer time and consequently was more oxygen depleted.

Critical comparisons between various metal electrodes have to be made on the same slide. To this end a slide was prepared on which the bottom electrodes were all aluminum and only the top electrodes differed. They were of gold, copper, aluminum, and indium. The results are listed in Table III. Gold achieved the largest storage and aluminum the least. This was also evident from a slide (Table IV) in which the top and bottom electrode were of the same metal. Unfortunately the barrier heights of these metals against Al_2O_3 published by Hurst and Ruppel (5) do not explain the variation in charge storage. More recent measurements of the Al-Al_2O_3-Al work function (6, 7), differ substantially from those of Hurst and Ruppel. For thermally oxidized aluminum Gundlach (6) measured 1.6-1.8 eV; for an aluminum electrode evaporated onto the oxide he measured values larger than 2.3 eV. Antula (8) also reports that the barrier in question depends on the process by which the Al_2O_3 film was made. This adds more complexity to the problem but may provide the key to the differences in conductivity of the various samples.

Under the assumption of the traps being distributed in the bandgap, Lindmayer (8) derived a 1/time dependence of the discharge current. Although we did find a 1/time dependence (Fig. 4) for some of the samples, a $1/t^m$ with $m = 0.35 \ldots 0.44$ was frequently found.

D-C Measurements

As mentioned earlier, the insulating films of the plates D_2 and D_4 were produced with low and high beam voltage, respectively. Correspondingly their charge storage differed widely. D_2 stored 45 nC and D_4 350 nC. These plates were chosen for the I-V measurements. A process considered relevant for the transport of electrons in the Al_2O_3 film is the Poole-Frenkel effect. The electrons tunnel into trap states from which they escape again by field-enhanced thermal excitation to be trapped again further down the field. This process repeats until the opposite metal electrode is reached. Following Mead's analysis (10) log I is plotted *vs.* $v^{1/2}$

Table III. Test slide with aluminum bottom electrode and alumina dielectric 6000 Å

Top electrode	Charge stored Top pos.	$\times 10^9$ coulombs Top neg.	Capacity, pf
Gold	2395 2449	2413 2874	2018
Copper	1705	1585 1899	1983
Indium	—	705	2015
Aluminum	391	341	1987

Table IV. Test slide with 6000 Å alumina film

Electrode material	Charge stored $\times 10^9$ coulombs
Gold-gold	75,630 67,760
Copper-copper	25,220 25,666
Indium-indium	25,160
Aluminum-aluminum	678 679

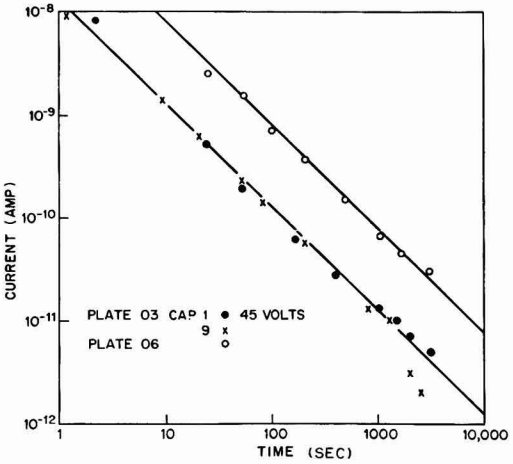

Fig. 4. Discharge current *vs.* time

in Fig. 5. The dashed line represents the slope obtained from the equation for space charge limited current using the static dielectric constant of $\epsilon = 8$. The corresponding current density is

$$J_1 = C_1 E \exp\{(\beta v^{1/2} - q\phi)/kT\} \quad [1]$$

with

$$\beta = \sqrt{q^3/\pi \epsilon \epsilon_0 d} \quad [2]$$

where C_1 is a constant, E the electric field, v the voltage, ϕ the depth of the trap potential well, q the electronic charge, and d the thickness of the film. If the current is controlled by the metal-insulator barrier rather than the bulk of the dielectric, the slope is half of the value in Eq. [2]. This is entered in Fig. 5 as a

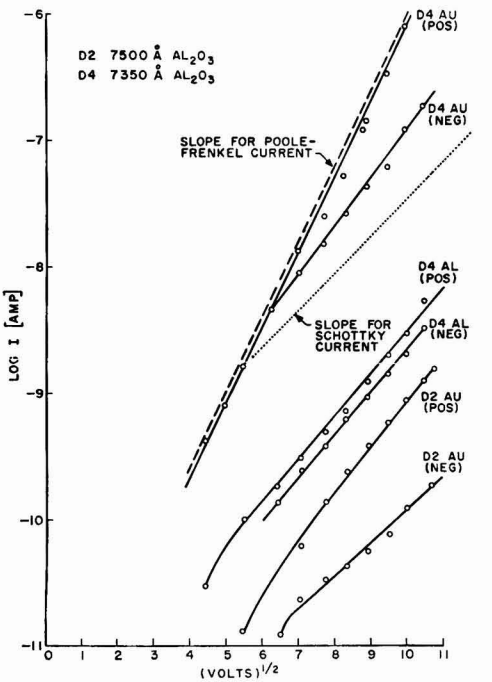

Fig. 5. Current-voltage characteristics

dotted line. For high fields the logarithm of the current followed a straight line. The current depended on the electrode material, the polarity, and it showed differences for oxides obtained under various conditions. Usually a dependence of current on polarity suggests an electrode-controlled transport mechanism. In the case presented here a sensitivity to polarity may be caused by differences in the oxide deposited at the beginning and the end of the evaporation as mentioned previously. The vertical position of the current-voltage curve is governed by the potential barrier ϕ and the density of the trap sites. The latter depends on the oxygen deficiency as derived from charge storage measurements. The slope of the straight section of the plot is controlled only by the dielectric constant and the thickness of the film. The question arises as to which dielectric constant should be used (11). The bulk dielectric constant of highly crystalline Al_2O_3 is as high as 13 from d-c to microwave frequencies and 3.1 at optical frequencies. The dielectric constants of these films were measured to be between 7.3 and 9.8, a difference too small to explain the differing slopes of the I-V characteristic in Fig. 5.

The current transport by means of trap states is temperature dependent as required by Eq. [1]. From charge storage measurements we recall that at some temperature below 0°C the movement in and out of traps was unmeasurable. Therefore, if we measure the dependence of the current on temperature we should find a corresponding behavior. This is indeed borne out by measurements plotted in Fig. 6. Below 260°K the current is independent of temperature as seen with sample D_6 which was typical of those measured over the available temperature range. Above 400°K the current rises steeply. The slopes of the straight portions of the current rise in Fig. 6 can be used to calculate the activation energy of the traps. To this end we write Eq. [1] as follows

$$\ln J = \ln C + \ln E - \frac{1}{T}\left(\frac{\beta v^{1/2}}{k} - \frac{q\phi}{k}\right)$$

where the term in brackets represents the slope of the straight portion of the curve (D4) and the remaining terms the current for $1/T = 0$. Both numbers are obtained from the graph and yield $\phi = 1.08$V and $C = 3.67 \cdot 10^{-4}$ A V^{-1} cm^{-1}.

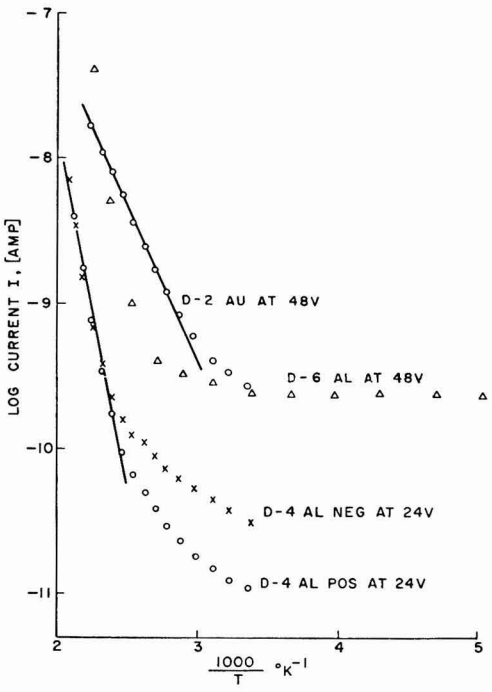

Fig. 6. Dependence of current on temperature

On the other hand we can write Eq. [1] as

$$\ln\left(\frac{J}{E}\right) = \ln C - \frac{q\phi}{kT} + \frac{\beta}{kT} \cdot v^{1/2}$$

and obtain from $\ln(J/E)$ for $V = 0$ again a value for ϕ by using the constant C calculated above. Sample D4 on Fig. 5 follows most closely the characteristics of a Poole-Frenkel mechanism and was chosen for the calculation. The trap depth found from this measurement was $\phi = 1.13$V. The agreement with the ϕ from the thermal analysis is sufficiently good to permit the Poole-Frenkel conduction to be assumed relevant for the current transport in this alumina film.

At low temperatures thermal excitation cannot be part of the electron transport through the film. A process that depends only on the field is more appropriate. Electrons are tunneling from traps into other traps further down the field and eventually into the conduction band. The current is given by (13)

$$I_2 = C_2\, E/E_0 \exp(-E_0/E)$$

where E_0 is a function of the energy level of the trap site and the effective electron mass. At liquid nitrogen temperatures the current depended linearly on the voltage and only above 10^6 V/cm did the current rise faster than ohmic.

Electron Microprobe Analysis

For this examination alumina films 0.30 μm thick were deposited with a beam current of 50 mA and the voltage set at various values between 3 and 7 kV. The material was Al_2O_3 pressed into pellets with a specified purity of 99.9%. The beam energy of the microprobe was 4 keV. The depth of the analyzed region was 0.17 μm, the x-ray emergence angle 41°, and the density of the film 3.15 g/cm^3. The peak-to-background ratios were for

	Typically	Best
Al	630/1	1026/1
O	38/1	80/1
Si	724/1	1682/1

the minimum detectability limits were for

	Typically	Best
Al	150 ppM	115 ppM
O	3000 ppM	1317 ppM
Si	160 ppM	90 ppM

In Fig. 7 the aluminum content in atomic per cent based on 12 analyses per point and the deposition rate is plotted *vs.* the beam power. The dashed line represents stoichiometric proportions allowing for an impurity of 0.14 atomic per cent (a/o) of silicon which was found in the average in all samples. An increase in aluminum content for the high beam power is apparent. This corroborates the conclusion that high beam power during evaporation of Al_2O_3 results in oxygen deficiency of the film; hence, its dark appearance and the large effect which annealing these films in oxygen had on the charge storage.

For the samples obtained with 4 and 5 kV beam voltage the microprobe has indicated less aluminum than would be expected for stoichiometric proportions. We cannot offer a simple explanation, but one could argue in the following manner: the dashed line in Fig. 7 would be at 40 a/o if the Al_2O_3 were absolutely pure. Because of the detected silicon content, the line has dropped to 39.86. If there were other impurities not detected by the microprobe, the line would run even lower and then fall close to the measured points of aluminum. For very low evaporation rates (3 kV beam voltage) the source material turned dark slowly, but

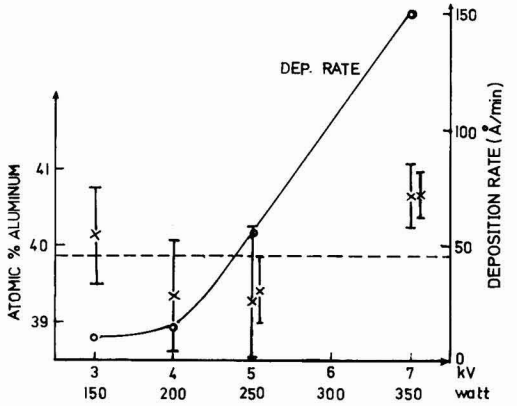

Fig. 7. The composition of the film and deposition rate for varying beam power.

because of the long times involved it became sufficiently oxygen depleted to result in poor films.

Summary

Aluminum oxide films deposited by an electron beam are aluminum rich; the degree of enrichment increasing the higher the beam power. The charge storage in the oxide is very sensitive to the degree of stoichiometry achieved. The charge storage capacity can be used to qualitatively grade the films and to study changes on postdeposition treatments. The d-c conductivity increases with decreasing oxygen content. For low conductivity, the oxide should be evaporated with a moderate beam power unless the method of Hoffman and Leibowitz is used. However, it is evident that even if electrons are prevented from striking and charging up the substrate, oxygen will still be lost through the pumping system and so not be available for complete stoichiometry of the oxide. Postdeposition heating in oxygen or air reduces both the charge storage capability and the conductivity as is expected from the trapping model used to interpret these experiments. There is a dependence on polarity due to the loss of oxygen from the source material during the whole evaporation time. This means that the source material becomes increasingly aluminum rich during the deposition process. These particular properties may become of importance if electron gun evaporated Al_2O_3 finds application in the manufacture of integrated circuits. It would also be a means of obtaining electrets (14).

Acknowledgment

I gratefully wish to express my appreciation for the careful electron microprobe analysis of Mr. D. R. Wonsidler and the constructive criticism of Prof. N. Klein.

Manuscript submitted Jan. 17, 1974; revised manuscript received June 17, 1974.

Any discussion of this paper will appear in a Discussion Section to be published in the December 1975 JOURNAL. All discussions for the December 1975 Discussion Section should be submitted by Aug. 1, 1975.

Publication costs of this article were partially assisted by the Institut fuer Angewandte Festkoerperphysik.

REFERENCES

1. R. A. Abott and T. I. Kamins, *Solid-State Electron.*, **13**, 565 (1970).
2. D. Hoffman and D. Leibowitz, *J. Vacuum Sci. Technol.*, **9**, 326 (1972).
3. D. A. Meyerhofer and S. A. Ochs, *J. Appl. Phys.*, **34**, 2535 (1963).
4. J. M. Calderwood and B. K. P. Scaife, *Proc. Roy. Soc.*, **269**, 217 (1971).
5. H. G. Hurst and W. Ruppel, *Z. Naturforsch.*, **19a**, 573 (1964).
6. K. H. Gundlach, in "Proc. of the International Symposium on Basic Problems of Thin Film Physics," Vandenhoeck and Ruprecht, Goettingen (1964).
7. S. R. Pollack and C. E. Morris, *J. Appl. Phys.*, **35**, 1503 (1964).
8. J. Antula, *Solid-State Electron.*, **9**, 825 (1966).
9. J. Lindmeyer, *J. Appl. Phys.*, **36**, 196 (1956).
10. C. A. Mead, *Phys. Rev.*, **128**, 2088 (1962).
11. S. M. Sze, *J. Appl. Phys.*, **38**, 2951 (1967).
12. M. O. Davies, Report Lewis Research Center, NASA, Feb. 1965.
13. A. G. Chynoweth, in "Progress in Semiconductors," Chap. 4, John Wiley and Sons, Inc., New York (1960).
14. L. W. Davies and R. E. Collins, *Electron. Letters*, **5**, 462 (1969).

Technical Notes

Synthesis of Rare Earth Oxysulfide Phosphors

Douglas W. Ormond*

IBM Thomas J. Watson Research Center, Yorktown Heights, New York 10598

and Ephraim Banks*

Department of Chemistry, Polytechnic Institute of New York, Brooklyn New York 11201

The rare earth oxysulfide phosphors have been of great interest recently due to their widespread applications in color television and in lighting (1, 2). Also these phosphor systems lend themselves easily to theoretical studies regarding luminescent mechanisms (3-5).

Though much information has been published about the synthesis of these compounds, a great deal has been deleted. This report describes the development of a clearly defined and reproducible method of synthesis of rare earth oxysulfides and phosphors derived from

* Electrochemical Society Active Member.
Key words: luminescence, phosphors, yttrium oxysulfide, lutetium oxysulfide, gadolinium oxysulfide, lanthanum oxysulfide.

them. The method involves the reaction of the sesquioxide with carefully controlled N_2:H_2O:H_2S gas mixtures at temperatures near 1200°C.

There are numerous routes that will yield rare earth oxysulfides. Some of them are as follows: (*i*) partial hydrolysis of the sesquisulfide (6); (*ii*) reaction between oxide and hydrogen sulfide (7, 8); (*iii*) direct union of oxide and sesquisulfide (9); (*iv*) reaction of oxide with thioacetamide (10); (*v*) reduction of sulfates with carbon monoxide or hydrogen (11, 12); (*vi*) reduction of sulfates with an inert atmosphere which contained a small amount of hydrogen and hydrogen sulfide (8); and (*vii*) solid-state reaction utilizing a flux (13).

At the time of this investigation we were required to choose the proper synthesis route that would insure phosphors of the highest chemical purity, the reason being the ultrahigh resolution spectroscopy that was being performed on the final product by Sovers and Yoshioka (14, 15). With ultrahigh purity of the final product as the guiding factor, it was felt that the direct reaction between the rare earth (RE) oxides and hydrogen sulfide gas would be the best approach.

Eastman and Brewer (16, 17) have published many papers regarding RE oxysulfide preparation using dry H_2S firings. Hayes and Brown (8) used a similar approach. We started our investigation trying to reproduce these early works. One problem cropped up again and again. The problem was that the RE oxide would either be underfired (excess oxide left) or overfired (higher sulfide, discoloration present). Temperature, concentration of H_2S, moisture present, starting materials, and firing time were all too critical under the conditions stated in the literature; but by varying the concentration of H_2S and also the amount of H_2O present, we were able to control the reaction significantly. The water vapor kept the reaction from going too far and forming higher sulfides. In addition, the concentration of H_2S needed to be controlled. This was accomplished by mixing the H_2S with an inert gas, namely nitrogen.

Experimental Procedure

In order to insure dispersion of the activator in a homogeneous manner, the 99.999% pure rare earth oxides were dissolved in a minimum amount of nitric acid and then precipitated as the oxalates by slowly adding a 100% excess oxalic acid solution to the nitrate solution. The dried oxalates were then ignited to the oxides by firing in air at approximately 1000°C for 2 hr. Tb- and Pr-containing oxides can be refired in dry H_2 to insure that the activator is in the +3 state.

A large variation of firing conditions was tried. Experimentation with a "dry" N_2:H_2S type of arrangement quickly proved that the synthesis parameters involved, such as N_2:H_2S ratio, firing temperature, firing time, and amount of charge in the firing vessel, were too critical. This procedure was usually too long and drawn out. It involved a series of firings to achieve the desired end product, Ln_2O_2S. Samples would usually be underfired (excess Ln_2O_3) or overfired (discoloration indicating higher sulfides).

In the former case, the remedy involved repeated "dry" N_2:H_2S firings, while in the latter case, a wet N_2 firing yielding Ln_2O_3, was prerequisite to subsequent "dry" N_2:H_2S firings. Though the rare earths are often supposed to behave chemically in the same manner, La_2O_3 was exceptionally sensitive to overreacting to form some sort of higher sulfide. Y_2O_3, Gd_2O_3, and Lu_2O_3 were not found to be as sensitive in this regard.

To be able to control the oxysulfide synthesis more precisely several "wet" H_2S firings were tried. Water was introduced into the system by bubbling H_2S through a heated flask of water. The temperature of the water was held constant by means of a hot plate. Through temperature control, one is able to regulate the amount of water vapor being mixed with the H_2S, utilizing the temperature dependence of the vapor pressure of water. Indeed, water was found to be effective in controlling the process.

Through a series of trial and error type experiments, close to optimum synthesis parameters were established for the general series of Ln_2O_2S phosphor systems, namely for La_2O_2S, Y_2O_2S, Gd_2O_2S, and Lu_2O_2S phosphors. During this final process, more water was added to the system, to extend the firing time of the reactions, thus allowing for better recrystallization to take place as indicated in Fig. 1. Also an even lower H_2S concentration was used since one experiment showed an increasing trend in brightness with lower H_2S concentration. The optimum conditions finally established for the general synthesis of Ln_2O_2S type phosphors are the following: nitrogen flow, 147.0 cm^3/min; H_2S flow, 35.0 cm^3/min; water temperature, 95° ± 2°C; firing temperature, 1150° ± 10°C; firing time, 1.5 hr; firing charge, approximately 2g; firing vessel, small 2 × ⅜ in. quartz boat.

Results and Discussion

The criteria used to arrive at the most suitable synthesis conditions were twofold: one being the x-ray diffraction data and the other being the phosphor's luminescent properties.

X-ray powder diffraction patterns were taken of each sample (18). These patterns were obtained utilizing Cu Kα radiation and scanning down at a rate of 1°/min from 60 to 20°. It must be noted that one may be easily misled in judging a sample's composition by x-ray diffraction alone. X-ray diffraction, as an analytical tool, is only good above about 5%, this figure becoming even larger in some cases, depending on the atomic scattering ability and crystallinity of the material (19, 20). It is, therefore, a common experience to obtain a powder pattern of a material which appears to be a single phase yet does in fact contain a second phase. Therefore, a second criterion was used to assess the variation in synthesis parameters, namely, the luminescent properties.

Both relative brightness of the photoluminescence and spectroscopic data were taken to evaluate the phosphors. Spectroscopic data showed that when the synthesis parameters were close to ideal the photoluminescence was completely due to Ln_2O_2S:RE with no trace of Ln_2O_3:RE fluorescence. The relative brightness of the photoluminescence was also recorded in order to peak the synthesis parameters toward producing an efficient phosphor. A Photovolt photomultiplier detection system was used to record the intensity of the total light output. Excitation was produced by a low

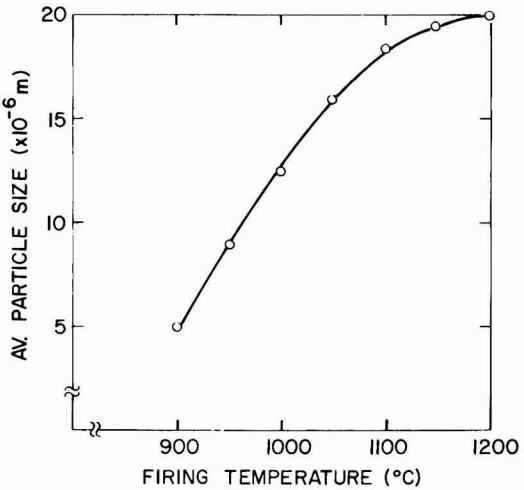

Fig. 1. Particle size vs. firing temperature

Table I. Processing parameters for $Y_2O_2S:Eu^{+3}$ (5 mole per cent)

A. Temperature series: dry H_2S, 1 hr firing time

Temperature (°C)	Body color	Relative brightness	X-ray analysis	Per cent weight gain	Per cent sulfur	Emission spectrum
1200	dark red	50.0		7.61	14.2	
1100	gradual change	43.7		6.71	12.5	
1000		37.5	100% Y_2O_2S	6.43	12.0	100% Y_2O_2S
900		31.2		5.60	10.5	
800		23.6		4.78	8.9	
700		—	~70% Y_2O_2S ~30% Y_2O_3	4.30	4.5	~70% Y_2O_2S ~30% Y_2O_3
600	light red	—	~90% Y_2O_3 ~10% Y_2O_2S	0.5	0.9	~90% Y_2O_3 ~10% Y_2O_2S

B. Gas composition variations: with 50°C H_2O temperature, ½ hr firing time at 1150°C

$H_2S:N_2$ ratio	Body color	Relative brightness	X-ray analysis	Per cent weight gain	Per cent sulfur	Emission spectrum
1:9	White	85.2		6.38	11.9	
1:4	White	85.0	100% Y_2O_2S	7.33	13.7	100% Y_2O_2S
3:7	Tan	81.2		6.77	12.6	

C. Gas composition variations: with 95°C H_2O temperature, 1½ hr firing time at 1150°C

$H_2S:N_2$ ratio	Body color	Relative brightness	X-ray analysis	Per cent weight gain	Per cent sulfur	Emission spectrum
1:9	White	93.7		6.71	12.5	
1:4	White	100.0	100% Y_2O_2S	7.10	13.3	100% Y_2O_2S
3:7	White	95.0		7.30	13.6	

pressure mercury vapor germicidal lamp. An ultraviolet filter, Corning No. 7-54, was used to allow only u.v. to pass through to the sample. A Wratten neutral density filter No. 0.5, was used to cut down on the light intensity to the detector.

The weight increases in going from oxide to oxysulfide were recorded for each sample to study possible correlations between relative brightness and nonstoichiometric oxysulfide. In addition, gravimetric analyses for sulfur and rare earth content were performed with the oxygen content taken as the difference between 100% and the sum of the rare earth and sulfur present. Table I shows representative data used to optimize processing parameters. Theoretically, in converting Y_2O_3 to Y_2O_2S, a net weight gain of 7.11% is expected. Overreaction produces a higher weight gain due to the formation of a higher sulfide, Y_2S_3, as indicated by gravimetric analysis. Underreaction yields a mixture of Y_2O_3 and Y_2O_2S thus producing a lower net weight gain with reduced sulfur content. It can be seen from Table I that the optimal brighness results from a phosphor which is close to stoichiometric in composition.

Phosphors prepared by the aforementioned method had the following properties. The x-ray powder diffraction patterns obtained essentially agree with those found by Haynes and Brown (8). Low resolution spectroscopy showed that the photoluminescence was 100% that of Ln_2O_2S:RE. No trace of Ln_2O_3:RE fluorescence was observed, although higher resolution spectroscopy, perhaps, would detect this type of photoluminescence in trace amounts. Also, no significant shifts in emission lines were detected in the Ln_2O_2S:RE samples. Firing conditions seemed to affect only the relative intensity of the patterns and in no way affected the wavelength. The intensity of the emission spectra followed the same trend as that of the over-all relative brightness measurements in that all peaks seem to increase or decrease in the same relative proportion to each other.

Summary

Through a series of trial and error type experiments, close to optimum synthesis parameters were established for the general series of Ln_2O_2S phosphor system, namely for La_2O_2S, Y_2O_2S, Gd_2O_2S, and Lu_2O_2S phosphors. Starting at first with a dry H_2S ambient, then switching to a moist H_2S ambient, and then finally succeeding with a moist H_2S-nitrogen ambient, a successive chain of events led to the development of a clearly defined and reproducible method of synthesis of rare earth oxysulfides and the phosphors derived from them. The criteria used to arrive at the most suitable synthesis conditions were twofold: one being the x-ray diffraction data and the other being the phosphor's luminescent properties. A gas-solid reaction was chosen to be the one most free of interfering foreign ions since careful theoretical work on the emission spectra was to be performed on the synthesized phosphors. The final method of synthesis involves the reaction of the rare earth sesquioxide with a carefully controlled $N_2:H_2O:H_2S$ gas mixture at a firing temperature of 1150°C using approximately 2g of material placed in a small quartz boat.

Manuscript submitted April 1, 1974; revised manuscript received Aug. 9, 1974.

Any discussion of this paper will appear in a Discussion Section to be published in the December 1975 JOURNAL. All discussions for the December 1975 Discussion Section should be submitted by Aug. 1, 1975.

REFERENCES

1. M. R. Royce, U.S. Pat. 3,418,246 (1968).
2. P. N. Yocom, U.S. Pat. 3,418,247 (1968).
3. F. C. Palilla, Paper 68 presented at Electrochemical Society Meeting, Dallas, Texas, May 7-12, 1967.
4. M. R. Royce and A. L. Smith, Abstract 34, p. 94, Electrochemical Society Extended Abstracts, Spring Meeting, Boston, Mass. 5-9, 1968.
5. R. E. Shrader and P. N. Yocom, *ibid.*, Abstract 35, p. 97.
6. J. Flahaut and E. Attal, *Compt. Rend.*, **238,** 682 (1954).
7. M. Picon and M. Patrie, *ibid.*, **242,** 516 (1956).
8. J. W. Haynes and J. J. Brown, Jr., *This Journal*, **115,** 1060 (1968).
9. L. Domange, J. Flahaut, and M. Guittard, *Compt. Rend.*, **249,** 697 (1959).
10. H. A. Eick, *J. Am. Chem. Soc.*, **80,** 43 (1958).
11. V. P. Surgutshii and V. V. Serebrennikov, *Russ. J. Inorg. Chem.*, **9,** 435 (1964).
12. J. J. Pitha, A. L. Smith, and R. Ward, *J. Am. Chem. Soc.*, **69,** 1870 (1947).
13. M. R. Royce, A. L. Smith, S. M. Thomsen, and P. N. Yocom, Paper 86 presented at Electrochemical Society Meeting, New York, N.Y., May 4-9, 1969.
14. O. J. Sovers and T. Yoshioka, *J. Chem. Phys.*, **49,** 4945 (1968).
15. O. J. Sovers and T. Yoshioka, *ibid.*, **51,** 5330 (1969).
16. E. D. Eastman, L. Brewer, L. A. Bromley, P. W. Gilles, and N. L. Lofgren, *J. Am. Chem. Soc.*, **72,** 2248 (1950).
17. E. D. Eastman, L. Brewer, L. A. Bromley, P. W. Gilles, and N. L. Lofgren, *ibid.*, **73,** 3896 (1951).
18. W. H. Zachariasen, *Acta Cryst.*, **2,** 60 (1949).
19. E. W. Nuffield, "X-Ray Diffraction Methods," John Wiley and Sons, Inc., New York (1966).
20. B. D. Cullity, "Elements of X-ray Diffraction," Addison-Wesley, Inc., Reading, Mass. (1959).

Deposition Rate and Phosphorus Concentration of Phosphosilicate Glass Films in Relation to $O_2/SiH_4 + PH_3$ Mole Fraction

Miyoko Shibata and Katsuro Sugawara*

Hitachi, Limited, Semiconductor and Integrated Circuits Division, Kodaira, Tokyo, Japan

Phosphosilicate glass (PSG) films have been widely used in the passivation (1, 2), solid-to-solid diffusion (3, 4), insulation for multilevel interconnections (1), and protection of aluminum electrodes (1) in the field of semiconductor devices. In spite of these applications, few reports (5-10) have been published which systematically investigate the deposition rate and phosphorus concentration by changing the deposition parameters over a wide range. In this note, the dependence of O_2 to SiH_4+PH_3 mole fraction on the deposition rate and phosphorus concentration during PSG film formation is reported.

A planetary-type CVD reactor (11) was used in this experiment. The bell jar was approximately 40 cm in diameter and 20 cm high. Clean silicon mirror-polished wafers, Czochralski-grown, boron-doped and (100)-oriented with resistivity of 30 ohm-cm, were placed on planetary rotation gears, then the bell jar was fixed and heating was effected. After reaching set temperatures of 300°, 350°, 400°, and 450°C, reaction was carried out by introducing SiH_4 (56 cm^3/min), PH_3 (4 cm^3/min), and O_2 (90-2000 cm^3/min). The carrier gas was N_2, and the total flow rate of 20 liters/min was maintained constant during deposition. The reaction time was set to obtain a PSG film of 3000-4000Å thickness. Thickness was measured by a "Talystep." The phosphorus concentration was determined by the sheet resistance after a predetermined diffusion in accordance with a calibration curve of sheet resistance and phosphorus concentration previously prepared by activation analysis. To determine the reacted SiH_4 concentration through the reactor system, the unreacted SiH_4 concentration of the vent gas was measured under the experimental conditions. A Hitachi EPI-S2 infrared spectrometer was used for this purpose. Absorption spectra were taken in the ranges of 2200 cm^{-1} and 900 cm^{-1} (8); the peak of 930 cm^{-1} was selected to avoid interference with the CO_2 peak near 2200 cm^{-1}. The transmittance through a 10 cm gas cell at the peak of 930 cm^{-1} shows the reacted SiH_4 concentration.

As shown in Fig. 1, the deposition rate of PSG films exhibited a tendency of increase-maximum-decrease when the O_2 flow rate increased at the constant flow rate of SiH_4 and PH_3. Mole fractions at these maximum ranges are approximately 3 at 300°C, 4-6 at 350°C, 8-12 at 400°C, and 14-22 at 450°C. The higher the temperatures of the deposition were, the larger the mole fractions and the wider the maximum range became. The phosphorus concentration rapidly increased with an increase of the O_2 flow rate, displaying a constant value at the maximum plateau range of the deposition rate, and then gradually increasing at the larger O_2 flow rate. The phosphorus concentration of the silicon wafers on which the PSG films were deposited, was determined after 30 min diffusion at 1100°C in dry nitrogen, using the calibration curve. Dependence of the oxygen mole fraction on the PSG film deposition is similar to that on CVD SiO_2 film formation (5-6, 9-10). At low O_2/SiH_4+PH_3 ratio, increase in the deposition rate was found as the temperature decreased. This fact may be explained by smaller reaction rate in the hot zone; the increased deposition rate at lower temperature was brought as the result of difference between total reaction and reaction in the hot zone. The abovementioned tendency was confirmed by the result of film thickness monitoring by a laser system (12).

Dependence of the oxygen mole fraction was also investigated in the case of various PH_3 flow rates. The oxygen flow rates were selected from 180 to 2000 cm^3/

* Electrochemical Society Active Member.

Key words: PSG film, SiH_4-PH_3-O_2 reaction, infrared gas measurement, retarding reaction.

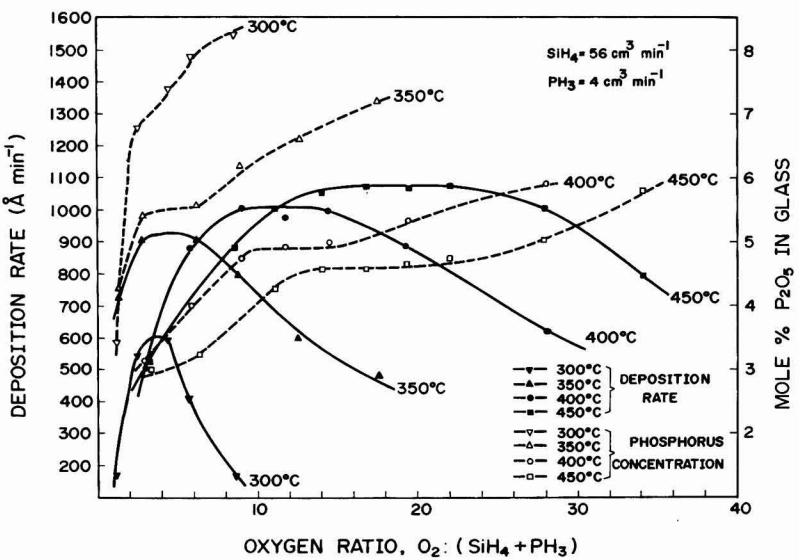

Fig. 1. O_2:(SiH_4 + PH_3) mole fraction vs. deposition rate and phosphorus concentration of PSG films.

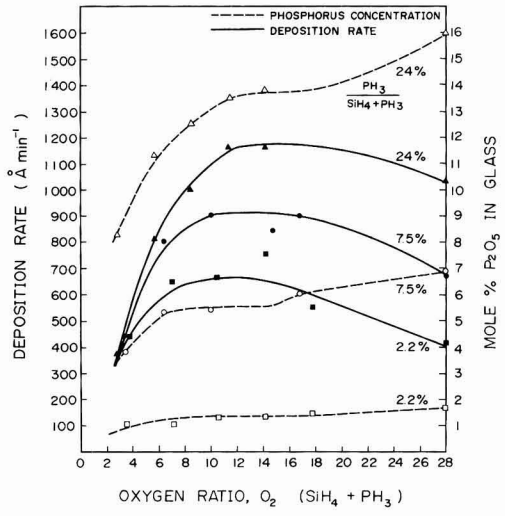

Fig. 2. Dependence of O_2:(SiH_4 + PH_3) mole fraction on the deposition rate and phosphorus concentration of PSG films in various PH_3 flow rates. Deposition temperature: 400°C.

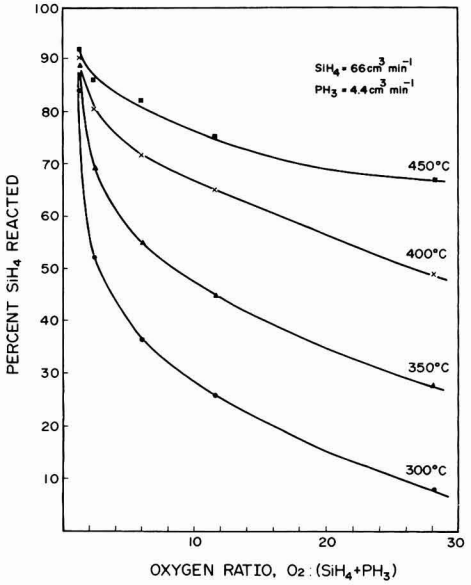

Fig. 3. O_2:(SiH_4 + PH_3) mole fraction vs. per cent SiH_4 reaction in the over-all reactor, measured by infrared absorption.

min at 1.8, 6.5, and 18.3 mole per cent (m/o) PH_3. Deposition was carried out at 400°C. Figure 2 shows that both deposition rate and phosphorus concentration became plateau at approximately constant value, 8-12 of O_2/SiH_4+PH_3.

The reacted per cent SiH_4 measured by the infrared absorption were plotted at various oxygen flow rates and deposition temperatures in Fig. 3. SiH_4-O_2 reaction was retarded as the oxygen flow rates increased. This retardation was remarkably noticeable when the film was deposited at the lower temperature. This result shows the same tendency as that of the undoped SiO_2 film formation (8).

The deposition rate and phosphorus concentration of PSG films formed by the SiH_4-PH_3-O_2 system was investigated in the temperature range of 300°-450°C by reaction with the O_2/SiH_4+PH_3 mole fraction and the deposition temperature. The deposition rate showed a tendency of increase-maximum-decrease with increasing O_2 flow rates. This maximum plateau range became larger and wider with increasing deposition temperature. The phosphorus concentration was kept constant at this range.

Acknowledgment

The authors express their sincere gratitude to Mr. S. Nishida and Mr. H. Mishimagi for the most helpful discussions. Appreciation is also due to Dr. N. Nagasima and Miss H. Suzuki for the activation analysis of phosphorus in PSG films, and to Miss Y. Tsukamoto for assistance in the experimental work.

Manuscript submitted July 30, 1973, revised manuscript received July 8, 1974.

Any discussion of this paper will appear in a Discussion Section to be published in the December 1975 JOURNAL. All discussions for the December 1975 Discussion Section should be submitted by Aug. 1, 1975.

Publication costs of this article were partially assisted by Hitachi, Limited.

REFERENCES

1. M. M. Schlacter, E. S. Schlegel, R. S. Keen, Jr., R. A. Lathlaen, and G. L. Schnable, *IEEE Trans. Electron Devices*, **ED-17,** 1077 (1970).
2. L. H. Kaplan and M. E. Lowe, *This Journal*, **118,** 1649 (1971).
3. A. W. Fisher, J. A. Amick, H. Hyman, and J. H. Scott, Jr., *RCA Rev.*, **29,** 533 (1968).
4. A. W. Fisher and J. A. Amick, *ibid.*, **29,** 549 (1968).
5. N. Goldsmith and W. Kern, *ibid.*, **28,** 153 (1967).
6. M. L. Hammond and G. M. Bowers, *Trans. Met. Soc. AIME*, **242,** 546 (1968).
7. W. Kern and R. C. Heim, *This Journal*, **117,** 562 (1970).
8. K. Strater, *RCA Rev.*, **29,** 618 (1968).
9. M. L. Barry, in "Chemical Vapor Deposition," John M. Blocher, Jr. and James C. Withers, Editors, p. 595, The Electrochemical Society Softbound Symposium Series, New York (1970).
10. B. J. Baliga and S. K. Ghandhi, *J. Appl. Phys.*, **44,** 990 (1973).
11. W. Kern, *RCA Rev.*, **29,** 525 (1968).
12. K. Sugawara, T. Yoshimi, H. Okuyama, and T. Shirasu, in "Chemical Vapor Deposition," Gene F. Wakefield and John M. Blocher, Jr., Editors, p. 205, The Electrochemical Society Softbound Symposium Series, Princeton, New Jersey (1973).

Deposition Rate and Phosphorus Concentration of Phosphosilicate Glass Films in Relation to $PH_3/SiH_4 + PH_3$ Mole Fraction

Miyoko Shibata, Takeo Yoshimi, and Katsuro Sugawara*

Hitachi, Limited, Semiconductor and Integrated Circuits Division, Kodaira, Tokyo, Japan

Phosphosilicate glass films (PSG films) have been widely used for the fabrication of semiconductor devices, such as stabilization of electric characteristics, insulation of multilayer interconnection, and protection of aluminum electrodes. In spite of these wide uses, few papers have reported the detailed relation of wide range deposition parameters to the deposition rate and the phosphorus concentration (1-5). The authors reported that the deposition rate and the phosphorus concentration of the PSG films showed little variation when the films were formed under the proper mole fraction O_2/SiH_4+PH_3, being dependent on the deposition temperature (5). In this range of O_2/SiH_4+PH_3, the dependence of PH_3 flow rate on the deposition rate and the phosphorus concentration is reported.

The same CVD reactor used in the previous paper (5) was of planetary type (6). In this reactor, silicon mirror-polished wafers [(100) oriented and boron doped with resistivity of 30 ohm-cm] were charged, and the PSG films 3000-4000Å in thickness were deposited on the wafers by SiH_4-PH_3-O_2 reaction at the temperatures of 350°, 400°, and 450°C. Flow rates were: N_2, 20 liters/min; SiH_4, 56 cm^3/min; O_2, plateau range of the small, variable deposition rate and phosphorus concentration and being fixed at the temperatures, *e.g.*, at 350°C, $O_2/SiH_4+PH_3 = 5$, at 400°C, $O_2/SiH_4+PH_3 = 12$, at 450°C, $O_2/SiH_4+PH_3 = 18$; PH_3, 0.7-14 cm^3/min. The thickness of the PSG films was measured by a "Talystep." The phosphorus concentration was determined by the sheet resistance in the previously prepared calibration curve between the phosphorus concentration by the activation analysis and the sheet resistance after the diffusion. To measure total amount of the reacted SiH_4 concentration with O_2 in the reactor, infrared gas absorption through a 10 cm gas cell was carried out, as reported in the previous paper (5). The reacted mole percentage of SiH_4 was detected by the transmittance of the cell, fixed at the absorption peak, 930 cm^{-1} of SiH_4, using Hitachi EPI-S2.

Figure 1 shows the deposition rates of the PSG films under various PH_3 flow rates at the O_2/SiH_4+PH_3 in the plateau range of the deposition rate. With increasing PH_3 flow rate, the deposition rate at 350°C shows a tendency of decrease-minimum-increase. After raising the deposition temperature in this experimental condition, the deposition rate became larger and showed the same tendency observed at 350°C. This was confirmed by the monitoring experiment using a 6328Å He-Ne laser system (7).

Figure 2 is the relation of PH_3/SiH_4+PH_3 mole fraction to the phosphorus concentration in the PSG films, represented as $P_2O_5/SiO_2+P_2O_5$ at the same experimental condition. With the increasing of the deposition temperature, P_2O_5 concentration in the PSG films decreased at the same PH_3/SiH_4+PH_3 flow ratio. The similar result of decreasing dopant materials in films was obtained in the cases of P, As, and Sb doping for silicon epitaxial layers (8-9) and in AsH_3 and PH_3 doping for polycrystalline silicon films (10). In this temperature range PH_3 was almost completely reacted, while SiH_4 tended to increase the reaction rate with O_2 at the higher temperature as can be seen in Fig. 1 and in the infrared absorption in the previous paper (5). Therefore, the phosphorus concentration was diluted as a consequence of the increased SiH_4 reaction.

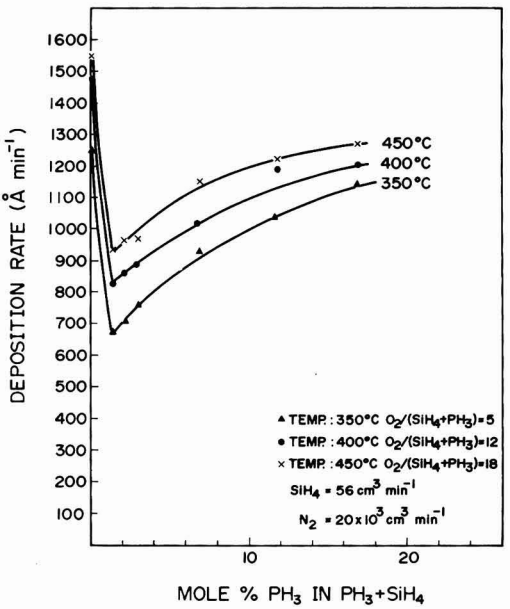

Fig. 1. Deposition rates of the PSG films vs. m/o PH_3 in $SiH_4 + PH_3$ in the plateau range of the deposition rate determined in terms of $O_2/SiH_4 + PH_3$ mole fraction.

When the reaction was effected under various PH_3 flow rates at the deposition temperature of 400°C, the result of the reacted percentage SiH_4 measured by the infrared absorption method is shown in Fig. 3, in which the O_2 flow rate is indicated as a parameter. The reacted SiH_4 concentration became suppressed independently of O_2 flow rates when PH_3 was added up to 2-3 mole per cent (m/o). With further increasing of PH_3 flow rates, the reacted SiH_4 increased. This tendency was dominant at larger O_2 flow rates.

When the PSG films were formed by the SiH_1-PH_3-O_2 reaction, it was previously reported that there existed O_2/SiH_4+PH_3 mole fraction, with little variation in the deposition rate and in the phosphorus concentration, and fixed at the deposition temperature. At this plateau range, the deposition rate showed the tendency of decrease-minimum-increase with increasing PH_3 flow rates. This tendency of the deposition rate was maintained in all reaction temperatures of this experiment.

Acknowledgment

The authors express their sincere gratitude to Mr. S. Nishida for his encouragement and helpful discussions, and to Miss Y. Tsukamoto for her assistance in the experimental work.

* Electrochemical Society Active Member.

Key words: SiH_4-PH_3-O_2 reaction, influence of PH_3 doping, infrared gas measurement, inhibiting reaction.

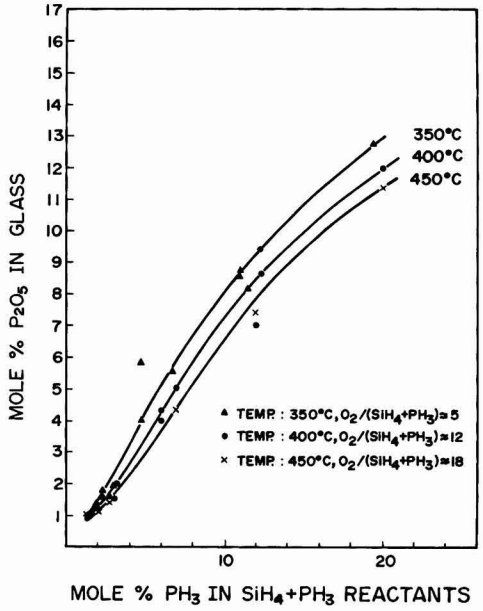

Fig. 2. M/o P_2O_5 in the PSG films vs. mole fraction PH_3 in SiH_4 + PH_3 reactants.

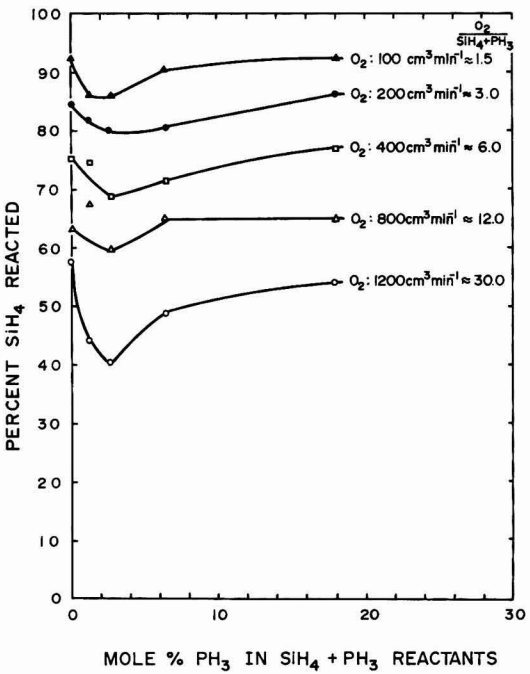

Fig. 3. Relation of m/o PH_3 to the total reacted SiH_4 concentration measured by the variation of transmittance through the infrared 10 cm gas cell.

Manuscript submitted Oct. 19, 1973; revised manuscript received July 8, 1974.

Any discussion of this paper will appear in a Discussion Section to be published in the December 1975 JOURNAL. All discussions for the December 1975 Discussion Section should be submitted by Aug. 1, 1975.

Publication costs of this article were partially assisted by Hitachi, Limited.

REFERENCES

1. N. Goldsmith and W. Kern, *RCA Rev.*, **28**, 153 (1967).
2. M. L. Hammond and G. M. Bowers, *Trans. Met. Soc. AIME*, **242**, 546 (1968).
3. M. L. Barry, in "Chemical Vapor Deposition, Second International Conference," J. M. Blocher, Jr. and J. C. Withers, Editors, p. 595, Electrochemical Society Softbound Symposium Series, New York (1970).
4. B. J. Baliga and S. K. Ghandhi, *J. Appl. Phys.*, **44**, 990 (1973).
5. M. Shibata and K. Sugawara, *This Journal*, **122**, 155 (1975).
6. W. Kern, *RCA Rev.*, **29**, 525 (1968).
7. K. Sugawara, T. Yoshimi, H. Okuyama, and T. Shirasu, in "Chemical Vapor Deposition, Fourth International Conference," G. F. Wakefield and J. M. Blocher, Jr., Editors, p. 205, Electrochemical Society Softbound Symposium Series, Princeton, New Jersey (1973).
8. W. H. Shepherd, *This Journal*, **115**, 541 (1968).
9. T. B. Swanson and R. N. Tucker, *ibid.*, **116**, 1251 (1969).
10. F. C. Eversteyn and B. H. Put, *ibid.*, **120**, 106 (1973).

JOURNAL OF THE ELECTROCHEMICAL SOCIETY

REVIEWS AND NEWS

JANUARY
1975

Division Activities during the New York Meeting of the Society

Battery Division. The head table at the Battery Division Luncheon and Business Meeting. Front (l-r): Per Bro, Joseph L. Weininger, Gerald Halpert, John P. Wondowski, James McBreen, Ralph J. Brodd. Back (l-r): Paul C. Milner, Karl Kordesch, Howard R. Karas, Eugene Y. Weissman, Samuel Ruben.

Corrosion Division. The following were at the head table during the Corrosion Division Luncheon and Business Meeting. Front (l-r): Paul P. Pemsler, Michael Clarke, Roger W. Staehle, Craig S. Tedmon, Jr. Back (l-r): Ken Nobe, Jerome Kruger, John Stringer, Mark Perakh.

Electrodeposition Division. Seated at the Electrodeposition Division Luncheon and Business Meeting head table were: (front, l-r): John L. Griffin, Michael Clarke, Richard Sard, Vladimir Hospadaruk; (back, l-r): Nathan Feldstein, Rolf Weil, David A. Vermilyea, Mark Perakh, and Fielding Ogburn.

Battery Division. Samuel Ruben (right) receives congratulations from Division Chairman Ralph J. Brodd (left) who is presenting him with a Certificate of Appreciation for his contributions to the battery field.

Battery Division Research Award—1974

The Battery Division has selected Dr. James McBreen to receive its Research Award for 1974. The selection was based on the article "Zinc Electrode Shape Change in Secondary Cells," published in the December 1972 issue of the Journal, pp. 1620-1628. The Award, which consisted of a scroll and Life Membership in the Society, was made at the Battery Division Luncheon and Business Meeting, October 14, 1974, at the New York Meeting of the Society.

The paper by Dr. McBreen reports on the results of an extensive study of the patterns of potential and current distribution on a cycling zinc electrode. The differences in current distribution are interpreted as arising from variations in electrode polarizability which were induced by changes in the secondary current distribution. The initiation and progress of shape change were explained on the basis of concentration cells which corrode zinc off the plate edges and deposit metal at the plate center.

James McBreen (left) receives the Battery Division Research Award from Ralph J. Brodd, Chairman, Battery Division.

Dr. McBreen is a native of Ireland and a graduate of University College, Dublin (B.S., 1961). He received his Ph.D. in physical chemistry from the University of Pennsylvania in 1965. From February 1965 through October 1968, Dr. McBreen carried out research on ambient temperature (zinc-silver, cadmium-silver, and zinc-air) battery systems for Yardney Electric Corporation. Since November 1968 he has worked on advanced battery systems for the Electrochemistry Department, Research Laboratories, General Motors Corporation, as a senior research chemist. Dr. McBreen is currently involved in research related to ambient temperature batteries, including the zinc, nickel oxide, and manganese dioxide electrodes, and is serving as group leader for this work.

Call for Recent News Papers, Toronto, Canada, Meeting, May 11-16, 1975

Triplicate copies of a 75-word abstract of Recent News Papers must be received by the Symposium Chairman (as indicated below) not later than April 1, 1975, to be considered for inclusion in the Recent News Papers Session.

ELECTRONICS DIVISION

Semiconductor General Session

Recent News Papers for the Semiconductor General Session are invited. Papers should be brief (15 minutes, including 3 minutes for questions) and timely, and should present information on:

1. The preparation and characterization of bulk or thin-film semiconductors and insulators including methods and mechanism of growth, surface and bulk properties, methods of evaluation, and new applications.
2. Semiconductor device fabrication methods and characterization including epitaxy, diffusion, ion implantation, passivation, metallization, photolithography, cleaning, etching, material evaluation, process control, and specific device fabrication such as solar cells, LED, IC, etc.
3. The evaluation and characterization of impurity and structural defects in semiconductor devices including analysis techniques, origin of defects, device fabrication induced defects and their minimization, the effect of defects on device characteristics, yield, and reliability.

The abstracts should be sent for receipt before April 1, 1975 to the Recent News Papers Session Chairman: Conrad Dell'Oca, Hewlett-Packard Laboratories, 1501 Page Mill Rd., Palo Alto, Calif. 94304.

Large-Scale Integration (LSI) Process Technology

Recent News Papers for the Large-Scale Integration (LSI) Process Technology Symposium are invited. Papers should present brief (15 minutes), timely, and broadly based information on:

1. Process modeling; process control, interrelation design/process/device performance; reliability improvement.
2. Diagnostic techniques; in-process measurements; analysis and evaluation.
3. Equipment and facilities for controlled LSI processing.
4. Material preparation and characteristics; influence on device performance.
5. Imaging and photolithography.
6. Doping techniques; diffusion; ion implantation, process-generated defects.
7. Insulator formation and properties; instability mechanisms.
8. Metallization; conductor technology.
9. Mounting and bonding; encapsulation.

Triplicate copies of 75-word abstracts should be sent to the Recent News Papers Session Chairman: Walter H. Schroen, Texas Instruments Inc., M.S. 72, P.O. Box 5012, Dallas, Texas 75222, for receipt on or before April 1, 1975.

Luminescence

Recent News Papers are being solicited for presentation at the Spring Meeting in Toronto. Papers should present brief (15 minutes), timely information on new materials, their applications, or better understanding of some aspects of luminescence.

A 75-word abstract, in triplicate, is due April 1, 1975, or sooner, for scheduling. Abstracts are to be sent to Recent News Papers Session Chairman: Charles W. Struck, RCA Laboratories, David Sarnoff Research Center, Princeton, N.J. 08540.

General Materials and Processes for Solar Energy Conversion

Recent News Papers on items of interest for solar energy conversion are invited. Papers should be brief (10-12 minutes) and based generally on materials and process aspects for solar energy conversion, including properties such as lifetime, diffusion length, mobility, charge generation, etc., and processes such as vapor growth, diffusion, evaporation, ribbon growth, etc. New materials, new devices, and new techniques for producing materials and devices for solar energy conversion are invited.

The abstracts should be sent to the Recent News Papers Session Chairman: Harold J. Hovel, IBM Research Laboratory, P.O. Box 218, Yorktown Heights, N.Y. 10598.

BATTERY AND ELECTRONICS DIVISIONS

Materials Problems in Battery and Fuel Cell Technology

Recent News Papers for inclusion in the symposium on Materials Problems in Battery and Fuel Cell Technology are invited in the following areas:

1. Materials science related to battery technology of materials used in anodes, cathodes, separators, and solid and liquid electrolytes.
2. Materials technology related to complete cell and battery systems. This will include applied materials preparation related to compatibility, aging, degradation, and corrosion studies of cell components.
3. Fuel cell technology related to electrode design. Specifically, this section will be concerned with catalyst selection (both noble and non-noble metal catalysts), matrix preparation, and porous electrode construction. Special interest will be focused on materials selection for high conversion efficiency and cost reduction of electrode fabrication.
4. Selection and design of materials related to over-all fabrication and testing of total fuel cell systems.

Triplicate copies of the 75-word abstracts should be sent to the Recent News Papers Session Chairman: J. Broadhead, Bell Laboratories, 600 Mountain Ave., Murray Hill, N.J. 07974.

ELECTRONICS AND ELECTROTHERMICS AND METALLURGY DIVISIONS

Growth and Processing of Large Crystals

Recent News Papers for the Growth and Processing of Large Crystals Symposium are invited. Papers should present brief (15 minutes) and timely information on any of the following subjects: the application of various techniques, such as the Bridgman, Czochralski, and Verneuil methods; the growth of large crystals of both metals and nonmetallic materials, such as silicon and garnets; the control of growth conditions; and methods for evaluation of the structure and properties of large diameter crystals.

Triplicate copies of 75-word abstracts should be sent to the Recent News Papers Session Co-Chairmen: John Rutter, University of Toronto, Dept. of Metallurgy and Materials Science, Toronto, Ont., Canada M5S 1A4, or Daniel F. O'Kane, IBM Corp., Dept. K15, Bldg. 282, Monterey-Cottle Rds., San Jose, Calif. 95193.

SECTION NEWS

Columbus Section

Report of Recent Activities

The Columbus Section of The Electrochemical Society continues to hold its noontime meetings once a month.

In September, Paul W. Cover, of Battelle's Columbus Laboratories, gave a talk entitled "Batteries and Fuel Cells—Alternatives to Petroleum Fuels." He said that before the year 2000 the motoring public will be saving gasoline and dollars by accumulating off-peak electricity each night in the batteries of their electric vehicles. At least 20% of our gasoline, or 5% of our electrical power capacity, can be replaced by batteries. Technologists will determine whether the batteries will be purchased by individuals, or by leasing agencies, or by the electric utility companies themselves. The present state of the art favors the economical lead-acid batteries in electric vehicles and fuel cells at dispersed locations in the electric utility network. Extended life is the most critical, but least mentioned, factor needed to promote more widespread application of batteries and fuel cells.

In October, John E. Slater, also of Battelle's Columbus Laboratories, talked about "The Removal of Chloride Ion from Reinforced Concrete Bridge Decks." The use of deicing salts can cause corrosion of the reinforcing struts. This corrosion ultimately gives cracks and spalls in the deck concrete, which successively mars the riding performance and structural integrity of the bridge. If the chloride can be removed from the concrete before severe corrosion occurs, and an impermeable membrane placed on the deck surface after removal, the deterioration process can be avoided. An electromigration technique has been developed at Battelle for the removal of chloride ion from contaminated concrete. Current is passed between the reinforcing shell (cathode) and a surface anode. The chloride ion that appears at the surface is then rendered harmless. Dr. Slater discussed the optimization of such parameters as anode materials, applied voltage, and duration of treatment.

Members of the Society interested in attending one or more meetings of the Columbus Section, and wishing to be placed on the advance notice mailing list, should contact Dr. Bryan McKinney, 505 King Avenue, Columbus, Ohio 43201, who is the Publicity Chairman.

Eric W. Brooman
Secretary-Treasurer

Cleveland Section

International Symposium on Manganese Dioxide

The Cleveland Section of The Electrochemical Society will sponsor a Symposium on Manganese Dioxide to be held in Crawford Hall, Case Western Reserve University, Cleveland, Ohio, October 1-2, 1975. The purpose of the symposium is to discuss various physical, chemical, and electrochemical properties of manganese dioxide, particularly those of the international common samples. Topics include those related to industrial interest (electrochemical activity, production processes, analytical procedures, and particle and pore size characterizations) as well as those related to basic properties of academic interest (structure, surface properties, x-ray diffraction, infrared absorption, NMR, etc.).

Manganese dioxide is a unique cathode material for dry batteries and one of the most important raw materials of today's primary cells, such as Leclanché cells and alkaline manganese cells. The Cleveland Section of The Electrochemical Society established the I.C. MnO_2 Sample Office (International Common Sample Office of Manganese Dioxide) in 1971. Since then ten MnO_2 samples have been distributed for research purposes. One of the most important functions of the I.C. Sample Office is to collect various experimental data of the I.C. MnO_2 samples, so that data can be distributed with the samples, thus making the samples more valuable in the future. It is hoped to present papers by workers in the various fields. The MnO_2 Symposium will be held immediately before the Leclanché Cell Symposium which is scheduled during the Dallas, Texas, Meeting of the Society, October 5-10, 1974, in the hope that maximum advantage can be taken from the related meetings.

Deadline for submission of the 75-word abstract is May 1, 1975; deadline for the full paper for inclusion in the symposium volume is July 1, 1975. These, as well as inquiries and suggestions, should be sent to Dr. A. Kozawa, Union Carbide Corporation, Parma Technical Center, P.O. Box 6116, Cleveland, Ohio 44101. The published Proceedings will be available during the Symposium. For the experiments to be presented during the Symposium, MnO_2 samples are available free of charge. For further information about the different samples available contact Dr. A. Kozawa at the above address. It is suggested that those wishing to attend the Symposium should make reservations at the Howard Johnson Motor Lodge, East 107th Street and Euclid Avenue, Cleveland, Ohio 44106. Phone (216) 231-6300.

R. J. Brodd and A. Kozawa
Symposium Co-Chairmen

NEW MEMBERS

It is a pleasure to announce the following new members of The Electrochemical Society as recommended by the Admissions Committee and approved by the Board of Directors in December 1974.

Active Members

Asao, I., New York, N.Y.
Baliga, B. J., Schenectady, N.Y.
Bobbin, L. D., Morristown, N.J.
Brummet, B. D., Bloomfield, N.J.
Campbell, J. F., Hightstown, N.J.
Caruso, J. M., Santa Clara, Ca.
DiGiacomo, G., Poughkeepsie, N.Y.
Dohmen, H. G., Kokomo, In.
Dunlop, A. K., Houston, Tx.
Espig, H. R., St. Paul, Mn.
Feria, G., Milan, Italy
Haberman, J. I., Linden, N.J.
Heerssen, G. O., Houston, Tx.
Karlin, J. J., Spotswood, N.J.
Kinloch, D. R., III, Eastlake, Oh.
Lin, P. T., Poughkeepsie, N.Y.
Lindsay, J. H., Clarkston, Mi.
Maggio, M. J., Boyertown, Pa.
Marcoux, L. S., Tustin, Ca.
Patigalia, E. N., Washington, D.C.
Siebert, O. W., Manchester, Mo.
Taylor, R. A., North Ridgeville, Oh.
Theus, G. J., Canton, Oh.
Thompson, J. F., St. Louis, Mo.
Thornton, C. G., Colts Neck, N.J.
Wagner, E. A., Abington, Pa.
Weitzel, C. E., Princeton, N.J.

Student

Angoran, Y. E., Cambridge, Ma.
Blum, J., Cambridge, Ma.
Gilboa, H., Troy, N.Y.
Siitari, D. W., Urbana, Il.
Yeh, P. P., Columbus, Oh.

Reinstatement

Zahavi, J., Haifa, Israel

Transfer

Dosaj, V. D., Hemlock, Mi.

NEW YORK NOSTALGIA

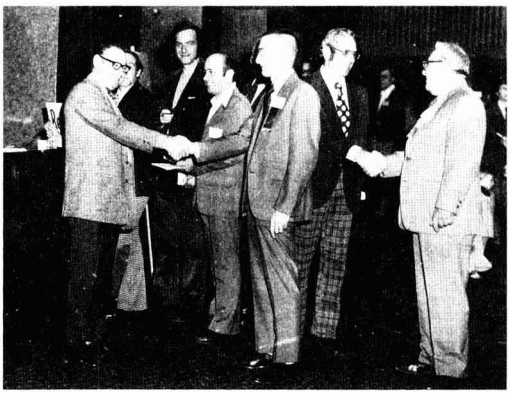

President Vermilyea (center) and Executive Secretary Enck (right) greet Monday morning's early registrants.

A friendly crowd gathered round to chat with ECS Headquarters staffer, Marie Krot, at the Advance Registration desk.

Our members and friends could check for messages at the Information Desk.

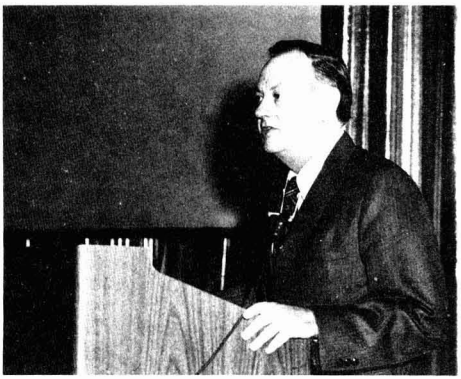

J. Herbert Holloman opened our 146th Meeting in New York at the Plenary Session. We all enjoyed his lecture entitled "Technology and the Changing Society."

ECS President, David A. Vermilyea, presented the Young Authors' Prizes for 1973 at the Awards and Recognition Session to (left to right): Daniel Simonsson, M. J. Bowden, and L. F. Thomson.

FALL MEETING 1974

The ladies enjoyed their coffee and rolls together every morning while Mrs. F. Kober (standing, center), our Ladies' Hostess, helped them plan their day.

ECS Officers, Past Presidents, and awardees were seated at the head table during the Awards and Recognition Session.

Cecil V. King, Past President of the Society and former Editor of This Journal, was awarded the Edward Goodrich Acheson Medal and Prize for 1974 by President Vermilyea. Congratulations!

Henry B. Linford, Past President and former Secretary of the Society and 1960 Acheson Medalist, was awarded Honorary Membership in the Society by President Vermilyea.

Sherlock Swann, Past President of the Society, became an Honorary Member of the Society. Here he is shown receiving his citation from President Vermilyea.

Secretary Milner (2nd right) and friends enjoy the delights of the punch bowl at the Acheson Medal Reception.

Well wishers wait to congratulate Dr. King on the receiving line at the Acheson Medal Reception. (l-r): John M. Blocher, Jr., Theodore D. McKinley, Mrs. T. D. McKinley, Sherlock Swann, Acheson Medalist Cecil V. King, Mrs. C. V. King, and David A. Vermilyea, President.

Harry C. Gatos to Receive The Electrochemical Society Award in Solid State Science and Technology

The Board of Directors is pleased to announce that Harry C. Gatos, Professor of Metallurgy and Materials Science at Massachusetts Institute of Technology, has been selected as the recipient of The Electrochemical Society Award in Solid State Science and Technology. The Award lecture will be given, and the Award presented, on Tuesday, May 13, 1975, during the 147th Meeting of the Society in Toronto, Canada, at the Royal York Hotel.

PEOPLE

Milan M. Jaksić, who is a member of The Electrochemical Society, has received the October Prize of the city of Belgrade, Yugoslavia. This prize was awarded this year in commemoration of Belgrade's 30 years of freedom on October 20. Dr. Jaksić won the award for, in the words of the Commission concerned, his "extraordinary contributions in the development of new technology for industrial electrolytic chlorate production." Dr. Jaksić was primarily judged by his work which was published in This Journal. Former winners of Belgrade's October Prize include A. R. Despić, D. Dražić, and the late P. S. Tutundžić.

BOOK REVIEW

"Electrical Conductivity in Ceramics and Glass," Part A, edited by N. M. Tallan. Published by Marcel Dekker, Inc., New York (1974). 311 pages; $26.50.

This volume is the first part of volume four of a five-volume set of monographs on the "Science and Technology of Ceramics and Glass." This book succeeds ably in its professed objective which is stated ". . . to provide the scientific basis for the technology of conduction of electronic ceramics. . ." . Chapter I, by D. Adler, treats electrical transport phenomena on a conceptual basis. The second chapter is an excellent and timely discussion of "Experimental Techniques" useful in studying electrical conduction in ceramics and glass. This chapter by R. N. Blumenthal and M. A. Seitz comprises half of the monograph and serves well the practitioner and the student as a refresher course or introduction, respectively, of the subject; the chapter closes with 183 references. Chapter III by R. J. Brook deals in a somewhat simplified fashion with the defect structure of ceramic materials. Much of this information is readily available in other places. While the subject matter is appropriate for this monograph, this reviewer feels that a somewhat more extensive treatment of the subject would have been justified. Chapter IV, "Electronic Conduction," by J. M. Wimmer and I. Bransky is again an excellent presentation of both the theory and measurement of electronic conduction in ceramics and glass.

It is regrettable that a book which has so much excellent material lacks an index which would greatly enhance its usefulness. Furthermore, the print, thin type photo-offset, is very hard to read. Both the authors and the readers have a right to expect a better presentation particularly at the high price of this monograph. Nevertheless, this book is a welcome addition to any library where people are concerned with the electrochemistry of insulating materials such as glasses and ceramics.

R. B. Frieser
IBM Corporation
Hopewell Junction, New York

Three $1000 Electrochemical Society Summer Fellowship Awards to be Granted

The Electrochemical Society will offer three fellowship awards for qualified graduate students for the summer of 1975. Each award will have a stipend of $1000 and its purpose is to assist the student to continue his graduate work during the summer months in a field of interest to The Electrochemical Society. These awards are to be known as The Edward Weston Fellowship Award, The Colin Garfield Fink Fellowship Award, and The Joseph W. Richards Fellowship Award.

Candidates' qualifications: "Each award shall be made without regard to sex, citizenship, race, or financial need. They shall be made to graduate students pursuing work between the degrees of B.S. and Ph.D., in a college or university in the United States or Canada, and who will continue their studies after the summer period. A previous holder of an award is eligible for reappointment."

Qualified graduate students are invited to apply for these fellowship awards. Applicants must complete an application form and supply the following information.

1. A brief statement of educational objectives.

2. A brief statement of the thesis research problem including objectives, work already accomplished, and work planned for the summer of 1975.

3. A transcript of undergraduate and graduate academic work.

4. Two letters of recommendation, one of which should be from his research adviser.

5. Successful recipients of fellowships shall agree not to hold other appointments or other fellowships during the summer of 1975.

Application forms are available from the Chairman of the Fellowship Awards Subcommittee, to whom completed applications and letters of recommendation should be sent: Professor G. J. Janz, Cogswell Laboratory, Rensselaer Polytechnic Institute, Troy, New York 12181.

Deadline for receipt of completed applications will be March 1, 1975, and award winners will be announced on May 1, 1975.

OBITUARY

Dr. Neal J. Johnson died on October 14, 1974, at the age of 65. After 40 years of service with the Carbon Products Division of Union Carbide Corporation, Dr. Johnson had retired earlier this year from his most recently held position there as manager of technical service for anode products.

After receiving his B.S., M.S., and Ph.D. degrees in chemistry from the University of Wisconsin, Dr. Johnson joined Union Carbide as a research chemist at its Niagara Falls laboratories in 1934. After various assignments in the development organization, he transferred to the marketing department in New York City in 1957. He moved to the Parma Technical Center in 1965.

A recognized authority in the use of graphite anodes in the electrochemical industry, Dr. Johnson had been active in the affairs of The Electrochemical Society, and in particular in those of its Industrial Electrolytic Division, for a number of years.

He is survived by his wife, his son and daughter, and six grandchildren.

OUT-OF-PRINT SOCIETY SYMPOSIUM VOLUMES

The following symposium volumes published by The Electrochemical Society, Inc. are now out-of-print. Xerographic copies* or reprints† of these volumes are available.

* **Vapor Plating.** C. F. Powell, I. E. Campbell, and B. W. Gonser, Editors. A 1955 symposium. 158 pages, **$8.40.**
* **The Structure of Electrolytic Solutions.** W. J. Hamer, Editor. A 1957 symposium. 441 pages, **$22.70.**
* **Technology of Columbium (Niobium).** B. W. Gonser and E. M. Sherwood, Editors. A 1958 symposium. 120 pages, **$6.50.**
* **Surface Chemistry of Metals and Semiconductors.** H. C. Gatos, J. W. Faust, Jr., and W. J. La Fleur, Editors. A 1959 symposium. 526 pages, **$27.00.**
* **Electrode Processes,** First Conference. E. Yeager, Editor. A 1959 symposium. 374 pages, **$19.50.**
* **Mechanical Properties of Intermetallic Compounds.** J. H. Westbrook, Editor. A 1959 symposium. 435 pages, **$22.50.**
* **Zirconium and Its Alloys.** J. P. Pemsler, E. C. W. Perryman, and W. W. Smeltzer, Editors. A 1965 symposium. 205 pages, **$15.10.**
† **Measurement Techniques for Thin Films.** B. Schwartz and N. Schwartz, Editors. 1965 and 1966 symposia. 347 pages, **$12.00** (softbound), **$15.00** (hardbound).
† **Electrode Processes,** Second Conference. E. Yeager, H. Hoffman, and E. Eisenmann, Editors. A 1966 symposium. 190 pages, **$5.00.**
* **Electrolytic Rectification and Conduction Mechanisms in Anodic Oxide Films.** P. F. Schmidt and D. M. Smyth, Editors. A 1967 symposium. 230 pages, **$11.80.**
* **Electrets and Related Electrostatic Charge Storage Phenomena.** L. M. Baxt and M. M. Perlman, Editors. A 1967 symposium. 150 pages, **$7.80.**
* **Dielectrophoretic and Electrophoretic Deposition.** E. F. Pickard and H. A. Pohl, Editors. A 1967 symposium. 138 pages, **$6.90.**
* **Electron and Ion Beam Science and Technology,** Third International Conference. R. Bakish, Editor. A 1968 symposium. 725 pages, **$35.80.**
* **Optical Properties of Dielectric Films.** N. Axelrod, Editor. A 1968 symposium. 325 pages, **$14.50.**
* **Thin Film Dielectrics.** F. Vratny, Editor. A 1968 symposium. 680 pages, **$34.20.**
* **Ohmic Contacts to Semiconductors.** B. Schwartz, Editor. A 1968 symposium. 356 pages, **$18.40.**
* **Semiconductor Silicon.** R. R. Haberecht and E. L. Kern, Editors. A 1969 symposium. 750 pages, **$38.90.**
* **Chemical Vapor Deposition,** Second International Conference. J. M. Blocher, Jr. and J. C. Withers, Editors. A 1970 symposium. 872 pages, **$43.55.**

* Order from University Microfilms, Inc., 300 North Zeeb Street, Ann Arbor, Mich. 48103. Enclose payment with order. Specify an Electrochemical Society volume.

† Order from Johnson Reprint Co., 355 Chestnut St., Norwood, N.J. 07648. Specify an Electrochemical Society volume. Prices subject to change without notice.

NEWS ITEM

Joint Program on Applied Electrochemistry

The School of Science of the Universidad de Los Andes and the Georgia Institute of Technology will start a joint program on Applied Electrochemistry, beginning January 1975.

The program is open to students from any university or other recognized institution who holds a graduate title in chemistry, physics, metallurgy, or related areas. Further information about this new program may be obtained by writing to Dr. P. J. Aragón, Facultad de Ciencias, Universidad de los Andes, Mérida, Venezuela.

ADVERTISERS' INDEX

POSITION AVAILABLE

The Ion Capacitor Corporation is seeking an electrochemical engineer with a minimum of ten years experience in the design and production of either commercial or computer grade electrolytic capacitors. Candidate should have minimum of a B.S. in electrical engineering and/or an M.S. in chemical engineering. Contact Ion Capacitor Corporation, Box 169, Columbia City, Indiana 46725.

POSITIONS WANTED

Please address replies to the box number shown, c/o The Electrochemical Society, Inc., P. O. Box 2071, Princeton, N. J. 08540.

Chemical Materials Interdisciplinary Engineer Scientist—Seeks academic, industrial position. 18 years industry, R&D, engineering, management, and adjunct teaching. Professor 9 years and consulting. Semiconductors, electronic properties, reactors, CVD. Member of eight societies. 32 publications, patents. Principals only please. Reply Box C-142.

Chemical/Electrochemical Engineer—Ph.D. December 1974. Background in applied electrochemistry, heat and mass transfer, thermodynamics. Research experience in electrochemical kinetics, corrosion, applied high rate dissolution process of metals. Seeking position in research, production, process development or design. Reply Box C-144.

Physicist—Metallurgist, materials oriented, with 25 years experience in device physics and electronics, epitaxy, III-V-compound device technology (LED) + electrooptics; Ph.D. Solid-State Physics and Ph.D. Electronics. 80 publications, 2 scientific books, 60 patents; Fellow IEEE, member APS, ECS, AVS etc. Seeking R&D-oriented consulting or position. Reply Box C-145.

Positions Wanted

Society members of any class may, at no cost and for the purposes of professional employment, place not more than three identical insertions per calendar year, not to exceed 8 lines each. Count 43 characters per line, including box number, which the Society will assign.

Electrochemical Kinetics & Solid-State Chemistry—Recent graduate (Ph.D.—1974) in Physical Chemistry and Materials Science, several years in industry, government, and academic research, publications and honors, desires opportunity to further pursue highly original work in electrode kinetics and metal surface chemistry.

Newly developed technique and sophisticated electrochemoptical instrumentation have led to a new understanding of lattice defect migration through very thin semiconductor structures. Concepts applicable in many fields (e.g., fuel cell and battery electrodics, manufacture & study of optical and special property oxide films, protective metallurgy, e.ectrocatalytic processing, metal substrate preparation for coatings, etc.).

Good background in oxidation, diffusion, phase transformations, circuit & semiconductor theory, surfaces, interfaces, computer graphics, ion-, electron-, and x-ray spectroanalytic methods, 3 western languages, lecturing, research management. Reply Box C-146.

THE ELECTROCHEMICAL SOCIETY BOOKS IN PRINT

Monograph Series

The following hardbound volumes are sponsored by The Electrochemical Society, Inc. and published by John Wiley & Sons, Inc., 605 Third Avenue, New York, N.Y. 10016. Members of the Society can receive a 33% discount by ordering from Society Headquarters. Books and invoice are mailed by publisher. Nonmembers (including subscribers) must order direct from the publisher. All prices subject to change without notice.

Corrosion Handbook, edited by Herbert H. Uhlig (1948). 1188 pages, **$30.25.**

Electrochemistry in Biology and Medicine, edited by Theodore Shedlovsky (1955). 369 pages, **$15.25.**

Arcs in Inert Atmospheres and Vacuum, edited by W. E. Kuhn. A 1956 Spring Symposium (1956). 188 pages, **$10.75.**

Ultrafine Particles, William E. Kuhn, Editor-in-Chief (1963). 561 pages, **$20.50.**

First International Conference on Electron and Ion Beam Science and Technology, edited by R. Bakish (1965). 945 pages, **$27.95.**

Chemical Physics of Ionic Solutions, edited by B. E. Conway and R. G. Barradas. A 1964 Spring Symposium (1966). 622 pages, **$31.00.**

The Electron Microprobe, edited by T. D. McKinley, K. F. J. Heinrich, and D. B. Wittry. A 1964 Fall Symposium (1966). 1035 pages, **$36.25.**

Vapor Deposition, edited by C. F. Powell, J. H. Oxley, and J. M. Blocher, Jr. (1966). 725 pages, **$27.75.**

The Stress Corrosion of Metals, by Hugh I. Logan (1966). 306 pages, **$19.75.**

The Corrosion of Light Metals, by H. P. Godard, W. B. Jepson, M. R. Bothwell, and R. L. Kane (1967). 360 pages, **$17.75.**

High-Temperature Materials and Technology, edited by I. E. Campbell and E. M. Sherwood (1967). 1022 pages, **$36.75.**

Alkaline Storage Batteries, by S. Uno Falk and Alvin J. Salkind (1969). 656 pages, **$36.75.**

The Primary Battery, Volume I, edited by George W. Heise and N. Corey Cahoon (1971). 500 pages, **$30.25.**

Zinc-Silver Oxide Batteries, edited by Arthur Fleischer and John J. Lander (1971). 544 pages, **$31.50.**

The Corrosion of Copper, Tin, and Their Alloys, by Henry Leidheiser, Jr. (1971). 411 pages, **$38.50.**

Corrosion in Nuclear Applications, by W. E. Berry (1971). 572 pages, **$28.00.**

Handbook on Corrosion Testing and Evaluation, edited by W. H. Ailor (1971). 873 pages, **$44.00.**

Modern Electroplating, edited by Frederick A. Lowenheim. Third Edition (1974). 801 pages, **$29.95.**

Society Symposium Series

The following softbound symposium volumes are sponsored and published by The Electrochemical Society, Inc., P.O. Box 2071, Princeton, N.J. 08540. Orders filled at the list price given, subject to availability. Enclose payment with order.

Vacuum Metallurgy. J. M. Blocher, Jr., Editor. A 1954 symposium. 216 pages, **$5.00.**

High-Temperature Metallic Corrosion of Sulfur and Its Compounds. Z. A. Foroulis, Editor. A 1969 symposium. 276 pages, **$9.00.**

Electron and Ion Beam Science and Technology, Fourth International Conference. R. Bakish, Editor. A 1970 symposium. 680 pages, **$15.00.**

Fundamentals of Electrochemical Machining. C. L Faust, Editor. A 1970 symposium. 365 pages, **$9.00.**

Electron and Ion Beam Science and Technology, Fifth International Conference. R. Bakish, Editor. A 1972 symposium. 420 pages, **$11.00.**

Electrochemical Contributions to Environmental Protection. T. R. Beck, O. B. Cecil, C. G. Enke, J. McCallum, and S. T. Wlodek, Editors. A 1972 symposium. 173 pages, **$8.00.**

Oxide-Electrolyte Interfaces. R. S. Alwitt, Editor. A 1972 symposium. 312 pages, **$9.00.**

Electrets. Charge Storage and Transport in Dielectrics. M. M. Perlman, Editor. A 1972 symposium. 700 pages, **$18.00.**

Marine Electrochemistry. J. B. Berkowitz, M. Banus, M. J. Pryor, R. Horne, P. L. Howard, G. C. Whitnack, and H. V. Weiss, Editors. A 1972 symposium. 416 pages, **$15.00.**

Semiconductor Silicon 1973. H. R. Huff and R. R. Burgess, Editors. A 1973 symposium. 936 pages, **$15.00.**

Electrochemical Bioscience and Bioengineering. H. T. Silverman, I. F. Miller, and A. J. Salkind, Editors. A 1973 symposium. 268 pages, **$8.00.**

Chemical Vapor Deposition, Fourth International Conference. G. F. Wakefield and J. M. Blocher, Jr., Editors. A 1973 symposium. 608 pages, **$16.00.**

Fine Particles. W. E. Kuhn and J. Ehretsmann, Editors. A 1973 symposium. Approx. 700 pages, **$15.00.**

Chlorine Bicentennial Symposium. T. C. Jeffery, P. A. Danna, and H. S. Holden, Editors. A 1974 symposium. 404 pages. **$11.00.**

Electrocatalysis. M. W. Breiter, Editor. A 1974 symposium. 378 pages, **$12.00.**

Corrosion Problems in Energy Conversion and Generation. C. S. Tedmon, Jr., Editor. A 1974 symposium. 474 pages, **$12.00.**

Call for Papers
148th Meeting, Dallas, Texas, October 5-10, 1975

Divisions which have scheduled sessions are listed on the overleaf, along with symposium topics.

1. Symposium Papers.

Authors desiring to contribute papers to a symposium listed on the overleaf should check first with the symposium chairman to ascertain appropriateness of the topic.

2. General Session Papers.

Each of the several Society Divisions which will meet in Dallas, Texas, can plan a general session. If your paper does not fit readily into a planned symposium, you should specify "General Session."

3. To Submit a Meeting Paper.

Each author who submits a paper for presentation at a Society Meeting must do three things:

A—Submit one original 75-word abstract of paper to be delivered. Use the form printed on the overleaf or a facsimile. **Deadline for receipt of 75-word abstract is May 1, 1975.**

B—Submit original and one copy of an Extended Abstract of the paper. **Deadline for receipt of Extended Abstract is June 1, 1975.** See (5) below for details.

C—Determine whether the meeting paper is to be submitted to the Society Journal for publication. See (6) below for details.

Send all material to The Electrochemical Society, Inc., P.O. Box 2071, Princeton, N.J. 08540.

Unless the 75-word and required Extended Abstracts are received at Society Headquarters by stated deadlines, the papers will not be considered for inclusion in the program.

4. Meeting Paper Acceptance.

Notification of acceptance for meeting presentation, along with scheduled time, will be mailed to authors with general instructions no earlier than two months before the meeting. Those authors who require more prompt notification are requested to submit with their abstracts a self-addressed postal card with full author-title listing on the reverse.

5. Extended Abstract Volume Publication.

All scheduled papers will be published in the EXTENDED ABSTRACTS volume of the meeting. The volume is published by photo-offset directly from typewritten copy submitted by the author. Therefore, special care should be given to the following instructions to insure legibility.

A—Abstracts are to be from 500 to 1000 words in length and should not exceed two pages, single spaced. The abstract should contain to whatever extent practical all significant experimental data to be presented during oral delivery.

B—Abstracts should be typed single spaced on the typing guide forms which are sent to each author after the submission of a short abstract. If it is necessary to use white bond paper, it should be 8½ x 11 inches with 1¼ inch margins on all sides. Submit all copy in black ink. Do not use handwritten corrections.

C—Title of paper should be in capital letters. Author(s) name and affiliation and address should be typed immediately below in capital and lower case letters. Please include zip code in address. It is not necessary to designate paper as "Extended Abstract" or to quote the divisional symposium involved.

D—If figures, tables, or drawings are used, they should follow the body of the text and should not exceed one page. Submit only the important illustrations and avoid use of halftones. Lettering and symbols should be no smaller than ⅛ inch in size. Figure captions should be typed beneath the figure and be no wider than the figure. Table titles should be typed above, and the same width as, the table.

E—Mail original and one copy of the abstract to: The Electrochemical Society, Inc., P.O. Box 2071, Princeton, N.J. 08540, unfolded.

Abstracts exceeding the stipulated length will be returned to author for condensation and retyping.

6. Manuscript Publication in Society Journal.

All meeting papers upon presentation become the property of The Electrochemical Society, Inc. However, presentation incurs no obligation to publish. If publication in Journal is desired, papers should be submitted as promptly as possible in full manuscript form in order to be considered. If publication elsewhere after presentation is desired, written permission from Society Headquarters is required.

Dallas, Texas, Meeting Symposia Plans—Fall 1975
October 5-10, 1975

a.) For receipt no later than May 1, 1975, submit a 75-word abstract of the paper to be delivered, on the form overleaf.
b.) For receipt no later than June 1, 1975, submit two copies of an extended abstract, 500-1000 words.
c.) Send all abstracts to The Electrochemical Society, Inc., P.O. Box 2071, Princeton, N.J. 08540. See details on preceding page.

BATTERY DIVISION

Leclanché Cells

Since the last Leclanché Cell Symposium (1966, in Philadelphia), considerable progress has been made in Leclanché cell technology. In order to review the present state of the art, the Battery Division has decided to have another symposium on Leclanche and related cells during the 1975 Fall Meeting in Dallas.

Even though the basic cell system is over 100 years old, Leclanché type cells are still the most important primary power sources in our society today. In the 1975 symposium, we would like to cover the new technology developed during the past 10 years and also the outlook with respect to future technological development on this cell system.

Papers related to the following topics and themes are being solicited:

1. Behavior of all zinc chloride electrolyte cells.
2. Leakage behavior and leakage mechanism.
3. Capacity decrease during storage (0°-70°C) and its causes.
4. Critical impurities which affect the cell capacity and the shelf-life.
5. Various zinc alloys relative to the corrosion in Leclanché and $ZnCl_2$ electrolytes.
6. Corrosion inhibitors for the zinc anode and function of mercury.
7. Acetylene blacks and graphites.
8. Cell construction and performance (regular cylindrical, inside-out type, flat layer type, thin electrode, etc.).
9. MnO_2 utilization in various cells at different discharge rates (2.25 ohm LIF, 25 ohm ratio tests, etc.). Review of the present technology.
10. Starch and separator layers.
11. Seals and gas venting.
12. Special electrolyte compositions of Leclanché cells.

Suggestions and inquiries should be directed to the Symposium Co-Chairmen: A. Kozawa, Union Carbide Corp., Parma Technical Center, P.O. Box 6116, Cleveland, Ohio 44101, or P. Ruetschi, Leclanché S.A., 1400 Yverdon, Switzerland.

Nonaqueous Cells

This symposium will include papers dealing with experimental and theoretical aspects of various types of electrochemical cells with nonaqueous electrolytes for the production of electrical energy. Emphasis will be placed upon recent advances and new systems of high specific energy and/or high specific power.

Appropriate systems include those with:

1. Inorganic solvent electrolytes.
2. Organic solvent electrolytes.
3. Molten salt electrolytes.
4. Solid electrolytes.

Suitable topics include:

1. Electrode kinetics and mechanisms.
2. Electrode and cell performance and lifetime.
3. Properties of new electrolytes.
4. Design theory.

Suggestions and inquiries should be directed to the Symposium Chairman: E. J. Cairns, Research Laboratories, General Motors Corp., General Motors Technical Center, Electrochemistry Dept., Warren, Mich. 48090.

General Session

The Battery Division will also hold a General Session. Suggestions and inquiries should be directed to: B. Agruss, Oakwood Garden Apts., 1515 Second St., Coronado, Calif. 92118.

CORROSION DIVISION

Repassivation Kinetics

This symposium will cover the kinetics of film repair and transient processes at film-free electrodes as well. Topics to be included are:

1. Nucleation and growth of protective films.
2. Transiently strained electrode.
3. Slowly strained electrode.
4. Triboellipsometry.
5. Potential jump.
6. Mechanical scratching.

Suggestions and inquiries should be directed to the Symposium Chairman: J. B. Lumsden, Dept. of Metallurgical Engineering, Ohio State University, 116 West 19th Ave., Columbus, Ohio 43210.

General Session

The Corrosion Division's program also includes a General Session. Suggestions and inquiries should be directed to: Roger W. Staehle, Dept. of Metallurgical Engineering, Ohio State University, 116 West 19th Ave., Columbus, Ohio 43210.

CORROSION, ELECTRONICS, ELECTROTHERMICS AND METALLURGY, AND DIELECTRICS AND INSULATION DIVISIONS

Techniques for Surface and Thin-Film Analysis and Depth Profiling

This symposium will discuss techniques for surface and thin-film analysis and problems related to depth profiling. The techniques will include, but are not necessarily limited to, x-ray photoelectron spectrometry, Auger electron spectrometry, ion scattering spectrometry, secondary ion mass spectrometry, ion microprobe mass spectrometry, nuclear backscattering, and glow discharge mass and optical spectrometry.

Relevant recent work on the analysis of corroding surfaces and corrosion films and on problems unique to depth profiling, such as changes in microstructure, ion bombardment induced diffusion, knock-on effects, altered layer effects, and molecular sputtered species, is solicited. Invited papers will be included in the program to provide an overview and to place the numerous techniques into perspective.

It is tentatively planned to have a symposium volume available at the meeting. Suggestions and inquiries should be directed to the Symposium Co-Chairmen: R. P. Frankenthal, Bell Laboratories, 600 Mountain Ave., Murray Hill, N.J. 07974, or E. Kay, IBM Corp., Research Laboratory, Monterey and Cottle Rds., San Jose, Calif. 95193.

DIELECTRICS AND INSULATION DIVISION

Dielectric Materials for Hybrid and Thin-Film Circuits

The main emphasis of this symposium will be on recent applications and new dielectric materials in hybrid and thin-film devices. In addition to the thin-film and thick-film materials, other forms such as encapsulants, substrates, transducer materials, etc. will be included. All papers should show a fundamental understanding of the relationship among material structure, properties, and circuit applications. Manufacturing art will not be included.

Suggestions and inquiries should be directed to the Symposium Chairman: L. D. Locker, Airpax Electronics, Inc., 6801 West Sunrise Blvd., Fort Lauderdale, Fla. 33313.

Thermal and Photostimulated Currents in Insulators

This symposium will deal with all aspects of the stimulation of current in bulk or thin-film insulating materials, by either an increase in temperature or exposure to light. Typical subjects include thermally stimulated currents, thermally stimulated depolarization, photorelease of electronic charge, and photocapacitance effects, both as subjects in themselves or for the study of the reorientation of ionic defect dipoles, defect association, solubility limits, electronic trapping states, electret behavior, etc. It is intended that the subject matter be broadly defined in order to encourage participation by workers from a variety of phenomenologically related fields.

It is planned to publish the proceedings of this symposium. In order to be included, final manuscripts must be submitted by the time of the meeting.

Keynote papers from invited speakers will be presented, and contributed papers are solicited. Suggestions and inquiries should be directed to the Symposium Chairman: D. M. Smyth, Materials Research Center, Lehigh University, Bethlehem, Pa. 18015.

General Session

Suggestions and inquiries should be directed to: B. H. Vromen, IBM Corp., Dept. 175, Bldg. 300-95, Hopewell Junction, N.Y. 12533.

DIELECTRICS AND INSULATION AND ELECTRONICS DIVISIONS

Recent Developments in MOS Technology

Contributions are solicited for a symposium on the subject of device and material problems in ultraminiaturization. This will include:

1. MOS processing technology.
2. Masking for local oxidation.
3. MNOS structures.
4. Yield considerations and limitations as affected by larger wafer size, increased chip size, and packing density.
5. Ion implantation, electron beam lithography, ion beam and plasma etching, reactive sputtering, and other technologies leading toward all-vacuum processing.
6. Applications of thin films in MOS technology.

Invited papers will also be presented within the above framework. Suggestions and inquiries should be directed to the Symposium Co-Chairmen: J. Rutledge, Motorola Inc., Semiconductor Products Div., M.S. A160, 5005 East McDowell Rd., Phoenix, Ariz. 85008, or K. A. Pickar, Bell-Northern Research, P.O. Box 3511, Station C, Ottawa, Ont., Canada K1Y 4H7.

ELECTRODEPOSITION DIVISION

General Session

Suggestions and inquiries should be directed to: J. L. Griffin, Research Laboratories, General Motors Corp., General Motors Technical Center, 12 Mile-and-Mound Rds., Warren, Mich. 48090.

ELECTRODEPOSITION, CORROSION, AND INDUSTRIAL ELECTROLYTIC DIVISIONS

Electrodeposition of Organic Coatings

The Electrodeposition, Corrosion, and Industrial Electrolytic Divisions have planned the joint symposium on Electrodeposition of Organic Coatings including corrosion protection by organic coatings.

Papers are solicited for this symposium which is concerned with the theoretical, experimental, and industrial aspects of electrocoating and the properties of electrodeposited organic films. Topics of interest include:

1. Polymers for electrodeposition.

2. Mechanism and kinetics of the electrodeposition of organic coatings.

3. Anionic and cationic electrodeposition.

4. Throwing power.

5. Effect of substrate and bath on film properties.

6. Effect of polymer structure, micell size, pigments, and curing temperature on film properties.

7. Corrosion protection by electrodeposited organic coating.

Suggestions and inquiries should be directed to the Symposium Co-Chairmen: W. B. Brown, Research Laboratories, General Motors Corp., General Motors Technical Center, Polymer Dept., Warren, Mich. 48090, or Z. Kovac, IBM Corp., Thomas J. Watson Research Center, P.O. Box 218, Yorktown Heights, N.Y. 10598, or R. J. Morrissey, Technic, Inc., P.O. Box 965, Providence, R.I. 02901, or R. A. Taylor, Glidden-Durkee Div. of SCM Corp., 900 Union Commerce Blvd., Cleveland, Ohio 44115.

ELECTRONICS DIVISION

Semiconductors

Electrochemical Techniques for Electronic Device Fabrication

The scope of this symposium includes any type of electrochemical technique that can be used in the fabrication of electronic devices. For the purpose of this symposium, the term electronic device includes both passive and active components; either conducting, semiconducting, or magnetic (bubble) types. The term electrochemical technique can include either an externally biased system or an internally generated electron transfer reaction. Topics of particular interest are:

1. Electrochemical etching and shaping.

2. Anodic oxide formation.

3. Electroplating of metallic components.

4. Displacement plating.

5. Selective surface reactions.

6. Surface cleaning and passivation.

7. Surface examination or evaluation.

Other topics will be included as warranted by the response of those active in the field. Suggestions and inquiries should be directed to the Symposium Chairman: B. Schwartz, Bell Laboratories, 600 Mountain Ave., Murray Hill, N.J. 07974.

General Session

The Semiconductor General Session will be devoted to a broad spectrum of theoretical and experimental areas of semiconductor and related technologies. Papers presenting original work in the following areas are requested:

1. Elemental and compound semiconductor materials preparation and characterization.

2. Thin-film semiconductor materials preparation, properties, and characterization.

3. Semiconductor device properties, fabrication, reliability, and processing technology.

4. Influence of material defects and imperfections (structural and impurity) on semiconductor materials and devices.

Suggestions and inquiries concerning the Semiconductor General Session should be directed to: R. D. Dupuis, Texas Instruments Inc., P.O. Box 5012, M.S. 12, Dallas, Texas 75222.

General Materials and Processes

General Sessions

An increasing variety of materials and processes have been covered in recent symposia by the Electronics Division. Frequently, however, those wishing to present or hear further work in these areas find the subject matter to be unsuitable for inclusion in the symposia or general sessions at subsequent meetings, often because the subject is not sufficiently "electronic" in nature. To remedy this situation, and to encourage the discussion of newly emerging areas of materials science and technology, Materials and Process General Sessions are being initiated. Papers are solicited in areas such as:

1. Solar energy and other methods of energy generation or storage, integrated optics, memory materials, laser windows, amorphous materials, etc.

2. Materials preparation and processing including crystal growth, etching, heat-treatment, diffusion, device fabrication, etc.

3. Other areas of interest.

Suggestions and inquiries should be directed to: F. A. Trumbore, Bell Laboratories, 600 Mountain Ave., Murray Hill, N.J. 07974.

ELECTROTHERMICS AND METALLURGY DIVISION

High Temperature Processes Induced in Materials by Absorption of Radiation

A symposium is planned to discuss high temperature phenomena induced in condensed phases by the absorption of intense electromagnetic radiation of various wavelengths. Temperatures involved would generally lie above 1°kK. Emphasis will be on the materials science aspects of the processes involved. Topics include:

1. Radiation sources, both continuous and pulsed, including lasers, solar and arc imaging furnaces, electron beams, flash lamps, nuclear reactors, and x-ray generators.

2. Diagnostics, including temperature and emittance measurements, spectroscopy, and calorimetry.

3. Physical processes, including shock and impulse generation, thermal expansion and fracture, phase changes, cavitation and nucleation phenomena, ablation, vaporization, and gasification.

4. Chemical processes, including ignition, decomposition, pyrolysis, and thermal deposition.

5. Control of absorption, including enhancement and protective measures, as in laser windows, and surface coatings.

6. Applications, such as cutting, welding, drilling, and crystal and fiber production.

Invited papers will present a general overview of the state of the art in the above topics. Papers are also being solicited for this symposium. Authors desiring to contribute papers should direct their suggestions and inquiries to the Symposium Co-Chairmen: L. S. Nelson, Sandia Laboratories, Chemical Technology Div. 5824, Albuquerque, N.M. 87115, or J. G. Kay, Dept. of Chemistry, Drexel University, Philadelphia, Pa. 19104.

General Session

The Electrothermics and Metallurgy Division's program will include a General Session. All suggestions and inquiries should be directed to: W. W. Smeltzer, Dept. of Metallurgy, McMaster University, Hamilton, Ont., Canada L8S 4M1.

ELECTROTHERMICS AND METALLURGY AND ELECTRONICS DIVISIONS

Liquid Phase and Molecular Beam Epitaxy: Electronic and Magnetic Materials

Contributed papers for this symposium are solicited covering all aspects of liquid phase and molecular beam epitaxy. Topics pertinent to this symposium are: phase diagrams, experimental and theoretical aspects of nucleation, growth kinetics, surface and interface morphology, growth methods, growth and materials characterization, and characterization of LPE devices such as magnetic bubble devices, laser diodes, and microwave devices.

The Molecular Beam Epitaxy program will include papers on the growth of epitaxial semiconductor films in UHV from one or more molecular and atomic beams, the doping of such films from impurity beams, the kinetics of beam-surface interactions, the electrical and optical properties of films grown by MBE, and the characteristics of MBE devices, e.g., diode lasers and superlatiice structures.

Suggestions and inquiries should be directed to the Symposium Co-Chairmen: (LPE Program) G. M. Blom, Phillips Laboratories, 345 Scarborough Rd., Briarcliff Manor, N.Y. 10510, or (MBE Program) J. R. Arthur, Bell Laboratories, 600 Mountain Ave., Murray Hill, N.J. 07974.

NEW TECHNOLOGY SUBCOMMITTEE AND ELECTROTHERMICS AND METALLURGY DIVISION

Energy Storage

The New Technology Subcommittee and the Electrothermics and Metallurgy Division will sponsor a symposium on methods and economics of storing large quantities of energy. The symposium will consider the merits and demerits of various energy storage devices, including batteries, regenerative fuel cells, flywheels, compressed fluids, pumped hydro, etc. Papers will cover the technical and economic aspects, requirements, and important obstacles to practical use.

A number of invited papers will be presented and contributed papers are solicited. Suggestions and inquiries should be directed to the Symposium Co-Chairmen: H. P. Silverman, TRW Systems, One Space Park, Redondo Beach, Calif. 90278, or J. B. Berkowitz, Arthur D. Little, Inc., Acorn Park, Cambridge, Mass. 02139.

75-Word Abstract Form

(Deadline for receipt—May 1, 1975)

DALLAS, TEXAS, MEETING—OCTOBER 5-10, 1975

Submit to: **The Electrochemical Society, Inc.**
P.O. Box 2071, Princeton, N.J. 08540

Schedule for ..... of .....
Symposium **ECS Division**

Abstract No. .....
(do not write in this space)

(Title of paper) .....

.....

(Authors) (Underline name of author presenting paper) .....

.....

(Business Affiliation and Address) .....

.....

.....
(ZIP Code) (Tel. No.)

(Type abstract in this area—double spaced.)

Do you require any audiovisual equipment?
☐ **35 mm (2 x 2 in.) slide projector**
☐ **vugraph**
☐ **other (specify)**
Is a full length paper on this work to be submitted for Society Journal publication?
☐ **Yes** ☐ **No**

Papers presented before a Society technical meeting become the property of the Society and may not be published elsewhere without written permission of the Society. Papers presented at Society technical meetings must be authored by a member or sponsored by an active member.

.....
Insert name of Society member author or sponsor

THE ELECTROCHEMICAL SOCIETY PATRON MEMBERS

Bell Telephone Laboratories, Inc.
Murray Hill, N.J.

Dow Chemical Co.
Inorganic Chemicals Dept., Midland, Mich.

General Electric Co.
Battery Business Section, Gainesville, Fla.
Chemical Laboratory, Knolls Atomic Power Laboratory, Schenectady, N.Y.
Electronic Capacitor & Battery Dept., Irmo, S.C.
Lamp Div., Cleveland, Ohio
Materials & Process Laboratory, Large Steam Turbine-Generator Dept., Schenectady, N.Y.
Research and Development Center, Physical Chemistry Laboratory, Solid State Physics Laboratory, Schenectady, N.Y.
Semiconductor Products Dept., Syracuse, N.Y.

The International Nickel Co., Inc.
New York, N.Y.

Olin Corporation
Chemicals Div., Research Dept., New Haven, Conn.

Philips Research Laboratories
Eindhoven, Holland

Union Carbide Corp.
Battery Products Div., Corporate Research Dept., New York, N.Y.

Westinghouse Electric Corp.
Electronic Tube Div., Elmira, N.Y.
Lamp Div., Bloomfield, N.J.
Semiconductor Div., Youngwood, Pa.
Research Laboratories, Pittsburgh, Pa.
K. W. Battery Co., Westinghouse Subsidiary, Skokie, Ill.

THE ELECTROCHEMICAL SOCIETY SUSTAINING MEMBERS

Airco Speer Carbon-Graphite
St. Marys, Pa.

Allied Chemical Corp.
Industrial Chemicals Division
Solvay, N.Y.

Aluminum Co. of America
New Kensington, Pa.

Aluminum Co. of Canada, Ltd.
Montreal, P.Q., Canada

American Gas & Chemicals, Inc.
New York, N.Y.

American Metal Climax, Inc.
New York, N.Y.

American Smelting and Refining Co.
South Plainfield, N.J.

AMP Incorporated
Harrisburg, Pa.

Analog Devices, Inc.
Norwood, Mass.

Applied Materials, Inc.
Santa Clara, Calif.

BASF Wyandotte Corporation
Wyandotte, Mich.

Beckman Instruments, Inc.
Fullerton, Calif.

Bell-Northern Research
Ottawa, Ont., Canada

Bethlehem Steel Corp.
Bethlehem, Pa.

Boeing Co.
Seattle, Wash.

The Borg-Warner Corp.
Roy C. Ingersoll Research Center
Des Plaines, Ill.

Brown, Boveri & Co., Ltd.
Research Center
Baden, Switzerland

Canadian Industries Ltd.
Montreal, P.Q., Canada

Carborundum Co.
Niagara Falls, N.Y.

Chrysler Corp.
Detroit, Mich.

Cominco Ltd.
Trail, B.C., Canada

Corning Glass Works
Corning, N.Y.

Crawford & Russell Inc.
Stamford, Conn.

The Detroit Edison Co.
Detroit, Mich.

Diamond Shamrock Corp.
Painesville, Ohio

E. I. du Pont de Nemours and Co.
Central Research Department
Wilmington, Del.

Eastman Kodak Co.
Rochester, N. Y.

Electrode Corporation
Chardon, Ohio

Eltra Corp.
Prestolite Div., Toledo, Ohio
C&D Batteries, Conshohocken, Pa.

Engelhard Minerals & Chemicals Corp.
Murray Hill, N.J.

ESB Inc.
Philadelphia, Pa. (2 memberships)

Esso Research and Engineering Co.
Engineering Technology Div.
Florham Park, N.J.

SUSTAINING MEMBERS (CONTINUED)

Ever Ready Co. (Holdings) Ltd.
Whetstone, London, England

Exmet Corporation
Bridgeport, Conn.

Fairchild Camera & Instrument Corp.
Research and Development Laboratory
Palo Alto, Calif.

Falconbridge Nickel Mines Ltd.
Thornhill, Ont., Canada

FMC Corp.
Inorganic Chemicals Div.
Buffalo, N.Y.

Foote Mineral Co.
Exton, Pa.

Ford Motor Co.
Dearborn, Mich.

GAF Corporation
Inorganic Chemicals Department
Glens Falls, N.Y.

General Motors Corporation
Delco Electronics Div., Kokomo, Ind.
Delco-Remy Div., Anderson, Ind.
Research Laboratories Div., Warren, Mich.

GTE Laboratories
Waltham, Mass.

B. F. Goodrich Chemical Co.
Cleveland, Ohio

Gould Inc.
Gould Laboratories, Rolling Meadows, Ill.
Gould Laboratories—Energy Research, St. Paul, Minn.
Gould Laboratories—Materials Research, Cleveland, Ohio

Great Lakes Carbon Corp.
New York, N.Y.

Harshaw Chemical Co.
Cleveland, Ohio (2 memberships)

Hill Cross Co., Inc.
West New York, N.J.

Honeywell, Inc.
Power Sources Center
Horsham, Pa.

Hooker Chemical Corp.
Niagara Falls, N.Y. (2 memberships)

HP Associates
Palo Alto, Calif.

Hughes Research Laboratories
Div. of Hughes Aircraft Co.
Malibu, Calif.

International Business Machines Corp.
New York, N.Y.

K. W. Battery Co.
Skokie, Ill.

Kaiser Aluminum & Chemical Corp.
Pleasanton, Ca.

Kawecki Berylco Industries, Inc.
Boyertown, Pa.

Kennecott Copper Corp.
New York, N.Y.

Kerr-McGee Corporation
Technical Center
Oklahoma City, Okla.

Arthur D. Little, Inc.
Cambridge, Mass.

Mallory Battery Company
Tarrytown, N.Y. (2 memberships)

Marathon Battery Co.
Cold Spring, N.Y.

The Marstolin Group
Hamilton, Bermuda

Matsushita Electric Industrial Co., Ltd.
Osaka, Japan

Microwave Associates, Inc.
Burlington, Mass.

Molybdenum Corporation of America
New York, N.Y.

Monsanto Company
St. Louis, Mo.

Motorola Inc.
Phoenix, Ariz.

M&T Chemicals Inc.
Detroit, Mich.

National Steel Corp.
Weirton, W. Va.

NL Industries, Inc.
New York, N.Y.

OKI Electric Industry Co., Ltd.
Tokyo, Japan

Olin Corporation
Metals Research Laboratories
New Haven, Conn.

Owens-Illinois Glass Co.
Toledo, Ohio

Phelps Dodge Refining Corp.
Maspeth, N.Y.

Philips Laboratories. Inc.
Briarcliff Manor, N.Y.

PPG Industries, Inc.
Chemical Div.
Pittsburgh, Pa.

RCA Corporation
Electronic Components and Devices
Lancaster, Pa.

Republic Foil
National Aluminum
A Unit of
National Steel Corp.
Danbury, Conn.

Reynolds Metals Co.
Reduction Research Div.
Sheffield, Ala.

Rockwell International
El Segundo, Calif.

SAFT America, Inc.
Metuchen, N.J.

Signetics Corp.
Sunnyvale, Ca.

Sobin Chemical Co.
Orrington, Maine

Sprague Electric Co.
North Adams, Mass.

Stackpole Carbon Co.
St. Marys, Pa.

Standard Telecommunication Laboratories Ltd.
Essex, England

Stauffer Chemical Co.
Dobbs Ferry, N.Y.

Teletype Corp.
Skokie, Ill.

Texas Instruments Inc.
Attleboro, Mass.
Dallas, Texas

Tokyo Shibaura Electric Co., Ltd.
Toshiba Research and Development Center
Kawasaki, Japan

Udylite Corp.
Detroit, Mich. (4 memberships)

United States Steel Corp.
Research Laboratory
Monroeville, Pa.

Varian Associates
Palo Alto, Calif.

Wacker Chemitronic
Burghausen, Germany

Xerox Corporation
Rochester, N.Y.

Yardney Electric Division
Pawcatuck, Conn.

Zenith Radio Corp.
Chicago, Ill.